Title
Growth Studies of CIGSe and CZTS Thin Films Fabricated by Pulsed Laser Deposition and Co-Electrodeposition Methods

Author
Beres, Matthew

Publication Date
2014

Peer reviewed|Thesis/dissertation

Growth Studies of CIGSe and CZTS Thin Films Fabricated by Pulsed Laser Deposition and Co-Electrodeposition Methods

by

Matthew Christian Beres

A dissertation submitted in partial satisfaction of the

requirements for the degree of

Doctor of Philosophy

in

Engineering – Mechanical Engineering

in the

Graduate Division

of the

University of California, Berkeley

Committee in Charge:

Professor Samuel S. Mao, Co-Chair
Professor Ralph Greif, Co-Chair
Professor Xiang Zhang
Professor Nathan Cheung

Fall 2014

Growth Studies of CIGSe and CZTS Thin Films Fabricated by
Pulsed Laser Deposition and Co-Electrodeposition Methods

By

Matthew Christian Beres

Abstract

Growth Studies of CIGSe and CZTS Thin Films Fabricated by
Pulsed Laser Deposition and Co-Electrodeposition Methods

by

Matthew Christian Beres

Doctor of Philosophy in Engineering – Mechanical Engineering

University of California, Berkeley

Professor Samuel S. Mao, Co-Chair

Professor Ralph Greif, Co-Chair

The reliable production of clean, inexpensive energy to meet the growing global demand remains one of the most significant challenges to modern society. As high-technology, high power-consumption machines and devices proliferate and as underserved populations around the globe come "on the grid," energy demand will significantly expand. Photovoltaic (PV) technologies represent one of the most direct paths to harvesting solar energy, converting solar energy directly into electricity with no moving parts, no pollution, and no greenhouse gas emissions. These technologies often utilize materials that may not exist in sufficient abundance to meet large-scale (TW) deployment demands. For instance, the highly successful $Cu(In,Ga)Se_2$ material system has achieved module efficiencies up to 15% [1] but contains In and Se, which are relatively scarce and expensive. Shafarman reports that the availability of In would limit total installed capacity to 0.1TW [2], far below the 10 – 20 TW required to meet global energy demand. Moreover, CIGSe devices typically involve processing with highly toxic H_2Se gas [2].

Therefore, significant research has recently been devoted to discovering and developing PV devices that use non-toxic, inexpensive, earth-abundant elements. Based on the success of the $Cu(In,Ga)Se_2$ material system, the development of the electronically analogous Cu_2ZnSnS_4 material system represents a natural next step. CZTS replaces the scarce Group III (In/Ga) elements with more abundant Group II (Zn) and Group IV (Sn) elements. Sulfur also replaces Selenium, allowing less-toxic processing conditions. With a direct band gap of 1.5eV and high

optical absorption > $10^4 cm^{-1}$, CZTS represents an ideal absorber layer for conventional single-junction solar cells [3]. Further, it is hoped that CZTS, which shares similar crystal structure and electronic attributes with CIGSe, may also share a similar resilience in its opto-electronic properties to grain boundaries and to stoichiometric deviations that has afforded CIGSe devices much success [2].

Devices with moderately high efficiencies of 12.6% have been fabricated using Se-alloyed CZTSeS absorber layers [4]. In general, however, the fabrication of high-quality CZTSeS absorber layers has been extremely challenging, due to the narrow phase formation region for CZTSeS [3, 5], elemental and compound volatility [3, 6-8], and phase decomposition at the surface and back contacts [9, 10]. Despite the moderately high device efficiencies achieved, all aspects of CZTS device design merit continued investigation. Scalable and reliable fabrication methods that are capable of producing phase-pure, void-free CZTSeS absorber layers have yet to be demonstrated. Such advancements will require better understanding of the crystal formation processes and defect behavior of CZTSeS. The work in this dissertation aims to improve understanding of the growth processes of CZTS thin films and to provide a pathway to fabrication of high-quality absorber layers for use in photovoltaic devices. Reliable growth of high-quality CZTS thin films will enable investigation of the fundamental properties of CZTS, as well as device and interface behavior, necessary to improve device efficiency.

This dissertation investigated the growth behavior of CIGSe and CZTS thin films developed for use as photovoltaic absorber layers. The CIGSe thin films were fabricated by pulsed laser deposition, and the CZTS thin films were fabricated by pulsed laser deposition and co-electrodeposition methods. The effects of deposition and annealing parameters on the film properties were systematically investigated, critical growth parameters identified, and optimized fabrication conditions recommended. In pulsed laser deposited CIGSe thin films, annealing in sulfur background significantly improved the electronic quality of the films, reducing carrier concentrations and increasing Hall mobilities. In pulsed laser deposition of CZTS thin films, proper adjustment of the laser fluence and sputtering target composition enabled films with the desired stoichiometries to be deposited at room temperature. A two-step temperature profile involving a long dwell at low temperature and short dwell at the crystal formation temperature yielded the most-stable films with the optimum structural properties. Proposed growth mechanisms and optimized fabrication processes are presented.

To study the deposition mechanisms active in the co-electrodeposition of S-containing CZTS precursors, cyclic voltammagrams were compared with varying potential depositions. Reduction mechanisms and peak assignments are proposed. Films deposited using a fabrication

process from literature demonstrated rough, powdery morphologies with Zn-poor, Sn-rich compositions. The morphology was attributed to diffusion-limited growth mechanisms with significant hydrogen co-deposition. However, removing tartaric acid from the deposition bath dramatically reduced the roughness and increased the uniformity of the films. To further improve film composition and morphology, bath component concentrations were systematically modified to yield Cu-poor, Zn-rich films. Optimum bath compositions were successfully identified, although a delayed onset of damaging hydrogen evolution reaction was observed during growth. Stopping the deposition before its onset limited the damage caused by this reaction, but films were limited to small thicknesses. Stirring, increasing bath concentration, and galvanostatic control were investigated as possible methods to increase the film thickness before the onset of this reaction. Optimized co-electrodeposition processes were identified, with linearly-swept potential and pulsed stirring methods representing the most promising processes. Similar to the pulsed laser deposited CZTS films, a two-step temperature profile yielded the most-stable films with the optimum structural properties.

Finally, co-electrodeposition of metallic CZT precursors was investigated. The as-deposited films were highly compact, uniform and free of damage, and the metal ratios in the film could be directly controlled by modifying the metal sulfate concentration ratios in the bath. Varying bath concentrations were investigated, in order to determine the effect on film thickness and composition. Optimized co-electrodeposition processes were identified. After sulfurization, films demonstrated ideal compositions and structures but also significant phase segregation, with the film laterally divided into regions of large-grained CZTS and small-grained ZnS phases. Annealing in Argon at low temperature prior to sulfurization significantly improved the film homogeneity, although a non-negligible density of pinholes remained. It is unclear if the lack of S-content in the precursors, the loss of sulfur overpressure, or both, contributed to the formation of voids and pinholes.

The work in this dissertation provides a comprehensive foundation on which to further improve the deposition of co-electrodeposited S-containing and metallic precursors. The growth of high-quality CZTS precursors was demonstrated and a pathway to additional optimization recommended. With minor adjustments in the electrodeposition process, and improved monitoring and control of the sulfur overpressure, it is believed that very high-quality CZTS films can be reliably fabricated using a two-step co-electrodeposition and sulfurization process. Notably, the co-electrodeposition method represents a simple fabrication method that utilizes low-toxicity components, complies with existing plating technologies, and provides high

throughput. The demonstration of such a process would represent a significant step forward in the development of the earth-abundant, low-toxicity CZTS material system.

References

[1] T. Unold, H.W. Schock, Nonconventional (Non-Silicon-Based) Photovoltaic Materials, Annual Review of Materials Research, 41 (2011) 297-321.

[2] W. Shafarman, S. Siebentritt, L. Stolt, Cu(InGa)Se_2 Solar Cells, in: A. Luque, S. Hegedus (Eds.) Handbook of Photovoltaics Science and Engineering, John Wiley & Sons, West Sussex, 2011.

[3] D. Mitzi, O. Gunawan, T. Todorov, K. Wang, S. Guha, The path towards a high-performance solution-processed kesterite solar cell, Solar Energy Materials & Solar Cells, 95 (2011) 1421 - 1436.

[4] W. Wang, M. Winkler, O. Gunawan, T. Gokmen, T. Todorov, Y. Zhu, D. Mitzi, Device Characteristics of CZTSSe Thin-Film Solar Cells with 12.6% Efficiency, Advanced Energy Materials, (2013).

[5] I.D. Olekseyuk, I.V. Dudchak, L.V. Piskach, Phase equilibria in the Cu_2S-ZnS-SnS_2 system, Journal of Alloys and Compounds, 368 (2004) 135 - 143.

[6] P.M.P. Salome, J. Malaquias, P.A. Fernandes, M.S. Ferreira, J.P. Leitao, A.F.d. Cunha, J.C. Gonzalez, F.N. Matinaga, G.M. Ribeiro, E.R. Viana, The influence of hydrogen in the incorporation of Zn during the growth of $Cu_2ZnSnSn_4$ thin films, Solar Energy Materials & Solar Cells, 95 (2011) 3482 - 3489.

[7] C. Platzer-Bjorkman, J. Scragg, H. Flammersberger, T. Kubart, M. Edoff, Influence of precursor sulfur content on film formation and compositional changes in Cu2ZnSnS4 films and solar cells, Solar Energy Materials & Solar Cells, 98 (2012) 110 - 117.

[8] A. Weber, R. Mainz, H.W. Schock, On the Sn loss from thin films of the material system Cu-Zn-Sn-S in high vacuum, Journal of Applied Physics, 107 (2010) 013516-013511 - 013516-013516.

[9] J. Scragg, T. Ericson, T. Kubart, M. Edoff, C. Platzer-Bjorkmann, Chemical Insights into the Instability of Cu_2ZnSnS_4 Films during Annealing, Chemistry of Materials, 23 (2011) 4625–4633.

[10] J. Scragg, J. Watjen, M. Edoff, T. Ericson, T. Kubart, C. Platzer-Bjorkman, A Detrimental Reaction at the Molybdenum Back Contact in $Cu_2ZnSn(S,Se)_4$ Thin-Film Solar Cells, J. Am. Chem. Soc., 134 (2012) 19330 - 19333.

To my loving wife, Britt,
for her unconditional love and limitless support
that helped guide me through the hardest challenges of my life

And to my parents, Carol and Dennis,
for their resolute support and belief in me

Acknowledgements

I can easily say the last 6 years have been the most challenging of my life. Without the love, support, encouragement, technical guidance, instrument access, financial support, and community provided by so many here, the task of completing this research would have been insurmountable. First, thanks to Dave Bugby for introducing me to heat transfer, teaching me how to be a research scientist, and supporting my application to graduate school. Thanks to my advisor Prof. Sam Mao for allowing me to work in his lab and to EETD at LBL for enabling me to complete my work. Many thanks to my dissertation co-chair Prof. Ralph Greif for his generous advice and encouragement through the years. To my dissertation committee members, Prof. Nathan Cheung and Prof. Xiang Zhang, thank you for your valuable feedback on my work. Dr. Kin Man Yu, thank you for supporting my research, providing invaluable access to critical processing and characterization tools, and teaching me how to conduct academic research.

I owe an enormous debt of gratitude to those at LBL, without whom I never could have completed my work, including Jaroslaw Syzdek, Xianglei Mao, Grace Lau, Ron Scholtz, Wladek Walukiewicz, Angelique Jarry, Dr. Robert Kostecki, and Dr. Joel Ager. To Michel Foure, Venkat Srinivasan, Rick Russo, and Vassilia Zorba, thank you for your support and unending patience while I completed my work. Susan Lauer, thank you for fighting for me and for supporting me.

To my many labmates and associates over the years, thank you for your technical insight, your support, your senses of humor, and your willingness to help: Mike Fina, Min Ting, Matt Lucas, Karen Bustillo, Tim Suen, Travis Owens, Alex Luce, Doug Detert, Maribel Jaquez, Maxwell Zhang, Xiaojun Zhang, Corsin Battaglia, Noah Bronstein, Jose Fonseca, Shaohua Shen, and so many others.

To my Berkeley community, thank you for helping to me to be less serious (sometimes) and making graduate school more memorable than I imagined possible.

This work was supported by the Department of Defense (DoD) through the National Defense Science & Engineering Graduate Fellowship (NDSEG) Program.

Table of Contents

1 INTRODUCTION

1.1 MOTIVATION

The reliable production of clean, inexpensive energy to meet the growing global demand remains one of the most significant challenges to modern society. As high-technology, high power-consumption machines and devices proliferate and as underserved populations around the globe come "on the grid," energy demand will significantly expand. The major energy sectors include Buildings, Industrial, Transportation, and Electricity, with Electricity representing ~13% of the total energy demand in 2010 [1]. Notably, the United States Energy Information Administration (EIA) projects the global electricity demand to double over the next 20 years, representing the fastest growing form of delivered energy [2]. More widespread adoption of electric vehicle technologies may further intensify this electricity demand.

While recent revolutions in natural gas and oil appears to be leading the United States toward energy independence, the production and use of fossil fuels carry environmental consequences that have been shown to impact the local environment as well as global climate change. Hydraulic fracturing or "fracking," the revolutionary technique in natural gas extraction, remains controversial, as it has been suggested that this technique may trigger earthquakes and contaminate the local water table. Government, academic, and industry institutions remain active in researching these connections [3, 4]. Further, the International Panel on Climate Change (IPCC) has determined that the release of anthropogenic greenhouse gases and other anthropogenic forcings "extremely likely" account for the majority of the increased global average temperature of 0.6 – 0.7°C over the last 60 years [5].

The panel further assesses that anthropogenic influences, particularly greenhouse gases, "likely" or "very likely" have contributed to: sea ice and glacial retreat, sea level rise, increased ocean salinity, and shifting global precipitation patterns [5]. Climate change models forecast the global average temperature using a range of forcings, representing best case and worse case predictions. In general, the average temperature scales linearly with the cumulative CO_2 concentration in the atmosphere [5], and stabilizing the global temperature requires halting release of anthropogenic CO_2. While the EIA projects the rate of CO_2 production in the United States to gradually decline, it also projects the global rate of CO_2 production to increase by 46% over the next 20 years [1, 6]. The goal of halting the release of greenhouse gases remains daunting, as production rates are expected to increase significantly.

As part of a review workshop on solar energy, the United States Department of Energy (DOE) released a report entitled "Basic Research Needs for Solar Energy Utilization" [7]. This report notes a yearly-averaged power consumption rate of ~10 terrawatts (TW) in 2005 with

expected growth to ~20TW by 2050 [7]. An inventory of various carbon-neutral energy sources, and their theoretical capacities, are also provided: solar radiation (120,000 TW), geothermal (12TW), wind (2–4 TW), tidal (2TW), and untapped hydroelectric (0.5TW) [7]. Nuclear energy could meet the expected demand, but would require the construction of thousands of new power plants [7], a prospect less likely in the wake of the Fukushima nuclear accident. As the most-abundant renewable energy reservoir, solar energy represents the most likely path to meeting the rising energy demand while also reducing carbon dioxide emissions. To realize the full potential of solar energy, however, issues associated with intermittency, material cost, and scaling must be overcome.

Photovoltaic (PV) technologies represent one of the most direct paths to harvesting solar energy, converting solar energy directly into electricity with no moving parts, no pollution, and no greenhouse gas emissions. Over the past 10 years PV has gained traction in the energy market through the aid of government subsidies, renewable portfolio standards (RPS) adopted by many states, economies of scale, and improved technology and manufacturing. However, PV costs ($0.13/kWh) remain comparatively high to conventional power plant technologies, such as coal and nuclear ($0.07 – 0.08kWh) [8], and so market penetration remains low with PV providing less than 1% of global electricity demand in 2010 [1].

As will be discussed in Section 1.2, photovoltaic technologies have evolved to improve device efficiency and reduce cost by improving material quality, reducing material use, and refining material fabrication techniques. Thin film PV technology was developed to meet these goals, using less material and increasing manufacturing throughput. However, thin film PV often utilizes materials that may not exist in sufficient abundance to meet large-scale (TW) deployment demands. For instance, the highly successful $Cu(In,Ga)Se_2$ material system has achieved module efficiencies up to 15% [9] but contains In and Se, which are relatively scarce and expensive. Shafarman reports that the availability of In would limit total installed capacity to 0.1TW [10], far below the 10 – 20 TW required to meet global energy demand. Moreover, $Cu(In,Ga)Se_2$ devices typically involve processing with highly toxic H_2Se gas [10]. Therefore, significant research has recently been devoted to discovering and developing PV devices that use non-toxic, inexpensive, earth-abundant elements. Based on the success of the $Cu(In,Ga)Se_2$ material system, the development of the Cu_2ZnSnS_4 material system represents a natural next step. CZTS represents an electronic analog to CIGSe, replacing the scarce Group III (In/Ga) elements with more abundant Group II (Zn) and Group IV (Sn) elements. Sulfur also replaces Selenium, allowing less-toxic processing conditions. This work focuses on the development of CZTS materials for photovoltaic applications and seeks to address some of the challenges identified in Section 1.3.

1.2 EVOLUTION OF PHOTOVOLTAICS

The photovoltaic effect, responsible for the direct conversion of solar energy into electricity, was first demonstrated by Edmund Bequerel in 1839 [11]. With the advent of Silicon-based p-n junctions, the first modern photovoltaic devices were developed by Bell labs in the 1950s. The basic **thin film** photovoltaic device consists of a transparent front contact, a single p-n junction, an optically absorbing semiconductor layer, and a reflecting back contact, shown below in Fig. 1-1. Incident solar radiation excites electrons in the optically absorbing semiconducting layer, creating an electron-hole pair. The p-n junction contains a built-in electric field which helps to separate the electron and hole, driving the electron through an external electric circuit where usable work can be extracted. Chapter 2 provides a more sophisticated description of photovoltaic device operation.

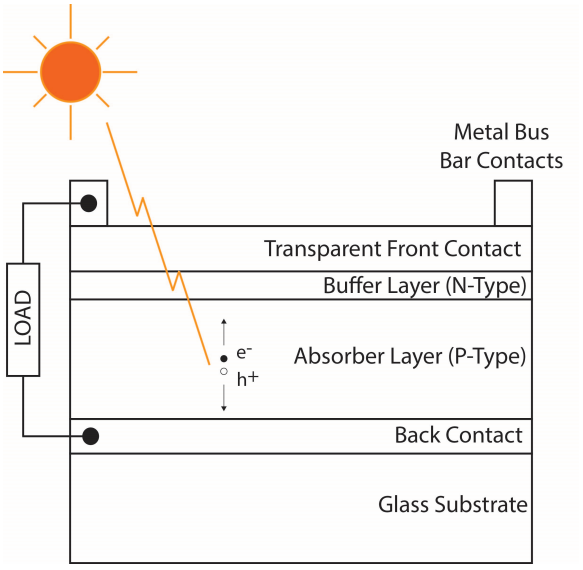

Fig. 1-1. Conceptual schematic of photovoltaic device

Photovoltaic technology evolution may be roughly divided into three generations: 1st generation (G1) devices utilize **bulk** wafer technology involving single crystalline and multi-crystalline materials, 2nd generation (G2) devices employ **thin film** technology involving polycrystalline and amorphous materials, and 3rd generation (G3) devices employing materials and devices that challenge the Shockley-Queisser limit of device efficiency [12]. G1 devices, primarily based on Silicon semiconductor technology, have demonstrated high efficiencies and constitute the majority of installed PV capacity. While Silicon is earth-abundant, G1 device costs have been shown to be largely dominated by material costs associated with the thick wafers [12]. Subsequently, growth techniques that reduce the overall amount of material used were explored, yielding conventional thin film fabrication techniques such as co-evaporation, sputtering, and chemical vapor deposition among others. G2 devices adopted materials and architectures suitable to these fabrication techniques, including the CdTe, $Cu(In,Ga)Se_2$ and amorphous Silicon material systems.

G1 and G2 devices conform to the single-junction device architecture, and their device efficiencies are subsequently constrained by the Shockley-Queisser limit, which theoretically approaches ~33% for a perfect crystallinity material and ~27% for polycrystalline thin films [9]. The Shockley-Queisser limit derives from a thermodynamic detailed balance approach using the solar spectrum and an ideal semiconductor with a single junction and band gap. In this model, the absorber perfectly absorbs the portion of the solar spectrum with energy larger than its band gap and perfectly transmits (e.g. does not absorb) the portion with energy smaller than its band gap. The portion of the spectrum not absorbed represents lost energy from the solar radiation. The band gap also determines the voltage of the cell and influences the power output of the PV device, so an optimum value exists: ~1.35eV for single-junction devices [9]. The electrons excited by photons with energies higher than the absorber band gap contain excess energy (e.g. energy above the conduction band); this model assumes that these electrons **thermalize** down to the conduction band edge, giving up this excess energy to the crystal lattice [9]. Finally, some of these electrons at the band edge recombine with holes in the valence band through **radiative recombination**, a fundamental loss which cannot be avoided [9]. Otherwise, the model assumes no reflection losses and no collection losses in the contacts [9].

G3 devices seek to further improve efficiency and reduce cost by exceeding the Shockley-Queisser limit through a number of potential avenues. Tandem and triple-junction cells aim to capture more of the incident sunlight by stacking absorber layers with varying band gaps that span the solar spectrum [12]. Multiband cells also intend to increase the optical absorption of incident sunlight but achieves this through the introduction of additional electronic bands in a single absorber layer [12]. Hot carrier extraction techniques focus on the collection of excited electrons before they thermalize to the band edge. Other efforts have focused on using the excess electron energies to promote further electron-hole pair generation through impact ionization [12]. Sophisticated nanofabrication techniques have been developed in recent years and may help to facilitate these G3 concepts by enhancing light collection and supporting novel device architectures.

1.3 CZTS STATE OF DEVELOPMENT

Recent thin film photovoltaic research has focused significant effort on the development of non-toxic, earth abundant absorber layers, in particular the Cu_2ZnSnS_4 (CZTS) material system. With a direct band gap of 1.5eV and high optical absorption > $10^4 cm^{-1}$, CZTS represents an ideal absorber layer for conventional single-junction solar cells [13]. Further, it is hoped that CZTS, which shares similar crystal structure and electronic attributes with $Cu(In,Ga)Se_2$, may also share a similar resilience in its opto-electronic properties to grain boundaries and to stoichiometric deviations that has afforded CIGSe devices much success [10].

Many investigations of CZTS have focused on fabrication by non-vacuum techniques, in part to enhance commercial viability, but also to mitigate stoichiometry control issues associated with the high vapor pressures of elemental Zn and SnS compounds [13-15]. As a true quaternary alloy, CZTS phase formation is complex and difficult to control, with a large number of possible binary and ternary phases formed during fabrication. The champion laboratory cell has achieved an efficiency of 12.6% using a nano-ink spin coating system with hydrazine as the solvent [16]. The reported device properties are as follows: short-circuit current density (J_{SC}) of 35.2mA/cm^2, open-circuit voltage (V_{OC}) of 513.4mV, and a fill factor (FF) of 69.8% [16]. The primary loss mechanisms in the champion cell remain similar to those previously reported by Mitzi, including interface recombination, series resistance, and short minority carrier lifetime [13, 16, 17].

The best performing devices, including the champion cells, have utilized CZTSSe absorber layers with Cu-poor, Zn-rich and S/Se-alloyed stoichiometries, with atomic ratios of Cu:[Zn+Sn] ~ 0.8 – 0.9, Zn:Sn ~ 1.1 – 1.2 and S:[S+Se] ~ 0.25 – 0.30, respectively [13]. The performance improvement in Cu-poor, Zn-rich film stoichiometries has been attributed to the minimization of deep-level Cu_{Zn} antisite defects and self-compensated defect pairs $[Cu_{Zn}^{-}+Zn_{Cu}^{+}]^0$, which have been identified as potential contributors to poor doping and charge separation properties [18]. The optimization of device performance with lower S:[S+Se] ratios has been possibly attributed to a shallower Cu_{Zn} defect level, a type-inversion at the P-N junction [19], or to a reduction of a blocking back contact barrier [17]. However, Barkhouse points out this detected blocking barrier may also be associated with the absorber-window layer interface or with grain boundaries in the absorber [17].

The device architecture for CZTSSe system has been almost universally borrowed from CIGSe and work remains to optimize the device layers. Indeed, all phases of research remain active for CZTSSe, including understanding and improving film growth, characterizing fundamental opto-electronic and defect properties of CZTSSe, and optimizing device architecture.

1.4 PURPOSE OF THIS WORK

Pulsed laser deposition and electrodeposition were chosen as the fabrication processes for CIGSe and CZTS absorber layers for several reasons, including our laboratory's capabilities and expertise in these methods. Pulsed laser deposition (PLD), particularly useful for multi-component systems like CIGSe and CZTS, represents a laboratory-scale synthesis tool that enables rapid evaluation of material combinations and layer interfaces. Moreover, the ability to deposit on insulating substrates facilitates the study of optical absorption and Hall Effect that cannot be performed for films deposited on conductive substrates, as needed for electrodeposited films. Electrodeposition (ED) represents a more commercially viable synthesis tool that also enables rapid thin film deposition. The scalability of electrodeposition has been demonstrated in

large-scale industrial deployment of conventional metallic plating, and also in the semiconductor industry through the use of copper damascene electroplating techniques [13].

Early work exposed significant difficulties in controlling CZTS thin film growth, using both PLD and ED. Pulsed laser deposited films demonstrated significant deviations in stoichiometry relative to the sputtering target (Sn-rich) during deposition and void formation during subsequent sulfur annealing steps. Using a fabrication recipe from [20], electrodeposited films exhibited severely rough, powdery morphologies, which appeared to deviate strongly from the reported behavior. These fabrication challenges, and the gaps in relevant literature necessary to address them, prompted the systematic investigation of the growth behavior of CZTS by PLD and ED that forms the core of this work.

Throughout this dissertation, my goals have frequently evolved as my understanding of the field grew, as equipment became available or unavailable, and as a new experimental results were evaluated. The overarching goals of this work, however, included the following:

(1) Fabricate device-quality CIGSeS thin films for use as reference standards against which the properties and behavior of CZTS thin films may be evaluated

(2) Characterize the growth behavior of pulsed laser deposited and electrodeposited CZTS thin films by systematically investigating relevant deposition and annealing parameters

(3) Identify the critical parameters in film growth, including the effects of deposition and annealing conditions and the precursor properties on the final CZTS film properties

(4) Demonstrate high-quality CIGSeS and CZTS absorber layers fabricated by PLD and ED

After many depositions and significant optimization effort, quality CZTS thin films were demonstrated using both pulsed laser deposition and co-electrodeposition methods. This work provides a greater understanding of the deposition parameters on the growth properties of CZTS thin films, and I believe it represents a significant achievement of this dissertation.

1.5 THESIS STRUCTURE

After the introduction, this thesis contains three background chapters which discuss the CIGSeS and CZTS material systems and devices (Chapter 2), the thin film fabrication methods (Chapter 3), and the characterization methods (Chapter 4) employed in this work. The next four chapters discuss the experimental work conducted for this dissertation, with each chapter composed of three main divisions: review of relevant literature, presentation of results, and discussion and interpretation of results. Chapter 5, the first experimental chapter, discusses the effects of growth conditions of CIGSeS thin films deposited by pulsed laser deposition, and it details the improvement of the electronic quality of the films with sulfur annealing and stoichiometry control. Chapter 6 discusses the effects of growth conditions of CZTS thin films

deposited by pulsed laser deposition, and it details the improvement of as-deposited films through the optimization of the sputtering target stoichiometry and the effects of sulfur annealing parameters. The effects of precursor composition and structure on the crystal formation of CZTS are discussed. Chapter 7 discusses the effects of growth conditions of sulfur-containing CZTS precursor films deposited by co-electrodeposition, and it details the critical role of pH and the hydrogen evolution reaction on the composition and morphology evolution of deposited films. Chapter 8 discusses the effects of growth conditions of metallic CZT precursor films deposited by co-electrodeposition, and the optimized deposition conditions and sulfur annealing parameters are presented. In the final chapter (Chapter 9), major conclusions are summarized and future work is recommended.

1.6 REFERENCES

[1] J. Conti, International Energy Outlook 2013, in: D.o. Energy (Ed.), 2013.

[2] U.S.E.I. Administration, International Energy Outlook 2013: Electricity, in, 2013.

[3] J. Rutqvist, A.P. Rinaldi, F. Cappa, G.J. Moridis, Modeling of fault reactivation and induced seimisicity during hydraulic fracturing of shale-gase reservoirs, Journal of Petroleum Science and Technology, 107 (2013) 31 - 44.

[4] Study of the Potential Impacts of Hydraulic Fracturing on Drinking Water Resources: Progress Report, in: O.o.R.a. Development (Ed.), 2012.

[5] Summary for Policy Makers, in: T.F. Stocker, D. Qin, G.K. Plattner, M. Tignor, S.K. Allen, J. Boschung, A. Nauels, Y. Xia, V. Bex, P.M. Midgley (Eds.) Climate Change 2013: The Physical Science Basis. Contribution of Working Group I to the Fifth Assessment Report of the Intergovernmental Panel on Climate Change, New York, 2013.

[6] AEO2014 Early Release Overview, in: D.o. Energy (Ed.), 2013.

[7] N.S. Lewis, G. Crabtree, Basic Research Needs for Solar Energy Utilization: Report of the Basic Energy Sciences Workshop on Solar Energy Utilization April 18 - 21, 2005, in, U.S. Department of Energy, 2005.

[8] Levelized Cost of New Generation Resources in the Annual Energy Outlook 2013, in: D.o. Energy (Ed.), 2013.

[9] T. Unold, H.W. Schock, Nonconventional (Non-Silicon-Based) Photovoltaic Materials, Annual Review of Materials Research, 41 (2011) 297-321.

[10] W. Shafarman, S. Siebentritt, L. Stolt, Cu(InGa)Se_2 Solar Cells, in: A. Luque, S. Hegedus (Eds.) Handbook of Photovoltaics Science and Engineering, John Wiley & Sons, West Sussex, 2011.

[11] J. Nelson, The Physics of Solar Cells, Imperial College Press, London, 2007.

[12] M. Green, Third generation photovoltaics: solar cells for 2020 and beyond, Physica E, 14 (2002) 65 - 70.

[13] D. Mitzi, O. Gunawan, T. Todorov, K. Wang, S. Guha, The path towards a high-performance solution-processed kesterite solar cell, Solar Energy Materials & Solar Cells, 95 (2011) 1421 - 1436.

[14] P.M.P. Salome, J. Malaquias, P.A. Fernandes, M.S. Ferreira, J.P. Leitao, A.F.d. Cunha, J.C. Gonzalez, F.N. Matinaga, G.M. Ribeiro, E.R. Viana, The influence of hydrogen in the incorporation of Zn during the growth of $Cu_2ZnSnSn_4$ thin films, Solar Energy Materials & Solar Cells, 95 (2011) 3482 - 3489.

[15] A. Weber, R. Mainz, H.W. Schock, On the Sn loss from thin films of the material system Cu-Zn-Sn-S in high vacuum, Journal of Applied Physics, 107 (2010) 013516-013511 - 013516-013516.

[16] W. Wang, M. Winkler, O. Gunawan, T. Gokmen, T. Todorov, Y. Zhu, D. Mitzi, Device Characteristics of CZTSSe Thin-Film Solar Cells with 12.6% Efficiency, Advanced Energy Materials, (2013).

[17] A. Barkhouse, O. Gunawan, T. Gokmen, T. Todorov, D. Mitzi, Device characteristics of a 10.1% hydrazine-processed $Cu_2ZnSn(Se,S)_4$ solar cell, Progressin Photovoltaics: Research & Applications, (2011).

[18] S. Chen, X.G. Gong, A. Wlash, S. Wei, Defect physics of hte kesterite thin-film solar cell absorber Cu_2ZnSnS_4, Applied Physics Letters, 96 (2010) 021902-021901 - 021902-021903.

[19] A. Walsh, S. Chen, S.-H. Wei, X.-G. Gong, Kesterite Thin-Film Solar Cells: Advances in Materials Modelling of Cu_2ZnSnS_4, Advanced Energy Materials, 2 (2012) 400 - 409.

[20] S.M. Pawar, B.S. Pawar, A.V. Moholkar, D.S. Choi, J.H. Yun, J.H. Moon, S.S. Kolekar, J.H. Kim, Single step electrosynthesis of Cu_2ZnSnS_4 (CZTS) thin films for solar cell application, Electrochimica Acta, 55 (2010) 4057-4061.

2 CHALCOGENIDE PHOTOVOLTAICS BACKGROUND

2.1 PHOTOVOLTAIC DEVICE BASICS

Photovoltaic devices convert sunlight directly into electricity. Semiconductor materials provide this conversion by transferring energy from incident photons to electrons in the material, and then driving these higher-energy electrons through a load (doing work in the process) before they can relax back down to their initial rest state. The following sections briefly describe the working principles of the photovoltaic device, including the properties of solar radiation, basic principles of semiconductor and device operation, and also the particular properties of thin film heterojunction photovoltaic device operation. For a more in-depth review, the reader is encouraged to consult one of the many good textbooks on the subject [1-5].

2.1.1 Solar Radiation

The Sun emits light at wavelengths spanning the ultraviolet to infrared regions of the electromagnetic spectrum [2]. The energy (wavelength) distribution approaches that of an ideal blackbody at 5760K and may be described by Planck's intensity relation for blackbodies [6]:

$$i_\lambda(T) = \frac{2hc^2}{\lambda^5}\frac{1}{e^{hc/(\lambda k_B T)} - 1} \tag{2-1}$$

where i_λ is the spectral intensity or radiation in units of $W/m^2 \cdot m \cdot sr$, h is Planck's constant, c is the speed of light, k_B is Boltzmann's constant, T is the temperature of the blackbody, and λ is the wavelength of light. The solid angle between the Earth and the Sun determines the portion of the emitted light intercepted by the Earth, and the AM0 (air mass 0) spectrum represents the real, extraterrestrial intensity distribution incident on the Earth (e.g. outside Earth's atmosphere) [2].

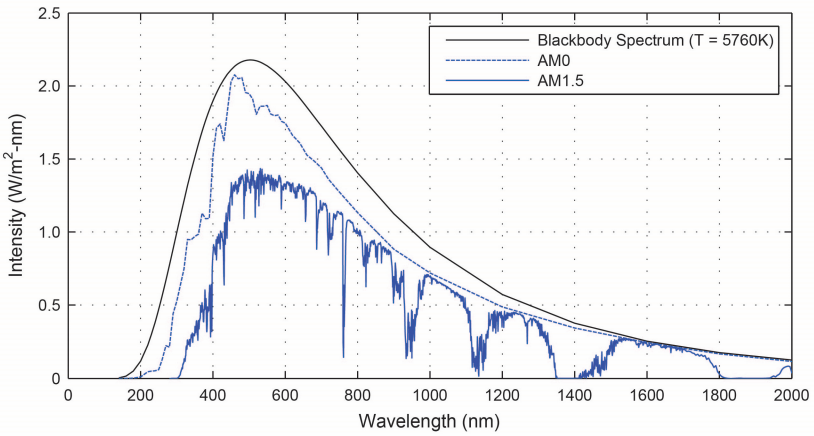

Fig. 2-1. Spectral intensity of radiation for blackbody, AM0, and AM1.5 – note: blackbody intensity scaled by solid angle of interception between Earth and Sun, data from [7, 8]

Sunlight gets absorbed as it passes through Earth's atmosphere, with some wavelengths highly filtered by strong H_2O and CO_2 absorption bands [2]. The amount of absorption increases with increasing path length, and the path length increases with increasing latitude. The standard spectrum, AM1.5, is taken at a latitude of 42° [2]. The standard blackbody, AM0, and AM1.5 spectra are shown in Fig. 2-1.

2.1.2 Fundamental Semiconductor Concepts

2.1.2.1 Introduction to Semiconducting Behavior

Semiconducting material properties result from the bonding and periodic arrangement of atoms in a lattice. Bohr originally theorized that electrons in an isolated atom may only take discrete, or **quantized**, energy levels governed by quantum mechanics [1]. Inner, lower energy electrons, are tightly bound to the atom, and they are referred to as **core electrons**. Outer, more weakly bound electrons are referred to as **valence electrons**. Valence electrons participate strongly in chemical reactions, while core electrons do not [1]. As atoms are brought into close contact, their valence electrons interact and modify their energy states. In periodically ordered crystalline materials, the atomic interactions lead to the development of **energy bands**, or sets of closely spaced allowed energy levels. **Valence band (VB)** refers to the lowest **mostly occupied** energy band, and **conduction band (CB)** refers to the next highest **mostly unoccupied** energy band [1]. In cases where these bands do not overlap, the **band gap** refers to the band of energies not allowed to be occupied. **Semiconductors** are defined as materials with band gaps between 0 – 4eV [9].

Semiconductor principles can often be described using the simplified **two-band model**, consisting of a valence band and conduction band of single energy values, E_v and E_c, as shown in Fig. 2-2. While electrons are **localized** around single atoms, excited electrons in a crystal are **de-localized** since the allowed electronic states (VB and CB) extend throughout the crystal [1]. That is, when crystal bonds are broken and electrons are excited from the valence band into the conduction band, which is empty or lightly populated, many electronic states are available allowing them to move easily through the crystal. Simultaneously, vacancies or **holes** form in the VB, mobilizing electrons in the VB [1]. The electron transport associated with these vacancies may be conceptually simplified by considering not the coordinated movement of the electrons but instead the movement of the hole. Thus, negatively charged electrons and positively charged holes describe the electron behavior in the CB and VB, respectively [1].

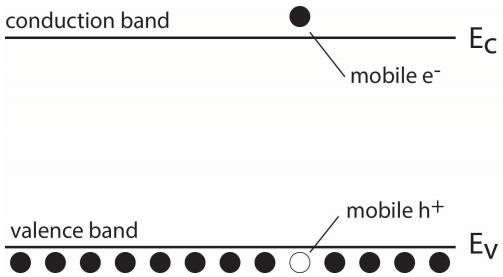

Fig. 2-2. Two energy band model

Electrons and holes **(charge carriers)** can be generated by **thermionic** and **optical excitation**. Doping refers to the introduction of carriers by thermionic emission (thermal excitation), either through intrinsic or native defects, or extrinsic dopants. In this case, defects are introduced into the crystal lattice, which possess either weakly bound electrons or holes [1]. These defects may include vacancies, antisite substitutions by native atoms, or intentional substitutions by foreign atoms. **P-type, acceptor** defects and dopants introduce holes into the material, and **N-type donors** introduce electrons. The concentration of these defects, the activation energy required to ionize the donors or acceptors, and the temperature of the semiconductor determine the concentration of carriers introduced into the material [1, 10]. Well-behaved dopants easily ionize (e.g. shallow) at room temperature and do not act as recombination centers for carriers.

2.1.2.2 Carrier Statistics

Carrier populations within a semiconducting material are governed by the distribution of allowed electronic states and the filling statistics associated with these states. The energy distribution of states, or **density of states**, corresponds to the electronic band structure of the material, a property dependent on its crystal structure and atomic chemistry [2]. While the band structure of a material can be quite complex, often the significant opto-electronic properties are dominated by behavior near the band edges [1]. This simplification allows us to approximate the valence and conduction bands as parabolas and to conceptualize the behavior using the two-band model. A **direct band gap** describes the condition when the conduction band minimum and valence band maximum occur at the same wavevector [2].

Electrons obey the Pauli exclusion principle and Fermi-Dirac statistics [4]. In thermodynamic equilibrium, the occupation distribution of electrons in the allowed energy states may then be described by the **Fermi function f**, which describes the probability that a given state may be occupied ($0 \leq f \leq 1$) [1]. Using the **parabolic approximation** of the band edges, relationships for the densities of states g_c and g_v may be formulated. By convolving and integrating these densities of states with the Fermi function, the **electron concentration n** in the conduction band and the **hole concentration p** in the valence band may be then directly calculated. Finally, with some algebraic manipulation, the **intrinsic carrier density n_i**, a constant property of the material, may be written as follows [2]:

$$n_i^2 = np = 4\left(\frac{m_n^* k_B T}{2\pi\hbar^2}\right)^{3/2}\left(\frac{m_p^* k_B T}{2\pi\hbar^2}\right)^{3/2} e^{-E_g/k_B T} \tag{2-2}$$

where m_n^* is the electron effective mass, m_p^* is the hole effective mass, E_g is the band gap, and $\hbar$ is the modified Planck's constant. This equation indicates an inverse relationship between electron and hole concentrations. Under intrinsic, undoped conditions, an **intrinsic potential E_i** may be defined that is equal to the Fermi level of the pure semiconductor in equilibrium and lies close to the center of the band gap [2]. A positioning of E_F in the midgap indicates that the electron and hole populations are equal [1].

Extrinsically doped materials typically involve shallow dopants that are fully ionized (e.g. electrically active) under standard room temperature conditions [1]. In this case, the carrier concentrations are dominated by the dopant concentrations, such that $n = N_D$ or $p = N_A$ for electrons (donors) and holes (acceptors), respectively [1]. It can be shown that the Fermi level, E_F, shifts towards the conduction band as the concentration of electrons increases and that E_F shifts towards the valence band as the concentration of holes increases [1]. When the doping concentrations are high enough, the Fermi level shifts into the conduction or valence band, a condition known as **degenerate** doping. In this condition, the semiconductor behaves more like a metal than a semiconductor [1].

2.1.2.3 Carrier Action

Carriers may be transported within the semiconductors by drift and diffusion, and they may be created or destroyed through generation and recombination processes. **Drift** involves the transport of charged particles (e.g. carriers) by electrostatic interactions with an applied electric field [1]. Scattering events involving collisions, for instance with ionized impurity atoms (dopants) and phonons, impede the drift motion, and a proportionality constant μ can be introduced which relates the drift current to the applied electric field [1]. Known as **mobility μ**, this constant relates proportionally to the mean free time between collisions and inversely proportionally to the effective mass of the carrier [1]. The **drift current densities** of electrons and holes may be written as $J_e=q\mu_e n\varepsilon$ and $J_h=q\mu_h p\varepsilon$, respectively, where q is the fundamental charge, μ_e is the electron mobility, μ_h is the hole mobility, n is the electronic concentration, p is the hole concentration, and ε is the applied electric field [1]. **Diffusion** involves the transport of carriers through random thermal motion that results in an overall migration of the particles when concentration gradients are present [1]. Using Fick's law, the 1-D diffusion current densities of electrons and holes may be written as $J_e=qD_e(dn/dz)$ and $J_h=-qD_h(dp/dz)$, respectively, where J_e is the electron diffusion current, J_h is the hole diffusion current, D_e is the electron diffusion constant, and D_h is the hole diffusion constant [1].

Generation and recombination processes, which create or destroy carriers, represent the forward and reverse actions of three primary electronic transitions: **direct (band-to-band)** transitions, **indirect (R-G center)** transitions, and **Auger** transitions [1]. These processes may operate in parallel [4], but frequently one recombination mechanism dominates the performance. Radiative recombination represents an unavoidable mechanism and thus yields a limit in the theoretical performance of operation (as mentioned in Ch1 discussion of the Shockley-Queisser limit) [11]. In thin film systems in particular, materials typically contain sufficient densities of R-G active defects, such that the devices are said to be **trap-limited** [2].

Direct, band-to-band transitions include photogeneration and radiative recombination. **Photogeneration**, the active process in optical absorption, involves the interaction of an incident photon ($E > E_g$) with the crystal, exciting an electron from the valence band into the conduction band and generating an electron-hole pair, as shown in Fig. 2-2. Electrons excited by photons with

energies larger than the band gap will quickly "thermalize" down to the band edges through vibrational interactions with the crystal lattice [1]. The photogeneration rate depends on the flux of incident photons and the absorption coefficient of the material, as well as its reflectance [2]. There also exists a probability that electrons in the conduction will spontaneously relax to the valence band, emitting a photon equivalent to the transition (band gap) energy, a process known as **radiative recombination** and given by the following relation [4]:

$$U_R = B(np - n_0 p_0) \tag{2-3}$$

where U_R is the radiative recombination rate, B is a material-specific proportionality constant, n and p are the electron and hole concentrations under arbitrary conditions, and n_0 and p_0 are the electron and hole concentrations under thermodynamic equilibrium conditions. This indicates an inherent restorative tendency, such that a carrier concentration product $np > n_0p_0$ will cause net recombination and a concentration product $np < n_0p_0$ will cause net generation [4]. Direct gap semiconductors typically have higher optical absorption coefficients and sharper absorption edges than indirect gap semiconductors because phonon (quantized vibrational excitation) interactions are not required to conserve momentum [1, 4]. Therefore direct gap transitions (photogeneration and radiative recombination) are more probable than indirect gap transitions [1, 4].

Indirect, R-G center transitions involve electronic transitions between the valence and conduction bands through intermediate trap states located within the band gap [1]. The transitions may result in the destruction or generation of electron-hole pairs, as shown Fig. 2-3, and involve either the transfer of thermal energy to or from the crystal to the electron [1]. As opposed to shallow donors, midgap R-G centers significantly lower the barrier to transitions between the bands and so represents a significant loss mechanism, as conduction band electrons may be lost with increasing probability before being separated and shuttled to the external circuit to do work [4]. The indirect, R-G center recombination process may be described by the **Shockley-Reed-Hall (SRH)** theory [1]:

$$U_T = \frac{np - n_0 p_0}{\tau_{h0}(n + n_i e^{(E_T - E_i)/k_B T}) + \tau_{e0}(p + n_i e^{(E_i - E_T)/k_B T})} \tag{2-4}$$

where U_T is the indirect recombination rate, n and p are the electron and hole concentrations under arbitrary conditions, n_0 and p_0 are the electron and hole concentrations under thermodynamic equilibrium, τ_{h0} and τ_{e0} are the average hole and electron lifetimes before relaxation, E_T is the energy of the R-G center (e.g. trap state), E_i is the intrinsic potential, k_B is Boltzmann's constant, and T is temperature.

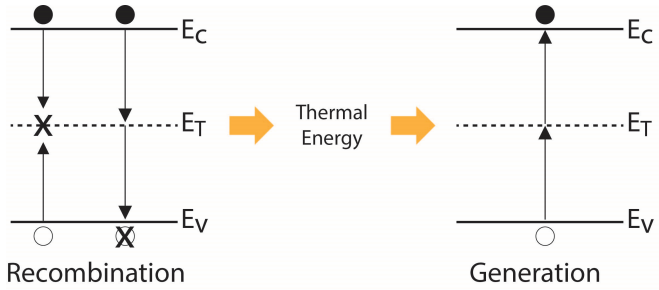

Fig. 2-3. Indirect (R-G center) transitions, adapted from [1]

Auger transitions involve the band-to-band transition by an electron, but instead of emitting or absorbing a photon, the electron transfers this energy to another electron which then gives this energy up to the crystal through thermalization to the band edge [1]. Since this transition involves more than one electron, the carrier concentrations must be large in order to have a significant probability of the event taking place. PV absorber layers typically target carrier concentrations between 10^{16} and 10^{17} cm^{-3}, a regime where Auger recombination and its converse, impact ionization, are much less active [4].

2.1.3 Device Physics

2.1.3.1 P-N Junctions Under Equilibrium and Under Bias

Formed by contacting P- and N-type layers, the P-N junction enables efficient charge carrier separation and acts as the heart of the photovoltaic device. As previously described and as shown in Fig. 2-4(a), the Fermi level shifts toward the conduction band and valence band edges for N-type and P-type semiconductors, respectively. **In thermodynamic equilibrium**, the Fermi level must remain constant throughout the entire material, and so when the P- and N-type layers are contacted, the difference in Fermi levels induces **bending in the bands**, as shown in Fig. 2-4(b) [1]. This band bending produces a **built-in electric field**, which enables electrons and holes to be separated and transported to the electrical load [1].

When the P- and N-type layers are contacted, concentration gradients between the hole-rich P-layer and the electron-rich N-layer initiate carrier diffusion currents. Holes from the P-layer diffuse into the N-layer, and electrons from the N-layer diffuse into the P-layer, leaving behind ionized acceptors and donors, respectively [1]. Holes diffusing into the N-layer readily recombine with majority electrons, and the electrons diffusing into the P-side readily recombine with majority holes, creating a region void of charge carriers known as the **depletion region** or **space charge region (SCR)** [1]. The stationary ionized donors and acceptors left behind create an electric field, which induces electron and hole drift currents that oppose the diffusion currents [1]. The junction establishes a dynamic equilibrium, such that the drift currents and diffusion currents balance out, leaving a zero net current within the device [1].

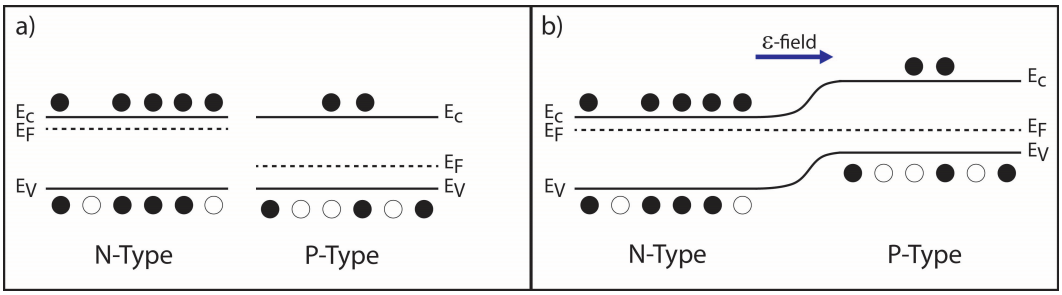

Fig. 2-4. P-Type and N-Type semiconductor materials a) separated and b) in contact (thermodynamic equilibrium)

The P-N junction fundamentally consists of three sections: the Quasi-Neutral P-type region, the Space Charge Region, and the Quasi-Neutral N-Type region [1]. The **Quasi-Neutral regions (QNRs)** are so named because they contain zero net charge density and carry no electric field [1]. The **depletion** or **Space Charge Region** contains net charge due to the stationary ionized donor and acceptors, and so carries an electric field [1]. The carriers (and therefore the ionized donors and acceptors) vary logarithmically between the QNRs and the depletion region, and therefore the charge densities of the donors and acceptors are commonly modeled as step changes, known as the **depletion approximation** [4].

Fig. 2-5 summarizes the effects of bias on the band bending, Fermi level, electric field, and the associated drift and diffusion currents in the P-N junction. Larger arrows indicate larger magnitude. **Under equilibrium ($V_A = 0$)**, the Fermi level remains constant across the junction, the barrier height to diffusion is qV_{bi}, and the individual drift and diffusion currents balance for both electrons and holes. **Under applied bias**, the Fermi level cannot be defined using a single level, since the device is no longer in equilibrium [1]. In the QNRs, however, the majority carrier concentrations are generally large such that deviations from equilibrium of the carrier populations, and therefore also the associated Fermi levels, are small especially far from the junction [1]. **Quasi-Fermi levels, E_{FP} and E_{FN}**, may then be defined in the QNRs, such that the applied bias V_A splits the Fermi level into quasi-Fermi levels as follows [1]:

$$E_{F_P} - E_{F_N} = -qV_A \tag{2-5}$$

Under forward-bias ($V_A > 0$), the Fermi level splits shifting E_{FP} down relative to E_{FN}, the barrier height reduces by qV_A, and the diffusion currents significantly increase for both electrons and holes as the barrier height decreases [1]. While the barrier height decreases linearly with the applied bias, the (diffusing) carrier concentrations at the band edge that are able to overcome the potential barrier increase exponentially with the applied bias [1]. The minority carrier populations in the QNRs that contribute to the drift current (e.g. electrons in P-layer and holes in N-layer) do not, however, change much [1]. Consequently, as indicated in Fig. 2-5(b), the **diffusion currents increase exponentially** with applied bias, while the drift currents remain the same, giving rise to a net current. This effectively injects minority carriers into the QNRs at the depletion region edges,

creating concentration gradients which cause diffusion of the minority carriers through the QNRs where they recombine with majority carriers supplied by the contacts [1].

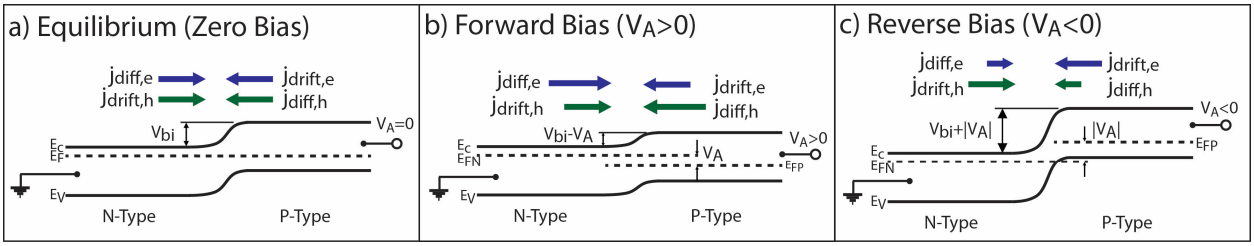

Fig. 2-5. P-N junctions under bias

Under reverse-bias ($V_A < 0$), the Fermi level splits shifting E_{FN} down relative to E_{FP}, the barrier height increases by $|qV_A|$, and the diffusion current significantly decrease for both electrons and holes as the barrier height decreases [1]. While the barrier height increases linearly with the applied bias, the (diffusing) carrier concentrations at the band edge that are able to overcome the potential barrier decrease exponentially with the applied bias [1]. Again, the minority carrier populations in the QNRs that contribute to the drift current (e.g. electrons in P-layer and holes in N-layer) do not change much [1]. Consequently, as indicated in Fig. 2-5(c), the **diffusion currents decrease exponentially** with applied bias, while the drift currents remain the same, giving rise to a net current in the opposite direction to that in forward bias. Unlike forward bias, however, the supply of minority carriers to contribute to the drift current is eventually exhausted leading to **saturation of the current** [1].

2.1.3.2 The Ideal Diode Equation

In typical thin film solar cell devices, the area of the device is large compared to the thickness, and so the physical behavior of the system corresponds to quasi-1D conditions. Classical electrostatics provides the link between electric field and potential ($\varepsilon = -dV/dz$), and **Poisson's equation** provides the link between electric field and the charge density [1]:

$$\frac{d\varepsilon}{dz} = \frac{\rho}{\in} = \frac{q}{\in}(p - n + N_D - N_A) \tag{2-6}$$

where ε is the electric field, ρ is the charge density (assuming fully ionized donors and acceptors), $\in$ is the material permittivity, p is the hole concentration, n is the electron concentration, N_D is the density of ionized donors, and N_A is the density of ionized acceptors.

Using the carrier transport, generation and recombination relationships previously detailed, the equations of state (e.g. the **continuity equations** for electrons and holes), may be written as Eqns. (2-7) and (2-8) where U and G are the rates of recombination and generation, respectively. These differential continuity equations provide a record keeping of carriers being transported through, created in, or destroyed in a given infinitesimal control volume at given point in the material.

$$\frac{1}{q}\frac{d}{dz}\left(q\mu_e n\varepsilon + qD_e\frac{dn}{dz}\right) = U - G \tag{2-7}$$

$$\frac{1}{q}\frac{d}{dz}\left(q\mu_h p\varepsilon - qD_h\frac{dp}{dz}\right) = -(U - G) \tag{2-8}$$

The **ideal diode equation** represents the steady-state relationship between current and voltage for a P-N junction diode. The derivation assumes quasi-1D behavior, no photogeneration, dilute minority carrier populations in the QNRs, the depletion approximation, and no recombination in the depletion region [1]. **In the QNRs**, the electric field is zero and carrier transport proceeds by diffusion only. **In the depletion region**, the electric field is non-zero and, under equilibrium conditions, the drift and diffusion currents cancel; under forward- and reverse-bias, the diffusion currents across the junction increase and decrease, respectively, modifying the drift-diffusion balance as shown in Fig. 2-5 and contributing to an overall current. It is noted that the overall current ($J = J_e + J_h$) must remain constant across the diode under steady-state conditions, although the individual contributions J_e and J_h may vary [1].

The general approach then involves solving the continuity equations within the P-type and N-type QNRs and the depletion regions and then splicing solutions together at the boundaries. **The ideal diode equation** may then be written as follows [1]:

$$J_{dark}(V) = J_0(e^{qV/k_BT} - 1) \tag{2-9}$$

$$J_0 \equiv q\left(\frac{D_e}{L_e}\frac{n_i^2}{N_A} + \frac{D_h}{L_h}\frac{n_i^2}{N_D}\right) \tag{2-10}$$

where J_{dark} is the **dark (diode) current density**, J_0 is the **saturation current density**, V is the applied bias, D_e is the electron diffusion constant, D_h is the hole diffusion constant, L_e is the electron diffusion length, L_h is the hole diffusion length, N_A is acceptor density, N_D is the donor density, and n_i is the intrinsic electron density. The **diffusion length** represents the average distance a carrier can travel before recombining [1].

2.1.3.3 P-N Junctions Under Illumination

In a highly-simplified model of P-N device operation under illumination, it is assumed that the **photogeneration rate G** acts uniformly throughout the device. Then, the continuity equations may be formulated as in the previous section but with constant generation terms in the QNR and depletions regions. The current-voltage relationship then becomes [4]:

$$J(V) = J_0(e^{qV/k_BT} - 1) - J_L = J_{dark}(V) - J_L \tag{2-11}$$

$$J_L \equiv qG(L_e + W + L_h) \tag{2-12}$$

where J is the current density of the device, J_{dark} is the diode current density with no illumination, J_L is the light-generated current density, G is the photogeneration rate, and W is the depletion region width.

The current-voltage equation (2-11) indicates that the junction behaves as though the dark (diode) current and the light-generated current are simply superposed on top of each other [4]. This assumption may break down when the light-generated current exhibits a voltage-dependence, not present in Eqn. (2-12), that can result due to depletion region-dependent collection, interface recombination and photocurrent barriers [5]. While more complex photogeneration models of the been developed as in [5], Eqn. (2-12) indicates that, under this simple model, all carriers generated within the depletion region and within a diffusion length on both sides of the junction are collected and contribute to the light-generated current [4].

2.1.3.4 Solar Cell Device Performance

The current density-voltage curves for a typical solar device (e.g. P-N junction device under illumination) are shown in Fig. 2-6. Important parameters are identified on the curves, including **short-circuit current density** (J_{SC}), **open-circuit voltage** (V_{OC}), **fill factor** (FF), and the associated **current density and voltage at maximum performance** (J_{MP}, V_{MP}).

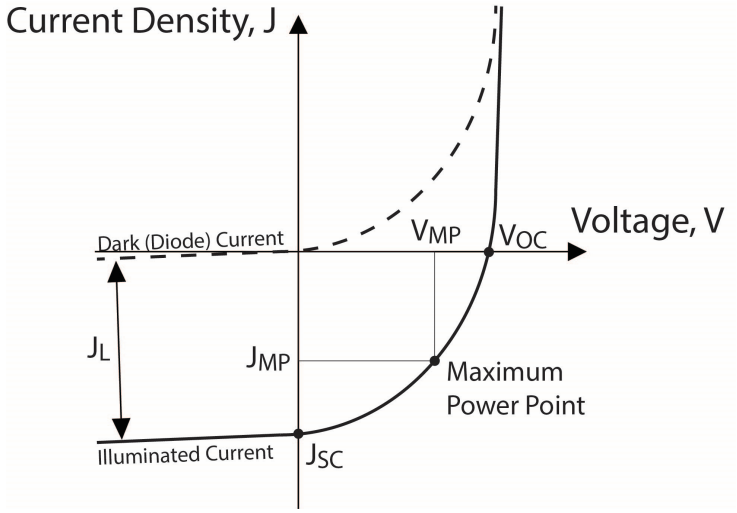

Fig. 2-6. Typical J-V Curve for Solar Cell Device

The power density delivered by the solar cell device equals the current density – voltage product (J·V), and there exists a **maximum power point** corresponding to J_{MP} and V_{MP}. The load resistance determines the (J,V) during operation, and so the optimum load resistance corresponds to V_{MP}/J_{MP} [2]. A load of infinite resistance prevents all current flow, and the voltage of the device corresponds to the **open-circuit voltage (V_{OC})**. At this point, the diode current and the light-generated current exactly cancel [2]. A load of zero resistance provides the maximum current density at zero voltage, ideally equivalent to the light-generated current density, known as the **short-circuit density (J_{SC})** [2]. The **fill factor**, Eqn. (2-13), represents the degree of "squareness" of the curve, such that a higher fill factor (e.g. more square J-V curve) corresponds to a higher

maximum power $J_{MP}V_{MP}$ [2]. Finally, the device efficiency, Eqn. (2-14), may be defined as the ratio of maximum power density output to supplied power density from the Sun, P_{SUN} [2].

$$FF = \frac{J_{MP}V_{MP}}{J_{SC}V_{OC}} \tag{2-13}$$

$$\eta = \frac{J_M V_M}{P_{SUN}} \tag{2-14}$$

In actual operation, solar cell devices may experience many types of losses in potential power output, such as optical losses, recombination losses, thermalization losses, and parasitic resistance losses. **Optical losses** include reflection, shading and transmission losses [12]. Due to the refractive index transition between air and the device, some light will be lost by reflectance at the device surface, particularly at high angles of incidence [2]. Antireflection (AR) coatings can mitigate this loss, but conventional coatings cannot completely eliminate it for all wavelengths or angles of incidence [2]. Metal bus bars are typically used to help shuttle the current from the P-N junction to the load, but these metals also block sunlight from the device [4]. Consequently, a trade-off exists between the electrical conductivity provided by these bus bars and the shading losses incurred by them [2]. Moreover, thin film devices frequently employ transparent conducting oxide layers (TCOs) as electrically conductive contacts, but light can be absorbed in these layers, which does not contribute to the light-generated current; for the most part, only light absorbed in the absorber layer contributes to the photogenerated current [2]. Finally, absorber layers that are not optically thick will not absorb all of the incident radiation, yielding transmission losses [2, 12]. Further, all the light with energy less than the band gap cannot be absorbed and so represents an inaccessible portion of the solar spectrum.

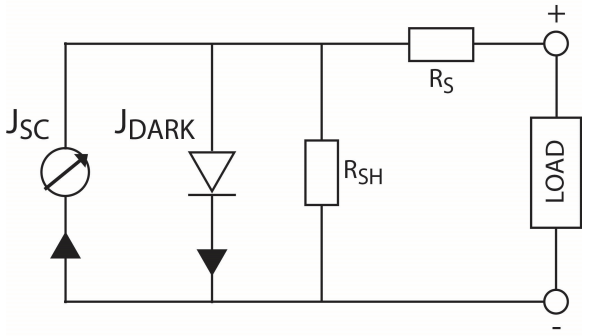

Fig. 2-7. Equivalent circuit for solar cell device, in the style of [2, 4, 12]

Charge carrier recombination can reduce the photogenerated current and increase the dark current, thereby reducing the power output of the device [5, 12]. Such losses may be severe, depending on the location and extent of the recombination. Recombination of minority carriers in the absorber layer can reduce the light-generated current, and recombination of carriers in the depletion region can significantly reduce the V_{OC}, as described in the following section, as well as

the FF [5, 12]. For most polycrystalline thin film systems, minimizing recombination losses represents the major challenge in achieving high performance devices.

Thermalization losses originate from the single-junction (single band gap) device structure. Band gaps help prevent recombination of electron-hole pairs long enough for the excited, conduction band electrons to be extracted and used to provide electrical work [2]. Within a band, the electron may easily exchange energy with the crystal lattice and move rapidly through the closely-spaced allowed energy levels [2]. This process, referred to as thermalization, progresses much more quickly than the recombination processes, and electrons cannot be extracted quickly enough to prevent it [2]. Subsequently, in single-junction, incident photons with energies greater than the absorber band gap will generate photoelectrons with energies above the conduction band edge (E_{photon}-E_g) that thermalize down to the band edge. This thermalization represents a fundamental loss mechanism associated with the Shockley-Queisser limit [4].

Parasitic resistance losses include series and shunt resistances within the PV device. Series resistances to current flow may include internal electrical resistance within the absorber or window layers or interfacial resistances at the front and back contacts [2]. Shunts, or parallel electrical paths, may develop across the P-N junction as a result of pinholes or voids in the absorber layer. If severe enough, these shunts may destroy the diode rectification action of the junction [2]. Conventional CIGSe devices employ an intrinsic ZnO layer between the buffer and window layer, at the expense of additional series resistance, in order to prevent shunt formation [13]. These parasitic series and shunt resistances may be modeled in an equivalent circuit, modeling the photovoltaic device as shown in Fig. 2-7. Including the effects of **series resistance R_S** and **shunt resistances R_{SH}** the current density – voltage relationship may be written as [2]:

$$J(V) = J_0(e^{q(V+JAR_S)/k_BT} - 1) + \frac{V + JAR_S}{R_{SH}} - J_L \tag{2-15}$$

where A is the active device area and J_L is the light-generated current.

2.1.4 Thin Film Heterojunctions

The previous section implicitly derived the performance relations for homojunction devices, in which the electron affinities and the band gaps across the P-type and N-type materials remain the same, simplifying the band alignment picture. **In heterojunctions**, however, the electron affinities and band gaps may vary significantly across the junction, giving rise to discontinuities at the interface [2]. Fig. 2-8 shows the different types of band alignments possible in heterojunctions [14].

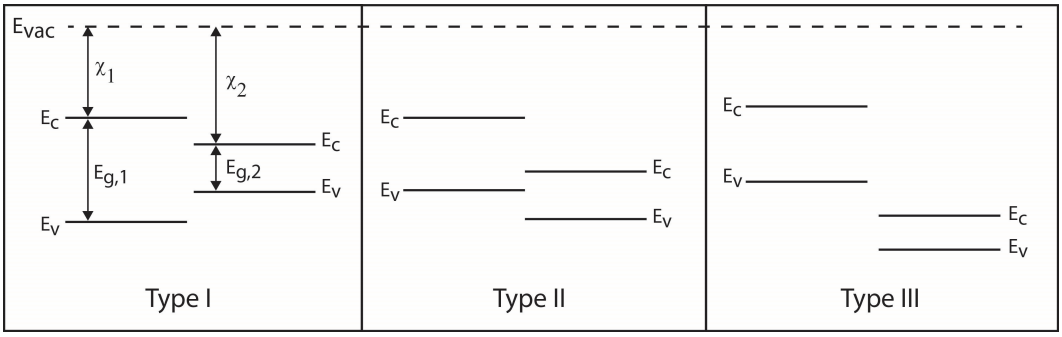

Fig. 2-8. Heterojunction band alignment types, adapted from [14]

2.1.4.1 Recombination Paths in Heterojunction Devices

The ideal diode equation assumes no recombination in the space charge region and no recombination at the P-N junction interface, allowing only for recombination in the Quasi-Neutral Region. However, thin film devices employ **heterojunctions**, which use different materials for the absorber and window layers, and which frequently experience recombination in these regions due to bulk and interfacial defects. Poor band alignments between the absorber and window layers can exacerbate these recombination mechanisms. Fig. 2-9 shows the most critical recombination paths in heterojunction devices [5]:

(A) Recombination in the QNR, with a recombination barrier height equal to the absorber band gap, $E_{g,abs}$

(B) Recombination in the Space Charge Region, with a recombination barrier height still equal to $E_{g,abs}$

(C) Recombination at the absorber-window layer interface, with a modified recombination barrier height due to band offset configuration. In the **cliff band offset** configuration shown, the barrier height to recombination decreases, such that $\phi_{b,int} < E_{g,abs}$

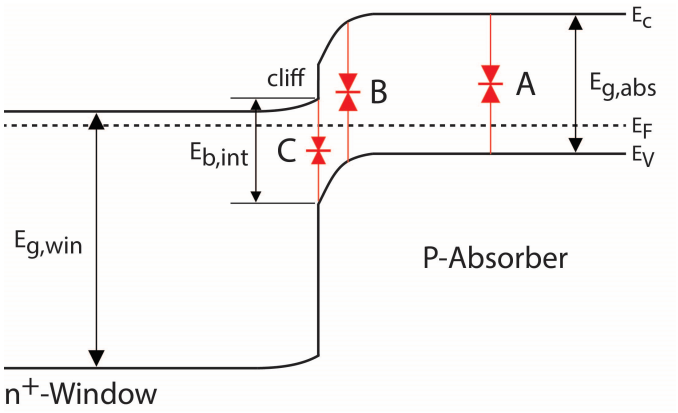

Fig. 2-9. Recombination paths in heterojunction devices, redrawn from [15]

Recombination within the space charge and interface regions introduces an additional diode current, referred to as a **recombination current**, which sums superpositionally with the nominal diode current [1]. In forward-bias, indirect (R-G) center recombination $J_{R\text{-}G}$ takes a

similar form to the nominal diode current J_{diff}, such that $J_{diff} \alpha (J_{0,diff})\cdot\exp(qV_A/k_BT)$ and $J_{R\text{-}G} \alpha (J_{0,R\text{-}G})\cdot(qV_A/2k_BT)$ [1]. Subsequently, the **diode ideality factor A** accounts for the relative contribution of the each term, such that an ideal diode with negligible recombination current has A~1 and a non-ideal diode dominated by the recombination current has A~2 [1]. The more general diode equation can then be written as follows [5, 16]:

$$J(V) = J_0\left(e^{\frac{q}{Ak_BT}(V-R_SJ)}\right)+\frac{V}{R_{SH}}-J_L \tag{2-16}$$

$$J_0 = J_{00}e^{\frac{-\phi_B}{Ak_BT}} \tag{2-17}$$

where J_0 is the diode saturation current density, A is the diode ideality factor, R_S is the series resistance, R_{SH} is the shunt resistance, J_L is the light-generated current, J_{00} is a reference current density, and ϕ_B is the activation energy associated with the dominant recombination mechanism. J_{00} represents a constant prefactor (e.g. only weakly dependent on temperature) that depends on the active recombination mechanism [5]. See Table 2.2 in [5] for a collection of J_{00} terms for the different recombination mechanisms. Using the general diode equation, the **open-circuit voltage** may also be redefined as follows [16]:

$$V_{OC} = \frac{\phi_B}{q} - Ak_BT\ln\left(\frac{J_{00}}{J_L}\right) \tag{2-18}$$

where **ϕ_B is the recombination barrier**. As interface recombination starts to dominate the diode current, the recombination barrier decreases, reducing the open-circuit voltage. Table 2-1 summarizes the relationships between the dominant recombination mechanisms and the diode ideality factor, recombination barriers and V_{OC} variation with band gap.

The shift to interface recombination, and the subsequent deficiency in V_{OC} rise with increasing bandgap **(E_g/q-V_{OC})**, can be explained in terms of the band alignment at the interface. A non-optimal **cliff** alignment can be seen in Fig. 2-9, while an optimal **spike** alignment can be seen in Fig. 2-10. The spike alignment shifts the Fermi level at the absorber interface closer to the conduction band, increasing the electron concentration and creating an inversion layer [11]. Photogenerated minority carriers in the P-type layer (electrons) that are transported across the depletion region then transit the interface with a lower population of holes, decreasing the probability of recombination and minimizing interface recombination [11]. This can be explained using Eqn. (2-4), which shows that R-G recombination experiences a maximum when hole and electron populations are equal, as would be the case with a E_F near the midgap [4]. The spike represents a barrier to the photogenerated electrons, but when kept small ($0 < \Delta E_C < 400$meV) the electrons can readily tunnel through it without detrimental effect to the device operation [11].

Table 2-1. The relationships between recombination mechanisms and device properties

Dominant Recombination Mechanism	Diode Ideality Factor, A	Recombination Barrier, ϕ_B (eV)	V_{OC} dependence on band gap E_g
QNR (A)	1	E_g	V_{OC} increases ~ linearly with E_g
SCR (B)	1 – 2	E_g	V_{OC} increases ~ linearly with E_g
I/F (C)	1 – 2	< E_g	V_{OC} may increase with E_g, depending on band alignment

The best performing CIGSe devices have utilized Ga:[In+Ga] ratios of ~25%, corresponding to a band gap of ~1.2eV [13]. For larger Ga concentrations, the V_{OC} does not increase linearly with E_g representing again the so-called **V_{OC}-deficit** [13]. With increasing Ga:[In+Ga] above ~25%, the conduction band alignment shifts from $\Delta E_C > 0$ to $\Delta E_C < 0$, reducing the inversion and increasing the interface recombination, thereby degrading the open-circuit voltage, as described above [17, 18]. The introduction of Ga has also been shown to influence the formation of characteristic deep-level (~300meV) defects in CIGSe. This defect level exhibits a minimum density near Ga:[In+Ga] ~ 30%, and therefore may also play a role in the increased recombination observed with increasing Ga-content [19].

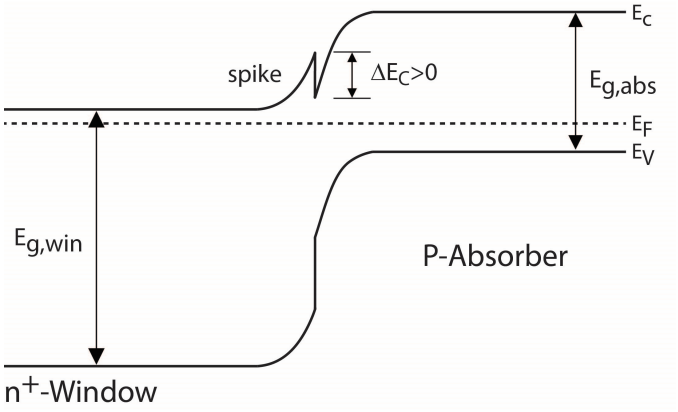

Fig. 2-10. Optimal ("spike") band alignment for heterojunction devices

Several manuscripts have reported theoretical or experimental band alignments for CIGSeS and CZTSeS devices, with varying absorber layer alloys and buffer-window layers. Table 2-2 and Table 2-3 summarize some of the reported conduction band alignments, where $\Delta E_C < 0$ denotes a cliff and $\Delta E_C > 0$ denotes a spike. This list is not exhaustive and is meant only to provide an introduction to the reported values.

Table 2-2. Reported conduction band alignments for CIGSeS-Buffer interfaces

Layer Configuration	ΔE_C (eV)	Method	Reference
CISe / CdS	0.38	X-Ray Photoelectron Spectroscopy	[19]
CISe / ZnS	1.26	Ultraviolet Photoelectron Spectroscopy	
CGSe / CdS	-0.16	Not Identified	
CIS / CdS	-0.45	Not Identified	

Table 2-3. Reported conduction band alignments for CZTSeS-Buffer interfaces

Layer Configuration	ΔE_C (eV)	Method	Reference
CZTS/ ZB-CdS	0.18 – 0.22	Density Functional Theory	[20]
CZTS/ W-CdS	0.28		
CZTS/ ZnS	1.29 – 1.36		
CZTS / CdS	-0.34	X-Ray Photoelectron Spectroscopy	[21]
CZTS / CdS	0.41	Ultraviolet Photoelectron Spectroscopy, Photoluminescence, and External Quantum Efficiency	[22]
$CZT(S_{0.45}Se_{0.55})_4$ / CdS	0.48		
CZTSe / CdS	0.48		
CZTS / CdS	-0.33	Ultraviolet and Inverse Photoelectron Spectroscopy	[23]

2.1.5 Design Guidelines for Heterojunction Devices

Scheer and Schock provide a useful summary of design guidelines for thin film heterojunction devices in [5]. For single junction devices, the absorber band gap should be between 1.0 and 1.6eV with a thickness greater than 2X the mean radiation penetration distance [5]. The absorber should be P-type because electrons (the active minority carriers) have higher mobilities, and it should have a hole concentration of 10^{15} – $10^{17}cm^{-3}$ to maintain an extended space

charge region with limited recombination [5]. Most device quality thin film CIGSe absorbers also exhibit Hall mobilities of 15 – 200cm^2/V·s [13]. The back electrical contact should make ohmic contact with the absorber. The buffer/window layer should have a large band gap, a low defect density and a high electrical conductivity [5]. Further, the conduction band alignment between the absorber and the buffer/window layer should form a small spike ($0 < \Delta E_c < 300$meV) to facilitate a surface layer inversion that minimizes interfacial recombination without significantly obstructing the photocurrent [5].

2.2 THE CIGSES MATERIAL SYSTEM

I would like to acknowledge Scheer and Schock [5] and Shafarman [13], as this CIGSeS material background section draws strongly from these works. For a more comprehensive review, the reader is strongly encouraged to visit these excellent texts.

2.2.1 Material Properties

2.2.1.1 Composition and Structure

$CuInSe_2$ is a P-type semiconductor material with a direct band gap (~ 1.04eV) and high optical absorption (>10^4 cm^{-1}) [5, 13, 24]. The $CuInSe_2$ (CISe) and the related $CuGaSe_2$ (CGSe) material system both adopt the chalcopyrite structure, with tetragonal bonding similar to the zinc blende structure [5, 13, 24]. In this II-VI analog, cations of the zinc blende structure (Zn) are alternately replaced by Cu and In, such that every Se atom tetragonally bonds with two Cu atoms and two In atoms, as in Fig. 2-11 [5, 13, 24].

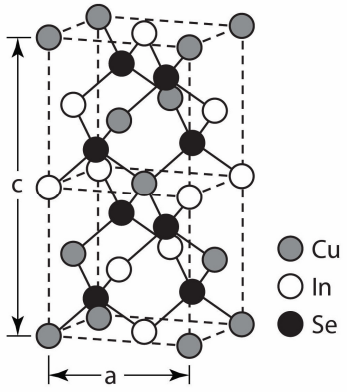

Fig. 2-11. Unit cell of Chalcopyrite CISe, reproduced from [13]

The chalcopyrite CISe structure has a reduced symmetry relative to the zinc blende structure, due to the chemical differences of the two cations, which doubles the unit cell size and yields more complex opto-electronic properties [5, 13, 25]. In particular, bond asymmetries between Cu-Se and In-Se cause two structural modifications to the crystal: tetragonal distortion of the unit cell and anion (Se) displacement from the ideal lattice site [5, 13]. The presence of Cu, a transition metal, further enhances differences in the CISe compared to other analogous II-VI

compounds, due to the strong participation of d-orbitals in bonding and their hybridization with anion (Se) sp states [5, 13, 25].

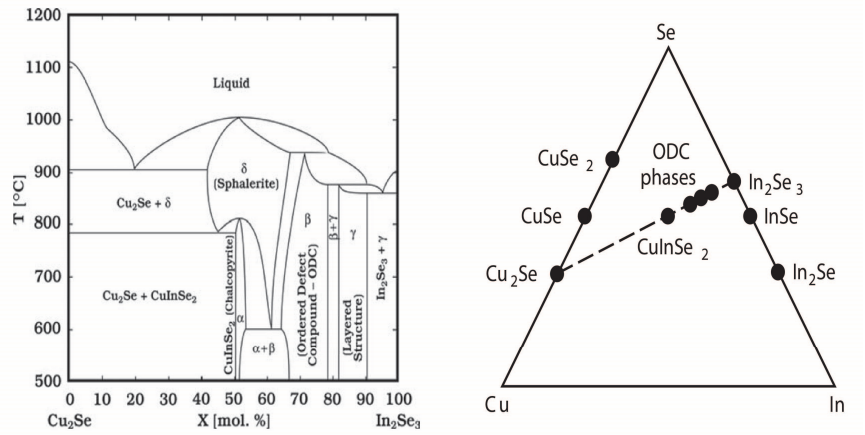

Fig. 2-12. Pseudobinary Cu_2Se - In_2Se3 phase diagram and ternary Cu-In-Se phase diagram, reproduced from [13]

A **pseudobinary isopleth** has been shown to connect **Cu_2Se** and **In_2Se_3** phases [5, 13]. In particular, literature has reported chalcopyrite CISe and a number of **ordered defect compounds (ODCs)**, such as $CuIn_3Se_5$ and $CuIn_5Se_8$, fall on or near this Cu_2Se-In_2Se_3 tie line under standard thin film growth conditions (e.g. under excess Se supply) [5, 13]. Consequently, the pseudobinary phase diagram shown in Fig. 2-12(a) has been used as a phase model to describe the growth behavior of CISe films under varying Cu:In ratios [5, 13, 24]. The ordered defect compounds are so named because they have a crystal structure described by the chalcopyrite structure with a "structurally ordered insertion of intrinsic defects" [13]. Phase diagrams represent systems in thermodynamic equilibrium, but some thin film deposition techniques (e.g. pulsed laser deposition) may involve non-equilibrium processes. As a general guide, however, phase formation of CIGSe thin films may be framed by the transitions prescribed by the relevant phase diagrams.

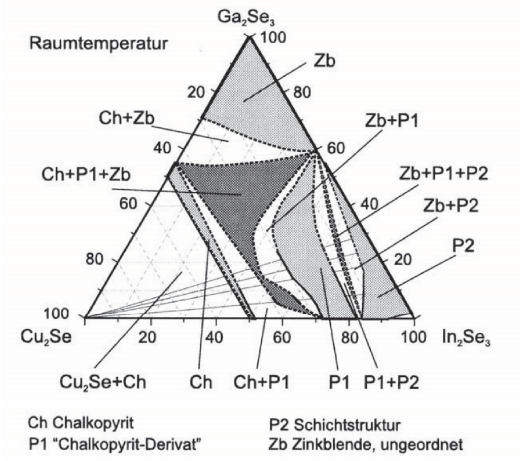

Fig. 2-13. Proposed isothermal quasi-ternary Cu_2Se-In_2Se_3-Ga_2Se_3 phase diagram, reproduced from [24]

Noting that most CISe films are grown at 500 – 550°C [5, 13], Fig. 2-12(a) shows that there exists a narrow region where **α-phase** (chalcopyrite) CISe may be formed. Films that are grown **Cu-rich** always exist as a combination of **α-CISe** and **Cu_2Se** phases. Films that are grown **Cu-poor** tend to exist as a combination **α-CISe** and **ODC** compounds, which develop from stable neutral defect complexes composed of Cu vacancies and In_{Cu} antisite subsitutions [$2V_{Cu}^{-} + In_{Cu}^{2-}$] [5, 13].

Frequently, $CuInSe_2$ films are alloyed with Ga in order to widen the band gap, as $CuGaSe_2$ has a direct band gap of 1.6eV [5, 13]. The effect of Ga-alloying on the phase diagram of CISe can be approximately described according to the **pseudo-ternary phase diagram** shown in Fig. 2-13. Again, the single-phase chalcopyrite region remains narrow, broadening slightly with increasing Ga:[In+Ga] and decreasing Cu concentration. This phase broadening can be attributed to the higher formation energy of Ga_{Cu} compared to In_{Cu}, which destabilizes defect clusters that contribute to the formation of the ODC compounds [13, 24].

2.2.1.2 Band Structure and Optical Properties

As described in the previous section, CISe has a direct band gap of ~ 1.04eV and CGSe has a direct band gap of 1.6eV, with both systems demonstrating high optical absorption (>10^4 cm^{-1}) above their band gaps. Typical optical absorption curves for device quality CISe and CGSe are shown in Fig. 2-14.

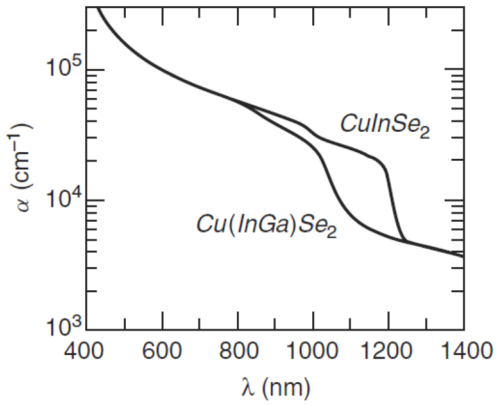

Fig. 2-14. Optical absorption curves for device quality $CuInSe_2$ and $CuGaSe_2$, reproduced from [13]

The **band gap variation** of CIGSe with **Gallium alloying**, Ga:[In+Ga], may be described according to the following [13]:

$$E_g = 1.04 + 0.65x - 0.26x(1-x) \tag{2-19}$$

where E_g is the band gap, x is the alloying ratio Ga:[In+Ga], and 0.26 is the bowing parameter. Further, exponential **Urbach tails**, which are associated with the degree of crystal disorder and described in more detail in Ch 4, are evident in CISe and CGSe absorbers (the linear portion of the

absorption curve below the band gap energy). For alloyed systems, the Urbach energy was shown to increase away from the pure ternary end points [5], consistent with increased alloy disordering.

To first order, the **optical functions** of ternary chalcopyrite compounds are similar to their binary analog compounds (zinc blende) [25]. However, crystal symmetry reductions and bonding asymmetries, previously noted, tend to remove degeneracies through crystal field and spin-orbit perturbations [25]. Further, the Cu-d states hybridize with the p-states, pushing up the valence band maximum and reducing the band gap compared to similar II-VI systems [5, 13, 25].

The **electronic band structure** of CISe and related chalcopyrite systems have been studied extensively using both theoretical and experimental methods. The band structures have been calculated theoretically using the analytical framework of Density Functional Theory (DFT) [26-28], and the band structures have been characterized experimentally by Angle-Resolved Photoemission Spectroscopy (ARPES) [29]. Optical characterization methods such as absorption spectroscopy and spectroscopic ellipsometry provide information about optical transitions within the material, which can yield indirect information about its electronic band structure. See references [5, 25, 28, 30] for more detailed descriptions of the electronic band structures and optical properties of CISe. Experimental **refractive indices** and **dielectric functions** for CISe and CGSe are given in [25].

2.2.1.3 Defect and Electronic Properties

CISe absorbers may be doped P-type and N-type by modulating off-stochiometry deviations [13]. **Cu-rich CISe** films are **always P-type**, with copper vacancies (V_{Cu}) and Cu antisite substitutions (Cu_{In}) acting as the dominant doping defects [5, 13]. **Cu-poor CISe** films may be doped **P-type or N-type** with Se-excess or Se-deficient annealing conditions, respectively [13]. Selenium acts an amphoteric defect, and its doping behavior depends on the Fermi level in the film and the formation of defect complexes with copper vacancies [5, 13]. **CGSe** films, on the other hand, are **always P-type** [5, 13, 19]. As E_F shifts towards the CB with increasing N-type doping, the defect formation energy of V_{Cu} drops rapidly, inducing the spontaneous creation of compensating acceptors and pinning the Fermi level [5, 31]. Further, the addition of Ga in CIGSe alloys tends to suppress the formation of the neutral defect complex $(2V_{Cu}^{-} + In_{Cu}^{2+})^{0}$, which causes V_{Cu} and $In(Ga)_{Cu}$ defects to remain active as recombination centers [5, 13].

CIGSe absorber layers in high quality devices are P-type with hole concentrations of 10^{15} – $10^{16}cm^{-3}$ [5, 13]. Hole mobilities of 15 – $200cm^2/V{\cdot}sec$ and 20 – 40 $cm^2/V{\cdot}sec$ have been reported in bulk crystals and polycrystalline films, respectively [5, 13]. Notably, thin film CIGSe grains are typically columnar, so that device operation will mostly involve intra-grain (or bulk) transport [5, 13]. However, hole mobilities are typically measured laterally in conventional Hall effect systems. Consequently, Hall measurements may not accurately represent the hole transport properties of polycrystalline films [5, 13].

Point Defects

Twelve intrinsic (native) point defects are possible in the $CuInSe_2$ system, as shown in Table 2-4. Depending on their charge states, these defects may exhibit varied transition energy levels and thus varied doping properties. For instance, $Cu_{In}^{(-/0)}$ acts as a **shallow** P-type dopant with transition energy ~300meV above the valence band edge, while $Cu_{In}^{(2-/-)}$ acts as a **deep** level defect with transition energy close to midgap [28]. The superscript (X/Y) on the defect label denotes a given transition of the defect, such that X corresponds to the initial charge state and Y the final charge state of the defect [32]. Defects that may act as either a P-type or N-type dopant (e.g. V_{Se}), depending on their charge state, are denoted **amphoteric**.

The creation of a defect depends on its **formation energy**, which varies with its electronic potential (e.g. Fermi level position) and its chemical potential (e.g. the composition of the film) [28]. Using first-principles calculations, Zhang showed that in **Cu-poor, P-type films**, defects with the lowest formation energies are ordered as: $V_{Cu} < In_{Cu} < V_{In} < Cu_{In} < I_{Cu}$ [28]. Domain showed a slightly different ordering: $V_{Cu} < Cu_{In} < V_{In} < In_{Cu} < I_{Cu}$ [5, 33]. For calculated defect formation energies, see [5, 28, 31, 33]. Copper vacancies (V_{Cu}), indium vacancies (V_{In}) and copper antisite substitutions (Cu_{In}) are all low-formation energy P-type dopants. However, V_{Cu} have shallow transition energies, and no charge states with deep level transition energies [28]. Therefore, copper vacancies represent the most benign P-type dopant, and compositions are typically grown Cu-poor, which lowers V_{Cu} formation energies and raises Cu_{In} formation energies [28].

Table 2-4. Native point defects in $CuInSe_2$ [5, 28]
(P-Type: $E_{defect} - E_{VB} < 300meV$, N-Type: $E_{CB} - E_{defect} < 300meV$)

Defect Type	Point Defect	Doping Type
Vacancies	V_{Cu}	P-Type
	V_{In}	P-Type / Deep
	V_{Se}	P-Type / N-Type
Interstitials	I_{Cu}	N-Type
	I_{In}	--
	I_{Se}	--
Antisite Substitution	Cu_{In}	P-Type / Deep
	In_{Cu}	N-Type
	Cu_{Se}	--
	Se_{Cu}	--
	In_{Se}	--
	Se_{In}	--

Anion-cation antisite substitutions, such as Cu_{Se}, are calculated to have prohibitively high formation energies (>5eV) [5]. Anion (Se) vacancies have shown complex behavior, acting as

amphoteric dopants and forming metastable defect complexes [5, 13]. It has been suggested that selenium vacancies predominately exist as defect complexes, (V_{Se} + V_{Cu}), as discussed in the following section [5].

The point defect properties of CIGSe films have been investigated using a variety of techniques, including photoluminescence spectroscopy, electroluminescence spectroscopy, deep level transient spectroscopy, and temperature-dependent Hall effect measurements [5, 13, 28].

Defect Complexes

Closely spaced point defects may interact with each other via charge transfer, electrostatic interaction, or atomic relaxation [28]. In some cases, these defects may significantly lower their formation energies through these interactions, forming ordered structures known as **defect complexes** [28]. In the $CuInSe_2$ system, a number of potential defect complexes have been modeled and investigated, including: $(2V_{Cu}^{-}+In_{Cu}^{2+})^0$, $(V_{Cu}^{2-}+I_{Cu}^{+})^0$, $(Cu_{In}^{2-}+2I_{Cu}^{+})^0$, $(Cu_{In}^{2-}+In_{Cu}^{2+})^0$, $(V_{Se}^{2+}+V_{Cu}^{-})^+$, and $(V_{Se}^{0}+V_{Cu}^{-})^-$ [5, 13, 28, 33, 34]. Uncharged complexes are referred to as **neutral defect complexes**.

The **$(2V_{Cu}^{-}+In_{Cu}^{2+})^0$ neutral defect complex** represents the most significant defect complex. This defect has formation energies less than or equal to zero in Cu-poor CISe crystals [5, 28], introduces minimal distortion into the unit cell [5], and reduces deep trap states by pushing V_{Cu} and In_{Cu} transition energies out of the midgap [5, 28]. Subsequently, large off-stoichiometries in the Cu-poor region of CISe may be accommodated, creating ordered defect compounds such as $CuIn_3Se_5$ and $CuIn_5Se_8$ [5, 13, 28, 34], while stabilizing V_{Cu} acceptors, removing recombination centers and remaining electrical inactive [13, 28].

The **(V_{Se} + V_{Cu}) charged defect complex** represents another significant defect complex in CIGSe films, which can cause metastable doping behavior [5, 13]. The binding energy (different than formation energy) for the (V_{Se} + V_{Cu}) complex in both CISe and CGSe are negative, indicating that the majority of selenium vacancies present in the crystal will be bound in this anion-cation defect complex [5]. Different bonding states of V_{Se} (0 and 2^+) yield different possible bonding states for the defect complex, with a positive charge state (donor) corresponding to the V_{Se}^{2+} configuration and a negative charge state (acceptor) corresponding to V_{Se}^{0} [5, 13].

2.2.1.4 Grain Properties

Polycrystalline thin films contain large numbers of grain boundaries (GBs), and the device performance associated with these absorbers depends on the size, orientation, and electronic properties of the grains and their boundaries. One of the major advantages of the CIGSe material system has been the **benign nature of the grain boundaries** in polycrystalline thin films [5, 13, 24]. In fact, polycrystalline absorbers have outperformed single-crystal absorbers, suggesting that the GBs may actually improve overall device performance [13]. This grain boundary behavior has been attributed to a lowering of the VB edge at the interface, due to Cu-depletion at the surface, which reduces GB recombination of the photogenerated minority carrier electrons. That is, GBs

tend to be Cu-deficient, possibly due to band-bending induced electromigration [13], which decreases the Cu-d electron states contributing to the uppermost part of the VB, thereby lowering the VB edge [5, 13, 24]. This dip in the VB edge creates a hole barrier, repelling holes away from the GBs, and consequently reducing recombination of minority carrier electrons [5, 13, 24].

As shown in Fig. 2-12(b), $CuInSe_2$ under Cu-rich conditions exists as a combination of Cu_2Se and chalcopyrite CISe. In these conditions, the $Cu_{2-X}Se$ phases preferentially segregate at the grain boundaries and the surfaces of the films [5, 13, 24]. Cu_2Se has the same Se-sublattice and a similar lattice constant to CISe [24]. **$Cu_{2-X}Se$** has been proposed to form **quasi-liquid phases** at the elevated temperatures of growth and annealing, which boost the atomic mobilities of the metal ions (Cu and In), thereby enhancing recrystallization and grain growth of the CISe phase [5, 13, 24]. Some studies, however, have indicated that this mechanism becomes less significant in the presence of Na and Ga in the films [13].

2.2.2 Absorber Fabrication Methods

Two fundamental approaches may be adopted to fabricate the CIGSe absorber layer: 1) a single-step fabrication including deposition (metals and chalcogen) and crystal formation, and 2) a two-step fabrication including precursor deposition (metals only) followed by annealing reaction with the chalcogen element [5]. A wide range of thin film deposition techniques have been applied to both of these fabrication methodologies, including pulsed laser deposition [35, 36], electrodeposition [37], sputtering [5, 13, 38], spray pyrolysis [39], and nanocrystal synthesis methods [40]. However a three-stage co-evaporation has yielded the highest efficiency cells [41]. Pulsed laser deposition, the primary fabrication tool for CIGSe in this dissertation, will be discussed in more detail in Ch 3, 5 and 6. The champion three-stage co-evaporation method and the basic deposition reaction method are briefly summarized here.

Design Properties of CIGSe Absorber Layers

Scheer summarizes the requirements for high quality CIGSe film growth as follows: 1) the substrate temperature should reach at least 500°C during crystal formation, the crystal formation should proceed under excess chalcogen (Se or S), and the final film composition should be Cu-poor with Ga:[In+Ga] = 0.2 – 0.3 and include Na-doping [5].

2.2.2.1 Co-Evaporation

Co-evaporation involves evaporation of multiple elements simultaneously under high-vacuum conditions, using Knusden-type effusion cells [13]. A major advantage of the method is its ability to carefully tailor growth conditions over time, taking advantage of the fortuitous **diffusion properties** of the metallic components in the film. Copper diffuses sufficiently fast during film growth in order to ensure a homogeneous distribution after film growth [24]. Indium and gallium, on the other hand, diffuse slowly, enabling the formation of through-thickness gallium gradients by altering the In/Ga flux rates [24]. Typically, two- and three-stage sequences, with varying elemental flux rates, are used to enhance film growth and to vary the through-thickness compositions.

The **sticking coefficients** of the metal components (Cu, In, and Ga) of CIGSe are very high, such that most of the particles that reach the surface, through evaporation or other physical vapor deposition processes, adsorb on the film [13]. Consequently, the flux rate of the elements roughly determines their deposition rate [13]. Selenium, however, has a higher vapor pressure and lower sticking coefficient than the metal components, and therefore it is evaporated in excess in order to maintain the proper film stoichiometries [13]. The higher overpressure associated with this excess Se also helps prevent re-evaporation of In_2Se and Ga_2Se, which have high vapor pressures [13].

As discussed in the previous section, CIGSe film growth under Cu-rich conditions can increase grain size. However, final film compositions should be Cu-poor, in order to improve their electronic quality [5]. Therefore, the two- and three-stage sequences employ Cu-rich growth periods followed by Cu-poor growth periods. Through-thickness gradients of Gallium, developed by altering the In and Ga flux rates over time, also aid device performance through the creation of a back surface fields that repel photogenerated minority carriers away from the back contact [5, 24]. Table 2-5 summarizes a representative **three-stage deposition sequence** [5, 13].

Table 2-5. Typical Three-Stage Co-Evaporation Process for CIGSe Thin Films

Stage	Element Fluxes	Substrate Temp
1	In + Ga + Se	300°C
2	Cu + Se	500 – 600°C
3	In + Ga + Se	500 – 600°C

In this three-stage process, Stage 1 involves the nucleation of In_xSe_y and Ga_xSe_y compounds [13, 42], which develop small grains in the absence of grain size-enhancing $Cu_{2-X}Se$ phases [5]. Stage 2 recrystallizes these small grains to form larger grains, a process enhanced by the $Cu_{2-X}Se$ growth mechanism [5]. Stage 3 discontinues the Cu element flux to yield overall Cu-poor films [5]**. In a typical two-stage process**, the first stage consists of a Cu-rich growth period, such that large grains nucleate on the substrate, leading to final films with large grains but also large surface roughness [5].

2.2.2.2 Deposition Reaction

The two-step deposition reaction method represents a simplified fabrication technique compared to three-stage co-evaporation. However, this method does not allow as much control of the through-thickness composition of the films or the growth properties of the films, since diffusion and reaction processes drive the crystal formation [5]. The **metal precursor** may be deposited in a Stacked Elemental Layer (SEL) configuration or as alloys or compounds [5]. The **chalcogen** may be introduced into the metal precursor film by a reactive gas (H_2Se or H_2S) or an evaporated elemental gas (Se_2 or S_2) [5]. The highest performing devices fabricated using the deposition reaction method have implemented surface sulfurization of the films, achieved by introducing H_2S gas at the end of the selenium (H_2Se) annealing sequence [5, 13]. The improved

performance has been attributed to a reduction of interface recombination, by widening of the band gap at the junction, and to passivation of recombination centers [5].

The final cation (metal) ratios are mostly dictated by the initial precursor ratios, although some In_2Se may be lost through the annealing process [5]. Fortunately, the inherent formation properties associated with $CuInSe_2$ and $CuGaSe_2$ yield favorable through-thickness compositions during the reaction [5]. $CuInSe_2$ crystallizes much faster than $CuGaSe_2$, and since the crystallization process originates at the solid(metal)-gas(chalcogen) interface, the films tend to have more CISe near the front surface and more CGSe near the back surface, creating approximately the desired Gallium-profile [5]. The use of compounds as precursors, through electrodeposition or nano-sintering, may introduce processing complexities, since the "recrystallization process competes with the decomposition of the compound. Optimization may therefore be more difficult" [5].

2.2.3 Photovoltaic Devices

The current champion laboratory cells (η~20.3%) [41] and commercial modules (η~16.6%) [43] have been produced using CIGSe absorber layers alloyed with Ga (Ga:[In+Ga] ~ 0.3) and fabricated by co-evaporation and sputtering processes, respectively. The highest performing devices have utilized a substrate (not superstrate) architecture with the conventional layer configuration shown in Fig. 2-15. The processing techniques conventionally used to fabricate the remaining device layers include sputtering of Mo, chemical bath deposition of CdS, sputtering of ZnO and ITO layers, and evaporation of Ni:Al collection grid [13].

A great number of works have investigated the effects of different layer materials and fabrication methods on the device performance of CIGSeS solar cells, well-documented in review articles and textbooks, including for example [5, 13, 44]. For a more detailed review of the device performance and tradeoffs associated with varying architectures, the reader is referred to these excellent texts.

The champion 20.3% device fabricated by the Centre for Solar Energy and Hydrogen Research Baden-Württemberg (ZSW) demonstrated a FF, V_{OC}, J_{SC}, E_g, and E_g/q-V_{OC} of 77.7%, 730mV, 35.7mA/cm^2, 1.14eV, and 0.410V, respectively [41, 45]. As described in Section 2.1.3.4, optical losses from shading, reflection, and incomplete absorption in the absorber layer cause short-circuit current density losses in the device. For the conventional CIGSe device architecture, the optical losses are identified, in decreasing magnitude, as reflection from the top surface of the device, incomplete generation in the CIGSe layer, absorption in the ZnO layer, shading from the Ni:Al collection grid, absorption in the CdS layer, and incomplete collection in the CIGSe layer [13]. Losses in FF and V_{OC} are attributed to primarily to SRH recombination in the SCR of the CIGSe layer [13]. As described in Section 2.1.4.1, advantageous conduction band alignment between CIGSe and CdS mitigates interface recombination via type-inversion at the junction [13]. The non-optimal band gap of 1.1 – 1.2eV used in high performance devices also represents a device performance loss. For single-junction devices, band gaps near 1.35eV provide the theoretically

maximum performance, accounting for the tradeoff between V_{OC} and J_{SC} [11]. However, as detailed in Section 2.1.4.1, wider gap CIGSe devices achieved by Ga-alloying have demonstrated high V_{OC} deficits and degraded device efficiency, attributed primarily to shifts in conduction band alignment at the junction from **spike** to **cliff** with increasing band gap [13].

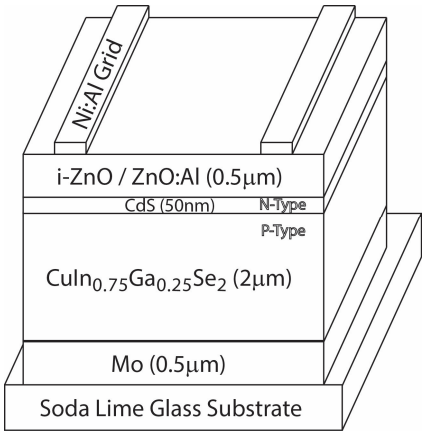

Fig. 2-15. Schematic of conventional CIGSe photovoltaic device, adapted from [13]

Sodium and **oxygen** have been shown to play significant roles in the performance of high-efficiency CIGSSe devices [5, 13, 24]. The **inclusion of Na** during CIGSSe thin film growth increases the net carrier concentration [24], increases the open circuit voltage [24], increases the FF [5, 24], and widens the chalcopyrite phase region [5] in particular for varying Cu composition [24]. These effects have been attributed to the electrical passivation of grain boundaries via Na-catalyzed oxygenation of dangling In-bonds [5, 13] and Na substitutions of Cu, In, and Ga sites [24]. Additional effects may include reduced Cu and In diffusion, enhanced chalcogen incorporation, and increased $MoSe_2$ formation at the back contact during film growth [5]. The **optimum doses of Na** for CIGSe and CIS thin films are ~ 0.1% and ~1%, respectively [5, 24, 44]. Higher doses tend to degrade performance and reduce adhesion by decreasing grain size and increasing film porosity [5, 24]. The **Na can be introduced** into the films by diffusion from a Na-containing substrate (e.g. Soda Lime Glass) or through a Na-containing precursor layer, such as NaF or Na_2S [5, 24, 44]. The method of introduction has been shown to have negligible effect on the behavior of the Na influence in the films [5, 24].

Thin film CIGSeS solar cells have been studied intensively for over 30 years, and both laboratory cells and modules have achieved very high efficiencies. Fundamental research into the material and device behavior of CIGSeS remains on-going, however, as debate still surrounds some aspects of its defect, grain boundary and junction physics [41]. Further, Jackson notes, the traditional device enhancement techniques used in silicon solar cell production have not been fully exploited in CIGSeS thin film technology [41]. Finally, in order to successfully scale production, the fabrication cost must be reduced and the throughput increased while still maintaining the high-quality device performance that has been demonstrated.

2.3 THE CZTSeS MATERIAL SYSTEM

I would like to acknowledge Persson [46], Olekseyuk [47] and Chen [48], as this CZTSeS material background section draws strongly from these works. For a more comprehensive review, the reader is strongly encouraged to visit these excellent texts.

2.3.1 Material Properties

2.3.1.1 Composition and Structure

Cu_2ZnSnS_4 is a P-type semiconductor material with a direct band gap (~ 1.5eV) and high optical absorption (>10^4 cm^{-1}) [46]. The Cu_2ZnSnS_4 (CZTS) and the related $Cu_2ZnSnSe_4$ (CZTSe) material systems (group I-II-IV-VI) both adopt the kesterite structure, with tetragonal bonding similar to the chalcopyrite structure. In this I-III-VI derivative, the group III cations (In) of the CISe crystal are alternately replaced by Zn and Sn, such that every Se atom tetragonally bonds with two Cu atoms, one Zn atom, and one Sn atom [49], as shown in Fig. 2-16.

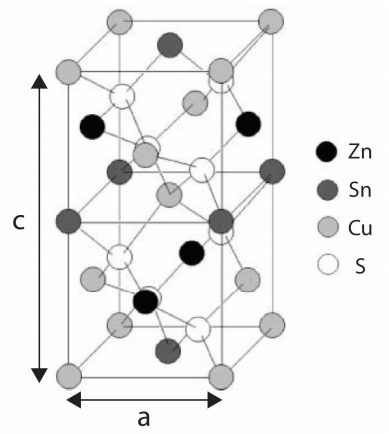

Fig. 2-16. Unit cell of Kesterite CZTS, reproduced from [50]

The CZTS(Se) crystal may also adopt a stannite structure, characterized by a slightly altered stacking arrangement of the cations as described in [46, 49] but with the S-anion still bonded to two Cu atoms, one Zn atom, and one Sn atom. First-principles calculations indicate that the kesterite structure has a slightly lower formation energy than the stannite structure, and so this kesterite structure has been typically designated as the prevailing phase [46, 49]. However, kesterite, stannite, and some disorder modifications, related through Cu and Zn intermixing in the Cu-Zn plane, exhibit similar formation energies and thus may coexist under equilibrium conditions [46]. Persson suggests that the coexistence of these phases may account for reported opto-electronic property variations and disorder observed in CZTSSe [46].

The kesterite CZTS structure has a reduced symmetry relative to the chalcopyrite CISe structure, due to chemical differences of the additional cations, which modifies its opto-electronic properties [46]. Like CISe, bond asymmetries between Cu-S and Zn-S and Sn-S cause two structural modifications to the crystal: tetragonal distortion of the unit cell and anion (S)

displacement from the ideal lattice site [46, 51]. These structural modifications alter the character of the band structure, as described in Section 2.3.1.2.

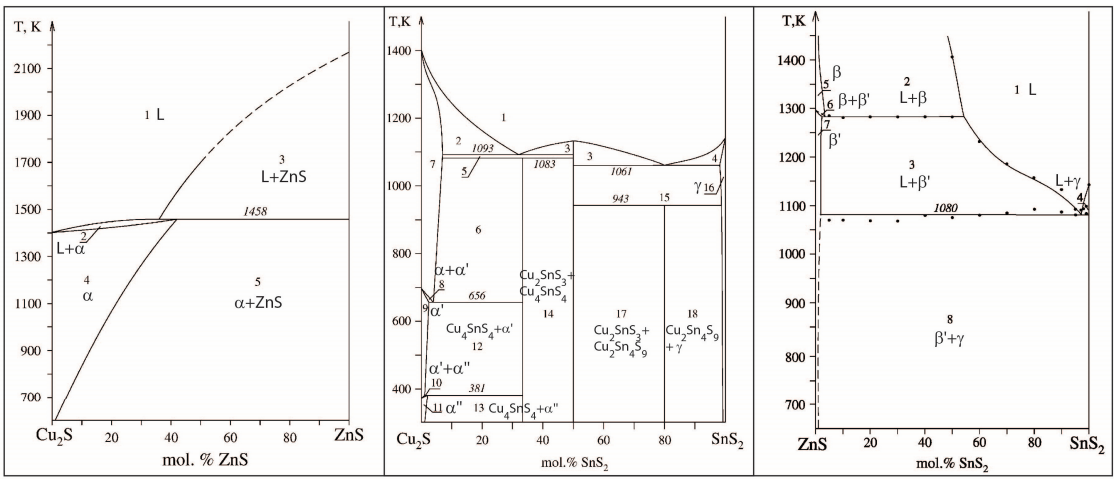

Fig. 2-17. Pseudobinary Cu_2S – ZnS, Cu_2S – SnS_2, and ZnS – SnS_2 phase diagrams, reproduced from [47]

Cu_2ZnSnS_4 represents a true quaternary alloy and so a description of it phase stability is inherently more complex. Olekseyuk's work on the phase equilibrium of the Cu_2S-ZnS-SnS_2 system [47] represents the basis for interpretation of phase formation behavior in most of the reported literature on CZTS, with many works including modified or annotated versions of his phase diagrams, for example [12, 52, 53]. **Pseudobinary isopleths** for the various binary limits are reported in [47], including Cu_2S – ZnS, Cu_2S – SnS_2, and ZnS – SnS_2, which are reproduced above in Fig. 2-17. Olekseyuk also provides an isothermal section of the pseudo-ternary phase diagram at 670K [47], as reproduced in Fig. 2-18.

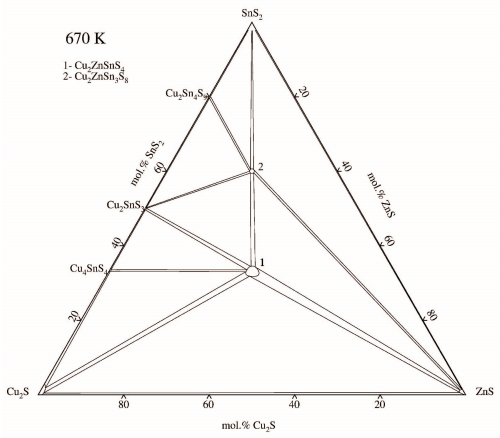

Fig. 2-18. Isothermal pseudo-ternary Cu_2S-ZnS-SnS_2 phase diagram, reproduced from [47]

CIGSe films have demonstrated resilience to off-stoichiometry deviations, under Cu-poor and Se-excess conditions, by forming well-behaved ordered defect compounds, as described in Section 2.2.1.1. CZTS films, on the other hand, have generally demonstrated the formation of detrimental secondary phases under off-stoichiometric conditions [48, 52, 54]. The best

performing devices have been fabricated under Cu-poor, Zn-rich conditions [54], conditions which have been shown to yield ZnS phases in coexistence with kesterite CZTS [55]. Many have framed this off-stoichiometric secondary phase formation in terms of the pseudo-ternary phase diagram in Fig. 2-18, relating the compositional variations in the films with the expected or identified secondary phases, such as [12, 52, 53]. Notably, however, other factors associated with the solid-state reaction pathway to CZTS crystal formation also strongly influence secondary phase formation. In particular, growth kinetics associated with the fabrication method and the film stability at the surface and the back contact play strong roles, as discussed in Chapter 3.

Frequently, Cu_2ZnSnS_4 films are alloyed with Se in order to improve the device performance and/or tune the band gap to lower values, as $Cu_2ZnSnSe_4$ has a direct band gap of 1.0eV [45, 56-58]. A review of the literature did not reveal any reported works investigating the effect of Se-alloying on the phase stability of kesterite CZTSSe. However, the phase equilibria of Se-based CZTSe was investigated in [59], and the single phase region of kesterite CZTSe at 670K appears similar in size to the single phase region of kesterite CZTS at 670K presented in [47]. Grossberg, however, suggests that the previous two reports indicate that the Se-based system may have a larger stoichiometry region where single-phase kesterite exists [60].

2.3.1.2 Band Structure and Optical Properties

As described in the previous section, CZTS has a direct band gap of ~1.5eV and CZTSe has a direct band gap of ~1.0eV, with both systems demonstrating high optical absorption (>10^4 cm^{-1}) above their band gaps [61-63]. Theoretically calculated optical absorption curves for CZTS and CZTSe, considering only direct optical transitions, are shown in Fig. 2-19 [46].

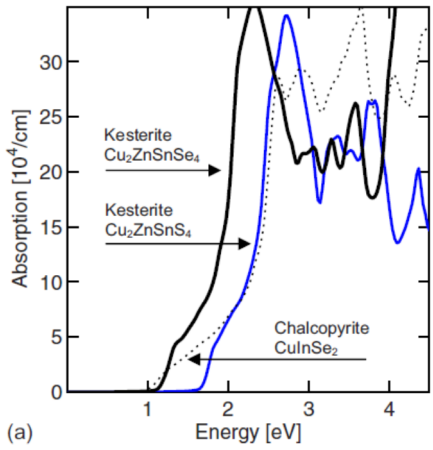

Fig. 2-19. Theoretical optical absorption curves for kesterite CZTS and CZTSe, with chalcopyrite $CuInSe_2$ shown for reference, reproduced from [46]

The **band gap variation** of CZTSSe with **Selenium alloying**, Se:[S+Se], may be described according to the following [61]:

$$E_g(x) = (1 - x)\mathrm{E_g}(CZTS) + xE_g(CZTSe) - bx(1 - x) \quad (2\text{-}20)$$

where E_g is the band gap of the S-Se alloy, E_g(CZTS) is the bandgap of CZTS, E_g(CZTSe) is the bandgap of CZTSe, x is the alloying ratio Se:[S+Se], and b is the bowing parameter. Chen calculated the theoretical bowing parameter as b = 0.07 – 0.10eV [61], and others [62, 63] measured the experimental bowing parameter as b = 0.06 – 0.08eV. The small value of the bowing parameter for this S-Se alloy is attributed to the small chemical differences between S and Se [61]. Experimental measurements of the optical absorption of polycrystalline CZTS and CZTSe have shown evidence of exponential **Urbach tails** below the band edge [64-66]. In one report [64], the Urbach energy was shown to decrease with increasing annealing temperature and increasing annealing time, consistent with decreased crystal disorder.

Similar to chalcopyrite CISe, crystal symmetry reductions and bonding asymmetries, previously noted, tend to remove degeneracies through crystal field and spin-orbit perturbations [46]. Further, like CIGSe, the upper most valence band derives mainly from the hybridization of Cu-d states with S-p states [46, 51, 67]. At lower band energies, Persson notes that Zn-spd, Cu-s and Sn-p also contribute to the valence band [46]. The lowest conduction band, on the other hand, derives mainly from the hybridization of Sn-s states with S-p states [46, 51, 67]. The optical absorption coefficients for CZTS and CZTSe have similar curves to CISe, as seen in Fig. 2-19, except that CZTS(Se) has higher absorption near the band edge, which can be attributed to the flatter dispersion of the lowest CB in this energy region [46]. Due to higher crystal field split-off energy in stannite crystal structures than kesterite, the dielectric functions of stannite demonstrate a higher anisotropy, which the author suggests could be used to help distinguish the presence of stannite and crystal structures in CZTS(Se) materials [46] .

The **electronic band structure** of CZTS and CZTSe systems, including kesterite, stannite and other disorder structures, have been studied using theoretical and experimental methods. The band structures have been calculated theoretically using the analytical framework of Density Functional Theory (DFT) [46, 49, 51, 67], and the band structures have been characterized experimentally by x-ray emission spectroscopy [68], optical absorption [68], and spectroscopic ellipsometry techniques [69, 70]. Experimental **refractive indices** and **dielectric functions** for CZTS are given in [25, 70].

2.3.1.3 Defect and Electronic Properties

CZTSeS absorbers may be doped P-type by native defects, with copper vacancies (V_{Cu}) and copper-zinc antisite substitutions (Cu_{Zn}) acting as the dominant doping defects [48, 57]. Chen indicates that the low formation energies of the acceptor defects compared to the donor defects make N-type doping of CZTSeS difficult to achieve [48]. As the Fermi level shifts towards the CB with increasing N-type doping, the defect formation energy of Cu_{Zn} drops rapidly, inducing the spontaneous creation of compensating acceptors and pinning the Fermi level [48].

Limited works report on the carrier concentration and mobility properties of CZTSeS films, in particular for those associated with champion devices. Mitzi summarizes the electronic properties for some early works in [54], which reports the lowest hole concentration of $2x10^{17}cm^{-3}$ and the highest hole mobility of ~$40cm^2/V$-s in CZTSe. In a high efficiency device (12.6%) using a CZTSeS alloy, Wang reports a drive-level capacitance defect concentration ~$10^{15}cm^{-3}$ and a capacitance-voltage defect concentration up to ~$10^{17}cm^{-3}$, generally associated with bulk and interface defects, respectively [45]. Significant work remains in characterizing the carrier and mobility properties for device quality CZTSeS, particularly under conditions that faithfully represent the films as they exist in devices [54]. Hall effect represents the simplest method to measure the majority carrier concentration and mobility but requires insulating substrates. As Mitzi notes [54] and as Scragg has demonstrated [71], the metal back contact can significantly influence the phase formation and defect properties of the films.

Point Defects

Thirteen intrinsic (native) point defects are commonly reported in the Cu_2ZnSnS_4 system, shown in Table 2-6, although many more defects are possible. Using first-principles calculations, Chen and Nagoya showed that in **Cu-rich films**, the defects with the lowest formation energies are ordered as: $Cu_{Zn} < Zn_{Sn} < Cu_{Sn}$ [48, 72]. Cu_{Zn} remain the lowest formation energy defect across the stable phase range of CZTS from Zn-poor to Zn-rich side and Sn-poor to Sn-rich side. The next highest formation energy defects do, however, vary with Zn and Sn concentrations [48, 72]. For **Cu-poor films**, the lowest formation energy defects are: $Cu_{Zn} < V_{Cu} < Zn_{Sn}$ [48, 72]. The phase stable region of CZTS is extremely small for these conditions, and therefore non-stoichiometric concentrations of Zn and Sn will cause the formation of secondary phases [72]. Anion-cation antisite substitutions (e.g. Cu_S) are not detailed in the few reports on CZTS defect physics, although similar calculations for CISe indicated such defects had prohibitively high formation energies [5].

For calculated defect formation energies, see [48]. Copper-Zn antisite substitutions (Cu_{Zn}), Cu vacancies (V_{Cu}), and Zn-Sn antisite substitutions (Zn_{Sn}) are all low-formation energy P-type dopants. Copper vacancies have shallow transition energies and no charge states with deep level transition energies [48]. Therefore, copper vacancies are considered the most benign P-type dopant. Film growth under Cu-poor, Zn-rich conditions can promote V_{Cu} formation and inhibit Cu_{Zn} formation, and the comparative success of solar devices fabricated using Cu-poor, Zn-rich absorbers [54] has generally been attributed to this defect behavior [57, 73].

The defect properties of CZTSeS films have been investigated using a variety of techniques, including for example photoluminescence (PL) spectroscopy [60, 74], capacitance-voltage and drive level capacitance profiling (DLCP) [45], and scanning transmission microscopy methods [74]. Broad intense PL peaks have been measured in CZTS at varying energies from 1.37 – 1.47eV [74]. In [60], the PL peaks in CZTSeS monograins were shown to narrow with increasing Se-content. Based on blue shifts with laser power, the PL peaks in CZTS have been attributed to donor-acceptor pairs (DAP); based on shifts in intensity with temperature, defect energy levels

have been calculated that indicate shallow donor and deep acceptor levels [74]. Aberration-corrected scanning transmission electron microscopy (STEM) measurements have confirmed Cu-Zn disorder in Cu-poor, Zn-poor films, demonstrating evidence of Cu_{Zn} and Zn_{Cu} antisite substitutions, as well as Cu_{Sn} antisite substitutions in Cu-rich films [74].

Table 2-6. Native point defects in Cu_2ZnSnS_4 [48]
(P-Type: $E_{defect} - E_{VB} < 300meV$, N-Type: $E_{CB} - E_{defect} < 300meV$)

Defect Type	Point Defect	Doping Type
Vacancies	V_{Cu}	P-Type
	V_{Zn}	P-Type
	V_{Sn}	P-Type / Deep
	V_S	Deep
Interstitials	I_{Cu}	N-Type
	I_{Zn}	N-Type
	I_{Sn}	N-Type / Deep
Antisite Substitution	Cu_{Zn}	P-Type
	Cu_{Sn}	P-Type / Deep
	Zn_{Cu}	N-Type
	Zn_{Sn}	P-Type
	Sn_{Cu}	N-Type / Deep
	Sn_{Zn}	N-Type

Defect Complexes

As described in Section 2.2.1.3, neutral defect complexes – in particular $(2V_{Cu}^{-} + In_{Cu}^{2+})^0$ – play critical roles in accommodating off-stoichiometric deviations and passivating recombination centers in the CIGSe material system. In the Cu_2ZnSnS_4 system, a number of potential neutral defect complexes have been modeled and investigated, including: $(V_{Cu}^{-}+Zn_{Cu}^{+})^0$, $(V_{Zn}^{2-}+Sn_{Zn}^{2+})^0$, $(Cu_{Zn}^{-}+Zn_{Cu}^{+})^0$, $(Cu_{Sn}^{3-}+Sn_{Cu}^{3+})^0$, $(Zn_{Sn}^{2-}+Sn_{Zn}^{2+})^0$, $(Zn_{Sn}^{2-}+2Zn_{Cu}^{+})^0$, $(Cu_{Zn}^{-}+I_{Cu}^{+})^0$, and $(Zn_{Sn}^{2-}+I_{Zn}^{2+})^0$ [48].

$(Cu_{Zn}^{-}+Zn_{Cu}^{+})^0$ exhibits the lowest calculated formation energy of the neutral defect complexes, and its value does not change with chemical potential (e.g. film composition) because the defect does not involve atom exchange with the external reservoir [48]. Chen notes that the calculated Zn_{Cu}^{+} level shifts up 0.07meV toward the CB edge when the defect complex forms, but the author does not note any change in the Cu_{Zn}^{-} [48]. From the figure in [48], the Cu_{Zn}^{-} level does not exhibit any significant shift. The Sn_{Cu}^{3+} deep gap defect, on the other hand, exhibits a major shift of 0.42eV towards the conduction band when the $(Cu_{Sn}^{3-} + Sn_{Cu}^{3+})^0$ defect complex forms.

Chen concludes that the favorable formation energies and electrical passivation behavior (e.g. pushing deep trap states toward the band edges) of the various neutral defect complexes in CZTS may yield similar benefits as in the CISe system [48]. Notably, however, neutral complex formation does not appear to significantly modify the trap energy of the dominant Cu_{Zn}^{-} doping defect, which has been identified as a potential source of V_{OC} loss in CZTS devices [57].

2.3.1.4 Grain Properties

As detailed in Section 2.2.1.4, one of the major advantages of the CIGSe material system has been the benign nature of the grain boundaries in polycrystalline thin films, which was attributed to band bending in the VB that results from Cu-deficiencies at the grain surfaces and that acts as a hole barrier. The electronic behavior of grain boundaries in CZTS films has been investigated both theoretically [75-77] and experimentally [77-79], but results have been mixed.

Theoretical calculations by Li [76] indicate that the grain boundaries in CZTS and CZTSe crystals introduce a greater density of midgap defect states into the bulk crystal compared to CISe. These defect levels are expected to increase detrimental carrier recombination [76]. Yin also found detrimental Fermi level pinning at the grain boundary defect states in CZTS [75]. In the same study, Zn_{Sn}, O_{Se}, and I_{Na}^{+} defects were predicted to electrically passivate the grain boundaries by neutralizing midgap defect states and creating hole barriers [75].

Experimental results, however, generally indicate that the grain boundaries are electrically passive. In [78], scanning Kelvin probe microscopy (SKPM) and conductive atomic force microscopy (c-AFM) measurements indicate decreases in the surface potentials and increases of the current at the grain boundaries compared to the bulk, for both CZTSSe and CIGSe films. The increase in current was attributed to greater local conductivity, resulting from increased electron mobility, near the grain boundaries [78]. In [79], also using the SKPM method, the surface potential variation between the bulk and the grain boundary was shown to depend on the film preparation method. The highest performing films were fabricated using a longer selenium anneal step and exhibited significantly larger grain sizes. In these higher performing films, the SKPM measurements indicated a comparatively larger decrease in the surface potentials at the grain boundaries compared to the bulk, similar to the results in [78].

Mendis examines the role of secondary phase precipitation on the electronic behavior of grain boundaries in CZTS [77]. In this study, $Cu_XSn_YS_Z$, ZnS and SnS phases were found, using electron backscattering and EDS, to precipitate at the grain boundaries in CZTS films. Using cathodoluminescence measurements, recombination velocities were calculated at the CZTS/$Cu_XSn_YS_Z$, CZTS/ZnS, and CZTS/SnS heterointerfaces [77]. The $Cu_XSn_YS_Z$ and ZnS heterointerfaces demonstrated low recombination velocities, while the SnS heterointerface demonstrated high recombination velocity. Mendis attributes the improved performance of $Cu_XSn_YS_Z$ and ZnS to the better lattice matching, and resulting decrease in strain, for these phases compared to SnS [77]. The precipitation of some secondary phases on the grain boundaries of CZTS can effectively passivate them, but the overall effect on device performance depends on the

properties of the secondary phases, including the band gap, the volume fraction in the film, the band offset at the heterointerface, and their location relative to the device P-N junction [77].

2.3.2 Absorber Fabrication Methods

Two fundamental approaches may be adopted to fabricate the CZTSeS absorber layer: 1) a single-step fabrication including deposition and crystal formation, and 2) a two-step fabrication including precursor deposition (with S(e)-containing CZTS(e) or metallic CZT precursors) followed by annealing reaction with sulfur/selenium. As detailed in [54, 80, 81], a wide range of thin film deposition techniques have been applied to both of these fabrication methodologies, including pulsed laser deposition, electrodeposition, sputtering, e-beam and thermal evaporation, spray pyrolysis, and nano-ink spin-coating. To date, nano-ink spin-coating has yielded the highest efficiency cells [45]. Pulsed laser deposition and electrodeposition, the primary fabrication tools for CZTS in this dissertation, are discussed in more detail in Chapters 3 and 6 – 9.

The fabrication of CZTS absorber layers remains a significant focus of research in the field, and no champion process has been adopted. The highest efficiency cells have been fabricated using a nano-ink spin-coating method that relies on hydrazine as the solvent [45], an undesirable processing chemical given its toxicity and instability. Since no industry standard fabrication method has been identified, a brief review of the general challenges and considerations of the CZTS fabrication process is provided below, including tradeoffs between single-step and two-step processes. **Three major challenges** have been identified in the fabrication of CZTSeS absorber layers: 1) narrow phase formation region for CZTSeS [47, 54]; 2) elemental and compound volatility [53, 54, 82, 83]; and 3) phase decomposition at the surface and back contacts [71, 84].

As shown in Fig. 2-18, phase-pure CZTS occupies a very narrow region of the compositional phase space. Even small stoichiometric deviations are expected to cause the formation of secondary phases that include metal sulfide binaries of the system ($Cu_{2-X}S$, ZnS, and SnS_X) and $Cu_XSn_YS_Z$ ternary phases. As discussed in Section 2.3.1.1, the best performing devices use Cu-poor, Zn-rich absorber layers, which are expected to consist of coexisting CZTS and ZnS phases. Generally, the phase formation of the crystal under equilibrium conditions depends on the temperature and composition of the system; however, some fabrication conditions have been shown to yield kinetically-limited growth processes, which may produce additional secondary phases [52]. Crystal formation processes associated with CZTS are discussed in more detail in Chapter 3, and the effects of secondary phases on device performance are discussed further in Section 2.3.3.

A significant challenge to the fabrication of quality CZTS absorber layers includes the loss of Zn, Sn and S during the crystal formation processes, either during heated deposition steps or post-annealing steps [54, 84]. While ZnS is relatively stable, elemental Zn has a high vapor pressure and may be evolved from the film under high temperature and low pressures [29, 51]. As Scragg notes, however, Zn is stable in the final CZTS film and when alloyed [19]. This work shows significant losses of Zn in films deposited by pulsed laser deposition at temperatures of 400°C

(10mtorr Ar_2), as detailed in Chapter 6. Moreover, many works have demonstrated the loss of Sn and S at elevated temperatures, and this loss has been attributed to the evolution of SnS from the films [83, 84]. The absence of S_2 and SnS overpressures during crystal formation at elevated temperatures has been shown to decompose CZTS at the surface into constituent binary metal sulfides (including SnS) [84]. The film may then evolve the SnS due its high vapor pressure [84]. This work also shows significant losses of Sn in films deposited by pulsed laser deposition at temperatures of 500°C (10mtorr Ar_2) and in films annealed at temperatures of 550°C without sulfur background, as detailed in Chapters 6 – 8.

Additional destabilizing reactions at the molybdenum back contact have been shown to degrade the quality of CZTS absorber layers; molybdenum can react with and decompose CZTS to form MoS_2 and metal-sulfide binaries [71]. Secondary phases at the back contact may cause increased recombination, and the MoS_2 formation reaction can yield crystal defects that may diffuse to the bulk and cause increased recombination [71]. Increasing the sulfur pressure can mitigate this decomposition reaction but increases the MoS_2 thickness, which can increase series resistance and decrease film adhesion [71]. These surface and back contact phase decomposition processes are discussed in more detail in Chapter 3.

The difficulty in providing a S_2 background during conventional physical vapor deposition processes, necessary to prevent the loss of Sn by SnS evolution at the desired crystal formation temperatures (>500°C) and to mitigate CZTS phase decomposition at the back contact interface, generally indicates the need for a two-step fabrication approach, with the precursor films deposited at low temperature followed by a high temperature annealing step in sulfur background. Scragg and others have reported similar conclusions regarding the comparative success of two-step approaches used to fabricate CZTS [54, 84].

Design Properties of CZTS Absorber Layers

Based on the available literature, the conditions that yield high-quality CZTSeS film growth are as follows: the substrate temperature should reach at least 500°C during crystal formation, the crystal formation should proceed under excess chalcogen (Se or S) to prevent phase decomposition of CZTS, and the final film composition should be Cu-poor and Zn-rich, Cu:[Zn+Sn] ~ 0.85 and Zn:Sn ~ 1.2. Assuming an average optical absorption coefficient of $2x10^4 cm^{-1}$ and using the design thickness for photovoltaic absorber layers from Section 2.1.5, the minimum design thickness for a CZTS absorber layer corresponds to approximately 1μm. Alternative back contact materials and barrier layers should be investigated in order to improve the stability at the back contact-absorber layer interface [71]. Other factors influencing the CZTS crystal formation processes, such as temperature profile and precursor composition, are discussed further in Chapter 3.

2.3.3 Solar Cell Devices

The current champion solar cell demonstrated a device efficiency of 12.6%, using a CZTSeS absorber layer fabricated with a hydrazine-based nano-ink spin-coating process and alloyed with a S-Se composition near Se:[S+Se] = 0.74 [45]. Reported CZTSeS solar devices, including the

current champion cell [45], have generally adopted the layer structure used in conventional CIGSe devices [85], as detailed in Section 2.2.3. This device architecture consists of a soda lime glass substrate, molybdenum back contact, CZTSeS absorber layer, CdS buffer layer, ZnO window layer, and ITO and Ni:Al top contact and collection grid, as shown in Fig. 2-20 below [45, 54, 56]. In the champion cell, conventional processing techniques are used to fabricate the remaining device layers: chemical bath deposition of CdS, RF magnetron sputtering of ZnO and ITO layers, and e-beam evaporation of Ni:Al collection grid [56].

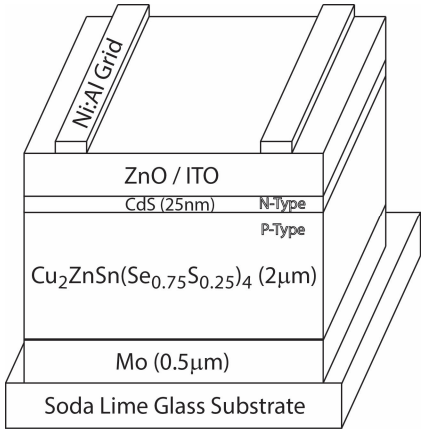

Fig. 2-20. Schematic of champion CZTSeS photovoltaic device, adapted from [13]

Only a limited number of works have reported performance of alternative device architectures, such as SLG/Mo/CZTS/a-Si/ITO and glass/FTO/TiO_2/In_2S_3/CZTS/Mo (superstrate configuration), where SLG refers to soda lime glass, FTO refers to F:SnO_2, and ITO refers to In:SnO_2 [85]. In fact, Delbos notes a general paucity of reported device properties in the literature, which the author attributes to the limited number of high-performance devices able to be fabricated [85]. Summaries of the reported device properties may be found in [54, 80, 81, 85].

The champion 12.6% device fabricated by IBM demonstrated a FF, V_{OC}, J_{SC}, E_g, and E_g/q-V_{OC} of 69.8%, 513.4mV, 35.2mA/cm^2, 1.13eV, and 0.617V, respectively [45]. For comparison, the champion 20.3% CIGSeS device fabricated by ZSW (detailed in Section 2.2.3) demonstrated parameter values of 77.7%, 730mV, 35.7mA/cm^2, 1.14eV, and 0.410V. The short-circuit current densities are similar for the CZTSeS and CIGSeS devices, but the CZTSeS devices show a significant drop in FF and V_{OC}. The low FF values have been attributed to large series resistances in the cell associated with a blocking back contact [45, 54], possibly caused by $Mo(S,Se)_2$ or other secondary phases at the interface [54, 85]. The significant V_{OC} deficits are attributed to SCR-recombination, possibly in the bulk or at the absorber-buffer interface, and to limited minority carrier lifetime [54, 85]. Comparison of capacitance-voltage and drive-level capacitance profiling suggests that interface recombination plays a significant role in the V_{OC} deficit observed in the champion device [45]. Interface recombination may result from defects or detrimental **cliff** band alignments at the interface [54], as detailed in Section 2.1.4.1. See Table 2-3 for reported conduction band alignments at CZTSeS – buffer layer interfaces.

As many review articles and manuscripts have noted, the best performing devices use Cu-poor, Zn-rich CZTS absorber layers, as discussed in prior sections [52, 54, 85]. Further, the champion cells have used S-Se alloyed absorber layers, despite CZTS possessing the optimal band gap for a single-junction solar cell device [57]. While much work remains to definitively identify the mechanisms by which Se-alloying improves device efficiency, Walsh suggests that the shallower level of the dominant Cu_{Zn} antisite defect in CZTSe and the possible type-inversion of CZTSe at the interface may be responsible for improved device performance with Se-alloying [57]. A reduction in series resistance and increase in device efficiency has also been attributed to a reduction of a back contact barrier height with increasing Se-content [54, 56, 85].

The formation of secondary phases in the absorber layer bulk and at the interfaces can significantly impact the device performance as briefly discussed in Section 2.3.1.4, through modification of the volume-averaged optical band gap of the absorber, degraded carrier collection or increased film resisitivity resulting from heterointerface formation, and decreased carrier lifetime resulting from lattice-mismatch induced defect formation at the heterointerface [77]. When present in sufficient quantities, secondary phases may change the effective (volume-averaged) band gap of the absorber, which significantly influences the short-circuit current density and V_{OC} of the device [77]. Further, heterojunction formation between CZTS and the secondary phases can either trap carriers in the smaller band gap material (type I junction) or increase film resisitivity through barrier formation (type II junction), depending on the heterojunction type [77]. Wide gap ZnS secondary phases are expected to yield large barriers to electron and hole transport [72, 77]. The presence of these resistive phases in the SCR increases the shunt resistance across the junction (e.g. non-detrimental impact), but the presence of these phases in the QNR increases the series resistance within the bulk, decreasing the FF [77]. As detailed in Section 2.3.1.4, ZnS and $Cu_XSn_YS_Z$ phases have low interfacial recombination velocities with CZTS, which may help passivate defects. ZnS, when formed in the SCR, may therefore possibly aid device performance [77]; etching studies, however, indicate improved device performance after preferential etching and removal of ZnS from the absorber layer surface [86]. The $Cu_XSn_YS_Z$ may also improve device performance, depending on the band gap of the phase and the heterojunction type formed, as described above [77]. SnS_X phases are shown to have high interfacial recombination velocities, indicating that they are detrimental to device performance [77].

Sodium has been shown to play a significant role in the performance of high-efficiency CIGSeS devices [5, 13, 24], and preliminary work shows similar behavior in CZTSeS devices [85]. In particular, the **inclusion of Na** during CZTSeS thin film growth significantly increased the grain size, improved the film compactness, and increased the film conductivity (both carrier concentration and hole mobility) [85, 87]. However, the diffusion of Na in CZTS appears less than that of Na in CIGSe, evident from lack of detection of Na on the surface of CZTS after film growth.

Moderately high device efficiencies of 12.6% have been achieved for CZTS, but all aspects of CZTS device design merit continued investigation. Scalable and reliable fabrication methods,

capable of producing phase-pure, void-free CZTSeS absorber layers have yet to be demonstrated. Such advancements will require better understanding of the crystal formation processes and defect behavior of CZTSeS. In particular, future improvements to the device performance will likely require the optimization of the device architecture for the CZTSeS material system, in order to enhance the stability and band alignments at the back contact and front contact interfaces.

2.4 REFERENCES

[1] R. Pierret, Semiconductor Device Fundamentals, Addison Wesley Longman, New York, 1996.

[2] J. Nelson, The Physics of Solar Cells, Imperial College Press, London, 2007.

[3] R. Muller, T. Kaims, Device Electronics for Integrated Circuits, Second ed., John Wiley & Sons, New York, 1986.

[4] M. Green, Solar cells: operating principles, technology, and system applications, Prentice Hall, Englewood Cliffs, 1982.

[5] R. Scheer, H.-W. Schock, Chalcogenide Photovoltaics: Physics, Technology, and Thin Film Devices, Wiley-VCH, Weinheim, 2011.

[6] R. Siegel, J. Howell, Thermal Radiation Heat Transfer, 4th ed., Taylor & Francis, New York, 2002.

[7] Standard Solar Constant and Zero Air Mass Solar Spectral Irradiance Tables, in: A.S.f.T.a.M.A. International (Ed.), 2006.

[8] Standard Tables for Reference Solar Spectra Irradiances: Direct Normal and Hemispherical on 37deg Tilted Surface, in: A.S.f.T.a.M.A. International (Ed.), 2012.

[9] P. Yu, M. Cardona, Fundamentals of Semiconductors: Physics and Materials Properties, Fourth ed., Springer, New York, 2010.

[10] C. Kittel, Introduction to Solid State Physics, John Wiley & Sons, New Yrok, 2005.

[11] T. Unold, H.W. Schock, Nonconventional (Non-Silicon-Based) Photovoltaic Materials, Annual Review of Materials Research, 41 (2011) 297-321.

[12] H. Flammersberger, Experimental study of Cu2ZnSnS4 thin films for solar cells, in: Engineering Sciences, Uppsala Universitet, 2010, pp. 121.

[13] W. Shafarman, S. Siebentritt, L. Stolt, Cu(InGa)Se_2 Solar Cells, in: A. Luque, S. Hegedus (Eds.) Handbook of Photovoltaics Science and Engineering, John Wiley & Sons, West Sussex, 2011.

[14] E. Schubert, Physical Foundations of Solid-State Devices, in, 2006.

[15] A. Neisser, Gallium as an Isovalent Substitution in $CuInS_2$ Absorber Layers for Photovoltaic Applications, in: Physics, Freie Universität Berlin, 2001.

[16] S. Hegedus, W. Shafarman, Thin-Film Solar Cells: Device Measurements and Analysis, Progress in Photovoltaics: Research & Applications, 12 (2004) 155 - 176.

[17] R. Herberholtz, V. Nadenau, U. Ruhle, C. Koble, H.W. Schock, B. Dimmler, Prospects of wide-gap chalcopyrites for thin film photovoltaic modules, Solar Energy Materials & Solar Cells, 49 (1997) 227 - 237.

[18] M. Gloeckler, J.R. Sites, Efficiency limitations for wide-band-gap chalcopyrite solar cells, Thin Solid Films, 480 - 481 (2005) 241 - 245.

[19] S. Siebentritt, Wide gap chalcopyrites: material properties and solar cells, Thin Solid Films, 403 - 404 (2002) 1 - 8.

[20] A. Nagoya, R. Asahi, G. Kresse, First-principles study of Cu_2ZnSnS_4 and the related band offsets for photovoltaic applications, Journal of Physics: Condensed Matter, 23 (2011) 404203-404201 - 404203-404206.

[21] A. Santoni, F. Biccari, C. Malerba, M. Valentini, R. Chierchia, A. Mittiga, Valence band offset at the CdS/Cu2ZnSnS4 interface probed by x-ray photoelectron spectroscopy, Journal of Physics D: Applied Physics, 46 (2013) 175101-175101 - 175101-175105.

[22] R. Haight, A. Barkhouse, O. Gunawan, B. Shin, M. Copel, M. Hopstaken, D. Mitzi, Band alignment at the $Cu_2ZnSn(S_xSe_{1-x})_4$/CdS interface, Applied Physics Letters, 98 (2011) 253502-253501 - 253502-253503.

[23] M. Bar, B.A. Schubert, B. Marsen, R.G. Wilks, S. Pookpanratana, M. Blum, S. Krause, T. Unold, W. Yang, L. Weinhardt, C. Heske, H.W. Schock, Cliff-like conduction band offsert and KCN-induced recombination barrier enhancement at the CdS/Cu_2ZnSnS_4 thin-film solar cell heterojunction, Applied Physics Letters, 99 (2011) 222105 - 222101 - 222105 - 222103.

[24] D. Rudmann, Effects of sodium on growth and properties of Cu(In,Ga)Se_2 thin films and solar cells, in: Physics, Swiss Federal Institute of Technology (ETH), Zurich, 2004.

[25] M.I. Alonso, K. Wakita, J. Pascual, M. Garriga, N. Yamamoto, Optical functions and electronic structure of $CuInSe_2$, $CuGaSe_2$, $CuInS_2$, and $CuGaS_2$, Physical Review B, 63 (2001) 075203-075201 - 075203-075213.

[26] A. Soni, A. Dashora, V. Gupta, C.M. Arora, M. Rerat, B.L. Ahuja, R. Pandey, Electronic and Optical Modeling of Solar Cell Compounds $CuGaSe_2$ and $CuInSe_2$, Journal of Electronic Materials, 40 (2011) 2197 - 2208.

[27] J.E. Jaffe, A. Zunger, Anion displacements and the band-gap anomaly in ternary ABC_2 chalcopyrite semiconductors, Physical Review B, 27 (1983) 5176 - 5179.

[28] S.B. Zhang, S. Wei, A. Zunger, Defect physics of the $CuInSe_2$ chalcopyrite semiconductor, Physical Review B, 57 (1998) 9642 - 9656.

[29] A. Hofmann, C. Pettenkofer, Electronic band structure of epitaxial $CuInSe_2$ films, Physical Review B, 84 (2011) 115109-115101 - 115109-115108.

[30] H. Neumann, Optical Properties and Electronic Band Structure of $CuInSe_2$, Solar Cells, 16 (1986) 317 - 333.

[31] C. Persson, Y. Zhao, S. Lany, A. Zunger, n-type doping of $CuInSe_2$ and $CuGaSe_2$, Physical Review B, 72 (2005) 035211-035211 - 035211-035214.

[32] A. Zunger, Theory of 3d Transition Atom Impurities in Semiconductors, Annual REview of Material Science, 15 (1985) 411-453.

[33] C. Domain, S. Laribi, S. Taunier, J.F. Guillemoles, Ab initio calculation of intrinsic point defects in $CuInSe_2$, Journal of Physics and Chemistry of Solids, 64 (2003) 1657-1663.

[34] S.B. Zhang, S. Wei, A. Zunger, Stabilization of Ternary Compounds via Ordered Arrays of Defect Pairs, Physics Review Letters, 78 (1997) 4059-4062.

[35] J. Levoska, S. Leppavuori, F. Wang, O. Kusmartseva, Pulsed Laser Ablation Deposition of $CuInSe_2$ and $CuIn_{1-x}Ga_xSe_2$ Thin Films, Physica Scripta, T54 (1994) 244-247.

[36] Y.H. Jo, B.C. Mohanty, Y.S. Cho, Crystallization and surface segregation in $CuIn_{0.7}Ga_{0.3}Se_2$ thin films on Cu foils grown by pulsed laser deposition, Applied Surface Science, 256 (2010) 6819-6823.

[37] N. Chaure, A. Samantilleke, R. Burton, J. Young, I. Dharmadasa, Electrodeposition of p^+, p, i, n and n^+-type copper indium gallium diselenide for development of multilayer thin film solar cells, Thin Solid Films, 472 (2005) 212 - 216.

[38] J. Botha, S. Schumacher, A. Leitch, V. Alberts, Homogeneity of single phase Cu(In,Ga)Se2 produced by selenisation of metal precursors: An optical investigation, Thin Solid Films, 511 - 512 (2006) 316 - 319.

[39] A. Katerski, A. Mere, V. Kazlauskiene, J. Miskinis, A. Saar, L. Matisen, A. Kikas, M. Krunks, Surface analysis of spray deposited copper indium disulfide films, Thin Solid Films, 516 (2008) 7110 - 7115.

[40] J. Lee, J. Chang, J.-H. Cha, Y. Lee, J.E. Han, D.-Y. Jung, E. Choi, B. Hong, Large-Scale, Surfactant-Free Solution Syntheses of $Cu(In,Ga)(S,Se)_2$ Nanocrystals for Thin Film Solar Cells, Eur. J. Inorg. Chem., (2011) 647 - 651.

[41] P. Jackson, D. Hariskos, E. Lotter, S. Paetel, R. Wuerz, R. Menner, W. Wischmann, M. Powalla, New world record efficiency for $Cu(In,Ga)Se_2$ thin-film solar cells beyond 20%, Progress in Photovoltaics: Research & Applications, 19 (2011) 894 - 897.

[42] M. Contreras, B. Egaas, D. King, A. Swartzlander, T. Dullweber, Texture manipulation of $CuInSe_2$ thin films, Thin Solid Films, 361 - 362 (2000) 167-171.

[43] E. Wesoff, CIGS Solar Update: Avancis Sets Thin-Film PV Module Efficiency Record, in: Greentech Media, 2014.

[44] F. Kessler, D. Rudmann, Technological aspects of flexible CIGS solar cells and modules, Solar Energy, 77 (2004) 685-695.

[45] W. Wang, M. Winkler, O. Gunawan, T. Gokmen, T. Todorov, Y. Zhu, D. Mitzi, Device Characteristics of CZTSSe Thin-Film Solar Cells with 12.6% Efficiency, Advanced Energy Materials, (2013).

[46] C. Persson, Electronic and optical properties of Cu_2ZnSnS_4 and $Cu_2ZnSnSe_4$, Journal of Applied Physics, 107 (2010) 053710-053711 - 053710-053718.

[47] I.D. Olekseyuk, I.V. Dudchak, L.V. Piskach, Phase equilibria in the Cu_2S-ZnS-SnS_2 system, Journal of Alloys and Compounds, 368 (2004) 135 - 143.

[48] S. Chen, J.-H. Yang, X.G. Gong, A. Walsh, S.-H. Wei, Intrinsic point defects and complexes in the quaternary kesterite semiconductor Cu_2ZnSnS_4, Physical Review B, 245204 (2010) 245204-245201 245204-245210.

[49] M. Ichimura, Y. Nakashima, Analysis of Atomic and Electronic Structures of Cu_2ZnSnS_4 Based on First-Principle Calculation, Japanese Journal of Applied Physics, 48 (2009) 090202-090201 - 090202-090203.

[50] G. Bernardini, D. Borrini, A. Caneschi, F. Benedetto, D. Gatteschi, S. Ristori, M. Romanelli, EPR and SQUID magnetometry study of Cu_2FeSnS_4 (stannite) and Cu_2ZnSnS_4 (kesterite), Phys. Chem. Minerals, 27 (2000) 453 - 461.

[51] S. Chen, X.G. Gong, A. Walsh, S.-H. Wei, Crystal and electronic band structure of Cu_2ZnSnX_4 (X = S and Se) photovoltaic absorbers: First-principles insights, Applied Physics Letters, 94 (2009) 041903-041901 - 041903-041903.

[52] J.J. Scragg, Studies of Cu_2ZnSnS_4 films prepared by sulfurisation of electrodeposited precursors, in: Chemistry, University of Bath, 2010, pp. 244.

[53] C. Platzer-Bjorkman, J. Scragg, H. Flammersberger, T. Kubart, M. Edoff, Influence of precursor sulfur content on film formation and compositional changes in Cu2ZnSnS4 films and solar cells, Solar Energy Materials & Solar Cells, 98 (2012) 110 - 117.

[54] D. Mitzi, O. Gunawan, T. Todorov, K. Wang, S. Guha, The path towards a high-performance solution-processed kesterite solar cell, Solar Energy Materials & Solar Cells, 95 (2011) 1421 - 1436.

[55] A. Fairbrother, X. Fontane, V. Izquierdo-Roca, M. Espindola-Rodriguez, S. Lopez-Marino, M. Placidi, L. Calvo-Barrio, A. Perez-Rodriguez, E. Saucedo, On the formation mechanisms of Zn-rich Cu_2ZnSnS_4 films prepared by sulfurization of metallic stacks, Solar Energy Materials & Solar Cells, 112 (2013) 97 - 105.

[56] A. Barkhouse, O. Gunawan, T. Gokmen, T. Todorov, D. Mitzi, Device characteristics of a 10.1% hydrazine-processed $Cu_2ZnSn(Se,S)_4$ solar cell, Progressin Photovoltaics: Research & Applications, (2011).

[57] A. Walsh, S. Chen, S.-H. Wei, X.-G. Gong, Kesterite Thin-Film Solar Cells: Advances in Materials Modelling of Cu_2ZnSnS_4, Advanced Energy Materials, 2 (2012) 400 - 409.

[58] J. He, L. Sun, N. Ding, H. Kong, S. Zuo, S. Chen, Y. Chen, P. Yang, J. Chu, Single-step preparation and characterization of $Cu_2ZnSn(S_xSe_{1-x})_4$, Journal of Alloys and Compounds, 529 (2012) 34-37.

[59] I.V. Dudkchak, L.V. Piskach, Phase equilibria in the Cu_2SnSe_3-$SnSe_2$-ZnSe system, Journal of Alloys and Compounds, 351 (2003) 145 - 150.

[60] M. Grossberg, J. Krustok, J. Raudoja, K. Timmo, M. Altosaar, T. Raadik, Photoluminescence and Raman study of $Cu_2ZnSn(Se_xS_{1-x})_4$ monograins for photovoltaic applications, Thin Solid Films, 519 (2011) 7403 - 7406.

[61] S. Chen, A. Walsh, J.-H. Yang, X.G. Gong, L. Sun, P.-X. Yang, J.-H. Chu, S.-H. Wei, Compositional dependence of structural and electronic properties of $Cu_2ZnSn(S,Se)_4$ alloys for thin film solar cells, Physical Review B, 83 (2011) 125201-125201 - 125201-125205.

[62] J. He, L. Sun, S. Chen, Y. Chen, P. Yang, J. Chu, Composition dependence of structure and optical properites of $Cu_2ZnSn(S,Se)_4$ solid solutions: An experimental study, Journal of Alloys and Compounds, 511 (2012) 129-132.

[63] S. Ji, T. Shi, X. Qiu, J. Zhang, G. Xu, C. Chen, Z. Jiang, C. Ye, A Route to Phase Controllable $Cu_2ZnSn(S_{1-x}Se_x)_4$ Nanocrystals with Tunable Enregy Bands, Scientific Reports, 3 (2013) 1 - 7.

[64] K. Zhang, J. Tao, J. He, W. Wang, L. Sun, P. Yang, J. Chu, Composition control in Cu_2ZnSnS_4 thin films by a sol-gel technique without sulfurization, Journal of Materials Science: Materials in Electronics, 25 (2014) 2703 - 2709.

[65] R.A. Wibowo, E.S. Lee, B. Munir, K.H. Kim, Pulsed laser deposition of quaternary $Cu_2ZnSnSe_4$ thin films, phys. stat. sol. (a), 204 3373-3379.

[66] M.A. Khan, S. Kumar, M. Alhoshan, A.S. Dwayyan, Spray pyrolysed Cu_2ZnSnS_4 absorbing layer: A potential candidate for photovoltaic applications, Optics & Laser Technology, 49 (2013) 196 - 201.

[67] J. Paier, R. Asahi, A. Nagoya, G. Kresse, Cu_2ZnSnS_4 as a potential photovoltaic material: A hybrid Hartree-Fock density functional theory study, Physical Review B, 79 (2009) 115126-115121 - 115126-115128.

[68] M. Bar, B.A. Schubert, B. Marsen, S. Schorr, R.G. Wilks, L. Weinhardt, S. Pookpanratana, M. Blum, S. Krause, Y. Zhang, W. Yang, T. Unold, C. Heske, H.W. Schock, Electronic structure of Cu_2ZnSnS_4 probed by soft x-ray emission and absorption spectroscopy, Physical Review B, 84 (2011) 035308-035301 - 035308-035306.

[69] J. Li, H. Du, J. Yarbrough, A. Norman, K. Jones, G. Teeter, F.L.T. Jr., D. Levi, Spectral optical properties of Cu_2ZnSnS_4 thin film between 0.73 and 6.5eV, Optics Expres, 20 (2012) A327 - A332.

[70] S. Levcenko, G. Gurieva, M. Guc, A. Nateprov, Optical Constants of Cu_2ZnSnS_4 Bulk Crystals, Moldavian Journal of the Physical Sciences, 8 (2009) 173 - 177.

[71] J. Scragg, J. Watjen, M. Edoff, T. Ericson, T. Kubart, C. Platzer-Bjorkman, A Detrimental Reaction at the Molybdenum Back Contact in $Cu_2ZnSn(S,Se)_4$ Thin-Film Solar Cells, J. Am. Chem. Soc., 134 (2012) 19330 - 19333.

[72] A. Nagoya, R. Asahi, Defect formation and phase stability of Cu_2ZnSnS_4 photovoltaic materials, Physical Review B, 81 (2010) 113202-113201 - 113202 - 113204.

[73] S. Chen, X.G. Gong, A. Wlash, S. Wei, Defect physics of hte kesterite thin-film solar cell absorber Cu_2ZnSnS_4, Applied Physics Letters, 96 (2010) 021902-021901 - 021902-021903.

[74] B. Mendis, M. Shannon, M. Goodjman, J. Major, R. Claridge, D. Halliday, K. Durose, Direct observation of Cu, Zn cation disorder in Cu_2ZnSnS_4 solar cell absorber material using aberration corrected scanning transmission electron microscopy, Progress in Photovoltaics: Research & Applications, 22 (2014) 24 - 34.

[75] W.-J. Yin, Y. Wu, S.-H. Wei, R. Noufi, M.M. Al-Jassim, Y. Yan, Engineering Grain Boundaries in Cu2ZnSnSe4 for Better Cell Performance: A First-Principle Study, Advanced Energy Materials, 4 (2013) 1300712-1300711 - 1300712-1300717.

[76] J. Li, D. Mitzi, V. Shenoy, Structure and Electronic Properties of Grain Boundaries in Earth-Abundant Photovoltaic Absorber Cu2ZnSnSe4, ACS Nano, 5 (2011) 8613 - 8619.

[77] B. Mendis, M. Goodman, J. Major, A. Taylor, K. Durose, D. Halliday, The role of secondary phase precipication on grain boundary electrical activity in Cu_2ZnSnS_4 (CZTS) photovoltaic absorber layer material, Journal of Applied Physics, 112 (2012) 124508-124501 - 124508-124510.

[78] J. Li, V. Chawla, B. Clemens, Investigating the Role of Grain Boundaries in CZTS and CZTSSe Thin Film Solar Cells with Scanning Probe Microscopy, Advanced Materials, 24 (2012) 720 - 723.

[79] G.Y. Kim, A.R. Jeong, J.R. Kim, W. Jo, D.-H. Son, D.-H. Kim, J.-K. Kang, Surface potential on grain boundaries and intragrains of highly efficient $Cu_2ZnSn(S,Se)_4$ thin-films grown by two-step sputtering process, Solar Energy Materials & Solar Cells, 127 (2014) 129 - 135.

[80] K. Ramasamy, M.A. Malik, P. O'Brien, Routes to Copper Zinc Tin Sulfide Cu_2ZnSnS_4 a Potential Material for Solar Cells, Chem. Commun., 48 (2012) 5703-5714.

[81] H. Wang, Progress in Thin Film Solar Cells Based on Cu_2ZnSnS_4, International Journal of Photoenergy, 2011 (2011) 801292-801291 - 801292-801210.

[82] P.M.P. Salome, J. Malaquias, P.A. Fernandes, M.S. Ferreira, J.P. Leitao, A.F.d. Cunha, J.C. Gonzalez, F.N. Matinaga, G.M. Ribeiro, E.R. Viana, The influence of hydrogen in the incorporation of Zn during the growth of $Cu_2ZnSnSn_4$ thin films, Solar Energy Materials & Solar Cells, 95 (2011) 3482 - 3489.

[83] A. Weber, R. Mainz, H.W. Schock, On the Sn loss from thin films of the material system Cu-Zn-Sn-S in high vacuum, Journal of Applied Physics, 107 (2010) 013516-013511 - 013516-013516.

[84] J. Scragg, T. Ericson, T. Kubart, M. Edoff, C. Platzer-Bjorkmann, Chemical Insights into the Instability of Cu_2ZnSnS_4 Films during Annealing, Chemistry of Materials, 23 (2011) 4625–4633.

[85] S. Delbos, Kesterite thin films for photovoltaics: a review, EPJ Photovoltaics, 3 (2012) 35004:p35001 - p35013.

[86] A. Fairbrother, E. Garica-Hemme, V. Izquierdo-Roca, X. Fontane, F. Pulgarin-Agudelo, O. Vigil-Galan, A. Perez-Rodriguez, E. Saucedo, Development of a Selective Chemical Etch to Improve the Conversion Efficiency of Zn-Rich Cu_2ZnSnS_4 Solar Cellss, J. Am. Chem. Soc., 134 (2012) 8018 - 8021.

[87] A. Nagaoka, H. Miyake, T. Taniyama, K. Kakimoto, Y. Nose, M. Scarpulla, K. Yoshino, Effects of sodium on electrical properties in Cu_2ZnSnS_4 single crystal, Applied Physics Letters, 104 (2014) 152101-152101 - 152101-152104.

3 THIN FILM FABRICATION METHODS

3.1 PULSED LASER DEPOSITION

3.1.1 Background

Fig. 3-1 illustrates a typical pulsed laser deposition (PLD) system. An externally-mounted, high-power laser focuses a beam through lenses onto a target material inside a vacuum chamber. The high-intensity irradiative flux vaporizes material from the surface of the target, ejecting a plume of material normal to the target surface and onto a heated substrate. The target holder rotates in order to provide undamaged ablation surface, and the substrate holder typically slides in order to adjust the target-substrate distance [1, 2]. Deposition takes place under vacuum (10^{-10} to 1 torr) and may include a reactive or inert deposition gas [1, 2]. A turbo pump with secondary rotary roughing pump provides the necessary vacuum pumping, and a mass flow controller adjusts the deposition gas pressure [1]. The thin films fabricated by PLD in this thesis were deposited either in high vacuum or in background Argon gas. The target surface can be cleaned of contaminants by laser cleaning in order to reduce exfoliational splashing, and a movable shutter prevents contamination of the substrate during the target surface cleaning [1].

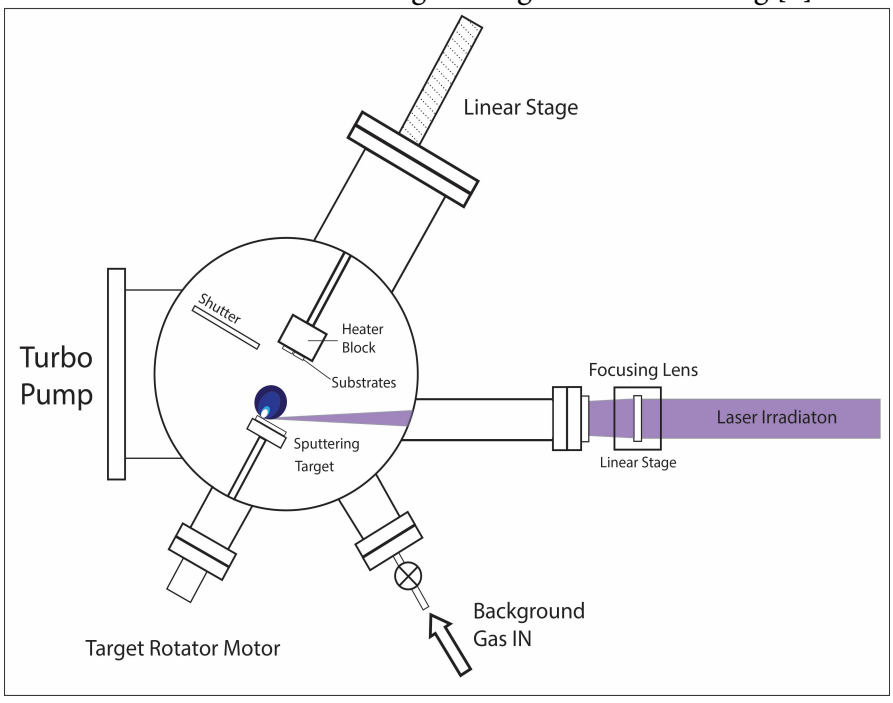

Fig. 3-1. Schematic of typical pulsed laser deposition system (representative of top-down view of EETD PLD system described later)

Pulsed laser deposition represents a useful laboratory-scale fabrication tool to quickly study different material combinations and layer interfaces. PLD systems offer flexibility in the choice of deposition materials and readily accommodates multilayer depositions by use of a rotating target

rack [3]. Furthermore, the nature of the laser-ablation processes, described in detail later, permits congruent deposition for nearly any target material [1, 2, 4], a particularly important deposition feature for complicated multi-component materials such as CZTS. This characteristic has been the driving force behind the adoption of PLD [1, 2, 5]. Finally, the higher kinetic energy content associated with laser ablation often means that the crystallinity of the film can be maintained with lower substrate temperatures during film growth [6], allowing a broader range of substrate materials to be employed [2].

Three main drawbacks have prevented more widespread adoption of PLD systems, including particulate deposition (**splashing**), film non-uniformity, and low throughput. Splashing involves the generation of micron-sized particulates during ablation, which then deposit on the film surface [2]. In semiconductor films, these splashed particulates can severely degrade electronic quality and serve as sources of shunting in multilayer devices [2]. Furthermore, laser-ablation plumes are highly forward-directed with a thin angular distribution, making uniform deposition over large areas difficult [2]. Decreasing the laser fluence and increasing the target-substrate distance can significantly reduce splashing and improve the thickness uniformity. However, as results of Chapters 5 and 6 demonstrate, optimal deposition conditions typically result in very low deposition rates. For a more detailed discussion of pulsed laser deposition and alternative physical vapor deposition techniques, the reader is referred to a few of the many available texts on the subject [2, 7-9].

3.1.2 Physical Processes of Deposition

Pulsed laser deposition involves many complicated physical processes, the effects which are not always distinguishable. However, the process can be roughly divided into four main stages: 1) laser-target interaction and ablation, 2) plume propagation, 3) plume-substrate interaction and deposition, and 4) nucleation and crystal growth of the thin film on the substrate. Fig. 3-2 shows a typical ablation plume.

Fig. 3-2. Pulsed laser ablation plume

The target absorbs the laser energy in a thin layer near the surface, resulting in evaporation and ejection of material according to various ablation mechanisms. These ejected particles form an ablation plume, consisting of atoms and ions with high kinetic energy content. When splashing

mechanisms are active, the plume will also contain micron-sized particulates. In the presence of a background gas, the ablation plume expands according to classical gas dynamics, with a highly forward-peaked distribution. Depending on the laser irradiance and wavelength, the laser irradiation may interact with the plume. Particles condense from the plume on to the substrate, and film nucleation and growth proceeds according to conventional growth modes. These growth models must be augmented to account for the high kinetic energy of the plume and the pulsed nature of the ablation.

3.1.2.1 Laser-target interaction and ablation

In pulsed laser deposition, laser irradiation ablates material from the surface of a target, which then deposits onto a substrate to form a thin film. The nature of the laser-target interaction varies widely depending on a variety of system parameters, including laser fluence, laser wavelength, laser pulse duration, target material, and target surface condition. Laser ablation divides roughly into two regimes: low fluence ($F < F_{abl}$) and high fluence ($F > F_{abl}$), where F_{abl} denotes the laser ablation fluence threshold [1, 2, 10, 11]. The **laser ablation fluence threshold** refers to a fluence level ($F_{abl} \sim 1$ J/cm^2), below which the ablation rate remains low, and above which the ablation rate increases steeply and a dense plume or plasma forms above the target surface [1, 10, 12-14]. Thermal ablation processes dominate the low fluence regime, and they are generally characterized by incongruent deposition [1, 14, 15], while electronic ablation processes dominate the high fluence regime and are characterized by congruent deposition [14].

Primary ablation mechanisms include thermal, electronic, hydrodynamic, and exfoliational [2, 10]. Both thermal and electronic ablation plumes consist of atomic-size particles released from the target surface [10]. Hydrodynamic and exfoliational ablation processes, on the other hand, liberate bulk-size material into the ablation plume [10]. Laser ablation processes are inherently complex, and often many ablation processes are active. Subsequently, these processes and their effects are often indistinguishable [2, 10, 11].

The conversion of incident laser energy to vibrational energy in the lattice prior to bond breaking corresponds to **classical thermal evaporation** [10]. In this case, the solid target surface is heated, melted, and finally vaporized. Classical evaporation dominates the low-fluence laser ablation regime, in which electronic ablation mechanisms are less active [10], and evaporation rates depend on the target material properties. Subsequently, thermal ablation of multi-component targets results in variable evaporation rates for the constituent species, thereby causing a loss of stoichiometry in the deposited film [1, 5]. Ablation rates associated with high-fluence, electronic mechanisms are less dependent on the material properties, increasing congruence of the deposition species and representing one of the major benefits of pulsed laser deposition [1, 2].

Electronic ablation involves chemical bond breaking resulting directly from electronic excitations with little or no energy transfer to lattice vibrations [10]. Various mechanisms and

models have been proposed to account for these electronic excitations and resulting ablation, including photochemical bond breaking, coulomb explosion, defect formation and surface plasmon excitation [1, 2, 10]. Laser irradiance and laser fluence values typically associated with electronic ablation are of the order 10^5 – 10^8 W/cm^2 and 1 – 10 J/cm^2, respectively [1, 2, 16]. Distinguishing the presence and individual effects of the various electronic mechanisms is often difficult, although electronic ablation processes generally share many similar characteristics [2, 11], including simply the existence of a threshold laser fluence. The ablation plumes contain non-thermodynamic yields of molecules, atoms, and ions, with high ionic (~10%) and kinetic energy content (KE ~ 0.2 – 50eV) [1, 2, 11]. The high ionic and kinetic energy content tends to increase the film crystallinity, as discussed in Section 3.1.2.3. Lastly, the plume contains relative species concentrations similar to the bulk target material, ostensibly the most important characteristic of electronic ablation processes [11].

Hydrodynamic ablation results when transient melting processes liberate bulk-sized material from the target surface [2, 10, 17], resulting in the deposition of spherical micron-sized particulates on the film substrate [10]. These transient melting processes include melt layer Taylor instabilities and subsurface boiling [2, 10, 17]. **Exfoliational ablation** involves the erosion of solid flakes from the target surface [2], which are then carried by the plume to the substrate. These eroded flakes are irregularly shaped, a feature that readily distinguishes exfoliated particulates from hydroynamically splashed particulates [2]. Recurring thermal shocks of the target form surface cracks [2], serving as energy-absorbing defects along which flakes separate [10]. Erosion of the target surface causes exfoliational ablation, and thus the presence of defects or contaminants will enhance this ablation mechanism [2].

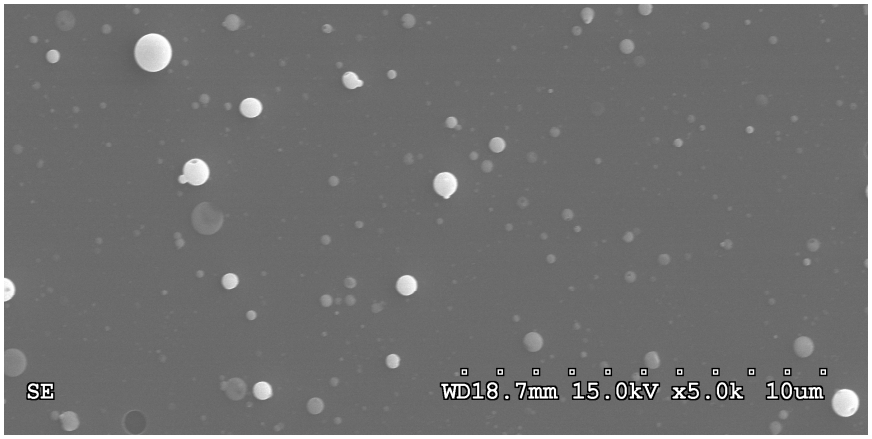

Fig. 3-3. Hydrodynamically-formed, spherical "splash" droplets

Splashing involves the formation and deposition of unwanted droplets in the film, ranging in diameter from a few hundred nanometers to several ten of micrometers [1]. Fig. 3-3 shows typical, hydrodynamically-formed droplets. Hydrodynamic and exfoliational ablation mechanisms, a collection of processes which are active for most target materials [2], cause

splashing. As a major source of degraded film quality, splashing has prevented more widespread adoption of pulsed laser deposition [1, 2, 11]. Therefore, splashing mitigation strategies have been a significant focus of PLD research over the past twenty years. Decreasing the laser wavelength, decreasing the laser fluence, increasing the target thermal conductivity, and increasing the quality of the target surface mitigate the sources of splashing and increase film quality [1, 2, 11]. In cases where the sources of splashing cannot be eliminated, additional strategies have been developed to prevent the micron-sized droplets from reaching the substrate [1]. However, these mitigation strategies are typically overly cumbersome and difficult to implement, or negatively impact the stoichiometry of the deposited films.

3.1.2.2 Plume propagation

Plume propagation behavior can be divided into two regimes: low-collision ($P \leq 300$mtorr) and high-collision ($P \geq 300$mtorr) [11]. In the low-collision regime, most common for PLD processes, collisions are infrequent and must be treated stochastically [10, 11], typically using a direct Monte Carlo method [10, 11]. The plume evolution associated with electronic ablation depends on the characteristics of the vapor-plasma layer, and the propagation can be considered in terms of conventional gas dynamics with some modifications made for the laser-plasma interactions [2, 10]. Plumes developed during both thermal and electronic ablation exhibit high-forward peaking of the kinetic-energy distributions ($\cos^4\theta$ to $\cos^{10}\theta$), resulting in highly directional (normal) propagation [2, 10].

Singh developed theoretical models of the laser-target interaction and subsequent plume evolution, yielding a number of important relationships between the deposition parameters and the structure of the plume and the deposited film [9]. For depositions in high-vacuum, there still exists a brief period in the initial ablation that classifies as high-collision, where continuum fluid mechanics hold. Singh models this initial plume formation as an isothermal expansion, which yields plume dimensions on the order of 1 – 4mm diameter and 20 – 100μm long (perpendicular to the target) [9]. Subsequent expansion proceeds according to low-collision, adiabatic expansion, which depends on the size and temperature of the plume, as well as the mass of the constituent species [9]. The species velocities depend strongly on the plume dimensions at the start of adiabatic expansion, such that the highest velocities proceed along the shortest lengths of the plume. That is, the highest velocities proceed perpendicular to the target, yielding the highly forward-directed plumes previously described [9]. Furthermore, the species velocities also depend on the species mass and the plume temperature.

Theoretically, species velocities show an inverse square root relationship with their masses, but interactions in the plume likely weaken this effect. Experimental measurements have shown variations in velocity according to $M^{-0.37}$ for some multi-component targets, where M is the mass [9]. The velocity decrease in higher mass species decreases their perpendicular to transverse velocity ratios, thereby spreading out the mass distribution in the plume and weakening the

forward-peaking [9]. Higher mass elements will spread more strongly in the plume (e.g. increase their FWHM), causing stoichiometry changes across the film, which depend on the location on the film relative to the center of the plume [9].

Increasing the temperature of the plume, by increasing the incident laser fluence, increases the velocities of all species within the plume, causing an overall increase forward-peaking of the plume and weakening the effect of species mass on particle distributions within the plume [9]. At high enough laser fluences, spatial variations in the stoichiometry across the film can effectively be eliminated [9].

3.1.2.3 Plume-substrate interaction and deposition

The deposition characteristics of the film and the deposition rate will to a large extent be determined by the particle characteristics within the plume and the target-substrate geometry. As described in Section 3.1.2.1, two distinct plume composition regimes exist for PLD processes corresponding to the two laser ablation regimes, low-fluence and high-fluence. In the **low laser-fluence** regime, thermal ablation dominates [14], yielding plumes containing kinetically low-energetic atomic species in non-stoichiometric concentrations relative to the target material [1, 2, 14, 15]. In the **high laser-fluence** regime, electronic ablation dominates [14, 15], yielding plumes containing kinetically energetic species in elemental concentrations similar to the target material [1, 2, 14].

Film properties depend strongly on the kinetic energy and compositional characteristics of the ablation plume. Increased film crystallinity has been attributed to the high ionic and kinetic energy content of high-fluence laser ablation plumes [2, 15]. The energetic ions are thought to enhance adatom surface diffusion and film annealing, mechanisms which support crystalline film growth and permit lower epitaxial growth temperatures [15, 16]. While generally beneficial to film growth, ions with too much kinetic energy may actually cause sputtering or damage to the substrate surface [15].

Within the high laser-fluence regime, decreasing laser fluence can aid film quality by reducing the density of splashed particulates and also by reducing sputtering damage to the film surface. Increasing the target-substrate distance reduces the solid angle of the plume intercepting the substrate, thereby sampling a narrower and more uniform portion of the plume. As previously discussed, this smaller solid angle makes alignment between the congruent, forward-peaked portion of the plume and substrate more critical. Moreover, the increased distance reduces the kinetic energy of particles impinging on the substrate helping to reduce any sputtering damage to the films. Decreasing the laser fluence and increasing the target-substrate distance as described above can significantly improve film quality, but this comes at the cost of dramatically reduced deposition rates [1].

3.1.2.4 Nucleation and crystal growth on substrate

Conventional film-nucleation and growth models assume steady-state deposition processes, well-representative of techniques such as molecular beam epitaxy (MBE) [2]. However, PLD differs from MBE in two fundamental ways. First, PLD is not a steady-state process, instead involving periodic bursts of rapid, near-instantaneous deposition [3]. Second, the kinetic energies of the deposition species are one to two orders of magnitude higher for PLD than for MBE [3]. Efforts have been focused on modifying conventional growth models to account for the periodic deposition and kinetically energetic deposition species [2, 3]. Indeed, experimental studies demonstrate similar morphological evolutions for MBE, thermal evaporation, and kinetically energetic laser ablation processes [3]. A brief review of conventional thin film growth models can be found in [2], including Volmer-Weber, Frank-van der Merwe, and Stranski-Krastinov models. Furthermore, Section 3.3 discusses the physics of crystal phase formation CIGSe and CZTS thin films, processes that are general to film growth associated with PLD and annealing.

Substrate deposition temperature also represents a significant parameter in nucleation and film growth, influencing both the crystallinity and the stoichiometry of the deposited film. Higher substrate temperatures increase adatom surface diffusivity, thereby increasing film crystallinity [1, 2]. However, high substrate temperatures in vacuum can also result in re-evaporation of elements from the film surface and decomposition of the films, a common problem associated with tin and sulfur elements in CZTS films, and discussed further in Section 3.3.2.2 [18].

3.1.3 Experimental Details

3.1.3.1 Equipment and Set-up

Pulsed laser deposition of thin films for this dissertation was performed using two different deposition systems, designated as **EETD** and **EMAT**. The following sections summarize the laser performance and deposition configuration for each of these systems.

EETD PLD System

The EETD pulsed laser deposition system is configured as shown schematically in Fig. 3-1. The deposition system utilizes a LambdaPhysik LPX 210i KrF excimer laser that produces a 248nm wavelength beam with 25ns pulse duration. The laser provides a stable energy between 150 – 450mJ and a repetition rate between 1 – 10Hz. Quartz plates and copper mesh are used in the beam line, in some cases, to attenuate the laser energy below its minimum stable value. The laser fluence can also be adjusted by modulating the spot size of the beam on the target, achieved by adjusting the distance of the focusing lens using a fine-tuning positional stage. The low ablation threshold of CIGSe sputtering targets generally required the use of attenuating optics, as well as spot size-tuning, to achieve the desired ablation characteristics.

During the course of deposition, the ablated material unintentionally deposits on the vacuum chamber optical window, reducing the transmitted laser energy to the target. To mitigate

this effect, the optical window employs a "sacrificial" quartz window that is replaced before each deposition. Despite this preventative maintenance, the laser energy decreases over long depositions and cannot be avoided.

Table 3-1. CIGSe Sputtering Target Compositions

Target ID	Molar Composition			
	Cu	In	Ga	Se
CIGSe - 1	1.00	0.75	0.25	2.00

Single layer films of CIGSe, 100–500nm thickness, were deposited onto soda lime glass substrates by PLD from a single, hot-sintered sputtering target with the composition specified in Table 3-1. The target was not polished between depositions out of concern for contaminating it with the polishing agent. Depositions were conducted under high-vacuum (~$5x10^{-5}$ torr).

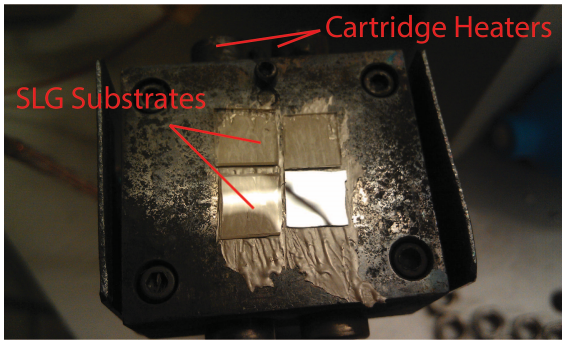

Fig. 3-4. Substrate holder for EETD PLD system

Four substrates were typically installed per deposition as shown in Fig. 3-4, using DuPont 4929N silver paste. The substrates were nominally located ~4 inches from the target. During deposition, the substrate temperatures were varied between room temperature and up to 450°C using a resistively heated mounting block. Substrates were allowed to cool passively back to room temperature after deposition.

EMAT PLD System

The EMAT pulsed laser deposition system is configured as shown in Fig. 3-5. The deposition system utilizes a Coherent Pro 205F KrF excimer laser that produces a 248nm wavelength beam with 20ns pulse duration. The laser provides a stable energy between 200 – 550mJ and a repetition rate between 1 – 30Hz. As originally configured, the laser spot size on the target was limited to ~6.14mm^2 due to the focal length of the condensing lens and the geometry of the chamber. In a few cases, copper mesh (same as in EETD) was used to attenuate the laser energy below 200mJ.

Similar to the EETD PLD system, the ablated material unintentionally deposits on the vacuum chamber optical window, reducing the transmitted laser energy to the target. As originally configured, no sacrificial window was used in the chamber. Over the course of several months, the

window became heavily coated, severely decreasing the incident laser energy during deposition. However, coating rates were sufficiently low that depositions performed consecutively within the same week experienced a negligible decline in the incident laser energy. Using a laser energy meter, the losses in the optics chain were measured, and to the best estimation, variations in the laser energy due to window coating are accounted for in the presented fluences in Chapter 6. Eventually, the chamber was re-configured to incorporate sacrificial quartz windows, which were then replaced weekly.

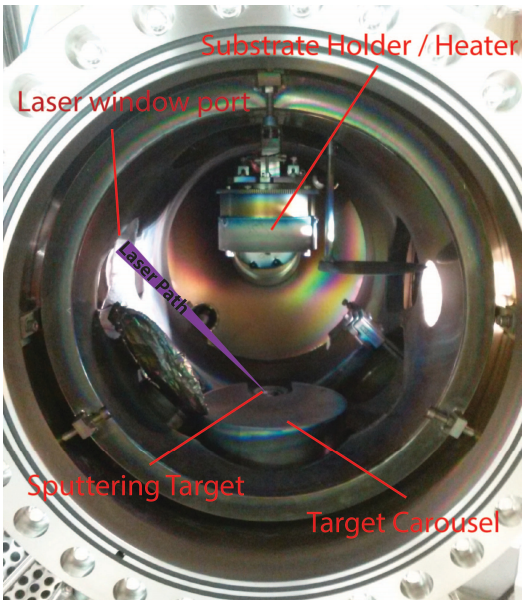

Fig. 3-5. Side view of EMAT PLD chamber

Single layer films of CZTS, 100 – 500nm thickness, were deposited on soda lime glass substrates by PLD from single, hot-sintered sputtering targets with the compositions specified in Table 3-2. After initial pumping to ultra-high vacuum ($\leq 10^{-7}$torr), films were deposited in Argon background (15mtorr) with a 2sccm flow rate. Nine substrates were installed per deposition using a metal mask and holder, at locations varying between 9 and 11cm from the target. During the deposition, substrate temperatures were varied between room temperature and up to 500°C using an infrared heater and silicon backing wafer. Substrates were allowed to cool passively back to room temperature after deposition.

Table 3-2. CZTS Sputtering Target Compositions

Target ID	Molar Composition			
	Cu	Zn	Sn	S
CZTS - 1	1.92	1.22	1.00	4.25
CZTS - 2	1.90	1.25	0.85	4.25
CZTS - 3	1.80	1.32	0.85	4.25

Materials

Sputtering targets with the compositions shown in Table 3-1 and Table 3-2 were purchased from American Elements. The sputtering targets were prepared via hot-sintering.

Table 3-3. Composition of Corning 0215 SLG substrates

Atomic %				
Si	**O**	**Na**	**Ca**	**Mg**
0.26	0.59	0.12	0.04	0.01

Corning 0215 soda lime glass substrates (SLG) were purchased from Ted Pella, P/N 26005. These substrates were used for all pulsed laser deposition studies, and Rutherford backscattering analysis of the substrate indicated the composition shown in Table 3-3.

3.1.3.2 Methodology

Prior to deposition, the soda lime glass substrates, 0.25-inches per side, were cleaned ultrasonically in acetone, alcohol, and ultra-high purity (UHP) water for 20min each cycle, and then blown dry with nitrogen gas. Substrates were then mounted in the sample holder, using either DuPont 4929N silver paste or a metal mask. To cure the silver paste, substrates were heated to 65°C for 35min prior to installation into the deposition chamber. Sacrificial quartz windows were then replaced.

The chamber was then pumped down to $\leq 5x10^{-5}$torr or $\leq 1x10^{-7}$torr for the EETD and EMAT deposition systems, respectively. After reaching the desired vacuum level, substrate temperatures were adjusted to the desired value using either the resistive or infrared heaters and allowed to stabilize. The background gas, if used, was then adjusted to the deposition pressure using the desired gas and flow rate. After the pressure stabilized, the substrates were either shuttered or moved as far back from the sputtering target as possible.

In the EETD chamber, the target rotator would then be started. In the EMAT chamber, the target rotator, sample holder rotator, and the rastering piezo would then be started. The laser was then turned on at the lowest stable energy and 1Hz repetition rate and the spot size/location adjusted as desired. The laser energy and repetition rate were then adjusted to the desired deposition condition, and run for several minutes to "clean" the sputtering target surface and to verify the plume stability. Finally, the sample holder would be moved to the desired target-substrate distance, and the shutter removed to initiate deposition.

3.2 ELECTROCHEMICAL DEPOSITION

Citations are provided and relevant texts are recommended throughout this section. However, I would like to acknowledge Scragg [19], Paunovic [20], and Bard [21], as this electrochemical deposition background section draws strongly from these works. For a more comprehensive review, the reader is strongly encouraged to visit these excellent texts.

3.2.1 Background

Fig. 3-6 illustrates a typical electrochemical cell used for electrodeposition of thin films. The **cathodic** deposition cell includes two conductive electrodes immersed in an aqueous solution that contains a mix of cationic (reducible) and anionic species. Typically, these electroactive species are introduced into the deposition bath in the form of metal salts (e.g. $CuSO_4$, $ZnSO_4$, $SnSO_4$), which form the cationic deposition species (e.g. Cu^{2+}, Zn^{2+}, Sn^{2+}) and anionic species (SO_4^{2-}) that supports the ionic current but does not participate in relevant reactions to the deposited film. The application of a sufficiently large external potential initiates a conduction current, indicated as the dashed line in Fig. 3-6. Conductive electrodes carry the current by electron drift, and the electrolyte bath carries an equal current by combinations of ionic drift (**migration**) and diffusion. At the metal-electrolyte interface of the working electrode, cationic species gain electrons and deposit on the electrode, according to the reaction (3-1) [19, 20]. At the anode, typically an inert material like platinum in three-electrode cells [21], a water splitting-reaction (3-2) completes the circuit. Section 3.2.2.2 describes three-electrode cells in more detail.

$$M^{z+}_{(aq)} + ze^- \rightarrow M^0_{(S)} \tag{3-1}$$

$$H_2O \rightarrow \frac{1}{2}O_2 + 2H^+ + 2e^- \tag{3-2}$$

The deposition reaction continues as long as the external potential remains applied, although conditions in the cell may evolve over time and modify the process [22]. As the deposition proceeds, the concentrations of cationic (deposition) species decrease unless they are replenished [19]. Commercial plating processes often employ the deposition metal as the anode material, which anodically dissolves in proportion to the deposition current, in order to maintain the concentration of cations [19]. Furthermore, the metal-solution interface changes as the deposition material coats the conductive substrate, and the interface may continue to evolve depending on the nucleation and film growth mode of the deposition.

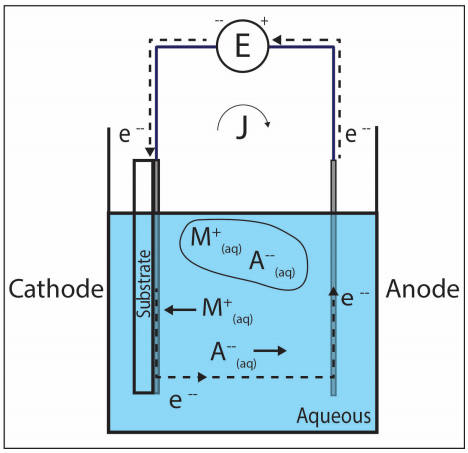

Fig. 3-6. Two-electrode electrochemical cell, adapted from [19]

The concentration of ionic species, reduction potential of the deposition species, the applied external potential, the mass transport properties, and the electrode configuration all play important roles in the growth behavior and the properties of electrodeposited films. The remainder of this section provides a brief review of relevant electrodeposition processes and electrochemistry theory; for a more detailed review, the reader is referred to a few of the many excellent texts on the subject [20-24].

3.2.1.1 Constant Current vs. Constant Potential

Constant current (**galvanostatic**) and **constant potential** (**potentiostatic**) control compose the two primary modes of operation during electrodeposition. In **galvanostatic control**, the external applied potential varies continuously in order to maintain a constant current throughout the deposition. In **potentiostatic control**, the external applied voltage remains constant throughout the deposition, allowing the deposition current to vary accordingly. The voltage device, known as a **potentiostat**, maintains the constant voltage or constant current by means of relatively simple op amp-based control circuitry [21]. Most of the work reported in this dissertation employs constant potential control, and the reader may assume potentiostatic control of presented experimental results unless otherwise noted.

3.2.1.2 Stacked Elemental Layer vs. Co-Deposition Processes

Three primary strategies have been employed to achieve Cu_2ZnSnS_4 thin films by electrodeposition, including: 1) stacked elemental layer (SEL) deposition of metal precursors with sulfurization reaction, 2) single-step co-deposition of metal precursors with sulfurization reaction, and 3) single-step co-deposition of all elemental components, which may or may not include further sulfurization.

SEL deposition of metal precursors involves the sequential deposition of each of the metal elements in the film, with the thickness of each layer adjusted to achieve the desired stoichiometric ratio. The metal precursor films are then annealed under sulfur background (e.g. H_2S or elemental sulfur) to incorporate sulfur and transform the film into the desired kesterite phase CZTS. An intermediate, low-temperature annealing step can promote metal alloying, helpful in the phase formation of kesterite CZTS [19]. The main advantages of this fabrication method include simplicity in deposition and flexibility in film stoichiometry. Due to the wide-ranging reduction potentials of the metals, there are some restrictions on the layering sequence of the metals [19]. Further, local variations in the film thicknesses of the metal precursors can lead to microscopic or macroscopic stoichiometric variations throughout the final films, decreasing the electronic quality of the films [19]. Even for highly uniform stacked layers, annealing and sulfurization must be properly controlled to achieve uniform mixing of the precursors.

Co-deposition of the metals can improve homogeneity of the metal precursor films, potentially yielding more uniform CZTS films [19]. In particular, the relaxed conditions on the

precursor film uniformity improve the adaptability of the fabrication method to commercial scale electrodeposition techniques. For instance, Scragg relied on the use of rotating disc electrode configurations to achieve the desired film uniformities [19], a process not readily scalable. However, finding deposition parameters that can simultaneously accommodate the electrodeposition of multiple elements represents a major challenge of the co-deposition approach [19]. For instance, the standard reduction potentials for copper, zinc, and tin vary widely, as shown in Table 3-4. A single deposition potential must be found which can concurrently reduce the metal elements at the correct rates to yield desired film stoichiometries, frequently requiring the use of complexing agents to shift the deposition potentials closer together [22, 23].

Moreover, literature has shown that the deposition behavior of multi-element semiconductors can be quite complex, resulting from metal-metal alloy and metal-chalcogen compound deposition mechanisms that significantly alter the reduction process [22, 25-27]. The interdependency of the ionic species stabilities, the elemental reduction mechanisms, and the alloy reduction mechanisms makes it difficult to optimize the deposition or alter the film stoichiometry in a predictable way [19], as the results of this dissertation will show. Once accomplished, the more highly-mixed and uniform co-deposited film may aid crystal phase formation of kesterite CZTS during sulfurization. Single-step deposition of all four elements Cu-Zn-Sn-S in the appropriate stoichiometries may also eliminate the need for sulfur background during post-annealing [28], which would dramatically simplify the fabrication process. Partial sulfur content in the precursor films (14 – 18%) has also been shown to improve the quality of annealed films through the reduction of voids [29], as discussed in Section 3.3.2.2.

3.2.1.3 Advantages and Disadvantages

As an atmospheric process, electrodeposition represents an attractive deposition method because it reduces the use of expensive vacuum equipment [18, 30]. Further, the scalability of electrodeposition has been demonstrated in large-scale industrial deployment of conventional metallic plating, and also in the semiconductor industry through the use of copper damascene electroplating techniques [18].

Frequently, however, electrodeposition involves the use of toxic processing materials, generating large volumes of chemical waste. Moreover, the quality of the films, in particular for the CZTS system, must improve in order to be competitive with other deposition techniques. To date, the best CZTS device deposited by electrodeposition (SEL method) has achieved 7.3% efficiency [31], while the champion CZTS device deposited by nano-ink spin-coating has achieved 12.6% efficiency [32].

3.2.2 Physico-Chemical Processes of Deposition

Electrodeposition involves many physico-chemical processes that depend on the following fundamental subjects: 1) the metal-electrolyte interface, 2) the equilibrium electrode potential, 3) the kinetics and mechanism of electrodeposition, and 4) nucleation and film growth. As

discussed in Section 3.2.1, the physico-chemical processes of deposition become increasingly more complex in transitioning from single-element electrodeposition of metals, to multi-element electrodeposition of alloys and compounds, to multi-element electrodepositions of alloys and compounds plus chalcogen components. In this section, the simplest process elements are discussed first, adding complexity where appropriate.

3.2.2.1 The Metal-Electrolyte Interface

Properties of Water and Ionic Solutions

Liquid water (H_2O) contains a collection of individual water molecules. The H-atoms and O-atom are covalently bonded, organizing into bonding sp3 orbitals with two lone electron pairs occupying the remaining two sp3 orbitals of the O-atom [20]. Electrons are more attracted to the atom with higher electron affinity (the O-atom), and bonding electrons spend more time around this atom than the other, inducing overall charging of the two bonding atoms and creating a **dipole moment** [20]. For this reason, water is a **polar molecule** and electrostatically interacts with other polar molecules, including itself [20].

Ionic crystals, or **salts**, are ionically bonded crystals consisting of alternating positive and negative ions [20]. These salts, such as $CuSO_4$ and $ZnCl_2$, are frequently dissolved in water to supply the necessary electroactive ions. All of the solutions used in this dissertation rely on metal and chalcogen salts to supply the depositing species: $CuSO_4$, $ZnSO_4$, $SnSO_4$, and $Na_2S_2O_3$. The dissolution process includes bond-breaking and separation from the lattice [20], and the dissolved ions may interact with water molecules or with other dissolved ions. In the former, ions interact with the dipole charges of the water molecules, causing the water molecules in the immediate vicinity to preferentially orient themselves according to the electrostatic forces between the charge of the ion and the dipole moment of the water molecule [20]. This forms a hydration shell which sheaths and moves with the ions as they move through the solution [20]; in this case, the ions are said to be **solvated**. These ion-water molecule interactions become particularly important in the development of the electric double-layer.

Properties of Metal Surfaces and Adsorption Processes

The surface of a metal refers to the topmost few layers of atoms, specifically those layers which are affected by the surface boundary and which interact with the electrolyte [20]. The outermost layer of atoms remains unbound on its free surface, causing a load imbalance which results in surface relaxation of the lattice [20]. Other surface defects may also be present in real surfaces, including: screw and edge dislocations, vacancies, substitutional defects, kinks, and adsorbed impurities [20]. Metal surface dislocation defects play important roles in adsorption and nucleation processes. Specifically, localized surfaces states may exist at the metal surface, which have energies within the forbidden regions associated with the bulk, and which effectively smear out the charge distribution at the surface [20]. Positive charges distribute inside the surface and

negative charges distribute outside the surface, yielding electron tails which may bond with adsorbed species [20].

Bard describes four methods of adsorption at the metal interface, including: purely electrostatic adsorption, specific ionic adsorption, adsorption of uncharged species (including dipoles), and chemisorption [33]. Purely **electrostatic adsorption** relies solely on long-range electrostatic forces to hold a given ionic species at the surface of the metal. **Specific ionic adsorption** implies the action of short-range forces that are *specific* to the given metal and adsorbate. **Adsorption of uncharged species** involves adsorption of a neutral species without significant chemical bond formation [33]. Finally, **chemisorption** achieves adsorption of an atom or molecule through the formation of chemical bonds with the metal surface, and it involves the highest adsorption energies [20, 33].

The Electric Double-Layer

The charge-transfer processes associated with deposition demonstrate **Faradaic behavior**, such that the extents of the reactions are proportional to the current flows [21]. In these processes, charge transfers across the solid-electrolyte interface. Additional **non-Faradaic processes** may also be active as a result of adsorption–desorption processes and structural changes to the solid-electrolyte interface that result from shifts in potential or electrolyte composition [21]. In non-Faradaic processes, no charge transfers across the interface [21]. The interface behaves similar to a capacitor in this case, and transient currents may flow [21]. While Faradaic processes predominate during deposition, the nature of the electric double-layer can strongly influence their behavior.

Due to the Fermi levels in the solid and electrolyte, the applied potential, the exchange of ions between the solid lattice and the electrolyte, and adsorption-desorption processes at the interface, the solid surface will develop a charge at the interface q_M [20, 21]. At equilibrium, no current flows, and the interface region must be charge neutral, such that an equal and opposite charge must exist within the electrolyte $-q_S$ [20]. Within a metal solid, the charge q_M will reside entirely at the surface as a sheet charge, due to the high conductivity of the metal (e.g. high carrier concentration). Within the solution, the charge will be supported by a distribution of cations, anions, and oriented solvent molecules near the solid surface [20]. Helmholtz originally represented the interface using a simple two-layer model, referred to as the **electric double-layer**. This model consists of two charge layers, q_M and q_S, separated by a distance d, defined by the closest approach of the solvated electroactive species and designated the **Helmholtz plane** [20]. In this case, the electric double layer behaves as a parallel-plate capacitor, obeying the classical relationship ($C=\varepsilon/4\pi d$), where C is the capacitance, ε is the dielectric constant between the metal surface layer and the Helmholtz plane, and d is the distance of the Helmholtz plane from the metal surface. A distribution of charge yields an electric field at the interface, which varies with the associated potential distribution at the interface. Subsequently, polar solvents such as water will

experience a force on the molecules near the metal surface which reorients their dipole moment in-line with the electric field.

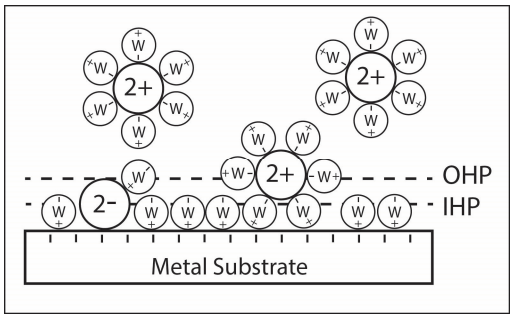

Fig. 3-7. Schematic of the electric double layer model, adapted from [20]

Others have since expanded on the solution-side layer to include multiple layers [21], although the original moniker **electric double layer** is still generally used. More recent models divide the solution side into the inner plane, the outer plane, and the diffuse layer. The inner plane contains the reoriented solvent molecules, as well as **specifically adsorbed ions**, and this **Inner Helmholtz Plane (IHP)** is defined by the centers of these molecules and ions [21]. The outer layer contains the closest-approach solvated ions, whose distance to the metal surface is limited by water molecules hydrating the ion, and the layer designated as the **Outer Helmholtz Plane (OHP)** is defined by the center of the ions [21]. These ions are called **nonspecifically adsorbed ions**, since they involve long-range Coulombic forces which are independent of the specific chemical properties of the ions [21]. The outermost diffuse layer consists of a distribution of the nonspecifically adsorbed ions between the OHP and the bulk of the solution. Fig. 3-7 shows the electric double layer model, including solvated cations (2+), specifically adsorbed ions (2-), and water molecules (W). Varying sizes of the ions and water molecules are intended to help identify them, and the radii shown are not to scale. See [21] for a more comprehensive description of the model. Note that the properties of the electric double layer can strongly influence the adsorption behavior of the system. For more information on this topic, the reader is referred to [21, 34].

3.2.2.2 The Equilibrium Electrode Potential

The Three-Electrode Cell

The most basic electrochemical cell consists of a cathode and an anode, as shown in Fig. 3-6. In cathodic electrodeposition of metals and semiconductors, the working electrode (e.g. the substrate) acts as the cathode, while the anode completes the electric circuit. A potentiostat connected between the cathode and anode maintains a constant potential on the cathode relative to the anode. An **ideal, non-polarizable electrode**, whose potential does not vary under current loading [21], provides the most accurate measure of changes in potential at the working electrode by maintaining a fixed reference potential.

However, such an ideal reference electrode placed in-line with the circuit measures not only the potential drop across the electric double-layer but also the potential drop associated with the resistance of the electrolyte [21]. In cases where this iR_s term is large, true for electrodeposition processes which involve large surface areas and comparatively high currents (mA), then it becomes necessary to introduce a third electrode. In this case, an auxiliary, or **counter electrode**, passes the current, and the reference electrode placed near the working electrode bypasses the majority of the ohmic drop in the electrolyte and conducts negligible current itself [21]. Only a small uncompensated resistance (R_u), which depends on the electrolyte conductivity and the electrode distance, remains. Fig. 3-8 shows a typical three-electrode cell.

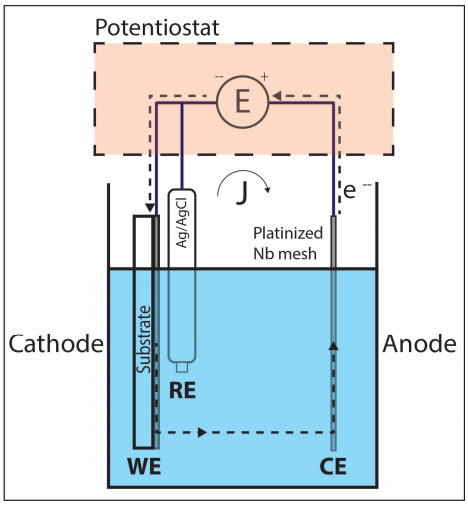

Fig. 3-8. Three-electrode electrochemical cell, adapted from [19]

Equilibrium Electrode Potential

Thermodynamics provides a powerful framework to relate the potential distributions through the electrochemical cell to the free energy changes in the system. However, thermodynamics inherently describes systems in equilibrium, and its applicability depends on the degree of *reversibility* in the system. In the case of electrodeposition, chemical reversibility and thermodynamic reversibility must be considered [21]. **Chemical reversibility** refers to the degree to which chemical reactions may proceed in forward and reverse directions. In a simplified view, if a net reaction cannot be reversed after reversal of the cell current, then the cell is not chemically reversible [33]. **Thermodynamic reversibility** refers to the ability of a reaction to reverse direction under an "infinitesimal reversal of the driving force" [21]. Real systems cannot exhibit true thermodynamic reversibility, since state changes through infinitesimal steps would take infinitely long to complete. However, a system may be **practically reversible,** such that it follows the **Nernst equation** relating the electrode potential to the species activity via the thermodynamic properties (free energies) of the system [21].

The change in **Gibbs free energy** of a charge transfer process, associated with cationic reduction during electrodeposition, can be related to the work done by the cell, as shown below [20, 21]:

$$|\Delta G| = W = qV = zF|\varepsilon| \tag{3-3}$$

where ΔG is the change in Gibbs free energy, W is the work performed by the cell, q is the total charge involved in the transfer, V is the voltage, z is the number of electrons transferred per atom, F is faraday's constant, and ε is the electromotive force [21]. **Electromotive force (emf)** relates the potential of the cell to a specific reaction, in order to assign a direction to a thermodynamic property otherwise inherently directionless [21]. A negative ΔG implies spontaneous reaction takes place, and by convention ε is defined as positive for this case, such that:

$$\Delta G = -zF\varepsilon \tag{3-4}$$

Under standard conditions, where all products and reactants are at unit activity, the standard Gibbs free energy, ΔG^0, and the standard emf, ε^0, of the reaction may be defined according to Eqn. (3-5) [21]:

$$\Delta G^0 = -zF\varepsilon^0 \tag{3-5}$$

From fundamental thermodynamics, the Gibbs free energy of the general reaction (3-6) may be expressed as Eqn. (3-7) [20]:

$$aA + bB + \ldots \rightleftharpoons mM + nN + \ldots \tag{3-6}$$

$$\Delta G = \Delta G^0 + RT \ln\left[\frac{a_M^m a_N^n, \ldots}{a_A^a a_B^b, \ldots}\right] = \Delta G^0 + RT \ln \frac{\Pi[a_{\text{prod}}]}{\Pi[\text{a}_{\text{react}}]} \tag{3-7}$$

where a, b, m, and n are stoichiometric coefficients, R is the universal gas constant, and T is the temperature of the reaction. Substituting (3-4) and (3-5) and dividing by -zF, Eqn. (3-7) may be rewritten in the terms of emf as follows. Eqn. (3-8) is known as the **Nernst Equation** [20, 21].

$$\varepsilon = \varepsilon^0 + \frac{RT}{zF} \ln \frac{\Pi[a_{react}]}{\Pi[\text{a}_{\text{prod}}]} \tag{3-8}$$

where ε is the equilibrium electrode potential and ε^0 is the standard potential of the electrode reaction. Historically, the Nernst equation has been described in terms of electrode *potentials*, although it is understood that the values technically represent the *electromotive force* [33]. Chemical activity, a_i, is defined as the ratio of the given species concentration in solution to a standard concentration (typically 1M) multiplied by an activity coefficient γ_i that varies with the concentrations of all species in the solution [20]. In dilute solutions (~0.01M), the concentration

approximately equals the activity [20]. By convention, the activities of atoms and electrons in a lattice are equal to 1 [20], and standard concentrations are 1M.

The **Nernst equation** describes the relationship between the equilibrium electrode potential and the contacting electrolyte composition [33]. **Standard electrode potentials** represent the equilibrium electrode potentials under standard-state conditions, for which the activities of all product and reactant species are equal to one and subsequently $\varepsilon = \varepsilon^0$ [33]. The standard electrode potentials for metal components in the CZTS system are shown in Table 3-4.

Table 3-4. Standard electrode potentials, from [20, 21]

Metal/Metal-Ion Couple	Electrode Reaction	Standard Value (V) vs. NHE
Cu/Cu^{2+}	$Cu^{2+} + 2e^- \rightleftharpoons Cu(s)$	0.342
Zn/Zn^{2+}	$Zn^{2+} + 2e^- \rightleftharpoons Zn(s)$	-0.762
Sn/Sn^{2+}	$Sn^{2+} + 2e^- \rightleftharpoons Sn(s)$	-0.138

Notably, a single electrode reaction does not represent a complete cell, and the Nernst derivation implicitly assumed a couple to a second half-reaction represented by the **normal hydrogen electrode (NHE)**, which has been accepted as the standard reference potential, where $\varepsilon^0 = 0$. Therefore, the emf of an overall cell reaction may be ascertained through the coupling of two half-reactions, each referenced vs. NHE [21]. For a more rigorous kinetic derivation of the Nernst equation, see [20].

$$\varepsilon_{cell} = \varepsilon_{right} - \varepsilon_{left} \tag{3-9}$$

Measuring Equilibrium Electrode Potentials: Reference Electrode

As discussed previously, an **ideal, non-polarizable** reference electrode provides a stable reference potential, which does not vary with composition or current. The **normal hydrogen electrode (NHE)** consists of a Platinum electrode in contact with hydrogen gas and an aqueous solution containing hydrogen ions, undergoing the reaction shown in Eqn. (3-10) [21]. The NHE equilibrium potential represents the standard potential against which other half-reactions are measured. Only changes in potential are relevant, and the NHE equilibrium electrode potential, under standard conditions, is arbitrarily set equal to zero [20].

$$2H^+ + 2e^- \rightleftharpoons H_2 \tag{3-10}$$

Another common type of reference electrode includes the **Metal-Insoluble Salt-Ion** electrode. A given reference electrode may be more well-suited to a given experiment based on the composition of the electrolyte and the expense of the electrode. A **silver-silver chloride (Ag/AgCl)** reference electrode, of this category, was used for all experiments performed in this

thesis. The electrode can be characterized by the following reaction, with the Nernst equation (3-8) applying as follows [20]:

$$AgCl(s) + e^{-} \rightleftharpoons Ag(s) + Cl^{-}(aq) \tag{3-11}$$

$$\varepsilon = 0.222 - 0.0592 \ln[a_{Cl^-}] \tag{3-12}$$

where 0.222 represents the standard electrode potential and a_{Cl^-} represents the activity of the chlorine ions. The reference electrode includes a self-contained solution of saturated KCl, which maintains a constant activity of chlorine ions in solution throughout the electrodeposition process. Under saturated KCl conditions, the equilibrium potential of the reference electrode Ag/AgCl is 0.197V vs. NHE [20].

Practical Considerations in Electrode Configuration

The choice of material for the counter electrode, as well as the electrode orientation and electrode spacing within the solution, can have a significant impact on the accuracy of the potential measurements and the quality of the electrodeposition. In general, the counter electrode should be conductive, inert and much larger than the working electrode in geometric size [21, 33].

The volume of electrolyte, defined by projecting path lengths along the outer edges of the working and counter electrodes, roughly defines the current-carrying portion of the bath [21]. Increasing the counter electrode area increases the size of this volume by increasing the average cross-sectional area, thereby reducing ohmic resistance in the electrolyte current path [21]. Notably, however, the resistance distribution will shift such that a greater portion of the potential will drop closer to the working electrode, due to the locally reduced cross-sectional area of the current path, thus increasing uncompensated resistance [21].

Electrodeposition involves the passage of relatively high currents (~10mA), which inherently give rise to potential variations in the electrolyte associated with its ohmic resistance. With large currents, these variations may be significant, yielding non-uniform current densities, and therefore non-uniform potentials, over the face of the working electrode [21]. The size and the placement of the working electrode relative to the counter electrode can, therefore, significantly impact the uniformity of the potential during deposition. To maintain a uniform current density and subsequently uniform potential, the working electrode must be parallel with the counter electrode and the electrolyte resistance reduced to the extent possible [21]. Large surface area working electrodes are more susceptible to these geometric variations.

3.2.2.3 Kinetics and Mechanisms of Electrodeposition

Thermodynamics describes the behavior of a system in equilibrium, and so describes only what processes nature will allow and not necessarily what processes will take place. **Kinetics** describes the rate and behavior of the reactions involved in the system, and so describes the way that systems change state and how quickly they will reach equilibrium [21]. Both thermodynamics

and kinetics are required to describe the behavior of real systems. In some cases, the thermodynamics may be favorable for a given transformation to occur; however, the kinetics of the reactions involved may be so slow that this transformation may never be realized on a practical timescale. For instance, the kinetics associated with hydrogen evolution reaction at a Platinum electrode are much faster than those at a Mercury electrode, and the reaction initiates at much more noble potentials on Platinum than on Mercury [35].

This section introduces some of the basic models associated with the kinetics of electrodeposition, building from the concepts of overpotential and one-step one-electron processes to develop a relationship between current and potential. For more detailed treatments, the following excellent references should be consulted: [20, 21, 23, 24, 35].

Overpotential

At equilibrium conditions within the electrochemical cell, there exists zero net current [21]. Under these conditions, the cathodic and anodic currents, i_c and i_a, associated with the electrode reactions are equivalent and referred to individually as the **exchange current, i_0,** such that $i_0 = i_c = i_a$ [21]. Applying a potential to the cell greater than the equilibrium potential for the electrode reaction (more negative in the case of cathodic deposition) will shift the balance of reaction such that $i_c > i_a$, and cathodic electrodeposition may proceed. In this case, the parameter of interest is the **overpotential, η,** which relates the applied bias to the equilibrium emf and represents, in simple terms, the **activation energy** required to drive the reaction:

$$\eta \equiv \varepsilon - \varepsilon_{eq} \tag{3-13}$$

where η is the overpotential, ε is the applied bias to the cell, and ε_{eq} is the equilibrium potential.

Four types of partial reactions take place in the cell during electrodeposition: **1) mass transfer** from the bulk to the electrode surface; **2) charge transfer** at the electrode surface; **3) chemical reactions** involved in the overall electrode reaction, including complex dissociation; and **4) other surface reactions**, including adsorption, desorption and crystallization [20, 21]. These four components proceed in series, each contributing to the overpotential; therefore, any one of the processes may be rate-limiting for the deposition [20]. The **total overpotential** may then be written as Eqn. (3-14):

$$\eta = \eta_{mt} + \eta_{ct} + \eta_{rxn} + \eta_{cryst} \tag{3-14}$$

where η is the total overpotential, η_{mt} is the mass transfer overpotential, η_{ct} is the charge transfer overpotential, η_{rxn} is the chemical reaction overpotential, and η_{cryst} is crystallization overpotential [20, 21].

As ions are consumed (e.g. deposited) at the electrode surface during a deposition process, a fresh supply of ions must be transported from the bulk electrolyte through the electric double-

layer to the electrode surface. This mass transport may be accomplished by a combination of migration, diffusion and/or convection [21]. In many cases, this transport proceeds under diffusion-limited conditions, increasing the **mass-transport overpotential** [20]. The deposition of a component involves the incorporation of an ion in solution into the lattice of the solid at the electrode surface, and this process requires an exchange of charge carriers between the oxidized deposition species (e.g Cu^{2+}) and the electrode ($2e^-$). The **charge-transfer overpotential** refers to the overpotential associated with the exchange of charge [20]. In addition to the charge-transfer, activation energies are associated with the actual incorporation of the atom into the lattice, and this process is separately associated with the **crystallization overpotential** [20]. Other **chemical reactions** may also be involved in the deposition chain. For instance, complexing agents are frequently used to alter the activities of one or more components. These complexed ions must be dissociated before the deposition species may be incorporated into the lattice [20].

Basic Kinetics Model

This section briefly summarizes the kinetics model of an elementary reaction with a **one-step, one-electron process**, derived in terms of the **standard free energy of activation**, which ultimately enables the current to be related to the overpotential applied during deposition.

Given the following reaction (3-15) involving a "discrete, chemical event" between two substances, A and B, that is driven by the forward and reverse rate constants, k_f and k_r, the rates of reaction may be written as (3-16) – (3-18) [21]:

$$A \underset{k_r}{\overset{k_f}{\rightleftharpoons}} B \tag{3-15}$$

$$v_f = k_f a_A \tag{3-16}$$

$$v_r = k_r a_B \tag{3-17}$$

$$v_{net} = v_f - v_r \tag{3-18}$$

where a_A and a_B are the activities of substances A and B, v_f is the rate of forward reaction, v_r is the rate of reverse reaction, and v_{net} is the net conversion rate of A to B.

The reaction rates, v_f and v_r, refer to the changes in the number of moles versus time in elements A and B, respectively [20]. The current contributions from each of the reactions may be formulated in terms of the reaction rate, the charge transferred per mole, zF, and the definition of current (I=dq/dt) to yield:

$$i_c = i_f = zFAv_f \tag{3-19}$$

$$i_a = i_r = zFAv_r \tag{3-20}$$

where z is the charge transferred per chemical event, F is Faraday's constant, A is the active area of the interfacial reaction, i_c is the cathodic current, and i_a is the anodic current [20, 21]. Substituting Eqn. (3-16) and (3-17) into (3-19) and (3-20), respectively, the net current may be defined as follow:

$$i_{net} = i_f - i_r = zFA(v_f - v_r) = zFA(k_f a_A - k_r a_B) \tag{3-21}$$

Expressions may be developed for the reaction rates, k_f and k_r, in Eqn. (3-21), which include potential-independent and potential-dependent components, as well as an additional **transfer coefficient term, α**, introduced to account for the asymmetry of the cathodic and anodic activation barriers [21]. The **Butler-Volmer equation** may then be written as follows [21]:

$$i = i_0 \left(e^{-(\alpha zF\eta)/RT} - e^{(1-\alpha)zF\eta/RT} \right) \tag{3-22}$$

where i is the net current, i_0 is the exchange current, α is the transfer coefficient, z is the charge transferred per chemical event, F is Faraday's constant, η is the overpotential, R is the universal gas constant, and T is the temperature of the process [21].

The development of Eqn. (3-22) assumes that the overpotential is charge-transfer limited, evident as treating the activity of the reactant a_A as a constant [20]. This relation holds for low currents, $i < 0.10(i_{L,c})$ or $< 0.10(i_{L,a})$, consistent with activities of reactants at the interface remaining within 10% of their values at bulk [21]. As the overpotential drives the cathodic currents higher, diffusion cannot supply the reactants fast enough to keep pace, eventually leading to a surface concentration of zero. In this case, reactants are consumed as fast as they can be supplied to the interface, and the deposition current reaches a **limiting current, i_L**. This case will be discussed in **Systems Under Diffusional Control** and Section 3.2.2.4. The various control regimes are demonstrated in Fig. 3-9 below.

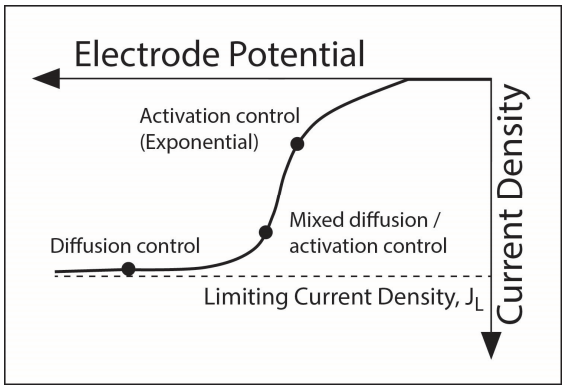

Fig. 3-9. Regimes in the current-potential relationship, adapted from [20]

Notably, the exchange current strongly impacts the shape of the current-potential under activation control [21]. A small exchange current indicates sluggish kinetics, thus requiring a larger overpotential to achieve a given net current [21]. Conversely, a small overpotential may

deliver large currents when the exchange current is high [21]. Increasing the exchange current has the effect of steepening the slope of the current in the activated control region of the current-potential curve [21].

In practice, the reactions involved in deposition are much more complicated than the one-step, one-electron process described in the derivation. Real processes typically contain multiple reaction steps, often involving complexation and dissociation, as well as adsorption and crystallization processes. While the current-potential relationships above do not strictly apply to these real systems, they do provide a qualitative understanding of the expected behavior in the system and may be used as a conceptual basis for interpreting results, such as those from cyclic voltammetry [21]. In addition to deposition reactions, other Faradaic reactions may be taking place in parallel, such as hydrogen evolution and extraneous surface reactions that do not result in the desired deposition. The overall current density may then be written as [19]:

$$J_{tot,ss} = J_{film\,dep} + J_{Hydrogen} + \sum_i J_i \tag{3-23}$$

where $J_{tot,ss}$ is the total current density at steady-state (e.g. only Faradaic reactions contribute), $J_{film\,dep}$ is current density due to film deposition, $J_{Hydrogen}$ is the current density to hydrogen evolution reaction, and J_i are component current densities resulting from other non-desired reactions [19].

Systems Under Diffusional Control

The electrodeposition of multi-element thin films frequently takes place under diffusional control, particularly for metal-chalcogenide systems involving cations and anions. The wide-ranging reduction potentials of the elements (or alloys/compounds) requires deposition at potentials more negative than the least noble element, which can quickly drive the more noble element reduction processes into the mass-transfer limited regime. Critically, diffusion allows oppositely charged components (e.g. the $S_2O_3^{2-}$ anion) to be transported in the same direction [22].

In systems under **diffusional control**, the rates of deposition reactions are limited by the rates that the electroactive species are diffusionally transported to the surface. Assuming quasi-one dimensional transport conditions (e.g. planar electrode and transport geometry), initially uniform concentration, step-function applied bias, surface concentration equal to zero for $t > 0$ (the condition for diffusional control), and applying the transport equations and mass conservation law, the time-dependent current density, known as the **Cottrell equation**, may be written as follows [20, 21]:

$$J = \frac{zF[M^{z+}]\sqrt{D}}{\sqrt{\pi t}} \tag{3-24}$$

where J is the deposition current density, $[M^{z+}]$ is the initial (or bulk) concentration of the electroactive species, D is the diffusion coefficient of the electroactive species under conditions of experiment, and t is the time after step-potential has been applied.

The diffusion current density described by Eqn. (3-24) represents a **limiting current density, J_L**, for a given deposition reaction. These limiting currents, $J_L A$, will be evident on potential sweeps (e.g. cyclic voltammetry studies) as current plateaus, as shown in Fig. 3-9. If current densities larger than J_L are forced through the electrode, the electric double layer will accumulate charge until the overpotential of the electrode initiates another reaction process, such as another deposition reaction or the hydrogen evolution reaction [20]. Note also that the presence of the $t^{-1/2}$ term in J_L signifies that the current density will decrease indefinitely. The flow of ions in the bath, however, will eventually induce a natural convection current, which partially replenishes the depleting concentration boundary layer, and yield a constant, steady-state current density composed of diffusion and convection currents [19]. Electrodeposition at current densities close to or exceeding the limiting current densities can often yield rough, powdery films [20, 36], as discussed further in Section 3.2.2.4.

Underpotential Deposition (UPD)

The standard electrode reactions and their associated reduction potentials, described in Table 3-4, implicitly assume that the depositing material and electrode material are the same. After initial deposition of several monolayers, the interface approaches this condition. **Underpotential deposition** refers to positive (noble) shifts in the reduction potentials of metals, relative to Nernstian equilibrium potentials, which result from deposition onto foreign substrates [24, 37]. In these cases, the depositing ions are more strongly bound to the foreign metal electrode than similar metals, where they are partially or completely reduced and deposited [24, 37]. Due to the complexity in chemical interactions at the interface, predicting the behavior of the underpotential deposition mechanism poses significant difficulty. Cyclic voltammetry, however, may be used to empirically identify the noble shifts in reduction potential [37].

The underpotential deposition mechanism represents a self-limiting process, as the effects of the foreign metal substrate will drop off after only a few monolayers [24]. Subsequently, such mechanisms are not typically relevant for the *bulk deposition*. The underpotential deposition mechanism may, however, play a role in the initial nucleation processes. Further, in the case of multi-element depositions, in which the electrode surface refreshes with new "foreign" deposits, the underpotential mechanism may remain more active.

Anomalous Co-deposition (ACD)

Under some conditions, the gain in free energy associated with compound formation yields a positive (noble) shift in the reduction potential of the less noble element [22]. Mechanisms of this type have been referred to as induced co-deposition, induced underpotential co-deposition,

anomalous co-deposition, or simply the Kroger mechanism [22, 25, 26, 38]. **Anomalous co-deposition** operates analogously to chemical vapor deposition (CVD), which involves self-regulating compound formation that leads to stoichiometric growth [39]. A brief review of the anomalous co-deposition mechanism for binary alloys and compounds originally developed by Kroger [25] is given below, in order to introduce basic concepts associated with the process. For a more rigorous treatment, the reader should refer to [22, 25, 26].

Kroger introduces the concept of the **quasi-rest potential (QRP)** to describe the effective equilibrium electrode potential (more noble) that exists as a result of alloy or compound formation. Specifically, the QRP represents the potential at the electrode that corresponds to the activities of the electroactive species taken as they are during deposition at the solid-electrolyte interface [25]. The potential at which co-deposition of the two elements proceeds then corresponds to the QRP plus an associated overpotential [25]. Four major factors influence the establishment of the QRPs: 1) the equilibrium potentials of the component species, 2) the thermodynamics associated with the compound formation, 3) the activities of the electroactive species at the solid-electrolyte interface during deposition, and 4) the relative magnitudes of the exchange currents for each component [25].

By accounting for the activities of the electroactive species, particularly as those values change according to the thermodynamics of compound formation, the possible shifts in equilibrium potentials may be accounted for using the Nernst equation. Consider the formation of compound M_rN_s, through the deposition of ionic species (present as M^{m+} and N^{n+}) and subsequent solid-state reaction, as follows:

$$M^{m+} + me^- \rightleftharpoons M(s) \tag{3-25}$$

$$N^{n+} + ne^- \rightleftharpoons N(s) \tag{3-26}$$

$$rM(s) + sN(s) \rightleftharpoons M_rN_s(s) \tag{3-27}$$

where m^+ represents the oxidation state of component M, n^+ represents the oxidation state of component N, (s) designates the solid state, and M_rN_s is the final compound. Here, N is arbitrarily taken as the more noble species (e.g. $\varepsilon_N > \varepsilon_M$). The QRP for a given component, X, may be written using the Nernst equation (3-8):

$$\varepsilon_X = \varepsilon_X^0 + \frac{RT}{xF}\ln\frac{a_{X^{x+}}}{a_X} \tag{3-28}$$

Calculating the equilibrium potential for a single metal is straightforward, as the activity of the component in a pure solid (e.g. a_M, a_N) would simply be equal to unity. Under standard conditions, $a_M{}^{m+}$ and $a_N{}^{n+}$ would also be taken as unity, yielding the standard reduction potential $\varepsilon_M = \varepsilon_{M,0}$. In this case, however, compound formation will modify the activities a_M and a_N, thereby causing

associated shifts in the equilibrium potentials ε_M and ε_N. From basic thermodynamics [40], the activities of components M and N in the deposit, a_M and a_N, respectively, may be calculated at chemical and thermodynamic equilibrium as follows:

$$\frac{a_{M_r N_s}}{a_M{}^r a_N{}^s} = \exp(-\Delta G/RT) \tag{3-29}$$

where a_{MrNs} is the activity of the compound and ΔG is the free energy changed associated with the reaction in (3-27). Assuming M_rN_s as the stable, most-abundant end phase, its activity approaches unity. Further, it is assumed that the compound formation is energetically favorable, such that $\Delta G < 0$. Subsequently, Eqn. (3-29) reduces to the following:

$$a_M{}^r a_N{}^s = \exp(\Delta G/RT) \tag{3-30}$$

Two different phase limits may then be examined: a) nearly pure M in coexistence with M_rN_s, and b) nearly pure N in coexistence with M_rN_s. By evaluating Eqn. (3-30) at these two limits, and substituting the activities into Eqn. (3-28), the **maximum shifts in the equilibrium potentials** associated with compound formation can be calculated as $\mathbf{\Delta\varepsilon_M=-\Delta G/rmF}$ (case a) and $\mathbf{\Delta\varepsilon_N=-\Delta G/snF}$ (case b). For further discussion, the reader again is referred to [22, 25, 26].

3.2.2.4 Nucleation and Film Growth

Electrodeposited film growth proceeds by the nucleation of adsorbed ion (adion) clusters and coalescence of these clusters to form coherent deposits [20]. The **nucleation process** involves approach and adsorption of the ion on the electrode surface, followed by transport of the adion on the electrode surface to the final nucleation site [20]. Isolated adions on electrode surfaces are unstable, due to their small binding energies. However, by forming clusters above a critical size, these adions can increase their stability through an increase in surface energy and a decrease in their free energy formation [20]. For 2D nucleation, the **critical cluster size N_C** can be described by the following [20]:

$$N_c = \frac{bs\varepsilon^2}{(ze\eta)^2} \tag{3-31}$$

where b is the aspect ratio of the cluster, s is the area occupied by on atom on the surface of the nucleus, ε is the edge energy, z is the charge associated with the adion, e is the fundamental unit of charge, and η is the overpotential. Notably, the critical cluster size exhibits a strong dependence on overpotential: $N_C \alpha \eta^2$. Stochastic processes govern the cluster formations, with statistical variations yielding some nucleation sites above the critical size [20].

Assuming a uniform nucleation probability across the electrode, the **first-order nucleation law** may be written as [20]:

$$N = N_0\left[1 - \exp(-At)\right] \tag{3-32}$$

where N is the number of nucleation sites, N_0 is the maximum number of nucleation sites on the surface, A is the nucleation rate constant, and t is time. For the initial stages of nucleation (e.g. t ~ small), two limiting cases exist, corresponding to very large and very small nucleation rate constants A. In **Instantaneous Nucleation (large A)**, $N \approx N_0$ and all available sites are instantaneously nucleated. In **Progressive Nucleation (small A)**, $N \approx AN_0t$ and the number of nucleation sites increases linearly with time [20].

Further growth of the nucleated sites may proceed independently, or they may experience overlap with other nucleated sites during their growth. Typically, independent site growth only proceeds in the very early nucleation stage, and later growth stages must account for the overlap of the nucleated sites [20]. **Multilayer film growth** (e.g. layers greater than one monolayer thick) may proceed by 2D layer growth or 3D nucleation-coalescence growth [20].

Two-dimensional layer growth progresses by mononuclear layer-by-layer growth or multi-nuclear step growth. In **mononuclear layer-by-layer growth**, the nucleus growth rate exceeds the nucleus formation rate, such that a single nucleus acts as the source of each monolayer [20]. This growth mechanism requires low nucleation rates, a condition typically corresponding to low overpotentials [20]. In **multi-nuclear step growth**, multiple nucleation sites form at the same time, such that layer growth progresses by the lateral spreading and merging of multiple step edges across its surface. The lateral growth proceeds generally faster than vertical growth, such that the coherent film depositions are formed approximately monolayer by monolayer [20].

Three-dimensional nucleation-coalescence growth progresses by the formation of isolated 3D nuclei that gradually coalesce to form a continuous film [20]. The adion surface mobility on the electron, the charge-transfer kinetics, the ion mass transfer properties, and the overpotential all influence the 3D nucleation and growth behavior. When the nucleation rate (vertical growth) exceeds the adion transport across the surface (lateral growth), 3D growth features become more pronounced because adions have less time to find low-energy step edge locations in the crystal [22, 36]. This growth condition corresponds to high overpotentials and diffusion-limited transport. As current densities increase relative to the limiting current, films exhibit degrading morphological features, such as ridges, polycrystalline blocks, dendrites and dispersed powders [20, 36].

Diffusion-Limited Growth

Under diffusion-limited growth conditions, mass transfer of the electroactive species from the bulk to the electrode surface represents the rate-limiting step in film growth. Effectively, the species are consumed by the deposition reaction as soon as they reach the electrode, such that their surface concentration remains close to zero. In this condition, three-dimensional growth mechanisms are exaggerated by the transport and nucleation behavior, yielding a range of

characteristic film morphologies, such as cauliflower deposits, spongy deposits, dendritic deposits, and powdery deposits [20, 41]. The type of morphology that develops depends strongly on the **exchange current density j_0** of the deposition reaction, which influences the nucleation rate [42]. Note the nucleation rate constant A given in Eqn. (3-32) varies inversely with j_0 [42]. In general, larger nucleation rates yield smoother, more compact films, since the grains have less time to grow before coalescence [42]. At very negative deposition potentials, however, low values of j_0 can increase film porosity due to increased hydrogen evolution reaction [42].

Surface irregularities on the surface of the electrode, resulting from nucleated grains or the substrate itself, cause variations in the deposition current density under mixed activation-diffusion and fully diffusion-limited control. The current density increases at the tip of the surface feature compared to the flat electrode surface as result of the effective decrease in the diffusion layer at this point [42]. Lateral (e.g. spherical) diffusion at the tip also increases the local current density [42]. Cauliflower growth can proceed from nucleated ellipsoidal grains, as shown in Fig. 3-10. The grain first grows vertically, and then grows hemispherically once high enough to facilitate spherical diffusion, giving rise to the **cauliflower** shape [42]. The nucleated grains must be spaced sufficiently far apart to allow spherical diffusion around the tip [42]. An example of cauliflower morphology in electrodeposited Cu is shown in Fig. 3-10. The development of cauliflower morphology corresponds to conditions of mixed activation-diffusion control [42].

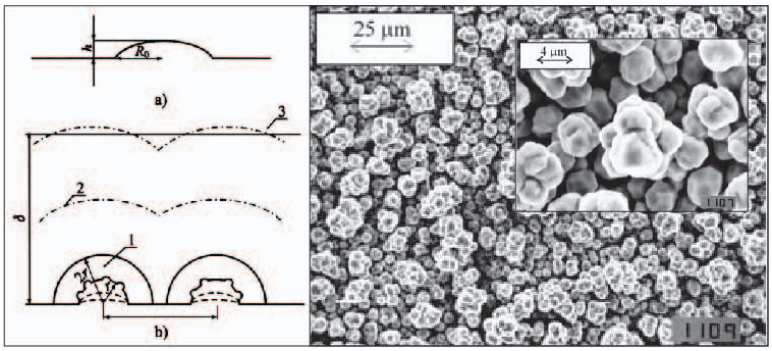

Fig. 3-10. Mechanism of cauliflower growth and example of Cu film with cauliflower morphology, reproduced from [42] and [43]

Systems fully under diffusional control can develop spongy, dendritic, or powdery deposits depending on the applied overpotential and exchange current density. Similar to cauliflower deposits, **spongy deposits** result from spherical diffusion around protrusions [42]. In particular, spongy deposits develop when film growth proceeds under fully diffusion-limited conditions with low nucleation rates (high current exchange densities), such that $j_L < j_0$. Since j_L depends proportionally on the concentration of the depositing ions, as shown in Eqn. (3-24), the morphology may be directly modulated by varying the ion concentration, as shown in [42].

Dendrites form under high overpotentials and high exchange current densities. They are defined by characteristic overpotentials, below which they do not form, and by ordered, branch-

like structures [42]. The dendrite growth mechanism consists of activation-controlled growth at the protrusion tip and diffusion-limited growth at the macroelectrode, which proceeds once the feature reaches a critical height [42]. The critical feature size depends directly on a critical overpotential that varies logarithmically with j_L/j_0 [42]. Therefore, lower overpotentials are required at higher exchange current densities, in order to initiate dendritic growth [42]. The **induction period** refers to the growth period of the protrusion prior to reaching the critical height to initiate the dendrite growth mechanism. The induction period and transition to dendrite growth can be evaluated from chrono-amperograms, evident as a well-defined shift in slope, as shown in Fig. 3-11. Since j_L varies proportionally with the concentration of the depositing species, decreasing species concentration increases j_L/j_0 and therefore increases the likelihood of dendrite formation [42]. Increasing the electrolyte conductivity and decreasing the solution velocity also enhance dendritic growth [42].

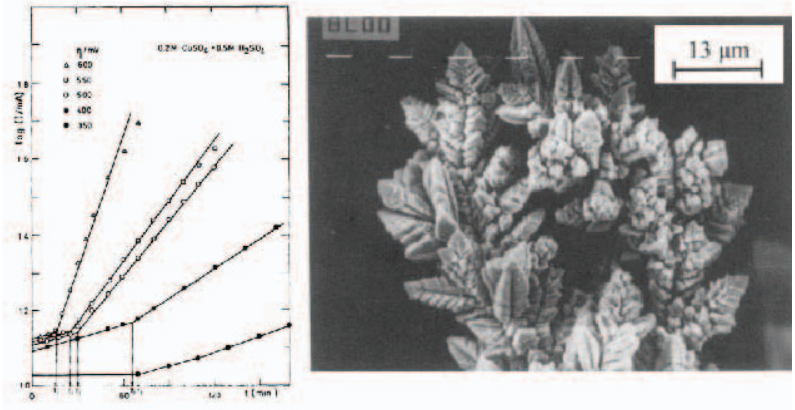

Fig. 3-11. Plot of log(I) vs. time illustrating transition to dendrite formation and example of Cu film exhibiting dendrite structure, reproduced from [42]

Powdery deposits represent loosely adhering dendrites that may form at very high current densities. This morphology develops above a critical current density, and the transition to powder formation was shown to be a constant product of the current density multiplied by the square root of time to formation. This time-dependence indicates a diffusion-limited process, and the onset of powder formation coincides with the transition to diffusion-limited control [42].

Higher overpotential yields smaller grain sizes [42]. Galvanostatic deposition typically yields less dendritic films, since the overpotential at the end of deposition is smaller than potentiostatic control [42]. Moreover, at high overpotentials, hydrogen co-deposition (e.g. hydrogen evolution reaction) may proceed in parallel with deposition. Hydrogen evolution can modify the film growth and morphology in several ways, including incorporating hydrogen into the film, forming voids in the film, and modifying the hydrodynamic layer and associated mass transfer [43]. In general, hydrogen co-deposition yields porous films with very high surface areas [43]. During hydrogen evolution, bubbles form on the surface of the film or electrode, which block further film growth at these sites, modify the local current density, and promote vertical

growth of protrusions around its edges. Fig. 3-12 shows example morphologies of electrodeposited Cu films that resulted from diffusion-limited growth with hydrogen co-deposition.

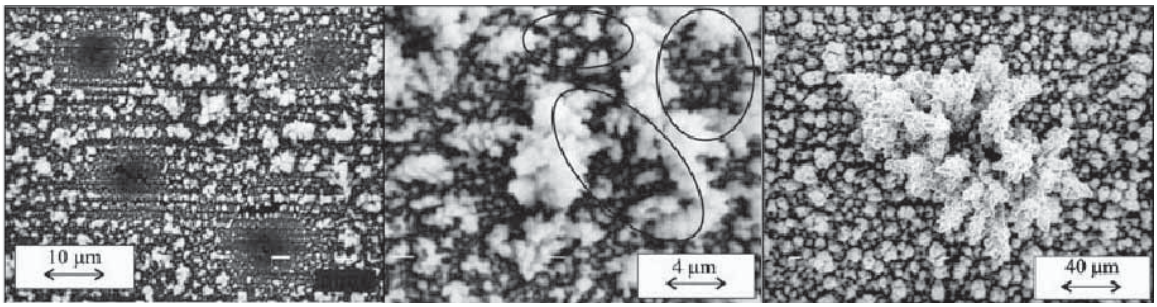

Fig. 3-12 Examples of Cu film morphologies resulting from diffusion-limited growth and hydrogen co-deposition, reproduced from [43]

3.2.3 The Electrochemical Window

The **electrochemical window**, as dubbed by Scragg, refers to the set of deposition conditions under which a desired thin film may be practically deposited [19]. Deposition potential, bath pH, substrate material, depositing species type and their concentrations primarily determine this window. For instance, standard reduction potentials of tin and zinc are -0.138V and -0.762 vs. NHE, respectively. Attempting to deposit tin onto a zinc substrate at a deposition potential of -0.138V vs. NHE would cause anodic dissolution of zinc, since the deposition potential is more noble than zinc's standard reduction potential [19].

Equilibrium phase diagrams, known as **Pourbaix diagrams**, provide maps of the thermodynamically stable phases (e.g. solid and ionic species) versus the electrode potential and pH [44]. As noted in Section 3.2.2.3, thermodynamics determines only which reactions are possible and not necessarily which reactions are likely. Therefore, the kinetics of the reactions must also be examined, in order to determine their reaction rate [44]. The **Hydrogen Evolution Reaction (HER)** and the **Oxygen Evolution Reaction (OER)** provide additional negative and positive deposition potential limits, respectively [19]. These reactions quickly dominate the deposition current after their onset, slowing and eventually preventing further deposition of the desired thin film elements [19].

3.2.3.1 Thermodynamic Phase Stability

Pourbaix Diagrams

Pourbaix diagrams represent maps of thermodynamically stable phases, constructed from the possible chemical and electrochemical equilibria in the given system [44]. These diagrams contain thermodynamic data regarding species stabilities, where thick solid lines delineate the predominant solid species, thin solid lines delineate the predominant solid-ionic species, and dashed lines delineate the predominant ionic species [44]. Along these coexistence lines, the activities of species on either side are equivalent [44]; in regions on either side of these lines, a given

species will predominate [44]. For aqueous solutions, water decomposition lines are usually indicated as well, where the stable region of water is defined by the onset of the Hydrogen Evolution Reaction (HER), described in the following section, and the Oxygen Evolution Reaction (OER), as originally noted in the Platinum anode reaction (3-2) [44].

Notably, the presence of **multiple elements** in the bath, as with the single-step electrodeposition of CZTS, modifies the Pourbaix diagrams and corrosion behavior in unpredictable ways. That is, the Pourbaix diagrams for each of the consistuents may not simply be superposed to describe the overall behavior of the system [44]. To construct a Pourbaix diagram for multi-element baths, the Gibbs free energies for each possible reaction, including reactions among the various consituents, must be evaluated. At a given Pourbaix coordinate (E_H,pH), the reaction with the lowest Gibbs free energy change per mole corresponds to the most stable species or compound in the given domain [44]. If at a given Pourbaix coordinate all possible reactions exhibit a positive Gibbs free energy change, then at thermodynamic equilibrium, the consistuent exists as stable solid in the immunity region [44]. The dependence of the Gibbs free energies of reactions on pH, potential, activities of products and reactants, as well as the activities of the various other aqueous species present [44], makes the calculation more challenging. However, various software programs, such as **Medusa** from the Swedith Royal Institute of Technology, have been developed to conduct these theoretical calculations.

Hydrogen Evolution Reaction (HER)

The **hydrogen evolution reaction**, described by (3-33) in acidic solutions and by (3-34) in neutral and alkaline solutions [19, 35], modifies the electrodeposition process in several significant ways. First, when HER activates at potentials more noble than the deposition potential of a given element or compound, then the HER reaction will compete with the deposition reaction, slowing or preventing it completely [19, 23]. In these cases, H-atoms may be included in the depositing film, possibly causing hydrogen embrittlement [36]. Second, HER produces H_2 bubbles on the surface of the working electrode, which locally block the deposition and create voids in the deposited thin film [43, 45]. Finally, the HER may induce significant changes in the solution pH, particularly near the electrode [19]. If HER proceeds by (3-33), then the pH may be altered through a local reduction in H^+ ions which are consumed by the process; if HER proceeds by (3-34), then the pH may be altered through the local generation of OH- ions generated by the water reduction. In both cases, the local pH shifts more alkaline, which can alter the thermodynamic stability of the substrate and depositing materials as described in the previous section [36, 45].

$$2H^+ + 2e^- \rightarrow H_2(g) \tag{3-33}$$

$$2H_2O + 2e^- \rightarrow H_2(g) + 2OH^-(aq) \tag{3-34}$$

The overall HER process, described here for acidic conditions (3-33), involves four steps: 1) transport of H^+ from the bulk to the Outer Helholtz Plane, 2) H^+ adsorption on the electrode surface, 3) H_{ad} combination and H_2 desorption from the electrode surface, and 4) H_2 gas transport from the electrode surface to the atomsphere. Any step may be rate-limiting and thus responsible for the overpotential required to advance the reaction. Further, the kinetics of these steps vary strongly with the electrode material and surface condition, leading to large variations in overpotentials, as Table 3-5 shows.

Table 3-5. Hydrogen Evolution Overpotentials for Various Electrodes, from [19]

Electrode Material	η_{H2} (V)
Pt	0.09
Mo	0.57
Cu	0.45
Zn	0.83
Sn	0.75

In neutral and alkaline solutions, the low concentration of H^+ ions requires the water-reduction reaction (3-34) to drive the HER, which increases the activation overpotential [35]. For more acidic solutions, the diffusion of H^+ ions drives the HER via (3-33), increasing the current density and reducing the overpotentials [35]. However, at high current densities, diffusion cannot supply H^+ ions fast enough to support the reaction, and the water-reduction once again drives the HER [35]. Very high current densities can be supported by the large concentration of H_2O available for reduction [35].

3.2.3.2 Cyclic Voltammetry

Cyclic voltammetry (CV) refers to an electroanalytical technique that provides "rapid observation of the redox behavior of the system over a wide potential range" [21, 46]. The technique involves cycling the applied potential, by linearly sweeping in the forward and reverse directions, and measuring the resulting current [21, 46]. For multi-element electrodepositions, cyclic voltammetry provides useful information on the reduction potentials for the different elements and compounds, as well as the overpotential for the HER, effectively determining the electrochemical window under which depositions may be suitably performed. Fig. 3-13 shows a typical cyclic voltammetry curve, known as **voltammagram**.

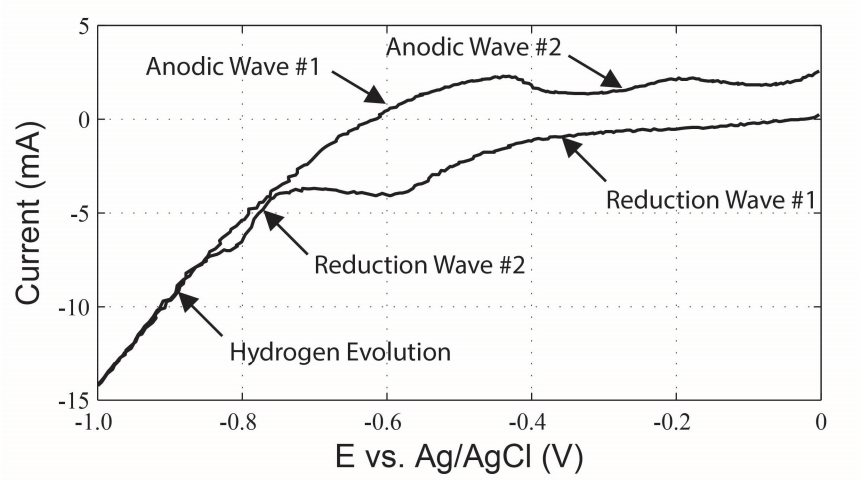

Fig. 3-13. Example cyclic voltammagram with various contributing reactions identified

CV measurements, which linearly sweep the potential at a slow rate (~10mV/s), provide a simplified way of quickly measuring the current response to a series of one-step potentials. By examining the current response to varying step changes in the applied potential, current-potential curves may be constructed and, in some cases, may be modeled with the Butler-Volmer equation [21]. **Under purely reversible conditions**, the i-E curves yield no information on the kinetics of the reaction, but they provide access to the thermodynamic parameters, including critically the formal potentials of the reactions [21]. **Under purely irreversible conditions**, the i-E curves yield no information on the thermodynamics of the reaction, but they provide access to kinetic parameters associated with the reaction, including the rate constant [21]. In both cases, the diffusion coefficient and bulk concentration of the electroactive species may be assessed via the shape of the curves. See [21] for a more detailed treatment of i-E curve modeling.

As the potential sweeps in the **negative (forward) direction** and passes through a reduction overpotential for a given reaction, the cathodic current rises. As the potential sweeps more negative, current passes through the mass transfer regime and saturates at the limiting current [19, 21]. In some cases, the electroactive species may quickly deplete, causing a reduction in the current with more negative potential. This increase in current, followed by saturation or depletion, is referred to as a **reduction wave, reduction peak or cathodic peak [21, 33]**. The current stays level (or decreases due to depletion), while the potential sweeps more negative, until the onset of the next reaction [21]. At high enough overpotentials (e.g. very negative deposition potentials), HER starts and quickly dominates the current, shown as a steep and eventually linear rise in the current [19, 21, 35]. As potential sweeps in the **positive (reverse) direction** and passes back through the anodic overpotential for a given reaction, the reaction reverses and creates a positive anodic current, which effectively strips the film away [19, 21].

3.2.3.3 Complexing Agents

In addition to the underpotential and anomalous co-deposition mechanisms, which may shift the deposition potentials of one or more components owing to favorable thermodynamic free energies, **complexing agents** may also modify the deposition potential of the metals through alteration of the electroactive species activities. In particular, the formation of complex ions, by the attachment of ligands, can dramatically reduce the activities of free and hydrated ions, achieving negative shifts in the reduction potential as high as 0.8V [23]. In some cases, increasing the concentration of the complexing agent allows a metal ion to be converted to higher complexes, thereby *further* reducing the activity and shifting negative the reduction potential [23]. The formation of the complex ion may be represented as follows [23]:

$$M^{n+} + qA^{p-} \rightarrow MA_q^{n-pq} \tag{3-35}$$

where q is the coordination number and A is the complexing ion of charge p.

The standard reduction potential for a free or hydrated metal ion under equilibrium conditions can be described according to the Nernst Equation (3-8), as described in Section 3.2.2.2. Accounting for the reduction in activity due to complexation, the reduction potential may be modified as follows [23]:

$$\varepsilon = \varepsilon^0_{M^{n+}} + -RT/nF\left[\ln K_f\right] + RT/nf\left[\ln\left(a^{n-pq}_{MA_q} / a^{q}_{A^{p-}}\right)\right] \tag{3-36}$$

where K_f is the thermodynamic formation constant for the complex, E is the standard reduction potential, R is the universal gas constant, T is the temperature, n is the oxidation number of the metal, F is Faraday's constant, a_{MXq} is the activity of the complex, and a_{Xp-} is the activity of the complexing agent. A stable complex implies a large value of K_f, and in this case, the second term dominates yielding a large negative shift in the reduction potential [23].

In addition to shifting the reduction potential, complexing agents can slow the reaction kinetics by adding charge transfer sequences, which if rate limiting, will slow the deposition rate [22]. This reduction in deposition rate can lead to an improvement in the film quality by altering nucleation and growth mechanisms [22]. Literature has shown that electrodeposition of $CuInSe_2$ with citrate complexing agents slowed the surface reactions and improved film crystallinity [22].

When complexing agents are applied in multi-element baths, such as those used in co-electrodeposition of CZTS, complexes may be formed that contain more than one element [26]. In these cases, speciation of the metal elements and complexes may be quite complicated, involving free and hydrate metal ions, single metal complex, and multi-metal complexes [26]. Single metal and alloy/compound deposition may then proceed via reduction of these various electroactive species, making peak identification on cyclic voltammagrams difficult [26].

Properties of Citrate Complexing Ions

Trisodium citrate ($Na_3C_6H_5O_7$) represents a common complexing agent in electrodepositions, and this complexing agent was used in nearly all depositions performed in this dissertation. The pH of co-electrodeposited CZTS baths have frequently been adjusted using **tartaric acid ($C_4H_6O_6$)** [28, 47], which also complexes mildly with Cu and Zn and complexes strongly with Sn [47]. The **citrate ion** (**$C_6H_5O_7$**) consists of three carboxylic groups and one alcoholic group and exhibits a wide range of charge states and hydrogenation that depend on the pH of the bath [26]. For pH-dependent speciation diagram of the citrate ion, see [26].

The primary citrate ion species shifts from $HCit^{2-}$ to Cit^{3-} as the pH shifts from 4.5 to 6 [26], the two bath conditions studied in this thesis, although the metal-citrate speciation depends strongly on the metal ion. With near-neutral pH and excess citrate, metal complexes of the form $M{\cdot}Cit_2^{4-}$ often predominate. For instance, under these conditions, nickel [26], copper [48] and zinc [49], were shown to primarily adopt this or similar complex structures. Higher charge state complexes have been shown to impede the electrodeposition [26, 48], which may improve the film quality by reducing the deposition rate. The metal complex forms according to the following [49]:

$$M^{2+} + Cit^{3-} + Cit^{3-} \rightarrow MCit_2^{4-} \tag{3-37}$$

Gougaud recently reported speciation calculations for Cu, Zn, and Sn in acidic and neutral baths, specifically for co-electrodeposition of Cu-Zn-Sn precursor layers, using citric acid complexing agent and tartaric acid buffer-complex agent [47]. The Cu and Zn complexed primarily with the citrate ligand, while Sn primarily complexed with the tartaric acid ligand. In the absence of tartaric acid and near-neutral pH values, Cu and Zn species shifted to non-hydrogenated, higher charge state complex species, and Sn species shifted to insoluble SnO compounds [47].

3.2.3.4 Effect of pH

The pH of the electrolyte can have profound effects on solution and film properties, including ion and complex stabilities, ionic mobility, electrode surface adsorption, and the HER overpotential [19, 23]. As discussed in the first part of this section, pH has a strong effect on thermodynamic of species in the solution, including their oxidation state. The stable forms of ionic and complexation species can significantly influence the nature of the deposition reaction, including the rate-limiting partial reaction, and the film quality. Therefore, **pH buffers**, which help maintain a constant pH, are frequently used to stabilize the desired species throughout the deposition. In some cases, these pH buffers may also act as complexing agents (e.g. tartaric acid).

The pH buffer species may reduce the ionic mobility of the deposition species, effectively reducing their diffusion to the working electrode surface [50]. This buffer species may also adsorb on the working electrode and block nucleation sites of the deposition species [50]. Finally, lowering of the pH (more acidic) reduces the overpotential of the HER, shifting its onset to more-noble electrode potentials. The HER can cause reduce the desired deposition current through

competition with the depositing species. As will be shown in Chapter 7, the bath pH strongly influences the film morphologies of co-electrodeposited CZTS thin films.

3.2.4 Experimental Details

3.2.4.1 Equipment and Set-Up

Electrodeposition and cyclic voltammetry studies performed in this work utilized an electrochemical cell that consisted of an Ag/AgCl reference, platinized Niobium-wire mesh counter electrode, and FTO-coated or Mo-coated glass substrate working electrodes, as shown in Fig. 3-14. The reference electrode (Pine Research Instrumentation, P/N RREF0021) was rotated approximately 30° from horizontal plane in both axes, in order to keep the tip as close to the working electrode as possible, while minimizing to the extent possible blocking of the working electrode face. The platinized Niobium-wire mesh counter electrode (Anomet Products) and the working electrode were connected via alligator clips to the potentiostat. Aluminum foil was used between the clips and the electrodes to improve electrical contact.

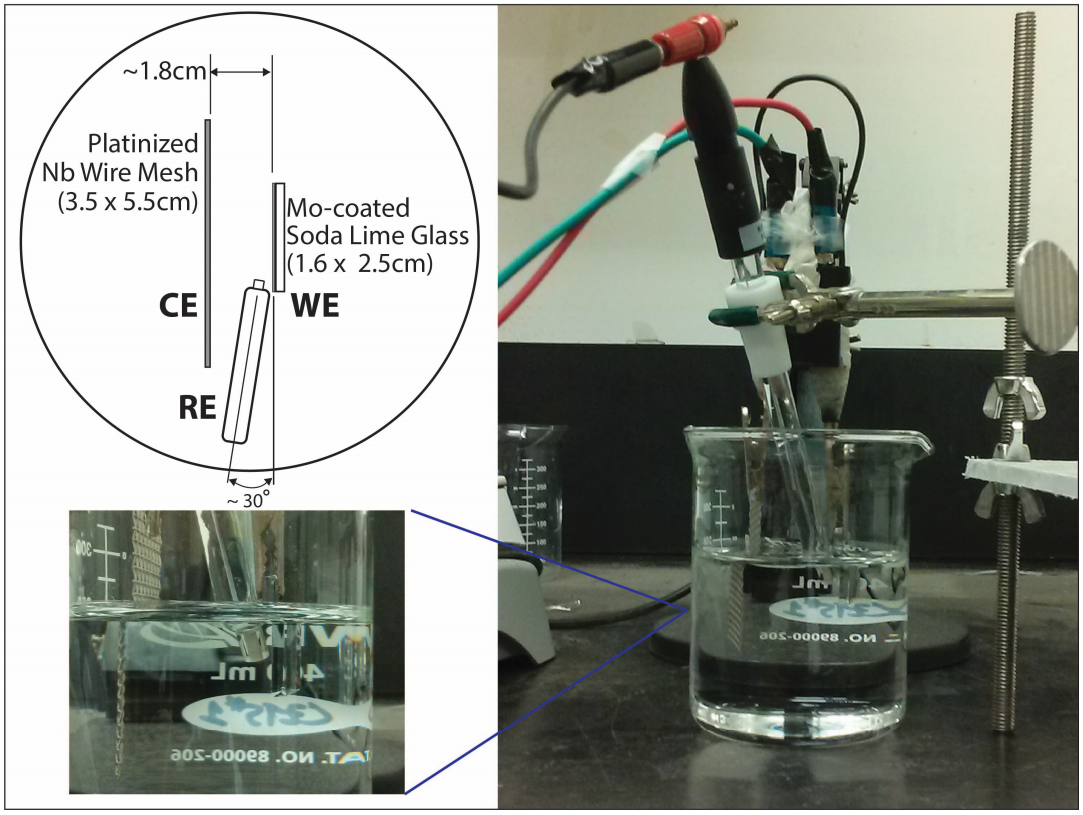

Fig. 3-14. Three-electrode electrodeposition set-up

The FTO-coated substrates used deposition areas of ~2 x 3cm or ~1.6 x 2.5cm, and the Mo-coated substrates used deposition areas of ~ 1.6 x 2.5cm, simply chosen based on the dimensions of the supplies. Nominally, electrochemical cell volumes of 250mL were employed, with volumes

varied up to 500mL. The working and counter electrodes were spaced approximately 1.8cm apart, chosen as close as possible while still providing access for the reference electrode.

Constant potential depositions were performed at -0.20 to -1.29V vs. Ag/AgCl, using an AFCBP1 or WaveDriver 20 biopoteniostat, both from Pine Research Instrumentation. Constant current depositions were performed at -1 to -5mA, using the WaveDriver 20. In some cases, stirring of the bath was performed during deposition (< 200rpm) using magnetic stir bars.

Materials

Commercial (TEC-7) FTO-coated films ~550nm thick (ρ~300μΩ-cm) on soda lime glass substrates were provided by Pilkington North America. Both in-house and commercially deposited Molybdenum films were investigated in this thesis. In-house (**EMAT**) molybdenum films ~300nm thick (ρ~150μΩ-cm) were deposited using RF sputtering under 10mtorr Argon background and with a deposition power of 300mW onto Corning 0215 soda lime glass slides. To investigate the effects of Molybdenum annealing on CZTS film growth, some EMAT Mo-substrates were rapid thermal annealed prior to electrodeposition, under flowing N_2 gas in an AG Associates HeatPulse 210. Commercial (**Guardian**) molybdenum films ~500nm thick (ρ~15μΩ-cm) on soda lime glass substrates were provided by Guardian Industries Corp.

Rutherford backscattering analyses of the substrates indicate the film compositions and thicknesses shown in Table 3-6. The soda lime glass in the FTO- and Mo-substrates demonstrated similar compositions to the soda lime glass composition shown in Table 3-3. The atomic density for FTO is taken from [51], and the atomic density for Mo is calculated from its mass density and molar mass, respectively. Note that the EMAT Mo films contain a significant amount of oxygen.

Table 3-6. Composition of substrates used in electrodeposition

Substrate	At %				Atomic Density (cm^{-3})	Film Thickness (nm)
	Sn	O	F	Mo		
FTO Coated Glass (Pilkington Tec-7)	0.33	0.65	0.02	-	FTO: 8.4e22	540
EMAT Mo (Corning 0215)	-	0.20	-	0.80	Mo: 6.4e22	250 - 275
Guardian Mo	-	-	-	1.00	Mo: 6.4e22	475

In order to characterize their possible contributions to the x-ray diffraction spectra of deposited thin films, x-ray diffraction measurements were performed on the FTO- and Mo-substrates, with the relevant diffraction data summarized below in Table 3-7.

Table 3-7. Diffraction data for substrates used in electrodeposition

Substrate	2-θ Peak Location (°)		Attributed Phase	Crystal Plane (hkl)
	Measured	Reference		
FTO-Coated Glass (Pilkington Tec-7)	26.57	26.54	SnO_2 (Tetragonal)	110
	33.78	33.81		101
	37.83	37.89		200
	51.58	51.67		211
	54.63	54.65		220
	61.67	61.76		310
	65.62	65.83		301
EMAT Mo (Corning 0215)	40.33	40.50	Mo (Cubic)	110
Guardian Mo	40.63	40.50	Mo (Cubic)	110

Notably, the EMAT Mo substrate shows significant tensile strain, evident as a leftward shift in the 2-θ location of the characteristic (110) peak. The Guardian Mo substrate, on the other hand, shows significant compressive strain, evident as a rightward shift in the 2-θ location of the characteristic (110) peak. Per conversations with Guardian, the properties of the Mo films had been optimized for other applications, and so the compressive strain was intentional. Stress/strain has been shown to influence the adhesion and the resistivity of sputtered Mo films [52, 53]. The peak width of the EMAT Mo film (0.79°) is also significantly larger than the peak width of the Guardian Mo film (0.33°), indicating significantly larger grain size in the Guardian Mo films. This can be expected since EMAT Mo films were deposited at room temperature and Guardian Mo films were fabricated using an industrially optimized process.

3.2.4.2 Methodology

Electrodeposition and Cyclic Voltammetry

Single-layer films of CZTS were deposited on FTO-coated glass and Mo-coated soda lime glass substrates using a single-step electrodeposition process adapted from [28]. Prior to deposition, the FTO-coated glass substrates were cleaned ultrasonically in acetone, alcohol, and ultra-high purity (UHP) water for 20min each cycle, and then blown dry with nitrogen gas. The FTO-glass substrates were cleaned in large batches and stored in the UHP water for weeks or months until required for deposition. Mo-coated glass substrates on the other hand were, immediately prior to deposition, thoroughly rinsed with alcohol and UHP water and then blown dry with nitrogen gas. Soaking and sonication were both shown to degrade the molybdenum layers in EMAT and Guardian Mo-substrates.

Table 3-8. Nominal bath composition and chemical source information

Chemical Formula	Chemical Name	Concentration [M]	Manufacturing Information
$Na_3C_6H_5O_7 \cdot 2H_2O$	Sodium Citrate Tribasic Dihydrate	0.20	Sigma Aldrich, ACS Reagent, 99.0% (P/N S4641-500G)
$C_4H_6O_6$	L-Tartaric Acid	0.10	Amresco, ACS Grade, (P/N 0501-500G)
$CuSO_4 \cdot 5H_2O$	Copper (II) Sulfate	0.02	Sigma Aldrich, ACS Reagent, 98.0% (P/N 209198-100G)
$ZnSO_4 \cdot 7H_2O$	Zinc (II) Sulfate	0.01	Sigma Aldrich, ACS Reagent, 99.0% (P/N 221376-100G)
$SnSO_4$	Tin (II) Sulfate	0.02	Sigma Aldrich, ACS Reagent, 95.0% (P/N 244635-100G)
$Na_2S_2O_3$	Sodium Thiosulfate	0.02	Amresco, Reagent Grade, (P/N 0393-500G)

Aqueous baths using ultra-high purity water (>18MΩ-cm), metal salts, a complexing agent, and a pH buffer were nominally prepared according to Pawar's formulation [28], as shown in Table 3-8. Chemical powders were massed and added to the solution in the order shown. During this weighing process, typically about 10–20min, the solution was stirred at 400RPM (room temperature) using a magnetic stir bar. After the components were mixed, the solution was stirred at 600RPM (room temperature) for an additional 30min, until the color effectively stopped changing. The nominal deposition bath had a dark green-light brown color, which varied as the bath composition changed. Once the bath was mixed, the magnetic stir bar was removed from the deposition beaker and the electrochemical cell configured, as shown in Fig. 3-14.

For electrodepositions, either constant potential or constant current were selected, and the deposition parameters were adjusted as described in Chapters 7 and 8. **For cyclic voltammetry**, a potential range of either 0 to -1.25V or 0 to -1.50V was specified, and the sweep rate set to 10mV/s.

After deposition, films were thoroughly rinsed in the ultra-high purity water and then either air-dried under the fumehood or blown dry with nitrogen gas. Films electrodeposited in acidic baths frequently developed thick, loosely adhering layers which were easily removed with rinsing. To prevent further damage, these films were typically air-dried. Films electrodeposited

in pH neutral baths developed more compact, well-adhering layers, and these films were typically blow dry with nitrogen after rinsing.

Sonication

Post-deposition sonication was investigated as a method to remove unwanted surface particulates. In these cases, sonication was performed for 20min using a VWR50 ultrasonic cleaner with samples oriented at ~60° from horizontal with the CZTS film facing down in a vial containing ultra-high purity water, acetone, or alcohol.

3.3 Annealing: Crystal Formation Processes of CIGSeS and CZTS Thin Films

I would again like to acknowledge Scragg [19] and Hergert [54, 55], as this annealing background sections draws strongly from these works. For a more comprehensive review, the reader is strongly encouraged to visit these excellent texts.

3.3.1 Background

As Sections 3.1.2.4 and 3.2.2.4 demonstrate, nucleation and film growth behavior depends strongly on the deposition method and conditions. In all cases, however, the deposited film must be transformed from the disordered precursor constituents into the desired ordered crystal phase(s). In order to form a film with extended, well-coordinated crystalline order, the constituent atoms must be able to diffuse to their particular equilibrium positions within the crystal, typically requiring extensive chemical bond breaking and re-formation [56]. This crystal formation requires energy to overcome the kinetic barriers associated with these formation reactions and atomic diffusion processes, which is typically supplied by heating of the film during and/or after its deposition [56]. As discussed in Section 3.1.2.3, the deposition process itself may supplement the required formation energy via the kinetic energies of the depositing species. Once sufficient energy has been supplied to the film to overcome the kinetic barriers of phase formation, the crystal will adopt the most thermodynamically stable phase with the lowest free energy [56, 57]. In the case of quaternary systems, like CZTS, the compositional window and temperatures under which pure phases may be formed can be quite small, as Fig. 2-18 in Chapter 2 shows.

In this thesis, **annealing** refers to the post-deposition heating of a film in order to alter its crystal phase and grain properties. Annealing may be performed in a variety of background environments, including vacuum, inert gas, and reactive gas environments. Vacuum annealing may be performed on deposited films, when the film does not decompose or form unstable phases under low pressures. CIGSe remains generally stable under vacuum. CZTS, however, has been shown to decompose into constituent binaries at high temperatures in the absence of S_2 and SnS gas overpressures, which can lead to irreversible losses of Sn through the evolution of SnS [58, 59]. In addition to aiding film stabilization, annealing in reactive background gases may be required in order to incorporate additional elemental components into films, in this case sulfur. As-deposited films may contain a sulfur-deficiency (as in the PLD films described in Chapter 6) or lack it

completely (as in the metal-only ED precursor films described in Chapter 8). Hydrogen sulfide (H_2S), elemental sulfur and tin-sulfide background gases have been used for both of these purposes. In the case of elemental sulfur and tin sulfide, several methods may be used to supply these gases: 1) sealed ampoule with elements, 2) partially-sealed graphite box with elements, and 3) tube furnace with carrier gas flowing the elements over the film during heating. Due to the high toxicity of H_2S, elemental sulfur was the only sulfur source used in this thesis.

3.3.2 Physical Processes of Annealing

3.3.2.1 CIGSeS Material System

Crystal Phase Formation

The crystal phase formation of chalcopyrite CIGSe has been investigated theoretically, using models based on epitaxially initiated solid-state formation reactions [54]. Thermodynamic analysis showed the ternary phase formation must proceed through the combination of binary phases [54]. Experimental proof, including in situ XRD, for the following reaction pathways to chalcopyrite CISe, CGSe, and CIGSe crystal formation was also provided in [54]:

$$CuSe + InSe \rightarrow CuInSe_2 \tag{3-38}$$

$$\frac{1}{2}Cu_2Se + InSe + \frac{1}{2}Se \rightarrow CuInSe_2 \tag{3-39}$$

$$\frac{1}{2}Cu_2Se + \frac{1}{2}In_2Se_3 \rightarrow CuInSe_2 \tag{3-40}$$

$$\frac{1}{2}Cu_2Se + \frac{1}{2}Ga_2Se_3 \rightarrow CuGaSe_2 \tag{3-41}$$

$$\frac{3}{4}CuInSe_2 + \frac{1}{4}CuGaSe_2 \rightarrow CuIn_{0.75}Ga_{0.25}Se_2 \tag{3-42}$$

Hergert recommends specific sets of annealing conditions to enhance grain growth based on the precursor film properties. For **stacked elemental layers (SEL)** with Cu-In precursor, metal precursors should be annealed in excess selenium at temperatures less than 377°C, in order to completely selenize the precursor while preventing thermal decomposition of γ-CuSe to β-Cu_2Se. Then, the temperature should be raised above 377°C to rapidly grow the α-$CuInSe_2$ crystal, via the fast reaction (3-40). This annealing sequence ensures the presence of high cationic conductivity β-Cu_2Se, which greatly enhances grain growth [54]. For **Ga-containing precursors**, Hergert recommends selenization of metallic precursors at 400°C and under selenium-poor conditions, prior to final crystallization at 500°C in excess selenium [54].

For **physical vapor deposited (e.g. co-evaporation) growth** of CISe, the fabrication process typically includes a two- or three-stage deposition sequence, with an In+Se phase followed by a Cu+Se phase, as described in Chapter 2. By growing slightly In-rich during the first phase of deposition, β–In_2Se_3 phases will be favored over γ–In_2Se_3. Hergert suggests that the layered structure of β–In_2Se_3 facilitates Cu^+ diffusion, thereby increasing grain growth and reducing defects [54].

Crystal Phase Decomposition at the Molybdenum Back Contact

By considering the free energy changes associated with possible reaction sequences of $CuInSe_2$ with the molybdenum back contact, assuming the final formation product of $MoSe_2$, the thermodynamic favorability of the given reactions may be evaluated [56].

$$2Cu_2Se + Mo \rightarrow 4Cu + MoSe_2 \tag{3-43}$$

$$2In_2Se_3 + Mo \rightarrow 4InSe + MoSe_2 \tag{3-44}$$

First considering the interactions between the binary components of CISe (Cu_2Se and In_2Se_3) with the molybdenum, Scragg evaluates the free energies of the reactions (3-43) and (3-44) shown above, as 5kJ/mol and 2.9kJ/mol [56]. Considering the additional energy that would be required to decompose the ternary CISe into the binaries and the positive values of the binary interactions, the formation of $MoSe_2$ can be generally considered thermodynamically unfavorable [56]. As will be shown in the next section, the thermodynamic stability of the Mo back contact in the CISe material is shown to be much higher than that of the thermodynamic stability of the Mo back contact in the CZTS(Se) material system [56, 60].

3.3.2.2 CZTS Material System

Crystal Phase Formation

The crystal phase formation of kesterite CZTS has been investigated both experimentally [19, 55] and theoretically, using models based on epitaxially initiated solid-state formation reactions [55]. Hergert's model predicts that kesterite CZTS may be formed via the following two reaction pathways [19, 55, 61]:

$$Cu_2S \,/\, Cu_2S \,/\, CuS + ZnS + SnS \,/\, SnS_2 (\pm S) \rightarrow Cu_2ZnSnS_4 \tag{3-45}$$

$$Cu_2S \,/\, Cu_2S \,/\, CuS + SnS \,/\, SnS_2 \rightarrow Cu_2SnS_3 \tag{3-46}$$

$$Cu_2SnS_3 + ZnS \rightarrow Cu_2ZnSnS_4 \tag{3-47}$$

where the "/" indicates "exclusive or" and components in Eqn. (3-45) and (3-46) must be added in stoichiometric combinations [55]. Hergert notes that the binary reaction (3-45) proceeds fastest when Cu_2S, ZnS, and SnS_2 compounds are involved; therefore, the author suggests that the annealing temperature be set where the conductive Cu_2S phase is stable and that sulfur be supplied

in excess in order to promote SnS_2 formation [55]. Epitaxial-assisted reactions may yield Cu_2SnS_3 phases in well-mixed precursor films, although experimental evidence indicates these compounds only form in Zn-deficient films [55].

Once the binary metal-sulfide precursors are formed, crystallization of the kesterite CZTS crystal has been predicted to proceed quickly [55] and verified experimentally to take 10 – 70sec to complete at 500°C [19]. Fabrication approaches that employ the two-step deposition reaction, in which metal precursors are first deposited and then reacted in a sulfur environment, include additional formation reactions which convert the metals and metal alloys into the binary metal-sulfide precursors.

Depending on the film precursor composition and the reaction temperature, a variety of formation reactions may take place. Further, the ramp rate to the reaction temperature can significantly influence the reaction pathways to crystallization [19]. **Low ramp rates** ensure that the diffusion of the reactive elements does not act as the rate-limiting step to crystal growth, and the reaction pathways lead to the most thermodynamically stable phases [19]. **High ramp rates** may lead to diffusion-limiting processes, which can alter the crystal growth [19].

Scragg suggests in [19] that Schurr's CZTS formation study in [62], which used a ramp rate of 0.8°C/s to 630°C, generally represents a low ramp rate annealing regime characterized by thermodynamically-limited processes. In this study, Schurr utilized co-electrodeposited metal precursor films, with Cu-rich films composed of Cu_3Sn and CuZn phases, and with Cu-poor/near-stoichiometric films containing additional Cu_6Sn_5 and Sn phases [62]. Note that Cu-Zn and Cu-Sn alloys may form under room temperature, due to the high diffusion coefficients of Zn in Cu and Cu in Sn, respectively [19]. Scragg summarizes Schurr's proposed reaction sequences, which are dependent on the precursor structure, as follows [19]. Note that in Schurr's study, the final film contained CZTS, as well as secondary phases of Cu_2SnS_3 and ZnS, indicating incomplete transformation of the film [19, 62].

(170-300°C) $$Cu_6Sn_5 + S \rightarrow SnS_2 + Cu_{2-x}S + Cu_3Sn \quad (3\text{-}48)$$

(< 570°C) $$Cu_2S + SnS_2 \rightarrow Cu_4SnS_6 \quad (3\text{-}49)$$

(510°C) $$2CuZn + 3S \rightarrow Cu_{2-x}S + ZnS \quad (3\text{-}50)$$

(570°C) $$Cu_4SnS_6 \rightarrow 2Cu_{2-x}S + SnS_2(melt) \quad (3\text{-}51)$$

(> 570°C) $$Cu_{2-x}S + SnS_2(melt) \rightarrow Cu_2SnS_3 \quad (3\text{-}52)$$

(575°C) $$Cu_2SnS_3 + ZnS \rightarrow Cu_2ZnSnS_4 \quad (3\text{-}53)$$

Scragg suggests, on the other hand, that his work on CZTS formation in [19], which used a ramp rate of 10°C/s to 500-550°C, generally represents a high ramp rate annealing regime characterized by kinetically-limited processes. In this work, Scragg utilized SEL metallic (Cu/Sn/Cu/Zn) precursors, including a short precursor anneal step at 250-270°C for 3 – 5min to improve element mixing [19]. These temperatures and short anneal times were chosen to promote mixing and alloying of the elements but to limit phase segregation and de-wetting that may occur if the alloying were allowed to proceed to completion [19]. After precursor annealing, the metal films contained Cu_5Zn_8, Cu_6Sn_5, and elemental Sn phases [19]. Scragg proposes the following reaction sequences for the high ramp annealing of CZTS, which are again dependent on the precursor structure, as the following reactions [19]:

(350°C) $$Cu_5Zn_8 + S_2(g) \rightarrow Cu_2S + ZnS \tag{3-54}$$

(400°C) $$Cu_6Sn_5(s) + 1.5S_2(g) \rightarrow 3Cu_2S(s) + 5Sn(l) \tag{3-55}$$

(500°C) $$Cu_2S + ZnS + Sn(l) + 2S \rightarrow Cu_2ZnSnS_4 \tag{3-56}$$

Under rapid thermal annealing in sulfur environment, Cu_2S and ZnS phases are observed forming on the surface of the film earlier than SnS_2 phases, indicating that crystallization proceeds from the top surface towards the back contact [19]. Sulfur then diffuses more slowly through the solid surface phases, yielding diffusion-limited growth of the amorphous regions toward the back contact, which remain Sn rich. Further Cu_2S growth proceeds through a copper vacancy diffusion mechanism, which effectively robs the Cu_6Sn_5 phase of Cu, decomposing Cu_6Sn_5 into Cu_3Sn and elemental Sn [19]. Cu atoms transport to the surface and react with adsorbed S_2 on the surface, yielding the overall reaction Eqn. (3-55). SnS_2 forms slowly in the subsurface region, due to slowed sulfur diffusion through the solid surface phases, and it is immediately consumed by the CZTS formation reaction, yielding the overall reaction Eqn. (3-56) [19].

This growth model was proposed, in order to explain the morphological features observed in films sulfur annealed under high ramp rates, including voids present at the back contact interface and bubbles/voids present in the bulk and surface. In this model, the copper vacancy diffusion mechanism yields voids at the back contact once all of the copper has been consumed [19]. The larger bubbles, both intact and collapsed, are attributed to the formation of liquid Sn in the subsurface of the films. This liquid Sn might enhance vacancy agglomeration, creating voids or bubbles [19]. For off-stoichiometric compositions, including Zn-rich and Zn-poor conditions, slightly modified reaction sequences are proposed in [19].

It is suggested that, since the Cu-Zn and Cu-Sn alloy phases must ultimately decompose before forming the metal-sulfide binaries, as shown in reactions (3-54) and (3-55), then there is no benefit to the precursor alloying employed in this study [19]. Scragg indicates that studies with and without the precursor alloying step showed similar results, although it is unclear under what

annealing conditions this might apply [19]. Notably, both high and low ramp rate regimes involve the transformation of metal alloys to metal-sulfide binaries before ultimate transformation to CZTS [19, 62]. Other studies [63], however, including original work presented in Chapter 8 of this thesis, do show benefits associated with precursor alloying.

Crystal Phase Decomposition at the Surface

As briefly detailed in Section 2.3.2, major challenges to the fabrication of quality CZTS absorber layers include the loss of Zn, Sn and S during the crystal formation processes, either during heated deposition steps or post-annealing steps [18, 59]. While ZnS and Zn alloys are relatively stable, elemental Zn has a high vapor pressure and may be evolved from the film under high temperature and low pressures [29, 61].

Many works have demonstrated the loss of Sn and S at elevated temperatures, and this loss has been attributed to the evolution of SnS from the films [58, 59]. The reverse reaction to Eqn. (3-45), with direct decomposition to gaseous SnS, was proposed by Weber as the mechanism for this loss [58]. However, thermodynamic models developed in [59] indicate that the decomposition must proceed in a slightly more nuanced two-step process, in which CZTS first decomposes into solid binary components and then solid SnS converts into gaseous SnS, as shown below:

$$Cu_2ZnSn^{IV}S_4(s) \rightleftharpoons Cu_2S(s) + ZnS(s) + Sn^{II}S(s) + \frac{1}{2}S_2(g) \tag{3-57}$$

$$SnS(s) \rightleftharpoons SnS(g) \tag{3-58}$$

Scragg emphasizes that the driving force for decomposition is not the volatility of SnS but in fact the thermodynamic instability of Sn(IV) in CZTS under conditions of high temperatures and low sulfur pressure [59]. The loss of SnS due to its high vapor pressure, driven by the final reaction step (3-58), simply makes the decomposition process irreversible [59].

In any case, Sn and S are lost from the film via evolution of SnS. In open systems, in which these evolution products may be swept away, the decomposition reactions are irreversible and the film loses Sn and S, frequently developing voids. Notably, these decomposition reactions have been shown to be reversible in the presence of sulfur and tin sulfide vapor [59, 64]. In order to achieve stable CZTS surfaces at 550°C, Scragg recommends maintaining sulfur partial pressure greater than $(2.3\pm0.7)\times10^{-4}$ mbar (~17mtorr) and the product of partial pressures $p_{SnS}(p_{S2})^{1/2}$ greater than $(3.8\pm1.2)\times10^{-5}$ mbar (~0.029mtorr) [59]. Note that for a sulfur partial pressure of 2.3×10^{-4} mbar (17mtorr), a SnS pressure greater than 2.5×10^{-3}mbar (~2mtorr) must be maintained to meet the criteria above.

Crystal Phase Decomposition at the Molybdenum Back Contact

In addition to phase decomposition induced at the surface of the CZTS films, detrimental phase decomposition also occurs at the molybdenum back contact as a result of an interfacial phase

formation reaction, MoS_2 [60]. Using thermodynamic models similar to those briefly described in Section 3.3.2.1, the interfacial reaction for CZTS with Mo may be described according to (3-59), which has a calculated negative free energy change of -150kJ at 550°C [60]:

$$2Cu_2ZnSnS_4 + Mo \rightarrow 2Cu_2S + 2ZnS + 2SnS + MoS_2 \quad (3\text{-}59)$$

This large negative free energy suggests a potent driving force for the reaction, although ultimately the kinetics (e.g. the active energy barrier) associated with the reaction will determine if, and how quickly, it proceeds [60]. If the reaction were to proceed, then it is expected that MoS_2 and the binary metal sulfide components shown in Eqn. (3-59) would be present at the back contact. Notably, annealing in a sulfur environment also generates interfacial MoS_2 phases by the direct reaction of diffusing sulfur with the molybdenum back contact [60].

To isolate these effects, annealing was performed using a glass cover in direct contact with the sample, such that sulfur overpressure was maintained without introducing additional sulfur into the film [60]. The experimental results support the reaction sequence described above, indicating decomposition of CZTS at the back contact into constituent metal sulfide binaries [60]. Maintaining high sulfur overpressures can mitigate the reaction in Eqn. (3-59) but can also cause the growth of thick MoS_2 layers. Scragg suggests, however, that thicker MoS_2 may be preferable to thinner MoS_2 with phase decomposition [60]. In either case, alternative back contact materials may provide improved performance [60].

Annealing Parameter Effects

Due to the difficulty in providing a reactive S_2 and/or SnS environment during growth of CZTS thin films (e.g. during physical vapor deposition), the best processes have involved two-step deposition reaction sequences [59]. In these two-step processes, metallic C-Z-T or sulfur-containing C-Z-T-S precursor films are deposited at low temperatures, followed by annealing at higher temperatures in S_2 and/or SnS environments [59]. Many research efforts have been made to investigate the effects of these annealing parameters on the properties of the films, including the reaction temperature, the temperature profile, and the background gas, as well as the effect of precursor film properties on the final sulfurized films.

Reaction Temperature

Most literature reports maximum reaction temperatures >500°C, see for example [18, 19, 31, 65-67]. Systematic investigations of the reaction temperature, such as those by Han [68] and Emrani [66] summarized below, provide experimental support for optimized reaction temperatures in the range of 500 – 550°C. Notably, these optimized reaction temperatures are significantly higher than the often referenced and generally accepted 400°C isothermal pseudo-ternary phase diagram by Olekseyuk [69]. As discussed in the previous sections, kinetics can alter the crystal reaction pathways, possibly driving the optimum kesterite CZTS phase formation temperature to these higher (>500°C) values.

Han investigated the effect of reaction temperature on annealing of sulfur-containing co-sputtered precursors. Using a tube furnace, annealing was performed under flowing nitrogen and H_2S (5%) for 1 hr at the maximum reaction temperature, which was varied from 250 – 550°C (ramp time not specified) [68]. At 250 and 300°C, the sulfur annealed films contained mostly phases of Cu_2SnS_3, SnS_2 and $Cu_{2-x}S$, as determined from Raman spectroscopy [68]. Above 300°C, the dominant $Cu_{2-x}S$ Raman mode declines rapidly to zero, and the standard assigned CZTS peaks dominate the spectra. Notably, however, all films annealed above 300°C also showed peaks near 167cm^{-1}, which the author designates unidentified [68]; this peak may be associated with a SnS phase [70].

Bright-field transmission electron microscopy (BF-TEM) imaging was performed on sample cross-sections, along with selected area electron diffraction (SAED), in order to study the crystallization behavior of the samples [68]. These measurements indicated that, at lower temperatures (250 – 300°C), crystallization processes started at the surface of the films and advanced toward the back contact, evident as a crystallized top section and amorphous bottom section. Notably, the thickness of this amorphous section decreased with increasing temperature [68]. Compositional gradients were observed on the lowest temperature (250°C) samples, which was attributed to segregation of $Cu_{2-x}S$ phases on the film surface [68]. From 350 – 550°C, the films were generally more uniform in composition, although some Cu-rich and Zn-rich regions could be seen, which were also attributed to phase segregation and included $Cu_{2-x}S$ and ZnS phases [68].

Emrani investigated the effect of reaction temperature on annealing of sputtered SEL metallic precursors [66]. Using a tube furnace, annealing was performed with unspecified carrier gas and H_2S (4-8%) for 2.5hr ramp times and 3 – 4hr dwell times at the maximum reaction temperature, which was varied from 500 – 575°C [66]. Increasing the reaction temperature was shown to increase the crystallite size, decrease the number of voids, and decrease the formation of secondary phases [66]. The best performing solar cell devices were fabricated using a 550°C annealing temperature; the degraded performance at 575°C was attributed to grain coarsening and associated deterioration of the junction [66]. Note, the cation ratios of Zn:Sn remain relatively constant with increasing reaction temperature, and the Cu:(Zn+Sn) ratios increase slightly with increasing temperature [66].

Ramp Time

Several groups have reported the effects of the temperature ramp rate during sulfur annealing on the morphological, compositional, and structural properties of the resulting films [19, 71, 72]. As detailed in an earlier section, Scragg proposes modifications to the reaction pathways based on the temperature ramp rate, discussing a low ramp rate regime (0.8°C/s) and a high ramp rate regime (10°C/s) [19]. High ramp rates may cause kinetically-limited growth behavior, thereby altering the reaction pathways to CZTS crystal formation. It is suggested in [19] that, for near-stoichiometric compositions, crystallization proceeds from the top surface towards

the back contact, due to the rapid formation of Cu_2S and ZnS near the surface. Sulfur then diffuses more slowly through the solid surface phases, yielding diffusion-limited growth of the amorphous regions toward the back contact, which remain Sn rich. This model was developed to explain morphological features observed in films sulfur annealed under high ramp rates, including voids present at the back contact interface and bubbles/voids present in the bulk and surface [19]. For off-stoichiometric compositions, including Zn-rich and Zn-poor conditions, slightly modified reaction sequences are proposed in [19].

Ge investigated the effects of two temperature ramp rates on the annealing of co-sputtered, partially-sulfurized precursors [71]. Using a gas reaction furnace, annealing was performed under flowing argon and H_2S (5%) for 1 hr at 550°C. The ramp time was varied between of 2°C/min (~0.033°C/s) and 21°C/min (~0.35°C/s), values considered in [19] as the low ramp rate regimes [71]. Varying precursor compositions were studied by varying the sputtering power of the CuSn target during deposition, although as-deposited compositions are not provided [71]. Notably, final film compositions, including those sulfur annealed under the slow and the fast ramp rates, were highly non-stoichiometric with severe Zn-deficiencies [71]. To eliminate the effect of film composition on the interpretation of results, only the near-stoichiometric films are discussed here, where the slow ramp rate sample is denoted s1 and the high ramp rate counterpart is denoted t1. The Cu and Zn concentrations decreased dramatically with high ramp rate annealing compared to low ramp rate annealing, with Cu:(Sn+Zn) decreasing from 0.96 to 0.67 and Zn:S decreasing from 0.93 to 0.53 [71]. The sulfur ratio in the films, S:metals, also increased significantly in the higher ramp rate sample, 1.46, compared to the lower ramp rate sample, 1.00. Ge attributed the higher Sn concentration in the high ramp rate films to the formation of surface phases of Cu_xS and SnS_x phases, which slowed sulfur diffusion into the film interior and protected a sub-surface layer of liquid Sn [71]. Bursted bubbles evident in the film under high ramp rates were attributed to the elemental liquid Sn, although the author did not detail this mechanism [71]. The proposed reaction sequence is similar to that presented in [19], except that Scragg argued that only Cu-S and Zn-S phases form at the surface, not SnS_x phases as Ge argues. The phase purity of the annealed samples cannot be adequately compared because the Raman spectra show only a narrow range of wavevectors, outside of which many of the secondary phases, such as SnS [70], fall. The main takeaways form this work are that higher temperature rates can cause: 1) severe morphology damage through the creation of voids and bubbles, and 2) severe Cu and Zn deficiencies in films.

Yoo investigated the effect of varying temperature profiles on the annealing of SEL metallic precursors [72]. A low temperature profile, denoted LT, included a 5min ramp to 440°C with 20min dwell time; the high temperature profile, denoted HT, included a 10min ramp to 440°C with 10min dwell time followed by a 5min ramp to 550°C with 25min dwell time. Using a two-zone tube furnace connected to a vacuum pump, annealing was performed using elemental sulfur heated to 180°C upstream of the sample. The LT annealing profile yielded highly non-uniform

films, with many voids and rough morphologies, as well as laterally inhomogeneous compositions [72]. The HT annealing profile improved the surface morphologies and the composition uniformity, but the films still appeared rough with many voids. Using a combination of XRD and Raman spectroscopy, SnS_2, $Cu_{2-x}S$, Cu_2SnS_3 and ZnS phases were identified in the LT samples [72]. The HT samples, on the other hand, showed only the typical CZTS peaks. Films showed significant losses of Sn using both LT and HT annealing profiles. Yoo attributed this Sn loss to insufficient sulfur overpressure during annealing [72].

Dwell Time

Fernandes investigated the effect of dwell time at the maximum reaction temperature on the annealing of Cu-poor, Zn-rich SEL metallic precursors [73]. Using a tube furnace, annealing was performed under flowing nitrogen and elemental sulfur at 520°C, with a 50min ramp time and dwell times varying between 10 – 60min [73]. By comparing front and back surface compositions using EDS, Fernandes determined that the interdiffusion of the metallic elements was incomplete after 10min, demonstrated by the widely varying atomic ratios of the elements. Compositional uniformity generally improved with increased time, but results were somewhat distorted by material losses from the film that were suggested by the decreasing film thicknesses with increasing sulfurization time [73]. Longer dwell times were also shown to increase the grain size and to increase the presence of a $Cu_{41}Sn_{11}$ phases. Other secondary phases were also identified in all films: Cu_4SnS_4, SnS and Cu_2S. KCN etching, however, was used to remove the unwanted Cu_2S phases. The best solar cell device performance was achieved using films annealed with the shortest dwell time of 10min, which Fernandes attributed to the presence of degrading Cu_xSn_y phases in longer dwell time samples [73].

In the reaction temperature study [68] summarized in a previous section, Han also investigated the effect of dwell time on the annealing of sulfur-containing co-sputtered precursors. Films were annealed at 500°C with dwell times varying between 10 – 60min [68]. Raman spectra indicated primarily CZTS peaks with additional SnS_2 peaks that increased in intensity with increasing dwell time. The SnS_2 emergence at longer dwell times was attributed to stoichiometric deviations that result from "overheating" [68]. The BF-TEM images and SAED measurements indicate that small crystallites form in the amorphous bulk matrix between 10 and 30min, indicating "partial crystallization". The size and density of the crystallites slowly increase with increasing dwell time, eventually achieving "full crystallization" after 60min [68].

Background Gas

The background gas environment during annealing plays an important role in the CZTS crystal formation process. Some works have suggested that CZTS film quality improves with the use of H_2S as the sulfur source during annealing compared to elemental sulfur vapor [61, 74], where the H_2S usually is mixed at 5% with either nitrogen or argon carrier gas [61, 71, 74, 75]. At least one report investigates the effect of H_2S concentration on film properties and device performance,

indicating an optimized concentration of around 3% [76]. **H_2S is highly toxic and less toxic elemental sulfur represents a preferred sulfur source** [74]. In [74], annealing similar composition metallic precursor films with similar thermal profiles, H_2S yielded much larger grains (5μm) compared to elemental sulfur sources (1μm). The samples annealed in H_2S also demonstrated higher optical absorption and lower carrier concentrations compared to elemental sulfur [74]. However, the films annealed in element sulfur demonstrated better film coverage and uniformity; films in annealed in H_2S contained large voids populated with MoS_2 phases and small Zn-S and Sn-S particles [74].

Salome noted the success of both H_2S annealing and precursors exposed to hydrazine, and so investigated the role H_2 might play in the annealing process [61]. CZTS films were fabricated by two methods, involving evaporation of Cu-Sn-S and annealing to form Cu_2SnS_3 followed by sputtering of ZnS or Zn layers: 1) Cu_2SnS_3 + ZnS or 2) Cu_2SnS_3 + elemental Zn. Using a tube furnace, final annealing to form CZTS was performed under flowing carrier gas and elemental sulfur at 530°C, with a 55min ramp time and dwell time of 20min. To investigate the effect of H_2, one set of samples was annealed using a carrier gas of 100% nitrogen and another set of samples was annealed using a carrier gas mixture of 95% nitrogen and 5% H_2 [61]. The presence of H_2 was shown to significantly enhance the diffusion of Zn in the films for the **ZnS precursor**. In the absence of H_2, Zn diffusion into the films consisting of ZnS precursor is very low. Zn diffusion into the films improved with Zn metal precursors, but the films also experienced Zn losses due to the high vapor pressure of elemental Zn. Therefore, the author recommends using ZnS precursor with an H_2 environment during annealing to achieve the best films [61].

The effect of the sulfur background pressure on the annealing of SEL metallic precursors was investigated in [19]. Using a rapid thermal annealing system with graphite container, described in detail in [19], samples were annealed at temperatures between 520 – 580°C with a background pressure of elemental sulfur varying between 6 – 140mbar. The grain size decreased dramatically with increasing background pressure (from 30mbar to 570mbar), while the number of voids decreased with increasing background pressure [19]. A clear shift in the stability of Sn in the films can be observed at pressures of 1mbar and 100mbar. The Sn concentration decreases dramatically after 10min of annealing at 550°C with 1mbar pressure, while the Sn concentration remains significantly more stable with 100mbar pressure [19].

Zhang also investigated the effect of background pressure on the sulfur annealing of sulfur-containing sol-gel deposited precursors [77]. Using a tube furnace, annealing was performed under flowing argon and elemental sulfur at 580°C, with a 60min dwell time (ramp time not specified). Base pressures in the furnace were adjusted to 1atm (0.1MPa) or 0.4atm (0.04MPa) [77]. The average sample compositions were largely unaffected by the base pressures investigated, with ideal Cu-poor, Zn-rich compositions measured by EDS. Similar to [19], the grain size decreased significantly with increasing pressure, varying from ~1.0um at 0.4atm to ~0.5um at

1atm. Films annealed under both base pressures exhibited compact morphologies with few voids [77]. A higher number of ZnS phases appeared to decorate the surface of the low pressure sample, although both high and low pressure samples showed these surface features. Other notable differences included a decrease in the thickness of interfacial MoS_2 from 230 to 110nm and a decrease in the band gap from 1.42 to 1.39eV with decreasing pressure from 1atm to 0.4atm [77]. Most significantly, however, device efficiency increased from 4.1% to 5.7% with decreasing base pressure. This efficiency improvement originated from the higher FF and V_{oc}, which the author attributes to the larger grain size and smaller SnS content in the low pressure annealed films [77].

As detailed in **Crystal Phase Decomposition at the Surface**, CZTS requires an overpressure of SnS during annealing in order to prevent film decomposition. At high enough sulfur background pressures, however, the required partial pressure of SnS drops to very low values ($3.8x10^{-5}$mbar) [59], suggesting that SnS background gas may not be necessary to prevent decomposition, especially for sealed or partially-sealed systems, in which the evolution of SnS will be self-limiting as SnS accumulates above the film. Redinger investigated the effect of including elemental Sn with elemental sulfur in a graphite annealing box during annealing at 560°C for 2hr, demonstrating dramatic improvement of device efficiency with the inclusion of the Sn [64]. These annealing conditions were not optimized, as Redinger notes, and so represents a somewhat limited perspective on the effectiveness of Sn atmosphere in improving the properties of annealed films [64]. A review of the literature did not reveal any other studies investigating the effects of Sn/SnS on the properties of annealed films.

Precursor Composition and Structure

As Platzer-Bjorkman summarizes in [29], reported literature has shown conflicting trends regarding the effects of precursor sulfur-content on the properties of annealed films. One study investigated sulfur annealing (H_2S) of metallic and sulfur-containing precursors deposited by e-beam evaporation, indicating a large increase in grain size and quality for the sulfur-containing precursors. The work detailed by Platzer-Bjorkman, however, demonstrated opposing and more nuanced results, which the author notes may result from variations in the precursor composition and structure, as well as the influence of the sulfur source (H_2S vs. elemental sulfur) [29].

The work in [29] investigated the effect of sulfur-content in the precursor films on the properties of the sulfur annealed films. Metallic and sulfur-containing (14 – 18% concentration) precursor films were fabricated by co-sputtering of CuSn targets and Zn (or ZnS) targets [29]. Using sealed quartz ampoules containing elemental sulfur, annealing was performed at 520°C with a 1hr ramp, 2hr dwell and 5 – 6 hour cooldown period. A range of cation ratios was investigated for the precursors, including Zn-poor, Zn-rich, Cu-poor and near-stoichiometric [29]. The sulfur-containing precursors were amorphous, while the metallic precursors were crystalline, exhibiting Cu_6Sn_5 and elemental Sn diffraction peaks. After annealing, the metal precursor films demonstrated increased grain size relative to sulfur-containing films, but sulfur-containing films

were generally more uniform and contained fewer voids [29]. Further, the metal precursors experienced greater Sn loss than sulfur-containing precursors. All films contained secondary phases [29].

The relative decrease in grain size of the sulfur-containing precursors after annealing was attributed to the formation of a higher number of crystal nuclei during annealing. These nuclei limit the grain growth, and therefore grain size, by inhibiting grain boundary migration and recrystallization processes [29]. The presence of the sulfur in the precursors facilitates the formation of these nuclei during the sputtering process and/or at the early part of the annealing process [29]. Metallic precursors, on the other hand, can only form crystallites where sulfur has been supplied (e.g. at the surface and as it diffuses), which constrains the number of nuclei formed and facilitates the growth of larger grains [29]. Finally, the smaller volume expansion that takes place with the sulfur-containing precursors (2 – 2.5X) compared to the metallic precursors (2 – 4X) likely reduces stress-cracking in the films [29].

Gurav investigated the effects of low-temperature annealing of co-electrodeposited metallic precursors on the properties of sulfur annealed films, using a similar approach to that presented in Chapter 8 of this thesis [63]. This precursor annealing operation, denoted **soft anneal**, was performed under 1atm of argon for 1hr at temperatures between 250 – 350°C [63]. Final sulfurization was performed under flowing nitrogen gas and H_2S (5%) at temperature of 580°C, with a 2hr dwell time (ramp time not specified). The compositions of the precursor films changed significantly after soft annealing, with Zn concentrations decreasing significantly with increasing temperature; the Cu:Sn ratio remains stable (varying < 10%) for the soft annealing temperatures investigated [63]. The Zn loss can be attributed to the high vapor pressure of elemental Zn, as previously discussed. X-ray diffraction showed the intensification of the Cu_6Sn_5 phase and the formation of Cu_5Zn_8 with increasing soft anneal temperature [63]. After sulfur annealing, the as-deposited sample gave the most uniform compact film without voids, at least for the SEM images presented. The sample soft annealed at 300°C showed relatively larger grains but contained pinhole voids. The sample soft annealed at 350°C exhibited large inhomogeneities. The compositions of the soft annealed precursors change considerably after sulfurization, with relative Zn concentrations increasing dramatically with sulfurization, although no explanation was provided. The S:metal ratio also increased with increasing soft anneal temperature, with the sample soft annealed at 300°C showing the nearest-stoichiometry composition with S:metal = 1.13 [63].

3.3.3 Experimental Details

3.3.3.1 Vacuum Annealing

Vacuum annealing was performed on pulsed laser deposited CIGSe thin films using the EETD PLD deposition chamber shown schematically in Fig. 3-1. Samples were mounted to the heater block using DuPont 4929N silver paste. The chamber was evacuated to < $5x10^{-5}$ torr. The

samples were then heated for 2hr at temperatures ranging from 300 – 500°C and allowed to cool passively back to room temperature.

3.3.3.2 Rapid Thermal Annealing (RTA)

Rapid thermal annealing was performed on CZTS films and Mo-coated glass substrates using an AG Associates Heat Pulse 210 rapid thermal processor. Samples were heated for 30 – 150sec at temperatures ranging from 300 – 550°C, while flowing dry nitrogen gas at 1atm over the samples. Samples were allowed to cool under nitrogen gas flow to < 150°C before removal from the processor.

3.3.3.3 Sulfur Annealing

Two generations of sulfur annealing chambers were built in order to investigate the effects of annealing on CIGSeS and CZTS thin films. **Caution**: **annealing samples in elemental sulfur environment may generate hazardous byproducts, such as H_2S and SO_2.** Consult your environmental health and safety group for additional guidance. The **first generation** design utilized a simplified, sealed chamber approach, in order to mitigate the risks associated with hazardous sulfur byproducts. The **second generation** design utilizes a Sulfatreat filter, in order to extract any trace quantities of H_2S or SO_2 that may be generated during the annealing process. In both cases, the enclosure volumes were minimized to the extent possible, in order to use the least amount of elemental sulfur possible during an annealing process (< 30mg). Secondary exhaust was provided on the chambers to further mitigate exposure.

Generation #1

The **Generation #1 sulfur annealing system** was configured as shown in Fig. 3-15. The system consisted of 2-inch diameter, thermal vacuum chamber components connected as shown to a high vacuum pumping system. The active chamber volume was heated up to 500°C using heater tape would around its exterior and sealed using a manual vacuum valve. In order to prevent overheating of the vacuum valve components (max continuous use temperature of 200°C), it was necessary to add another chamber section to thermally isolate the valve. Therefore, the sealed chamber volume consisted of the actively heated volume, shown in Fig. 3-15 with the heater tape, and a cooler section to the right used to isolate the valve.

The sample was installed into the system, along with a small quantity (~13mg) of elemental sulfur, and the chamber was then evacuated to < 10^{-3}torr and sealed. Samples were subsequently heated for 1hr at temperatures ranging from 300 – 500°C, then allowed to cool passively back to room temperature. This system was used only for the sulfur annealing of pulsed laser deposited CIGSe thin films. Notably, the Gen#1 sulfur annealing system did not achieve significant sulfur incorporation into the CIGSe thin films, with surface sulfur concentrations < 15at% and compositional gradients through the thickness clearly evident. This low sulfur incorporation is attributed to two sources: 1) low background pressures associated with the small masses of

elemental sulfur used relative to the chamber volume, and 2) rapidly declining sulfur pressures caused by condensation of the elemental sulfur in the cooler sections of the chamber. The low sulfur incorporations into CIGSe films actually proved fortuitous, as high levels of incorporation were later shown to displace too much of the Se, degrading the crystallinity and the electronic quality of the films.

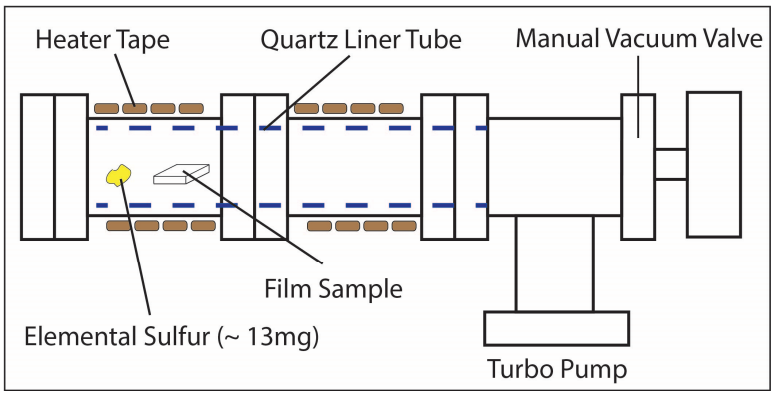

Fig. 3-15. Schematic of Generation #1 sulfur annealing chamber

Generation #2

The **Generation #2 sulfur annealing system** was configured as shown in Fig. 3-16. The system consisted of a small thermal vacuum chamber with a graphite annealing box assembly. The graphite box (Graphite Machining Inc.) was match-machined to provide a tight fitting lid, providing a reasonable but imperfect seal. A heater block assembly, utilizing a Firerod cartridge heater, provided heating up to 600°C. The graphite box was bolted to the heater block assembly with high-temperature Inconel Belleville washers (Solon Mfg), in order to maintain clamping load as the bolts thermally expanded at high temperatures. The entire assembly was contained within a stainless steel sheet metal radiation shield, in order to minimize radiation losses during heating. Inlet and exit meter valves were used to control the Argon flow through the chamber during annealing. A vacuum valve was used to isolate the roughing pump from the chamber, as shown. A MassVac inline filter with Sulfatreat insert was used at the inlet of the roughing pump to prevent any trace H_2S or SO_2 from corroding the pump and to minimize potential exposures. All annealing operations were performed under negative gauge pressures (-150torr) to further minimize gas escape.

Films were installed into the graphite box with a small quantity (3–25mg) of elemental sulfur. The chamber was then evacuated to < 10^{-3}torr and purged twice with Argon gas up to atmosphere. A constant background pressure of 600torr was maintained with a small Argon flow (< 5sccm), adjusted using the meter valves. The ramp rates and dwell times were then programmed into the temperature controller, typically 7min ramp with a 10min dwell at 560°C for 10min. After annealing, the graphite box was passively cooled under flowing Argon to < 120°C.

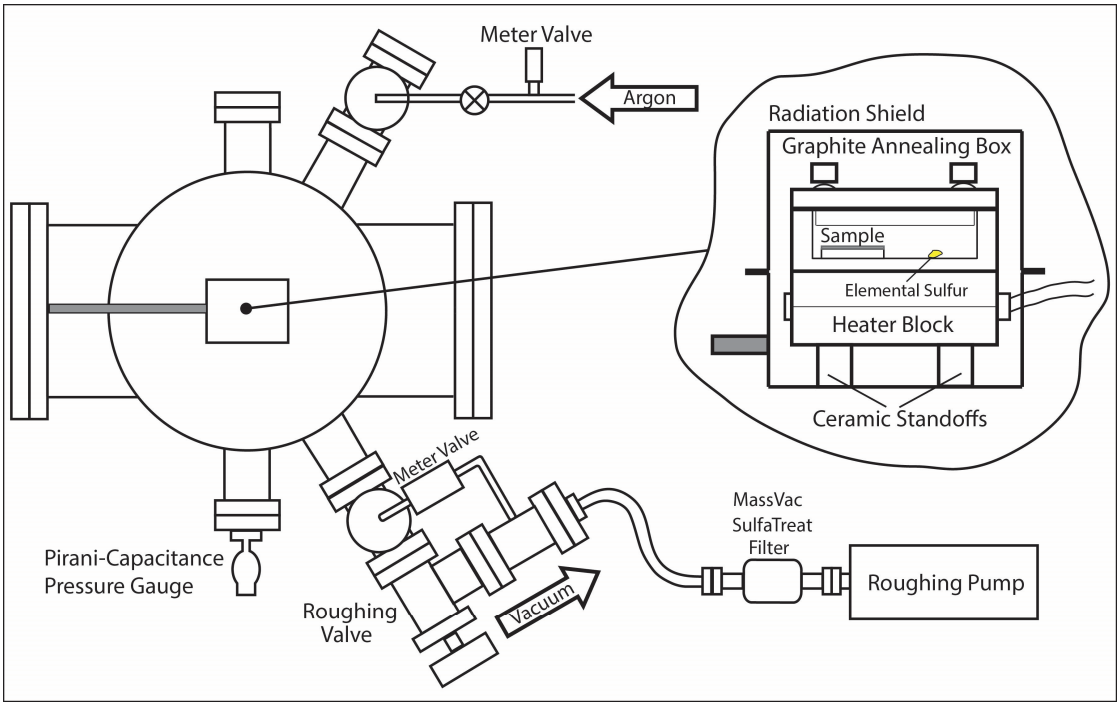

Fig. 3-16. Schematic of Generation #2 sulfur annealing chamber

The graphite box was based on the design reported in [19], but the lid was bolted in this case to improve the seal and to remove the reliance on background pressure to modulate the sulfur pressure in the box. Based on the mass of elemental sulfur and the volume of the graphite box, the maximum sulfur gas pressure can be estimated as described in the next section. Due to out-diffusion of the sulfur, the pressure likely decreases at the annealing temperature; for this reason annealing times are frequently kept short. The machine drawings for the graphite box are shown below in Fig. 3-17 and Fig. 3-18. The graphite base variation without the hole (flag feature 1) was used to perform sulfur annealing and prevent sulfur escape; the graphite base variation with the hole was used to perform low-temperature Argon annealing of the precursor films.

Properties of Sulfur

For this thesis, elemental sulfur (Sigma Aldrich, 99.998% metals basis, P/N: 213292-250G) contained in a closed or partially-closed volume, provides the background sulfur pressure necessary to achieve proper crystal phase formation. In order to ensure that proper sulfur pressures are maintained during annealing, as discussed in **Crystal Phase Decomposition at the Surface**, the proper amount of elemental sulfur must be included in the volume with the sample. To this end, a brief summary of the properties of elemental sulfur is provided here.

Elemental sulfur vapor consists of a mixture of sulfur molecules, S_n (n = 2…8), which have partial pressures that vary with both temperature and total pressure [78]. At 550°C and under saturation conditions, Rau reports that the S_6 – S_8 species of sulfur dominate the mixture with a total saturation pressure of 3.6atm [79]. The internal volume of the graphite annealing box used

in this work is approximately 3.36cm^3. Using experimental density data provided in [79] and this fixed internal volume of the graphite box, the following fitting can be used between 0.5atm (2.3mg) and saturation pressure of 3.56 atm (m_S = 38mg):

$$p_{S_{tot}} = 0.08677 m_S + 0.297 \tag{3-60}$$

where $p_{S,tot}$ is the total sulfur pressure in atm and m_S is the mass in mg of elemental sulfur included in the graphite box. At masses larger than 38mg, some elemental sulfur will condense; at masses smaller than this value, the vapor will become superheated. The mole fractions (e.g. the partial pressures) of the sulfur components at saturation (dominated by S_6 – S_8) are presented in [79]. As the vapor superheats (e.g. as the mass of the sulfur decreases), however, the speciation will shift towards higher mole fractions of lower n S_n-molecules [78]. Sulfur masses of 3.0mg, 4.5mg, 9.0mg, and 25mg were used in this thesis, corresponding to sulfur vapor pressures of 0.56atm, 0.69atm, 1.1atm, and 2.5atm, respectively. Notably, all sulfur masses employed yield much greater sulfur pressures than the 2.3x10^{-4}mbar recommended in [59]. The lowest sulfur pressure of 0.56atm requires an associated SnS pressure greater than 1.7x10^{-6}torr according to [59]. In some cases, elemental Sn (Alfa Aesar, 100mesh, 99.85%, P/N: AA00941-22) was also included in the graphite box to investigate its effect on film stability and formation.

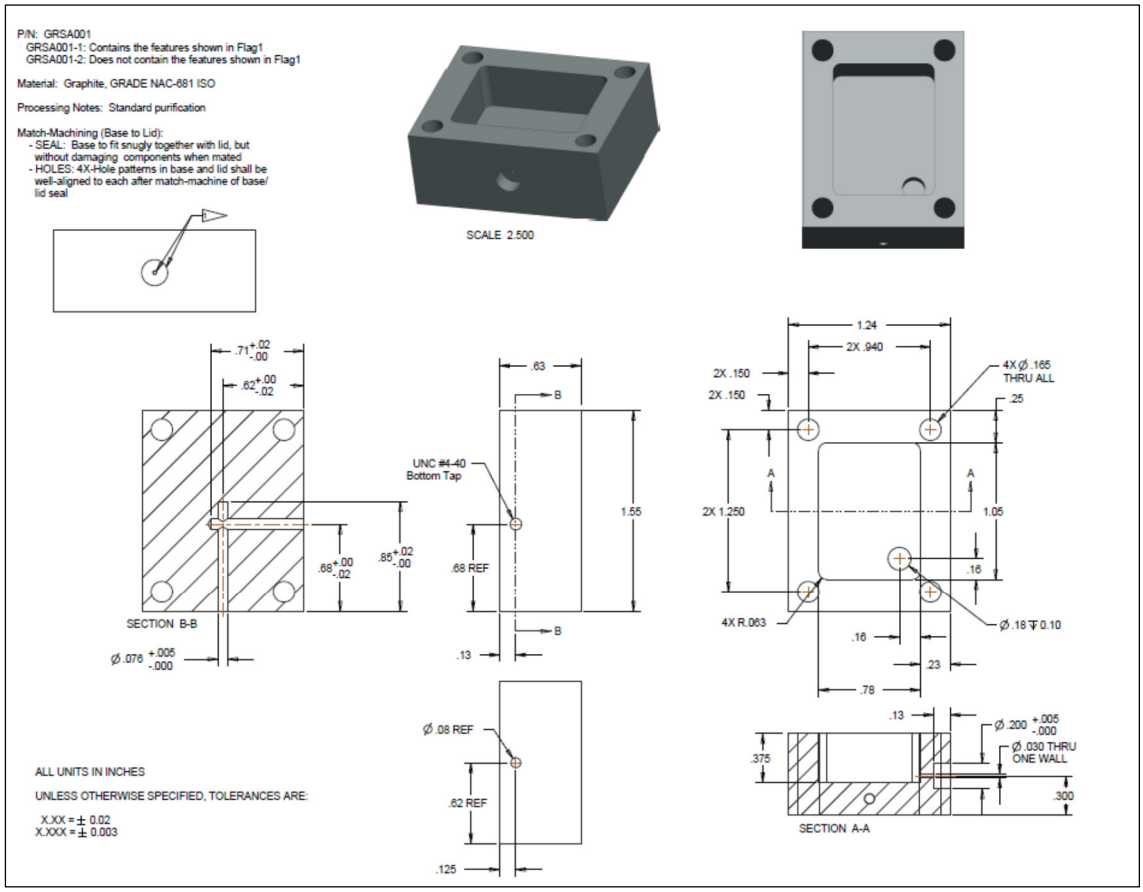

Fig. 3-17. Graphite annealing box design: Base

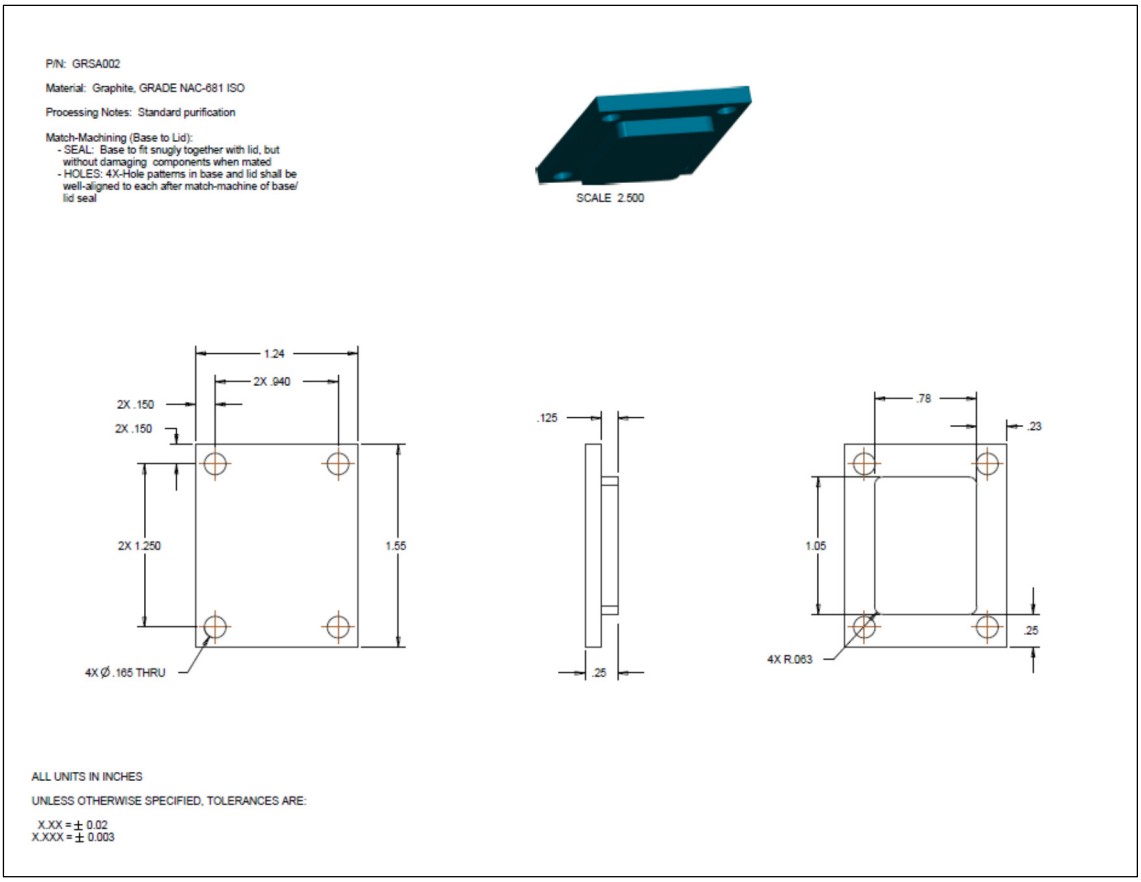

Fig. 3-18. Graphite annealing box design: Lid

3.4 REFERENCES

[1] T.J. Jackson, S.B. Palmer, Oxide superconductor and magnetic metal thin film deposition by pulsed laser ablation: a review, J. Phys. D: Appl. Phys., 27 (1994) 1581-1594.

[2] D.C.G. Hubler, Pulsed Laser Deposition of Thin Films, John Wiley & Sons, New York, 1994.

[3] M.J. Aziz, Film growth mechanisms in pulsed laser deposition, Appl Phys A, 93 (2008) 579-587.

[4] J.M. Camacho, R. Castro-Rodriguez, J.L. Pena, Transparent conductive oxide thin films of CdTe-doped indium oxide prepared by pulsed-laser deposition, Optics & Laser Technology, 40 (2008) 895-900.

[5] T. Venkatesan, S.M. Green, Pulsed Laser Deposition: Thin Films in a Flash, The Industrial Physicist, 2 (1996) 22-24.

[6] M. Ratzke, M. Kappa, D. Wolfframm, S. Kouteva-Arguirova, J. Reif, PLD of High-k Dielectric Films on Silicon, in: I. Miyamoto, H. Helvajian, K. Itoh, F. Kobayashi, A. Ostendorf, K. Sugioka (Eds.) Fifth International Symposium on Laser Precision Microfabrication, Proceedings of SPIE, Bellingham, 2004, pp. 406-411.

[7] R. Eason, Pulsed Laser Deposition of Thin Flims: Applications-Led Growth of Functional Materials, John Wiley & Sons, Hoboken, 2007.

[8] D. Smith, Thin-Film Deposition: Principles and Practice, McGraw-Hill, Inc., 1995.

[9] R.K. Singh, J. Narayan, Pulsed-laser evaporation technique for deposition of thin films: Physics and theoretical model, Physical Review B, 41 (1990) 8843-8861.

[10] C.P. Grigoropoulos, Transport in Laser Microfabrication: Fundamentals and Applications, Cambridge University Press, New York, 2009.

[11] M. Lorenz, Pulsed-Laser Deposition of ZnO-Based Thin Films, in: K. Elmer, A. Klein, B. Rech (Eds.) Transparent Conductive Zinc Oxide, Springer Berlin Heidelberg, Berlin, 2007, pp. 303-357.

[12] K. Byrappa, T. Ohachi, Crystal Growth Technology, Williams Andrew, Inc., Norwich, 2003.

[13] J.R. Ho, C.P. Grigoropoulos, J.A.C. Humphrey, Computational study of heat transfer and gas dynamics in the pulsed laser evaporation of metals, J. Appl. Phys., 78 (1995) 4696-4709.

[14] S.A. Reid, W. Ho, F.J. Lamelas, Pulsed Laser Ablation and Sn and SnO_2 Targets: Neutral Composition, Energetics, adn Wavelength Dependence, J. Phys. Chem. B, 104 (2000) 5324-5330.

[15] H. Sankur, R. Hall, Thin-film deposition by laser-assisted evaporation, Applied Optics, 24 (1985) 3343-3347.

[16] H. Sankur, Properties of thin PbF_2 films deposited by cw and pulsed laser assisted evaporation, Applied Optics, 25 (1986) 1962-1965.

[17] X. Zhang, S.S. Chu, J.R. Ho, C.P. Grigoropoulos, Excimer laser ablation of thin gold films on a quartz crystal microbalance at various argon background pressures, Appl Phys A, 64 (1997) 545-552.

[18] D. Mitzi, O. Gunawan, T. Todorov, K. Wang, S. Guha, The path towards a high-performance solution-processed kesterite solar cell, Solar Energy Materials & Solar Cells, 95 (2011) 1421 - 1436.

[19] J.J. Scragg, Studies of Cu_2ZnSnS_4 films prepared by sulfurisation of electrodeposited precursors, in: Chemistry, University of Bath, 2010, pp. 244.

[20] M. Paunovic, M. Schlesinger, Fundamentals of Electrochemical Deposition, John Wiley & Sons, Hoboken, 2006.

[21] A.J. Bard, L.R. Faulkner, Electrochemical Methods: Fundamentals and Applications, Second ed., John Wiley & Sons, Hoboken, 2001.

[22] M. Bouroushian, Electrochemistry of Metal Chalcogenides, Springer, Berlin, 2010.

[23] J.A. Abys, S.R. Brankovic, e. al., Modern Electroplating, Fifth ed., John Wiley & Sons, Hoboken, 2010.

[24] E. Budevski, G. Staikov, W.J. Lorenz, Electrochemical Phase Formation and Growth: An Introduction to the Initial Stages of Metal Deposition, VCH, New York, 1996.

[25] F.A. Kroger, Cathodic Deposition and Characterization of Metallic or Semiconducting Binary Alloys or Compounds, Journal of the Electrochemical Society: Solid-State Science and Tehcnology, 125 (1978) 2028 - 2034.

[26] N. Eliaz, E. Gileadi, Induced Codeposition of Alloys of Tungsten, Molybdenum, and Rhenium with Transition Metals, in: C. Vayenas (Ed.) Modern Aspects of Electrochemistry, Springer, New York, 2008.

[27] W. Septina, S. Ikeda, A. Kyoraiseki, T. Harada, M. Matsumura, $Cu_2ZnSn(S,Se)_4$ Thin Film Prepared from a Single-step Electrodeposited Cu-Zn-Sn-Se Precursor, in: Photovoltaic Specialists Conference (PVSC), 2012 38th IEEE, Austin, 2012, pp. 002702-002706.

[28] S.M. Pawar, B.S. Pawar, A.V. Moholkar, D.S. Choi, J.H. Yun, J.H. Moon, S.S. Kolekar, J.H. Kim, Single step electrosynthesis of Cu_2ZnSnS_4 (CZTS) thin films for solar cell application, Electrochimica Acta, 55 (2010) 4057-4061.

[29] C. Platzer-Bjorkman, J. Scragg, H. Flammersberger, T. Kubart, M. Edoff, Influence of precursor sulfur content on film formation and compositional changes in Cu2ZnSnS4 films and solar cells, Solar Energy Materials & Solar Cells, 98 (2012) 110 - 117.

[30] S. Taunier, J. Sicx-Kurdi, P.P. Grand, A. Chomont, O. Ramdani, L. Parissi, P. Panheleux, N. Naghavi, C. Hubert, M. Ben-Farah, J.P. Fauvarque, J. Connolly, O. Roussel, P. Mogensen, E. Mahe, J.F. Guillemoles, D. Lincot, O. Kerrec, $Cu(In,Ga)(S,Se)_2$ solar cells and modules by electrodeposition, Thin Solid Films, 480 - 481 (2005) 526 - 531.

[31] S. Delbos, Kesterite thin films for photovoltaics: a review, EPJ Photovoltaics, 3 (2012) 35004:p35001 - p35013.

[32] W. Wang, M. Winkler, O. Gunawan, T. Gokmen, T. Todorov, Y. Zhu, D. Mitzi, Device Characteristics of CZTSSe Thin-Film Solar Cells with 12.6% Efficiency, Advanced Energy Materials, (2013).

[33] L.M. Abrantes, N. Amir, e. al., Electrochemical Dictionary, Springer, Berlin, 2008.

[34] P. Hiemenz, R. Rajagopalan, Principles of Colloid and Surface Chemistry, Third ed., Taylor & Francis Group, Boca Raton, 1997.

[35] Springer Handbook of Metrology and Testing, Springer-Verlag, New York, 2011.

[36] D. Pletcher, F. Walsh, Industrial Electrochemistry, Second ed., Springer Science + Business Media, LLC, 1990.

[37] V. Sudha, M.V. Sangaranarayanan, Underpotential deposition of metals - Progress and prospects in modelling, J. Chem. Sci., 117 (2005) 207 - 218.

[38] J. Mosby, D. Johnson, A. Prieto, Evidence of Induced Underpotential Deposition of Crystalline Copper Antimonide via Instantaneous Nucleation, Journal of the Electrochemical Society, 157 (2010) E99 - E105.

[39] D. Lincot, Electrodeposition of semiconductors, Thin Solid Films, 487 (2005) 40 - 48.

[40] Y.A. Cengel, M.A. Boles, Thermodynamics: An Engineering Approach, Sixth ed., McGraw Hill Higher Education, Boston, 2008.

[41] R. Winand, Electrodeposition of Metals and Alloys - New Results and Perspectives, Electrochimica Acta, 39 (1994) 1091 - 1105.

[42] K. Popov, S. Djokic, B. Grgur, Fundamental Aspects of Electrometallurgy, Kluwer Academic Publishers, New York, 2002.

[43] N. Nikolic, K. Popov, Hydrogen Co-deposition Effects on the Structure of Electrodeposited Copper, in: S. Djokic (Ed.) Electrodeposition: Theory and Practice, Springer, New York, 2010.

[44] Uhlig's Corrosion Handbook, John Wiley & Sons, Hoboken, 2011.

[45] J. Gustavsson, In-situ activated hydrogen evolution from pH-neutral electrolytes, in: Chemical Science and Engineering, Kungliga Tekniska Högskolan (KTH), Stockholm, 2012.

[46] P.T. Kissinger, W.R. Heineman, Cyclic Voltammetry, Journal of Chemical Education, 60 (1983) 702 - 706.

[47] C. Gougaud, D. Rai, S. Delbos, E. Chassaing, D. Lincot, Electrochemical Studies of One-Step Electrodeposition of Cu-Sn-Zn Layers from Aqueous Electrolytes for Photovoltaic Applications, Journal of the Electrochemical Society, 160 (2013) D485-D494.

[48] F.I. Tzec, G. Oskam, Electrodeposition of Copper in Trenches from a Citrate Plating Bath, ECS Transactions, 25 (2010) 195-201.

[49] R.B. Martin, pH as a variable in free zinc ion concentration from zinc-containing lozenges, Antimicrobial Agents and Chemotherapy, 32 (1988) 608 - 609.

[50] C. Sene, M.E. Calixto, K.D. Dobson, R.W. Birkmire, Electrodeposition of $CuInSe_2$ absorber layers from pH buffered and non-buffered sulfate-based solutions, Thin Solid Films, 516 (2008) 2188-2194.

[51] S.-K. Song, Characteristics of SnO_x films deposited by reactive-ion-assisted deposition, Physical Review B, 60 (1999) 11137 - 11148.

[52] J. Scofield, A. Duda, D. Albin, B.L. Ballard, P.K. Predecki, Sputtered molybdenum bilayer back contact for copper indium diselenide-based polycrystalline thin-film solar cells, Thin Solid Films, 260 (1995) 26-31.

[53] S. Marsillac, H. Khatri, Study of CIGS Solar Cells Back Contact, Mater. Res. Soc. Symp. Proc., 1012 (2007).

[54] F. Hergert, S. Jost, R. Hock, M. Purwins, A crystallographic description of experimentally identified formation reaction of $Cu(In,Ga)Se_2$, Journal of Solid Sate Chemistry, 179 (2006) 2394 - 2415.

[55] F. Hergert, R. Hock, Predicted formation reactions for the solid-state syntheses of the semiconductor materials Cu_2SnX_3 and Cu_2ZnSnX_4 (X=S,Se) starting from binary chalcogenides, Thin Solid Films, 515 (2007) 5953 - 5956.

[56] J. Scragg, P. Dale, D. Colombara, L. Peter, Thermodynamic Aspects of the Synthesis of Thin-Film Materials for Solar Cells, Chem. Phys. Chem., 13 (2012) 3035 - 3046.

[57] F. Abbona, S. Balint, e. al., Springer Handbook of Crystal Growth, Springer, New York, 2010.

[58] A. Weber, R. Mainz, H.W. Schock, On the Sn loss from thin films of the material system Cu-Zn-Sn-S in high vacuum, Journal of Applied Physics, 107 (2010) 013516-013511 - 013516-013516.

[59] J. Scragg, T. Ericson, T. Kubart, M. Edoff, C. Platzer-Bjorkmann, Chemical Insights into the Instability of Cu_2ZnSnS_4 Films during Annealing, Chemistry of Materials, 23 (2011) 4625–4633.

[60] J. Scragg, J. Watjen, M. Edoff, T. Ericson, T. Kubart, C. Platzer-Bjorkman, A Detrimental Reaction at the Molybdenum Back Contact in $Cu_2ZnSn(S,Se)_4$ Thin-Film Solar Cells, J. Am. Chem. Soc., 134 (2012) 19330 - 19333.

[61] P.M.P. Salome, J. Malaquias, P.A. Fernandes, M.S. Ferreira, J.P. Leitao, A.F.d. Cunha, J.C. Gonzalez, F.N. Matinaga, G.M. Ribeiro, E.R. Viana, The influence of hydrogen in the incorporation of Zn during the growth of $Cu_2ZnSnSn_4$ thin films, Solar Energy Materials & Solar Cells, 95 (2011) 3482 - 3489.

[62] R. Schurr, A. Holzing, S. Jost, R. Hock, T. Vob, J. Schulze, A. Kirbs, A. Ennaoui, M. Lux-Steiner, A. Weber, I. Kotschau, H.W. Schock, The crystallisation of Cu2ZnSnS4 thin film solar cell absorbers from co-electroplated Cu-Zn-Sn precursors, Thin Solid Films, 517 (2009) 2465 - 2468.

[63] K.V. Gurav, S.M. Pawar, S.W. Shin, M.P. Suryawanshi, G.L. Agawane, P.S. Patil, J.H. Moon, J.H. Yun, J.H. Kim, Electrosynthesis of CZTS films by sulfurization of CZT precursor: Effect of soft annealing treatment, Applied Surface Science, 283 (2013) 74 - 80.

[64] A. Redinger, D.M. Berg, P.J. Dale, S. Siebentritt, The Consequences of Kesterite Equilibria for Efficient Solar Cells, J. Am. Chem. Soc., 133 (2011) 3320 - 3323.

[65] H. Araki, Y. Kubo, K. Jimbo, W.S. Maw, H. Katagiri, M. Yamazaki, K. Oishi, A. Takeuchi, Preparation of Cu_2ZnSnS_4 thin films by sulfurization of co-electroplated Cu-Zn-Sn precursors, Phys. stat. sol. (c), 6 (2009) 1266-1268.

[66] A. Emrani, P. Vasekar, C. Westgate, Effects of sulfurization temperature on CZTS thin film solar cell performances, Solar Energy, 98 (2013) 335 - 340.

[67] A. Fairbrother, X. Fontane, V. Izquierdo-Roca, M. Espindola-Rodriguez, S. Lopez-Marino, M. Placidi, L. Calvo-Barrio, A. Perez-Rodriguez, E. Saucedo, On the formation mechanisms of Zn-rich Cu_2ZnSnS_4 films prepared by sulfurization of metallic stacks, Solar Energy Materials & Solar Cells, 112 (2013) 97 - 105.

[68] J. Han, S. Shin, M. Gang, J. Kim, J. Lee, Crystallization behaviour of co-sputtered Cu2ZnSnS4 precursor prepared by sequential sulfurization processes, Nanotechnology, 24 (2013) 095706-095701 - 095706-095708.

[69] I.D. Olekseyuk, I.V. Dudchak, L.V. Piskach, Phase equilibria in the Cu_2S-ZnS-SnS_2 system, Journal of Alloys and Compounds, 368 (2004) 135 - 143.

[70] P.M. Nikolic, L.J. Miljkovic, P. Mihajlovic, B. Lavrencic, Splitting and coupling of lattice modes in the layer compound SnS, Journal of Physics C: Solid State Physics, 10 (1977) L289 - L292.

[71] J. Ge, Y. Wu, C. Zhang, S. Zuo, J. Jiang, J. Ma, P. Yang, J. Chu, Comparative study of the influence of two distinct sulfurization ramping rates on the properties of Cu2ZnSnS4 thin films, Applied Surface Science, 258 (2012) 7250 - 7254.

[72] H. Yoo, J. Kim, L. Zhang, Sulfurization temperature effects on the growth of Cu_2ZnSnS_4 thin film, Current Applied Physics, 12 (2012) 1052 - 1057.

[73] P.A. Fernandes, P.M.P. Salome, A.F. Sartori, J. Malaquias, A.F.d. Cunha, B.A. Schubert, J.C. Gonzalez, G.M. Ribeiro, Effects of sulphurization time on Cu_2ZnSnS_4 absorbers and thin films solar cells obtained from metallic precursors, Solar Energy Materials & Solar Cells, 115 (2013) 157 - 165.

[74] J.J. Scragg, P.J. Dale, L.M. Peter, Synthesis and characterization of Cu_2ZnSnS_4 absorber layers by an electrodeposition-annealing route, Thin Solid Films, 517 (2009) 2481 - 2484.

[75] S. Shin, S.M. Pawar, C. Park, J. Yun, J. Moon, J. Kim, J. Lee, Studies on Cu_2ZnSnS_4 (CZTS) absorber layer using different stacking orders in precursor thin films, Solar Energy Materials & Solar Cells, 95 (2011) 3202 - 3206.

[76] K. Maeda, K. Tanaka, Y. Fukui, H. Uchiki, Influence of H_2S concentration on the properties of Cu_2ZnSnS_4 thin films and solar cells prepared by sol-gel sulfurization, Solar Energy Materials & Solar Cells, 95 (2011) 2855 - 2860.

[77] K. Zhang, Z. Su, L. Zhao, C. Yan, F. Liu, H. Cui, X. Hao, Y. Liu, Improving the conversion efficiency of Cu_2ZnSnS_4 solar cell by low pressure sulfurization, Applied Physics Letters, 104 (2014) 141101-141101 - 141101-141104.

[78] H.R. Alvarez, Growth mechanisms of $CuInS_2$ formed by the sulfurization of thin metallic films, in, der Technischen Universitat Berlin, 2010.

[79] H. Rau, T.R.N. Kutty, J.R.F.G.d. Carvalho, Thermodynamics of sulphur vapour, Journal of Chemical Thermodynamics, 5 (1973) 833 - 844.

4 THIN FILM CHARACTERIZATION METHODS

4.1 ELEMENTAL COMPOSITION

Characterization techniques that investigate elemental composition typically involve firing high-energy particles or x-rays at a substance and detecting either the spectrum of scattered particle energies or the spectrum of radiatively re-emitted fluorescence from the substance. Neighboring elements on the periodic table can exhibit similar physical and electronic properties, and so their effects on the physical scattering or re-emission processes can be difficult to deconvolute. In the case of Rutherford backscattering, Cu and Zn have significant peak overlaps in the resulting scattering spectra, yielding a high degree of uncertainty in the analytical fitting of the results. In x-ray emission based techniques, such as particle-induced x-ray emission (PIXE), x-ray fluorescence (XRF) and energy dispersive x-ray spectroscopy (EDS), Cu and Zn have partially overlapping emission peaks, which require analytical deconvolution. Some elements may share common x-ray emission peaks due to the nature of their electronic structure, despite largely varying atomic chemistry, such as sulfur Kα and molybdenum Lα peaks. Table 4-1 summarizes the key overlaps for characteristic element peaks in RBS and x-ray emission based techniques.

Table 4-1. Summary of elemental peak overlaps in RBS and x-ray emission based methods

Overlap Elements	RBS		PIXE/XRF/EDX	
	Within Layer	Between Layers	Within Layer	Between Layers
Cu – Zn	X		X	
Sn – FTO		X		X
Sn – Ca				X
S – Mo				X
Cu,Zn,Sn,S – Mo		X		X

Rutherford backscattering provides greater accuracy, when peaks can be resolved, than x-ray emission techniques [1], and it also provides information about the elemental concentrations as a function of film depth [2]. Subsequently, a combination of RBS and PIXE measurements are used to evaluate the elemental concentrations in the thin films. Specifically, PIXE measurements are used to estimate the Cu:Zn ratios in the films, as described in Section 4.1.2.2, and the RBS models are developed using these Cu:Zn ratios as additional fitting constraints.

4.1.1 Rutherford Backscattering (RBS)

4.1.1.1 Background and Experimental Set-up

Rutherford Backscattering (RBS) represents a non-contacting, non-destructive characterization tool used to probe the depth-resolved atomic composition of a sample. The

technique relies on a phenomenon known as **Rutherford scattering** that involves scattering of mono-energetic alpha-particles (ionized Helium atoms) by atomic nuclei within the sample [2]. RBS spectra are obtained by measuring the quantities and energies of backscattered ions. Fig. 4-1 shows a schematic of the RBS and PIXE experimental set-up. Measurements were performed using a National Electrostatics Corporation 5SDH pelletron tandem accelerator, with a 3.04MeV, $^{4}He^{++}$ ion beam (~1mm^2 spot size), detected at a 168° scattering angle. The beam energy (3.04MeV) was tuned to resonance with oxygen.

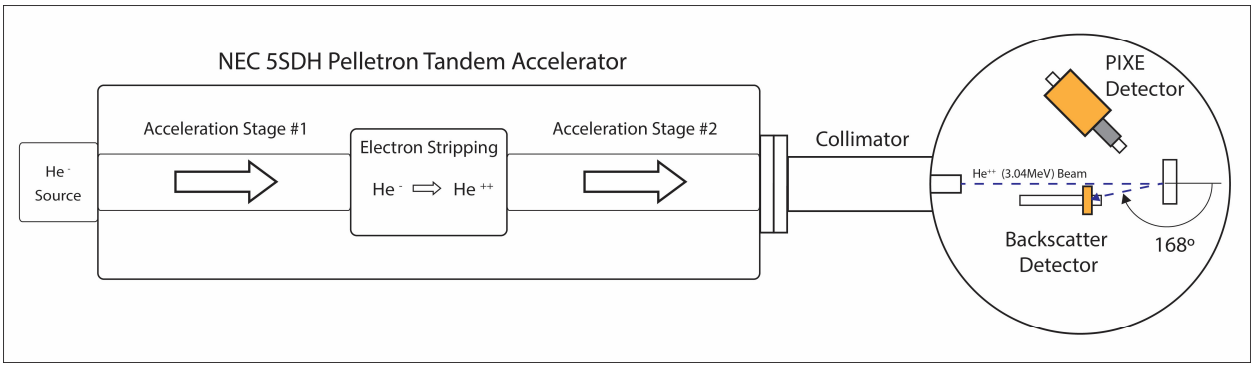

Fig. 4-1. RBS and PIXE Experimental Set-up

The energies of the scattered particles depend on the energy of the incident ions, the kinematic recoil factors and scattering cross-sections of the film atoms, and the depth of penetration of the scattered particles [2]. As one might expect, the scattered particle energy increases with increasing energy of the incident ions. The **kinematic recoil factor** represents the efficiency of energy transfer in elastic collisions, and its value increases with increasing mass of the film atoms [2]. Consequently, scattered particle energies also increase with increasing atomic mass of the elements.

The intensity of a given backscattering signal (e.g. the number of counts) depends on the rate of scattering interactions between incident ions and film atoms, which in turn depends on the concentration of a given element and its scattering cross-section [2]. The **scattering cross-section** represents the probability that an incident ion of a given energy will scatter into a given direction, in this case the backscattering direction [2]. The scattering cross-sections can depend strongly on the incident ion energy, demonstrating intense resonances at certain energies. The non-resonant, **Rutherford scattering cross-section** scales with the square of the atomic masses of the colliding ions, as shown in Eqn. (4-2). The non-resonant and resonant scattering cross-sections, and associated **reactions**, are described in more detail in Section 4.1.2.2.

As the incident ion penetrates deeper into the film, the particle loses energy due to Coulombic interactions with electrons in the film during both ingress and egress. The characteristic **stopping powers** of the elements may be used to correlate the loss of scattering energy with the depth distribution of the retarding atoms in the film [3]. Notably, this ion braking

represents a stochastic process and yields statistically varying energy losses for a given ion penetrating the same distance into the same material. These variations are described by the **energy straggle** and cause a broadening of the scattered energy spectrum [2], thereby limiting the depth-resolution of composition profiling.

Spectrum Trends

This section describes the trends associated with peak locations, peak shapes, and peak intensities, in order to more efficiently apply the model fitting parameters. Fig. 4-2 graphically demonstrates the effects of the physical parameters of the experiment on the behavior of the backscattering spectra, while Table 4-2 summarizes these results. Figures were generated using simulation spectra from SIMNRA [4].

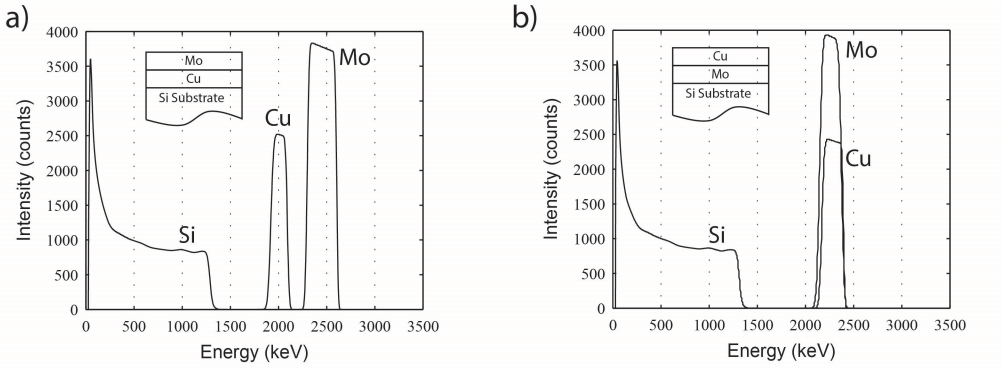

Fig. 4-2. Spectrum Trends in RBS with a) Favorable and b) Unfavorable layer configurations

With the physical principles described in the previous section, the **incident ion beam energy**, **element mass**, and **element distribution** may be related to trends in the backscattering spectra. As the incident ion penetrates deeper into the film, it loses more energy due to electronic breaking. Consequently, the right-most, high-energy side of the peak corresponds to the outermost surface of the layer containing that element; the left-most, low-energy side of the peak corresponds to its innermost surface [2]. As the layer thickness increases, the width of the elemental peak also increases due to the wider spread of backscattering energies. Furthermore, as the element depth increases, the ion must penetrate deeper into the film before being scattered by it, thereby decreasing the backscattering energy and shifting the element peak to the left [2]. Conversely, a reduction of thickness or a reduction of mass above a given element in the film will increase its backscattering energy and shift the element peak location to the right [2].

As previously detailed, the backscattering energies of the particles increase with increasing incident ion beam energy and with increasing mass of the scattering element, thereby shifting the element peak location to the right. Finally, increasing element concentration increases the number of backscattered particles, thereby increasing the peak intensity [2]. Based on these trends, the most favorable layer configuration for element peak resolution and analysis can be defined, such that outermost layers contain the highest mass elements and inner layers contain lighter mass

elements in sequence. This configuration tends to separate out the peaks, preventing overlap and ensuring the easiest and the most accurate fit of the simulated spectrum to the measure spectrum, as shown in Fig. 4-2 ($Z_{Si} < Z_{Cu} < Z_{Mo}$) [2].

Table 4-2. Summary of RBS backscattering spectrum trends

Category	Effect	Cause
Peak Locations	Element peak shifts left (lower E)	Increasing depth
	Element peak shifts right (higher E)	Increase He ion energy Increasing mass of that element Decreasing mass of element(s) above it Decreasing thickness of element above it
Peak Thickness	Peak thickness increases	Increasing thickness of layer containing that element
Peak Intensity	Peak intensity increases	Increasing element concentration
Peak Shape	Slope of left-most (lower E) edge flattens	Increasing film roughness
	Left-most (lower E) edges smoothen	Energy straggle Detector resolution

Film roughness and energy straggle both modulate the shapes of element peaks. Film roughness causes effective variations in the thickness of the layer, due to changes in the path length of the backscattered particle, and results in a sloping of the left-most, low-energy side of the element peak [2]. Energy straggle, resulting from the randomness of ion collisions with the elements in the film, yields a statistical distribution of energies that tends to smooth out the left-most edges of the element peaks and typically limits depth resolution to 10 – 20nm [2]. Detector resolution can further smooth edges as a result of statistical variations in detection [2].

4.1.1.2 Analysis and Modeling

Software

SIMNRA 6.0 software, developed by Matej Mayer at the Max-Planck-Institut fur Plasmaphysik, simulates backscattering spectra for high-energy ion beams [4]. The user inputs properties of the experimental configuration, the target (e.g the sample), and the relevant element reactions. Experimental conditions include incident ion type and energy, scattering detection geometry, and energy calibration parameters; relevant values for the RBS system used in this thesis are shown in Table 4-3.

Table 4-3. Experiment parameters implemented in SIMNRA models

Ion Type	4He
Energy	3040 keV (±5keV)
Incident Angle	0
Exit Angle	12.99
Scattering Angle	168.00
Calibration offset	-14.000keV (±15keV)
Energy per Channel	2.9500 (±0.05keV)
Particles*sr	1.80×10^{11}

The **target** consists of a collection of layers, which simulate the deposited film(s) and substrate. The user specifies the properties of each layer, including thickness (at/cm^2), elemental composition (at%), and roughness (at/cm^2). Each layer represents a discrete thickness, such that the properties remain constant within the layer. Through-thickness variations may be effectively captured by discretizing the layers into smaller thicknesses, and slowly varying the composition of each layer. SIMTarget was developed by J.L. Calaux to facilitate the modeling of such complex film compositions, and the software includes models for inter-layer Boltzmann diffusion [5]. Note that layer thickness values are entered in terms of atomic surface densities, where the conversion to film thickness is given by the following:

$$t_{film}(nm) = \frac{t_{film}(at/cm^2)}{N_{film}(at/cm^3)}\left(\frac{1nm}{1x10^{-7}cm}\right) \tag{4-1}$$

where N_{film} is the atomic density of the layer. After the reaction list for the elements present in the target are inputted, as described below, the user calculates the simulated spectrum. Using lattice parameters from [6] and [7], atomic densities of $CuIn_{0.75}Ga_{0.25}Se_2$ and Cu_2ZnSnS_4 were calculated as 4.1×10^{22}at·cm^{-3} and 5.0×10^{22}at·cm^{-3}, respectively.

Reaction List

The scattering cross-sections for many elements follow the simple relationship first described by Rutherford [3]:

$$\sigma = \left(\frac{Z_1 Z_2 e^2}{E_0}\right)^2 \left[\sin^4\left(\frac{\theta}{2}\right)\right]^{-1} \tag{4-2}$$

However, many low-Z elements exhibit nuclear resonances at certain incident ion energies, which dramatically alter the behavior of their scattering cross-sections [2]. These non-Rutherford scattering cross-sections depend on the element and on the incident ion energy. Accurate analysis of simulated backscattering spectra typically requires the use of non-Rutherford scattering cross-sections for *elements lighter than Silicon* [8]. These non-Rutherford scattering processes involve

nuclear reactions, and relevant data are typically referred to as **reaction data**. Reaction data are available at the Nuclear Data Service's Ion Beam Analysis Nuclear Data Library (IBANDL) [9].

Table 4-4. Table of scattering reactions used in SIMNRA modeling

Element	Non-Rutherford	Rutherford
O	Alphas on O16: 1769 – 5028keV	RBS 170, RBS 180
Na	Alphas on Na: 2000 – 6000keV	None
Si	Alphas on Si: 2000 – 6000keV	None
Ca	Alphas on Ca: 2200 – 8800keV	None
Mg	Alphas on Mg: 2000 – 9000keV	None
Cu, Zn, Sn, S, In, Ga, Se, Mo, Ti	None	ALL

As previously described, the RBS laboratory at Lawrence Berkeley National Laboratory (LBNL) tunes the energy of the ion beam to 3.04MeV at resonance with oxygen, allowing improved detection limits. When in direct resonance, RBS allows detection of the element at very low concentrations, but it does not provide accurate quantitative analysis of the absolute concentration [2]. Table 4-4 summarizes the scattering reactions used in quantitative modeling.

Sources of Error

The accurate determination of thin film composition by RBS analysis depends on a number of factors, including the measurement of the ion beam energy, the backscattering ion detector efficiency and energy resolution, the scattering cross-sections and electronic stopping powers of modeled atoms [1]. Other factors, such as energy straggle and film roughness, must also be properly captured in the modeling [1]. Literature has reported the investigation of measurement uncertainties and absolute accuracies of RBS analyses, performed under precise calibration, yielding values of ~1.25% and ~1%, respectively [1, 10]. Dominant sources of error in the RBS analyses were determined to be inaccuracies in electronic stopping powers of the modeled atoms [1]. Given that such extreme calibration steps are not performed under everyday lab conditions, it is expected that the RBS analyses of film compositions in this dissertation likely have a higher degree of error. However, it also expected that the majority of quantitative error in the analysis resides in misfits between the simulated and measured spectra, and so the overall composition errors of films analyzed in this dissertation are characterized according to these fitting errors.

The SIMNRA software contains an optimization routine in which the energy calibration, the particles*sr, the layer composition and thickness, and the layer roughness may be optimized to improve the fit accuracy and to calculate the fit error. However, this optimization may only performed on one layer at a time, and frequently visually improved fits were attained by manual iteration of the simulation parameters. In this vein, error was determined by assessing the range of compositions that provided a visually "good" or "acceptable" fit. The composition variation for

each element in a layer that satisfies these conditions represents the measurement error in the element concentration. In most cases, such error analysis proves quite cumbersome, and also unnecessary for the purposes of the analysis. Where error bars are presented on measured compositions, values were determined using the method discussed above.

As previously detailed, the thickness of the layers are inputted into the software as atomic surface densities (at/cm^2), requiring knowledge of the volumetric atomic densities of the films to convert to physical thickness values. Energy straggle contributes to limits in depth resolution on the order of 10 – 20nm. However, uncertainties in the volumetric atomic density likely dominate depth resolution in most cases. Structural variations, multiple phases, point defects, strain, and compositional gradients may all contribute to uncertainties in the volumetric atomic density, thereby limiting certainty in a given layer thickness. As Eqn. (4-1) shows, measured film thickness, and therefore its uncertainty, scales directly with volumetric atomic density and its uncertainty.

Film compositions and thicknesses were characterized using a combination of Rutherford backscattering and particle-induced x-ray emission spectroscopy (PIXE) analyses. As shown in Table 4-1, Cu and Zn element peaks strongly overlap in the RBS spectra, and PIXE measurements are required to calculate the Cu:Zn ratios in the film, as described in Section 4.1.2.2. Since PIXE measurements cannot provide depth-resolved information of the element concentrations, the individual through-thickness variations of Cu and Zn cannot be determined. Subsequently, it is assumed in the RBS fittings that the Cu:Zn ratio remains constant through the film thickness.

As stated in the previous section, the tuning of the ion beam energy to resonance with oxygen enables detection of the oxygen at low concentrations but does not permit accurate quantitative analysis of absolute concentrations. Notably, electrodeposition often involves co-deposition of hydrogen (see Chapter 3), which can yield hydrogen evolution but also hydrogen incorporation in the films. With a He ion source, H atoms cannot be detected in the backscattered configuration, although forward-scattering ion beam techniques have been used to detect hydrogen content in thin films [11]. Such evaluation of hydrogen concentration would be valuable, as a review of the literature on electrodeposition of CZTS found no reports of the H-content of the films, and this remains for future work. Electrodeposited films also frequently contain other impurities and inclusions, such as metal-complex ions and additives [12], suggesting the possible presence of carbon in the films (e.g. tartaric acid: $C_4H_6O_6$). However, the light carbon atoms cannot be reliably evaluated in the RBS spectra, due to their weak signal and overlap with substrate elements. In Chapters 7 and 8, the reported oxygen concentrations are provided as guides only, since the oxygen cannot be modeled with high quantitative accuracy and carbon and hydrogen may contribute to the balance of components in the film. Critically, the ratios of the Cu, Zn, Sn, and S remain unaffected by this particular uncertainty.

Measurement uncertainty was estimated according to the range of visually acceptable fits, and subsequently, uncertainty values varied according to signal quality and interpretation.

Calculated film thicknesses are intended as a relative guide only, and we do not provide error estimates. Further, many RBS fittings allow multiple solutions due to element peak overlap in the spectrum that results from the following: 1) composition distribution in the film; 2) severe surface roughness; or 3) incomplete film coverages of the substrate. In these cases, PIXE spectra were used to help *qualitatively* guide the RBS fittings, through scaling of the element peaks, although solutions were not always conclusive. These PIXE analyses are considered qualitative, since the x-ray production cross-sections are not well-known for elements besides Cu and Zn, and frequently elements in the PIXE spectrum overlap, as summarized in Table 4-1. It will be noted where compositions may not be quantitatively reliable. Finally, in many cases, through-thickness film compositions varied, and in these cases, weighted-average compositions are provided.

4.1.2 Particle-Induced X-Ray Emission (PIXE)

4.1.2.1 Background and Experimental Set-up

Particle-Induced X-Ray Emission (PIXE) represents a non-contacting, non-destructive characterization tool used to probe the atomic composition of a sample. The technique relies on the emission of **characteristic x-rays** that result from the ionization, by bombarding He^{++} ions, of core-shell electrons in the analyzed atoms [13-15]. Core-shell vacancies are quickly repopulated by outer shell (higher energy) electrons, and these de-excitations are accompanied by radiative x-ray emissions [13-15]. X-ray emissions that result from transitions of outer shell electrons to the inner most shell are denoted as **K x-rays**, emissions resulting from transitions to the next-most inner shell are denoted as **L x-rays**, etc. [13-15].

PIXE measurements are taken at the same time as RBS measurements, using the experimental set-up shown in Fig. 4-1. X-ray emissions from the film are detected using a PX4 Digital Pulse Processor with Si-PIN detector (energy resolution of ~150eV at 5.9keV) [16].

Spectrum Trends

This section describes general trends associated with peak intensities of characteristic x-rays. Notably, emission spectra depend only on the chemistry of the atoms probed, and so variations in characteristic peak locations result only from energy calibration errors associated with the x-ray detector. In this thesis, possible elements present in the sample are known, and small errors in peak location do not prevent definitive elemental identification. Relevant x-ray emission data may be found in [17].

Peak intensity increases with **increasing concentration** and **increasing x-ray production cross-section** of the element [13]. The x-ray production cross-section of an element generally increases with decreasing atomic mass (the ionization cross-section increases faster than the fluorescence yield declines) and with increasing projectile energy [15]. However, **fluorescence yield** drops rapidly for elements below Al (Z=13), detection efficiency drops rapidly, and x-ray absorption by the sample increases significantly, thereby limiting the peak intensities [13-15].

The background radiation generated during PIXE measurements largely determines the signal-to-noise ratio of the resulting spectra. **Bremsstrahlung emission** composes the primary source of background radiation and results from He^{++} ion braking by Coulombic-interactions with sample electrons [13, 14]. This background signal decreases substantially with increasing mass of incident particles, representing one of the major advantages of PIXE over EDS [13].

4.1.2.2 Analysis and Modeling

Similar to Energy Dispersive X-Ray Spectroscopy (EDS) and Electron Microprobe Analysis (EMPA), PIXE measurements provide information on the elemental concentrations within the sample by analysis of the x-ray emission spectra. Commercial and institutional software programs, such as GUPIX, PIXAN, and GEOPIXE, include sophisticated models that simulate the emission spectra [18]. In this dissertation, PIXE was primarily used qualitatively to identify elements present in the films and quantitatively only to estimate the Cu:Zn atomic ratios.

The **ionization cross-section** represents the probability that an interaction between the bombarding He^{++} ion and an atom in the film will result in ejection of an electron from the atom core shell [15]. However, the **x-ray production cross-section** (4-3) represents a more useful quantity for chemical analysis [15], since it directly relates the sample being probed to the parameter detected (e.g. the emitted x-ray).

$$\sigma_{prod} = \sigma_{ion} w k \tag{4-3}$$

where σ_{ion} is the ionization cross-section, w is the fluorescence yield, and k is the relative line intensity. The ionization and x-ray production cross-sections vary with both the bombarding ion mass and the sample atom chemistry [15]. Substantial bodies of data exist on the x-ray production cross-sections for a wide range of atomic masses interacting with ionized proton (H^+) beams.

Many beam lines, including the RBS lab at Lawrence Berkeley National Laboratory, use heavier He^{++} ions, and the x-ray production cross-sections must be properly scaled before use in any quantitative analysis. According to [19], the ionization cross-sections may be scaled as follows:

$$\sigma_{proj}(E_1) = Z_1^{\,2}\sigma_{prot}\left(\frac{E_1}{A_1}\right) \tag{4-4}$$

where σ_{proj} is the ionization cross-section of a projectile with atomic number Z_1 and mass number A_1, σ_{prot} is the ionization cross-section of an ionized proton. The values in parentheses indicate the energies at which the ionization cross-sections are evaluated. Scaling the x-ray production cross-sections from [15] using Eqn. (4-4), the Kα x-ray production cross-sections for **Cu** and **Zn** are **75barns** and **58barns**, respectively.

The intensity of an element peak, defined as the integrated area under the peak, scales with the concentration and the x-ray production cross-section of the element [15]. The Cu:Zn atomic ratios may then be calculated as follows:

$$\frac{\mathrm{Cu}}{\mathrm{Zn}} = \left(\frac{\mathrm{Cu}_{k\alpha}\text{Peak Area}}{\sigma_{\mathrm{prod}}(\mathrm{Cu}_{k\alpha})} \right) \Bigg/ \left(\frac{\mathrm{Zn}_{k\alpha}\text{Peak Area}}{\sigma_{\mathrm{prod}}(\mathrm{Zn}_{k\alpha})} \right) \tag{4-5}$$

Sources of Error

The accurate determination of the Cu:Zn atomic ratio depends on the accuracies of the calculated peak areas and the x-ray production cross-sections for Cu and Zn. The Cu and Zn Kα peaks are closely spaced (8.048keV and 8.640keV), and so the detector efficiency and associated counting errors for each element should be similar. Subsequently, errors in the calculation of peak areas are expected to result primarily from errors in deconvolution and fitting of Gaussian peaks to the overlapping Cu and Zn peaks.

The x-ray production scattering cross-sections for Cu and Zn, however, likely represent the largest sources of errors in the analysis. X-ray production cross-sections are estimated by scaling proton-induced x-ray production cross-sections of Cu and Zn in [15] according to Eqn. (4-4). The proton-induced x-ray production cross-sections contain a certain amount of measurement uncertainty, and the values were linearly interpolated from a table further introducing uncertainty. Without knowing the measurement uncertainties of the proton-induced x-ray cross-sections or the scaling equation, it is impossible to estimate the overall uncertainty in the calculation. However, for Cu and 2MeV incident proton, a measurement of uncertainty of ~2% was reported by [13], representing a lower bound. The absolute error in the calculated x-ray production cross-sections likely exceeds 10%, although Cu:Zn ratios calculated this way should provide useful information regarding trends in film compositions.

4.2 STRUCTURE AND MORPHOLOGY

4.2.1 X-Ray Diffraction (XRD)

4.2.1.1 Background and Experimental Set-up

X-Ray Diffraction (XRD) represents a non-contacting, non-destructive characterization tool used to probe the structural properties of a sample, which can be used to identify material phase, crystal structure, grain size, and film stress [20]. The technique relies on a phenomenon known as **diffraction** that involves **constructive interference** of scattered monochromatic x-rays at discrete angles that relate to the underlying crystal structure of the sample [20]. X-ray diffraction measurements were performed using a Siemens D500 x-ray diffractometer with a Cu anode (Cu-Kα wavelength 0.154 nm). Voltage and current were maintained at 40kV and 30mA, respectively. Wide scan 2θ measurements (20 – 70°) were nominally performed with a 0.05° step size and 1 sec/step accumulation. Narrow scan 2-θ measurements were performed on peaks of

interest with higher resolution 0.02° step sizes. In all cases, 0.3° slits were used on the source and detector sides. The x-ray diffractometer was configured with a stationary x-ray source and rotating sample holder and detector, as shown schematically in Fig. 4-3.

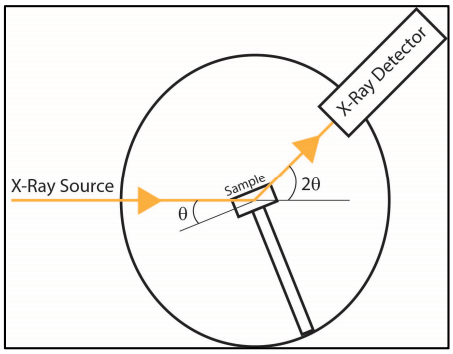

Fig. 4-3. Schematic of Diffractometer

Atoms within the crystal scatter the incident x-rays in all directions. Due to the periodicity of atoms within the crystal, however, only certain scattering angles will interfere constructively such that the x-rays are in-phase. All other angles will interfere destructively, effectively canceling out the scattered x-ray [20]. The condition for constructive interference is known as **Bragg's law**, and may be written as:

$$n\lambda = 2d\sin\theta \tag{4-6}$$

where n is the whole number of wavelengths, λ is the wavelength of the x-ray, d is the lattice plane spacing, and θ is the scattering angle. Fig. 4-4 shows a simple model of Bragg diffraction.

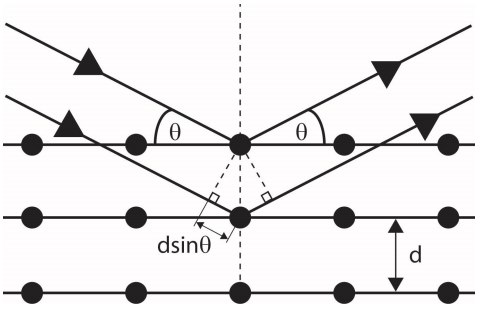

Fig. 4-4. Schematic of Bragg diffraction

In a single crystal, only the family of planes perpendicular to the surface will be probed. However, in powder or polycrystalline samples with randomly oriented crystal grains, all possible diffracting planes will be probed. A number of factors influence the relative intensity of diffraction peaks in "perfectly" randomized powders, including structure factor, multiplicity factor, Lorentz-polarization factor, absorption factor, and temperature factor [20]. The structure factor and the multiplicity factor influence the relative peak intensities most strongly under standard measurement conditions.

The location 2θ of a diffraction peak nominally depends on the periodicity of the crystal and therefore the underlying lattice [20]. However, the intensities of the peaks further depend on the atomic positions within the crystal (e.g. the basis), which are effectively captured in the **structure factor** [20]. Depending on the basis arrangement, the structure factor can weaken or eliminate completely certain diffraction peaks that would otherwise be present based on the underlying lattice [20]. The **multiplicity factor** represents the amplification of intensity in a given diffraction peak caused by the presence of multiple plane families with the same lattice spacing in a crystal, which reinforce a given peak signal [20].

Spectrum Trends

This section describes the general trends associated with peak locations, peak shapes, and peak intensities. Bragg's law, Eqn. (4-6), indicates that the diffraction angle θ varies inversely with the lattice plane spacing and therefore also the crystal unit cell size. Subsequently, decreasing the unit cell size increases (shifts right) the diffraction angle θ. The crystal unit cell size may be decreased through introduction of vacancies, smaller atom substitutions (as with S-Se alloying in the CZTSSe system), and uniform lattice strain. Alignment errors in the x-ray diffraction tool can also lead to erroneous shifts in the peak locations [20].

Table 4-5. Summary of x-ray diffraction spectrum trends

Category	Effect	Cause(s)
Peak Location	Peak shifts to the right	Decreasing unit cell size (e.g. vacancies, substitution of smaller atom) Increasing compressive (uniform) strain of film
Peak Width	Peak width broadens	Decreasing the crystallinity (grain size) Increasing non-uniform strain Increasing instrument profile (e.g. increasing slit size and beam divergence) Increasing the temperature
Peak Intensity	Peak intensity increases	Increasing the multiplicity factor Increasing the crystallinity (grain size) Decreasing the temperature Increasing the concentration of phase in mixture

Diffraction peak widths, typically defined as the full-width half-maximum (FWHM) values of the peaks, are determined by a number of factors including film geometry (crystallite size and film thickness), instrument profile, and film strain. Sharp diffraction peaks depend on constructive interference at the characteristic diffraction angles but also on destructive interference at the remaining scattering angles. To achieve complete destructive interference of scattered x-

rays from a given layer of atoms, another layer of atoms must be available to scatter x-rays at exactly 180° out-of-phase [20]. For films of limited thickness or crystallite size, these deeper layers that are fully out-of-phase may not be available, and so the x-rays scattered near to but offset from the primary diffraction angle are not completely cancelled out, resulting in broadening of the diffraction peak [20]. This effect can be exploited to determine the average grain size in films as described in Eqn. (4-7).

The instrument itself also contributes to the broadening of diffraction peaks, such that perfect crystals will exhibit finite peak diffraction widths. Two main factors contribute to this broadening, collectively referred to as the **instrument profile**, including beam divergence ($\Delta\theta$) and finite spectral range ($\Delta\lambda$) of the monochromatic incident x-rays [20]. Decreasing instrument slit size mitigates beam divergence but also decreases incident flux, thereby reducing peak intensities for a given accumulation time.

For a pure, perfectly randomized powder sample, the relative peak intensities of different reflection planes (hkl) vary as described in the previous section. Peak intensities also increase with increasing crystallinity (e.g. grain size) of the sample. Effectively, a greater number of coherent, constructively interfering reflection planes are available in large-grained samples. Based on this concept, the relative concentration of phases present in a mixture may be evaluated using their relative peak intensities after adjusting for the relative line intensity effects (e.g. structure factor, multiplicity factor, etc) [20]. For the same reason the peak intensity increases with increasing grain size, the peak intensity of a phase in a mixture increases with increasing concentration [20].

4.2.1.2 Analysis and Modeling

Phase Identification

Material phase and structure may be identified by comparing x-ray diffraction measurements of samples against standards. An international organization known as the International Centre for Diffraction Data (previously the Joint Committee on Powder Diffraction Standards) has been working since 1969 to catalogue a standard database of sample powder diffraction profiles [20]. In cases where JCPDS standards were unavailable, relevant literature was consulted. The x-ray diffraction reference standards used in this dissertation, for CIGSeS and CZTS, are listed in Table 4-6 and Table 4-7, respectively.

Table 4-6. Powder diffraction files of CIGSeS and commonly formed phases

Phase	Crystal Structure	JCPDS #	Phase	Crystal Structure	JCPDS #
$CuInSe_2$	Chalcopyrite	89-5649	Cu_2Se	Berzelianite	88-2044
$CuGaSe_2$	Chalcopyrite	81-0903	$Cu_{1.8}Se$	Cubic	88-2460
$CuIn_{0.7}Ga_{0.3}Se_2$	Chalcopyrite	35-1102	CuSe	Klockmannite	89-7391
$CuInS_2$	Chalcopyrite	89-6095	$CuIn_5Se_8$	Ordered Defect Compound	[6]
$CuGaS_2$	Chalcopyrite	65-1571	-	-	-

The diffraction spectra for a given material represents a chemical-structural fingerprint, and therefore the more peaks that can be matched the higher the confidence in the identification. Film texturing and peak overlap complicate phase identification. **Film texturing** results in a preferred (non-random) orientation of grains in a polycrystalline film, thereby reducing the number of diffraction peaks in the spectra [20]. In this case, the polycrystalline shifts the diffraction spectra towards that of a single-crystalline film (singular orientation of crystal face) and away from that of a powder (perfectly random orientation of crystal faces).

Table 4-7. Powder diffraction files of CZTS and commonly formed phases

Phase	Crystal Structure	JCPDS #	Phase	Crystal Structure	JCPDS #
Cu_2ZnSnS_4	Kesterite	26-0575, 34-1246	Cu	Cubic	89-2838, 03-1015
CuS	Cubic	89-2073	Zn	Hexagonal	87-0713
$Cu_{1.8}S$	Rhombohedral	85-1693	Sn	β-Tetragonal	89-4898
$Cu_{1.95}S$	Cubic	89-2072		α-Cubic	89-4789
Cu_2S	α-Cubic	84-1770		Tetragonal	89-2565
	Chalcocite	89-2670		Tetragonal	65-5224
ZnS	Rhombohedral	89-2351	S	Monoclinic	78-0793
	Hexagonal (Wurtzite 4H)	89-7385		Triclinic	89-6764
	Rhombohedral (Wurtzite 15R)	89-7386	Mo	Cubic	89-5156
SnS	Cubic	89-2755		Cubic	88-2331
SnS_2	Hexagonal (Bermdtite 4H)	89-3198	CuZn	Cubic	06-0657
	Hexagonal (Berndtite-2T)	83-1706		Cubic (Zhangengite)	02-1231
MoS_2	Hexagonal (Molybdenite 2H)	75-1539		Rhombohedral	26-0571
	Rhombohedral (Molybdenite3R)	89-2905	Cu_3Zn	Cubic	65-6567
CuO	Monoclinic	89-5899	Cu_4Zn	Hexagonal	65-6066
Cu_2O	Cubic (Cuprite)	78-2076	Cu_5Zn_8	Cubic	71-0397
ZnO	Cubic	77-0191	Cu_3Sn	Orthorhombic	65-4653
	Hexagonal	89-1397, 89-0511		γ-Cubic	65-4374
SnO	Tetragonal (Romarchite)	78-1063	$Cu_{10}Sn_3$	Hexagonal	71-0339, 65-3632
SnO_2	Orthorhombic	78-1063	Cu_6Sn_5	Monoclinic	65-2303
	Tetragonal	77-0452, 88-0287	Cu_2SnS_3	Tetragonal	89-4714
MoO_2	Monoclinic (Tugarinovite Titanian)	78-1073	Cu_3SnS_4	Orthorhombic (Kuramite)	36-0218
Cu_4SnS_4	Orthorhombic	71-0129	$Cu_4Sn_7S_{16}$	Rhombohedral	89-4713

The texturing may be so significant that only a single diffraction peak appears, making definitive phase identification nearly impossible without strong inherent knowledge of the film properties. Many factors may cause texturing in thin films, including non-uniform growth rates along different crystal faces, epitaxial orientation, and crystal face stability [21, 22]. Moreover, many phases may have close or identical peak locations, which may make phase identification difficult. For instance, CZTS shares many common peak locations with commonly formed binary and ternary compounds, such as ZnS and Cu_2SnS_3. In this case, a combination of composition and structural characterization tools must be used to identify the material phases and structures present in the film.

Grain Size Estimation

As described in 4.2.1.1, decreasing crystallite size results in a broadening of the diffraction peak. This relationship can be exploited to determine the size of small crystallites (< 500nm). Based on simple geometric considerations, the **average crystallite size** may be given by **Scherrer's formula** [20]:

$$d = \frac{0.9\lambda}{B\cos\theta_B} \tag{4-7}$$

where d is the crystallite size, λ is the wavelength of monochromatic x-rays, B is the FWHM of the primary diffraction peak in radians, and θ_B is the angular location of the peak in radians. The 0.9 pre-factor represents a geometric factor associated with the shape of the crystallite [20]. Instrument profile and film strain may also contribute to peak broadening and must be subtracted to provide an accurate determination of crystallite size. As the crystallite size increases, and the peak width decreases, the instrument profile will comprise a larger portion of the broadening and the calculations becomes less accurate [20]. Frequently, researchers use the Scherrer formula to qualitatively compare the changes in crystallite size between different samples. In this work, the instrument profile was not subtracted from the peak broadening, and calculations therefore represent a lower limit to the possible crystallite size. Therefore, no quantitative authority is assigned to these measurements, and calculations are used to provide a qualitative comparison of relative grain sizes.

In order to separate the contributions of crystallite size and film strain to the broadening of diffraction peaks, a Williamson-Hall plot may be constructed. The widths, B, of all strong diffraction peaks are measured. Then, $B\cos\theta$ is plotted vs. $\sin\theta$ (the Williamson-Hall plot). If $B\cos\theta$ is unchanging, then the crystallite size dominates the peak broadening. If $B\cos\theta$ is a linear function of $\sin\theta$, then film strain dominates the peak broadening.

Sources of Error

A number of factors may contribute to errors in diffraction peak locations, peak widths and peak intensities. As previously discussed, beam divergence and finite wavelength bands

contribute to instrument profile and it associated peak broadening. System misalignment in the source-sample-detector path may contribute to erroneous shifts in peak location [20]. Detector inefficiencies may cause miscounts in the peak intensities, and background radiation from fluorescence and diffuse scattering by the specimen may degrade the signal-to-noise ratio [20].

Table 4-8. Diffraction data for reference metal foils

Substrate	2-θ Peak Location (°)			Attributed Phase	Crystal Plane (hkl)
	Measured	Reference	Δ (°)		
Cu Foil	43.42	43.40	-0.02	Cubic	111
	50.56	50.41	-0.15		200
Zn Foil	36.34	36.29	-0.05	Hexagonal	002
	39.04	38.99	-0.05		100
	43.26	43.22	-0.04		101
	54.37	54.32	-0.05		102
Sn Foil	32.06	32.02	-0.04	β-Tetragonal	101
	45.01	44.90	-0.11		211
	55.43	55.34	-0.09		301
	62.60	62.52	-0.08		112
	64.67	64.59	-0.08		321

While x-ray diffraction is used to estimate crystallite sizes in some samples for this dissertation, the technique is primarily used to identify material phases/structures present in the samples. As such, the peak locations represent the most critical parameter measured in the films, and possible errors must be characterized in order to understand the tolerance values used in peak searching and identification. In order to determine the accuracy and repeatability of peak locations, a series of calibration and repeatability measurements were performed on reference foils and films. Calibration measurements are summarized in Table 4-8, and the repeatability measurements are summarized in Fig. 4-5 and Table 4-9.

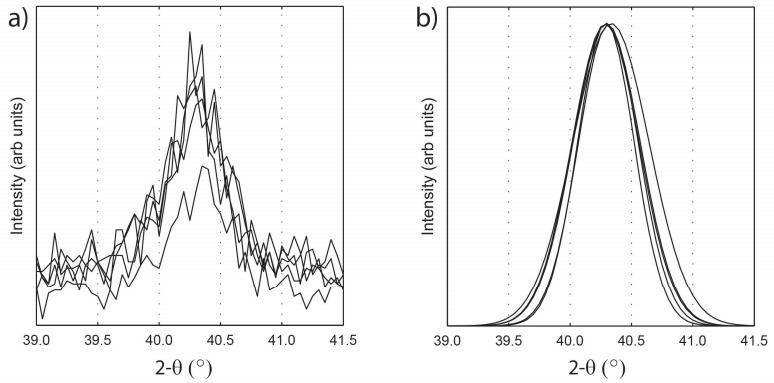

Fig. 4-5. a) X-ray diffractograms of measured EMAT Mo (110) peak for 5 different installations of the same sample; b) scaled and fitted peaks to the measured diffraction spectra

Table 4-9. Repeatability measurements of EMAT Mo on SLG

Substrate	Measurement #	2-θ Peak Location (°)	Average 2-θ Peak Location (°)	σ (°)
EMAT Mo (Corning 0215)	1	40.33	40.30	0.02
	2	40.29		
	3	40.29		
	4	40.31		
	5	40.30		

Based on the measured diffraction spectra of the metal foils and the Mo-coated SLG substrates, the repeatability (e.g. the precision) of the measurements, ± 0.02°, remains within the accuracy bounds of the measurements, +0.05/-0.15°. While this collection of data represents a distinctly small sample-size from which to draw broad statistical trends, a reasonable tolerance on the peak matching criterion may be established such that a measured peak matches a reference peak if the following condition is met:

$$2\theta_{meas} - 0.15° \leq 2\theta_{ref} \leq 2\theta_{meas} + 0.05° \tag{4-8}$$

Given the large number of closely-spaced diffraction peaks among possible phases in the CZTS system, this large tolerance band represents a substantial challenge in positive peak identification.

4.2.2 Raman Backscattering Spectroscopy

4.2.2.1 Background and Experimental Set-up

Raman Backscattering Spectroscopy represents a non-contacting, non-destructive characterization tool used to probe the vibrational properties of a sample, which can be exploited to identify material phase, crystal structure, film stress, defects and impurities [23]. The technique relies on an optical scattering phenomenon known as **Raman scattering** that involves **inelastic scattering** of monochromatic light. Raman backscattering measurements were performed using a Horiba Jobin-Yvon LabRam Raman confocal microscope with 1800 grating and interference filter. A 0.5mW, 488nm wavelength Coherent Argon laser was used as the monochromatic light source, and scattered light was detected at 180°.

The incident light interacts with **elementary excitations** of the medium (e.g. **phonons, plasmons**) and results in either the creation or destruction of one of these excitations. The creation of a phonon (e.g. excitation) reduces the frequency of the scattered light by the frequency of the associated phonon, causing a positive **Stokes shift** in the wavelength of the light. The destruction of a phonon (e.g. de-excitation) causes a negative **Anti-Stokes shift** in the wavelength of the light. At room temperature, where the population of excited phonons remains small compared to those in the ground state, Stokes processes predominate [24]. In practice, Stokes and Anti-Stokes shifts

provide similar information, so room temperature Raman spectroscopy typically involves analyzing only the Stokes components [23]. Stokes and Anti-Stokes energy shifts are shown below:

$$\text{Stokes: } \hbar\omega_i - \hbar\omega_s = \hbar\Omega_s \tag{4-9}$$

$$\text{Anti-Stokes: } \hbar\omega_s - \hbar\omega_i = \hbar\Omega_s \tag{4-10}$$

where $\hbar\omega_i$ is the energy of the incident photon, $\hbar\omega_s$ is the energy of the interacting phonon, and $\hbar\Omega_s$ is the energy transferred to the interacting phonon from the incident photon [24].

In addition to Raman scattering, samples will also exhibit **elastic Rayleigh scattering,** which results in re-emission of the incident light at the same wavelength. This remains the strongest scattering mechanism (by a factor of 10^6-10^9) [23], and optical filters must be used to remove the large background signal, as well as to protect the CCD from oversaturation [24]. When the incident light has a wavelength (e.g. energy) close to that of an inherent opto-electronic transition within the sample, the Raman scattering cross-sections significantly increase, yielding higher intensities [25]. Scattering under these conditions is referred to as **Resonant Raman Scattering** [25].

In order for incident light to interact with a given material, the electric field of the light must be able to deform the electron cloud within the material and induce an **oscillating electric dipole moment** thereby providing the mechanism of scattering [26]. **Polarizability** refers to the ability of an electric field to induce these dipole moments, and **electric susceptibility** χ refers to the relative degree to which a material is polarizable [24]. Conservation laws, as well as crystal symmetries, contribute to the Raman selection rules that determine which phonons may be active in Raman scattering. For instance, energy and quasi-momentum conservation require that the wave vector of single phonon scattering processes, and that the sum of wave vectors of multi-phonon scattering processes, lie close to the Brillouin zone origin [24].

The Raman selection rules may be assessed via the **Raman tensor,** which depends on the orientation and symmetry of the crystal and relates proportionally to the **Raman polarizability** ($\partial\chi/\partial A$), where χ is the electric susceptibility and A is the vibration amplitude [24]. In general, **Raman active** vibration modes are those that yield changes in Raman polarizability, **infrared (IR) active** vibration modes are those that yield changes in the dipole moment, and **silent modes** are those that yield no changes in either [24]. Crystal imperfections, such as point defects or grain boundaries, relax the selection rules due to a loss of symmetry in the crystal [24].

Spectrum Trends

This section describes the general trends, summarized in Table 4-10, associated with Raman scattering peak locations, peak widths, and peak intensities. As Eqn. (4-9) indicates, the frequency (and therefore wave vector) of the Raman shift depends on the frequency of the

interacting vibrational crystal mode. Therefore, changes to the vibrational mode frequencies of the sample will yield changes in the Raman scattering peak locations. A simplified vibrational model, known as the **simple harmonic oscillator**, yields the following relationship:

$$\omega = \sqrt{\frac{K}{\mu}} \tag{4-11}$$

where ω is the oscillation frequency, K is the force constant, and μ is the reduced mass. Of course, real systems are more complicated, and more complex modeling via the Raman tensor and material physics is required to accurately predict the Raman scattering behavior. However, by framing changes in a material system using this highly simplified model, some general trends may be observed. Increasing the frequency of the vibrational crystal mode involved in the Raman scattering process increases the Raman shift (shifts the peak to the right). Consequently, increasing the force constant or decreasing the reduced mass of the oscillator shifts the Raman peak to the right. And indeed, this trend appears in the alloyed CIS_xSe_{1-x} alloy system, with a shift of the dominant A_1-band from 173 → 290cm^{-1} as the lighter sulfur atom substitutionally replaces the heavier Se atom (x=0 → x=1) [23].

Anharmonicity in the vibrational behavior increases with **increasing temperature**, as the force constant begins to change and higher order terms in the taylor expansion of the vibrational potential become non-negligible [27]. The effects of anharmonicity on the frequency shifts of vibrational modes has been investigated in [27], and these shifts Δω(T) are shown generally to be negative, such that **increasing temperature** decreases the mode frequency and shifts the Raman peak to the left [27]. Such temperature-related shifts may be associated with laser heating of the sample during the measurement. **Strain** can also influence the force constant by modifying interatomic distances within the crystal. In general, compressive strain, which decreases the interatomic spacing, increases the force constant and shifts the associated Raman scattering peak to the right; tensile strain shifts the Raman peak to the left [23]. In a similar way, point defects in the crystal can alter the average force constants of bonding. Vacancies have been found in some cases to effectively weaken the force constant and shift the Raman peak left [23].

Raman scattering peak shapes depend strongly on the **effective correlation length** of the crystal, which represents a metric for crystalline order. The correlation length may be limited by defects within the crystal or by the size of the crystal, in the case of nano-grained samples [23]. The phonon frequency and the Raman scattering cross-section depend primarily on the local crystal order, and defect-free crystal grains above ~100nm diameter demonstrate Raman scattering behavior close to that of a perfect crystal [23]. For correlation lengths less than about ~100nm, symmetry breaking in the crystal relaxes the quasi-momentum conservation requirements and activates non-Brillouin center phonon modes [23]. Depending on the phonon dispersion

relationship, these non-center phonon modes often cause the development of a low-frequency or high-frequency shoulder in the Raman peak [23].

More generally, a decrease in the correlation length of the crystal causes a broadening and shift of its Raman scattering peak [23]. As the sample becomes more amorphous, and the quasi-momentum conversation rules more relaxed, any phonon may participate in the Raman scattering process and the phonon density of states (DOS) dictates the probability of a scattering event [23]. In these cases, the Raman spectra broaden and reflect the phonon DOS [23]. In summary, the peak width of a Raman band increases with decreasing correlation length, which in turn decreases with an increase in defect density and a decrease in the grain size. The phonon lifetime, which depends on the density of scattering defects, varies inversely with the peak width [23]. Temperature has also been shown to broaden the Raman peaks, due to thermal population effects and multi-phonon decay processes [27].

Table 4-10. Summary of Raman backscattering spectrum trends

Category	Effect	Cause(s)
Peak Locations	Peak shifts to the left	Alloying of crystal with heavier atoms Increasing tensile strain of films Increasing temperature Decreasing correlation length (increasing defect density)
Peak Width	Peak width broadens	Decreasing correlation length (increasing defect density) Increasing temperature
Peak Shape	Shoulders appear Very broad peak (α phonon DOS)	Decreasing correlation length Amorphous film
Peak Intensity	Peak intensity decreases	Increasing excitation laser wavelength Decreasing excitation laser power Decreasing polarizability of the film Decreasing concentration of Raman scattering species Increasing temperature

Crystalline defects may include **point defects**, such as vacancies, interstitials and antisites, or line and **surface defects**, such as dislocations and grain boundaries [23]. These defects may broaden and shift the Raman scattering peaks, as described above, but they may also introduce Raman-active **local vibrational modes (LVMs)** that alter their characteristic spectra [23]. For

instance, nitrogen impurities in GaAs, and cation disorder in CISe films, have been shown to introduce additional Raman peaks [23].

Raman peak intensities, in general, depend on the laser wavelength and power, the material polarization, the type of vibrational mode involved in the Raman scattering process, and the concentration of Raman active species. The intensity of Raman signals scale as λ^{-4} with laser wavelength [28] and linearly with laser power [23]. That is, the intensity of the Raman signal increases with decreasing laser wavelength and increasing laser power. As described earlier in this section, interaction of the incident light with the sample requires the material to be polarizable, and the strength of this interaction scales with the material's Raman polarizability [23]. For instance, Raman signals involving vibrational modes of highly polarizable atoms, such as sulfur or iodine, are more intense [26]. Finally, the Raman signal intensity typically increases linearly with increasing concentration of the detected species, with the proportionality constant dependent on its scattering cross-section [26]. Raman intensities may vary between measurement runs due to changes in the experimental set-up, and so each peak intensity should ideally be scaled using a standard of known concentration embedded within the sample [26].

As described above, **alloying** shifts Raman peak locations by modifying the force constants and masses associated with the vibrational modes [23]. Alloying effects, however, can vary widely and may exhibit one-mode or two-mode behavior [23, 26]. **One-mode behavior** involves a linear shift in peak position with alloying concentration [23]. **Two-mode behavior** involves splitting of the Raman peak with alloying, where each split mode represents the end phase [23, 26]. For instance, $Ga_{1-x}Al_xAs$ alloying results in generation of a GaAs-like and AlAs-like mode [26]. Elemental mass differences have been proposed to cause the differences between one- and two-mode behavior, but research remains on-going [25].

4.2.2.2 Analysis and Modeling

Micro-Raman (2-D Mapping) Measurements

The LabRam Raman system, which includes a focusing microscope, represents a micro-Raman system, with a spot diameter on the order of 1μm. The small spot size facilitates 2-D mapping of sample surfaces with reasonable spatial resolution. In most cases, spatial Raman maps of 4 – 16 μm^2 with measurement spacings of 0.25 – 1μm were used to characterize samples. These spectra were then averaged to provide a representation of the overall bulk sample.

Software

Raman spectra were recorded and analyzed using LabSpec, a commercial software installed with the Raman tool. As described above, average spectra taken from a mapping of the surface were used to characterize film samples. Each spectrum was corrected to remove baseline features and γ-radiation spikes.

For this work, baselines were calculated using "Lines"-type fitting and spectrum-anchored attach points. Anchor points were chosen such that the baseline followed closely the natural curves of the acquired spectra and such that baselines contained no sharp features. Such a fitting process relies on visual estimation of the "natural" curves of the spectra, and so the baselines contain inherent and unknown measurement uncertainties. Another method for assessing the baseline involves measuring the spectrum of a clean, well-known reference standard with distinct Raman peaks, and fitting the baseline as described above. Then, this baseline function, properly scaled, may be subtracted from the other measured sample spectra [26]. In this work, however, more consistent results were obtained using separate baseline fittings of each spectrum. Notably, fitted baselines usually represent a significant source of error in Raman spectra [26]. Fig. 4-6 shows a sample spectrum with and without the baseline removed.

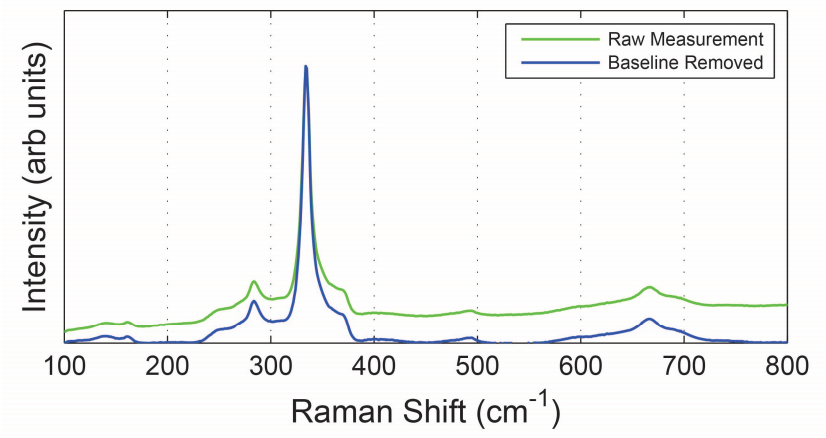

Fig. 4-6. Raman spectra of the as-measured signal and with baseline removed

Raman peaks were fitted using the peak fitting function in the LabSpec software. Spectra were fitted using the minimum number of peaks that adequately simulated the measured spectra. Peak locations, peak intensities, and peak widths were optimized by the software to minimize the standard error between the simulated spectra and the measured spectra.

Phase Identification

Material phase and structure may be identified by comparing Raman backscattering measurements of samples against standards. As with diffraction, the Raman scattering spectrum for a given material represents a chemical-structural fingerprint, and therefore the more peaks that can be matched the higher the confidence in the identification. Contrary to x-ray powder diffraction, however, there are no well-established repositories for Raman scattering data, perhaps in part because of the variation in sample spectra resulting from defects, disordering, and experimental conditions to which this technique is particularly sensitive. For this reason, matching peaks and identifying material phases-structures proves significantly more difficult than for x-ray

diffraction. Reference Raman scattering data used in this dissertation, for CIGSeS and CZTS, are listed in Table 4-11 and Table 4-12, respectively.

Table 4-11. Raman scattering references for CIGSeS and commonly formed phases

Phase	Crystal Structure	Reference	Phase	Crystal Structure	Reference
$CuInSe_2$	Chalcopyrite	[6]	$Cu_{2-x}Se$	Not Specified	[6]
$CuGaSe_2$	Chalcopyrite	[6]	$Cu_{2-x}S$	Not Specified	[6]
$Cu(In,Ga)Se_2$	Chalcopyrite	[6, 29]	Cu-In-Se	ODC	[6]
$CuInS_2$	Chalcopyrite	[6]	$CuIn_5S_8$	Not Specified	[6]
$CuGaS_2$	Chalcopyrite	[6]	-	-	-

Table 4-12. Raman scattering references for CZTS and commonly formed phases

Phase	Crystal Structure	Reference	Phase	Crystal Structure	Reference
Cu_2ZnSnS_4	Kesterite	[7, 30-34]	CuO	Monoclinic	[35, 36]
CuS	Covellite	[37, 38]	Cu_2O	Cuprite	[39, 40]
Cu_2S	Chalcocite	[38, 41]	ZnO	Wurtzite	[24, 42]
ZnS	Zinc Blende	[37, 43]	SnO	Layered	[44-46]
	Wurtzite	[43]	SnO_2	Rutile	[44, 47, 48]
SnS	Layered	[37, 49, 50]	MoO_2	Monoclinic	[51-53]
SnS_2	2H, 4H Polytypes	[37, 50]	Cu_2SnS_3	Tetragonal	[54-56]
Sn_2S_3	-	[37, 50]		Cubic	
S	Rhombic	[57]	$Cu_2Sn_3S_7$	-	[54]
MoS_2	Hexagonal Layered	[58, 59]	Cu_3SnS_4	Orthorhombic	[55]
-	-	-		Tetragonal	[56]

4.2.3 Secondary Phase Identification in CZTS: XRD and Raman Spectroscopy

Literature has frequently reported on the use of combined XRD and Raman spectra, in order to determine the phase-purity of CZTS thin films [30, 34, 37, 60]. Typically, diffraction spectra are examined first to evaluate which phases might be present. Cu_2ZnSnS_4 shares nearly identical diffraction peaks with ZnS and Cu_2SnS_3 [30], both of which are commonly formed secondary phases as the pseudo-ternary phase diagram in Chapter 2 and the CZTS formation reaction sequence in Chapter 3 suggest. Cheng notes, however, that the presence of peaks at 37.0° (202), 37.9° (211) and 44.9° (105/213) can be used to definitely confirm the presence of CZTS in the films; it does not, however, rule out the presence of the other two ZnS and Cu_2SnS_3 phases [30].

In textured films, where these differentiating peaks are weak or absent, Raman may sometimes be used to identify secondary phases and confirm the presence of CZTS in the film. However, many of the secondary phases also share common Raman modes [60], as one might expect given their similar crystal structure. Similar to the case above, Scragg notes the existence of

a unique CZTS Raman mode at 287cm^{-1}, which can be used to confirm the presence of CZTS but also not rule out the presence of ZnS and Cu_2SnS_3 phases [60]. For films deposited on Mo, however, a MoS_2 phase may also be present at 287cm^{-1}, as shown in [61, 62] and as evident in sulfur annealed samples discussed in Chapters 7 and 8 of this work.

Certainly, not all films will fit the general pattern described above, although similar lines of reasoning must be pursued to properly identify to the extent possible the phases present. Like samples with textured x-ray diffraction, not all Raman modes will always be visible and the peak shapes and locations may change, as described in preceding sections. Reference standards fabricated using similar processing conditions and with known composition structure should be used whenever possible.

The wavelength of the excitation laser used in Raman spectroscopy has also been shown to play a critical role in secondary phase identification, in particular for ZnS [34, 37, 62]. UV laser excitation has demonstrated significantly improved detection of ZnS phases by Raman spectroscopy, attributed to resonant scattering enhancement with the 3.84eV band gap of ZnS [62]. By varying the laser excitation wavelength over a large range, other similar resonances may be found which might enhance detection of both CZTS and secondary phases [34]. In fact, Dimietrievska does find changes in the intensities of characteristic CZTS Raman bands with wavelength. For instance, peaks at 255, 271, 316 and 347cm^{-1} were intensified when using a 325nm versus 514.5nm laser wavelength [34]. In that study, Raman spectra were generated for the following laser excitation wavelengths of 325.0, 457.9, 514.5, 632.8, 785.0 and 830.0nm [34]. As the relative peak intensities were expected to change with excitation wavelength, this study was intended to provide a baseline for which to evaluate the presence of secondary phases [34]. In this case, the relative peak intensities for CZTS Raman modes should be considered in a manner analogous to the relative peak intensities in powder diffraction data. A comprehensive list of active Raman modes for CZTS, both theoretical and experimental, are provided in [34].

4.2.4 Scanning Electron Microscopy and Energy Dispersive X-ray Spectroscopy

4.2.4.1 Background and Experimental Set-up

Scanning Electron Microscopy (SEM) represents a non-contacting, minimally destructive characterization tool used to probe the surface morphologies of thin films. The technique relies on the emission of **secondary electrons** from the sample by an incident beam of high energy electrons [63]. The emission of these secondary electrons varies with the material properties of the sample and depends most strongly on the path length of the incident electron beam. Morphological features alter this path length, which varies according to the incident angle and provides the primary source of feature contrast [63]. By scanning the incident electron beam and detecting the secondary electrons, a visual image of the sample surface may be reconstructed [63]. Film morphologies were primarily evaluated using a Hitachi S-4300 SE/N Schottky-Emission or

S-4700 scanning electron microscope, with electron beam accelerating voltages of 5 – 25kV and probe currents of ~2nA. Many studies were also performed using a JSM-7500F Field-Emission SEM.

Frequently, **energy dispersive x-ray emission spectroscopy (EDS)** measurements are performed at the same time as SEM imaging. EDS represents a non-contacting, minimally destructive characterization tool used to probe the laterally-resolved atomic composition of a sample. In addition to the emission of secondary electrons, the incident electron beam also causes the emission of characteristic x-rays of the constituent elements in the sample. EDS behaves similarly to PIXE, except electrons provide the bombarding particle source instead of He^{++} ions. EDS measurements were performed on the Hitachi and Jeol SEM systems using the Noran System Six x-ray microanalysis system and Oxford instruments system, respectively, with electron beam accelerating voltages of 15 – 25kV.

4.2.4.2 Applications

Software and Analysis

Quantitative analysis by EDS relies on the scaling of element peak intensity with the concentration of the element in the sample. By comparing the measured element peak intensity of an unknown sample with the element peak intensity of a sample with known composition, the element concentration in the unknown sample may be determined, as given by the following [64]:

$$\frac{C_i}{C_{(i)}} = \frac{I_i}{I_{(i)}} = k_i \tag{4-12}$$

where C_i is the concentration of element i in the unknown, $C_{(i)}$ is the concentration of element i in the standard sample, I_i is the peak intensity of element i in the unknown, $I_{(i)}$ is the peak intensity of element i in the standard sample. **I(i)** is known as the **standard intensity** and $\mathbf{k_i}$ as the **k ratio** [64]. Quantitative EDS analysis may include either **standards-based** or **standardless** methodologies. In standards-based analysis, standard intensities are measured on samples of known composition. In standardless analysis, standard intensities are calculated from first principles or semi-empirically derived from a suite of baseline standards measured on representative equipment [64]. Frequently, pure element targets, that represent the elements in a given film, are used as the standards basis. While this standard intensity measurement will not aid in the calibration of matrix effects, it nominally will include measurement effects such as detector efficiency and detector geometry [64]. Consequently, standardless analysis generally includes larger measurement uncertainties, and the experimental conditions must be accurately modeled in the standardless analysis in order to provide reasonable estimates [64].

EDS spectra were recorded and analyzed using Noran System Six (NSS), a commercial software installed with the EDS tool. Compared to RBS/PIXE, EDS provides better spatial

resolution but lesser quantitative accuracy in the film composition. Subsequently, EDS was used only qualitatively to assess surface decorations and film homogeneity by comparing relative peak intensities.

Sources of Error

EDS and PIXE characterization tools both measure characteristic x-rays emitted from the sample, and so both employ similar detector types. Consequently, the calibration and broadening errors associated with the detector will be similar for both, and the reader is referred back to Section 4.1.2. EDS differs from PIXE, however, in that the method typically provides spatially-resolved information about the composition. The **volume of interaction** of the electron within the sample determines the spatial resolution of the EDS measurement. Primary electrons fired at the sample penetrate its surface and then are scattered within the material through random scattering processes, creating a rain drop or pear-shaped volume of interaction [64]. Atoms within this volume may emit, and also absorb, x-rays as a result of these interactions [64]. At 20keV accelerating voltage, a low-density, low-atomic number sample will typically exhibit an interaction volume of ~ 1μm [64]. As mentioned in the previous section, EDS was used only for qualitative analysis in thesis, so further discussion of error analysis is omitted here. For a more detailed account of the errors in quantitative analysis associated with EDS, the reader is referred to [64].

4.3 Optical Properties

4.3.1 Absorption Spectroscopy

4.3.1.1 Background and Experimental Set-up

Absorption spectroscopy represents a non-contacting, non-destructive characterization technique used to probe the optical absorption properties of a sample, which can be exploited to identify optical transitions, including the band gap, of the material [65]. The technique relies on the optical absorption of light, which results from the photo-excitations of electrons in the sample into higher energy states [65]. Transmission and reflection measurements are used to calculate the optical absorption coefficient of the sample, as described in the following section. Transmission and reflection measurements were performed using a Scientific Computing International FilmTek 3000SE spectroscopic ellipsometer using the maximum wavelength range 240 – 1050nm, or a Perkin Elmer Lambda 950 UV/VIS/NIR spectrophotometer using a wavelength range of 200 – 2500nm.

From fundamental radiation theory, the variation of light intensity within an optically-participating sample with uniform optical absorption may be written as the Beer-Lambert law [66]:

$$I_\lambda(x) = I_{i,\lambda} \exp(-\alpha_\lambda x) \tag{4-13}$$

where $I_\lambda(x)$ is the intensity of light at distance x into the sample, $I_{i,\lambda}$ is the intensity of light incident on the sample after accounting for reflection losses, α_λ is the optical absorption coefficient, and λ denotes the spectral dependence of the variables. The transmittance of the films represents the percentage of incident light transmitted through the sample and may be defined as the ratio of transmitted to incident light. The transmittance τ_λ and the optical absorption coefficient α_λ, accounting for reflection losses at the front surface only or for both the front and back surfaces of the films, may then be written as follows [63]:

Table 4-13. Transmittance and optical absorption coefficient, including front and back surface reflections

Surface Reflections	τ_λ	α_λ (cm^{-1})
Front Surface Only	$(1-\rho_\lambda)\exp(-\alpha_\lambda d)$	$-\frac{1}{d}\ln\left(\frac{\tau_\lambda}{(1-\rho_\lambda)}\right)$
Front and Back Surfaces	$\frac{(1-\rho_\lambda)^2\exp(-\alpha_\lambda d)}{1-\rho_\lambda{}^2\exp(-2\alpha_\lambda d)}$	$-\frac{1}{d}\ln\left(\frac{\sqrt{(1-\rho_\lambda)^4+4\tau_\lambda{}^2\rho_\lambda{}^2}-(1-\rho_\lambda)^2}{2\tau_\lambda\rho_\lambda{}^2}\right)$

where ρ_λ is the reflectance, d is the film thickness, and λ again denotes the spectral dependence of the variables. Knowing the film thickness, the optical absorption coefficient may then be determined at each wavelength by directly substituting the measured values of transmittance and reflectance, τ_λ and ρ_λ.

4.3.1.2 Analysis and Modeling

Calculating Band Gap

Optical absorption involves the photo-excitation of electrons from the valence band to the conduction band, and so the transition process depends strongly on the joint density of states of the valence band and conduction band. Near the fundamental band edge (within a few 100meV), the bands may be approximated as parabolas and a simplified model of the joint density of states developed [66]. For direct band gap materials, the absorption coefficient may then be written in the following form [65, 67, 68]:

$$\alpha(h\nu)\cdot h\nu = \alpha_0\left(h\nu - E_g\right)^{1/2} \tag{4-14}$$

where $h\nu$ is the energy of the incident photon, h is Planck's constant, ν is the frequency of the incident photon, E_g is the fundamental band gap of the material, and α_0 is a material-dependent constant. By plotting $(\alpha h\nu)^2$ vs. $h\nu$, fitting a straight line near the band edge and extrapolating to zero, the direct allowed bandgap E_g may be evaluated [66, 67]. At this zero location, the material constant α_0 drops out.

$$(\alpha \cdot h\nu)^2 = \alpha_0 (h\nu - E_g) = 0 \rightarrow h\nu = E_g\big|_{(\alpha \cdot h\nu)^2 = 0} \quad (4\text{-}15)$$

The direct (forbidden), indirect gap, and indirect (forbidden) interband transitions may also be shown to follow the general form $(\alpha \cdot h\nu)^n = \alpha_0 (h\nu - E_g)$, where the exponent n is given by those in Table 4-14 [67, 68].

Table 4-14. Exponential relationships for optical transitions

Transition Type	n
Direct Allowed	2
Direct Forbidden	2/3
Indirect Allowed	1/2
Indirect Forbidden	1/3

Fitting the Urbach Tail

Frequently, materials exhibit **exponential (Urbach) absorption tails** that result from impurities or crystal disorder [65]. Despite wide-ranging underlying physics associated with the varying sources of disorder, the exponential tail develops almost universally in disordered solids [69]. Proposed mechanisms for this tail include electron band tails resulting from impurity states [69], as well as exciton-phonon interactions and associated free exciton absorption [70, 71]. The absorption tail may be empirically fitted with following equations [70, 71]:

$$\alpha = \alpha_0 \exp\left[\frac{\sigma(h\nu - E_0)}{k_B T}\right] \quad (4\text{-}16)$$

where α_0 and E_0 are characteristic material parameters, k_B is Boltzmann's constant, and σ is the steepness parameter [71]. A plot of $\ln(\alpha)$ vs. $h\nu$ will yield a straight line below the absorption edge, and extrapolation of this line for varying temperature measurements usually converges on (α_0, E_0).

Related to the structural disorder within the crystal, the Urbach tail provides an indication of the material quality. A perfectly crystalline direct gap thin film will show a steep rise in absorption at the fundamental band gap with negligible absorption below the band gap. As the crystalline structure becomes more disordered, the steepness of the absorption at the edge will decrease due to the development of a band tail. The Urbach energy, $E_U = kT/\sigma$, captures this relationship, varying inversely proportionally with the steepness parameter [71]. A direct relationship between the magnitude of the Urbach energy and the degree of structural disorder has been suggested [71].

Sources of Error

Calculation of the optical absorption coefficient from transmission and reflection data may include errors due to absorption in the substrate, diffuse reflection from the film, and detector inefficiencies in the ellipsometer. The thin film samples analyzed by absorption spectroscopy are

deposited on glass substrates, which also absorb a portion of the transmitted light. The transmittance of the glass is large over the wavelength range analyzed (τ ~ 91%), except with a transmission cutoff below ~350nm (3.5eV). In calculating the band gap, the change in the optical absorption coefficient, not the absolute magnitude, matters most, as described by Eqn. (4-15). Subsequently, as long as the transmittance of the glass does not vary much over the wavelength of interest, the absorption in the substrate will have negligible impact on the band gap calculation. Substrate effects on absorption are neglected in this work. The ellipsometer measures reflection and transmission only at 0° incidence (in-line). Subsequently, any diffusely reflected light will not be exhibited in the reflectance measurement, and this will contribute to an overestimation of the optical absorption within the sample. The detectors used to measure the intensity amplitude of reflected and transmitted light contain some measurement uncertainties as well.

Calculation of the band gap from the optical absorption curves may include errors due to inaccuracies in the absorption measurements, and fitting errors resulting from non-crystalline films and the choice of fitting range for the linear extrapolation described in the previous section. Since the calculation of band gap depends directly on the optical absorption coefficient, any errors in the value of optical absorption will contribute to errors in the calculated value of band gap. Further, the band gap calculation depends on the linear extrapolation of a linearly-sloped region of the $(\alpha h\nu)^n$ curve near the band edge. In some cases, no well-defined linear region exists, due to the structural disorder within the film, making fitting difficult or impossible. Further, the derivation depends on the parabolic approximation, which is only valid within several 100meV of the band edge. This small region is then extrapolated out several eV. Consequently, the choice of the fitting region may contribute to significant errors in the extrapolated value of the band gap, depending on the characteristic of the $(\alpha h\nu)^n$ curve near the band edge.

4.3.2 Photomodulated Reflectance (PR)

4.3.2.1 Background and Experimental Set-up

Photomodulated Reflectance (PR) spectroscopy represents a non-contacting, non-destructive characterization tool used to measure optical transitions, including the band gap and higher order transitions, of the sample [72]. The technique measures changes in the sample reflectance that result from periodic modulations of the internal electric field by optically injected carriers [63, 72]. A chopped laser incident on the sample injects carriers by photo-exciting electrons into the conduction band; a second broadband lamp, spectrally dispersed by a monochromator, probes the reflectances of the sample at varying wavelengths, measuring the photo-induced changes in these values $\Delta R/R$ using a photodiode [63, 72].

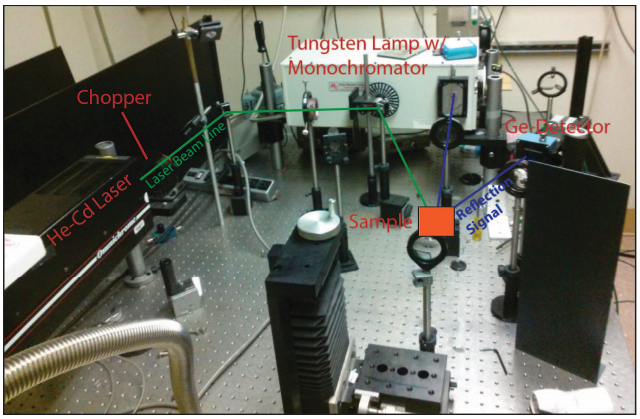

Fig. 4-7. Photomodulated reflectance (PR) spectroscopy experimental set-up

Fig. 4-7 shows the PR spectroscopy experimental set-up. The band gaps of the samples were measured by photomodulated reflectance at room temperature. Radiation from a 300W halogen tungsten lamp dispersed by a 0.5m monochromator was focused on the samples as a probe beam. A chopped HeCd laser beam (λ=442 nm) provided the photomodulation. PR signals were detected by a Ge photodiode using a phase-sensitive lock-in amplification system.

4.3.2.2 Analysis and Modeling

The measured photomodulated reflectance values ΔR/R may be related to the dielectric function ($\varepsilon = \varepsilon_1 + i\varepsilon_2$) of the sample according to the following:

$$\frac{\Delta R}{R} = \alpha(\varepsilon_1, \varepsilon_2)\Delta\varepsilon_1 + \beta(\varepsilon_1, \varepsilon_2)\Delta\varepsilon_2 \tag{4-17}$$

where α and β are the Seraphin coefficients and $\Delta\varepsilon_1$ and $\Delta\varepsilon_2$ are the photo-induced changes in the real and complex parts of the dielectric constant [72].

The dielectric function relates to the band structure of the material, most notably, through the presence of Van Hove singularities that occur at the interband critical points [73]. While the dielectric constants remain finite under all conditions, at these critical points (e.g. interband transitions) the derivatives diverge, yielding sharp peaks that improve the signal to background ratio [63, 73]. Consequently, peaks or oscillations in the PR curves may then be assigned to the band gap and other interband optical transitions of the sample.

4.4 Electronic Properties

4.4.1 Hall Effect

4.4.1.1 Background and Experimental Set-up

The **Hall Effect measurement** represent a contacting, non-destructive characterization technique used to probe the electronic properties of a sample, including carrier concentration and

type, majority carrier mobility and film resistivity [63]. The **Hall Effect** refers to the development of a transverse electric potential on a sample, when the sample conducts current in the presence of a perpendicular magnetic field [74]. This potential develops as a result of the Lorentz force exerted on the carriers (e.g. holes or electrons) by the magnetic field as the carriers move through the conductor [74]. Hall effect measurements were performed at room temperature in the Van de Paaw geometry using an Ecopia HMS-3000 device.

The **Van de Paaw method** of performing four-point probe analysis eliminates the need to construct the contacts in a specific geometry or with exactly known locations [63]. The method relies on the following assumptions: 1) the contacts are located at the periphery of the sample, 2) the contact size is small compared to their spacing, 3) the sample thickness is uniform, and 4) the sample is contiguous [63]. By consecutively measuring across pairs of contacts, the geometry factors associated with the contact placement effectively drop out.

4.4.1.2 Analysis and Modeling

Carrier Concentration and Mobility Calculation

By balancing the magnetic and Hall-field forces, required under steady-state conditions, **the Hall voltage** for **P-type materials** may be written as follows [63]:

$$V_H = \frac{1}{t}\left(\frac{IB}{qp}\right) = \frac{R_{H,hole} IB}{t} \tag{4-18}$$

$$R_{H,hole} = \frac{1}{qp} \tag{4-19}$$

where t is the film thickness, I is the current, B is the magnetic field, q is the carrier charge, p is the density of hole carriers, and $R_{H,hole}$ is the **Hall coefficient** for holes. The Hall voltage and Hall coefficient may be written similarly for **N-type materials,** except $R_{H,electron}$ takes a negative sign [63].

The Hall voltage, current, magnetic field, and film thickness are all measured or known quantities, thereby allowing determination of the Hall coefficient. **Majority carrier densities** may be calculated directly from the Hall coefficients in Eqn.(4-19) and the N-type equivalent, where positive value of R_H indicates that the majority carriers are holes, and a negative value indicates that majority carriers are electrons. Finally, the **Hall mobility**, which provides a measure of the majority carrier mobility and therefore the electronic quality of the material, can be defined as follows [63]:

$$\mu_H = \frac{|R_H|}{\rho} \tag{4-20}$$

where R_H is the Hall coefficient and ρ is the film electrical resistivity measured under zero magnetic flux. Notably, the Hall mobility differs from the conductivity mobility by the Hall scattering factor, r, which is usually close to 1 and previously neglected in the definition of R_H [63]. The film resistivity can be measured under zero magnetic flux using the four-point probe method, described elsewhere [63].

Sources of Error

Hall effect measurements may include errors due to thickness non-uniformities, doping non-uniformities, high film resistance (including non-ohmic contact), poor contact configuration and conducting substrates. As Eqns. (4-18) and (4-19), the Hall coefficients depend on the film thickness, which the analysis nominally considers to be uniform and without holes. Similarly, the derivation assumes a uniform doping concentration, and so films with non-constant doping profiles will not be accurately represented by Eqns. (4-18) – (4-20).

Films with high resistance (>10MΩ), due either to low film conductivity or non-ohmic contact to the measurement system, will carry very low currents (~nA) which are not accurately detected by the equipment, introducing error into the calculated values of the Hall coefficients. Mobilities < 1cm^2/V·sec frequently give unreliable Hall measurements. If the contacts between the film and the measurement system, typically pressed indium, are large compared to the dimensions of the sample, the electric field associated with the metal-semiconductor interface can introduce additional uncertainty in the measurement. To minimize this effect, the contact dimensions should be < 10% the length of their separation. Finally, conducting substrates (or other film layers) introduce additional parallel paths across which the sample current can be carried. Therefore, circuit models must be used to separate the contributions of each layer to the overall Hall measurement.

4.5 REFERENCES

[1] C. Jeynes, N.P. Barradas, E. Szilagyi, Accurate determination of Quantity of Material in thin films by Rutherford backscattering spectrometry, Analytical Chemistry, 84 (2012).

[2] W.-K. Chu, J. Mayer, M. Nicolet, Backscattering Spectrometry, Academic Press, Inc., Boston, 1978.

[3] W.K. Chu, J.W. Mayer, M.A. Nicolet, T.M. Buck, G. Amsel, F. Eisen, Principles and Applications of Ion Beam Techniques for the Analysis of Solids and Thin Films, Thin Solid Films, 17 (1973) 1-41.

[4] M. Mayer, SIMNRA User's Guide, Report IPP 9/113, in, Max-Planck-Institut für, Plasmaphysik, Garching, Germany, 1997.

[5] J.L. Calaux, SIMTarget, in, University of Namur, Belgium, 2013.

[6] R. Scheer, H.-W. Schock, Chalcogenide Photovoltaics: Physics, Technology, and Thin Film Devices, Wiley-VCH, Weinheim, 2011.

[7] A. Khare, B. Himmetoglu, M. Johnson, D. Norris, M. Cococcioni, E. Aydil, Calculation of the lattice dynamics and Raman spectra of copper zinc tin chalcogenids and comparison to experiments, Journal of Applied Physics, 111 (2012) 083707-083701 - 083707-083709.

[8] M. Mayer, Rutherford Backscattering Spectrometry (RBS), in: Workshop on Nuclear Data for Science and Technology: Materials Analysis, Trieste, 2003.

[9] Ion Beam Analysis Nuclear Data Library, in: I.A.E. Agency (Ed.), http://www-nds.iaea.org/ibandl/, 2013.

[10] G. Boudreault, C. Jeynes, E. Wendler, A. Nejim, R.P. Webb, U. Watjen, Accurate RBS measurement of ion implant doses in silicon, Surface and Interface Analysis, 33 (2002) 478-486.

[11] G. Morello, Hydrogen content of amorphous PECVD SiN_x:H films by infrared spectroscopy and hydrogen forward scattering results, Journal of Non-Crystalline Solids, 187 (1995) 308 - 312.

[12] J.A. Abys, S.R. Brankovic, e. al., Modern Electroplating, Fifth ed., John Wiley & Sons, Hoboken, 2010.

[13] S.A.E. Johansson, J.L. Campbell, PIXE: A Novel Technique for Elemental Analysis, John Wiley & Sons, New York, 1988.

[14] S. Johansson, J. Campbell, K. Malmqvist, Particle-Induced X-Ray Emission Spectrometry (PIXE), John Wiley & Sons, New York, 1995.

[15] Sven A.E. Johansson, T.B. Johansson, Analytical Application of Particle Induced X-Ray Emission, Nuclear Instruments and Methods, 137 (1976) 473-516.

[16] PX4 User's Manual, in: Amptek (Ed.) Amptek, http://www.amptek.com, 2013.

[17] A. Thompson, J. Kirz, D. Attwood, E. Gullikson, M. Howells, J. Kortright, Y. Liu, A. Robinson, Center for X-Ray Optics Advance Light Source: X-Ray Data Booklet, in: A. Thompson (Ed.), Lawerence Berkeley National Laboratory, Lawrence Berkeley National Laboratory, 2009.

[18] S. Fazinic, Intercomparison of PIXE spectrometry software packages, in, International Atomic Energy Agency, Vienna, 2003.

[19] C.M. Romo-Kroger, An empirical curve describing the ionization cross-sections in atomic collisions involving heavy ions, Nuclear Instruments and Methods in Physics Research B, 164-165 (2000) 349 - 352.

[20] B.D. Cullity, S.R. Stock, Elements of X-Ray Diffraction, Third ed., Prentice Hall, Upper Saddle River, NJ, 2001.

[21] M. Paunovic, M. Schlesinger, Fundamentals of Electrochemical Deposition, John Wiley & Sons, Hoboken, 2006.

[22] S.B. Zhang, S.H. Wei, Reconstruction and energetics of the polar (112) and (112) versus the nonpolar (220) surfaces of $CuInSe_2$, Physical Review B, 65 (2002) 081402: 081401 - 081404.

[23] J. Alvarez-Garcia, V. Izquierdo-Roca, A. Perez-Rodriguez, Raman Spectroscopy on Thin Films for Solar Cells, in: D. Abou-Ras, T. Kirchartz, U. Rau (Eds.) Advanced Characterization Techniques ofr Thin Film Solar cells, Wiley-VCH Verlag GmbH & Co., Berlin, 2011.

[24] M. Schumm, ZnO-based semiconductors studied by Raman spectroscopy: semimagnetic alloying, doping, and nanostructures, in: Physics and Astronomy, Julius Maximilian University of Würzburg, 2008.

[25] Raman Scattering in Materials Science, Springer, New York, 2000.

[26] Analytical Raman Spectroscopy, John Wiley & Sons, New York, 1991.

[27] G. Lucazeau, Effect of pressure and temperature on Raman spectra of solids: anharmonicity, Journal of Raman Spectroscopy, 34 (2003) 478-496.

[28] P. Vandenabeele, Practical Raman Spectroscopy: An Introduction, John Wiley & Sons, West Sussex, 2013.

[29] Y.M. Shin, D.H. Shin, J.H. Kim, B.T. Ahn, Effect of Na doping using Na_2S on the structure and photovoltaic properties of CIGS solar cells, Current Applied Physics, 11 (2011) S59-S64.

[30] A.J. Cheng, M. Manno, A. Khare, C. Leighton, S.A. Campbell, E.S. Aydil, Imaging and phase identification of Cu_2ZnSnS_4 thin films using confocal Raman spectroscopy, J. Vac. Sci. Technol. A, 29 (2011) 051203-051201 - 051203-051211.

[31] K. Wang, B. Shin, K. Reuter, T. Todorov, D. Mitzi, S. Guha, Structural and elemental characterization of high efficiency Cu_2ZnSnS_4 solar cells, Applied Physics Letters, 98 (2011) 051912-051911 - 051912-051913.

[32] P.A. Fernandes, P.M.P. Salome, A.F.d. Cunha, Growth and Raman scattering characterization of Cu_2ZnSnS_4 thin films, Thin Solid Films, 517 (2009) 2519 - 2523.

[33] M. Altosaar, J. Raudoja, K. Timmo, M. Danilson, M. Grossberg, J. Kurstok, E. Mellikov, $Cu_2Zn_{1-x}Cd_xSn(Se_{1-y}S_y)_4$ solid solutions as absorber materials for solar cells, Physica Status Solidi (a), 205 (2008) 167 - 170.

[34] M. Dimietrievska, A. Fairbrother, X. Fontane, T. Jawhari, V. Izquierdo-Roca, E. Saucedo, A. Perez-Rodriguez, Multiwavelength excitation Raman scattering study of polycrystalline Cu_2ZnSnS_4 thin films, Applied Physics Letters, 104 (2014) 021901-021901 021901-021905.

[35] A.P. Litvinchuk, A. Moller, L. Debbichi, P. Kruger, M.N. Iliev, M.M. Gospodinov, Second-order Raman scattering in CuO, Journal of Physics: Condensed Matter, 25 (2013).

[36] T. Wei, Raman Scattering of Cuprous Oxide (CuO), in: Department of Physics, Simon Fraser University, 1990.

[37] A. Fairbrother, X. Fontane, V. Izquierdo-Roca, M. Espindola-Rodriguez, S. Lopez-Marino, M. Placidi, L. Calvo-Barrio, A. Perez-Rodriguez, E. Saucedo, On the formation mechanisms of Zn-rich Cu_2ZnSnS_4 films prepared by sulfurization of metallic stacks, Solar Energy Materials & Solar Cells, 112 (2013) 97 - 105.

[38] S.-Y. Wang, W. Wang, Z.-H. Lu, Asynchronous-pulse ultrasonic spray pyrolysis deposition of Cu_xS (x=1,2) thin films, Materials Science & Engineering B, 103 (2003) 184 - 188.

[39] H. Solache-Carranco, G. Juarez-Diaz, M. Galvan-Arellano, J. Martinez-Juarez, G. Romero-Paredes, R. Pena-Sierra, Raman Scattering and Photoluminescence Studies on Cu_2O, in: 5th International Conference on Electrical Engineering, Computing Science and Automatic Control, 2008.

[40] P.F. Williams, S.P.S. Porto, Symettry-Forbidden Resonant Raman Scattering in Cu_2O, Physical Review B, 8 (1973) 1782 - 1785.

[41] B. Minceva-Sukarova, M. Najdoski, I. Grozdanov, C.J. Chunnilall, Raman spectra of thin solid films of some metal sulfides, Journal of Molecular Structure, 410 - 411 (1996) 267 - 270.

[42] F.J. Manjon, B. Mari, J. Serrano, A.H. Romero, Silent Raman modes in zinc oxide and related nitrides, Journal of Applied Physics, 97 (2005) 053516-053511 - 053516-053514.

[43] Y.C. Cheng, C.Q. Jin, F. Gao, X.L. Wu, W. Zhong, S.H. Li, P.K. Chu, Raman scattering study of zinc blende and wurtzite ZnS, Journal of Applied Physics, 106 (2009) 123505-123501 - 123505 - 123505.

[44] J. Geurts, S. Rau, W. Richter, F.J. Schmitte, SnO Films and Their Oxidation to SnO_2: Raman Scattering, IR Reflectivity and X-Ray Diffraction Studies, Thin Solid Films, 121 (1984) 217 - 225.

[45] R. Ahmad, M. Distaso, H. Azimi, C. Brabec, W. Peukert, Facile synthesis and post-processing of eco-friendly, highly conductive copper zinc tin sulphide nanoparticles, Journal of Nanoparticle Research, 15 (2013).

[46] V.G. Kravets, Photoluminescence and Raman Spectra of SnO_x Nanostructures Doped with Sm Ions, Optics and Spectroscopy, 103 (2007) 766 - 771.

[47] R.S. Katiyar, P. Dawson, M.M. Hargreave, G.R. Wilkinson, Dynamics of the rutile structure III. Lattice dynamics, infrared and Raman spectra of SnO_2, Journal of Physics C: Solid State Physics, 4 (1971) 2421 - 2431.

[48] J.F. Scott, Raman Spectrum of SnO_2, Journal of Chemical Physics, 53 (1970) 852 - 853.

[49] P.M. Nikolic, L.J. Miljkovic, P. Mihajlovic, B. Lavrencic, Splitting and coupling of lattice modes in the layer compound SnS, Journal of Physics C: Solid State Physics, 10 (1977) L289 - L292.

[50] L.S. Price, I.P. Parkin, A. Hardy, R. Clark, Atmospheric Pressure Chemical Vapor Deposition of Tin Sulfides (SnS, Sn_2S_3, and SnS_2) on Glass, Chemistry of Materials, 11 (1999) 1792 - 1799.

[51] L. Kumari, Y. Ma, C. Tsai, Y. Lin, S. Wu, K. Cheng, Y. Liou, X-ray diffraction and Raman scattering studies on large-area array and nanobranched structure of 1D MoO_2 nanorods, Nanotechnology, 18 (2007) 1-7.

[52] G. Smudde, P. Stair, The oxidation of Mo(100) studied by XPS and surface Raman spectroscopy: the onset of MoO_2 formation and the formation of surface polymolybdate, Surface Science, 317 (1994) 65 - 72.

[53] M. Dieterle, G. Mestl, Raman spectroscopy of molybdenum oxides: Part II. Resonance Raman spectroscopic characterization of the molybdenum oxides Mo_4O_{11} and MoO_2, Phys. Chem. Chem. Phys., 4 (2002) 822 - 826.

[54] D. Berg, R. Djemour, L. Gutay, S. Siebentritt, P. Dale, X. Fontane, V. Izquiero-Roca, A. Perez-Rodriguez, Raman analysis of monoclinic Cu_2SnS_3 thin films, Applied Physics Letters, 100 (2012) 192103-192101 - 192103-192104.

[55] P.A. Fernandes, P.M.P. Salome, A.F.d. Cunha, A study of ternary Cu2SnS3 and Cu3SnS4 thin films prepared by sulfurizing stacked metal precursors, Journal of Physics D: Applied Physics, 43 (2010) 1-11.

[56] H. Guan, H. Shen, C. Gao, X. He, Structural and optical properties of Cu_2SnS_3 and Cu_3SnS_4 thin films by successive ionic layer adsorption and reaction, Journal of Materials Science: Materials in Electronics, 24 (2013) 1490 - 1494.

[57] A.T. Ward, Raman Spectroscopy of Sulfur, Sulfur-Selenium, and Sulfur-Arsenic Mixtures, Journal of Physical Chemistry, 72 (1968).

[58] J.L. Verble, T.J. Wieting, Lattice Mode Degeneracy in MoS_2 and other Layer Compounds, Physical Review Letters, 25 (1970) 362 - 365.

[59] H. Li, Q. Zhang, C. Yap, B. Tay, T. Edwin, A. Olivier, D. Baillargeat, From Bulk to Monolayer MoS_2: Evolution of Raman Scattering, Advanced Functional Materials, 22 (2012) 1385 - 1390.

[60] J.J. Scragg, Studies of Cu_2ZnSnS_4 films prepared by sulfurisation of electrodeposited precursors, in: Chemistry, University of Bath, 2010, pp. 244.

[61] S. Sandoval, D. Yang, R.F. Frindt, J.C. Irwin, Raman study and lattice dynamics of single molecular layers of MoS_2, Physical Review B, 44 (1991) 3955 - 3962.

[62] X. Fontane, L. Calvo-Barrio, V. Izquierdo-Roca, E. Saucedo, A. Perez-Rodriguez, J.R. Morante, D.M. Berg, P.J. Dale, S. Siebentritt, In-depth resolved Raman scattering analysis for the identification of secondary phases: Characterization of Cu_2ZnSnS_4 layers for solar cell applications, Applied Physics Letters, 98 (2011) 181905-181901 181905-181903.

[63] D. Schroder, Semiconductor Material and Device Characterization, Third ed., John Wiley & Sons, Hoboken, 2006.

[64] J. Goldstein, D. Newbury, D. Joy, C. Lyman, P. Echlin, E. Lifshin, L. Sawyer, J. Michael, Scanning Electron Microscopy and X-Ray Microanalysis, Third ed., Springer Science + Business Media, New York, 2003.

[65] J. Essick, R. Mather, Characterization of a bulk semiconductor's band gap via nearabsorption edge optical transmission experiment, American Journal of Physics, 61 (1993) 646 - 649.

[66] J. Nelson, The Physics of Solar Cells, Imperial College Press, London, 2007.

[67] M.S. Dresselhaus, Solid State Physics. Part II: Optical Properties of Solids, in, 2013.

[68] A.M. Elkorashy, Indirect Forbidden Fundamental Absorption Edge in Germanium Selenide Single Crystals, phys. stat. sol. (b), 135 (1986) 707 - 713.

[69] S. John, C. Soukoulis, M. Cohen, E.N. Economou, Theory of Electron Band Tails and the Urbach Optical-Absorption Edge, Physical Review Letters, 57 (1986) 1777 - 1780.

[70] S. Chichibu, T. Mizutani, T. Shioda, H. Nakanishi, T. Deguchi, T. Azuhata, T. Sota, S. Nakamura, Urbach-Martienssen tails in a wurtzite GaN epilayer, Applied Physics Letters, 70 (1997) 3440 - 3442.

[71] T. Shioda, S. Chichibu, T. Irie, H. Nakanishi, T. Kariya, Influence of nonstoichiometry on the Urbach's tails of absorption spectra for CISe single crystals, Journal of Applied Physics, 80 (1996) 1106 - 1111.

[72] J. Misiewicz, G. Sek, R. Kudrawiec, P. Sitarek, Photomodulated reflectance and transmittance: optical characterisation of novel semiconductor materials and device structures, Thin Solid Films, 450 (2004) 14 - 22.

[73] P. Yu, M. Cardona, Fundamentals of Semiconductors: Physics and Materials Properties, Fourth ed., Springer, New York, 2010.

[74] R. Muller, T. Kaims, Device Electronics for Integrated Circuits, Second ed., John Wiley & Sons, New York, 1986.

5 GROWTH BEHAVIOR OF PULSED LASER DEPOSITED CIG(SE,S)

5.1 PURPOSE

Thin film solar cells using CIGSe absorber layers have achieved high efficiencies, both in laboratory cells as well as commercial modules, as detailed in Section 2.2.3 [1, 2]. Although the CIGSe material system has been studied for over two decades and commercial products are available on the market, a complete understanding of the defect, grain and junction physics of CIGSe remains lacking [3]. Further, significant effort has been focused on the development of Cd-free buffer-window layers with better band alignment than CdS for wide gap CIGSe absorbers [1, 4].

Research into the CIGSe material system remains relevant not only for continuing investigation into its fundamental defect and grain properties but also because it serves as a standard against which the next generation CZTS material system can be evaluated. As a less complex and more mature material system, CIGSe represents a useful starting material for thin film research. Pulsed laser deposition (PLD), particularly valuable for multi-component systems like CIGSe and CZTS, represents a laboratory-scale synthesis tool that enables rapid evaluation of material combinations and layer interfaces.

However, existing literature [5-7] shows that PLD of CISe and CIGSe thin films typically yielded materials with high carrier concentration ($>10^{18}$ cm^{-3}) and low hole mobilities (<10 $cm^2/V\text{-}s$) not adequate for use in photovoltaic (PV) device and interface studies. It has been reported that for PV applications, optimum doping concentrations of 10^{15} – $10^{17}cm^{-3}$ and hole mobilities of 20 – $200cm^2/V\text{-}s$ are needed [1, 2]. High hole concentrations have been correlated with large Cu:[In+Ga] ratios (>1) and attributed to acceptor-type Cu_{In} or V_{In} defects, as well as the formation of $Cu_{2-X}Se$ phases on the film surface [5-8].

This chapter explores pulsed laser deposition and annealing of CIGSe thin films with the intent to understand the effects of film composition and defects on the electronic behavior of the material and to achieve device quality films for use as reference standards in studies of CZTS films. Practically, this work was intended to help develop the expertise in thin film fabrication and characterization methods necessary to investigate the more complex CZTS material system. Lessons learned from the development of the Gen #1 sulfur annealing chamber supported the design and fabrication of the Gen #2 chamber critical in the fabrication of CZTS.

5.2 BACKGROUND

This section provides a brief review of the existing literature on pulsed laser deposition of thin film CISe and CIGSe [19-36]. Most of the reported works utilized excimer lasers for PLD: ArF (193nm), KrF (248nm), or XeCl (308nm). As indicated in Chapter 3, the use of ultraviolet-wavelength lasers mitigates the generation of splashed particles. Further, most literature reported the use of stoichiometric $Cu(In,Ga)Se_2$ sputtering targets, usually single-crystalline or poly-crystalline; the targets were prepared by Bridgman-growth or pressing-sintering methods. Table 5-1 shows typical deposition parameters demonstrated in the literature, and Table 5-2 shows reported effects of the deposition parameters on the properties of CISe and CIGSe films.

Pulsed laser deposition studies of CISe and CIGSe thin films in literature have focused on characterizing their growth behavior and fundamental properties, including doping, alloying, and opto-electronic properties. Notably, this author found no reported device efficiencies for solar cells using pulsed laser deposited CISe or CIGSe absorber layers.

Table 5-1. Typical deposition parameters for CISe and CIGSe (literature results)

Deposition Parameter	Value	Reference
Background Pressure	Vacuum: $< 10^{-5}$ torr	[5-7, 9-11]
Laser Energy (Fluence)	10 – 300mJ/pulse 2 – 5 J/cm^2	[6, 7, 9-15]
Laser Pulse Frequency	5 – 20Hz	[5-7, 9, 12, 13]
Substrate-Target Distance	3 – 6cm	[5, 6, 9-15]

As-deposited films tended to be slightly Cu-rich, slightly In/Ga-poor, and moderately Se-poor relative to the target compositions [5, 7, 9, 12], which Jo attributes to the higher vapor pressures of In, Ga, and Se [5]. While increasing substrate temperature did not significantly alter this compositional trend [5, 9, 12], increasing the background pressure using Argon gas was shown to mitigate Se-loss in the films [14]. These target-film composition trends were evident in depositions performed with excimer lasers and pressed and/or sintered polycrystalline targets; works reporting the use of Nd:Yag lasers and single-crystal targets did not provide compositional data of the target.

Strong (112) texturing developed in as-deposited, and also post-annealed, films on amorphous glass substrates [9]. Polycrystalline CIGSe films frequently exhibit strong (112) texturing, owing to the relatively low surface energy of this polar face, particularly under Cu-poor conditions [16, 17]. Epitaxial orientation of CISe and CIGSe on single-crystal substrates was demonstrated by Lowndes and Levoska, respectively [9, 18].

Increasing substrate temperature has been shown to increase film crystallinity [9, 12, 14], although additional annealing at the same temperature did not further improve crystallinity [12]. At least one study, however, indicated little change in grain size with substrate temperature [5]. Kuranouchi demonstrated slight increases in Cu-richness [12], and Jo showed an apparent increase in the size and density of macro-particulates on the surface, with increasing substrate deposition temperature [5, 6]. Jo attributed this increase in surface particulates to enhancement of thermally-activated aggregation processes, which transport and combine smaller surface particulates [5].

Increasing the laser energy above 300mJ has been shown to yield Cu-rich films with evidence of secondary elemental Cu and $Cu_{2-X}Se$ phases in the x-ray diffractograms of films studied in [6]. While these peaks were well-defined at the higher laser energies, peak shoulders evident in the x-ray diffractograms of lower laser energy depositions may also imply the presence of these secondary phases, contrary to the interpretation in [6]. Further, preferential evaporation of elements with higher vapor pressures (e.g. In and Se) was attributed to heating of the target at higher laser energies [6], implying classical thermal evaporation processes were active. This preferential evaporation was proposed to cause "selective extraction" of the In and Se, leaving the plumes Cu-rich [6]. Likely, however, these secondary phase peaks sharpen at higher laser energies due to increased crystallization or greater forward-peaking of the lighter Cu element. Film compositions at the varying laser energies were not provided, and so this explanation cannot be confirmed. The influence of laser energy (fluence) on the surface morphology of as-deposited films was not discussed in any of the reviewed literature. However, SEM images presented in [6] for laser energies of 200 and 350mJ indicate negligible impact of laser energy on the size and density of macro-particulates on the surface.

X-ray diffraction studies have indicated peak sharpening of the primary (112) CIGSe peaks with increasing pulse repetition rate, which the author attributed to either an increase of the film thickness associated with the increasing repetition rate or increasing crystallite size [6]. Decreasing the target-substrate distance was shown to have a negligible impact on the film stoichiometry [15]; the author provided no explanation, but this result likely indicates that the densities of atomic components do not vary strongly across the plume. Yoshida also reported that the density of splashed particulates and the grain size both increased with decreasing target-substrate distance [15].

Table 5-2. Process control variables and effects: CISe and CIGSe (literature results)

Process Parameter	Variation	Film Effect	Rationale
Target Stoichiometry	--	Cu-rich, slightly In/Ga-poor, and slightly to moderately Se-poor (relative to target)	Re-evaporation losses higher for In, Ga, and Se due to higher vapor pressures
Background Gas Pressure	Increasing	(1) Decreases deposition rate (2) Reduces Se-loss from film	(1) Increases # collisions and diffuses plume (e.g. less forward-peaking) (2) Over pressure reduces re-evaporation from the deposited film
Substrate	--	(1) Significant (112) texturing on most substrates (2) Epitaxial growth on single-c substrates at elevated substrate temp	(1) Surface (112) most stable, low-energy (2) Higher temperatures increase surface adatom diffusion
Substrate Temperature	Increasing	(1) Increases film crystallinity (2) Increases size and density of macro-particulates on surface	(1) Increases adatom surface diffusion (2) Enhanced thermally-activated aggregation processes on surface
Laser Energy (Fluence)	Increasing	Increases dep rate, eventually saturating	Higher laser energies eject more material, until plume begins to absorb incident laser energy
Laser Pulse Frequency	Increasing	Sharpens diffraction peaks	Increasing film thickness or increasing grain size reduces FWHM
Substrate-Target Distance	Decreasing	(1) Does not affect film stoichiometry (2) Increases size and density of deposited macro-particulates (3) Increases film crystallinity	(1) Likely uniform atomic densities across the plume (2) Greater solid angle of plume sampled, yielding increased density of lower-velocity macro-particulates (3) Decreases # collisions prior to deposition, thus increases KE of deposition species

Electronic properties of PLD CISe and CIGSe films are not frequently reported; this may be due to poor electronic quality of the films. Resistivity values are reported in some cases [10, 11, 19, 20], but these values alone do not give information about the electronic quality of the films. Shafarman reports that quality CIGSe layers have hole concentrations of ~ 10^{17}cm^{-3} and hole mobilities of ~ 200cm^2/V-s, yielding resitivities of ~ 0.5ohm-cm [1]. However, a film with a hole concentration of 10^{19} cm^{-3} and a hole mobility 2cm^2/V-s will yield a similar resistivity value of 0.5ohm-cm, despite having significantly worse electronic quality. Almost universally, works that reported Hall effect measurements of pulsed laser deposited CISe and CIGSe thin films demonstrated high carrier concentrations (≥10^{18}cm^{-3}) and low hole mobilities (≤5cm^2/V-s) [6, 7,

15], particularly at deposition temperatures above 200°C [6, 7]. Deposited films were typically Cu-rich and thus likely contained secondary $Cu_{2-X}Se$ phases, as discussed in Section 2.2.1.1.

Nearly all reported works on PLD CISe and CIGSe used stoichiometric targets [5, 6, 9-12, 15, 18-22], and studies have shown that films tend to be Cu-rich relative to the target [5, 7, 9, 12]. This fact suggests most reported films are Cu-rich. Since Cu-rich films have a strong tendency to form $Cu_{2-X}Se$ phases [2, 23], and large hole concentrations have been attributed to the formation of these phases [6, 24], the generally poor electronic quality of pulsed laser deposited films may possibly be attributed to the near-universal choice of stoichiometric targets. The use of a Cu-poor target may improve the electronic quality of the deposited films by suppressing the growth of $Cu_{2-X}Se$ phases; notably, the best performing CIGSe devices contain overall Cu-poor films [2]. However, growing films in a Cu-poor stoichiometry may limit their overall grain sizes, as deposition under Cu-rich conditions has been shown to significantly improve grain size in CIGSe films through liquid-epitaxy type growth mechanisms associated with the $Cu_{2-X}Se$ phases [2]. Co-evaporation has the inherent advantage of modulating individual element effusion rates, thereby allowing films to be grown Cu-rich for a period of time, in order to enhance grain size, and then finished Cu-poor for a period of time, in order to optimize electronic quality [1]. A single-step pulsed laser deposition process does not allow this composition optimization; a multi-step PLD deposition may facilitate modulation of the composition but also limits the utility of the approach.

5.3 EXPERIMENTAL DETAILS

Single layer films of CIGSe, 100 – 130nm thickness, were deposited onto soda lime glass substrates by PLD from the CIGSe-1 ($Cu_{1.00}In_{0.75}Ga_{0.25}Se_{2.00}$) sputtering target, as specified in Table 3-1. Using the EETD PLD system described in Section 3.1.3.1, films were deposited in vacuum (~$5x10^{-5}$ torr) with a fixed laser energy ~110mJ and repetition rate of 7Hz. The substrate temperature was varied between room temperature and 450°C and allowed to cool passively back to room temperature after deposition. Vacuum annealing was performed for 2hr at temperatures of 300 – 500°C, as described in Section 3.3.3.1. Sulfur annealing was performed for 1hr at temperatures of 300 – 500°C, using the Generation #1 annealing system, as described in Section 3.3.3.3. Films used for the vacuum and sulfur annealing studies were initially deposited at 450°C.

Film compositions and thicknesses were characterized using Rutherford backscattering (RBS) analysis, crystal structures were analyzed by x-ray diffraction (XRD) and Raman backscattering spectroscopy, electronic properties were evaluated by Hall effect in the Van de Paaw geometry, morphologies were assessed using scanning electron microscopy (SEM), and band gaps were determined using photomodulated reflectance spectroscopy, as detailed in Chapter 4. Film compositions were modeled using SIMNRA 6.06 [25] and fitted to the raw RBS

data. Measurement uncertainty was estimated according to the range of visually acceptable fits, and subsequently, uncertainty values vary according to signal. See Section 4.1 for further details.

5.4 RESULTS AND DISCUSSION

The effects of substrate temperature (ST), vacuum annealing (VA), and sulfur annealing (SA) on the film composition, structure and opto-electronic properties are investigated in the following sections. Note that all films measured P-type conductivity in this study.

5.4.1 Effects of Substrate Temperature

Using the CIGSe-1 sputtering target and the laser parameters detailed in Section 5.3, films were grown with substrate temperatures varied between room temperature and 450°C. The deposition rate decreased slightly with substrate heating, but all film thicknesses remained near ~100nm.

The CIGSe-1 target composition was chosen with stoichiometric element ratios and the optimum In/Ga-alloying ratio of Ga:[In+Ga] = 0.25 [1-3]. The compositions of the as-deposited ST films, and the associated carrier concentration and transport properties, are summarized in Table 5-3.

Table 5-3 Composition and electronic properties of films in substrate temperature (ST) study

Substrate Temperature	Atomic %				Hole Density (cm^{-3})	Hall Mobility ($cm^2/V{\cdot}s$)
	Cu	In	Ga	Se		
RT	26.0	17.8	6.90	49.2	$3x10^{20}$	1.2
250°C	26.0	17.7	7.00	48.5	$8x10^{19}$	1.1
350°C	25.9	18.2	7.00	49.4	$8x10^{19}$	0.2
450°C	26.0	17.4	7.30	47.6	$7x10^{19}$	1.2

The relevant element ratios are summarized below in Fig. 5-1 (dashed line indicates stoichiometric ratios). The as-deposited ST films are Cu-rich and Se-deficient, with the deviation from stoichiometry showing no strong correlation with deposition temperature. The increase in Cu:[In+Ga] and the decrease in Se:metals relative to the target composition are consistent with the literature [5, 7, 9, 12]. In general, lighter elements exhibit slightly greater forward-peaking in the plume, as detailed in Section 3.1.2.2, and this may account for the relative increase in Cu in the films compared to the sputtering target. Further, Se has a higher vapor pressure and lower sticking coefficient than the metal elements, and Se typically requires evaporation in excess to maintain stoichiometry and mitigate $(In,Ga)_2Se$ re-evaporation losses, as detailed in Section 2.2.2.1. The Se-deficiency can therefore be attributed to the lack of Se excess in the plume, which

may also contribute to the increase in relative Cu concentration by increasing In and Ga re-evaporation losses.

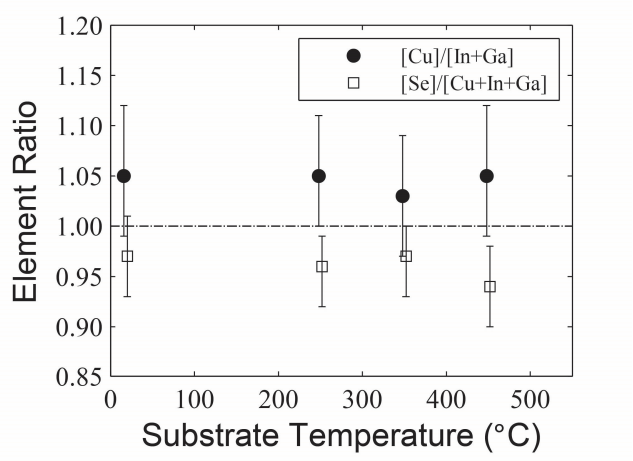

Fig. 5-1. Element composition ratios for ST films

Fig. 5-2 shows x-ray diffractograms for each of the as-deposited ST films. All ST films indicate chalcopyrite structure with strongly-preferred (112)-orientation. No other peaks or phases are evident in the XRD scans, although Raman spectroscopy confirms the presence of a small amount of $Cu_{2-X}Se$ phases in the films deposited at 450°C, as shown in Fig. 5-3 and Fig. 5-7. Raman measurements were not performed on the other ST films. As others in literature have noted, CuSe and Cu_2Se have diffraction peaks at 26.6–26.7° (JCPDS 89-7391 and 88-2044) that may be masked by the $CuIn_{0.7}Ga_{0.30}Se_2$ (112) peak near 26.9° (JCPDS 35-1102).

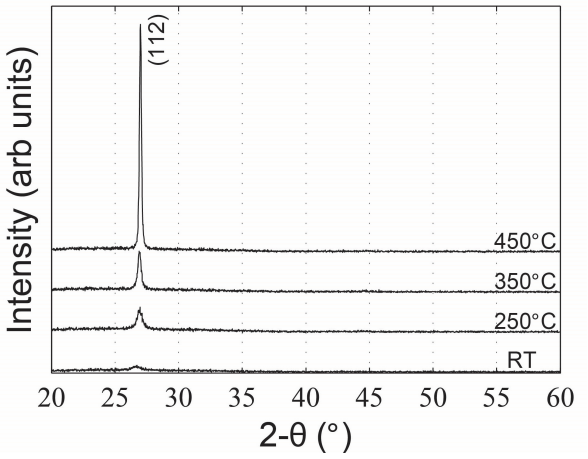

Fig. 5-2. X-ray diffractograms for as-deposited ST films

As expected, grain size increases significantly with increasing deposition temperature, evident as a decreasing (112) diffraction peak width. Grain sizes were estimated using the Debye-Scherrer equation (4-7), ignoring other broadening effects. As the substrate deposition temperature increases from room temperature to 450°C, grain sizes increase from approximately

50nm to 250nm, respectively. The calculated values agreed well with visually estimated grain size estimates from SEM images (not shown).

Hole carrier concentrations do not change significantly with substrate deposition temperature, as Table 5-1 shows, remaining greater than 10^{19} cm^{-3} for all as-deposited ST films. The high carrier concentrations are attributed to the Cu-rich film stoichiometries, which may contribute large hole concentrations through Cu_{In} antisite substitutions [8] or high conductivity $Cu_{2-X}Se$ phases [6, 24], as discussed further in Section 5.4.3. Hole mobilities also show no strong correlation with substrate deposition temperatures, remaining less than 1.2 $cm^2/V{\cdot}s$ for all as-deposited ST films. Grain sizes of the films increased with increasing substrate temperature, but hole mobilities did not increase. This stagnation of mobility with increasing grain size suggests that scattering by defects or possibly secondary phases, and not scattering by grain boundaries, primarily limits the mobility in as-deposited films. Selenium vacancies and $Cu_{2-X}Se$ likely contribute to this detrimental scattering behavior.

5.4.2 Effects of Vacuum Annealing

Using films deposited at 450°C (as in Section 5.4.1), vacuum annealing was performed for 2hr at 300 to 500°C, as detailed in Section 5.3. As-deposited samples used for this section were slightly thicker (~130nm) than similar depositions in Section 5.4.1, attributed to laser energy instabilities in the deposition system. The film thickness exhibits minimal change with vacuum annealing, indicating negligible evaporation losses.

Table 5-4. Composition and electronic properties of films in vacuum annealing (VA) study

Anneal Temperature	Atomic %				Hole Density (cm^{-3})	Hall Mobility ($cm^2/V{\cdot}s$)
	Cu	In	Ga	Se		
No Anneal	26.6	17.8	8.10	47.5	$2x10^{20}$	1.1
300°C	26.5	17.2	7.10	47.4	$2x10^{20}$	0.7
400°C	27.1	17.6	7.00	48.5	$2x10^{20}$	0.7
500°C	28.8	17.5	6.60	47.4	$2x10^{20}$	0.5

The compositions of the VA films, and the associated carrier concentration and transport properties, are summarized in Table 5-4. The Cu concentration monotonically increases and the Ga concentration monotonically decreases with increasing annealing temperature, evident as increasing Cu:[In+Ga] and decreasing Ga:[In+Ga] ratios, respectively. The relative increase in Cu can only be accomplished through the loss of other elements, and this loss of In and Ga is attributed to the re-evaporation of volatile $(In,Ga)_2Se$ phases as detailed in the previous section.

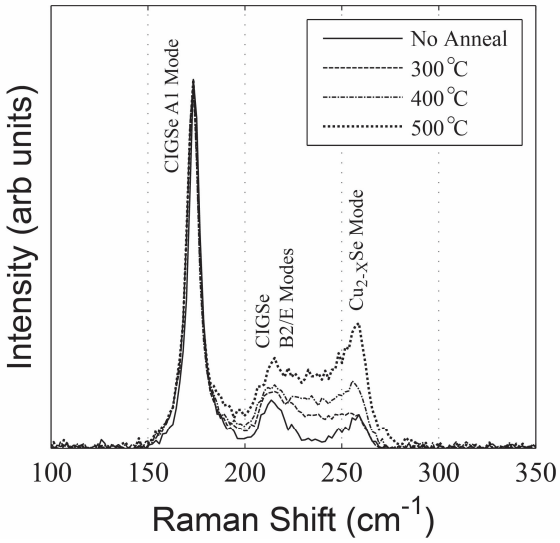

Fig. 5-3. Raman spectra for VA films

For all VA films, x-ray diffractograms (not shown) indicate only the presence of chalcopyrite (112) peaks associated with CIGSe. Raman spectroscopy was used to detect secondary $Cu_{2-X}Se$ phases that may impact the electronic properties of the films but that may not be identifiable by x-ray diffraction, as previously discussed. Fig. 5-3 shows the Raman spectra taken for VA films using single-spot measurements. Spectra are normalized to the primary mode peak intensity.

Raman spectra for all films exhibit the characteristic A1 chalcopyrite mode (~175cm^{-1}) and secondary B2/E (214 and 226cm^{-1}) modes associated with CIGSe [26]. The Raman spectrum for the as-deposited film also shows a well-defined peak at 260cm^{-1} (with weaker shoulder near 240cm^{-1}) attributed to $Cu_{2-x}Se$ [2]. This peak grows monotonically with increasing anneal temperature, consistent with the increasing Cu:[In+Ga] ratios exhibited in the films.

After vacuum annealing, films remain highly conductive with hole concentrations of $10^{20}cm^{-3}$, which do not shown any variation with anneal temperature. Hall mobilities, on the other hand, show a small monotonic decrease from 1.1 to 0.5$cm^2/V{\cdot}s$ as the anneal temperature increases to 500°C. The Se:metals ratio increases and then decreases with anneal temperature, which is attributed either to variations of Se-content in the as-deposited films or to deviations associated with $(In,Ga)_2Se$ loss. Notably, the concentration of $Cu_{2-x}Se$ phases in the film increases monotonically with increasing anneal temperature. These trends suggest that $Cu_{2-X}Se$ plays a more significant role than Se-deficiencies in the poor mobilities demonstrated in these films.

5.4.3 Effects of Sulfur Annealing

Using films deposited at 450°C (as in Section 5.4.1), sulfur annealing was performed for 1hr at 300 to 500°C, as detailed in Section 5.3. As-deposited samples used for this section were

similar thickness (~130nm) to those used in the VA studies. The film thickness exhibits minimal change with sulfur annealing, indicating negligible evaporation losses. The compositions of the SA films, and the associated carrier concentration and transport properties, are summarized in Table 5-5.

Table 5-5. Composition and electronic properties of films in sulfur annealing (SA) study

Annealing Temperature	Atomic %					Hole Density (cm^{-3})	Hall Mobility (cm^2/V-s)
	Cu	In	Ga	Se[a]	S[a]		
No Anneal	26.2	17.1	6.90	47.1	-	$2x10^{20}$	1.1
300°C	26.2	17.1	6.80	44.0	4.30	$7x10^{16}$	16.6
400°C	25.0	17.0	6.90	36.0	8.50	$5x10^{16}$	19.3
500°C	25.7	17.1	6.70	35.5	14.0	$1x10^{17}$	8.5

[a] Sulfurization yields films with graded chalcogen profiles; Se and S values shown correspond to model surface-most layer

Annealing in elemental sulfur environment dramatically modifies the material properties. First, we notice that SA yielded graded composition films with the maximum sulfur concentrations located at the film surfaces. Fig. 5-4a shows the sulfur concentration profiles through the films in which the relatively large error bars arise from the weak sulfur signals in RBS measurements (due to low elemental concentrations and the low atomic number of S). The surface concentration of sulfur increased with increasing annealing temperature, consistent with increasing sulfur gas pressures. Notice that the sulfur distributions are in good agreement with the complementary error function fit of the data (solid lines).

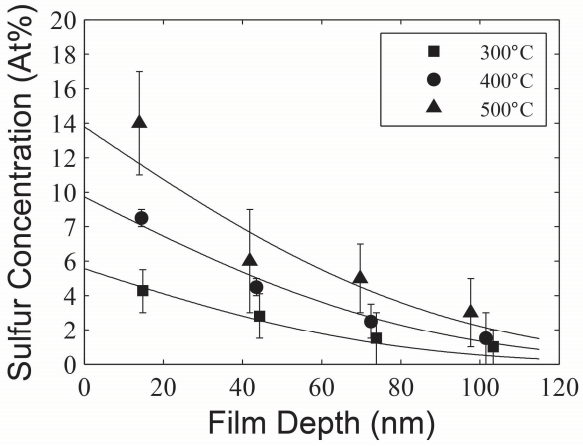

Fig. 5-4. Elemental sulfur concentrations in SA films (solid lines represent erfc fits of the indicated data)

The relevant element ratios are summarized below in Fig. 5-5 (dashed line indicates stoichiometric ratios). Fig. 5-5 indicates that the overall chalcogen concentration [S+Se]:metals increases after sulfur annealing, as expected. Within the measurement uncertainty, the total

chalcogen concentration remains approximately constant through the thickness, suggesting that S likely occupies the films as Se-sublattice substitutions instead of as interstitials. However, the increase in total chalcogen content after sulfur annealing indicates that incorporated sulfur must also occupy some selenium vacancies. A filling of Se vacancies by S would enlarge the unit cell size and decrease the band gap, while substitutions of Se by S would shrink the unit cell size and increase the band gap.

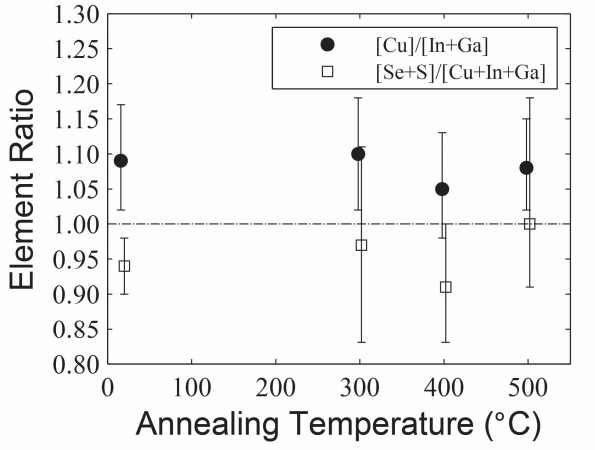

Fig. 5-5. Element composition ratios for SA films

The sulfur incorporation mechanism remains unclear, however, as photomodulated reflectance (PR) measurements shown in Fig. 5-6 indicate negligible effect of sulfur annealing on the band gap (at ~1.17 eV) of the material. However, we point out that the regions of significant sulfur incorporation remain limited to small surface layers (< 40nm), likely resulting in the mitigated effect on the band gap measured by PR. The measured band gap of 1.17eV is in excellent agreement with the predicted band gap for Ga:[In+Ga] ~ 0.28 in literature [1].

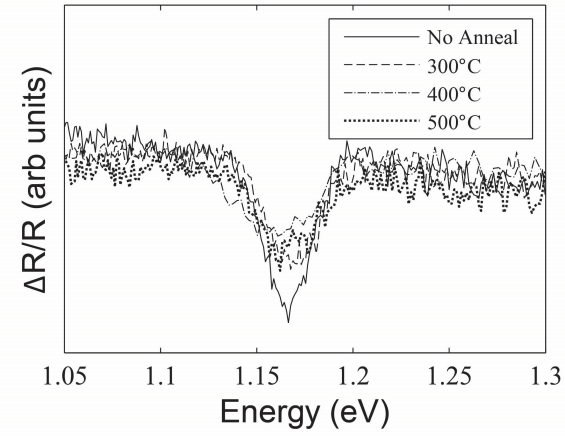

Fig. 5-6. PR measurements for SA films

For all SA films, x-ray diffractograms (not shown) indicate only the presence of chalcopyrite (112) peaks associated with CIGSe. As for VA films, Raman spectroscopy was used for SA films to detect secondary $Cu_{2-X}Se$ phases that may not be identifiable by x-ray diffraction. Fig. 5-7 shows the Raman spectra for sulfur annealed films, averaged for 360 data points taken over a film surface area of 75x25μm and normalized to the primary mode peak intensity.

Raman spectra for all films exhibit the characteristic A1 chalcopyrite mode (~175cm^{-1}), as well as secondary B2/E (214 and 226cm^{-1}) modes, associated with CIGSe [26]. The Raman spectrum for the as-deposited film also shows a well-defined peak at 260cm^{-1} attributed to $Cu_{2-x}Se$. This is consistent with previous reports that showed the presence of $Cu_{2-x}Se$ phases in Cu-rich CIGSe films synthesized by PLD [5, 7, 27]. The 300°C SA film demonstrates a small red (right) shift of the $Cu_{2-x}Se$ peak (266cm^{-1}) and the appearance of a well-defined $Cu_{2-x}S$ (460cm^{-1}) peak [28]. As the sulfur anneal temperature increases to 500°C, the $Cu_{2-x}Se$ peak decreases and further red shifts, while the $Cu_{2-x}S$ peak dramatically decreases and then disappears, as shown in Fig. 5-7b and c. Notably, at 500°C a small $Cu_{2-x}Se$ peak remains, but at 400°C the $Cu_{2-x}Se$ peak disappears completely. Further, a characteristic A1 mode for $CuInS_2$ peak (293cm^{-1}) appears at 500°C [29].

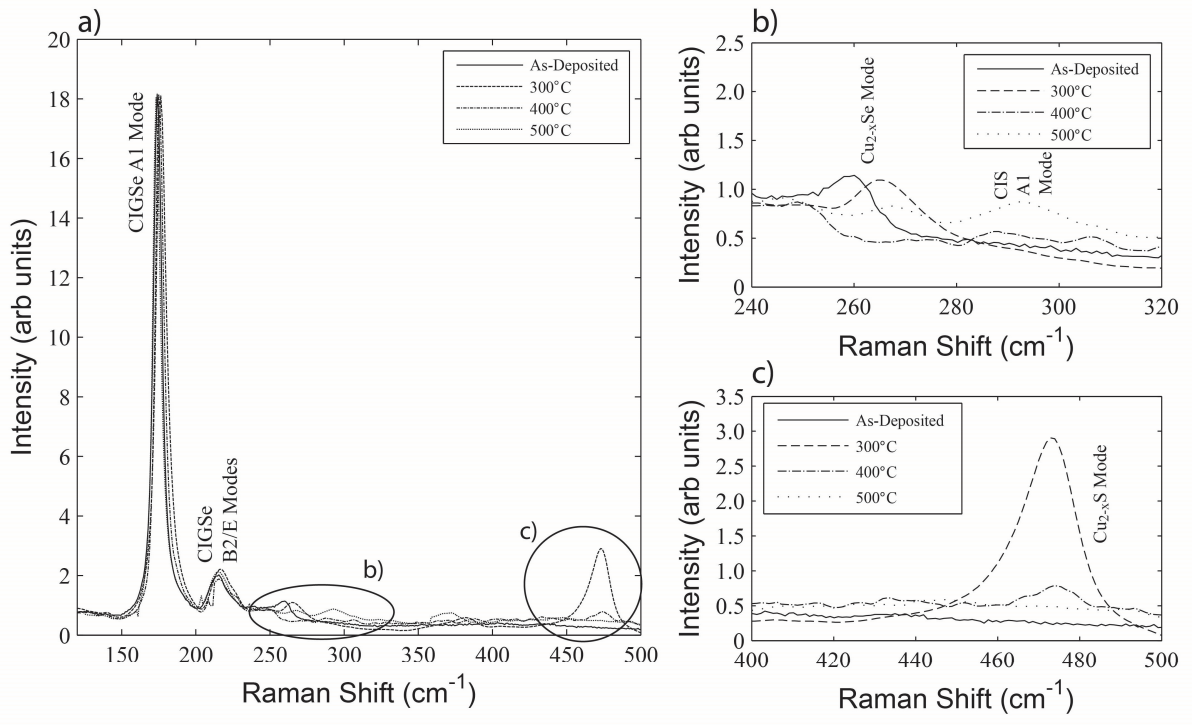

Fig. 5-7. Raman spectra for SA films

In contrast to vacuum annealing, sulfur annealing yields a dramatic reduction in film conductivity. Fig. 5-8 summarizes the electronic properties of the SA samples. Hole

concentrations decreased by more than three orders of magnitude, and mobilities increased by at least one order of magnitude, for all sulfur annealed samples.

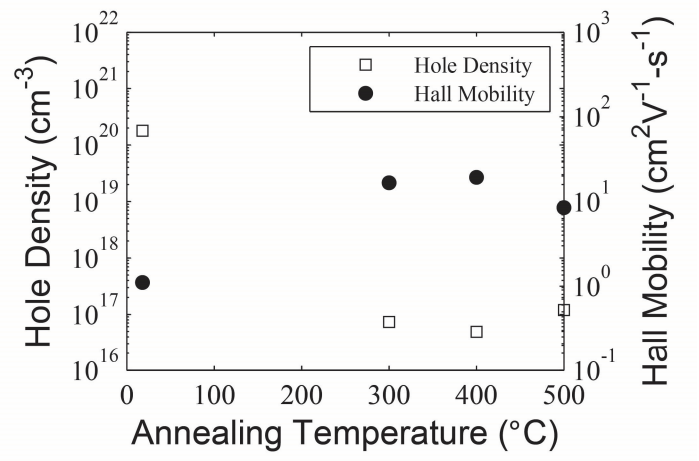

Fig. 5-8. P-Type carrier concentrations and Hall mobilities for SA films

A decrease in carrier concentration with sulfurization of CIGSe films has been attributed to an increase in the ionization energies of the acceptor levels associated with the Se-sublattice substitution by S [30]. However, in our case the SA films indicated no substantial widening of the band gap and hole concentrations do not show a dependence on the amount of sulfur incorporated in the films; subsequently, shifting ionization energies do not appear to properly account for the decreases in hole concentrations.

Notably, the highest electronic quality film (e.g. minimum hole concentration and maximum mobility) corresponds to the least Cu-rich composition with the smallest $Cu_{2-X}Se$ Raman peak. The concentration of $Cu_{2-X}S$ phases decreases with increasing anneal temperature, as evidenced by decreasing Raman peak intensity, but these variations does not appear to influence the electronic behavior.

It has been reported that $Cu_{2-x}Se$ and $Cu_{2-x}S$ phases tend to precipitate on film surfaces during the growth of copper-rich CIG(Se,S) thin films, and KCN has been used to selectively etch and remove these unwanted phases [2]. To investigate the possibility that $Cu_{2-x}Se$ phases were contributing the excessive carrier concentrations and low mobilities, an as-deposited film was etched in 1.5M KCN for 3 minutes. Raman spectra in Fig. 5-9 confirm the removal of the $Cu_{2-x}Se$ phases by KCN etching. Fig. 5-10 shows SEM images for the as-deposited and KCN-etched films.

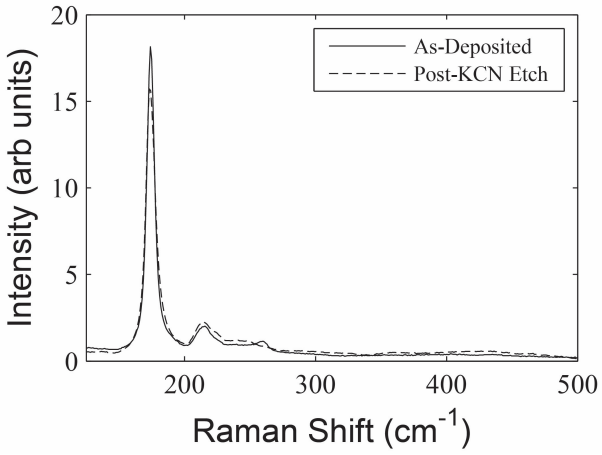

Fig. 5-9. Raman spectra for as-deposited and KCN-etched CIGSe films

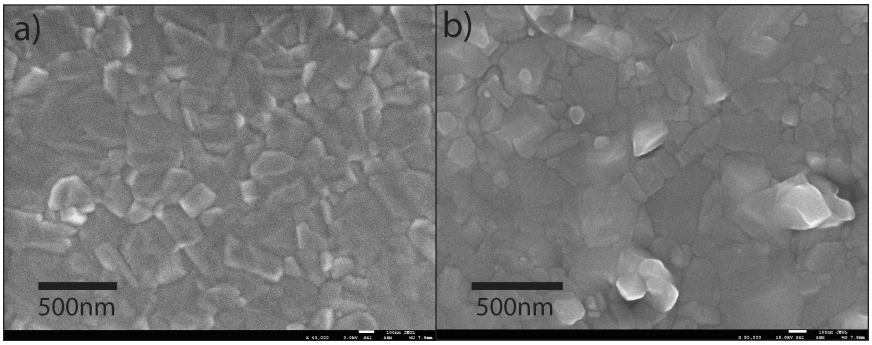

Fig. 5-10. SEM images of a) as-deposited CIGSe film, b) KCN-etched CIGSe film

After etching, the film conductivity decreased dramatically, such that Hall effect measurements were not possible. This suggests that the $Cu_{2-x}Se$ phases are mainly on the surface and also decorating the CIGSe grains, such that their removal by etching disrupts the lateral transport and makes the Hall measurement inconclusive. In summary:

- **Increasing vacuum annealing temperature**: increased the relative Cu and Se concentrations, monotonically increased the concentration of $Cu_{2-X}Se$ phases, and monotonically decreased the mobilities by small amounts. Hole concentrations remained very high.

- **Increasing the sulfur annealing temperature**: increased the amount of sulfur incorporated into the films, monotonically decreased the concentration of $Cu_{2-X}S$ phases, and decreased the concentration of $Cu_{2-X}Se$ phases (minimum at 400°C). Hole mobilities increased substantially and hole concentration decreased substantially for all sulfur annealed samples, and both values appear to correlate to some extent with the presence of $Cu_{2-X}Se$ phases but not the presence of $Cu_{2-X}S$ phases. Notably, however, the as-deposited

and the 300°C sample both had similar $Cu_{2-X}Se$ peak magnitudes but exhibited significantly different hole concentrations and mobilities.

- **KCN etching** of the as-deposited samples: removed $Cu_{2-X}Se$ phases from the film and decreased the film conductivity to the extent that it was not measurable by Hall effect.

Both $Cu_{2-X}Se$ and $Cu_{2-X}S$ phases exhibit low resistivities (< 1Ω·cm) and high carrier concentrations (10^{19} – $10^{20}cm^{-3}$), depending on their stoichiometric deviations [31]. The presence of these phases in similar quantities in films with very high hole concentrations, as well as films with the desired hole concentrations, indicates that these phases are not predominately responsible for the changes in hole concentration behavior observed. In the vacuum annealed and sulfur annealed films, small changes in the mobilities were observed to correspond with the concentration of $Cu_{2-X}Se$ phases. The dramatic drop in film conductivity with KCN etching likely indicates that $Cu_{2-X}Se$ phases decorate the grain boundaries, such that their removal by etching disrupts the lateral transport between grains, particularly in the very thin films (~100nm) investigated here. We conclude, then, that the $Cu_{2-X}Se$ phases form on the grain boundaries in small quantities and mildly degrade the mobility of the films. These phases are not, however, responsible for the overall very high hole concentrations and low mobilities observed in the as-deposited and vacuum annealed films.

The orders of magnitude of the shifts for hole concentration and hole mobilities remain independent of both the amount of sulfur incorporation and the amount of secondary phases, indicating that the incorporation of sulfur, in any amount, improves the electronic properties of the film. Thermal annealing of CIGSe absorbers in sulfur environment has been shown to quench electrically active deep level defects [2, 32], although the defect involved and the nature of the passivation have not been definitively identified. The order of magnitude increase in mobilities with sulfur annealing is consistent with the view of deep level defect passivation by the S atoms. While it is noted that sulfur-containing CISeS alloys have demonstrated low hole concentrations, it is expected that these decreases would be accompanied by shifts in the band gap, which we do not observe. In the sulfur annealed films, the coincidental reduction of hole concentration and increase of mobility with incorporation of sulfur suggests, however, that the defect being passivated also might be associated with the high acceptor concentrations.

5.5 SUMMARY OF RESULTS

We have investigated the structural and electrical properties of thin chalcopyrite-phase CIGSe films synthesized by pulsed laser deposition and annealed under varying conditions. As-deposited films demonstrated Cu-rich, Se-deficient composition with high hole carrier concentrations and low hall mobilities. Increasing the substrate temperature, either during

deposition or through vacuum annealing, increased the grain size but had negligible effect on the electronic performance of the films. This decoupling of grain size and electronic performance suggests that scattering by defects or secondary phases, not grain boundaries, dominate the electronic quality of these films. The incorporation of sulfur into the films, even in small quantities, substantially decreases carrier concentration and increases hall mobility. This is mainly attributed to a reduction in stoichiometry-related defects, defect passivation, and improved film connectivity associated with sulfur incorporation.

The results of this study indicate that sulfur annealing represents a feasible processing route for improving the electronic quality of pulsed laser deposited CIGSe thin films for use in photovoltaic device studies. After sulfurization, films demonstrate hole carrier concentrations and Hall hole mobilities within the range of values typically associated with device-quality films.

5.6 REFERENCES

[1] W. Shafarman, S. Siebentritt, L. Stolt, Cu(InGa)Se_2 Solar Cells, in: A. Luque, S. Hegedus (Eds.) Handbook of Photovoltaics Science and Engineering, John Wiley & Sons, West Sussex, 2011.

[2] R. Scheer, H.-W. Schock, Chalcogenide Photovoltaics: Physics, Technology, and Thin Film Devices, Wiley-VCH, Weinheim, 2011.

[3] P. Jackson, D. Hariskos, E. Lotter, S. Paetel, R. Wuerz, R. Menner, W. Wischmann, M. Powalla, New world record efficiency for Cu(In,Ga)Se_2 thin-film solar cells beyond 20%, Progress in Photovoltaics: Research & Applications, 19 (2011) 894 - 897.

[4] C. Lee, L. Larina, Y. Shin, E. Al-Ammar, B. Ahn, Design of energy band alignment at the $Zn_{1-x}Mg_xO$/Cu(In,Ga)Se_2 interface for Cd-free Cu(In,Ga)Se_2 solar cells, Phys. Chem. Chem. Phys., 14 (2012) 4789–4795.

[5] Y.H. Jo, B.C. Mohanty, Y.S. Cho, Crystallization and surface segregation in $CuIn_{0.7}Ga_{0.3}Se_2$ thin films on Cu foils grown by pulsed laser deposition, Applied Surface Science, 256 (2010) 6819-6823.

[6] Y.H. Jo, B.C. Mohanty, Y.S. Cho, Enhanced electrical properties of pulsed laser-deposited $CuIn_{0.7}Ga_{0.3}Se_2$ thin films via processing control, Solar Energy, 84 (2010) 2213-2218.

[7] D.H. Yeon, B.C. Mohanty, Y.H. Jo, Y.S. Cho, Preparation and electrical properties of $CuInSe_2$ thin films by pulsed laser deposition using excess Se targets, J. Mater. Res., 25 (2010) 1936-1942.

[8] S.M.F. Hasan, M.A.S.K.M. Mannan, The optical and electrical properties of copper indium di-selenide thin, Optical Materials, 14 (2000) 329-336.

[9] J. Levoska, S. Leppavuori, F. Wang, O. Kusmartseva, Pulsed Laser Ablation Deposition of $CuInSe_2$ and $CuIn_{1-x}Ga_xSe_2$ Thin Films, Physica Scripta, T54 (1994) 244-247.

[10] E. Ahmed, A.E. Hill, J. Leppavuori, R.D. Pilkington, R.D. Tomlinson, J. Levoska, O. Kusmartseva, A Comparative Study of Uplsed Laser Deposition and Flash Evaporation of $CuIn_{0.75}Ga_{0.25}Se_2$ Thin Films, Advanced Materials for Optics and Electronics, 4 (1994) 423-429.

[11] P. Victor, J. Nagaraju, S.B. Krupanidhi, Pulsed laser excimer laser ablated copper indium diselenide thin films, Solid State Communications, 116 (2000) 649-653.

[12] S. Kuranouchi, A. Yoshida, Annealing effects of $CuInSe_2$ films prepared by pulsed laser deposition, Thin Solid Films, 343-344 (1999) 123-126.

[13] P. Luo, C. Zhu, G. Jiang, Preparation of CuInSe2 thin films by pulsed laser deposition the Cu-In alloy precursor and vacuum selenization, Solid State Communications, 146 (2008) 57-60.

[14] A. Tverjanovic, E.N. Borisov, E.S. Vasilieva, O.V. Tolochko, I.E. Vahhi, S. Bereznev, Y.S. Tveryanovich, $CuInSe_2$ thin films deposited by UV laser ablation, Solar Energy Materials & Solar Cells, 90 (2006) 3624-3632.

[15] A. Yoshida, N. Tanahashi, T. Tanaka, Y. Demizu, Y. Yamamoto, T. Yamaguchi, Preparation of CuInSe2 thin films with large grain by excimer laser ablation, Solar Energy Materials & Solar Cells, 50 (1998) 7-12.

[16] S.B. Zhang, S.H. Wei, Reconstruction and energetics of the polar (112) and (<u>112</u>) versus the nonpolar (220) surfaces of $CuInSe_2$, Physical Review B, 65 (2002) 081402: 081401 - 081404.

[17] D. Liao, {112} Polar Surfaces of $Cu(In,Ga)Se_2$: Properties and Effects on Crystal Growth, in: Department of Materials Science and Engineering, University of Illinois.

[18] D.H. Lowndes, C.M. Rouleau, D.B. Geohegan, A.A. Puretzky, M.A. Strauss, A.J. Pedraza, J.W. Park, J.D. Budai, D.B. Poker, Pulsed Laser Ablation Growth and Doping of Epitaxial Compound Semiconductor Films, in: Mater. Res. Soc. Symp. Proc., Materials Research Society, 1996, pp. 107-118.

[19] I.V. Bodnar, V.P. Gremenok, E.P. Zaretskaja, I.V. Victorov, Preparation and properties of laser-evaporated $CuGa_{0.1}In_{0.9}Se_2$ thin films, Thin Solid Films, 207 (1992) 54-56.

[20] S. Leppavuori, J. Levoska, A.E. Hill, R.D. Tomlinson, J.Frantti, O. Kusmartseva, H. Moilanen, R.D. Pilkington, Laser ablation deposition as a preparation method for sensor materials, Sensors and Actuators A, 41-42 (1994) 145-149.

[21] V.F. Gremenok, E.P. Zaretskaya, I.V. Bodnar, Y.V. Rud', M.A. Magomedov, Photosensitivity of In-p-$CuIn_xGa_{1-x}Se_2$ thin film structures, Thin Solid Films, 232 (1993) 139-141.

[22] V.V. Kindyak, A.S. Kindyak, V.F. Gremenok, A.A. Kutas, Optical transitions in laser-evaporated thin $CuInSe_2$ films, Thin Solid Films, 240 (1994) 114-115.

[23] A. Rockett, F. Abou-Elfotouh, D. Albin, M. Bode, J. Ermer, R. Klenk, T. Lommasson, T.W.F. Russell, R.D. Tomlinson, J. Tuttle, L. Stolt, T. Walter, T.M. Peterson, Structure and chemistry of $CuInSe_2$ for solar cell technology: current understanding and recommendations, Thin Solid Films, 237 (1994) 1-11.

[24] L. Zhang, Q. He, W. Jiang, F. Liu, C. Li, Y. Sun, Effects of substrate temperature on the structural and electrical properties of $Cu(In,Ga)Se_2$ thin films, Solar Energy Materials & Solar Cells, 93 (2009) 114 - 118.

[25] M. Mayer, SIMNRA User's Guide, Report IPP 9/113, in, Max-Planck-Institut für, Plasmaphysik, Garching, Germany, 1997.

[26] Y.M. Shin, D.H. Shin, J.H. Kim, B.T. Ahn, Effect of Na doping using Na_2S on the structure and photovoltaic properties of CIGS solar cells, Current Applied Physics, 11 (2011) S59-S64.

[27] Y.H. Jo, B.C. Mohanty, Y.S. Cho, Enhancedelectrical properties of pulsed laser-deposited $CuIn_{0.7}Ga_{0.3}Se_2$ thin films via processing control, Solar Energy, 84 (2010) 2213–2218.

[28] A.J. Cheng, M. Manno, A. Khare, C. Leighton, S.A. Campbell, E.S. Aydil, Imaging and phase identification of Cu_2ZnSnS_4 thin films using confocal Raman spectroscopy, J. Vac. Sci. Technol. A, 29 (2011) 051203-051201 - 051203-051211.

[29] M. Berruet, M. Valde´s, S. Cere´, M. Va´zquez, Cost-effective solar cells containing copper indium chalcogenides prepared by SILAR method, J Mater Sci, 47 (2012) 2454–2460.

[30] B. Eisener, D. Wolf, G. Muller, Influence of sulphur on the electrical and optical properties of p-type $CuIn(S_xSe_{1-x})_2$ single crystals, Thin Solid Films, 361-362 (2000) 126-129.

[31] O. Madelung, Semiconductors: Data Handbook, Springer, New York, 2004.

[32] U.R.M. Schmitt, F. Engelhardt, O. Seifert, J. Parisi, W. Riedl, J. Rimmaschb, F. Karg, Impact of Na and S Incorporation on the Electronic Transport Mechanisms of $Cu(In,Ga)Se_2$ Solar Cells Solid State Communications, 107 (1998) 59-63.

6 GROWTH BEHAVIOR OF PULSED LASER DEPOSITED CZTS

6.1 PURPOSE

CZTS thin films represent ideal absorber layers for single-junction photovoltaic devices, due to its direct band gap of ~1.5eV and high optical absorption > $10^4 cm^{-1}$ above the band edge [1]. Devices with achieve high device efficiencies of 12.6% have been fabricated using Se-alloyed CZTSeS absorber layers [2]. In general, however, the fabrication of high quality CZTSeS absorber layers has been extremely challenging, due to the narrow phase formation region for CZTSeS [1, 3], elemental and compound volatility [1, 4-6], and phase decomposition at the surface and back contacts [7, 8]. The difficulty in preventing Zn and SnS loss during film growth, associated with CZTS phase decomposition and the high vapor pressures of these components, has resulted in the comparative success of two-step (deposition reaction) fabrication processes over more conventional single-step processes (e.g. coevaporation) [1, 7].

The champion CZTSeS device was fabricated using a two-step process, in which the absorber layer was deposited at low temperature using a nano-ink spin-coating process and then annealed in S(Se) background to complete the crystal formation [2, 9] – S(Se) overpressure helps prevent phase decomposition and SnS evolution [7]. The primary loss mechanisms in the champion cell remain similar to those previously reported by Mitzi, including interface recombination, series resistance, and short minority carrier lifetime [1, 2, 9]. Secondary phases, native defects and poor band alignment have been shown to play significant roles in these losses, but they are generally not well-understood [1, 2, 10].

Despite the moderately high device efficiencies achieved, all aspects of CZTS device design merit continued investigation. Scalable and reliable fabrication methods, capable of producing phase-pure, void-free CZTSeS absorber layers have yet to be demonstrated. Such advancements will require better understanding of the crystal formation processes and defect behavior of CZTSeS. For instance, the S-content in precursor films has been shown to significantly influence grain growth and void formation during annealing [5], and kinetically-limited growth processes and decomposition reactions have been shown to play significant roles in secondary phase formation [7, 8, 11]. Future improvements to the device performance will also likely require the optimization of the device architecture for CZTSeS, in order to enhance the stability and band alignments at the back contact and front contact interfaces. Only a limited number of works, however, have reported on the performance of alternative device architectures [10].

As discussed in Chapters 1,3 and 5, pulsed laser deposition (PLD) represents a useful laboratory-scale fabrication tool to quickly study different material combinations, and the ability

to deposit on insulating substrates facilitates the study of optical absorption and Hall Effect measurements. This work explores the pulsed laser deposition of CZTS thin films, deposited and annealed under varying conditions, with the following objectives:

- Characterize the effects of pulsed laser deposition parameters on film composition and morphology.
- Compare one-step and two-step film growth processes using pulsed laser deposition.
- Investigate the role of the precursor composition and structure on crystal and secondary phase formation processes, and determine their influence of film properties.
- Demonstrate high quality films for use in fundamental material and interface studies.

6.2 BACKGROUND

This section provides a brief review of the existing literature on pulsed laser deposition of thin film CZTS and CZTSe [12-23]. Most of the reported works utilized KrF (248nm) excimer lasers for PLD [12-19, 23], with only one work reporting use of a solid-state, continuous-wave Nd:Yag (1.06 μm) laser [21]. The sputtering targets were typically prepared using pressing/sintering methods, with a wide range compositions reported. Table 6-1 below shows typical deposition parameters demonstrated in the literature, and Table 6-2 shows reported effects of the deposition parameters on the properties of CZTS and CZTSe films.

Table 6-1. Typical pulsed laser deposition parameters for CZTS and CZTSe (literature results)

Deposition Parameter	Value	Reference
Background Pressure	Vacuum: $\leq 10^{-4}$ torr Argon: ~10mtorr	[12-21] [23]
Laser Energy (Fluence)	200 – 300mJ/pulse 0.7 – 3 J/cm^2	[19-21] [12-18, 23]
Laser Pulse Frequency	5 – 10Hz	[12-15, 19, 21, 23]
Substrate-Target Distance	3 – 5cm	[12-15, 18-21, 23]

Pulsed laser deposition studies of CZTS and CZTSe thin films in literature have focused on characterizing their growth behavior and fundamental properties, including the effects of stoichiometry on their opto-electronic properties, the alloying behavior of S-Se substitutions and the development of secondary phases. Device efficiencies up to 3.14% have been reported for solar cells using pulsed laser deposited CZTS absorber layers [15].

He reported on the fabrication of sintered-powder sputtering targets [22]. For pure sulfur compositions (not alloyed with Se), Cu_2S, ZnS and SnS_2 powders were mixed in stoichiometric proportions, except with 5% excess of S to offset evaporation losses. After pre-sintering at 500°C for 2h and final sintering at 700°C (time not specified), final element ratios were determined as follows: Cu:[Zn+Sn] = 0.94, Zn:Sn = 1.03, and S:metals = 0.83 [22]. For near-stoichiometric powders, others have reported similarly extreme deficits in S after sintering [13, 16, 18, 21]; on the other hand, wide variations in the metal element ratios have been reported, with target compositions ranging from Cu-poor to Cu-rich and Zn-poor to Zn-rich [13, 16, 18, 21, 22]. Frequently, only the initial powder ratios are reported [12, 17, 19, 20], and subsequently the sputtering target composition likely varies widely from nominal stoichiometry, as described above.

Due to widely varying deposition and post-annealing conditions in reported works, in addition to frequently unspecified target compositions and incompletely specified deposition conditions, drawing conclusions regarding the relationship between compositions in the sputtering target and the as-deposited films remains challenging. Notably, the as-deposited composition also depends strongly on the substrate temperature during deposition, due to the high vapor pressures of elemental Zn and SnS(Se) [4, 6], which can modify the film compositions by re-evaporation. Comparing depositions performed under similar conditions, the limited available literature shows conflicting trends regarding the element transfer between the target and the deposited film [21, 23]. For instance, for films deposited in high-vacuum at temperatures > 400°C, He shows that relative to the target, the Cu:[Zn+Sn] decreases slightly, Zn:Sn decreases significantly, and [S+Se]:metals increases slightly [23]; Wibowo, on the other hand, shows that Cu:[Zn+Sn] does not change, Zn:Sn increases significantly, and Se:metals does not change [21].

He attributes the Cu-poor, Zn-poor, and S-rich transfer of elements to the non-homogeneous distribution of elements in the plume according to atomic mass and also to the high vapor pressure of Zn. The author states that the relatively light S-atoms tend to be more forward-directed and therefore preferentially deposited; similarly, variations of Cu in the plume lead to deficiencies at the "large" target-substrate distances employed [23]. However, since Cu is lighter than Zn and Sn, films should be Cu-rich if the degree of forward-peaking in the plume was determined by the atomic mass. Wibowo similarly argues that greater forward-peaking of the lighter elements causes the stoichiometric deviations relative to the target that are observed in the films. However, in that case, Cu and Zn are both preferentially deposited over Sn and Se [21].

Literature has reported a wide range of effects of substrate temperature on film properties. With increasing substrate temperatures, the S(e):metals ratios were generally shown to decrease and then increase, exhibiting minimums between 300 and 400°C [17, 19, 21]. Sekiguchi and Sun demonstrated increases in the Cu:[Zn+Sn] ratio up to 350°C and 400°C, respectively, followed by

declines with further increases in the temperature [17, 19]. Wibowo reported Cu:[Zn+Sn] ratios that exhibited small oscillations near stoichiometry with increasing substrate temperature [21]. Finally, with increasing substrate temperature, Sekiguchi and Sun showed steady increases in Zn:Sn [17, 19], and Wibowo showed a decline then rise in Zn:Sn [21]. Notably, Sekiguchi and Sun deposited films using UV-wavelength excimer lasers [17, 19], while Wibowo deposited films using a long-wavelength Nd:Yag laser, complicating the comparisons [21].

Table 6-2. Process control variables and effects: CZTS and CZTSe (literature results)

Process Parameter	Variation	Film Effect	Rationale
Target Stoichiometry	–	Note: Sintering of CZTS(Se) powders in near-stoichiometric proportions likely yields highly S-deficient targets with variations in the cation ratios dependent on the preparation method Slightly Cu-poor and S(Se)-rich, Zn and Sn concentrations may vary (relative to target)	Varying atomic masses distribute elements differently within plume
Substrate Temperature	Increasing	(1) Effect on composition unclear (2) Likely increases surface roughness, but conflicting trends reported	Unclear trends
Laser Energy (Fluence)	Increasing	(1) Increases film crystallinity ▪ Critical value exists (2.5J/cm^2), above which film crystallinity degrades (2) Increases surface roughness, and size/density of macro-particulates	(1) Increases KE content of depositing species ▪ Above critical value, dep rates hinder crystallization (2) Increases thermal penetration depth, enhancing splashing
Laser Pulse Frequency	Increasing	Increases film crystallinity ▪ Critical value exists (10Hz), above which film crystallinity degrades	Reduces pulse duration, yielding higher average thermal values as successive layers deposit ▪ Above critical value, increased deposition rates hinder crystallization

Sekiguchi, Sun, and Wibowo showed inconsistent results regarding the effects of substrate temperature on the surface morphologies of deposited films. Sekiguchi provides little commentary, but SEM images appear to show surfaces increasing in microscopic roughness from 300°C to 400°C but decreasing in macroscopic roughness (e.g. fewer splashed particles) [17]. Wibowo shows a similar increase in microscopic surface roughness of the films with increasing substrate temperature, with the root mean square (RMS) roughness increasing linearly from RT to

500°C [21]. On the other hand, Sun shows an apparent decrease in microscopic surface roughness attributed to coalescence of Volmer-Weber type islands at higher temperatures [19].

Increasing laser fluence was shown to increase film crystallinities [12], as well as increase microscopic and macroscopic film surface roughnesses [12, 16]. The author states that the improvement in film crystallinities, evident as sharpened diffraction peaks, results from the increase in plasma density and associated increase in kinetic energies of the ejected species [12], consistent with the explanation summarized in Chapter 3. Above a critical laser fluence (2.5J/cm^2), Pawar noted a decline in the film crystallinity, which the author attributes to excessive deposition rates at the higher fluences that prevent adequate time for the adatoms to diffuse to the lattice sites [12, 24]. The deposited species are "overlaid and solidified by the succeeding species" [24], leading to smaller crystallites but bulkier overall grains [12]. Notably, the surface roughness trends remain similar in samples that have been post-annealed in H_2S background [12], suggesting that the morphologies of as-deposited films strongly influences the final morphologies of annealed films.

Increasing laser pulse repetition rate was shown to increase film crystallinities, evident as sharpened diffraction peaks of as-deposited films and larger grains in SEM images of post-annealed films [13]. The author attributed this improvement crystallinity to the decreased pulse duration, which yielded an increase in the average thermal energy still present in the deposited species when the next deposition pulse arrives, thereby enhancing crystal growth [13]. Above a critical laser repetition rate (10Hz), however, decline in the film crystallinity was observed, attributed to a reduction of the island ripening time to below a critical value, thereby yielding smaller average island sizes and degraded crystallinity [13]. Notably, the impact of pulse repetition rate on film crystallinity, and its associated critical value, behaves similarly to the mechanism of laser fluence on crystallinity, as described above.

6.3 EXPERIMENTAL DETAILS

Single layer films of CZTS, 50 – 550nm thickness, were deposited onto soda lime glass substrates by PLD from the CZTS-1 ($Cu_{1.92}Zn_{1.22}Sn_{1.00}S_{4.25}$), CZTS-2 ($Cu_{1.90}Zn_{1.25}Sn_{0.85}S_{4.25}$) and CZTS-3 ($Cu_{1.80}Zn_{1.32}Sn_{0.85}S_{4.25}$) sputtering targets, as specified in Table 3-2. Using the EMAT PLD system, set-up and methodology described in Section 3.1.3.1, films were deposited in Ar_2 background (15mtorr) with a 2sccm flow rate. Laser fluence was varied between 0.8 – 6.0 J/cm^2, the repetition rate was varied between 5 – 15Hz, and substrates were heated between room temperature and 500°C using an infrared heater and a silicon backing wafer. Sulfur annealing was performed using the Generation #2 annealing system design and methodology described in Section 3.3.3.3. Samples were nominally annealed with 4.5mg elemental sulfur at 560°C for 10min, with a 7min ramp, and passively cooled under flowing Argon to < 120°C.

Film compositions and thicknesses were characterized using Rutherford back scattering (RBS) and particle-induced x-ray emission spectroscopy (PIXE) analyses, as detailed in Chapter 4. Crystal structures were analyzed by x-ray diffraction and Raman backscattering spectroscopy, morphologies were assessed using scanning electron microscopy, and electronic properties were evaluated by Hall effect in the Van de Paaw geometry, as detailed in Chapter 4. Using the SCI FilmTek 3000SE for shorter wavelength ranges (band gap calculations) and the Perkin Elmer Lambda 950 spectrophotometer for longer wavelength ranges (optical absorption spectra), transmission and reflection measurements were taken as described Section 4.3.1.1. The optical absorption coefficients were calculated, accounting for front surface reflections only, according to the relations in Table 4-13. The band gap was calculated using the fitting procedure for direct band gap materials, Eqn. (4-14) and (4-15), described in Section 4.3.1.2.

6.4 RESULTS AND DISCUSSION

The effects of the pulsed laser deposition parameters (laser fluence, target-substrate distance, pulse repetition rate, and sputtering target composition) on the composition, structural and morphological properties of the films are investigated in Sections 6.4.1 – 6.4.5. The effects of precursor properties and sulfur annealing parameters on the composition, structural, morphological and opto-electronic properties are investigated in Section 6.4.6. Key growth parameters are identified and crystal and secondary phase formation processes discussed.

6.4.1 Effects of Laser Fluence

Using the CZTS-1 sputtering target, a target-substrate spacing of 10cm, and a repetition rate of 5Hz, films were grown at room temperature with the following laser fluences: 0.8J/cm^2 (52mJ), 1.3J/cm^2 (82mJ), 2.6J/cm^2 (160mJ), and 3.9J/cm^2 (240mJ). The deposition rate increases approximately linearly with increasing laser fluence, with film thicknesses varying between 60 and 280nm.

Table 6-3. Compositions and thickness of pulsed laser deposited CZTS films with varying laser fluences

Laser Fluence (J/cm^2)	Atomic %					Cu:Zn	Zn:Sn	S:Metals	Thick (nm)
	Cu	Zn	Sn	S	O				
0.8	15	17	21	40	8.0	0.87	0.83	0.76	60
1.3	18	15	18	39	9.0	1.2	0.86	0.76	90
2.6	26	14	15	39	6.0	1.8	0.91	0.70	205
3.9	25	15	16	40	5.0	1.7	0.94	0.71	280

The CZTS-1 target composition was chosen with the desired metal element ratios, Cu:Zn (1.57) and Zn:Sn (1.22), assuming stoichiometric transfer to the film; S was included in excess to

account for re-evaporation losses during deposition. The as-deposited film compositions are summarized in Table 6-3.

The element ratios of the as-deposited films are graphically summarized in Fig. 6-1, and the dashed lines indicate the desired element ratios for the film. Fig. 6-1 indicates the presence of an ablation threshold between 1.3 and 2.6J/cm^2, above which the deposited film stoichiometry remains approximately constant with increasing laser fluence. Below the ablation threshold, the film stoichiometries deviate strongly from the target stoichiometry, exhibiting severely Cu-deficient compositions.

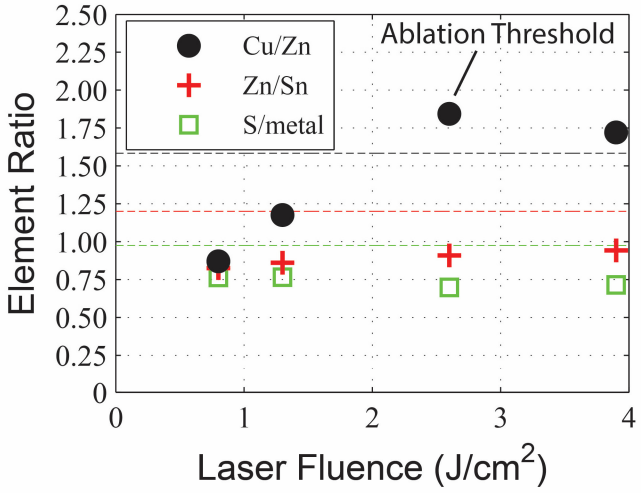

Fig. 6-1. Film element ratios vs. laser fluence

For all laser fluences, films are significantly S-deficient, despite the target containing S in stoichiometric excess. Dissimilar deposition parameters, including background pressure, temperature, and laser fluence, make comparisons to literature difficult. However, the decrease in S:metals ratio in the films relative to the target contradicts reported trends in the limited literature, which has shown small increases [16, 23]. This S-deficiency can be readily mitigated with a short sulfur annealing operation. Deviations in the metal element ratios, on the other hand, are more difficult to correct through post-deposition processing.

At fluences above the ablation threshold, where the composition stabilizes, films are slightly Zn-poor and highly Sn-rich relative to stoichiometric CZTS, which literature has indicated yields poor electronic behavior [1]. CZTS devices with stoichiometries close to that of the *nominal target* (Cu:Zn = 1.57, Zn:Sn = 1.22, and S:metals = 1.03) have yielded the best performance [1].

The Cu:Zn ratios at laser fluences of 2.6 and 3.9J/cm^2 are near the target stoichiometry, but the Zn:Sn ratios are very low, indicating highly Sn-rich conditions. In general, heavier elements exhibit slightly less forward-peaking in the ablation plume and therefore demonstrate slightly lower concentrations in the deposited film [25]. Mass-related plume effects are thus not likely to

cause increased incorporation of the *heavier* Sn elements. While the cause of the Sn concentration deviations between the target and deposited films cannot currently be identified, it will be shown in Section 6.4.6.1 that the Sn concentration in the films can be corrected by proportionally reducing the Sn concentration in the target by the desired amount.

The slightly reduced Zn concentration, evident as larger than expected Cu:Zn ratios, may result from re-evaporation of elemental Zn before it can form stable Zn-compounds [11, 26], slightly greater forward-peaking in the plume of the lighter Cu elements [19], or errors associated with Eqn. (4-5). The near-target Cu:Zn ratios and the correctable S-deficiencies indicate that high Sn concentrations represent the main obstacle to achieving desired film stoichiometries.

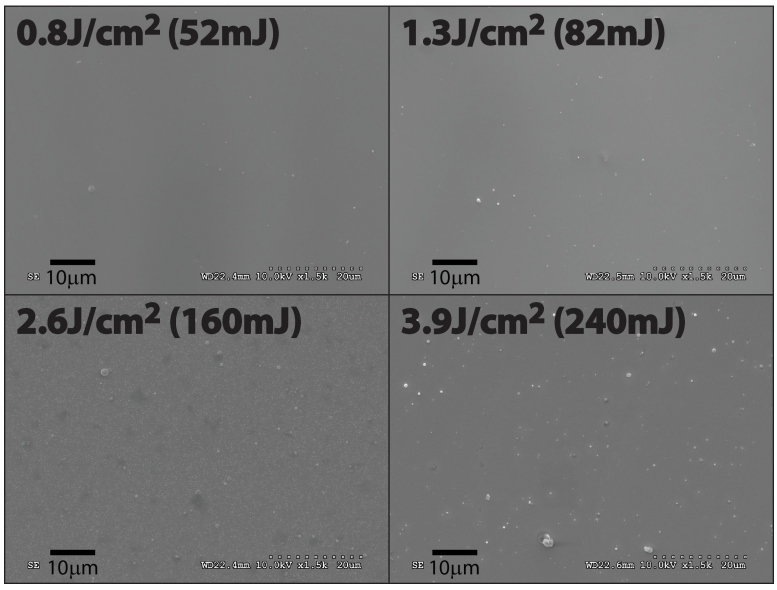

Fig. 6-2. SEM images of films deposited with varying laser fluences

Film surface morphologies were investigated using SEM, as shown in Fig. 6-2. The density of micron-sized splashed and exfoliated particles increases slightly with increasing laser fluence, consistent with other works [12, 18]. Consequently, the optimum film will be deposited at the lowest laser fluence that yields the most-stoichiometric transfer from the target: in this case, a laser fluence of $\geq 2.6 J/cm^2$.

6.4.2 Effects of Target-Substrate Distance

Using the CZTS-1 sputtering target, a laser fluence of $2.6 J/cm^2$, and a repetition rate of 5Hz, films were grown at room temperature with the following target-substrate distances: 9cm, 10cm, and 11cm. The deposition rate decreases approximately linearly with increasing target-substrate distance, with film thicknesses varying between 265 and 165nm. As-deposited film compositions are summarized in Table 6-4.

Table 6-4. Compositions of films deposited at varying target-substrate distances

Distance (cm)	Atomic %					Cu:Zn	Zn:Sn	S:Metals	Thick (nm)
	Cu	Zn	Sn	S	O				
9	25	15	15	38	8.0	1.6	0.98	0.69	265
10	26	14	15	39	6.0	1.8	0.91	0.70	205
11	23	14	15	39	10	1.6	0.95	0.77	165

No clear trends in the metal element concentrations are observed with target-substrate distance, with the Cu:Zn and Zn:Sn ratios varying non-monotonically. The S:metals ratio increases monotonically with increasing target-substrate distance, although the absolute S concentration does not vary significantly. Subsequently, the increase in S:metals ratio can primarily be attributed to variations in the metal concentrations rather than increased deposition rates of S. Essentially, the film compositions do not depend strongly on the target-substrate distances. However, the chamber limits the target-substrate distances to the values shown, and so trends in composition may not be clear due to the small range of values investigated.

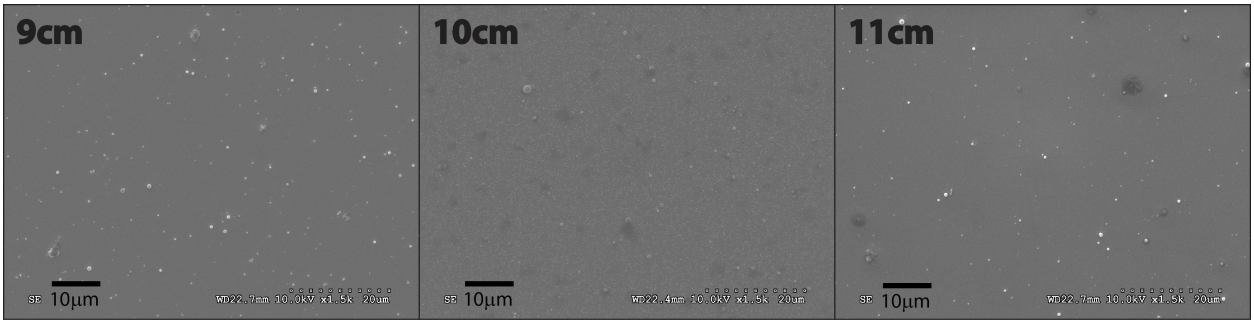

Fig. 6-3. SEM images of films deposited at various target-substrate distances

The surface morphologies of these films are shown in Fig. 6-3. The density of micron-sized splashed and exfoliated particles decreases slightly with increasing target-substrate distance. Based on the composition and morphology trends, the optimum target-substrate distance is: 10 – 11cm.

6.4.3 Effects of Laser Pulse Repetition Rate

Using the CZTS-1 sputtering target, a laser fluence of 2.6J/cm^2, and a target-substrate distance of 10cm, films were grown at room temperature with the following repetition rates: 5Hz, 10Hz, and 15Hz. The deposition rate increases approximately linearly with increasing pulse repetition rate, with film thicknesses varying between 200 and 540nm. As-deposited film compositions are summarized in Table 6-5.

The relative concentrations of Zn, S, and O monotonically increase with increasing repetition rate, evident as decreasing Cu:Zn and increasing Zn:Sn ratios, increasing S:metals ratio, and increasing O:elements ratio, respectively. Note the element ratios in Table 6-5 are calculated

using non-truncated composition values. Zn, S and O tend to have lower sticking coefficients than Cu and Sn [26-30]. It has also been suggested that Zn requires compound formation with S [26] or other alloys [11] to remain stable on the film surface, particularly at high temperatures and/or low pressures [4]. Increasing repetition rate may then counteract the loss of unstable species by capping them with the next material layer before they have time to desorb.

Table 6-5. Compositions of films deposited at varying laser pulse repetition rates

Rep Rate (Hz)	Atomic %					Cu:Zn	Zn:Sn	S:Metals	Thick (nm)
	Cu	Zn	Sn	S	O				
5	26	14	15	39	6.0	1.8	0.91	0.70	205
10	24	14	15	38	9.0	1.7	0.95	0.74	395
15	21	14	14	38	13	1.5	0.97	0.78	540

The surface morphologies of these films are shown in Fig. 6-4. The size of micron-sized splashed and exfoliated particles increases with increasing repetition rate. Higher repetition rates may cause additional heating of the target, which tends to exacerbate hydrodynamic splashing mechanisms [31].

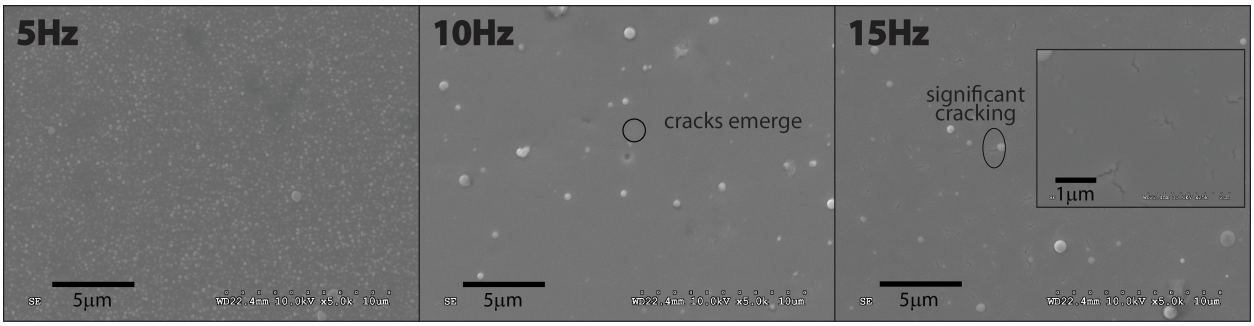

Fig. 6-4. SEM images of films deposited at varying laser pulse repetition rates

More significantly, however, cracks emerge in the films at a repetition rate of 10Hz, and they grow in size and density at 15Hz. Increased growth rates and increased film thickness at higher repetition rates may yield greater film strain which causes crack formation. Notably, however, 1µm thick films were deposited under similar conditions with 5Hz repetition rate, and no significant cracking was observed. While no significant temperature rises were observed in the substrate holder, the atomic species arrive at the substrate with significant kinetic energies [25, 32]; local heating of the films [32], with subsequent relaxation, is therefore expected. With higher repetition rates, larger volumes of deposited material may be involved in this relaxation process, thereby increasing the strain. To prevent cracking in the films, repetition rates of 5Hz should be employed for depositions at room temperature.

6.4.4 Effects of Substrate Temperature

Using the CZTS-1 sputtering target, a laser fluence of 2.6J/cm^2, a repetition rate of 5Hz, and a target-substrate distance of 10cm, films were grown at the following substrate temperatures: room temperature, 400°C, and 500°C. The deposition rate decreases significantly with increasing temperature, with film thicknesses varying between 200 and 115nm. The decreased deposition rate is attributed to re-evaporation from deposited films. The as-deposited film compositions are summarized in Table 6-6.

Table 6-6. Compositions of films deposited at varying substrate temperatures

Substrate Temp (°C)	Atomic %					Cu:Zn	Zn:Sn	S:Metals	Thick (nm)
	Cu	Zn	Sn	S	O				
RT	26	14	15	39	6.0	1.8	0.91	0.70	205
400	27	11	17	45	0.0	2.4	0.67	0.80	160
500	35	17	5.0	43	0.0	2.0	3.5	0.76	115

Two notable trends may be observed with increasing substrate temperature. First, the relative Zn concentration decreases from RT to 400°C and then increases from 400°C to 500°C. Second, the relative Sn concentration increases from RT to 400°C and then drops dramatically from 400°C to 500°C. The relative S concentration also increases from RT to 400°C and then decreases slightly from 400°C to 500°C. Other works have reported similarly non-monotonic trends in Zn, Sn and S concentrations [17, 19, 21]. For instance, Sun similarly demonstrated a decrease in relative Zn concentrations from 300 to 350°C, followed by steady increases from 350 to 450°C. Contrary to our results, however, the same study showed S concentrations decreasing from 300 to 400°C, followed by an increase from 400 to 450°C [19].

The sharp decrease in Zn at 400°C and the sharp decrease in Sn at 500°C are attributed to shifts in the thermodynamic and phase properties of the system at these two temperatures. Near 400°C, the vapor pressure of elemental zinc rises to ~7mtorr [33], roughly the background pressure (15mtorr) of the deposition, significantly raising the likelihood of Zn sublimation from the depositing film. The remaining Zn in the film likely remains stable due to its incorporation into either ZnS or CZTS phases. CZTS, as well as SnS, phases are clearly evident at 400°C in the Raman spectra presented in Fig. 6-5 [34-37]. While ZnS phases are not observed in Fig. 6-5, ZnS requires resonant, UV wavelength excitation to be reliably detected in Raman spectra [34, 37, 38]. The Raman system here used a 488nm wavelength laser.

Significant losses of Sn in the form of SnS have been demonstrated during processing of CZTS thin films at high temperatures, particularly at low background pressures [6, 7]. This loss of SnS has been shown to be driven by the decomposition of CZTS into metal-sulfide binaries and subsequent irreversible evaporation of SnS, when insufficient partial pressures of S_2 and SnS are

maintained [6, 7], as discussed in detail in Section 3.3.2.2. Per [39], the vapor pressure of SnS is ~ 0.3mtorr at 500°C. The high kinetic energy of the impinging species may further lower the barrier to sublimation of SnS. As Fig. 6-5 shows, SnS peaks are reduced at 500°C, consistent with loss of Sn through the evaporation of SnS. The partial recovery of Zn concentration in the film, evident as decline in Cu:Zn ratio between 400°C and 500°C, may be attributed to the enhanced formation of more stable ZnS and CZTS phases. However, without better detection of ZnS, this hypothesis cannot be confirmed. Notably, Weber explains similar losses in Zn and Sn, during multi-step evaporation of CZTS thin films, as re-evaporation losses of elemental Zn and SnS [40].

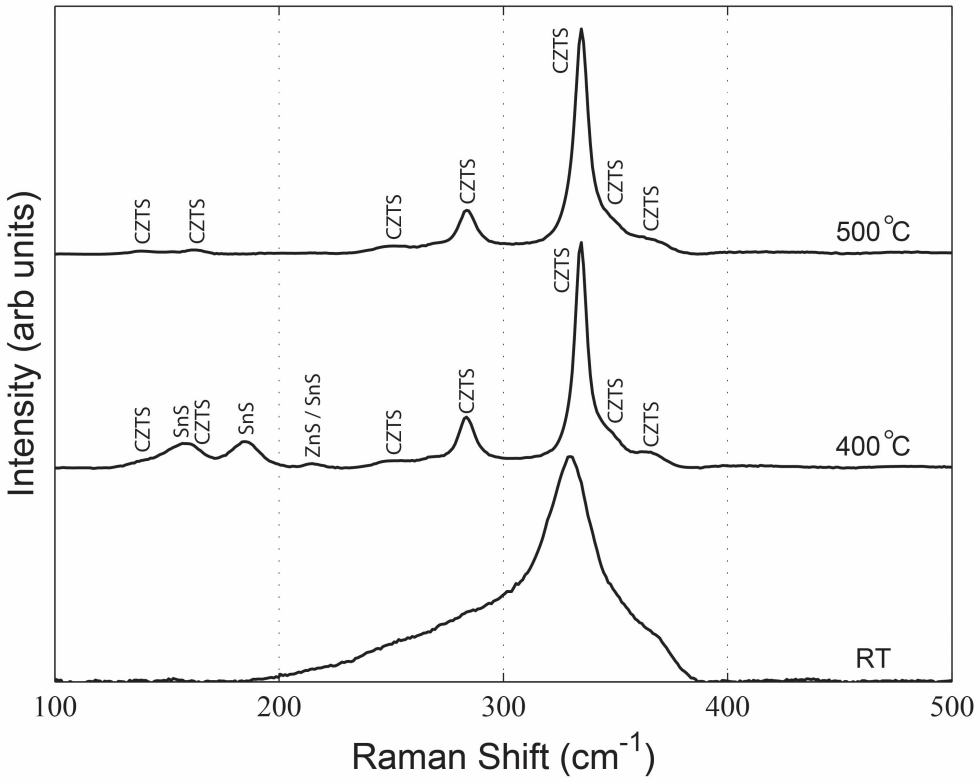

Fig. 6-5. Raman spectra of films deposited at varying substrate temperatures

The surface morphologies of these films are shown in Fig. 6-6 below. The lower magnification images in the figure show that the size and density of micron-sized splashed and exfoliated particles remain roughly similar among the various deposition temperatures. The finer morphology (shown in the insets) varies significantly, however. The inset in Fig. 6-6 (RT) shows tightly packed spheres approximately 100-200nm in diameter on the surface of the as-deposited film. This morphology represents anomalous behavior relative to other depositions performed under similar conditions. Note, however, the film surface does not show any well-defined crystal grain structures. At 400°C substrate temperature, relatively large grains (200 – 500nm) are clearly evident in the Fig. 6-6 (400°C) inset. Similar grain structure can be seen for the 500°C substrate

temperature, shown in Fig. 6-6 (500°C) inset. However, the 500°C film appears to be rougher and contain a higher density of smaller crystallites (50 – 200nm).

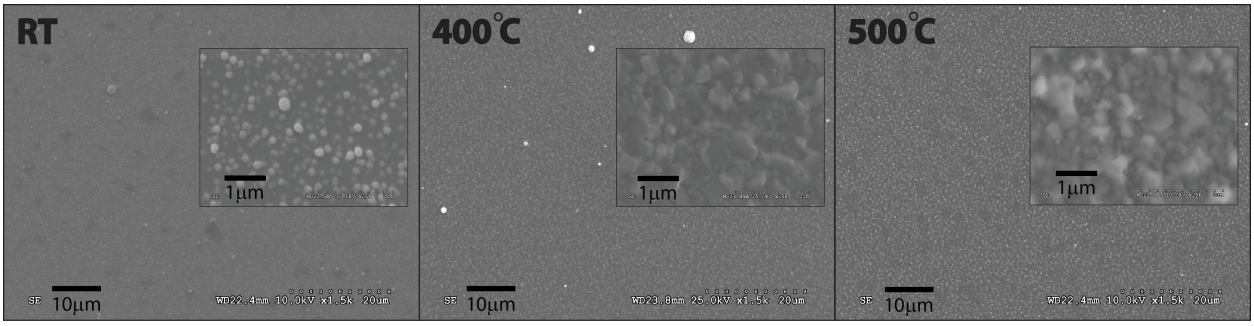

Fig. 6-6. SEM images of films deposited under various substrate temperatures

The evaporative losses of Zn and Sn at deposition temperatures > 400°C indicate the need for a two-step fabrication approach, with the precursor films deposited at room temperature followed by a high temperature annealing step in sulfur background. Scragg and others have previously reported similar conclusions regarding the comparative success of two-step approaches used to fabricate CZTS [1, 7]. Further, for growth on Mo-coated substrates, detrimental reactions at the back contact must also be considered [8]. If sufficient sulfur overpressures are not maintained during CZTS formation, then MoS_2 formation at the back contact interface may lead to phase decomposition of CZTS into the binary metal-sulfides [8]. By employing a two-step fabrication approach, the back contact decomposition can be mitigated by forming CZTS under S-rich environment [7].

For glass substrates, Sn losses likely cannot be offset at temperatures > 500°C, due to the overpressure requirements for S_2 and SnS, which are not compatible with operation of the pulsed laser deposition chamber. However, Zn losses in heated substrates might be overcome by decreasing the substrate temperature <400°C, increasing the Zn concentration in the target, or supplementing Zn during deposition through effusion of a ZnS source.

6.4.5 Effects of Sputtering Target Composition

Using a laser fluence of ~3.5J/cm^2, a repetition rate of 5Hz, and a target-substrate distance of 10cm, films were grown at room temperature with the CZTS-2 and CZTS-3 sputtering targets (see Table 3-2). The as-deposited film compositions are summarized in Table 6-7.

Table 6-7. Film compositions for varying sputtering target compositions

Target ID	Atomic %					Cu:Zn	Zn:Sn	S:Metals	Thick (nm)
	Cu	Zn	Sn	S	O				
CZTS-2	18	12	10	37	22	1.5	1.2	0.91	320
CZTS-3	18	13	10	36	23	1.4	1.3	0.86	325

With adjusted Sn concentrations in the CZTS-2 and CZTS-3 sputtering targets, the desired film stoichiometries are achieved. From Table 6-7, the Cu:Zn ratios in the as-deposited films, 1.50 and 1.38, are close to the ratios in CZTS-2 and CZTS-3 targets, 1.52 and 1.36, respectively. Further, the Zn:Sn ratios are in the desired Zn-rich (1.2 – 1.3) range. Note the CZTS-2 and CZTS-3 films are S-deficient and contain significant oxygen. As the following shows, however, sulfur annealing successfully adds the required sulfur and significantly reduces the concentration of oxygen in the films. Depositions were also performed at 400°C (results not shown), but the increased Zn concentration in CZTS-3 was not enough to counter the severe Zn losses at temperature.

6.4.6 Effects of Sulfur Annealing

All pulsed laser deposited films in this study also require a post-deposition annealing operation in sulfur background, in order to realize acceptable quality films. Films deposited at room temperature are S-deficient and amorphous, evidenced by XRD measurements (not shown), and subsequently they require sulfur annealing to crystallize the films and to adjust the chalcogen concentration. Films deposited at higher temperatures (400°C) are more crystalline, but also S-deficient, and so they also require sulfurization.

6.4.6.1 Sn-Rich Films

To examine the impact of annealing on Sn-rich samples, the 400°C samples from Section 6.4.4 were sulfur annealed as described in Section 6.3. To ensure sulfur overpressure was maintained throughout, longer anneal times were achieved by performing the nominal procedure twice, denoted as **SA (2X)**. The compositions of the as-deposited and sulfur annealed films are summarized in Table 6-8. Film thickness increases slightly after sulfur annealing, from 160 to 175nm, and additional annealing (**SA 2X**) does not change the film thickness. No composition gradients are observed in the RBS spectra.

Table 6-8. Composition of films as-deposited and after sulfur annealing performed repeated times

Annealing Condition	Atomic %					Cu:Zn	Zn:Sn	S:Metals	Thick (nm)
	Cu	Zn	Sn	S	O				
None	27	11	17	45	0.0	2.4	0.67	0.80	160
SA (1X)	24	9	12	46	9.0	2.5	0.82	1.0	175
SA (2X)	24	10	12	48	5.0	2.4	0.83	1.0	175

Note that as-deposited films are significantly Zn-poor, evident as too high a Cu:Zn ratio. The Zn:Sn ratio increases after sulfur annealing, as a result of Sn loss, while the Cu:Zn ratio remains roughly constant. The S:metal ratio of 1.0 indicates complete sulfurization of the film after sulfur annealing. Sulfur annealing can, therefore, effectively mitigate some deviations from desired stoichiometry, by evolving Sn and incorporating S. It was found that additional annealing, identified as **SA (2X)**, does not further change the stoichiometry except to incorporate additional

S and decrease O in the film. This indicates that Sn loss from the film stabilizes once near-stoichiometric concentrations are achieved.

The surface morphologies of the as-deposited and sulfur annealed films are shown in Fig. 6-7. Notably, the sulfur annealed film contains a high density of voids, as seen in Fig. 6-7b-c. These voids are attributed to SnS evolution, evident as the significant decrease in Sn concentration in the film and the disappearance of SnS Raman modes (160cm^{-1}, 188cm^{-1}) previously identified in as-deposited films and shown in Fig. 6-5 (400°C)Fig. 6-10. As the following section will show, as-deposited films containing concentrations of Sn closer to stoichiometry demonstrate corresponding decreases in the density of voids.

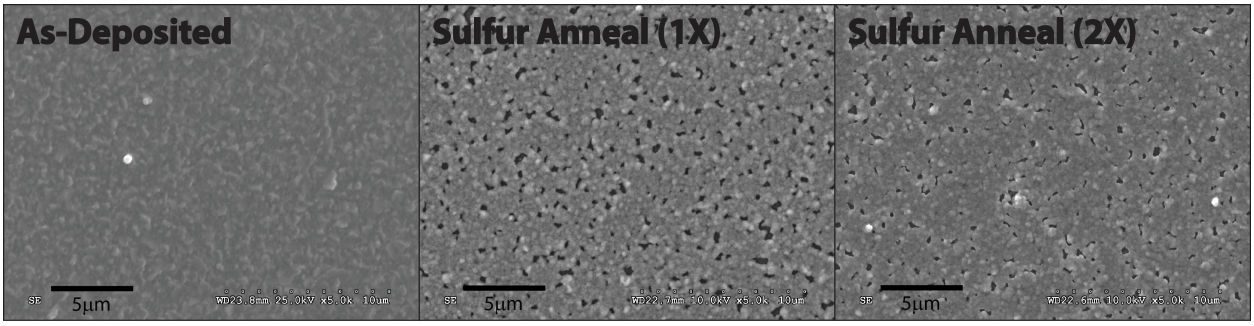

Fig. 6-7. SEM images of films as-deposited and after sulfur annealing performed repeated times

Fig. 6-7 (**SA 2X**) indicates that, after the Sn concentration stabilizes, the number of voids does not increase. In fact, it appears that additional annealing may help heal the voids by coalescing the remaining film. Subsequently, sulfur annealing can mitigate mild stoichiometric deviations in Sn and S, but the as-deposited film compositions must be closer to the ideal stoichiometries to prevent the severe void formation observed here.

6.4.6.2 Cu-Poor, Zn-Rich Films

By modifying the sputtering target compositions, the desired film stoichiometries were achieved for room temperature depositions, as described in Section 6.4.5. Using the CZTS-2 samples from Section 6.4.5 (see Table 6-7), temperature ramp times, dwell times, and temperature profiles of the sulfur annealing process were varied, in order to improve the structural and opto-electronic properties of the films.

Ramp Time

Using the nominal sulfur annealing process with a dwell time of 10min and temperature of 560°C, the ramp times were varied from 7 – 40min. The compositions of the as-deposited and sulfur annealed films are summarized in Table 6-9. Film thickness decreases with increasing ramp time and stabilizes at ramp times greater than 20min, with an as-deposited thickness of 320nm and annealed thicknesses of 290nm at 20min and 40min ramp times.

Table 6-9. Compositions of films as-deposited and sulfur annealed for 10min at 560°C with varying ramp times

Ramp Time	Atomic %					Cu:Zn	Zn:Sn	S:Metals	Thick (nm)
	Cu	Zn	Sn	S	O				
None	18	12	10	37	22	1.5	1.2	0.91	320
7min	19	13	10	45	12	1.5	1.3	1.1	315
20min	21	16	11	48	5.0	1.3	1.4	1.0	290
40min	21	15	11	49	4.0	1.4	1.4	1.0	290

Several notable trends in films composition emerge with increasing ramp time. First, the relative Zn concentration increases with increasing ramp time, evident as a monotonically increasing Zn:Sn ratio and generally decreasing Cu:Zn. Second, the S:metal ratio rises significantly for the 7min ramp time compared to the as-deposited film, but then stays nearly constant with increasing ramp time. Finally, oxygen concentration monotonically decreases with increasing ramp time.

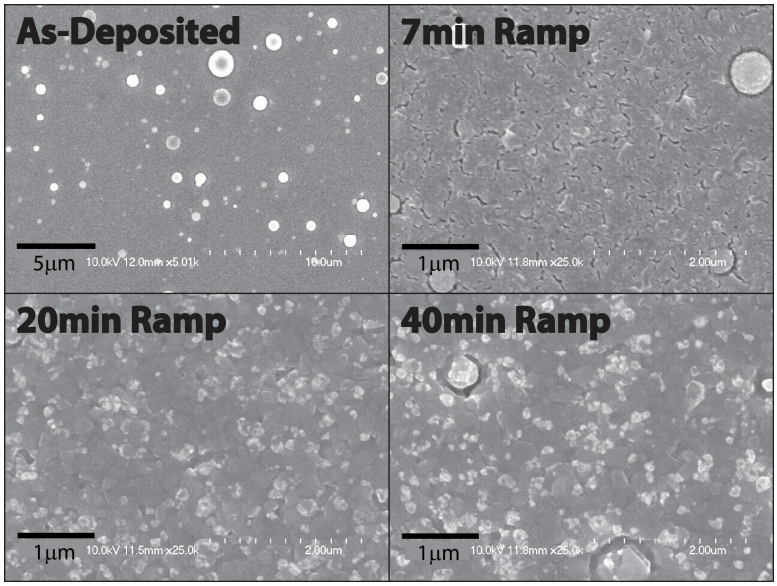

Fig. 6-8. SEM images for films as-deposited and sulfur annealed for 10min at 560°C with varying ramp times

Rutherford backscattering measurements (not shown) indicate decreases of 5–15at% in Sn concentration at the surfaces of sulfur annealed films. The increase in Zn:Sn ratio in the annealed films can therefore be primarily attributed to the loss of Sn at the surfaces of the films. Note that the film composition (including the Sn gradient) and the film thickness both stabilize at ramp times longer than 20min. As described in Chapter 4, the Cu-Zn RBS peaks contain significant overlap, and the PIXE measurements used to resolve the Cu:Zn ratios are not able to provide depth-resolved composition information. Therefore, while the combined Cu-Zn RBS peak does

not show any through thickness variation, opposing grading of the Cu and Zn elements in the film could mask individual variations. The S peaks show no concentration gradients.

The surface morphologies of the as-deposited and sulfur annealed films are shown in Fig. 6-8. The as-deposited films contain a significant number of large particles on the surface, which we attribute to the large laser fluences (3.5J/cm^2) used to ensure deposition above the ablation threshold and to degraded surface quality of the sputtering target caused by the deposition history.

The 7min ramp sample shows a significant density of elongated voids several 100nm in length. The samples with longer ramp times of 20min and 40min show fewer voids and more light colored surface decorations. These lighter surface decorations are attributed to ZnS phases, since the films are Zn-rich and likely to co-form ZnS and CZTS phases during crystal formation as detailed in Chapters 2 and 3. Further, these surface decorations increase with increasing relative Zn concentration in the films, and similar features have been attributed to ZnS in [41]. Finally, ZnS has been shown to be selectively etched by hydrochloric acid [42], and etching for 3min in 1.5M HCl effectively removed these surface decorations. However, no significant changes in the film composition or in the structure (Raman spectra) were observed, preventing additional confirmation of the removal of Zn or ZnS from the film.

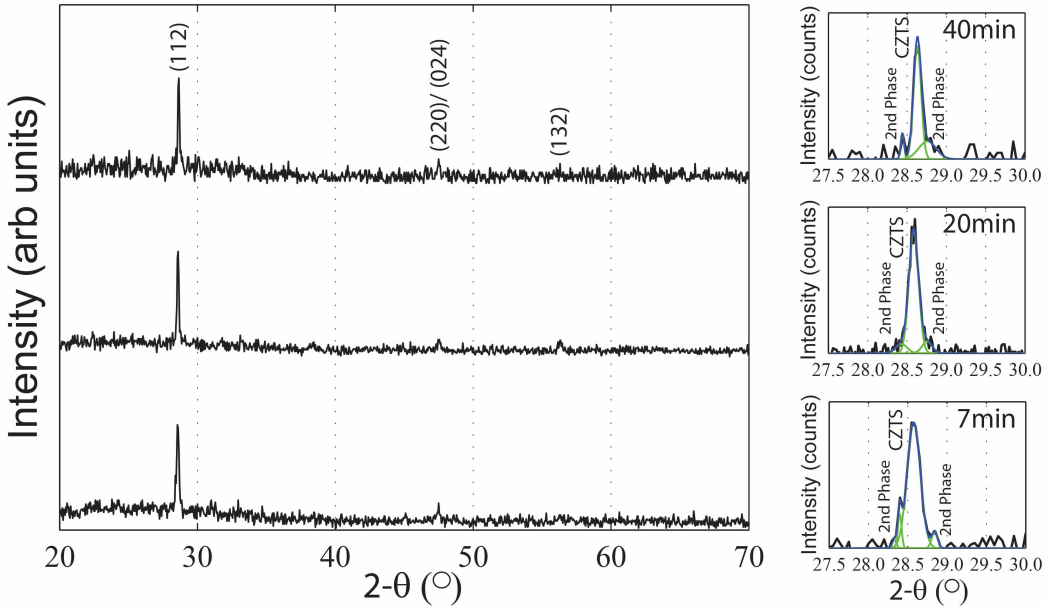

Fig. 6-9. X-ray diffractograms for films sulfur annealed for 10min at 560°C with varying ramp times

Sulfur annealed films show more pronounced voids around the splashed surface particles, which likely increase the local instability of the films as a result of their increased surface area to volume ratios. Consequently, lower laser fluences and target reconditioning should be investigated in the future, in order to reduce the number of splashed particles and to improve the as-deposited film surface quality.

Fig. 6-9 shows x-ray diffractograms for the sulfur annealed films, and Table 6-10 shows the 2-θ positions and widths of the characteristic (112) peaks. Note the as-deposited film (not shown) does not exhibit any diffraction peaks. All sulfur annealed films indicate likely kesterite structure with strongly-preferred (112)-orientation. Small (220)/(024) and (132) peaks associated with kesterite CZTS are also visible in the wide-scan diffractograms.

Narrow-scan diffractograms, shown in the right side of Fig. 6-9, indicate the presence of a dominant peak near 28.58°, attributed to CZTS (112), with two smaller peaks near 28.4° and 28.8°, attributed to secondary phases. As summarized in Table 6-10, the fitted (112) peak shifts from 28.58° to 28.63° as the ramp time increases from 7min to 40min, which may indicate either a decrease in CZTS lattice constant or increase in secondary phase. The fitted (112) peak widths also decrease with increasing ramp time, indicating an increase in the crystallite size, as expected with effectively longer times above minimum CZTS formation temperature (e.g. longer ramp times).

Table 6-10. Structural properties of films as-deposited and sulfur annealed for 10min at 560°C with varying ramp times

Ramp Time	(112) 2-θ (°)	(112) FWHM (°)	A-Mode (cm^{-1})
None	-	-	-
7min	28.58	0.197	335
20min	28.59	0.143	337
40min	28.63	0.113	336

The shoulders on both sides of the (112) peak likely indicate the presence of secondary phases. Based on the accuracy limits of the x-ray diffractometer, described in Chapter 4, possible assignments for the peaks near 28.4° include cubic-SnS (111), Hex(P-3m1)–SnS_2 (100), cubic (F-43m)–Cu_2SnS_3 (111) [43], orthorhombic(Pmn21)-Cu_3SnS_4 [43], $Cu_4Sn_7S_{16}$ (202/116), and various ZnS phases. Possible assignments for the peaks near 28.8° include cubic–CuS (111), orthorhombic–Cu_3SnS_4 (222), and orthorhombic–Cu_4SnS_4 (102/410). Reference peak locations are taken from the JCPDS files identified in Table 4-7, unless otherwise specified in previous list.

Raman spectroscopy was performed on the films, in order to help differentiate the presence of secondary phases. Fig. 6-10 shows Raman spectra for the sulfur annealed films, and Table 6-10 notes the wavevector positions of the dominant A-mode peak for CZTS. Characteristic CZTS Raman modes are evident at 252cm^{-1} (E-TO mode), 286cm^{-1} (A-mode), 336cm^{-1} (A-mode), 353cm^{-1} (E-TO mode) and 373cm^{-1} (B-LO mode). Like x-ray diffraction, however, many of the common secondary phases share similar Raman mode locations, as noted in Section 4.2.3. The Raman spectra generally have the characteristic shapes associated with kesterite CZTS [11, 37]. The dominant CZTS A-mode (335-337cm^{-1}) indicates decreasing peak width and increasing

Raman shift (e.g. shift to right) with increasing ramp time. Since the other characteristic CZTS modes do not shift with ramp time, we attribute the decrease in the peak width and associated shift right in the peak maximum to decreases in secondary phase Raman modes near 310 – 320cm^{-1}. Raman modes in this range have been attributed to SnS_2, $Cu_2Sn_3S_7$ and Cu_3SnS_4 [34, 36, 43-45]. A subtle peaks near 308cm^{-1}, identified with an arrow in Fig. 6-10, suggests the presence of Cu_2SnSn_3 phases [43].

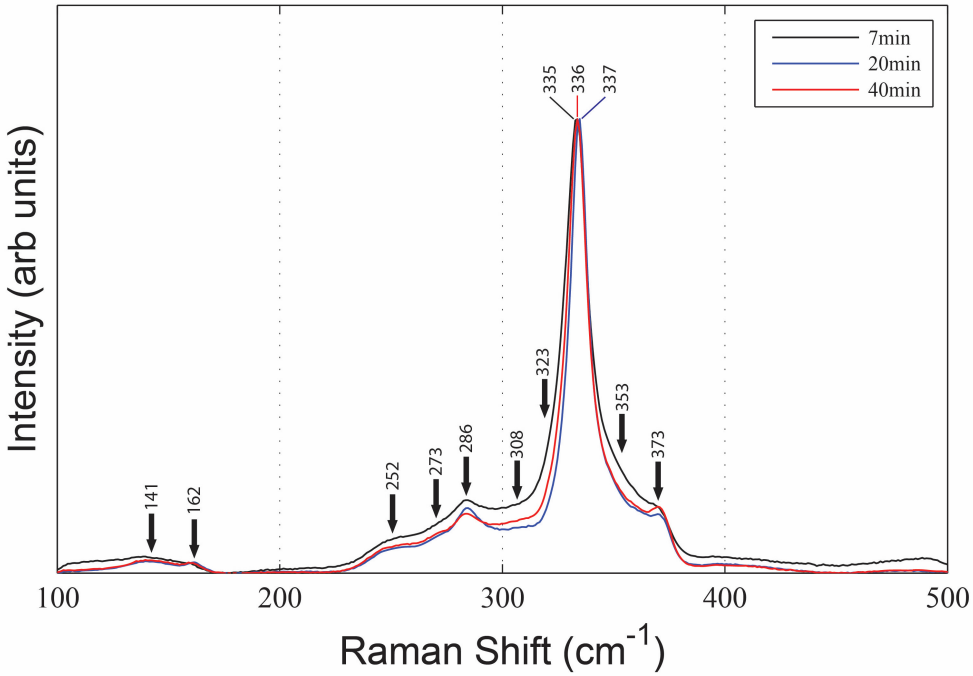

Fig. 6-10. Raman spectra for films sulfur annealed for 10min at 560°C with varying ramp times

Small but well-defined peaks observed near 141, 162, and 273cm^{-1} have been associated with CZTS Raman modes in [37]. Since varying sulfur anneal conditions do not significantly modify the relative intensity of these modes compared to the other characteristic CZTS modes, we assign these small peaks to CZTS. The 141cm^{-1} mode may possibly be assigned to CuS, but we observe no evidence of the typically dominant 475cm^{-1} mode [34, 46]. Similarly, the 162cm^{-1} mode may be possibly be assigned to SnS, but we observe no evidence of the sister 190cm^{-1} mode [34-36], as exhibited in Fig. 6-5.

Considering the possible phases identified in Raman, we may then restrict the likely phases contributing to the 28.4° diffraction peak to SnS_2, Cu_2SnS_3 and Cu_3SnS_4 phases. Similarly, the 28.8° peak may be attributed to Cu_3SnS_4 and/or Cu_4SnS_4 phases. ZnS phases may also contribute to the 28.4° and 28.8° shoulders of the CZTS peak, as interpreted in [34] for right-shouldered (112) peaks, although these phases cannot be reliably detected with 488nm excitation, as previously discussed.

Fig. 6-11 and Fig. 6-12 show the optical absorption and $(\alpha \cdot h\nu)^2$ vs. hν plots for the as-deposited and sulfur annealed films, respectively. The optical absorption coefficients and band gaps were calculated as noted in Section 6.3, and the band gaps are summarized in Table 6-11.

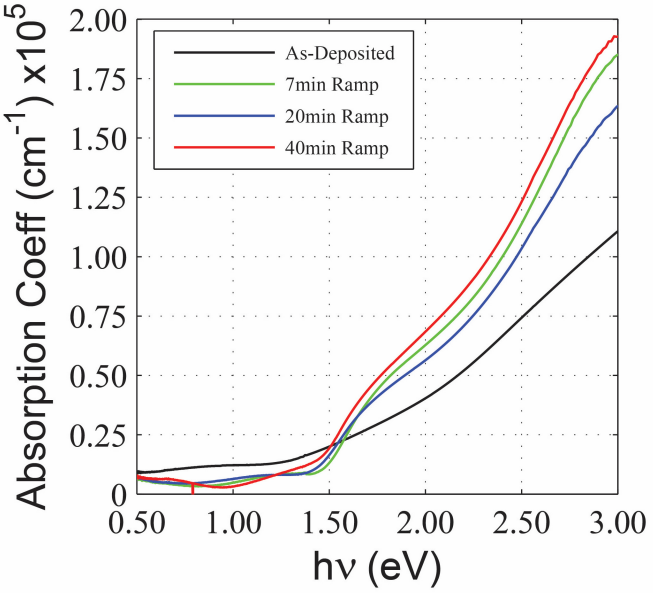

Fig. 6-11. Optical absorption coefficient curves for films sulfur annealed for 10min at 560°C with varying ramp times: 7min – 40min

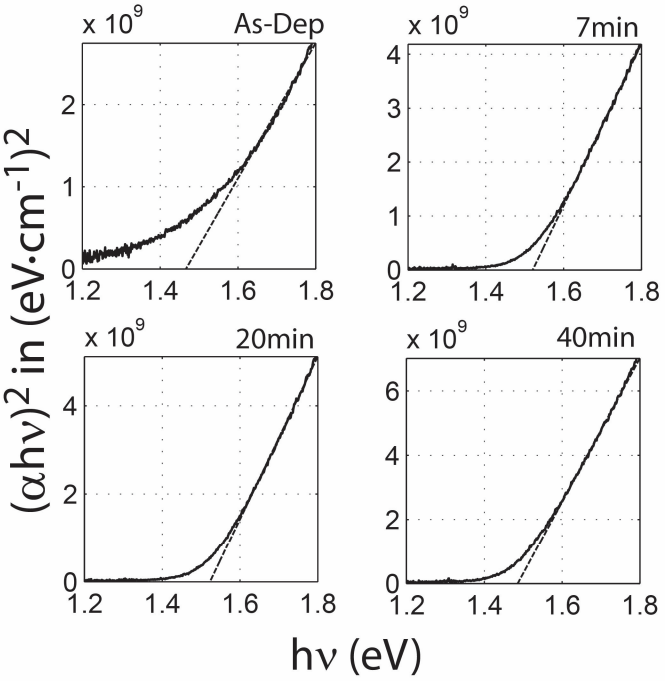

Fig. 6-12. Plots of $(\alpha \cdot h\nu)^2$ vs. (hν) for films sulfur annealed for 10min at 560°C with varying ramp times

The optical absorption curves indicate high absorption values (>$10^4 cm^{-1}$) at photon energies just above the band edge near 1.5eV. As expected, the absorption edges for the sulfur annealed films sharpen significantly compared to the room temperature, as-deposited films, consistent with improving crystallinity. Moreover, the staircase shapes observed in the sulfur annealed films (steep rise – shallower rise – steeper rise) are generally consistent with the theoretically predicted curves in [47], although the slopes and the transition energies are shifted.

The slope of the absorption curve at the band edge decreases and the band gaps decrease in energy with increasing ramp time, as shown, respectively, in Fig. 6-11 and Fig. 6-12. The band gap variations measured (1.52eV –1.49eV) are negligible, howver, given the inherent fit errors associated with this method of calculation.

Table 6-11. Opto-electronic properties of films as-deposited and sulfur annealed for 10min at 560°C with varying ramp times

Ramp Time	ρ (ohm·cm)	E_g (eV)
None	-	-
7min	7.6e1	1.52
20min	1.1e2	1.53
40min	3.2e1	1.49

Due to low Hall mobilities, carrier concentrations and Hall mobilities could not be reliably calculated. The film resistivities, however, were measured as shown in Table 6-11. Note that the 7min ramp contains a significant number of voids, which may alter the measured resistivity. The film resistivities correlate most reliably with the Raman CZTS A-mode peak location and width: the smaller the peak width and the closer to 337cm^{-1}, the higher the film resistivity. This correlation likely indicates that the film resistivity depends strongly on the presence of secondary phases, to which variations in A-mode peak width and location have been attributed.

Dwell Time

Using the nominal sulfur annealing process with a ramp time of 20min and temperature of 560°C, the dwell times were varied between 10 and 30min. The compositions of the as-deposited and sulfur annealed films are summarized in Table 6-12. Film thickness decreases with increasing dwell time, stabilizing at ramp times greater than 20min, with as-deposited thickness of 320nm and annealed thicknesses of 290nm at 10min and 30min dwell times.

Two notable trends in films composition emerge with increasing dwell time, similar to those observed with varying ramp time. After sulfur annealing for 10min dwell time, the Zn:Sn ratio increases significantly and the Cu:Zn ratio decreases, indicating a general increase in the relative Zn concentration in the films. Further, the S:metal ratio rises to stoichiometric ratio of 1

and the oxygen content decreases to ~ 5%. With the longer anneal time of 30min, however, no significant changes in the film composition are observed. Film thicknesses for the two sulfur annealed samples are both ~ 290nm, and Rutherford backscattering measurements show similar decreases of ~15% in Sn concentration at the surfaces. Like the samples annealed with varying ramp time, the film composition, including the Sn gradient, as well as the film thickness, stabilizes under longer annealing times (in this case longer dwell time).

Table 6-12. Compositions of films as-deposited and sulfur annealed 20min ramp to 560°C and varying dwell times

Dwell Time	Atomic %					Cu:Zn	Zn:Sn	S:Metals	Thick (nm)
	Cu	Zn	Sn	S	O				
None	18	12	10	37	22	1.5	1.2	0.91	320
10min	21	16	11	48	5.0	1.3	1.4	1.0	290
30min	21	15	11	47	6.0	1.4	1.4	1.0	290

The surface morphologies of the sulfur annealed films are shown in Fig. 6-13, and the as-deposited film may be found in Fig. 6-8. As Fig. 6-13 shows, the number of elongated voids increases significantly with increasing dwell time. Further, the 30min dwell time sample shows a decrease in the number of lighter surface decorations, previously attributed to ZnS. The film surface morphology for the 20min ramp – 30min dwell sample looks quite similar to the surface morphology observed in the 7min ramp – 10min dwell sample, shown previously in Fig. 6-8.

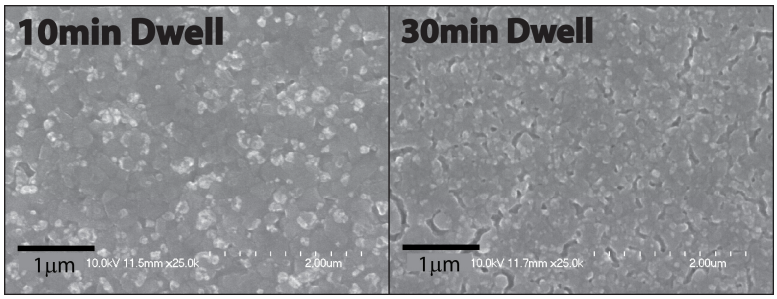

Fig. 6-13. SEM images for films sulfur annealed with 20min ramp to 560°C and varying dwell times

The wide 2-θ scan diffractograms for the 10min and 30min dwell samples (not shown) appear similar to those in Fig. 6-9, with only the (112), (220)/(024) and (132) peaks again evident; thus, the wide-scan diffractograms are omitted here. The middle inset in Fig. 6-9 shows the magnified view of the (112) peak for the 20min ramp – 10min dwell sample, and Fig. 6-14 shows the magnified view for the 20min ramp – 30min dwell sample. Table 6-14 shows the 2-θ positions and widths of the characteristic (112) peaks.

The narrow-scan diffractogram, shown in Fig. 6-14, indicates the presence of a dominant peak near 28.59°, attributed to CZTS (112), with the smaller peak near 28.7°, attributed to secondary phases. As summarized in Table 6-13, the fitted (112) peak location remains constant

but the peak width increases significantly with increasing dwell time, indicating a decrease in film crystallinity. This width increase is unexpected, as additional annealing should improve crystallinity. Similar to the previous section, possible assignments for the peak near 28.7° include cubic–CuS, orthorhombic–Cu_3SnS_4, orthorhombic–Cu_4SnS_4, and ZnS.

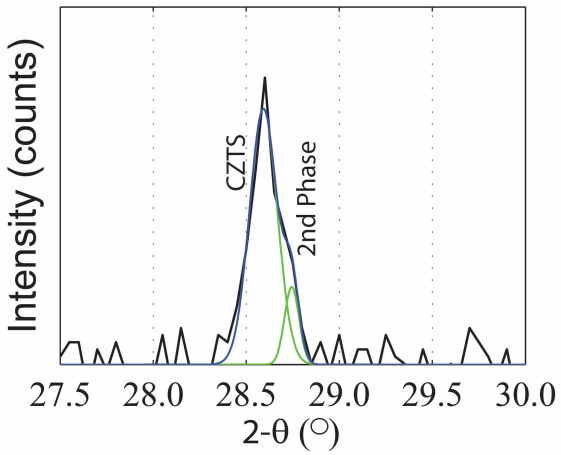

Fig. 6-14. X-ray diffractogram (magnified) for film sulfur annealed with 20min ramp–30min dwell at 560°C

Fig. 6-15 shows Raman spectra for the sulfur annealed films. The characteristic CZTS Raman modes are again evident at 251cm^{-1}, 286cm^{-1}, 335cm^{-1}, 353cm^{-1}, and 372cm^{-1}, with the additional peaks at 140, 161, and 274cm^{-1} also assigned to CZTS. The dominant CZTS A-mode (335-337cm^{-1}) indicates increasing peak width and decreasing Raman shift (e.g. shift to left) with increasing dwell time. As described in the previous section, this increase in the peak width and associated shift left in the peak maximum can be attributed to increases in secondary phase Raman modes near 310 – 320cm^{-1}, possibly SnS_2, $Cu_2Sn_3S_7$ and Cu_3SnS_4 phases [34, 36, 43-45]. A subtle peak near 308cm^{-1}, identified with an arrow in Fig. 6-15, again suggest the presence of Cu_2SnSn_3 phases [43]. Similar to the previous section, we may then restrict likely phases contributing to the 28.8° diffraction peak to Cu_3SnS_4, Cu_4SnS_4, and/or ZnS phases.

Table 6-13. Structural properties as-deposited and sulfur annealed with 20min ramp to 560°C and varying dwell times

Ramp Time	(112) 2-θ (°)	(112) FWHM (°)	A-Mode (cm^{-1})
None	-	-	-
10min	28.59	0.143	337
30min	28.59	0.175	335

Despite the development of voids in the 30min anneal sample, the film composition and film thickness remain stable, indicating no significant additional Sn loss compared to the 10min

dwell sample. However, the XRD spectrum indicates a decrease in crystallinity, evident as a decrease in (112) peak width, and the Raman spectrum indicates the presence of secondary Cu-Sn-S phases, evident as a broadening and shift in CZTS A-mode peak. At the longest (40min) ramp time, the Raman A-mode also showed a similar broadening and shift, although to a lesser extent. The 40min ramp sample, however, showed a continued decrease in the (112) peak width.

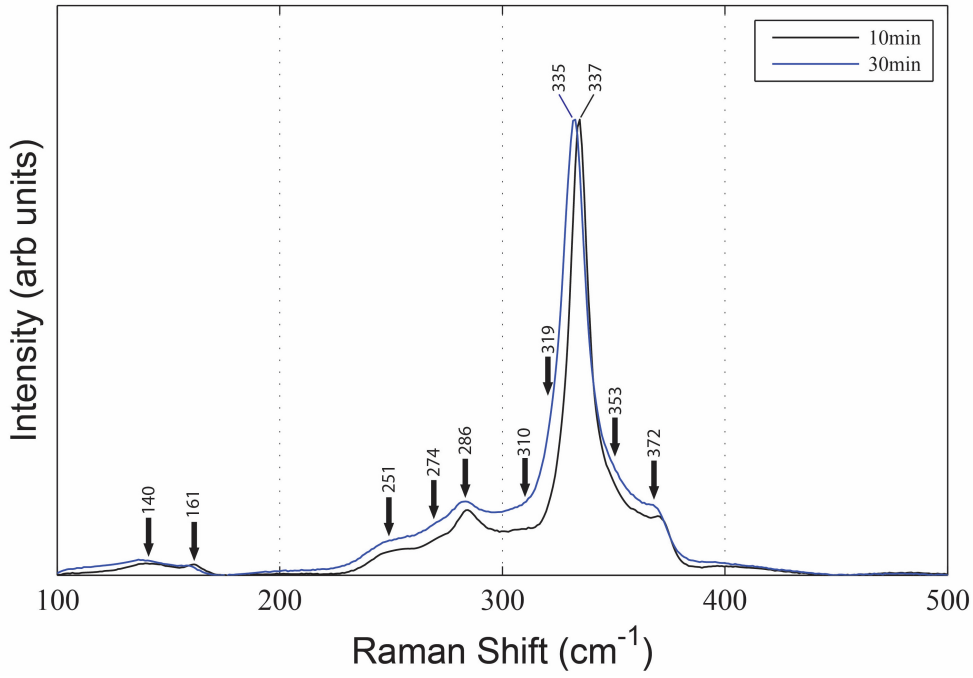

Fig. 6-15. Raman spectra for films sulfur annealed with 20min ramp to 560°C and varying dwell times

The increase in voids and decrease in crystallinity are difficult to explain given the relative stability in the film composition and thickness. If film decomposition were active, as detailed further in Section 6.4.6.3, due to a loss in sulfur overpressure with the longer dwell times, additional losses in Sn and film thickness would be expected.

Table 6-14. Opto-electronic properties as-deposited and sulfur annealed with 20min ramp to 560°C and varying dwell times

Dwell Time	ρ (ohm·cm)	E_g (eV)
None	-	-
10min	1.1e2	1.53
30min	2.3e1	1.50

The optical absorption and $(\alpha \cdot h\nu)^2$ vs. $h\nu$ plots for the varying dwell time samples appear similar to those in Fig. 6-11 and Fig. 6-12, respectively; subsequently, they are omitted here.

Relevant band gap data, as well as film resistivities, however, are summarized in Table 6-14. As with the varying ramp time samples, the films resistivities track most reliably with the Raman CZTS A-mode peak location and width. In this case, the resistivity decreases with increasing anneal time, as the A-mode peak widens and shifts to lower values.

Temperature Profile

Using the nominal sulfur annealing process with a temperature of 560°C, the temperature profiles were varied as detailed in Table 6-15 below.

Table 6-15. Summary of annealing temperature profiles

ID	Ramp (min)	Dwell (min)	Temp (°C)
TP1	7	10	560
TP2	TP1 profile, 3X		
TP3	5/ 5	30/ 10	200/ 560

The compositions of the as-deposited and sulfur annealed films are summarized in Table 6-16. First, we note that the film composition of the multiple anneal sample (TP2) appears similar to the stabilized film compositions observed with the long ramp and long dwell time samples. The film thickness of this sample also remains at a similar value (290nm) to those of the long ramp and long dwell time samples. Moreover, the multiple annealed sample (TP2) also exhibited similar loss Sn concentration near the surface, compared to the single anneal sample (TP1).

Table 6-16. Compositions of films as-deposited and sulfur annealed at 560°C with varying temperature profiles

ID	Atomic %					Cu:Zn	Zn:Sn	S:Metals	Thick (nm)
	Cu	Zn	Sn	S	O				
None	18	12	10	37	22	1.5	1.2	0.91	320
TP1	19	13	10	45	12	1.5	1.3	1.1	315
TP2	21	15	11	48	5.0	1.4	1.4	1.0	290
TP3	20	14	11	47	9.0	1.4	1.4	1.1	300

The multiple anneal sample (TP2), seen in Fig. 6-16, exhibits similar surface morphology to those of the long ramp (short dwell time only) samples. The voids evident in the single anneal sample (TP1) do not appear in the multiple anneal sample (TP2), and the TP2 surface contains a significant number of lighter colored decorations previously attributed to ZnS phases.

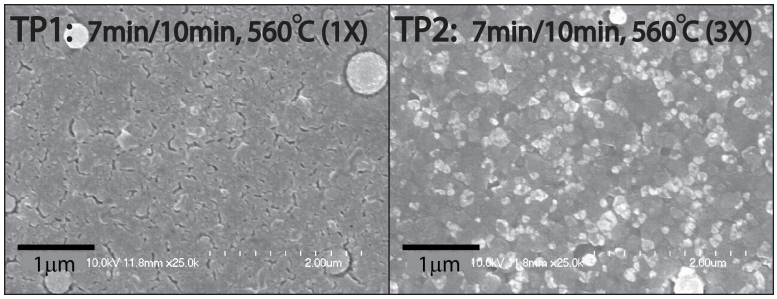

Fig. 6-16. SEM images for films sulfur annealed at 560°C with temperature profiles: TP1 (1X) and TP2 (3X)

The film annealed with temperature profile (TP3) exhibits a composition between the high ramp anneal sample (TP1) and the longer ramp (40min) samples, with the stabilized compositions previously discussed. The oxygen content was also in between these samples, indicating that time at the higher temperatures are required in order to purge the films of the oxygen. Moreover, the film thickness of the TP3 sample (~300nm) lies between the TP1 sample and longer anneal samples, with the Sn-deficiency confined to a smaller region near the film surface.

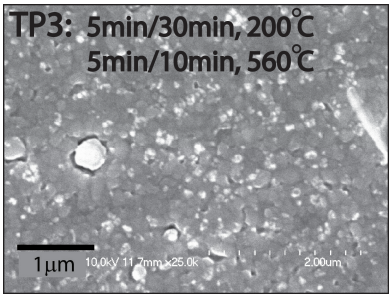

Fig. 6-17. SEM images for film sulfur annealed at 560°C with temperature profile, TP3

The surface morphology of the TP3 sample, shown in Fig. 6-17, indicates a morphology in between those of the short ramp (TP1) and the longer ramp (40min) samples. TP3 contains some elongated voids, but at a much lower density, and the surface contains some light colored surface decorations but also at a lower density than the longer ramp (40min) samples.

The wide 2-θ scan diffractograms for the TP2 and TP3 temperature profile samples (not shown) appear similar to those in Fig. 6-9, with only the (112), (220)/(024) and (132) peaks again evident; thus, the wide-scan diffractograms are omitted here. The bottom inset in Fig. 6-9 shows the magnified view of the (112) peak for the 7min ramp – 10min dwell sample (TP1), and Fig. 6-14 shows the magnified views for the TP2 and TP3 samples. Table 6-14 shows the 2-θ positions and widths of the characteristic (112) peaks.

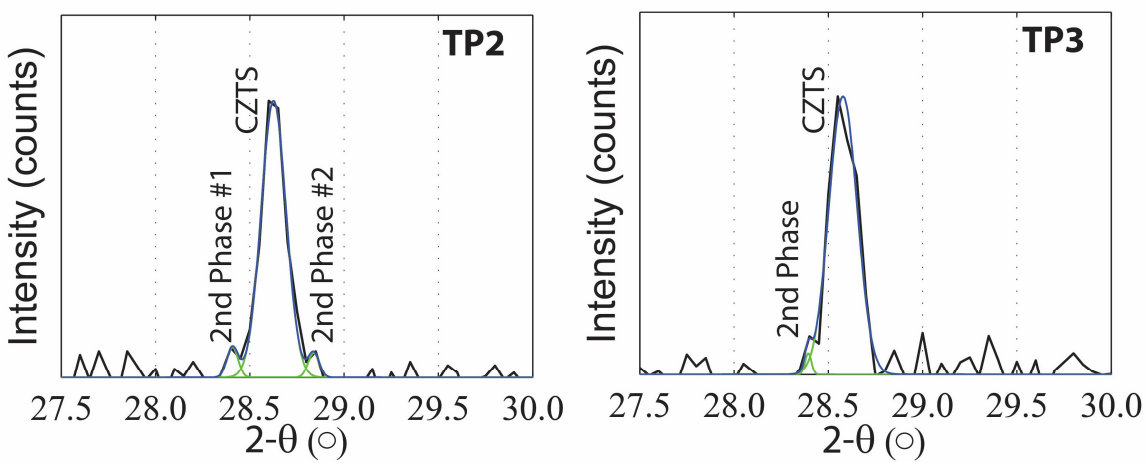

Fig. 6-18. X-ray diffractograms for films sulfur annealed at 560°C and varying temperature profiles

The narrow scan diffractograms, shown in Fig. 6-18, indicate the presence of dominant peaks attributed to CZTS (112), with smaller peaks near 28.4° and 28.8° attributed to secondary phases. As summarized in Table 6-17, the (112) peak shifts from 28.58° (TP1) to 28.63° (TP2) with multiple anneals. As before, this shift may be associated with a smaller lattice constant, or with a secondary phase. Multiple annealing improves the crystallinity of the deposited film, with FWHM decreasing from 0.197° (TP1) to 0.157° (TP2). The TP1 and TP2 diffractograms, shown in Fig. 6-9 and Fig. 6-18, respectively, show secondary phase peaks at 28.4° and 28.8°. Similar to previous sections, possible assignments for the peaks near 28.4° include cubic-SnS, Hex–SnS_2, cubic–Cu_2SnS_3, orthorhombic-Cu_3SnS_4, $Cu_4Sn_7S_{16}$, and various ZnS phases. Possible assignments for the peak near 28.8° include cubic–CuS, orthorhombic–Cu_3SnS_4, orthorhombic–Cu_4SnS_4, and ZnS.

Table 6-17. Structural properties of films as-deposited and sulfur annealed at 560°C with varying temperature profiles

ID	(112) 2-θ (°)	(112) FWHM (°)	A-Mode (cm^{-1})
None	-	-	-
TP1	28.58	0.197	335
TP2	28.63	0.156	335
TP3	28.58	0.176	336

More significantly, Fig. 6-18 shows negligibly small secondary phases present near the (112) peak for TP3; if present, the small peak at 28.4° may be assigned as above. The (112) peak width of TP3 improves compared to the fast ramp sample (TP1), but remains small compared to longer ramp samples (20min and 40min) described in previous sections.

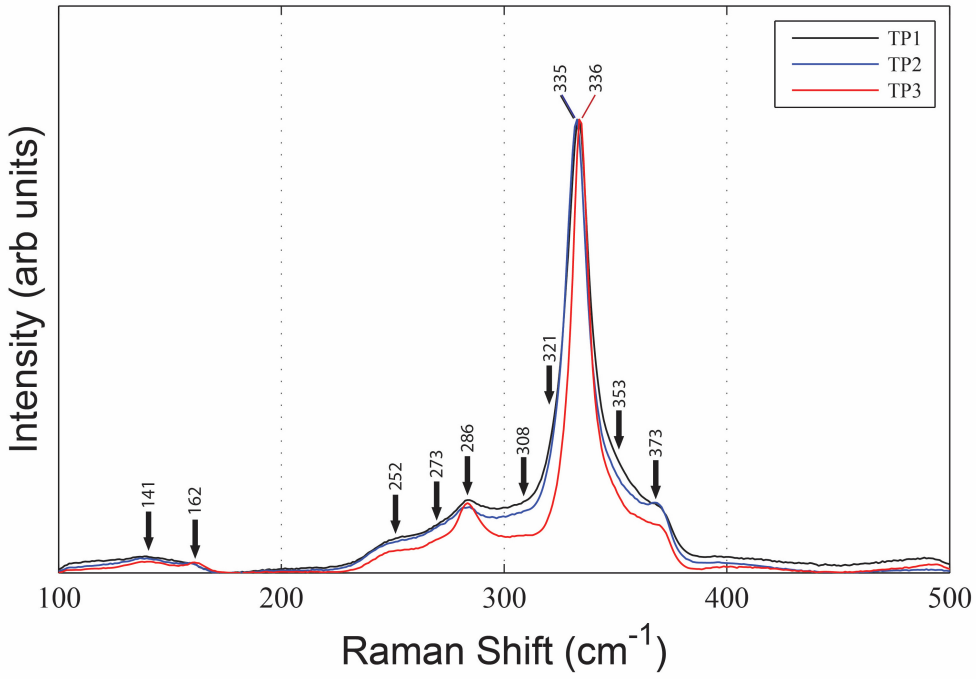

Fig. 6-19. Raman spectra for films sulfur annealed at 560°C and varying temperature profiles

Fig. 6-19 shows Raman spectra for the sulfur annealed films. The characteristic CZTS Raman modes are again evident at 252cm^{-1}, 286cm^{-1}, 336cm^{-1}, 353cm^{-1}, and 373cm^{-1}, with the additional peaks at 141, 162, and 273cm^{-1} also assigned to CZTS. With multiple anneals (TP2), the dominant CZTS A-mode (335cm^{-1}) slightly widens and decreases (e.g. shifts to left) compared to the single anneal (TP1). As described before, the general widening and shifting of the A-mode can be attributed to increases in secondary phase Raman modes near 310 – 320cm^{-1} (possibly SnS_2, $Cu_2Sn_3S_7$ and Cu_3SnS_4 phases), and the smaller peak near 308cm^{-1} suggests the presence of Cu_2SnSn_3 phases. Similar to the previous section, we may then restrict likely phases contributing to the 28.4° diffraction peak to SnS_2, Cu_2SnS_3, Cu_3SnS_4 and/or ZnS phases, and the phases contributing to the 28.8° peak to Cu_3SnS_4, Cu_4SnS_4, and/or ZnS phases.

Table 6-18. Opto-electronic properties of films as-deposited and sulfur annealed at 560°C with varying temperature profiles

ID	ρ (ohm·cm)	E_g (eV)
None	-	-
TP1	7.6e1	1.52
TP2	4.3e1	1.49
TP3	8.2e2	1.55

More significantly, the film annealed with temperature profile (TP3) exhibited the sharpest A-mode peak with one of the highest Raman shifts of 336cm^{-1} (e.g. closest to ideal position) of all

the pulsed laser deposited films, consistent with a significant decline in the secondary phase modes near 310 – 320cm^{-1}. Further, the (112) peak exhibited minimal shoulder, thus also indicating minimal contribution from secondary phases.

The optical absorption and $(\alpha \cdot h\nu)^2$ vs. $h\nu$ plots for the varying dwell time samples appear similar to those in Fig. 6-11 and Fig. 6-12, respectively; subsequently, they are omitted here. Relevant band gap data, as well as film resistivities, however, are summarized in Table 6-15. As with the varying ramp time and varying dwell time samples, the films resistivities track most reliably with the Raman CZTS A-mode peak location and width. In this case, the sample annealed with temperature profile TP3 achieved the highest resistivity (820 Ω-cm) by a significant margin. As discussed above, this sample also had the narrowest Raman A-mode band and smallest secondary phases peaks accompanying the (112) diffraction peak.

6.4.6.3 Proposed Growth Mechanisms

Sulfur annealing decreased the film thickness, decreased the Sn concentration near the surface of the films, and formed voids with varying severity in the films. The film thickness and the Sn-loss in the films stabilized at increasing ramp times and increasing dwell times. However, while increasing ramp time decreased the concentration of voids, increasing the dwell time increased the concentration of voids. This increased in voids with dwell time is unexpected, given the relative stability in the film thickness and composition. The two-step temperature profile TP3 yielded a film thickness in between the short ramp-short dwell time sample and the long ramp and the long dwell time samples. Sn-loss was also confined to a smaller region near the film surface.

The Sn-loss near the surface of the films and the overall decrease in film thickness must result from the evolution of unstable phases in the film. However, the stabilization of film compositions and thicknesses at ramp times greater than 20min and dwell times greater than 10min suggests that these loss mechanisms are most active early in the sulfur annealing process. This time-dependent stabilization may indicate kinetically-limited crystal growth.

According to [48] (see Section 3.3.2.2), kesterite Cu_2ZnSnS_4 may form according to the following two reaction pathways:

$$Cu_2S + ZnS + SnS + \frac{1}{2}S_2 \rightleftarrows Cu_2ZnSnS_4 \tag{6-1}$$

$$Cu_2SnS_3 + ZnS \rightleftarrows Cu_2ZnSnS_4 \tag{6-2}$$

where Cu_2SnS_3 forms by reaction of Cu_2S and SnS. Reaction (6-1) and the Cu_2SnS_3 formation may actually proceed by any stoichiometric combination of the metal-sulfide binary variants [48]. Hergert, however, notes experimental evidence that Cu_2SnS_3 phases would likely only emerge in well-mixed, *Zn-poor* CZTS films [48]. Further, using Olekseyuk's phase diagram [3], Scragg shows

the various metal-rich regions for CZTS and the likely secondary phases formed [11]. Cu_2SnS_3 and Cu_4SnS_4 phases are shown to form in Cu-rich/Zn-poor films [11]. Consequently, if we attribute the (112) diffraction peak shoulders and the Raman CZTS A-mode broadening at 310 – 320cm^{-1} to Cu-Sn-S secondary phases, such as Cu_2SnS_3 and Cu_3SnS_4, then these phases do not likely emerge as a result of decomposition of the Zn-rich CZTS films according to reaction (6-2). If films are decomposing according to reaction (6-1) as described in [7], then evidence of the metal-sulfide binary decomposition products (Cu_2S, SnS and ZnS) should be evident in the films, in particular Cu_2S and ZnS, corresponding to Sn-poor compositions [11]. While ZnS may not be identified, as detailed before, characteristic Cu_2S and SnS Raman modes of any significance are notably absent.

To investigate the effect of potential sulfur loss from the graphite annealing box, the 40min ramp sample was repeated with 9.0mg of sulfur (compared to 4.5mg). No significant changes in the composition, morphology, or structure were observed. In particular, the Sn-concentration gradient through the films remained identical. If the Sn loss were induced by phase decomposition resulting from loss of sulfur overpressure, increasing the elemental sulfur in the graphite box should delay its onset and reduce the Sn-concentration gradient in the film. Consequently, decomposition of the films resulting from a loss of S-overpressure seems less likely, at least for the 40min ramp profile examined.

Instead, we suggest that amorphous Cu-Sn-S phases and amorphous CZTS are present in the as-deposited films. The existence of these phases reduces the diffusion of the metallic and binary metal-sulfides, which leads to kinetically-limited crystal formation. Salome examined the formation reaction of CZTS using Cu_2SnS_3 and ZnS precursor layers [4]. In that study, ZnS was shown to have poor diffusion in the Cu_2SnS_3 leading to incomplete mixing and crystal formation [4]. Hydrogen gas (H_2) background was shown to improve this ZnS diffusion. The Raman spectrum of the as-deposited CZTS-2 sample is similar to the room temperature as-deposited CZTS-1 sample, shown in Fig. 6-5. Amorphous CZTS bands, and likely other Cu-Sn-S bands, are evident between 200 – 400cm^{-1}. Annealing likely involves a large number of nuclei early in the growth, resulting from amorphous seed phases, further slowly diffusion and formation. This slower crystal growth might allow evaporation of segregated volatile phases, possibly SnS or SnS_2.

The behavior exhibited by sulfur annealing of Sn-rich films supports this growth model. The films deposited at 400°C exhibited predominately CZTS phases with large grains, as well as significant SnS phases. The films demonstrated a significant voids after sulfur annealing, but film thickness increased and the Sn-concentration remained uniform the film depth. That is, the CZTS phase remained stable, while secondary SnS phases were evolved. Similarly, in the room temperature (CZTS-2) deposited film investigated in this section, the film composition does not

change significantly once the CZTS films are formed and stabilized. However, during the time it takes to react and form the stable CZTS phases, unstable secondary phases (likely SnS) are evolved.

Note that the loss of SnS phases, regardless of the crystal growth mechanism, is unexpected given the high background pressure of elemental sulfur. In [7], the predicted partial pressure of SnS required to prevent evaporation is given by $p_{SnS}(p_{S2})^{1/2} > (3.8\pm1.2)x10^{-5}$ mbar. As given in Section 3.3.3.3, 4.5mg of sulfur corresponds to a total sulfur pressure of 0.69atm. At 550°C and saturation conditions, the S_2 partial pressure is 300mbar [7]. While the sulfur is not at saturation, we note that the S_2 species mole fraction increases with superheating, such that a reasonable approximation to its partial pressure may be given as 300mbar, under the given annealing conditions. Reference [49] and see Section 3.3.3.3 for further discussion. Given p_{S2} of 300mbar, then the minimum SnS partial pressure is $2.2x10^{-6}$mbar.

CZTS has an atomic density of ~$5.0x10^{22}cm^{-3}$, as noted in Section 4.1.1.2. With approximately 1 Sn atom for every 8 CZTS atoms, the Sn in the film has an atomic density of ~$6.2x10^{21}cm^{-3}$. Assuming SnS behaves as an ideal gas, a reasonable approximation given the low pressures, then the thickness of film that must be evaporated in order to stabilize the evolution of SnS may be calculated as follows (for 0.6x0.6cm film):

$$n_{SnS} = \frac{p_{SnS}V_{graphite}}{RT} = \frac{(2.2x10^{-7}kPa)(3.36cm^3)}{(8314.47kPa\cdot cm^3/mol\cdot K)(823K)} = 1.1x10^{-13}mol \quad (6\text{-}3)$$

$$N_{Sn} = N_A n_{SnS} = (6.022x10^{23}at/mol)(1.1x10^{-13}mol) = 6.5x10^{10}at \quad (6\text{-}4)$$

$$t_{film} = \frac{1}{A_{film}}\left(\frac{N_{Sn}}{\rho_{Sn(CZTS)}}\right) = \left(\frac{1}{0.60x0.60cm^2}\right)\left(\frac{6.5x10^{10}at}{6.2x10^{21}at/cm^3}\right) = 2.9x10^{-11}cm \quad (6\text{-}5)$$

where n_{SnS} is the number of moles SnS, p_{SnS} is the partial pressure of SnS, $V_{graphite}$ is the volume of the graphite annealing box (see Section 3.3.3.3), R is the universal gas constant, T is the annealing temperature (550°C = 823K), N_{Sn} is the number of Sn atoms, N_A is Avogadro's number, t_{film} is the film thickness, A_{film} is the film area, and $\rho_{Sn(CZTS)}$ is the atomic density of Sn in the CZTS film. Although this analysis represents a significant oversimplification of the annealing environment, it indicates that very low Sn concentrations are required to maintain stabilizing partial pressures of SnS. Note, however, that leaks from the graphite box and adsorption of SnS molecules on the interior walls of the graphite box may also act as sinks for the evolved phases, thereby exacerbating Sn-losses from the films. Better control and monitoring of the annealing background environment

would enable more definitive evaluation of the evolution mechanism and optimization of the crystal formation processes. This remains for future work as noted in Sections 9.2.4 and 9.3.

Sulfur annealing with temperature profile TP3 yielded the best performing film properties. The film composition ($Cu_{1.82}Zn_{1.27}Sn_{1.00}S_{4.27}$) remains close to the ideal Cu-poor, Zn-rich stoichiometry of the as-deposited film, and the Sn concentration varies less through the thickness than other sulfur annealed samples. The densities of voids and ZnS phases (light colored surface decorations) are moderated compared to the end range properties exhibited by the other sulfur annealing samples. Most importantly, the sample exhibits the highest phase purity, with negligibly small secondary phases evident in the diffraction spectrum and the narrowest CZTS Raman A-mode band. The film also showed the highest resistivity of all the sulfur annealed films measured by a significant margin, which may indicate lower carrier concentrations.

The low temperature annealing step employed in temperature profile TP3 may help anneal out defects in the amorphous state, which can subsequently reduce the number of nucleation sites. Reducing the number of nucleation sites may mitigate the kinetically-limited growth effects previously described, by facilitating diffusion within the crystal. Longer ramp times may act in a similar way, although average temperatures are maintained significantly higher than the 200°C step used in TP3, which may limit their utility. Notably, annealing of the as-deposited film in Argon at 200°C sharpened the Raman spectrum (not shown), but the film remains characteristically amorphous.

6.5 SUMMARY OF RESULTS

CZTS thin films were fabricated by pulsed laser deposition and annealing in elemental sulfur, and films were characterized using Rutherford backscattering, SEM imaging, x-ray diffraction, Raman spectroscopy, optical absorption spectroscopy, and Hall effect measurements.

The effects of laser fluence, pulse repetition rate, target-substrate distance, substrate temperature, and sputtering target composition on the deposited film properties were investigated. A laser ablation threshold fluence of ~2.5J/cm^2 was identified, above which the film composition no longer varied significantly with fluence. Splashed and exfoliated particles were shown to increase with increasing laser fluence. In order to improve the surface quality of deposited films, the lowest fluence above the threshold (2.5J/cm^2) and sputtering target reconditioning are recommended. Laser pulse repetition rates > 5Hz caused microcracking in the deposited films, attributed to higher strains in the films associated with the higher deposition rates. Modifying the target-substrate distance showed little change in film composition or quality, over the range of distances (9 – 11cm) investigated.

Substrate temperature was shown to significantly impact the composition and quality of the deposited film. While smoother, larger-grained films were achieved at temperatures of 400 and 500°C, significant losses in Zn and Sn were demonstrated. These losses were attributed to losses of elemental Zn and SnS phases caused by their high vapor pressures at these elevated temperatures. It is not considered practical to limit the loss of Sn at temperatures greater than 500°C without the use of a sulfur overpressure during deposition. However, reducing the substrate temperature during deposition to < 400°C and incorporating excess Zn, either in the sputtering target or from a separate effusion cell (preferably the more stable ZnS compound), may enable the improved deposition quality of the films, while mitigating the Zn losses in the films.

At laser fluences above the ablation threshold, as-deposited films were shown to be slightly Zn-poor, significantly Sn-rich, and S-poor compared to the sputtering target. The reason for the severe deviation in Sn concentration was not well-understood. However, the sputtering target compositions were shown to be reliably modified, in order to improve the cation ratios in the as-deposited films, achieving the desired Cu-poor, Zn-rich stoichiometries.

Annealing in elemental sulfur was investigated, in order to achieve stoichiometric concentrations of sulfur in the films and to form the kesterite CZTS phase. Sulfur annealing of the Sn-rich samples showed that annealing can improve the film stoichiometries, evolving the excess Sn through SnS phases. The film compositions stabilized at near-stoichiometry conditions after the initial loss of Sn. However, this evolution resulted in the development of significant voids in the films.

Using the films deposited with the optimized sputtering target compositions, the effects of ramp time, dwell time, and temperature on the annealed film properties was investigated. Increasing the ramp time was shown to increase the film crystallinity, evident as a sharper (112) diffraction peak, but also increased the number of secondary phases present, evident both in shoulders developed near the (112) peak and in the peak broadening of the dominant CZTS Raman A-mode. Longer ramp samples also exhibited less voids but increased surface decorations, attributed to ZnS.

Increasing the dwell time from 10min to 30min was unexpectedly shown to decrease the film crystallinity, evident as a broader (112) diffraction peak, and also increased the number of secondary phases present. The 20min ramp – 30min dwell sample also unexpectedly developed elongated voids, similar to those exhibited by the high ramp sample.

Sulfur annealed films, in general, exhibited a decrease of Sn at the film surface and a decrease in overall film thickness, which stabilized at longer ramp times and longer dwell times. This time-dependent stabilization was explained in terms of kinetically-limited crystal growth,

which we believe results from the large number of amorphous Cu-Sn-S and CZTS phase present in as-deposited films, and the associated large number of nucleation sites therefore formed. These amorphous phases formed, despite room temperature deposition, via the high kinetic energies associated with pulsed laser deposition, similar to the possible seed phases noted in S-containing CZTS precursors deposited by sputtering in [5]. While the slow crystal growth proceeds, volatile SnS phases are evolved from the films. The exact mechanism for this evolution remains unclear, however, as the sulfur overpressures employed during annealing should prevent their evaporation.

The inclusion of a low-temperature (200°C) anneal prior to crystal formation at 550°C was shown to significantly improve the phase purity and resistivity of the annealed film. This temperature profile (TP3) exhibits a (112) diffraction peak with the most negligible shoulder and the A-mode with the smallest peak width. The TP3 film also demonstrated a decreased loss of Sn in the film, which was restricted to a smaller layer near the surface. We attribute this reduction in secondary phase formation, and the reduction of Sn loss, to the healing of defects in the amorphous state, which reduces the number of nucleation sites and improves the kinetics associated with crystal formation. The improvement in phase purity likely yields the improved film resistivity.

6.6 REFERENCES

[1] D. Mitzi, O. Gunawan, T. Todorov, K. Wang, S. Guha, The path towards a high-performance solution-processed kesterite solar cell, Solar Energy Materials & Solar Cells, 95 (2011) 1421 - 1436.

[2] W. Wang, M. Winkler, O. Gunawan, T. Gokmen, T. Todorov, Y. Zhu, D. Mitzi, Device Characteristics of CZTSSe Thin-Film Solar Cells with 12.6% Efficiency, Advanced Energy Materials, (2013).

[3] I.D. Olekseyuk, I.V. Dudchak, L.V. Piskach, Phase equilibria in the Cu_2S-ZnS-SnS_2 system, Journal of Alloys and Compounds, 368 (2004) 135 - 143.

[4] P.M.P. Salome, J. Malaquias, P.A. Fernandes, M.S. Ferreira, J.P. Leitao, A.F.d. Cunha, J.C. Gonzalez, F.N. Matinaga, G.M. Ribeiro, E.R. Viana, The influence of hydrogen in the incorporation of Zn during the growth of $Cu_2ZnSnSn_4$ thin films, Solar Energy Materials & Solar Cells, 95 (2011) 3482 - 3489.

[5] C. Platzer-Bjorkman, J. Scragg, H. Flammersberger, T. Kubart, M. Edoff, Influence of precursor sulfur content on film formation and compositional changes in Cu2ZnSnS4 films and solar cells, Solar Energy Materials & Solar Cells, 98 (2012) 110 - 117.

[6] A. Weber, R. Mainz, H.W. Schock, On the Sn loss from thin films of the material system Cu-Zn-Sn-S in high vacuum, Journal of Applied Physics, 107 (2010) 013516-013511 - 013516-013516.

[7] J. Scragg, T. Ericson, T. Kubart, M. Edoff, C. Platzer-Bjorkmann, Chemical Insights into the Instability of Cu_2ZnSnS_4 Films during Annealing, Chemistry of Materials, 23 (2011) 4625–4633.

[8] J. Scragg, J. Watjen, M. Edoff, T. Ericson, T. Kubart, C. Platzer-Bjorkman, A Detrimental Reaction at the Molybdenum Back Contact in $Cu_2ZnSn(S,Se)_4$ Thin-Film Solar Cells, J. Am. Chem. Soc., 134 (2012) 19330 - 19333.

[9] A. Barkhouse, O. Gunawan, T. Gokmen, T. Todorov, D. Mitzi, Device characteristics of a 10.1% hydrazine-processed $Cu_2ZnSn(Se,S)_4$ solar cell, Progressin Photovoltaics: Research & Applications, (2011).

[10] S. Delbos, Kesterite thin films for photovoltaics: a review, EPJ Photovoltaics, 3 (2012) 35004:p35001 - p35013.

[11] J.J. Scragg, Studies of Cu_2ZnSnS_4 films prepared by sulfurisation of electrodeposited precursors, in: Chemistry, University of Bath, 2010, pp. 244.

[12] S.M. Pawar, A.V. Moholkar, I.K. Kim, S.W. Shin, J.H. Moon, J.I. Rhee, J.H. Kim, Effect of laser incident energy on the structural, morphological and optical properties of Cu_2ZnSnS_4 (CZTS) thin films, Current Applied Physics, 10 (2010) 565-569.

[13] A.V. Moholkar, S.S. Shinde, A.R. Babar, K.-U. Sim, Y.-b. Kwon, K.Y. Rajpure, P.S. Patil, C.H. Bhosale, J.H. Kim, Development of CZTS thin films solar cells by pulsed laser deposition: Influence of pulse repetition rate, Solar Energy, 85 (2011) 1354-1363.

[14] A.V. Moholkar, S.S. Shinde, G.L. Agawane, S.H. Jo, K.Y. Rajpure, P.S. Patil, C.H. Bhosale, J.H. Kim, Studies of compositional dependent CZTS thin film solar cells by pulsed laser deposition technique: An attempt to improve the efficiency, Journal of Alloys and Compounds, 544 (2012) 145-151.

[15] A.V. Moholkar, S.S. Shinde, A.R. Babar, K.-U. Sim, H.K. Lee, K.Y. Rajpure, P.S. Patil, C.H. Bhosale, J.H. Kim, Synthesis and characterization of Cu_2ZnSnS_4 thin films grown by PLD: Solar cells, Journal of Alloys and Compounds, 509 (2011) 7439-7446.

[16] K. Moriya, K. Tanaka, H. Uchiki, Fabrication of Cu2ZnSnS4 Thin-Film Solar Cell Prepared by Pulsed Laser Deposition, Japan Society of Applied Physics, 46 (2007) 5780-5781.

[17] K. Sekiguchi, K. Tanaka, K. Moriya, H. Uchiki, Epitaxial growth of Cu_2ZnSnS_4 thin films by pulsed laser deposition, phys. stat. sol. (c), 3 (2006) 2618-2621.

[18] K. Moriya, K. Tanaka, H. Uchiki, Cu_2ZnSnS_4 Thin Films Annealed in H2S Atmosphere for Solar Cell Absorber Prepared by Pulsed Laser Deposition, Japan Society of Applied Physics, 47 (2008) 602-604.

[19] L. Sun, J. He, H. Kong, F. Yue, P. Yang, J. Chu, Structure, composition and optical properites of Cu_2ZnSnS_4 thin films deposited by Pulsed Laser Deposition method, Solar Energy Materials & Solar Cells, 95 (2011) 2907-2913.

[20] L. Sun, J. He, Y. Chen, F. Yue, P. Yang, J. Chu, Comparative study on Cu2ZnSnS4 thin films deposited by sputtering and pulsed laser deposition from a single quaternary sulfide target, Journal of Crystal Growth, 361 (2012) 147-151.

[21] R.A. Wibowo, E.S. Lee, B. Munir, K.H. Kim, Pulsed laser deposition of quaternary $Cu_2ZnSnSe_4$ thin films, phys. stat. sol. (a), 204 3373-3379.

[22] J. He, L. Sun, S. Chen, Y. Chen, P. Yang, J. Chu, Composition dependence of structure and optical properites of $Cu_2ZnSn(S,Se)_4$ solid solutions: An experimental study, Journal of Alloys and Compounds, 511 (2012) 129-132.

[23] J. He, L. Sun, N. Ding, H. Kong, S. Zuo, S. Chen, Y. Chen, P. Yang, J. Chu, Single-step preparation and characterization of $Cu_2ZnSn(S_xSe_{1-x})_4$, Journal of Alloys and Compounds, 529 (2012) 34-37.

[24] X.L. Tong, D.S. Jiang, L. Liu, Z.M. Liu, M.Z. Luo, Effect of the laser fluence on structural and optical characterization of thin CdS films synthesized by femtosecond pulsed laser deposition, Optics Communications, 270 (2007) 356-360.

[25] R.K. Singh, J. Narayan, Pulsed-laser evaporation technique for deposition of thin films: Physics and theoretical model, Physical Review B, 41 (1990) 8843-8861.

[26] M. Friz, F. Waibel, Coating Materials, in: N. Kaiser, H.K. PUlker (Eds.) Optical Interference Coatings, Springer-Verlag Berlin Heidelberg, New York, 2003.

[27] R. Cadoret, Growth by Vacuum Evaporation, Sputtering, Molecular Beam Epitaxy, and Chemical Vapor Deposition, in: B. Mutaftschiev (Ed.) Interfacial Aspects of Phase Transformations, D. Reidel Publishing Company, Boston, 1981.

[28] C. Lee, T. Yen, J. Lin, Light emission from an oxygen covered copper surface by ion bombardment, Surface Science, 488 (2001) 379 - 386.

[29] C. Lee, T. Lin, Oxygen sticking coefficient and sputtering yields at an Al(111) surface by ion bombardment, Surface Science, 471 (2001) 219 - 224.

[30] A. Fontell, E. Arminen, Direct collection of some metal ions in an electromagnetic isotope separator and related surface effects, Canadian Journal of Physics, 47 (1969) 2405 - 2414.

[31] T.J. Jackson, S.B. Palmer, Oxide superconductor and magnetic metal thin film deposition by pulsed laser ablation: a review, J. Phys. D: Appl. Phys., 27 (1994) 1581-1594.

[32] M. Lorenz, Pulsed-Laser Deposition of ZnO-Based Thin Films, in: K. Elmer, A. Klein, B. Rech (Eds.) Transparent Conductive Zinc Oxide, Springer Berlin Heidelberg, Berlin, 2007, pp. 303-357.

[33] Zinc Smelting from a Chemical and Thermodynamic Viewpoint, in: U.S.D.o. Commerce (Ed.), Government Printing Office, Washington, D.C., 1930.

[34] A. Fairbrother, X. Fontane, V. Izquierdo-Roca, M. Espindola-Rodriguez, S. Lopez-Marino, M. Placidi, L. Calvo-Barrio, A. Perez-Rodriguez, E. Saucedo, On the formation mechanisms of Zn-rich Cu_2ZnSnS_4 films prepared by sulfurization of metallic stacks, Solar Energy Materials & Solar Cells, 112 (2013) 97 - 105.

[35] P.M. Nikolic, L.J. Miljkovic, P. Mihajlovic, B. Lavrencic, Splitting and coupling of lattice modes in the layer compound SnS, Journal of Physics C: Solid State Physics, 10 (1977) L289 - L292.

[36] L.S. Price, I.P. Parkin, A. Hardy, R. Clark, Atmospheric Pressure Chemical Vapor Deposition of Tin Sulfides (SnS, Sn_2S_3, and SnS_2) on Glass, Chemistry of Materials, 11 (1999) 1792 - 1799.

[37] M. Dimietrievska, A. Fairbrother, X. Fontane, T. Jawhari, V. Izquierdo-Roca, E. Saucedo, A. Perez-Rodriguez, Multiwavelength excitation Raman scattering study of polycrystalline Cu_2ZnSnS_4 thin films, Applied Physics Letters, 104 (2014) 021901-021901 021901-021905.

[38] X. Fontane, L. Calvo-Barrio, V. Izquierdo-Roca, E. Saucedo, A. Perez-Rodriguez, J.R. Morante, D.M. Berg, P.J. Dale, S. Siebentritt, In-depth resolved Raman scattering analysis for the identification of secondary phases: Characterization of Cu_2ZnSnS_4 layers for solar cell applications, Applied Physics Letters, 98 (2011) 181905-181901 181905-181903.

[39] V. Piacente, S. Foglia, P. Scardala, Sublimation study of the tin sulphides SnS_2, Sn_2S_3, and SnS, Journal of Alloys and Compounds, 177 (1991) 17 - 30.

[40] A. Weber, H. Krauth, S. Perlt, B. Schubert, I. Kotschau, S. Schorr, H.W. Schock, Mult-stage evaporation of Cu_2ZnSnS_4 thin films, Thin Solid Films, 517 (2009) 2524 - 2526.

[41] K. Zhang, Z. Su, L. Zhao, C. Yan, F. Liu, H. Cui, X. Hao, Y. Liu, Improving the conversion efficiency of Cu_2ZnSnS_4 solar cell by low pressure sulfurization, Applied Physics Letters, 104 (2014) 141101-141101 - 141101-141104.

[42] A. Fairbrother, E. Garica-Hemme, V. Izquierdo-Roca, X. Fontane, F. Pulgarin-Agudelo, O. Vigil-Galan, A. Perez-Rodriguez, E. Saucedo, Development of a Selective Chemical Etch to Improve the Conversion Efficiency of Zn-Rich Cu_2ZnSnS_4 Solar Cellss, J. Am. Chem. Soc., 134 (2012) 8018 - 8021.

[43] P.A. Fernandes, P.M.P. Salome, A.F.d. Cunha, A study of ternary Cu2SnS3 and Cu3SnS4 thin films prepared by sulfurizing stacked metal precursors, Journal of Physics D: Applied Physics, 43 (2010) 1-11.

[44] D. Berg, R. Djemour, L. Gutay, S. Siebentritt, P. Dale, X. Fontane, V. Izquiero-Roca, A. Perez-Rodriguez, Raman analysis of monoclinic Cu_2SnS_3 thin films, Applied Physics Letters, 100 (2012) 192103-192101 - 192103-192104.

[45] H. Guan, H. Shen, C. Gao, X. He, Structural and optical properties of Cu_2SnS_3 and Cu_3SnS_4 thin films by successive ionic layer adsorption and reaction, Journal of Materials Science: Materials in Electronics, 24 (2013) 1490 - 1494.

[46] S.-Y. Wang, W. Wang, Z.-H. Lu, Asynchronous-pulse ultrasonic spray pyrolysis deposition of Cu_xS (x=1,2) thin films, Materials Science & Engineering B, 103 (2003) 184 - 188.

[47] C. Persson, Electronic and optical properties of Cu_2ZnSnS_4 and $Cu_2ZnSnSe_4$, Journal of Applied Physics, 107 (2010) 053710-053711 - 053710-053718.

[48] F. Hergert, R. Hock, Predicted formation reactions for the solid-state syntheses of the semiconductor materials Cu_2SnX_3 and Cu_2ZnSnX_4 (X=S,Se) starting from binary chalcogenides, Thin Solid Films, 515 (2007) 5953 - 5956.

[49] H.R. Alvarez, Growth mechanisms of $CuInS_2$ formed by the sulfurization of thin metallic films, in, der Technischen Universitat Berlin, 2010.

7 GROWTH BEHAVIOR OF CO-ELECTRODEPOSITED SULFUR-CONTAINING CZTS PRECURSORS

7.1 PURPOSE

As discussed extensively in previous chapters, CZTS thin films represent ideal absorber layers for single-junction photovoltaic devices, due to its direct band gap of ~1.5eV and high optical absorption > 10^4 cm^{-1} above the band edge [1]. The fabrication of high quality CZTSeS absorber layers has been extremely challenging, due to the narrow phase formation region for CZTSeS [1, 3], elemental and compound volatility [1, 4-6], and phase decomposition at the surface and back contacts [7, 8]. In particular, the difficulty in preventing Zn and SnS loss during film growth, associated with CZTS phase decomposition and the high vapor pressures of these components, has resulted in the comparative success of two-step (e.g. deposition reaction) fabrication processes over more conventional single-step processes (e.g. coevaporation) [1, 7].

Despite the moderately high device efficiencies achieved (12.6%) [2], all aspects of CZTS device design merit continued investigation. Scalable and reliable fabrication methods, capable of producing phase-pure, void-free CZTSeS absorber layers have yet to be demonstrated. Electrodeposition (ED) represents a commercially viable synthesis tool that also enables rapid thin film deposition. The scalability of electrodeposition has been demonstrated in large-scale industrial deployment of conventional metallic plating, and also in the semiconductor industry through the use of copper damascene electroplating techniques [13].

Significant efforts have been devoted to the investigation and optimization of CZTS thin films fabricated by the electrodeposition of metallic precursors in the stacked elemental layer (SEL) configuration; see for example [3-5]. As discussed in Section 3.2.1.2, however, single-step co-electrodeposition of the elements may improve the film homogeneity, while reducing the need for precise control of the film thickness. In the SEL configuration, the layer thicknesses correspond to directly the final film composition. Co-electrodeposition of metallic CZT and S-containing CZTS precursors have both been successfully demonstrated [6-9]. As discussed in detail in Section 3.3.2.2, the S-content in the precursor films has been shown to significantly influence grain growth and void formation during annealing [10]. In particular in [10], S-content of 14-18at% in the precursor films significantly reduced Sn-loss and void formation, although also decreased the grain size, in the final films. Consequently, the co-electrodeposition of S-containing CZTS precursors may provide advantages over metal-only precursors.

To this author's knowledge, the first successful single-step co-electrodeposition of S-containing CZTS precursors with near-stoichiometric compositions was demonstrated by Pawar

et. al [6]. As a first step for work in this dissertation, the co-electrodeposition process from [6] was reproduced. However, films fabricated using this method exhibited severely rough, powdery morphologies and highly Zn-poor, Sn-rich compositions, which deviated strongly from the reported film properties in the original work. A later investigation by Gougaud noted the potential precipitation of insoluble species using this fabrication method [9]. In working to reconcile the deviations in deposition behavior, a gap in the literature was noted regarding the effects of the deposition parameters on the growth behavior of co-electrodeposited S-containing CZTS precursors. Consequently, in order to understand the growth behavior and to improve the quality of as-deposited films, the effects of the deposition parameters on the film properties were systematically investigated.

Note the as-deposited precursors reported in [6] were fully-sulfurized, and crystal formation was originally achieved by annealing in inert Nitrogen background gas. Later work by the same group demonstrated that annealing in H_2S background significantly improved film quality by increasing the grain size and shifting the band gap closer to the predicted value of 1.5eV for CZTS [11]. Despite being fully-sulfurized, the CZTS precursor still required annealing in sulfur environment to achieve high quality films. More generally, a reaction at the Mo back contact requires crystal formation to be conducted under sulfur overpressure, in order to prevent decomposition of the CZTS film at the interface, as discussed in Section 3.3.2.2. Consequently, it is unlikely that deposition of fully-sulfurized CZTS precursors will eliminate the need for annealing in sulfur environment. In fact, S-deficiencies in the precursors enhance grain growth, and an optimum S-content between metals-only and full-sulfurized likely exists, as explored in [10].

Notably, co-electrodeposited S-containing CZTS precursors demonstrated in this dissertation are always S-deficient, with values ranging from approximately 12 – 35at%, precisely the range investigated in [10], a fortuitous coincidence. A wide range of precursor compositions are investigated in this dissertation, providing a broad overview of the effects of the precursor composition on crystal formation: the pulsed laser deposited films in Chapter 6 are highly-sulfurized, the co-electrodeposited films in this chapter are partially-sulfurized, and the co-electrodeposited films in Chapter 8 contain no sulfur.

This chapter explores the co-electrodeposition of S-containing CZTS precursors, deposited and annealed under varying conditions, with the following objectives:

- Characterize the effects of the co-electrodeposition parameters on the as-deposited film compositions and morphologies.
- Determine deposition parameters that achieve the optimum as-deposited film composition and morphology. From Section 1.3 and 2.3.2, the desired film stoichiometry corresponds

to a Cu:Zn:Sn metal ratio of approximately 1.8:1.2:1.0, and 1μm represents the minimum film thickness necessary for use in photovoltaic absorber layers.

- Investigate the role of the precursor composition and structure on crystal and secondary phase formation processes and determine their influence on film properties.
- Demonstrate the fabrication of high-quality films for use in fundamental material, interface studies, and device studies.

7.2 BACKGROUND

This section provides a brief review of the existing literature on co-electrodeposition of S-containing CZTS thin film precursors [6, 8, 12-27]. Most of the reported works performed the electrodepositions under constant potential using three-electrode cells, with varying reference electrodes, platinum or graphite counter electrodes, and Mo-coated or ITO/FTO-coated glass substrates [6, 8, 12, 13, 15-22, 26, 27]. Metal sulfates or metal chlorides typically provided the Cu, Zn, and Sn sources in the deposition bath, while sodium thiosulfate or sodium sulfate most frequently provided the S source [6, 8, 12, 13, 15, 17-19, 21, 22, 26]. Other complexing agents have been investigated, but most works used combinations of tri-sodium citrate and tartaric acid [6, 15, 17-22, 27]. Table 7-1 shows typical deposition parameters demonstrated in the literature, and Table 7-2 shows reported effects of the deposition parameters on the properties of S-containing CZTS precursor films.

Table 7-1. Typical co-electrodeposition parameters for S-containing CZTS precursors (literature results)

Deposition Parameter	Value	Reference
$[Cu^{2+}]$	0.02 – 0.12	[6, 8, 12, 13, 15, 18-22, 26]
$[Zn^{2+}]$	0.01 – 0.14	
$[Sn^{2+}]$	0 – 0.13	
$[S_2O_3^{2-}]$	0.001 – 0.16	
[Citrate]	0.2 – 1.36	
Bath pH	4 – 7	[6, 12, 15, 17, 18, 20-22, 27]
Deposition Potential (vs. Ag/AgCl)	-0.8 to -1.4V	[6, 8, 12, 13, 15, 17-19, 21, 22, 26, 27]
Deposition Time	3 – 60min	[6, 8, 12, 13, 17-19, 21, 22, 26, 27]
WE-CE Distance	2cm	[20, 25]
Stirring	None	[6, 8, 12, 13, 21, 22]

In literature, studies of the co-electrodeposition of S-containing CZTS thin film precursors have focused on characterizing the precursor growth behavior, including the effects of bath composition and deposition potential on the as-deposited film compositions, structures and morphologies. Device efficiencies of 1.21 – 3.68% have been reported for solar cells using CZTS absorber layers fabricated by a two-step co-electrodeposition of S-containing CZTS precursors and sulfurization [8, 20, 22, 26].

To this author's knowledge, the first successful single-step co-electrodeposition of S-containing CZTS precursor with near-stoichiometric composition was demonstrated by Pawar et. al [6], hereafter denoted **Pawar's method**. This method has served as the basis for many other co-electrodeposition approaches, including the work to follow in this thesis. Given its significance and prevalence, a brief review of Pawar's method is given here. CZTS thin films were electrodeposited from aqueous baths containing simple component salts and two complexing agents. The component sources included: copper sulfate ($CuSO_4$), zinc sulfate ($ZnSO_4$), tin sulfate ($SnSO_4$), and sodium thiosulfate ($Na_2S_2O_3$). The complexing agents include tri-sodium citrate ($Na_3C_6H_5O_7$) and tartaric acid ($C_4H_6O_6$) [6]. Note: the tartaric acid also acted as a pH buffering agent, and it was added in sufficient concentration to maintain a pH of 4 – 5 [6]. Complexing agents were used to shift closer the reduction potential of the depositing species, as discussed more generally in Section 3.2. While a comprehensive study of the deposition mechanisms remains noticeably lacking in the literature, most reports that use similar deposition parameters and bath compositions to Pawar's method have attributed the deposition of metallic components according to simple cathodic reduction mechanisms [6, 15, 16]:

$$Cu^{2+} + 2e^- \rightarrow Cu(s) \tag{7-1}$$

$$Zn^{2+} + 2e^- \rightarrow Zn(s) \tag{7-2}$$

$$Sn^{2+} + 2e^- \rightarrow Sn(s) \tag{7-3}$$

where the dissolved metal sulfates provide Cu^{2+}, Zn^{2+}, and Sn^{2+} ions in solution. The sulfur deposition has been attributed to the cathodic reduction of the thiosulfate ion ($S_2O_3^{2-}$) [15, 16], as described in detail in [28]. Near the zero-charge potential, thiosulfate ion reduction may proceed according to the following [16, 28]:

$$S_2O_3^{2-} + 2e^- \rightarrow S^{2-} + SO_3^{2-} \tag{7-4}$$

At potentials more negative than the zero-charge potential, the cathodic reduction process proceeds through reactions with atomic hydrogen ions, as follows [16, 28]:

$$S_2O_3^{2-} + H^+ + OH^- \rightarrow S^{2-} + SO_3^{2-} + H_2O \tag{7-5}$$

Higher hydrogen evolution overpotentials and higher current densities have been shown to increase the rate of reaction (7-5) by increasing the concentration of H^+ ions available to react [28]. The S-incorporation into the deposit has generally been described in terms of the overall formation reaction, such that the Cu-, Zn-, and Sn-cations react with the S_2O_3-anion to form CZTS + SO_3^{2-} (+H_2O), depending on the thiosulfate reduction process [16, 19, 27]. Anomalous co-depositions involving metal-sulfide compounds (e.g. SnS) may also be active, as detailed in Section 3.2.2.3, with at least one report identifying these compounds in as-deposited samples electrodeposited from baths composed of chloride- and nitrate-based metal salts and sodium thiosulfate [27]. As mentioned previously, however, comprehensive kinetics studies are lacking.

In the original paper detailing Pawar's method, as-deposited films were amorphous with rough, porous morphologies characterized by "non-uniform distributions of agglomerated particles with well-defined boundaries" [6]. Note that only high magnification images (20kX) are provided and the macroscopic film uniformity may not be evaluated. Another work [19] using Pawar's method showed similar film morphologies under high magnification. In this thesis, however, poorly adherent, powdery films were demonstrated using similar deposition parameters. In [12], depositions were performed using similar bath compositions but with Na_2SO_4 and $SnCl_2$ as the S- and Sn-sources, respectively. In that study, loose, powdery films were observed at sufficiently negative deposition potentials, which were attributed to increased hydrogen evolution and sulfur deposition. Degraded film qualities were also correlated with high sulfur concentrations in the films in [13, 16]. It is noted in [9] that the $Na_2S_2O_3$-containing baths from Pawar's method are unstable due to disproportionation reactions and the precipitation of insoluble species. In the original work by Pawar, film morphologies were shown to improve after annealing [6] with best results obtained in H_2S (5%) atmosphere with nitrogen carrier gas [11, 22].

A review of the literature found no works reporting the effects of metal cation concentrations, or the metal cation sources, on the properties of as-deposited films. As noted in Section 3.2.1.2, interdependencies among electroactive species in the bulk and the associated deposition mechanisms suggest that the deposition process might not be optimized in a predictable manner. The effects of varying $Na_2S_2O_3$ concentration on the film properties were investigated in [13], using a similar bath composition to Pawar's method but replacing tartaric acid with potassium tartrate. As expected, the S concentration in the as-deposited films increased with increasing $Na_2S_2O_3$ concentration, evident as an increase in S:metal ratio. Less expected, the Zn concentration in the film decreases with increasing $Na_2S_2O_3$ concentration, while the Cu and Sn concentrations vary unpredictably [13]. The author suggested that sulfur interactions with metal ions in the bulk may form secondary phases, thereby modifying the deposition rates [13]. As-deposited film morphologies were not presented, but it was noted that the films delaminated at the

highest $Na_2S_2O_3$ concentrations [13]. In addition to sodium thiosulfate, sodium sulfate [12] and thiourea [20] have been used as S-sources, but their effects on growth behavior were not discussed.

Using Pawar's method, two works systematically investigated the effects of varying tri-sodium citrate concentration on the properties of as-deposited films [18, 21]. When no tri-sodium citrate was included in the bath, films exhibited severe cracking and large surface features [21]. The addition of 0.2M tri-sodium citrate yielded rougher, but more uniform, films with fewer large surface features [21]. However, additional increase in tri-sodium citrate concentrations caused increased roughness and increased density of large surface feature [21]. Films deposited with 0.2M tri-sodium citrate were the most stoichiometric, with the lowest S concentration, while films deposited without tri-sodium citrate and in larger concentrations contained S concentrations greater than 65at% [21]. It was concluded that 0.2M tri-sodium citrate represented an optimum value, evidenced by better morphologies and sharper diffraction peaks after annealing [21].

The effects of tri-sodium citrate concentration on the deposited film properties were also reported in [18]; however, volumes of the citrate concentration were reported without giving the overall cell volume, so the molar concentrations are unknown. Consequently, only general trends associated with increasing concentration may be detailed. Both the morphology and composition trends appear different for this study compared to [21]. In this study, the S concentration monotonically increases from 13.5at% at the lowest concentration to 50.0at% in the highest concentration baths [18]. This study also shows much larger dendrites on the surface, which appear to grow more compact with increasing tri-sodium citrate concentration [18].

Many works have also reported the use of complexing agents besides tri-sodium citrate and tartaric acid, including potassium tartrate [8, 13, 26] and potassium thiocyanate [16]. The complexing behavior of potassium tartrate, the potassium salt of tartaric acid, is expected to act similarly to tartaric acid due to their similar chemical structure. The complexing behavior for the thiocyanate ion will differ from the citrate ion, owing to its different chemical structure, and the stability constants of different metal-thiocyanate complexes are summarized in [16]. Insufficient data are available to compare the effectiveness of tri-sodium citrate and potassium thiocyanate.

The effects of deposition potential on the properties of as-deposited films were investigated in [12] and [16]. In [12], films were co-electrodeposited from baths similar to Pawar's method but using $SnCl_2$ and $NaSO_4$ as alternate Sn- and S-sources, respectively. All as-deposited films were severely Sn-rich. The onset of Zn reduction was demonstrated between -1.2V and -1.4V vs. Ag/AgCl. With increasingly negative potential, the Cu:Sn ratios stayed approximately constant. The Zn and S concentrations, however, exhibited a jump between -1.2V and -1.4V, with slight increases thereafter [12]. At deposition potentials more negative than -1.4V, the films were powdery and easily removed with rinsing after deposition, attributed to hydrogen evolution and

excess sulfur deposits [12]. Despite using a significantly different bath composition, including potassium thiocyanate complexing agent and acetic acid buffering agent, Iljina demonstrated similar results in [16]. The Cu:Sn ratio remained constant, while Zn and S concentrations in the films increased with increasingly negative deposition potential [16]. Further, a threshold value of deposition potential was identified, above which HER reaction initiated, the S concentration increased significantly, and films developed poor adhesion [16]. This work also noted a significant increase in the S:metals ratio with increasing deposition time, which the author attributes to a reduction of the HER overpotential once the film has been covered with Cu-Zn-Sn-S and to an associated increase in the rate of $S_2O_3^{2-}$ reaction (7-5). However, the $S_2O_3^{2-}$ reduction reaction should decrease with increasing HER rate, due decreasing concentration of H^+ species available to react. However, the increase in HER may also signify an increase in H^+ species, which could increase the reaction rate of both HER and $S_2O_3^{2-}$ reduction mechanisms.

Table 7-2. Process control variables and effects: S-containing CZTS precursors (literature results)

Process Parameter	Variation	Film Effect	Rationale
Metal Cation Ratios	Not Reported	-	-
Sulfur Source Concentration	Increasing	(1) Increasing [S] in film (2) Decreasing [Zn] in film (3) Delamination at high [Na_2SO_4]	(1) Increasing source concentration (2) S- metal ion interactions in bulk (3) Not discussed
Complexing Agent	None	Severe cracking, with large surface features	Not discussed
	Increasing [$Na_3C_6H_5O_7$]	Increasing [S] in film	Not discussed
Deposition Potential	Increasingly negative	(1) Increasing [Zn] in film (2) Increasing [S] in film (3) Fixed [Cu]:[Sn] (4) Increasing HER (5) Powdery, dendritic films	(1) Onset of Zn reduction wave (2) Increased S_2O_3 reduction • Attributed to increased HER (3) Not discussed (4) Onset of HER (5) Increased [S] in films and HER
Deposition Time	Increasing	(1) Increase in [S] in film (2) Powdery, dendiritic films	(1) Increased HER • Lower overpotential on deposited C-Z-T-S (vs. Mo) (2) Increased [S] in film and HER
Bath pH	Decreasing (more acidic)	Less compact films	Not discussed

No comprehensive studies of the effects of pH on film growth were found in the literature. However, in [15], films were depositing using a similar bath composition to Pawar's method, but NaOH was used to adjust the pH to 6 – 7. The films contained some large, micron-sized surface

deposits but were overall much more compact than those observed in [6]. Note that the bath components were supplied in different ratios and at significantly higher overall concentrations (e.g 0.12M vs. 0.02M) than in [6], possibly influencing the film morphologies.

Co-electrodeposition of S-containing CZTS precursors has been performed using Mo-coated [6, 13, 15, 17-22, 26], ITO-coated [6, 8, 13, 16, 22], and FTO-coated glass substrates [12, 27]. A review of the literature revealed no studies of the effects of the substrate on the deposition behavior. In general, however, it should be noted that the Molybdenum back contacts have been shown to cause detrimental secondary phase formation by reaction with CZTS during annealing operations [3] and sulfur annealing of films deposited on ITO substrates has been shown to degrade the ITO film resistivity [8].

Finally, various deposition control methods have been investigated in order to improve the as-deposited film quality, including pulsed potential [20], two-step potential [26], and electrochemical atomic layer deposition (EC-ALD) [27] methods. The highest efficiency (3.6%) solar cell device reported was fabricated using a two-step deposition potential method presented in [26]. In this method, similar bath compositions to Pawar's method were employed, but component concentration ratios were adjusted and potassium tartrate replaces tartaric acid [26]. The highest efficiency device was fabricated with a -1.15V vs. Ag/AgCl potential held for 10min followed by a -1.10V potential held for 10min [26]. Films deposited at constant potential (-1.10V and -1.15V) exhibited bilayer morphologies, composed of a denser, small-grain underlayer and a rougher, less compact and large-grained top layer [26]. The two-step deposition potential, on the other hand, shows a single, well-densified layer with small grains. Further, the two-step deposition potential films are fully-sulfurized while the single-step potential films have S:metal ratios < 1 [26]. No explanations were given, however, for the comparative success of the two-step potential method or its influence on growth behavior.

7.3 EXPERIMENTAL DETAILS

Film compositions and thicknesses were characterized using Rutherford back scattering (RBS) and particle-induced x-ray emission spectroscopy (PIXE) analyses, as detailed in Chapter 4. To help qualitatively identify compositions of large surface features, such as the copper grains seen in Fig. 7-26, point-and-shoot EDS spectra were measured. In most cases, the through-thickness film composition varied, and weighted-average compositions are provided. Crystal structures were analyzed by x-ray diffraction and Raman backscattering spectroscopy, and morphologies were assessed using scanning electron microscopy, as detailed in Chapter 4. Using the Perkin Elmer Lambda 950 spectrophotometer, transmission and reflection measurements were taken as detailed in Chapter 4. Optical absorption coefficients were calculated, accounting for front surface

reflections only, according to the relations in Table 4-13. The band gap was calculated using the fitting procedure for direct band gap materials, Eqn. (4-15) and (4-16), described in Section 4.3.1.2.

7.3.1 Depositions with Tartaric Acid (pH~4.5)

Single-layer films of CZTS, up to ~2μm thickness, were deposited on FTO-coated and Mo-coated soda lime glass substrates using **Pawar's method** [6]. The FTO-coated substrates (TEC-7) used deposition areas of ~2 x 3cm, and the Mo-coated substrates (EMAT) used deposition areas of ~1.6 x 2cm, chosen simply for the dimensions of the supplies. To investigate the effects of substrate condition on CZTS film growth, some (EMAT) Mo-substrates were rapid thermal annealed prior to deposition, as detailed in Section 3.3.3.2. Note that this annealing of the substrates prior to deposition was not shown to strongly affect the growth behavior. EMAT Mo-substrates rapid thermally annealed at 400°C for 60s were used for the following studies: Time-Evolution of Morphology (Section 7.4.1.3) and Effects of Sulfur Annealing (Section 7.4.1.7). All other sections used unannealed substrates.

S-containing CZTS precursor films were deposited from aqueous electrolyte baths with the nominal compositions shown in Table 7-3, as originally demonstrated in [1]. Constant potential depositions were performed at -0.20 to -1.20V vs. Ag/AgCl, using an AFCBP1 bipotentiostat. The substrates were prepared according to the general methodology described in Section 3.2.4. Post-deposition sonication was investigated as a method to remove unwanted surface particulates; sonication was performed using a VWR50 ultrasonic cleaner, as detailed in Section 3.2.4. Details specific to individual studies are presented in the following sections.

Table 7-3. Nominal bath composition used with Pawar's method [6]

Chemical Formula	Concentration [M]
$Na_3C_6H_5O_7$	0.20
$C_4H_4O_6$	0.10
$Cu(II)SO_4$	0.02
$Zn(II)SO_4$	0.01
$Sn(II)SO_4$	0.02
$Na_2S_2O_3$	0.02

Sulfur annealing was performed using the Generation #2 annealing system design and methodology described in Section 3.3.3.3. Samples were nominally annealed with 4.5mg elemental sulfur at 560°C for 10min, with 7min ramp, and passively cooled under flowing Argon to < 120°C.

7.3.2 Depositions without Tartaric Acid (pH~6)

Single-layer films of CZTS, up to ~2μm thickness, were deposited on Mo-coated and FTO-coated soda lime glass substrates using **Pawar's method**, **less the tartaric acid** [6]. The Mo-coated

substrates (Guardian and EMAT) and the FTO-coated substrates (TEC-7) used deposition areas of ~1.6 x 2cm. Due to the low quality of in the in-house (EMAT) Mo-substrates (e.g. small grains and high oxygen content), commercial (Guardian) Mo-substrates were pursued. All depositions performed in this section use the (Guardian) Mo-substrates, except as noted in Section 7.4.2.4.

CZTS precursor films were deposited from aqueous electrolyte baths with the nominal composition shown in Table 7-3, less the tartaric acid ($C_4H_4O_6$). Constant potential depositions were performed at -0.20 to -1.20V vs. Ag/AgCl, using an AFCBP1 or WaveDriver 20 bipoteniostat. Constant current depositions were performed at -0.34 to -1.59mA/cm^2, using the WaveDriver 20. In some cases, stirring of the bath was performed during deposition using a magnetic stir bar. The substrates were prepared according to the general methodology described in Section 3.2.4. Details specific to individual studies are presented in the following sections.

Sulfur annealing was performed using the Generation #2 annealing system design and methodology described in Section 3.3.3.3. Samples were nominally annealed at 560°C and passively cooled under flowing Argon to < 120°C. The masses of elemental sulfur and the temperature profiles used for annealing are noted in the discussion.

7.4 RESULTS AND DISCUSSION

Note that all deposition potentials referenced in this section refer to the Ag/AgCl reference electrode. For ease of discussion, the term **FTO film** shall be interchangeable with the expression **CZTS precursor film deposited on FTO-substrate**. Similarly, **Mo films** shall refer to films deposited on Mo-substrate.

The following results are divided into two main sections: depositions with tartaric acid (Section 7.4.1) and depositions without tartaric acid (Section 7.4.2). In Section 7.4.1, using Pawar's method as the baseline, deposition studies investigated the properties of as-deposited films, including the potential- and time-dependence of film composition, structure, and morphology. The properties of the nominal bath are also investigated by cyclic voltammetry. With an understanding of the baseline behavior of the deposition, the bath composition was then systematically modified to determine the effects of component concentrations on the film properties, in order to improve film composition and morphology. Mechanical methods to improve the film morphology are also explored. Finally, results of sulfur annealing of as-deposited and sonicated films are presented.

It is shown in Section 7.4.1 that the removal of tartaric acid from the bath dramatically improves the surface morphologies of the as-deposited films. In Section 7.4.2, deposition studies were performed using Pawar's method, less the tartaric acid, as the baseline. Similar to Section 7.4.1, the properties of the baseline films and baths were characterized. Then, the bath

composition, bath concentration, stirring, and control methods (e.g. galvanostatic) were systematically modified to determine their effects on the properties of as-deposited films. Finally, results of sulfur annealing of optimized films are presented.

7.4.1 Depositions with Tartaric Acid (pH~4.5)

7.4.1.1 Baseline Film Properties

This section attempts to reproduce Pawar's method and describes the film properties and deposition characteristics associated with the original bath conditions (see Table 7-3). Baseline films were deposited from the nominal bath composition at a constant potential of -1.00V for 25 minutes.

After deposition, samples were thoroughly rinsed in ultra-high purity water. Both **FTO films** and **Mo films** possessed loose, powdery top layers that were easily removed by rinsing. These powdery layers were much thinner for **FTO films** than the **Mo films**, evidenced as less material volume removed by rinsing. While no such layer was discussed in [6], other works have noted the formation of loose, powdery films under conditions of high hydrogen evolution and high sulfur deposition, as noted in Section 7.2.

FTO films exhibited poor surface morphologies with large, non-uniform growth features, as shown in Fig. 7-1. In this work, these surface features were characteristic of all films deposited from baths containing tartaric acid. Such features were not shown or noted in films presented in the original work [6].

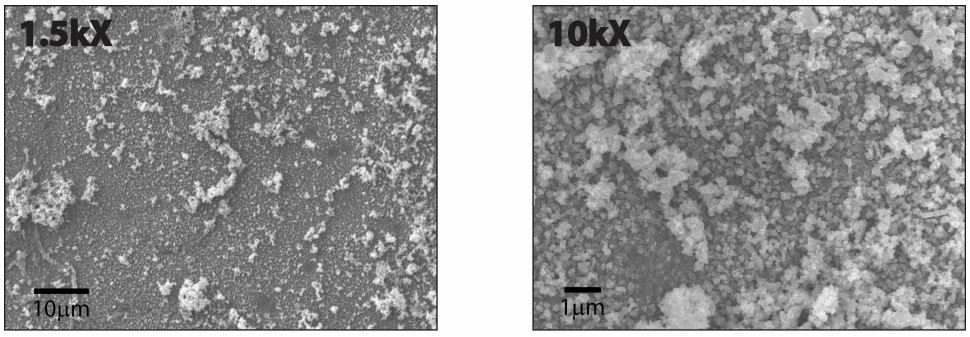

Fig. 7-1. SEM images of co-electrodeposited CZTS precursor on FTO-substrate, using Pawar's method [6]

The high degree of roughness and non-uniformity of the films make accurate fitting of the RBS spectra difficult, introducing uncertainty into the measured film compositions and thicknesses. Table 7-3 shows the best estimates for the compositions and thicknesses of the deposited CZTS precursor films on FTO- and (EMAT) Mo-substrates.

In this work, **FTO films** were Zn-poor, severely Sn-rich, and severely S-poor. The original work [6] did not clearly delineate which results applied to ITO-substrates and to Mo-substrates,

but presented results indicated that as-deposited films were near-stoichiometric with slightly Zn-poor and S-rich composition [10]. The causes for the large discrepancies between compositions and morphologies of films fabricated in this work and those reported in literature cannot be discerned without more information about the substrate properties and electrochemical cell used in [6]. Note the **FTO film** was significantly thinner than the **Mo film**, consistent with the much lower current density evident on the cyclic voltammagram for the FTO-substrate (see Fig. 7-3).

Table 7-4. Compositions of baseline co-electrodeposited CZTS precursors on FTO- and (EMAT) Mo-substrates

Substrate	Atomic %					Cu:Zn	Zn:Sn	S:Metals	Thick (nm)
	Cu	Zn	Sn	S	O				
FTO	15	5	25	11	56	3.1	0.11	0.24	240
(EMAT) Mo	23	5	15	25	32	4.3	0.36	0.58	820

Mo films exhibited more extreme surface morphologies than the **FTO films**, with many-micron thick growth features, as shown in Fig. 7-2. These morphologies were consistent with the thick top-layers of loose, powdery film that were removed with rinsing. The **Mo film** was severely Zn-deficient but included more S than the **FTO film**, evident as a larger S:metals ratio.

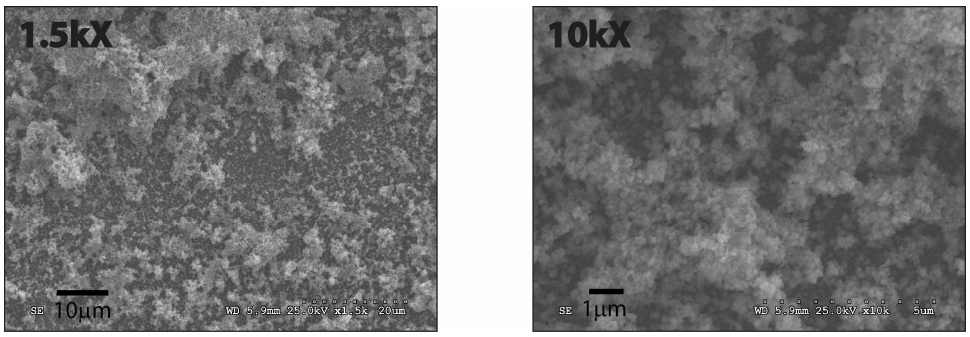

Fig. 7-2. SEM images of co-electrodeposited CZTS precursor on (EMAT) Mo-substrate, using Pawar's method [6]

As will be discussed in Section 7.4.1.6, sonication of the samples was explored as a possible method to mechanically remove the surface overgrowths (e.g. powdery top layer). This method proved effective, significantly reducing film roughness and exposing a compact underlayer primarily free of these surface overgrowths. By comparing the measured composition of the samples before and after sonication, the composition of these surface features could be deduced. After removal of the surface features, the films were much smoother and more uniform, allowing more accurate fitting of the RBS spectra. The film compositions and thicknesses after sonication are shown below in Table 7-5.

Notably, the compositions of the **FTO film** and the **Mo film** converge after sonication, indicating that the compact underlayers have similar compositions. The composition of the **FTO film** did not change significantly with sonication, possibly indicating that the composition of the

surface features were similar to the compact underlayer. The Sn concentration cannot be reliably fitted using RBS, however, due to unclear transition between Sn in the film and in the FTO substrate. On the other hand, Cu and S possess unique, resolvable element peaks in the PIXE spectra and therefore provide a reasonable qualitative estimation of changes in the Cu:S ratio in the film. This Cu:S peak ratio remains constant after sonication, suggesting these quantities do not change substantially.

Table 7-5. Compositions, after sonication, of baseline co-electrodeposited CZTS precursors on FTO- and (EMAT) Mo-substrates

Substrate	Atomic %					Cu:Zn	Zn:Sn	S:Metals	Thick (nm)
	Cu	Zn	Sn	S	O				
FTO	19	8	27	12	32	2.4	0.29	0.22	75
Mo	23	2	24	14	37	13	0.07	0.28	95

The surface features of the **Mo film**, on the other hand, can be deduced to be S-rich and Zn-rich, while containing significantly less Sn than the underlayer. Note again, however, that significant peak overlap, resulting from thick, rough films, makes reliable composition analysis by RBS difficult in the as-deposited film. In PIXE spectra, Mo and S element peaks coincide and so cannot provide reliable information regarding the changes in S concentration in the film. However, Cu and Sn possess unique, resolvable element peaks in PIXE spectra and therefore provide a reasonable qualitative estimation of changes in the Cu:Sn ratio in the film. This Cu:Sn peak ratio decreases significantly with sonication, consistent with the reported compositions in Table 7-4 and Table 7-5. Based on the SEM images and the calculated film thicknesses before and after sonication, the **Mo film** clearly contains a much higher effective thickness of surface features compared to the **FTO film**, which may allow changes in composition with sonication to be more easily identified.

The properties of as-deposited films on FTO- and (EMAT) Mo-substrates may then be summarized as follows:

- Films possess a bilayer structure, consisting of compact underlayers and rough, non-uniform surface layers that are poorly adhering
- **Mo films** possess thick layers of loosely adhering surface features, which were determined to be S-rich, Zn-rich, and Sn-poor compared to the compact underlayers. This powdery layer was much thicker for the **Mo film** than the **FTO film**.
- After sonication, the **FTO film** and **Mo film** demonstrated approximately similar thicknesses and compositions, with the final films showing severely Zn-poor, S-poor and Sn-rich stoichiometries.

A study of the time evolution of the surface morphology of CZTS on (EMAT) Mo-substrates is presented in Section 7.4.1.3. Growth mechanisms for the surface features are explored in Section 7.4.1.5, including possible explanations for the dissimilarity of surface features on FTO- and (EMAT) Mo-substrates. The hydrogen evolution reaction (HER) is believed to play a strong role in both the Zn-deficiencies and the surface feature growth properties.

7.4.1.2 Cyclic Voltammetry and Peak Assignments

In order to control and improve the stoichiometries and morphologies of as-deposited films, the relationship between the growth conditions and the deposition reaction pathways must be established. As a first step, the composition of deposited species must be correlated with the reduction peaks in the cyclic voltammagrams. Then, potential reaction pathways may be suggested.

FTO-Substrate

A cyclic voltammetry spectrum for the FTO-substrate with nominal bath conditions was measured from 0 to -1.25V at 10mV/s, as shown in Fig. 7-3. The voltammagram indicates a series of cathodic peaks labeled I – VIII. The onset of hydrogen evolution reaction (HER) occurs near -1.10V.

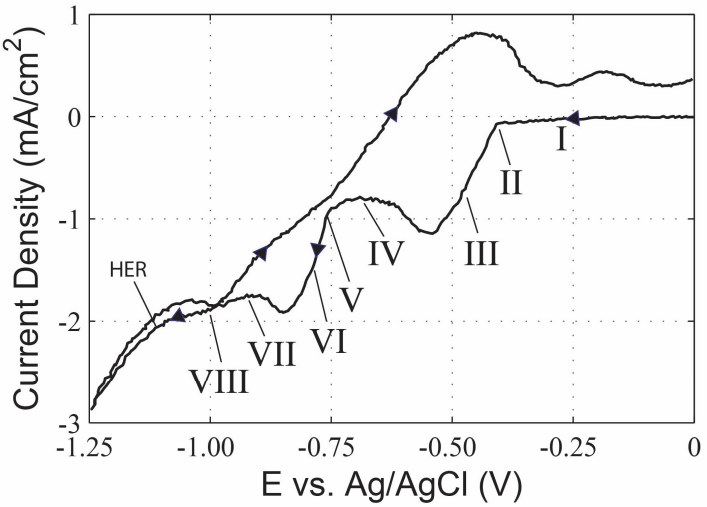

Fig. 7-3. Cyclic voltammagram of nominal bath composition with FTO-substrate

The dominant cathodic peaks at -0.41V (II), -0.75V (V), and -0.91V (VII) show sharp, well-defined drop-offs in cathodic current density consistent with mass-transfer limited conditions. Weaker peaks, evident as shifts in current density slope, appear at -0.21V (I), -0.49V (III), -0.68V (IV), -0.80V (VI), and -1.00V (VIII). The dominant cathodic peak locations are generally consistent with those evident on the cyclic voltammagram (for full electrolyte on Mo-substrate) presented in [6]: -0.45V, -0.64V, -0.84V, and -0.95V. A series of anodic oxidation peaks are also evident on the reverse voltage sweep.

To identify the reduction processes associated with the FTO-substrate, depositions were performed at varying potentials corresponding to the most significant regions identified on Fig. 7-3. The compositions, morphologies, and crystal structures of these films deposited at varying potentials are summarized in Table 7-6, Fig. 7-4, and Fig. 7-5 respectively. Elemental peak overlap and poor surface morphologies prevent reliable determination of the composition by RBS, but PIXE spectra support the reported trends in element ratios in the films.

Table 7-6. Composition of co-electrodeposited CZTS precursors on FTO-substrates deposited at varying potentials, * incomplete film coverage, + element detected in PIXE but peak negligible, ◊ element or film cannot be reliably fitted

Potential	Atomic %					Cu:Zn	Zn:Sn	S:Metal	Thick (nm)
	Cu	Zn	Sn	S	O				
-0.20V*	0	0	0	0	0	-	-	-	-
-0.33V*	0	0	0	0	0	-	-	-	-
-0.45V*	◊	0	0	+	◊	-	-	-	-
-0.50V*	◊	0	0	◊	◊	-	-	-	-
-0.65V	30	0	6	16	48	-	-	0.45	950
-0.80V	24	1	15	32	28	32	0.05	0.81	290
-0.95V	18	3	22	37	20	7.2	0.11	0.87	560
-1.00V	15	5	25	11	56	3.1	0.19	0.25	240
-1.10V	12	7	31	12	38	1.6	0.23	0.24	170
-1.20V	12	11	30	12	35	1.1	0.35	0.23	140

As Table 7-6 and Fig. 7-4 show, no significant deposits are evident at -0.20V and -0.33V. At -0.45V, large, micron-sized grained copper deposits partially cover the substrate. Sn incorporation could not be ruled out by RBS, due to incomplete coverage of the deposits and subsequently convoluted spectra. However, a comparison of PIXE spectra for the sample and the substrate-only indicates negligible increase in Sn concentration. S is similarly difficult to detect by RBS, but PIXE indicates a very small S peak present at -0.45V. PIXE confirms the absence of Zn in the film from -0.20 to -0.50V. The x-ray diffractogram, shown in Fig. 7-5, confirms the presence of elemental copper with a small peak near cubic (111) peak 43.4°. At -0.50V, RBS, SEM, and XRD confirm the presence of large-grained Cu-deposits on the substrate surface. However, the density of the deposits covering the surface significantly decreases.

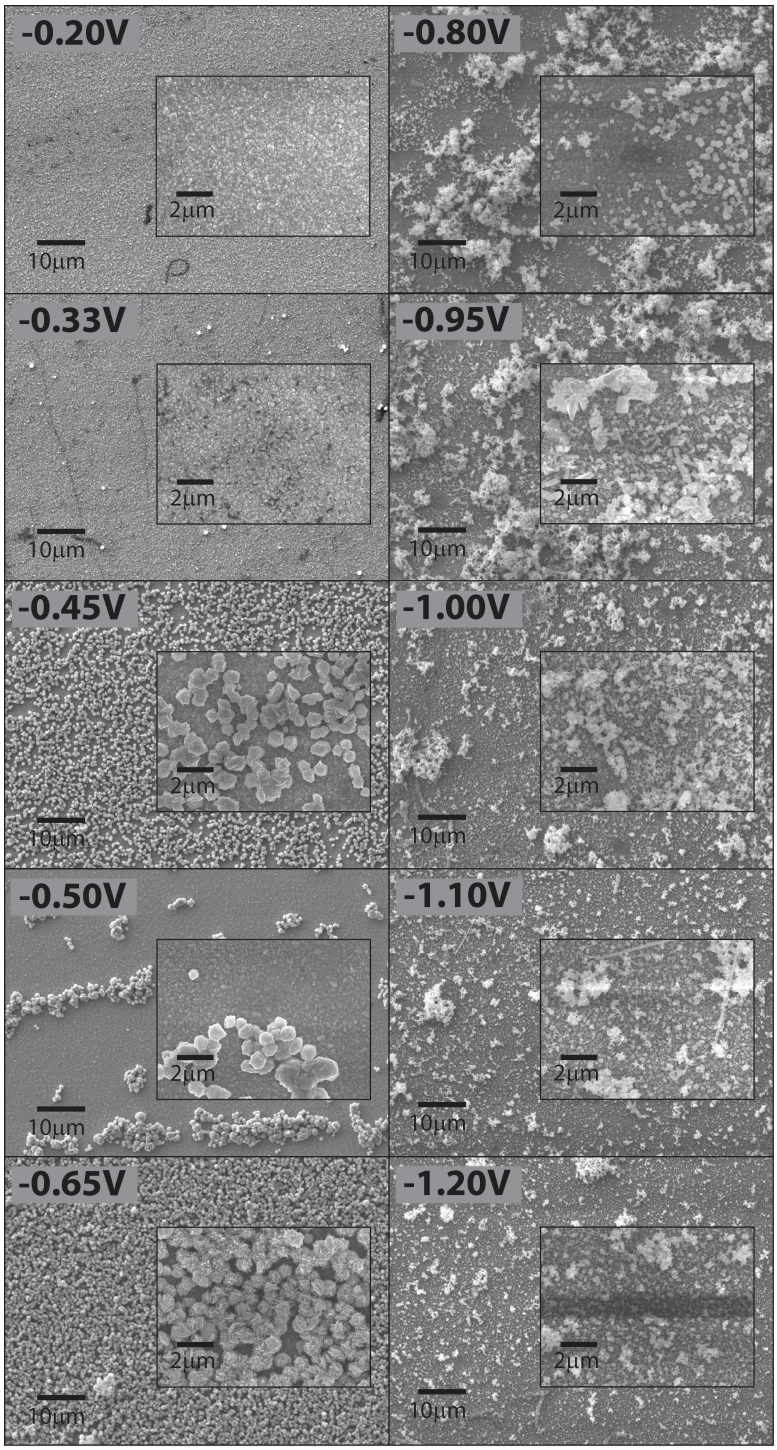

Fig. 7-4. SEM images of co-electrodeposited CZTS precursors on FTO-substrates deposited at varying potentials (nominal bath composition)

At -0.65V, the density of nucleated grains on the substrate increases substantially. The films are not compact, however, as voids are evident in between the micron-sized grains. RBS and PIXE confirm the onset of non-negligible concentrations of Sn and S in the films. The film

thickness of 950nm is consistent with the diameter of the grains shown in Fig. 7-4. The x-ray diffractogram confirms the presence of Cu_2O phase near 36.5° and also indicates a small peak near 42.8°, which may be attributed to a $Cu_{10}Sn_3$ phase. As noted in [3], the high diffusion rate of Cu in Sn frequently leads to the room temperature formation of Cu-Sn alloys. Subsequently, the presence of these phases does not imply the deposition of Cu and Sn through alloy reaction pathways. PIXE confirms the absence of Zn in the deposited film. The onset of Sn and S at the same potential could indicate a compound formation mechanism (e.g. deposition by SnS). Depositions at more negative potentials clearly indicate, however, the presence of elemental Sn phases, suggesting that individual element reduction processes are more likely. Raman spectra measured for this series of films were inconclusive and could not provide confirmation of any metal-sulfide binary phases in the as-deposited films.

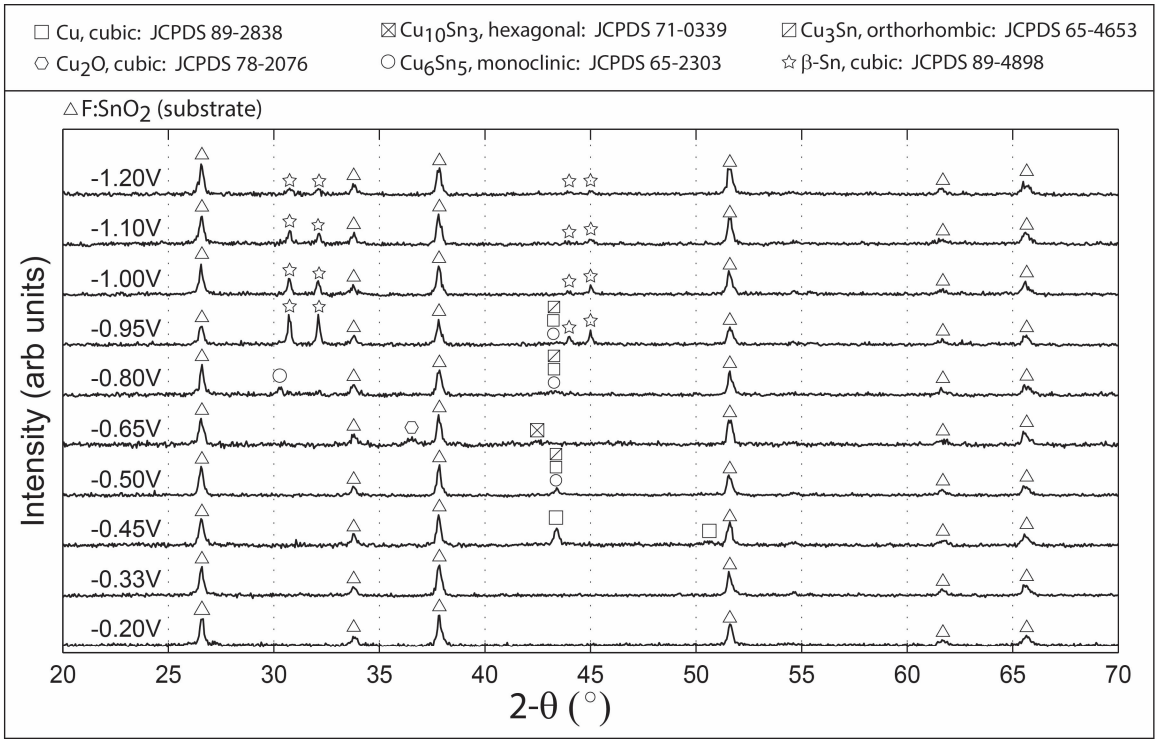

Fig. 7-5. X-ray diffractograms of co-electrodeposited CZTS precursors on FTO-substrates deposited at varying potentials (nominal bath composition)

At -0.80V, an abrupt transition of the film morphology is observed. A dense, small-grained film fully covers the surface with large, patchy clusters of growths decorating the film surface, as shown in Fig. 7-4. An abrupt transition in film composition is also evident at -0.80V, with large increases in Sn and S evident in the films, as shown in Table 7-6. PIXE confirms the onset of non-negligible concentrations of Zn in the films. Cu-Sn alloy phases are evident in the x-ray diffractogram, with a peak near 30.3° attributed to Cu_6Sn_5 and a peak near 43.3° attributed to Cu_3Sn, $Cu_{10}Sn_3$, or Cu_6Sn_5 phases.

At -0.95V, the Sn concentration increases significantly, while the Cu concentration drops off significantly. S concentrations in the film remain high. PIXE confirms a slight increase in the relative Zn concentration compared to the film deposited at -0.80V. The morphology of the film appears similar to the one deposited at -0.80V, characterized by a compact, small-grained film decorated with large, patchy clusters of overgrowths. Notably, the -0.80V and -0.95V sample have the highest S concentrations and also the highest density of surface overgrowths. Well-defined diffraction peaks for elemental Sn are evident in the x-ray diffractogram, while a very weak Cu-Sn alloy peak near 43.3° remains. The increase in intensity of the elemental Sn peaks is attributed to the highly Sn-rich film stoichiometry.

At -1.00V (baseline potential), the Cu concentration decreases slightly, while the Zn and Sn concentrations increase slightly. Notably, however, the S concentration drops dramatically compared to the deposition -0.95V. With increasingly negative deposition potential, at -1.10V and -1.20V, the Cu concentration slowly continues to monotonically decrease, while the Zn concentration slowly continues to monotonically increase. Sn increases and then levels out, staying near 30at%. The S concentration remains low, below 20at%. The morphology of the film deposited at -1.00V appears similar to the one deposited at -0.95V, characterized by a compact, small-grained film decorated with large, patchy clusters of overgrowths. The density of these surface overgrowths decreases with increasingly negative potential from -0.95V to -1.20V, and the measured film thickness also decreases. The decrease in elemental Sn diffraction peak intensity in Fig. 7-5 with increasingly negative deposition potential is attributed to the decrease in film thickness.

Based on the onset of deposition for the different elements, the following assignments may be made for the cathodic peaks on the cyclic voltammagram:

- Dominant cathodic peak at -0.41V (I): elemental Cu reduction
- Weak cathodic peak near -0.68V (IV): Sn and S reduction processes (elemental and SnS_X compound reduction possible)
- Dominant cathodic peak at -0.75V (V): Sn, S and Zn reduction processes, including potentially citrate deprotonation and hydrogen evolution processes (as detailed below)

The peak at -0.41V (I) may clearly be assigned to elemental copper, supported by RBS and XRD identification of the deposited grains. The onset of Sn and S deposition at -0.65V suggests that the weak cathodic peak near -0.68V (IV) may be assigned either to elemental or SnS_X compound reduction. Note that Raman analysis found no evidence of Sn_XS in the deposited films. The strong cathodic peak at -0.75V may be associated with further Sn and S reduction processes, or possibly the onset of Zn reduction processes. However, the near linear increase in Sn concentration in the

film with increasing deposition potential from -0.65V to -0.95V suggests that the sudden increase in current density evident at -0.75V on the cyclic voltammagram likely is not associated with a sudden onset of other Sn reduction processes. Similarly, the relatively small Zn concentrations evident in the film at -0.80V suggest that the steep cathodic current at -0.75V likely is not attributed to the Zn reduction process. However, the rapid rise in S concentration and subsequent leveling off with increasing deposition potential from -0.65V to -0.95V suggests that the peak at -0.75V may be associated with a S reduction process. Further, Gougaud has noted a strong reduction peak between -0.65V and -1.05V associated with deprotonation of sodium citrate (citric acid) and subsequent hydrogen evolution [9]. Such a process may enhance S reduction process through increased H^+ concentrations at the electrode, through reaction (7-5) for instance. See Section 8.2 and Eqn. (8-5) and (8-6) for further details on the citrate deprotonation process.

Note that the film composition shows monotonic trends in the cation element ratios with increasingly negative deposition. After the onset of Zn deposition at -0.80V, the Cu:Zn ratio steadily decreases and the Zn:Sn ratio steadily increases with increasingly negative deposition potential, indicating relative increases in Zn concentration. The S:metal ratio exhibits a large rise between -0.80V and -0.95V, decreases abruptly at -1.00V then remains level through -1.20V. X-ray diffraction indicates the presence of elemental and metal alloy phases, which are easily formed at room temperature.

(EMAT) Mo-Substrate

A cyclic voltammetry spectrum for the (EMAT) Mo-substrate with nominal bath conditions was measured from 0 to -1.25V at 10mV/s, as shown in Fig. 7-6. The voltammagram indicates a series of cathodic peaks labeled I – IV. The onset of HER occurs near -0.85V.

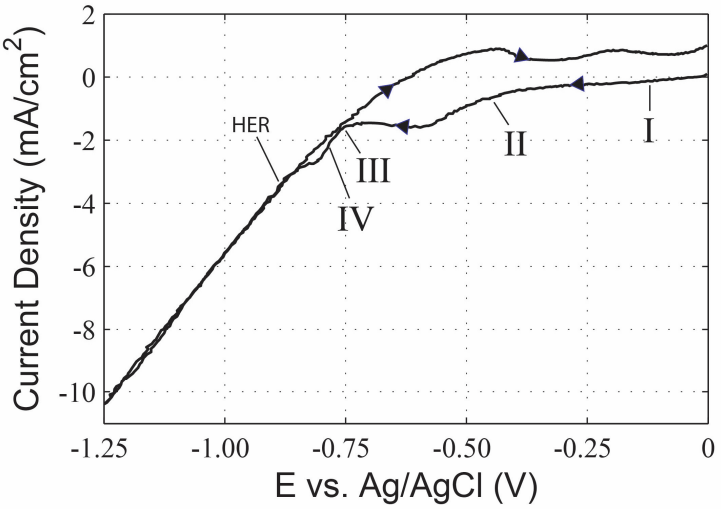

Fig. 7-6. Cyclic voltammagram of nominal bath composition with (EMAT) Mo-substrate

The dominant cathodic peaks at -0.45V (II) and -0.75V (III) show sharp, well-defined drop-offs in cathodic current density consistent with mass-transfer limited conditions. These peaks agree well with those observed on the FTO-substrate, although additional, more negative reduction peaks are likely masked by the onset of HER at much lower overpotential. Weaker peaks, evident as shifts in current density slope, appear at -0.13V (I) and -0.78V (IV). A series of anodic oxidation peaks are also evident on the reverse voltage sweep.

To identify the deposition processes associated with the (EMAT) Mo-substrate, depositions were performed at varying potentials correlating to the most significant regions on Fig. 7-6. The compositions, morphologies, and crystal structures of these films deposited at varying potentials are summarized in Table 7-7, Fig. 7-7, and Fig. 7-8, respectively. Elemental peak overlap and poor surface morphologies prevent reliable determination of the composition by RBS, but PIXE spectra support the reported trends in the element ratios in the films.

Table 7-7. Compositions of co-electrodeposited CZTS precursors on (EMAT) Mo-substrates deposited at varying potentials, * incomplete film coverage, + element detected in PIXE but peak negligible, ◊ element or film cannot be reliably fitted

Potential	Atomic %					Cu:Zn	Zn:Sn	S:Metals	Thick (nm)
	Cu	Zn	Sn	S	O				
-0.20V*	+	0	+	0	0	-	-	-	-
-0.33V*	◊	0	+	0	◊	-	-	-	-
-0.45V	◊	0	+	3	◊	-	-	-	-
-0.50V	◊	0	+	3	◊	-	-	-	-
-0.65V	65	0	3	8	24	-	-	0.11	635
-0.80V	◊	+	◊	◊	◊	53	-	-	1800
-0.95V	21	6	14	25	34	3.6	0.42	0.62	870
-1.00V	23	5	15	25	32	4.3	0.36	0.58	820
-1.10V	18	7	19	12	44	2.6	0.38	0.28	320
-1.20V	22	10	15	14	39	2.2	0.66	0.30	675

Copper nucleation appears at lower potentials on Mo-substrates compared to FTO-substrates, with a few nucleated grains evident at -0.20V and moderate coverage of the substrate evident at -0.33V, as shown in Fig. 7-7. These Cu deposits are consistent with the cyclic voltammagram in Fig. 7-6, which indicates the onset of cathodic current around -0.13V and a softer reduction peak edge near -0.45V. At -0.45V, the density of nucleated grains on the substrate increases substantially. The grains are smaller and more tightly packed than comparable Cu-grains deposited on FTO-substrate at -0.45V. Sn incorporation could not be ruled out by RBS, due to incomplete coverage of the Cu-deposits and subsequently convoluted spectra. However, a comparison of PIXE spectra for the sample and the substrate-only indicates negligible increase in Sn concentration.

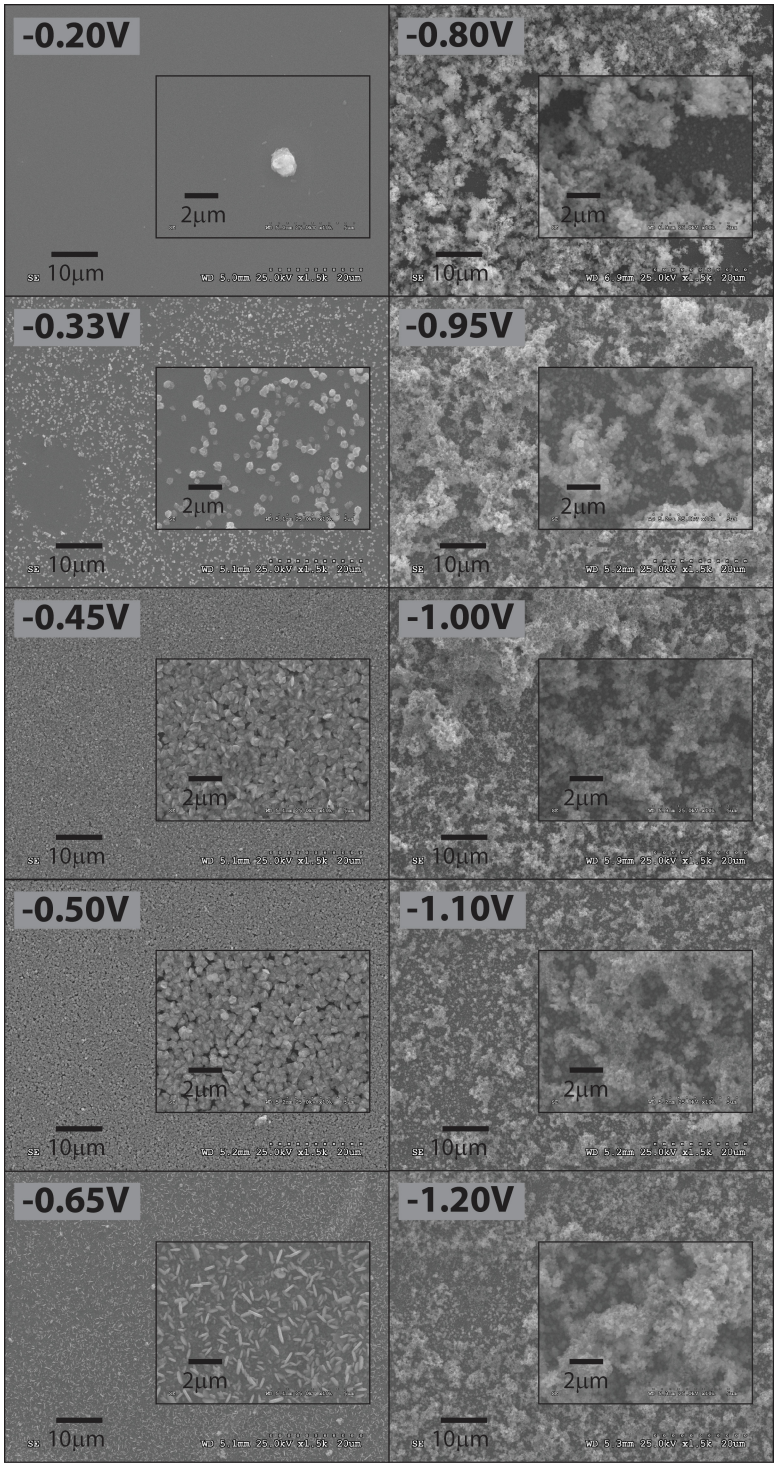

Fig. 7-7. SEM images of co-electrodeposited CZTS precursors on (EMAT) Mo-substrates deposited at varying potentials (nominal bath composition)

Due to peak overlap with Mo, S cannot be detected by PIXE. However, a small but distinct edge in the RBS spectra clearly indicates the presence of a small quantity of S in the films deposited at -0.45V. PIXE confirms the absence of Zn in the film from -0.20 to -0.50V. The x-ray

diffractogram, shown in Fig. 7-8, confirms the presence of elemental copper with a small peak near cubic (111) peak 43.4°. At -0.50V, no significant changes in composition, morphology, or crystal structure are observed.

At -0.65V, a clear morphology transition is evident in Fig. 7-7. Compared to films deposited at -0.50V, films deposited at -0.65V are more compact, with smaller grains. Embedded in these films are larger, vertically-oriented, plate-like grains, which may indicate the presence of another phase, such as SnS (see Fig 3.12 in [29]). The x-ray diffractogram shows a very small peak near 36.5°, which is attributed to Cu_2O, and also shows a small, more well-defined peak near 43.3°, which may be attributed to a Cu-Sn alloy phase. Notably, x-ray diffraction does not indicate the presence of SnS, which may be due to its absence or due to a weak signal resulting from small domain size or amorphous structure. Raman spectroscopy measurements (not shown) indicates a small shoulder near 190cm^{-1}, which may be associated with SnS or the stronger background signal of Cu_2O. The onset of deposition of Sn and S are evident in the RBS and PIXE spectra. PIXE confirms the absence of Zn in the deposited film. Similar to the films deposited on FTO-substrates, the presence of elemental Sn phases at more negative deposition potentials suggests that individual element reduction processes are more probable than a compound SnS_X deposition mechanism.

At -0.80V, another more abrupt transition of the film morphology is observed. A dense, small-grained film fully covers the surface with large, patchy clusters of growths decorating most of the film surface, as shown in Fig. 7-7. The RBS spectrum could not be reliably fitted, although Cu, Sn, and S elements are clearly evident in significant concentrations. PIXE confirms the deposition onset of Zn. The x-ray diffractogram for -0.80V shows three well-defined peaks near 30.3°, 36.5° and 43.2°, which are attributed to Cu_6Sn_5, Cu_2O, and Cu-Sn alloys, respectively. Similar diffraction peaks appear for the film deposited at -0.80V on FTO-substrate, except the strong Cu_2O peak occurs at -0.65V for FTO.

Between -0.65V and -0.95V, the Cu concentration decreases significantly, and the Zn, Sn and S concentrations increase significantly. At more negative deposition potentials, the absolute Zn concentration generally continues to increase, consistent with the onset of the Zn reduction. Further, unlike the FTO-substrate, the relative Zn concentrations in the films on Mo-substrates, evident in the Cu:Zn and Zn:Sn ratios, do not show a monontonic trend with the more negative potentials; however, the ratios do generally decrease and increase, respectively, as expected. Further, the maximum S concentrations were observed at -0.80V and -0.95V on FTO-substrates, while maximum S concentrations are observed at -0.95V and -1.00V on (EMAT) Mo-substrates. Like the films deposited on FTO-substrates, films deposited on (EMAT) Mo-substrates between -0.95V and -1.20V primarily exhibit elemental Sn peaks on the x-ray diffractrogram. A pair of weak Cu-Sn alloy peaks are also observed at -1.20V in Fig. 7-8.

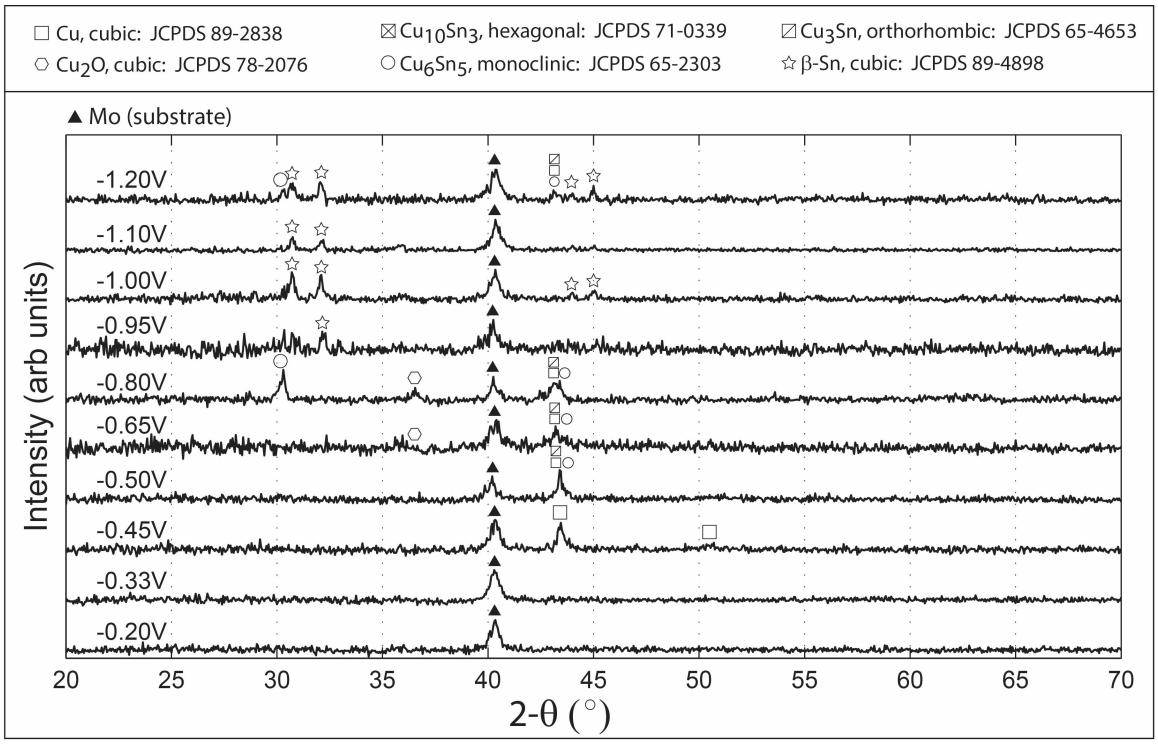

Fig. 7-8. X-ray diffractograms of co-electrodeposited CZTS precursors on (EMAT) Mo-substrates deposited at varying potentials (nominal bath composition)

Based on the onset of deposition for the different elements, the following assignments may be made for the cathodic peaks on the cyclic voltammagram:

- Weak cathodic peak at -0.13V (I): initial nucleation of elemental Cu
- Dominant cathodic peak at -0.45V (II): elemental Cu reduction
- At -0.65V (reduction peak not clearly evident in Fig. 7-6): Sn and S reduction processes (elemental and SnS_X compound reduction possible)
- Dominant cathodic peak at -0.75V (III): Sn, S and Zn reduction processes, including potentially citrate deprotonation and hydrogen evolution processes
- No cathodic peaks evident beyond -0.85V due to hydrogen evolution reaction

The peaks at -0.13V (I) and -0.45V (II) may clearly be assigned to elemental copper, supported by RBS and XRD identification of the deposited grains. The onset of Sn and S deposition at -0.65V suggests that the presence of a weak cathodic peak, not clearly apparent on the cyclic voltammagram in Fig. 7-6, which may be assigned either to elemental or SnS_X compound reduction. Note that Raman analysis found no clear evidence of Sn_XS in the deposited films. The strong cathodic peak at -0.75V may be associated with further reduction processes associated with Sn and S, or possibly the onset of Zn reduction processes. Similar to the films deposited on FTO-

substrates, the lack of large increases in the Sn and Zn concentrations at -0.80V suggests that the significant increase in current density evident at -0.75V (III) on the cyclic voltammagram likely is not associated with a sudden onset of other Sn or Zn reduction processes. The RBS spectra for the film deposited at -0.80V on (EMAT) Mo-substrate could not be reliability fitted but clearly indicates Sn and Zn concentrations in between those deposited at -0.65V and -0.90V. The rapid rise in S concentration and subsequent leveling off with increasing deposition potential from -0.65V to -1.00V suggests that the peak at -0.75V may be associated with a S reduction process. As previously noted, deprotonation of sodium citrate may enhance S reduction process through increased H^+ concentrations at the electrode.

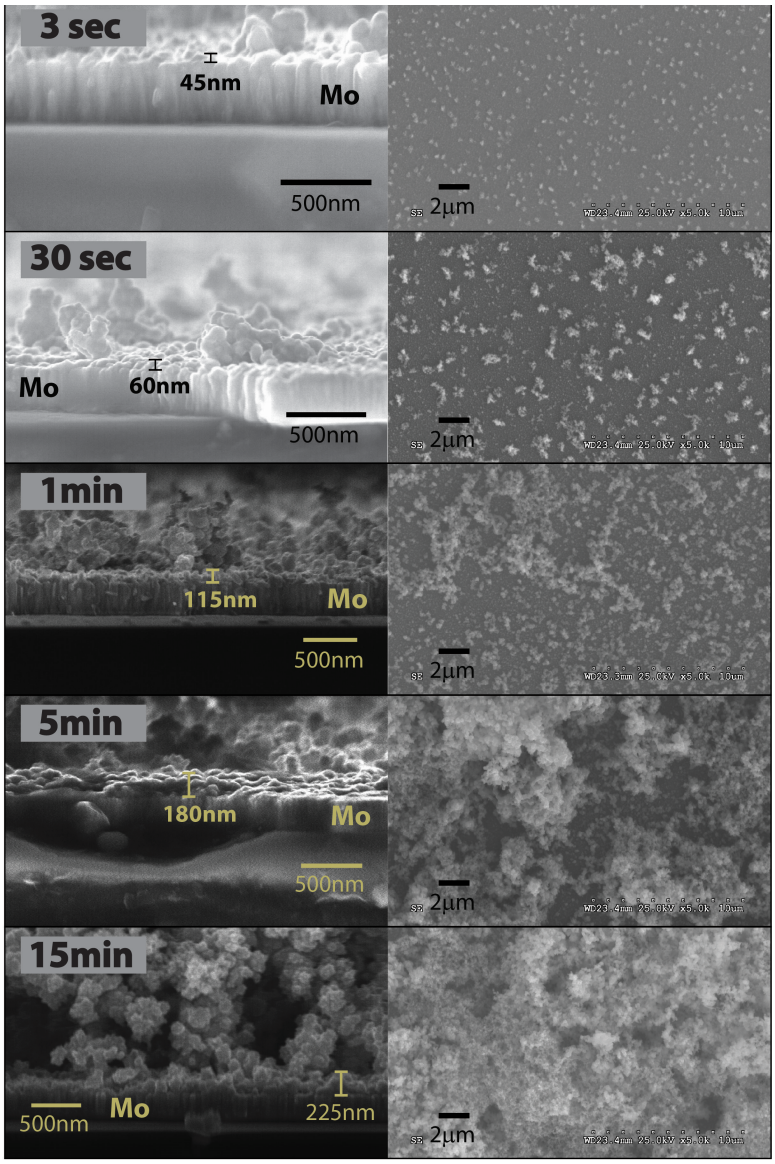

Fig. 7-9. Top-down and cross-sectional SEM images of co-electrodeposited CZTS precursors on (EMAT) Mo-substrates for deposition times of 3sec - 15min

7.4.1.3 Time Evolution of Morphology

In order to investigate the growth behavior of the large surface features that decorate the film and that yield unstable, powdery surface layers, films were prepared with varying deposition times: 3sec, 30sec, 1min, 5min, and 15min. Using the nominal bath composition (see Table 7-3), depositions were performed on (EMAT) Mo-substrates at -1.00V. The morphologies of as-deposited films with increasing deposition time are shown below in Fig. 7-9.

Uniformly distributed, three-dimensional surface features on the order of 100nm are evident after only 3sec of growth. Their sizes increase with increasing deposition time, suggesting preferential nucleation at these sites. These "overgrowths" may therefore result from nucleation-coalescence or diffusion-limited, dendritic growth mechanisms. Multi-micron sized dendrites have been demonstrated with co-electrodeposition processes that used similar electrolyte baths less the S-source (sodium thiosulfate) [9]. The growth mechanisms of these overgrowths are explored further in Section 7.4.1.5.

After approximately 5min of growth, these loosely packed overgrowths cover nearly the entire film surface. However, the SEM images also show the formation of a compact, well-adhering "underlayer" which grows with time as shown in Fig. 7-9 and Fig. 7-10. Bilayer structures of electrodeposited CZTS films, characterized by thin, dense nano-grained underlayers and thicker, rougher, large-grained top layers were also demonstrated in [26]. The rough surface layers in [26] were considerably more compact, however, and more in agreement with the films observed in Section 7.4.2.3, which were fabricated from baths without tartaric acid.

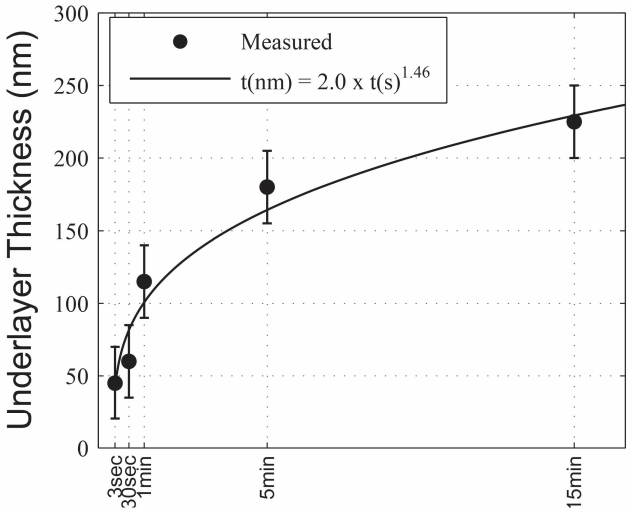

Fig. 7-10. Underlayer film thickness vs. deposition time

As Fig. 7-10 shows, the underlayer exhibits power-law type growth, significantly leveling off after 5min of deposition. This leveling off is consistent with the increasing surface coverage by

the overgrowths, suggesting that these overgrowths effectively shadow the underlayer and severely inhibit further growth.

7.4.1.4 Effects of Bath Composition

The dependence of the as-deposited CZTS precursor compositions and morphologies on the bath composition was investigated for (EMAT) Mo-substrates by varying each bath component while holding the others constant. Due to interactions of the electroactive species in solution, it was not expected that the film composition would change linearly with the bath component concentrations. In all cases, deposition was performed for 25min at constant potential of -1.00V.

As with the films discussed in Section 7.4.1.1 and 7.4.1.2, elemental peak overlap and poor surface morphologies of many of the films prevent reliable determination of the compositions by RBS, but PIXE spectra support the reported trends in the element ratios in the films.

$CuSO_4$ Concentration

Using the nominal bath composition (see Table 7-3), the $CuSO_4$ concentration was decreased from its nominal value of 0.02M to 0.01M. The resulting compositions and morphologies are summarized in Table 7-8 (bold indicates nominal) and Fig. 7-11 (* indicates nominal), respectively.

Table 7-8. Compositions of co-electrodeposited CZTS precursors deposited with varying $CuSO_4$ concentrations

[$CuSO_4$]	Atomic %					Cu:Zn	Zn:Sn	S:Metals	Thick (nm)
	Cu	Zn	Sn	S	O				
0.010M	19	4	35	20	22	4.6	0.12	0.34	820
0.015M	21	5	28	20	26	4.4	0.17	0.38	660
0.020M	23	5	15	25	32	4.3	0.36	0.58	820

As expected, the relative Cu concentration in the film increases with increasing $CuSO_4$ concentration, evident as an increase in the Cu:[Zn+Sn] ratio. Conversely, the relative Sn concentration monotonically decreases with increasing $CuSO_4$ concentration. Notably, the changes in Cu:Sn ratios in the film were greater than the changes in the $CuSO_4$:$SnSO_4$, suggesting an interaction between the Cu and Sn deposition mechanism. This inverse Cu and Sn relationship, associated with varying $CuSO_4$ concentration, is observed in all $Na_2S_2O_3$-containing baths with and without tartaric acid.

Unexpectedly, the relative Zn concentration, evident as the Cu:Zn ratio, increases with increasing $CuSO_4$ concentration. The changes in Zn concentration are small, however, and may be considered negligible compared to the accuracy of the calculation. Similarly, the absolute S concentration appears to increase with increasing $CuSO_4$ concentration, but the S concentrations

cannot be reliably determined from RBS or PIXE due to S peak overlaps with Mo. The increase in S:metal ratio with increasing $CuSO_4$ concentration can be primarily attributed to the associated decrease in Sn concentration in the film.

Note the non-monotonic change in film thickness with increasing $CuSO_4$ concentration. This most likely can be attributed to the non-uniformity and/or instability of the surface layer. An RBS measurement of the film at location of less coverage, such as the upper left region of Fig. 7-11 (0.010M $CuSO_4$), would yield a smaller measured thickness. Further, inherent variability in the amount of surface layer removed with rinsing after deposition also can impact the measured film thickness.

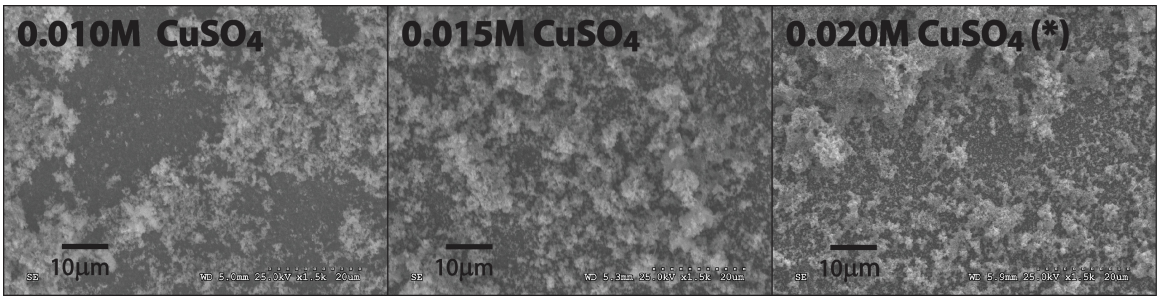

Fig. 7-11. SEM images of co-electrodeposited CZTS precursors on (EMAT) Mo-substrates deposited with varying $CuSO_4$ concentrations

The surface morphologies of as-deposited films did not vary strongly with increasing $CuSO_4$ concentration, as shown in Fig. 7-11. The films all exhibited bilayer structures, consisting of compact underlayers and loosely-adhering surface layers. The overgrowths did not exhibit any notable changes in size or coverage with $CuSO_4$ concentration.

$ZnSO_4$ Concentration

Using the nominal bath composition (see Table 7-3), the $ZnSO_4$ concentration was increased from its nominal value of 0.01M to 0.02M. The resulting compositions and morphologies are summarized in Table 7-9 (bold indicates nominal) and Fig. 7-12 (* indicates nominal), respectively.

Table 7-9. Compositions of co-electrodeposited CZTS precursors deposited with varying $ZnSO_4$ concentrations

[$ZnSO_4$]	Atomic %					Cu:Zn	Zn:Sn	S:Metals	Thick (nm)
	Cu	Zn	Sn	S	O				
0.010M	23	5	15	25	32	4.3	0.36	0.58	820
0.020M	21	11	15	25	28	2.0	0.71	0.53	780

As expected, the relative Zn concentration in the film increases significantly with increasing $ZnSO_4$ concentration, evident as a decrease in Cu:Zn and increase in Zn:Sn ratios. In fact, a doubling in the $ZnSO_4$ concentration yields an approximately two-fold increase in the

absolute Zn concentration in the film. The other component concentrations (e.g. Cu, Sn and S) remain approximately constant with increasing $ZnSO_4$.

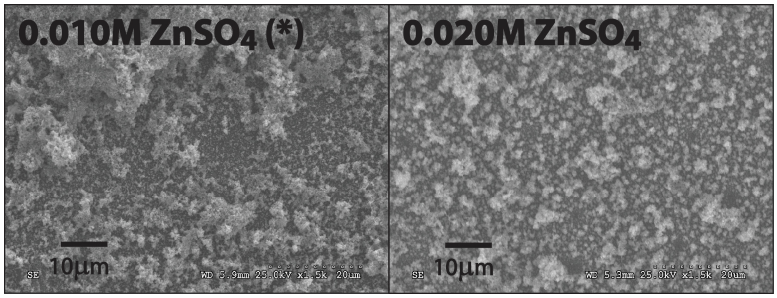

Fig. 7-12. SEM images of co-electrodeposited CZTS precursors on (EMAT) Mo-substrates deposited with varying $ZnSO_4$ concentrations

With increasing $ZnSO_4$ concentration, the surface morphologies of as-deposited films showed a decrease in large well-connected surface features to smaller, more isolated surface features that were more uniformly distributed, as shown in Fig. 7-12. The increase in film uniformity at 0.020M $ZnSO_4$ coincides with a reduction in steady-state deposition current (not shown) that is consistent with a lower rate of hydrogen evolution reaction. Films both exhibited bilayer structures, consisting of compact underlayers and loosely-adhering surface layers.

$SnSO_4$ Concentration

Using the nominal bath composition (see Table 7-3), the $SnSO_4$ concentration was decreased from its nominal value of 0.02M to 0.005M. The resulting compositions and morphologies are summarized in Table 7-10 (bold indicates nominal) and Fig. 7-13 (* indicates nominal), respectively.

Table 7-10. Compositions of co-electrodeposited CZTS precursors deposited with varying $SnSO_4$ concentrations

[$SnSO_4$]	Atomic %					Cu:Zn	Zn:Sn	S:Metals	Thick (nm)
	Cu	Zn	Sn	S	O				
0.005M	25	13	1	18	43	1.9	10	0.44	840
0.010M	25	12	4	17	42	2.0	3.0	0.41	720
0.020M	23	5	15	25	32	4.3	0.36	0.58	820

As expected, the relative Sn concentration in the film increases with increasing $SnSO_4$ concentration, evident as an increase in the Sn:[Cu+Zn] ratio. Conversely, the relative Cu concentration monotonically decreases with increasing $SnSO_4$ concentration. This inverse Sn and Cu relationship, associated with varying $SnSO_4$ concentration, is similar to that observed with varying $CuSO_4$ concentration. Similarly, changes in Cu:Sn ratios in the film were greater than the changes in the $CuSO_4$:$SnSO_4$. In both cases, much larger variations are observed in the absolute Sn concentrations compared to absolute Cu concentrations.

The relative Zn concentration increases with decreasing $SnSO_4$ concentration, evident as decreased Cu:Zn and increased Zn:Sn element ratios. A similar trend is also observed in baths with varying $CuSO_4$ concentration. With increasing $CuSO_4$ concentration, the Sn concentration in the film decreases, while the Cu:Zn ratio increases. These trends suggest that the Sn deposition mechanism may influence the Zn incorporation in the film, particularly at very low Sn deposition rates.

The S concentration appears to increase with increasing $SnSO_4$ concentration, evident as increasing S:metals ratio, but the calculated S concentrations cannot be reliably determined from RBS or PIXE due to S peak overlaps with Mo. The non-monotonic change in film thickness with increasing $SnSO_4$ concentration can most likely be attributed to the non-uniformity and/or instability of the surface layer, as detailed in the previous section.

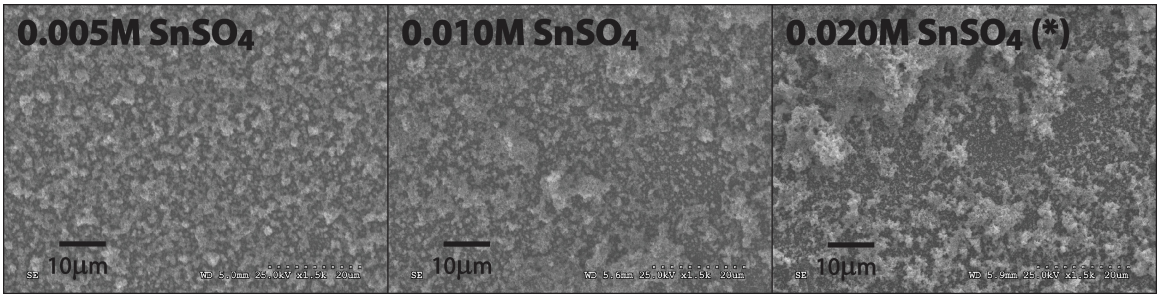

Fig. 7-13. SEM images of co-electrodeposited CZTS precursors on (EMAT) Mo-substrates deposited with varying $SnSO_4$ concentrations

With decreasing $SnSO_4$ concentration, the surface morphologies of as-deposited films showed a decrease in large well-connected surface features to smaller, more isolated surface features that were more uniformly distributed, as shown in Fig. 7-13. The increase in film uniformity at 0.005M $SnSO_4$ coincides with a reduction in steady-state deposition current (not shown) that is consistent with a lower rate of hydrogen evolution reaction. The films all exhibited bilayer structures, consisting of compact underlayers and loosely-adhering surface layers.

$Na_2S_2O_3$ Concentration

Using the nominal bath composition (see Table 7-3), the $Na_2S_2O_3$ concentration was varied from its nominal value between 0.01M and 0.03M. The resulting compositions and morphologies are summarized in Table 7-11 (bold indicates nominal) and Fig. 7-14 (* indicates nominal), respectively.

No clear correlation exists between the S concentration in the films and the $Na_2S_2O_3$ concentrations in the bath. Counterintuitively, the S concentration appears to decrease with increasing $Na_2S_2O_3$ concentration. However, the calculated S concentrations cannot be reliably determined from RBS or PIXE due to S peak overlaps with Mo. Moreover, the film thickness also

decreases by almost 50%, possibly indicating a significant loss of the film during rinsing, due to poor adhesion, which may influence the measured composition. The thickness may also decrease as a result of increased hydrogen evolution reaction or modification of the species stabilities with increasing $Na_2S_2O_3$. As described in Section 7.4.1.5, thiosulfate can cause sulfur and metal-sulfide colloid formation and metal-thiosulfate complex formation.

Table 7-11. Compositions of co-electrodeposited CZTS precursors deposited with varying $Na_2S_2O_3$ concentrations

$[Na_2S_2O_3]$	Atomic %					Cu:Zn	Zn:Sn	S:Metals	Thick (nm)
	Cu	Zn	Sn	S	O				
0.010M	28	8	25	26	13	3.7	0.30	0.43	850
0.020M	23	5	15	25	32	4.3	0.36	0.58	820
0.030M	24	6	19	13	38	4.2	0.29	0.27	435

With increasing $Na_2S_2O_3$ concentration, the surface morphologies of as-deposited films show slight reductions in the densities of surface features, as shown in Fig. 7-12. Films all exhibited bilayer structures, consisting of compact underlayers and loosely-adhering surface layers.

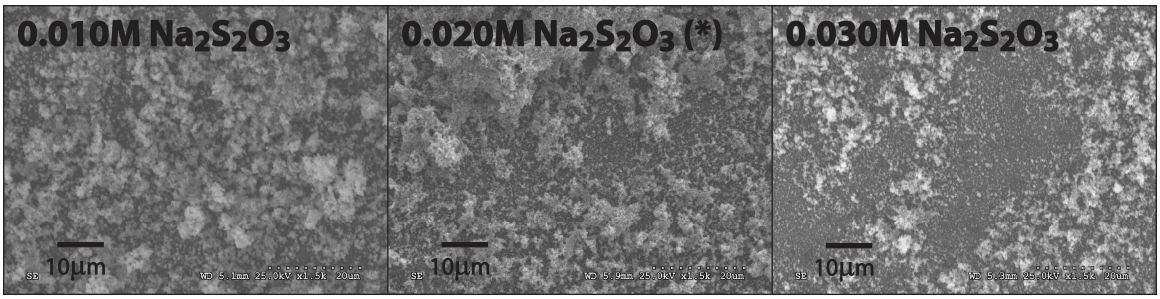

Fig. 7-14. SEM images of co-electrodeposited CZTS precursors on (EMAT) Mo-substrates deposited with varying $Na_2S_2O_3$ concentrations

Citrate Concentration

Using the nominal bath composition (see Table 7-3), the Citrate ($Na_3C_6H_5O_7$) concentration was varied from its nominal value between 0 and 0.3M. Note that the removal of tartaric acid from the bath decreases the pH from ~4.5 to ~0. The resulting compositions and morphologies are summarized in Table 7-12 (bold indicates nominal) and Fig. 7-15 (* indicates nominal), respectively.

The removal of the citrate from the bath reduced the pH to 0 and significantly modified the growth characteristics of the bath. During deposition, dendrites up to ~10mm, were evident on the film surface. After removal of the sample from the deposition bath, most of these dendrites and the deposited film was removed by rinsing, leaving only a thin 90nm thick layer present, as shown in Table 7-12. The remaining film contained very little Zn, evident as a large Cu:Zn and a

small Zn:Sn ratio. The dramatic increase in dendrite growth may be related to the significantly lower pH or the removal of complexing agent.

Table 7-12. Compositions of co-electrodeposited CZTS precursors deposited with varying Citrate concentrations

[Citrate]	Atomic %					Cu:Zn	Zn:Sn	S:Metals	Thick (nm)
	Cu	Zn	Sn	S	O				
None	31	4	23	33	9	8.1	0.17	0.56	90
0.10M	22	10	16	20	32	2.3	0.63	0.42	980
0.20M	23	5	15	25	32	4.3	0.36	0.58	820
0.30M	25	5	21	15	34	4.5	0.21	0.34	335

For baths containing Citrate, the relative Zn concentration decreases with increasing Citrate concentration, evident as an increase in Cu:Zn and a decrease in Zn:Sn ratios. No strong trends are observed in the S concentration in the films, contrary to [21], which demonstrated monotonic increases in S concentration with increasing Citrate concentration. Note the film thickness decreased with increasing Citrate concentration, consistent with other studies of $CuInSe_2$ electrodeposition that demonstrated a decreasing deposition rate and slowing interfacial reaction kinetics in the presence of citrate ions [29].

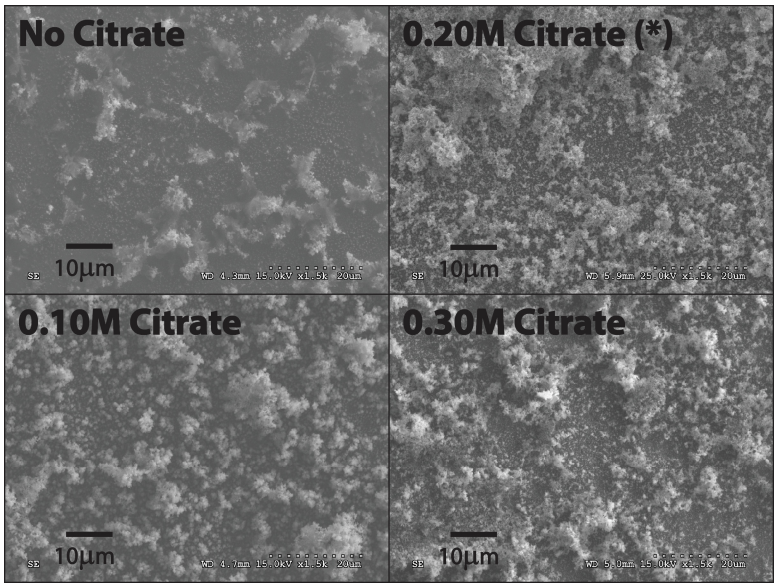

Fig. 7-15. SEM images of co-electrodeposited CZTS precursors on (EMAT) Mo-substrates deposited with varying Citrate concentrations

As described above, removal of the Citrate significantly modified the morphology of the deposited film, yielding multi-mm length dendrites and a loose, powdery film almost entirely removed after rinsing. For baths containing Citrate, increasing the Citrate concentration did not

significantly modify the film surface morphologies, as shown in Fig. 7-15. Films all exhibited bilayer structures, consisting of compact underlayers and loosely-adhering surface layers.

Tartaric Acid Concentration

Using the nominal bath composition (see Table 7-3), the tartaric acid ($C_6H_4O_6$) concentration was varied between its nominal value of 0.1M and 0M. Note that the removal of tartaric acid from the bath increases the pH from ~4.5 to ~6. The resulting compositions and morphologies are summarized in Table 7-13 (bold indicates nominal) and Fig. 7-16 (* indicates nominal), respectively.

Table 7-13. Compositions of co-electrodeposited CZTS precursors deposited with varying tartaric acid concentrations

[Tartaric]	Atomic %					Cu:Zn	Zn:Sn	S:Metals	Thick (nm)
	Cu	Zn	Sn	S	O				
None	32	8	17	20	23	3.9	0.47	0.35	1330
0.10M	23	5	15	25	32	4.3	0.36	0.58	820

The removal of tartaric acid yields films with compositions closer to stoichiometry, achieved primarily by the reduction of relative Sn concentration in the film. The Cu:Zn ratio remains near 4, but the Zn:Sn ratio increases from 0.36 to 0.47. Most significantly, the Cu:Sn ratio increases from 1.5 to 1.9. The trend is even more exaggerated when considering the composition of the sonicated sample, which has a Cu:Sn ratio of 0.96 (see Table 7-5). On the other hand, the S:metals ratio decreased significantly with the removal of the tartaric acid.

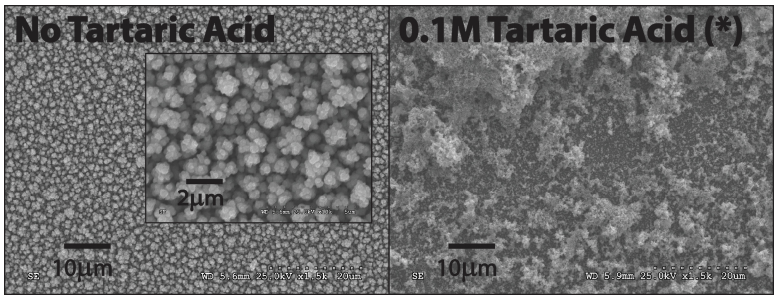

Fig. 7-16. SEM images of co-electrodeposited CZTS precursors on (EMAT) Mo-substrates deposited with varying Tartaric acid concentrations

The surface morphologies of as-deposited films dramatically improved with the removal of tartaric acid from the bath, as shown in Fig. 7-16. While the film deposited without tartaric acid still showed a high degree of roughness, consistent with diffusion-limited growth mechanisms, it exhibited much greater uniformity with no evidence of the overgrowths present on all previous samples. Note the steady-state deposition current decreases by approximately a factor of 4 with the removal of tartaric acid, indicating a reduction in the hydrogen evolution reaction. Removing the tartaric acid may improve film quality by increasing the bath pH (and thereby reducing HER)

or by modifying the complexing behavior of species in the bath, as discussed in more detail in Section 7.4.1.5. Work reported in Section 7.4.2 will demonstrate that, for baths without tartaric acid, further improvement in the surface morphologies can be achieved through optimization of the bath and deposition parameters.

The effects of bath composition on the composition and morphology of as-deposited films may then be summarized as follows:

- The metal elements (Cu, Zn, and Sn) increased in concentration in the deposited films with increasing concentrations of their precursor metal sulfates, as expected.
- The S concentration did not increase with increasing $Na_2S_2O_3$ concentration, and may in fact decrease. Accurate measurement of S concentrations in the films was difficult, however, due to significant peak overlap of Mo and S in RBS and PIXE spectra.
- The Cu and Sn concentrations in the films demonstrated an inverse relationship. For instance, increasing the $CuSO_4$ increased the Cu and decreased the Sn concentrations in the films. Conversely, increasing the $SnSO_4$ increased the Sn and decreased the Cu concentrations in the films. However, shifts in the Sn concentrations were significantly more pronounced than Cu in both cases.
- The Zn concentration correlated inversely with Sn concentration when varying $CuSO_4$ and $SnSO_4$ concentrations, with this dependence particularly strong at low Sn concentrations (< 10at%). However, varying the $ZnSO_4$ concentration was not shown to strongly affect the relative Sn concentration in the film.
- Changes in component precursors ($CuSO_4$, $ZnSO_4$, $SnSO_4$, and $Na_2S_2O_3$) did not yield strong changes in the surface morphologies of the as-deposited films. The films, in general, exhibited bilayer structures, consisting of compact underlayers and loosely adhering, surface layers.
- The removal of Citrate drove the bath strongly acidic (pH ~ 0) and generated multi-mm length dendrites during deposition. The deposited film was severely inadhesive, and most of the film was removed after rinsing.
- In baths containing Citrate, increasing the Citrate concentration decreased the relative Zn concentrations in the films and negligibly modified the as-deposited surface morphologies.
- The removal of tartaric acid significantly improved both the composition and morphology of the as-deposited film, reducing the relative Sn concentration and eliminating detrimental overgrowths. As-deposited films exhibited dendritic growth

features, but they were significantly more uniform and well-adhering. The steady-state deposition current decreased by a factor of 4, indicating significantly decreased hydrogen evolution reaction.

7.4.1.5 Proposed Deposition Mechanisms

Substrate Damage

After electrodepositions, visible changes to molybdenum layers are observed, while FTO layers remain unchanged. Both (EMAT) Mo- and (Guardian) Mo-substrates demonstrate changes in physical appearance after deposition, but the changes and their impacts on the deposited film morphology differ considerably. Prior to deposition, the backside of the (EMAT) Mo film viewed through the glass is highly specular and smooth; after deposition, the molybdenum film is significantly less reflective and more matted in appearance. No pits are evident and the film remains intact. However, since the molybdenum layer is optically thick, changes in the appearance of the back (glass-side) surface must indicate modifications to the Mo film itself. The (Guardian) Mo films completely delaminated after deposition from baths containing tartaric acid, attributed to the significant compressive-strain and multi-layer structure of the Mo films, as described in Section 3.2.4.1 and Section 7.4.2.9. For this reason, results for depositions on (Guardian) Mo-substrate are not reported for baths containing tartaric acid

The depositions do not cause noticeable changes in the compositions or structures of the (EMAT) Mo- or FTO-layers, as evidenced by RBS and x-ray diffraction. Due to peak overlap in RBS, however, small changes in the oxygen contents of the Mo films, which might result from oxidation, may not be detected. The cause of the visible changes to the (EMAT) Mo films remains unclear. However, for baths with tartaric acid, the poor surface morphologies of the films remain the predominant limiting factor in the development of useful absorber layers, and their possible origins are discussed further below.

Possible Growth Processes and Side Reactions

The co-electrodeposition of a multi-element system represents an inherently complex process, frequently demonstrating modified deposition behavior resulting from interaction of two or more of the elements. Anomalous co-deposition, as detailed in Section 3.2.2.3, can cause noble shifts in the reduction potential of electroactive species by lowering their free energies through compound and alloy formation [30]. Subsequently, co-electrodeposition of CZTS precursors may involve many single- and multi-element reduction processes occurring in parallel. Most reported works, however, propose that the co-electrodeposition of CZTS precursors proceeds primarily by parallel single-element reduction processes, as detailed in Section ⊠ and described by reactions (7-1) – (7-5). In [9], an additional citrate deprotonation and hydrogen evolution reaction were noted for baths containing citrate complexing agents. As this work shows, hydrogen evolution

reaction and possibly other chemical reactions likely also play important roles in the deposition process, particularly from baths containing tartaric acid. This section first discusses the general chemistry of the deposition, noting additional reaction pathways and side reactions beyond conventionally assigned mechanisms that may be active. Then, mechanisms are proposed for the reduction processes of deposition, the morphology evolution of the films, and the observed trends in film composition.

In addition to the conventionally assigned reduction processes (7-1) - (7-5), precipitation of sulfur colloids, precipitation of binary metal-sulfide compounds, precipitation of metal hydroxides, and cathodic electrodeposition of binary metal-sulfide compounds (Cu_2S, ZnS, SnS) have been shown to be active in similar electrodeposition processes. Due to chemically unstable disproportionation reactions in acidic baths, thiosulfate plays a strong role in heterogeneous and homogeneous chemical reactions during deposition. The thiosulfate ion also acts as an additional metal complexing agent.

Sodium thiosulfate provides $S_2O_3^{2-}$ anions in solution. In addition to the cathodic reduction processes described by (7-4) and (7-5), many other thiosulfate ion reactions are possible. In particular, acidic baths of thiosulfate are known to readily form sulfur colloids in bulk solution by disproportionation reaction with hydrogen ions as follows [29]:

$$S_2O_3^{2-}(aq) + H^+(aq) \rightarrow S(colloid) + HSO_3^{2-} \qquad (7\text{-}6)$$

Reaction (7-6) is commonly referred to as the **clock reaction**, since the kinetics may be evaluated by measuring the time required for the solution to turn opaque by the sulfur colloid suspension.

In general, compounds may precipitate out of solution when their ionic product exceeds their solubility product, a condition known as **supersaturation** [31, 32]. The lower a compound's solubility product, the more likely it is that the compound will precipitate [31, 32]. Temperature, solvent, and particle size are the main factors affecting the solubility constant [31]. Chemical bath deposition (CBD) exploits this property to deposit low solubility compound thin films in the absence of an electrochemical potential [31, 32]. When the solution becomes supersaturated, ions combine to form precipitate compounds in bulk solution (homogeneous) and on the substrate (heterogeneous) [31]. Thin films of Cu_2S [31, 33] and SnS [31, 34, 35] have been fabricated by CBD from solutions containing metal salts and $Na_2S_2O_3$, typically described by thiosulfate reduction via reaction (7-5) or (7-6) and final compound formation via reaction (7-9). Chemical bath deposition proceeds via two pathways: ion-by-ion growth and colloidal aggregation [29]. In ion-by-ion growth, the metal and chalcogen ions are separately adsorbed on the substrate surface, followed by compound formation as in Eqn. (7-8) [29]. In colloidal aggregation, the metal-sulfide

compounds precipitate in solution, then adsorb and coalesce on the film [29]. In CBD of CdS, rough, powdery films have been attributed to colloidal aggregation growth mechanisms [36].

The thiosulfate ion has also been shown to effectively complex metals, such as Cu and Sn [33, 37]. In fact, the cathodic co-electrodeposition of Sn an S has been possibly attributed to the complex formation between the two elements [37]. Thiosulfate has been shown to reduce as well as complex Cu ions, according to the following reactions [38]:

$$2Cu^{2+}(aq) + 2S_2O_3^{2-}(aq) \rightarrow 2Cu^{+}(aq) + S_4O_6^{2-}(aq) \quad (7\text{-}7)$$

$$2Cu^{+}(aq) + 2S_2O_3^{2-}(aq) \rightarrow Cu_2(S_2O_3)_2^{2-}(aq) \quad (7\text{-}8)$$

Grozdanov attributes the deposition of Cu_2S instead of CuS by chemical bath deposition method to this reduction of Cu^{2+} to Cu^{+} by the thiosulfate ion [33].

Similar to metal sulfides, many metal hydroxides are also highly insoluble [39, 40]. In more basic (alkaline) solutions, metals may react with hydroxide ions to form metal hydroxides. While the deposition baths investigated in this dissertation are all moderately (pH~4.5) to weakly (ph~6) acidic, depending on the presence of tartaric acid, hydrogen evolution reaction can cause large rises in the local pH at the working electrode [29]. For highly acidic baths or moderately high rates of hydrogen evolution, H_2 gas generation proceeds via reaction (3-33). At high enough reaction rates, H^+ ions are consumed faster than they can be replenished by transport from the bulk, leaving an excess of OH^- ions near the site of the HER (e.g. the working electrode). For very high rates of hydrogen evolution reaction, H_2 gas generation proceeds via water reduction (3-34), yielding high concentrations of OH^- ions. The rise in local pH can be particularly extreme when buffering agents are not used, and metal hydroxides may precipitate on the surface of the working electrode.

In co-electrodeposition studies of $CuInSe_2$, indium hydroxide particulates (~100nm) have been shown to precipitate on the surface of deposited films [41]. These precipitates are attributed to local pH rises at the working electrode resulting from hydrogen evolution reaction [29, 41, 42]. The use of complexing and buffering agents has been shown to mitigate indium hydroxide formation by reducing pH variations. In [9], the chemical stabilities of baths similar to Pawar's method (less $Na_2S_2O_3$) are investigated. The study notes that the pH must be maintained less than 7 to prevent precipitation of copper and zinc oxides and less than 5 to prevent precipitation of tin oxide [9]. While these species stabilities are undoubtedly modified by the presence of $Na_2S_2O_3$ used in these depositions, the work in [9] suggests additional routes to the precipitation of insoluble oxide species that might be associated with local rises in pH caused by hydrogen evolution reaction.

The cathodic co-electrodeposition of Cu_2S, ZnS, and SnS have been reported from $Na_2S_2O_3$-containing baths [37, 43-50]. However, the deposition mechanism is generally described

according to parallel reduction processes of the metal and the S^{2-} ion, as in (7-1) - (7-4), with the final compound formation given by the following [47-50]:

$$\frac{2}{n} M^{n+}(aq) + S^{2-}(aq) \rightarrow M_{(2/n)}S(s) \tag{7-9}$$

where M is the given metal, n is the oxidation state of the metal (typically 2), and S^{2-} is the sulfide ion. Compound formation was typically confirmed with x-ray diffraction. The reviewed literature did not suggest that anomalous co-deposition mechanisms, which would regulate the film stoichiometries, were active in the compound deposition process [47-50]; instead, deposition parameters were adjusted to achieve the desired flux rates and stoichiometries [51]. In one study of electrodeposited ZnS from alkaline baths with $Na_2S_2O_3$ sulfur-source, however, voltammetry data suggested that Zn deposition proceeded by a S-induced underpotential mechanism or another co-reduction mechanism with sulfur [29]. Other studies have demonstrated induced underpotential deposition of Sn in the presence of Cu [52, 53]. However, the deposited Sn concentrations remained relatively low (<10at%) in the underpotential regime [52, 53].

Many factors may contribute to the poor surface morphologies observed in S-containing co-electrodeposited CZTS precursors, including: diffusion-limited growth modes and high overpotentials; precipitation of particulates resulting from HER-induced pH changes at the substrate; and precipitation of sulfur and metal-sulfide compounds proceeding in parallel with electrodeposition. Diffusion-limited growth mechanisms are discussed in detail in Section 3.2.2.4. The possible precipitation of copper, tin, and zinc oxides, as well as metal hydroxides, as a result of HER-induced pH changes at the electrode was discussed above. Finally, colloidal sulfur and metal-sulfide compounds may possibly form in the bulk and deposit on the film, as discussed above. Sulfur colloid formation, according to the **clock reaction** (7-6), is expected to proceed at room temperature. In CBD on the other hand, baths are typically maintained above room temperature to facilitate the compound formation, but some metal-sulfide depositions have been successfully performed at room temperature using $Na_2S_2O_3$-containg baths [32]. Therefore, it is possible that some metal-sulfide compounds may precipitate at room temperature.

Reduction Mechanisms

Examining the peak assignments for FTO- and (EMAT) Mo-substrates from Section 7.4.1.2, the onset of significant Cu deposition occurs at -0.45V, the onset of significant Sn and S deposition occurs at -0.65V, and the onset of significant Zn deposition occurs at -0.95V. The strong peak at -0.75V may be associated with a Sn reduction process, a S reduction process, citrate ion deprotonation and hydrogen evolution, or possibly a mix of all these mechanisms. The highest S concentrations are found in films deposited at potentials between -0.80 and -1.00V.

The deposition of Cu associated with the reduction peaks at -0.41 to -0.45V in the voltammagrams can be attributed to an elemental reduction process, as in Eqn. (7-1). Additional decomplexation of Cu-citrate and Cu-thiosulfate molecules may also be associated with the deposition. Well-defined grains, identified with x-ray diffraction and EDS, confirm the deposition of elemental Cu at these potentials. As seen in Table 7-6 and Table 7-7, small S concentrations are also shown to incorporate into the films at these deposition potentials. The very small quantities present, however, suggest that the S does not deposit via an active reduction mechanism. That is, S reduction or $Cu_{2-X}S$ anomalous co-deposition do not likely play active roles in the Cu deposition at this potential. Sulfur incorporation could result from incomplete Cu-thiosulfate decomplexation or from colloid formation and entrapment.

The deposition of Sn and S associated with the reduction peaks at -0.65 to -0.68V in the voltammagrams can be attributed most likely to parallel reduction processes, as given by Eqns. (7-3) and (7-5), respectively. The film deposited at -0.65V on (EMAT) Mo-substrate shows the formation of nanodisks, which have been attributed to SnS phases in other works depositing films from baths with $SnCl_2$ or $SnSO_4$ and $Na_2S_2O_3$ [46, 51]. Note, however, those depositions were performed in baths maintained above room temperature. In any case, the formation of the SnS compound was not attributed to anomalous co-deposition but instead to parallel Sn and S reduction process that formed the final compound in the deposited film via reaction (7-8) [51]. In particular, increasing the overpotential was shown to increase the Sn:S ratio in the deposited film, similar to the behavior observed in Section 7.4.1.2 for both FTO- and (EMAT) Mo-substrates. Therefore, the nanodisks formed at -0.65V for (EMAT) Mo-substrates, and which are tentatively attributed to SnS, most likely result from fortuitous growth conditions that provide suitable Sn and S deposition rates to form SnS phases.

In a cyclic voltammetry study of a SnO_2 working electrode and acidic baths containing $SnCl_2$ and $Na_2S_2O_3$, a strong reduction peak was found at -0.53V attributed to Sn and $S_2O_3^{2-}$ reduction, followed by a weaker peak at -0.71V (vs. Ag/AgCl) [37]. In [37], the onset of Sn and S reduction peak was shifted significantly more-noble than the value of -0.65V demonstrated in this work, but the peak shapes in the cyclic voltammagrams appeared similar, including the presence of a second weak peak spaced approximately 0.16 – 0.18V more negative. The deep peak after Sn onset in the cyclic voltammagram in [37] suggests that the strong peak observed at -0.75V may be associated with the Sn and S reduction processes, but the contribution of the citrate deprotonation reaction described by Eqns. (8-5) and (8-6) cannot be ruled out.

The Zn deposition mechanism remains generally unclear. For both FTO- and (EMAT) Mo-substrates, Zn incorporation into the films first appears at -0.80V, although significant concentrations do not appear until -0.95V. It will be shown in Chapter 8 that in the absence of

$Na_2S_2O_3$ (and tartaric acid), Zn deposition is delayed until < -1.14V. Tartaric acid is not shown to strongly impact the Zn deposition, however. This noble shift in deposition onset suggests that the thiosulfate may induce Zn deposition by underpotential or anomalous co-deposition mechanism. S-induced Zn deposition or co-reduction of Zn and S has been reported in the literature [29]. As Bouroushian notes, however, there are not many reports on the electrodeposition of ZnS, which might be attributed to the comparative success of CBD techniques [29]. Additional investigation is required to discern the deposition mechanism of Zn in this bath.

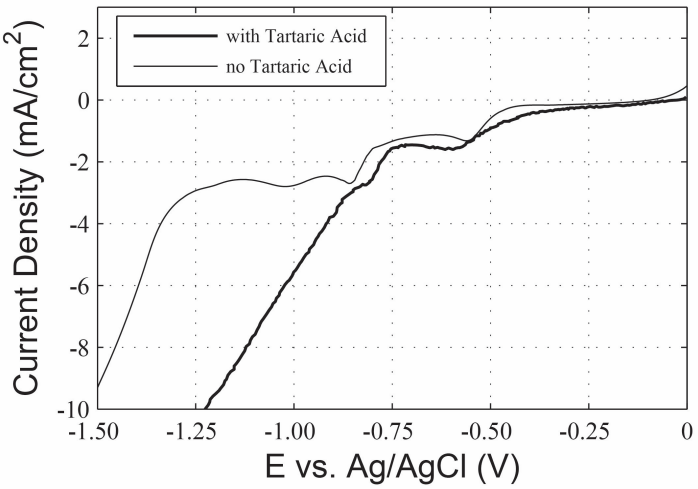

Fig. 7-17. Cyclic voltammagrams of nominal bath composition, with and without tartaric acid, on (EMAT) Mo-substrate

The cyclic voltammagrams (only forward sweep shown for clarity) for nominal baths with and without tartaric acid are shown in Fig. 7-24. The voltammagrams share the same general shape but exhibit two clear distinctions. First, the cathodic peaks for the baths without tartaric acid are shifted up to ~ 0.05V more negative. The removal of tartaric acid shifts the reduction peak potentials up to ~0.05V more negative. Tartaric acid complexes strongly with Sn [9]; subsequently, the removal of tartaric acid should increase the activity and shift the Sn reduction peak more-noble, contrary to the observed behavior. The increase in overpotentials might therefore be associated with shifts in the charge states of the predominant electroactive species caused by the shift in pH from 4.5 to 6 in the absence of tartaric acid. The predicted pH dependencies of the chemical stabilities of Cu, Zn, and Sn species in citrate-containing baths are shown in [9]. These species stabilities are calculated for baths without $Na_2S_2O_3$, so they are not directly representative of the baths here [9]. However, the speciation diagrams do generally indicate a shift to higher charge states for the predominant (complexed) Cu- and Zn-species with higher pH [9].

Second, the hydrogen evolution reaction, indicated in Fig. 7-24, shifts significantly negative (~0.4V) compared to the bath with tartaric acid. This large shift cannot be completely accounted for by a shift in the equilibrium potential caused by reduced H^+ activity at higher pH. Assuming

the shift results entirely from the H^+ activity shift described by the Nernst equation [3], HER would shift ~ 0.07V more negative for a pH of 6 vs. 4.5. At the higher pH values, the chemical stabilities of the Cu- and Zn-complex species may shift to less hydrogenated species, reducing the co-deposition of hydrogen when the metal-complexes are reduced. Shifts to non-hydrogenated metal-complex species with increasing pH have been reported for both citrate and tartaric complexing agents [9, 54, 55].

Morphology Trends

As demonstrated in Section 7.4.1.1 and 7.4.1.2, the **FTO films** and **(EMAT) Mo films** exhibit bilayer structures, consisting of compact underlayers with loosely-agglomerated, non-uniformly distributed growths on their surfaces. For both FTO- and (EMAT) Mo-substrates, abrupt transitions to these bilayer structures are observed at potentials greater than -0.80V. These growths appear to have maximum densities between -0.80V and -1.00V, tapering off at potentials of -1.10 and -1.20V. The formation of these overgrowths was more severe in films deposited on (EMAT) Mo-substrates than on the FTO-substrates. The surface morphologies of the **FTO** and **(EMAT) Mo films** shown in Fig. 7-1 and Fig. 7-2 are consistent with the powdery surface morphologies of Cu films from [56] that were deposited under diffusion-limited conditions with hydrogen co-deposition (see Fig. 3-12). For the **(EMAT) Mo film** deposited at -1.00V, the powdery surface layer was determined to be S-rich, Zn-rich, and Sn-poor compared to the compact underlayers. The co-electrodeposition process represents the sum of multiple parallel deposition processes for the elements in CZTS. A surface layer rich in S and Zn may indicate their deposition proceeds under more diffusion-limited conditions.

A study of the time evolution of the morphology on (EMAT) Mo-substrates, at -1.00V deposition potential, indicates the formation of three-dimensional growth features after only 3sec, which are uniformly distributed on the film surface. Between 3 and 30sec, three-dimensional growth proceeds preferentially at the nucleated sites, with well-defined islands of growth clusters evident. This growth mechanism is consistent with spherical diffusion around the protrusions, providing further evidence that morphologies of the films are controlled by diffusion-limited growth mechanisms. Additional deposition time results in the connection of these islands, eventually yielding thick, porous layers of these overgrowths that cover most of the sample surface. The compact underlayer exhibits a power-law type growth with time, leveling off significantly after 5min and remaining less than 250nm after a 15min deposition. The slowing of film growth with increasing deposition time is attributed to the shadowing of the compact underlayer by the growing layer of powdery surface deposits.

Modifying the concentrations of $CuSO_4$, $ZnSO_4$, and $SnSO_4$, and $Na_2S_2O_3$ in the bath had little effect on the film morphology, with the large overgrowths evident for all bath compositions

studied. The removal of citrate from the bath caused significant acidification (pH~0) and dramatically enhanced three-dimensional growth of the film. Dendrites up to ~10mm were evident on the film surface during deposition, and most of the film was removed by rinsing after deposition. Increased electrolyte conductivity and increased hydrogen evolution caused by decreased pH likely enhance the dendrite formation, as detailed in Section 3.2.2.4. In baths containing citrate, modifying the citrate concentration had little effect on the film morphology. Removing tartaric acid from the deposition bath, however, dramatically improved the morphology of the as-deposited film. As shown in Fig. 7-16, the film deposited without tartaric acid shows a high degree of roughness but also exhibits much greater uniformity with no evidence of the overgrowths present. Further, a clear transition from powdery to cauliflower morphology is evident, with the appearance similar to the characteristic cauliflower morphology in the electrodeposited Cu film from [56] (see Fig. 3-10).

The improvement in morphology with the removal of tartaric acid is unexpected, since literature has shown the complexing agent to be an effective brightener in the electrodeposition of Sn and Zn films [55, 57, 58]. Removing the tartaric acid clearly reduces hydrogen co-deposition, evident as a much larger HER overpotential in the cyclic voltammagram, a visible reduction in the bubbles generated during deposition, and the deposition of a thicker film with lower current density. The reduction in HER can be attributed to a decrease in H^+ ions and possibly to a shift to non-hydrogenated metal-complex species with increasing bath pH from 4.5 to 6. The transition from powdery to cauliflower morphology also likely indicates a transition from fully-diffusional controlled growth to mixed activation-diffusion growth mode. The effect of the tartaric acid on this transition remains unclear, however. Typically, the presence of a complexing agent slows the reaction kinetics, which would mitigate mass-transfer limitations. The exchange current density of the Cu reduction increases in the absence of tartaric acid, evident as a steeper slope at the onset of Cu deposition in the cyclic voltammagram (Fig. 7-17), but the other reduction peak shapes do not change significantly. The reduction peak potentials are shifted up to ~0.05V more negative in the absence of tartaric acid, possibly attributed to shifts of the metal-complex species to higher charge states, as discussed previously. However, the morphology transition cannot be attributed to the slight decreases in overpotential associated with the observed negative shifts of reduction potentials. As shown in Section 7.4.2.2, powdery deposits do not appear on (Guardian) Mo-substrates until deposition potentials of -1.20V.

It is unclear if the hydrogen evolution induces the three-dimensional growth modes that lead to powdery deposits or simply accompanies these growth modes under high overpotentials, as described in Section 3.2.2.4. A clear correlation exists between the two, however, in baths with and without tartaric acid. For baths with tartaric acid, the improved morphologies of the **FTO films** compared to **(EMAT) Mo films** correlates with the reduced hydrogen co-deposition, evident

as a much larger HER overpotential in the cyclic voltammagram (Fig. 7-3) and a visible reduction in the bubbles generated during deposition. For baths without tartaric acid, the onset of visible hydrogen evolution consistently accompanies morphology transitions to rougher more powdery films, as shown in Section 7.4.2. Clearly, the removal of tartaric acid from the deposition bath reduces hydrogen evolution and mitigates severe diffusion-limited growth behavior. However, a more detailed study of the deposition kinetics is required in order to discern the mechanisms by which tartaric acid modifies the reduction processes and transport behavior of the system. This remains for future work.

The film morphologies demonstrated from baths with tartaric acid are consistent with diffusion-limited growth with hydrogen co-deposition. However, it is possible that colloidal deposition proceeds in parallel with this growth mechanism. To investigate the possible precipitation of insoluble species within the electrolyte, solutions were examined for particle formation using SEM imaging and Raman spectroscopy. SEM images (not shown) appear to confirm the formation of particles up to several microns in diameter, and Raman spectra (not shown) exhibit bands that might be associated with sulfur species. However, the studies are considered inconclusive, since the measurements themselves may introduce or modify the precipitated species. That is, the evaporation of the solution may induce particle formation, and laser excitation used with Raman analysis may cause photochemical formation of elemental sulfur and metal-sulfides [1]. While colloidal deposition may be active, it does not appear likely to strongly influence the deposition.

Composition Trends

As demonstrated in Section 7.4.1.4, the Cu and Sn concentrations in the film demonstrated an inverse relationship, such that increasing the $CuSO_4$ (and decreasing $SnSO_4$) concentration increased the Cu and decreased the Sn concentrations in the films. The changes in Cu:Sn ratios in the film were greater than the changes in the $CuSO_4$:$SnSO_4$, suggesting an interaction between the Cu and Sn deposition mechanism. Varying $CuSO_4$ and $SnSO_4$ concentrations both caused shifts in the relative Sn concentrations, evident in the Zn:Sn ratio, that were significantly more pronounced than Cu concentrations. This trend is observed in baths with and without tartaric acid. However, this trend is not observed in baths without $Na_2S_2O_3$ (as in Chapter 8). Consequently, the thiosulfate ions appear to mediate the interaction between Cu and Sn in the deposition process, possibly through metal-thiosulfate complex formation. Complexation with thiosulfate can modify the activities of the metal ions, as described in Section 3.2.3.3, and also possibly modify the adsorption behavior at the electrode [59]. A large noble shift in the Cu reduction peak with the absence of thiosulfate (see Table 8-5) suggests possibly significant Cu-thiosulfate complexation. However, additional investigations of the species stabilities and deposition kinetics are required to identify the mechanism(s) of Cu-Sn interaction.

The Zn concentration correlated inversely with Sn concentration when $CuSO_4$ and $SnSO_4$ concentrations were varied, with this dependence particularly strong at low Sn concentrations (< 10at%). However, varying the $ZnSO_4$ concentration was not shown to strongly affect the relative Sn concentration in the film. The most significant example of increasing Zn concentration with decreasing Sn concentration corresponds to depositions with low $SnSO_4$ concentrations, as shown in Table 7-10. The film thickness remains approximately constant despite decreasing $SnSO_4$ concentrations and significantly decreasing steady-state deposition currents (not shown). In fact, the steady-state deposition current monotonically decreases with decreasing $SnSO_4$ concentration, with the steady-state current at 0.005M $SnSO_4$ approximately half of the steady-state current at 0.02M $SnSO_4$. The unchanging deposition rate (e.g. constant film thickness) with decreasing deposition current indicates decreasing hydrogen co-deposition rates. Zinc deposition rates may therefore increase as a result of decreasing competition with HER. However, the removal of tartaric acid also significantly reduced HER, but a similarly large increase in the relative Zn concentration is not observed. Reduced hydrogen evolution partially accounts for the increased Zn deposition rates, but additional interactions between Zn and Sn deposition are likely.

The removal of tartaric acid increased the film thickness and decreased the relative Sn concentration, evident as a decrease in Sn:[Cu+Zn]. With the removal of tartaric acid, the steady-state deposition current decreases by approximately a factor of 4, yet the film thickness increases by approximately 50%, indicating a dramatic reduction in hydrogen co-deposition. The decrease in relative Sn concentration with the removal of tartaric acid is unexpected. Tartaric acid strongly complexes Sn ions, and its removal from the bath was expected to increase the reaction rates for Sn. The increase in pH with the removal of tartaric acid likely enhances the oxidation of tin (e.g. precipitation of tin oxide) [9, 60] and decreases the dissolution of $SnSO_4$ [52], which may also influence the species stability of Sn^{2+} ions. The decrease in hydrogen evolution reaction with the removal of tartaric acid is attributed to the reduction of H^+ ions and the shift towards non-hydrogenated metal-complex species at higher pH values.

7.4.1.6 Mechanical Removal of Particulates

Two paths exist to improving the morphology of the films: a) mechanically remove the overgrowths on the film surface to expose the compact underlayer; and b) prevent the deposition and formation of the overgrowths through modification of the electrolyte and/or working electrode.

As demonstrated in Section 7.4.1.4, deposition from baths without tartaric acid can dramatically improve the as-deposited morphology of CZTS thin films. Section 7.4.2 explores this path to improve deposition quality. For acidic baths containing tartaric acid, mechanical processing to remove the overgrowths represents the most direct path to improving the

morphology of as-deposited films. To this end, sonication was investigated as a possible post-deposition processing technique.

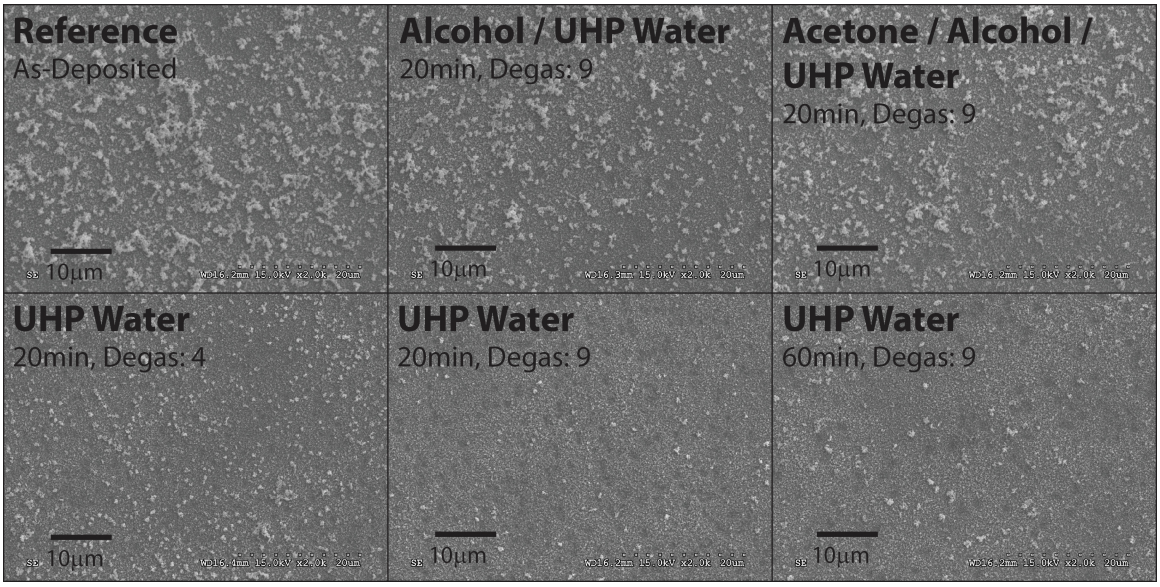

Fig. 7-18. SEM images of co-electrodeposited CZTS precursors on FTO-substrates after varying sonication conditions

A series of sonication experiments, using CZTS films electrodeposited on FTO-glass substrates, demonstrated that sonication of the films in UHP water for 20minutes on the most vigorous setting most effectively removed the overgrowths. Acetone and alcohol were less effective sonication media, and additional sonication time did not cause any further overgrowth removal. These results are summarized in Fig. 7-18. Sonication of CZTS films deposited on (EMAT) Mo-substrates was shown to be similarly effective at removal of the surface features.

The removal of the surface overgrowths can leave voids in the dense underlayer, indicated as the darker regions in Fig. 7-18, for UHP Water, 20min, and Degas 9 (most vigorous setting). These voids would cause shunting in the junctions of PV devices. As Section 7.4.1.3 showed, however, the compact underlayers reach a maximum thickness of only ~300nm due to the surface overgrowths. Hence, a multi-deposition/sonication cycle would be needed to deposit films of sufficient thickness. In doing so, the film voids left by sonication might effectively be filled by subsequent depositions. Note: such a process was not pursued because of the demonstrated improvement in film quality with removal of tartaric acid from the deposition bath.

7.4.1.7 Effects of Argon and Sulfur Annealing

Without Sonication

As-deposited films, fabricated from baths containing tartaric acid, exhibited poor morphologies consisting of compact underlayers and loose, powdery top layers. In [9], the successful densification of severely dendritic films was reported using a 15min selenium annealing

operation at 550°C. Based on the SEM image in that work, however, those films appeared porous but significantly more uniform than the as-deposited films produced here. In any case, to densify the films and possibly improve the porous morphologies observed in this work, annealing in sulfur and argon environment was investigated.

Films were deposited by Pawar's method (nominal bath), using a constant potential of -1.00V and a deposition time of 5min. After deposition, films were thoroughly rinsed with ultra-high purity water and air dried; no sonication was performed. Films were then annealed in Argon background or elemental sulfur background (4.5mg), using the nominal procedure detailed in Section 7.3.1, including a 10min dwell time at 560°C with a 7min ramp. The morphologies of as-deposited and annealed films are shown in Fig. 7-19.

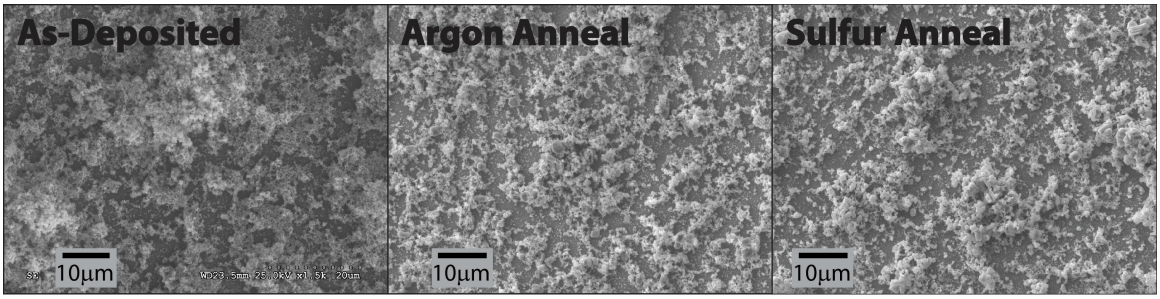

Fig. 7-19. SEM images of co-electrodeposited CZTS films on (EMAT) Mo-substrates as-deposited and after annealing

As the SEM images show, annealing had no significant effect on the surface morphologies. Large, patchy clusters of overgrowths remained non-uniformly distributed across the substrate surface. Increasing the anneal time may further improve the film morphology. However, the highly non-uniform distributions of the surface features in as-deposited films makes it unlikely that annealing under any conditions will yield uniform film thicknesses and compositions.

With Sonication

Sonicating the samples in UHP water for 20min after deposition was shown to improve the surface morphologies of the films by removing the loosely adhering surface overgrowths, as demonstrated in Section 7.4.1.6. To investigate the viability of this fabrication method, sonicated films were then sulfur annealed in order to fully sulfurize the films and complete the crystal formation of CZTS. Noting that the sonicated baseline films, fabricated using the nominal bath composition and deposition potential from Pawar's method, were severely Zn-poor (see Table 7-5), samples were deposited from the nominal bath for 25min at a more negative deposition potential of -1.10V in attempt to incorporate more Zn in the film. After deposition, samples were sonicated in ultra-high purity water for 20min at the most vigorous setting. Finally, films were annealed in elemental sulfur background (4.5mg), using the nominal procedure detailed in Section 7.3.1, including a 10min dwell time at 560°C with a 7min ramp. After sulfur annealing, the film

composition was measured by RBS as the following: $Cu_{1.32}Zn_{0.23}Sn_{1.00}S_{3.41}$. The film was severely Cu-poor and severely Zn-poor, deviating strongly from stoichiometry. The S:metals ratio is greater than 1, however, indicating that the film was fully sulfurized. The metal element ratios Cu:Zn:Sn could be improved by increasing the $ZnSO_4$ and decreasing the $SnSO_4$ concentrations in the deposition bath, as demonstrated in Section 7.4.1.4.

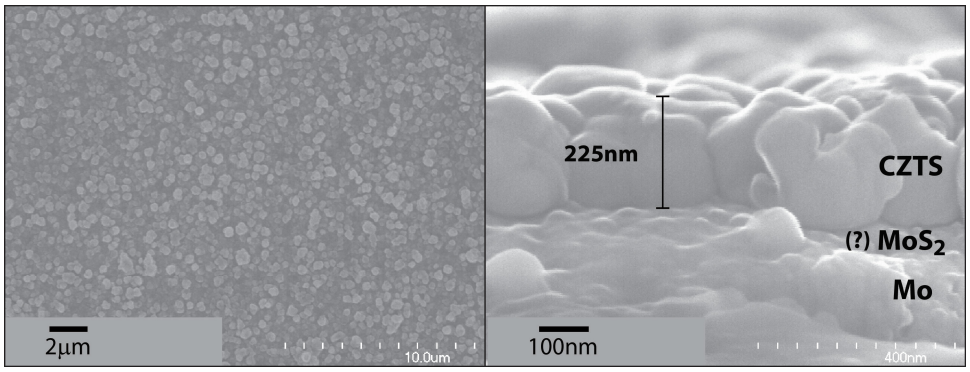

Fig. 7-20. Top-down and cross-sectional SEM images of CZTS film after co-electrodeposition, sonication and sulfur annealing

Fig. 7-20 shows the surface morphology of the sonicated and sulfur annealed film. The SEM images show that the film was uniform and compact, with no evidence of the large overgrowths present on the film surface. Notably, however, the film was thin (225nm) and contained a significant number of voids, as expected from the time evolution of morphology and sonication studies in Sections 7.4.1.3 and 0, respectively. Voids are evident as the darker spots in the top-down SEM image. However, the film forms compact, columnar grains as shown in the cross-sectional SEM images in Fig. 7-20.

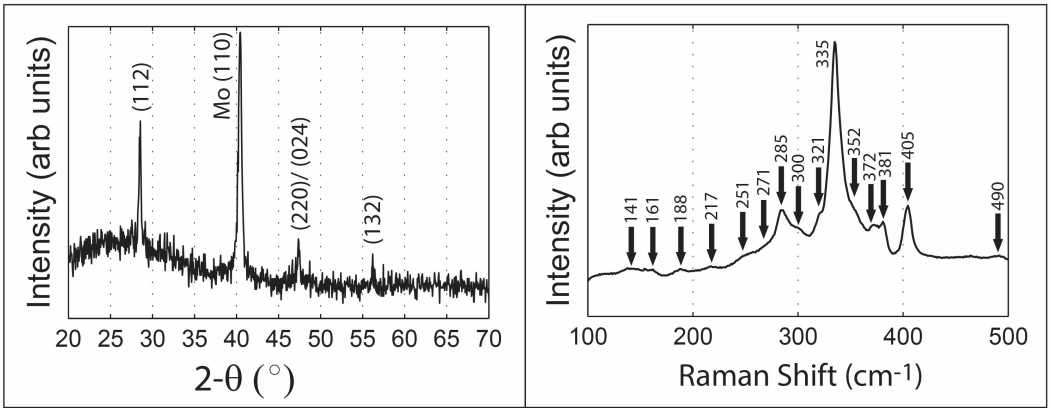

Fig. 7-21. X-ray diffractogram and Raman spectrum for CZTS film after co-electrodeposition, sonication and sulfur annealing

The structural properties of the sulfur annealed film are presented in Fig. 7-21. The x-ray diffractrogram indicates the presence of strong (112) peak at 28.52° and two small (220)/(024) and (132) peaks, which are attributed to kesterite CZTS. Similar to the pulsed laser deposited films

from Chapter 6, the diffractogram indicates a shoulder in the (112) peak near 28.3°, evident under greater magnification, that suggests the presence of a secondary phase. Similar to the pulsed laser deposited films in Section 6.4.6.2, cubic-SnS, Hex–SnS_2, cubic–Cu_2SnS_3, orthorhombic-Cu_3SnS_4, $Cu_4Sn_7S_{16}$, and various ZnS phases may contribute this shoulder to the diffraction peak.

Characteristic CZTS Raman modes are evident at 251cm^{-1} (E-TO mode), 285cm^{-1} (A-mode), 335cm^{-1} (A-mode), 352cm^{-1} (E-TO mode) and 372cm^{-1} (B-LO mode). As determined in Section 6.4.6.2, the weak modes near 141, 161, and 271cm^{-1} are likely attributed to CZTS, as well. Like x-ray diffraction, however, many of the common secondary phases share similar Raman mode locations, as noted in Section 4.2.3. It was shown in Section 6.4.6.2 that properties of the dominant A-mode (near 338cm^{-1}) provide some indication of the phase-purity of the film, such that a widening and blue shift in the peak can be attributed to increases in secondary phase Raman modes near 310 – 320cm^{-1}. Raman modes in this range have been attributed to SnS_2, $Cu_2Sn_3S_7$ and Cu_3SnS_4 [61-65]. The peak near 321cm^{-1} in the Raman spectra may be associated with these phases. The small peak at 300cm^{-1} identified in Fig. 6-14 suggests the presence of Cu_2SnS_3 or Cu_3SnS_4 phases [63]. The small peaks 188 and 217cm^{-1} indicate SnS phase. Using a reference MoS_2 sample, in which a Mo-substrate was annealed in elemental sulfur environment, the Raman modes at 381 and 405cm^{-1} may be definitively attributed to MoS_2. The presence of a significant concentrations of secondary phases are expected, given the large deviation in film composition from stoichiometry.

If the composition of as-deposited films were optimized to achieve the desired cation ratios, and if multiple deposition/sonication cycles could be successfully implemented to eliminate voids and increase film thickness, then the sonication/annealing approach used here may facilitate the growth of quality films. However, this approach is not optimal, given the increased time required for processing. If other modifications to the deposition process yield thicker, less powdery films, sonication may still prove useful as a single-step tool to improve film morphology.

7.4.1.8 Summary of Results

Films deposited on FTO- and (EMAT) Mo-substrates, using Pawar's method and the original bath composition, exhibited bilayer structures with compact underlayers and loose, powdery surface layers. The as-deposited films were Zn-poor, Sn-rich and S-poor. Cyclic voltammetry and deposition potential studies suggest that Cu, Sn, and S are deposited by elemental reduction mechanisms given by Eqns. (7-1), (7-3), and (7-5), respectively. A noble shift in the Zn reduction peak in the presence of $Na_2S_2O_3$ suggests that Zn deposits by S-induced underpotential or anomalous co-deposition mechanism with sulfur. The Cu and Sn concentrations in the film demonstrated an inverse relationship, such that increasing the $CuSO_4$ (and decreasing $SnSO_4$) concentration increased the Cu and decreased the Sn concentrations in the films. The changes in Cu:Sn ratios in the film were greater than the changes in the $CuSO_4$:$SnSO_4$, suggesting an

interaction between the Cu and Sn deposition mechanism, which was possibly attributed to interactions mediated by the thiosulfate ion.

The rough morphologies of the films are attributed to diffusion-limited growth modes and hydrogen co-deposition. Removal of the tartaric acid from the bath increases the bath pH, decreases the hydrogen evolution, and significantly improves the film morphologies. In particular, the film transitions from powdery to cauliflower morphology-type in the absence of tartaric acid, likely indicating a transition from fully-diffusional controlled growth to mixed activation-diffusion growth mode. The reduction in hydrogen evolution and apparent slowing of the deposition kinetics are attributed primarily to the increase in bath pH, which decreases the H^+ ions available for HER and likely shifts the metal-complexes to higher charge-state, non-hydrogenated species. Additional kinetics and species stability studies are required to confirm the mechanisms by which tartaric acid modifies the reduction process and transport behavior in the system.

In addition to removing tartaric acid, sonication of the samples in water was shown to significantly improve the surface morphologies of the films by effectively removing the powdery surface layer and exposing the compact underlayer. Due to shadowing effects by the powdery surface layer, the compact underlayers were limited to < 300nm, films too thin for use as photovoltaic absorber layers. Further, the removal of partially-buried growth features created voids in the films. To assess the viability of this approach, sonicated films were sulfur annealed using the nominal procedure. Although non-optimized stoichiometries were investigated, x-ray diffraction and Raman spectroscopy confirm the formation of kesterite CZTS. Significant secondary phases were also identified, as expected, given the large stoichiometric deviations. SEM images confirm the formation of well-defined grains with smooth surfaces, although voids are present, which are attributed to sonication damage. If the composition of as-deposited films may be optimized to achieve the desired cation ratios, and if multiple deposition/sonication cycles could be successfully implemented to eliminate voids and increase film thickness, then the sonication/annealing approach used here may facilitate the growth of quality films. However, this approach is not optimal, given the increased time required for processing.

The removal of tartaric acid significantly improves the quality of the deposited films, and all remaining investigations in this dissertation pertain to that deposition method. If other modifications to the deposition process yield thicker, less powdery films, sonication may still prove useful as a single-step tool to improve film morphology.

7.4.2 Depositions without Tartaric Acid (pH~6)

Films were deposited using a modified version of Pawar's method [6], most significantly altered through elimination of tartaric acid in the deposition bath. The work in Section 7.4.1.4

showed that removing tartaric acid from the deposition bath significantly improved as-deposited surface morphologies, effectively eliminating the large surface overgrowths from the films.

This section documents studies to characterize the dependence of film composition and morphology on the deposition parameters, in order to improve the quality of as-deposited films. The (Guardian) Mo-substrates were used for all studies in this section except Section 7.4.2.4, which compares the deposition behavior of these commercial substrates to the in-house fabricated (EMAT) Mo-substrates and FTO-substrates. Semi-transparent FTO-substrates were also used to study the optical properties of co-electrodeposited and sulfur annealed films in Section 7.4.2.12.

7.4.2.1 Baseline Film Properties

This section describes the baseline film properties and deposition characteristics associated with the original bath conditions (Table 7-3) less the tartaric acid. As discussed in Section 7.4.1.4, the bath without tartaric acid has a measured bath pH ~ 6. Baseline films were deposited from the nominal bath composition at constant potential of -1.00V for 25 minutes.

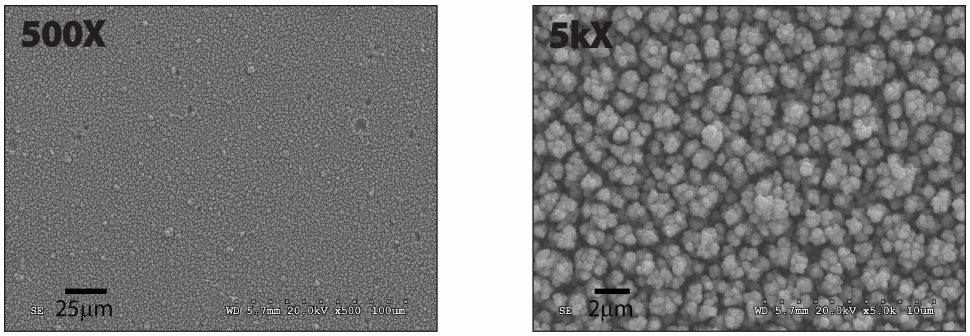

Fig. 7-22. SEM images of co-electrodeposited CZTS precursor on (Guardian) Mo-substrate, using Pawar's method [6] less tartaric acid

Unlike films deposited from baths with tartaric acid, the baseline films here are well-adhering and do not possess loose, powdery top layers. Rinsing and light nitrogen blow drying caused no visible loss of material from the films. The morphologies of these as-deposited films were highly uniform, exhibiting diffusion-limited growth features consistent with cauliflower or dendrite growths, as shown in Fig. 7-22. Voids in the films, attributed to hydrogen evolution, may also be seen in the SEM image.

Table 7-14. Composition of baseline co-electrodeposited CZTS precursor on (Guardian) Mo-substrate

Atomic %					Cu:Zn	Zn:Sn	S:Metals	Thick (nm)
Cu	Zn	Sn	S	O				
35	9	18	21	17	3.8	0.52	0.34	1950

Note the large film thickness, estimated as ~2µm by RBS measurements, and the significant surface roughness prevent reliable determination of the composition by RBS. Table 7-14 shows the

best estimate of the film composition. The film was severely Zn- and S-deficient, although the Cu:Sn ratio of 1.94, however, was close to the stoichiometric ratio of 2.

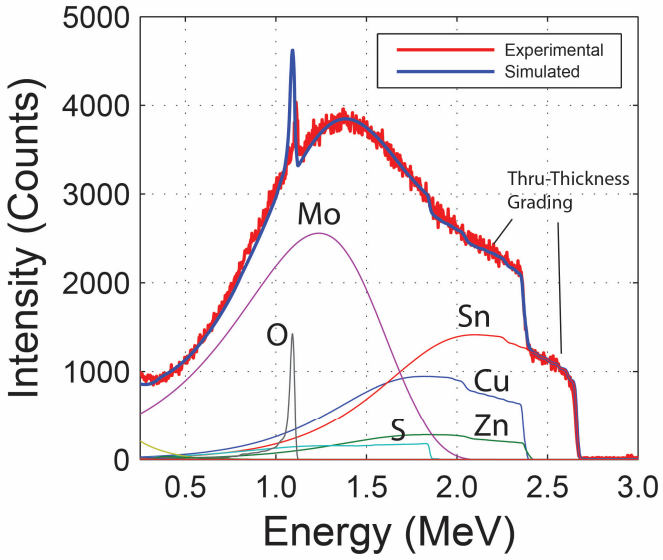

Fig. 7-23. Experimental and simulated RBS spectra of co-electrodeposited CZTS precursor on (Guardian) Mo-substrate

The RBS spectrum, shown in Fig. 7-23, indicates significant through-thickness variation in the composition, with Cu-Zn and Sn concentrations much higher near the substrate than at the surface and the lower concentrations near the film surface offset by higher oxygen concentration.

7.4.2.2 Cyclic Voltammetry and Peak Assignments

A cyclic voltammetry spectrum for the (Guardian) Mo-coated glass substrate with nominal bath conditions was measured from 0 to -1.50V at 10mV/s, as shown in Fig. 7-24. The voltammagram indicates a series of cathodic peaks labeled I – VI. The onset of hydrogen evolution reaction (HER) occurs near -1.29V.

The dominant cathodic peaks at -0.55V (II), -0.77V (IV), and -0.90V (V) show sharp, well-defined drop-offs in cathodic current density consistent with mass-transfer limited conditions. Weaker peaks, evident as shifts in current density slope, appear at -0.055V (I), -0.73V (III), and -1.14V (VI). The dominant cathodic peak locations are generally consistent with the dominant peaks observed for the FTO- and (EMAT) Mo-substrates from Section 7.4.1.2: -0.41V to -0.45V, -0.75V, and -0.91V. A series of anodic oxidation peaks are also evident on a reverse voltage sweep.

The relationships between growth conditions and the deposition reactions are here investigated, in order to control and improve the stoichiometries of as-deposited films. To help correlate the cathodic peaks with the deposition reactions, depositions were performed for 10min at varying potentials corresponding to the regions of interested identified on Fig. 7-24. Shorter

deposition times were used to improve RBS fittings by reducing film surface roughness and peak overlap in the spectra. In films with graded compositions, weighted-average atomic concentrations are presented. Compositions, morphologies and crystal structures of these films deposited at varying potentials are summarized in Table 7-15, Fig. 7-25 and Fig. 7-28, respectively.

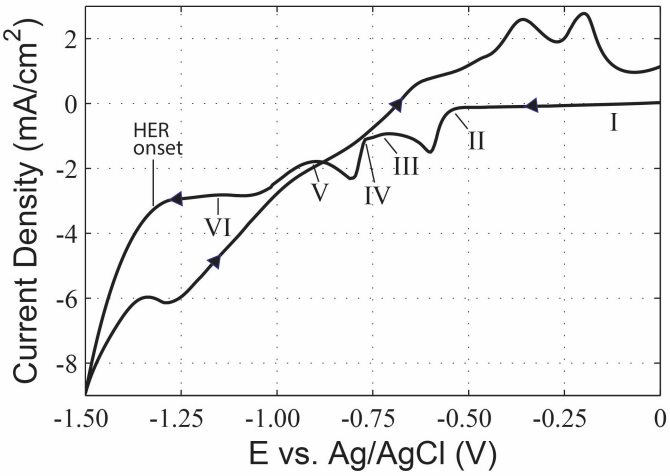

Fig. 7-24. Cyclic voltammagram of nominal bath composition with (Guardian) Mo-substrate

At -0.45V, nucleated copper grains periodically decorate the substrate surface, with more moderate coverage achieved at -0.55V, as shown in Fig. 7-25. Point-and-shoot EDS measurements (not shown) confirm the 500nm – 1μm grains are copper. Incomplete film coverage complicates the RBS fitting, and the inclusion of a small amount of sulfur cannot be ruled out. EDS and PIXE cannot be used to confirm the presence of S due to peak overlap with Mo. Zn and Sn, however, are clearly absent in the film as evidenced by the PIXE and RBS spectra. The x-ray diffractogram, Fig. 7-28, confirms the presence of elemental copper with a small peak near the cubic (111) peak at 43.4°.

Table 7-15. Compositions of co-electrodeposited CZTS precursors on (Guardian) Mo-substrates deposited at varying potentials, * incomplete film coverage, + element detected in PIXE but peak negligible, ◊ element cannot be reliably fitted

Potential	Atomic %					Cu:Zn	Zn:Sn	S:Metals	Thick (nm)
	Cu	Zn	Sn	S	O				
-0.45V*	100	-	-	-	-	-	-	-	-
-0.55V*	100	-	-	-	-	-	-	-	-
-0.75V	50	+	10	◊	39	-	-	-	360
-0.80V*	24	1	◊	◊	◊	33	-	-	375
-1.00V	32	8	16	13	31	4.2	0.48	0.23	660
-1.20V	16	6	12	13	54	2.7	0.48	0.39	350

At -0.75V, a clear morphology transition is evident. A small-grained film fully covers the substrate with very large particulates (~10μm) periodically decorating the surface, as shown in Fig. 7-25. RBS and PIXE measurements clearly show the onset of Sn deposition. A generally well-fitted RBS spectrum indicates the film is highly oxygenated with a Cu:Sn ratio near 5. PIXE confirms the onset of Zn in the films, with a very small peak. The presence of S cannot be completely ruled out due to possible peak overlap with Mo in the RBS and PIXE spectra. However, in the RBS spectrum, no clear peak edge appears for S and, if present, the concentrations remain small. Point-and-shoot EDS measurements, shown in Fig. 7-26, indicate the large surface features seen in the SEM image (-0.75V) are composed of Cu and Sn. These large particulates are highly Sn-rich, with the Sn:Cu peak heights increasing from ~0.6 to 2.7 in the bulk surface and the particulate, respectively. The x-ray diffractogram, Fig. 7-28, indicates the presence of Cu_6Sn_5 phase in the film. As previously noted, the high mobility of Cu in Sn typically results in the formation of Cu-Sn alloy phases at room temperature conditions [3]. Subsequently, the presence of these phases does not imply the deposition of Cu and Sn through alloy reaction pathways.

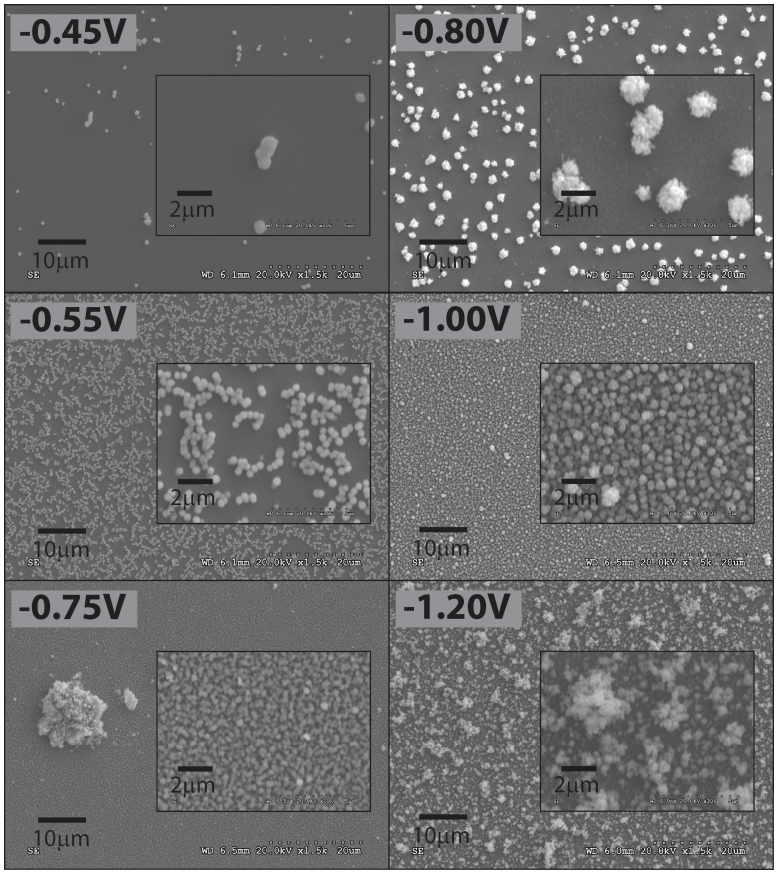

Fig. 7-25. SEM images of co-electrodeposited CZTS precursors deposited at varying potentials (nominal bath composition)

At -0.80V, another significant change in morphology appears. Again, a small-grained film fully covers the substrate, but the particulates decorating the film surface decrease in size and increase in population density compared to the deposition at -0.75V. The small-grained film is also more compact than the one deposited at -0.75V. The partial coverage of the film by a high density of large particulates make fitting of the RBS spectra quite difficult. The Cu peak is reasonably well-fitted, but significant peak overlap exists in the Sn and S regions. A small edge in the RBS spectra does confirm the onset of S deposition at this potential; however, the S peak cannot be reliably fitted. PIXE again confirms the presence of Zn, but the peak remains very small. Point-and-shoot EDS measurements, shown in Fig. 7-27, indicate that the large surface particulates seen in the SEM image (-0.80V) are composed of Cu and Sn. These large particulates are Sn-rich, with the Sn:Cu peak heights increasing from ~1.0 to 1.8 in bulk surface and particulate, respectively. Notably, the particulates are less Sn-rich than those observed on the surface at -0.75V. The x-ray diffractogram, Fig. 7-28, indicates the presence of Cu_6Sn_5 phase in the film with well-defined peaks near 30.2 and 40.3°.

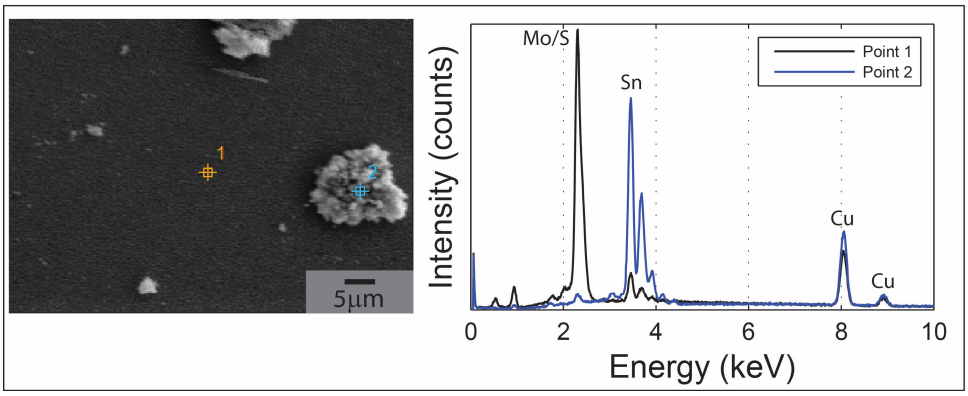

Fig. 7-26. Point-and-shoot EDS spectra for co-electrodeposited CZTS precursor (-0.75V)

At -1.00V, the large surface features decorating the surface at lower potentials disappear and the film shows a uniform morphology characterized by relatively densely packed small grains, as shown in Fig. 7-25. Notably, this potential corresponds to the baseline film presented in Section 7.4.2.1. The composition of this film (10min deposition time) is slightly Zn-deficient and moderately S-deficient compared to the baseline film (25min deposition time), shown in Table 7-14. These Zn- and S-deficiencies may result from inherent variations in the deposition process, depletion effects associated with longer deposition times, or fitting errors associated with the PIXE and RBS measurements. In particular, the thicker sample exhibits significantly more peak overlap in the RBS spectra, making definitive evaluation of S concentration particularly difficult. The x-ray diffractogram, Fig. 7-28, indicates the presence of Cu_6Sn_5 phase in the film with a well-defined peak near ~ 30.2°. An additional peak near 43.2° may be associated with Cu_6Sn_5, Cu_5Zn_8, or elemental Zn.

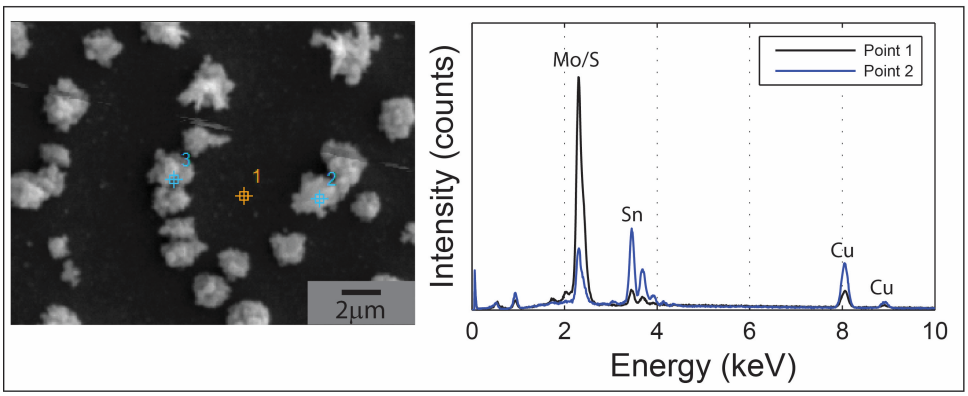

Fig. 7-27. Point-and-shoot EDS spectra for co-electrodeposited CZTS precursor (-0.80V)

Deposition of Zn at -1.00V likely indicates an active underpotential or anomalous co-deposition mechanism. For instance, deposition from a similar bath that excludes $Na_2S_2O_3$ causes the delay of Zn deposition until < -1.14V (see Chapter 8). Possible S-induced underpotential deposition of Zn or Zn-S co-deposition has been previously reported, although the exact mechanism was not well understood [29]. X-ray diffraction does not indicate the presence of any ZnS phases, although amorphous ZnS may be present. While Raman measurements cannot definitively confirm its presence, a small Raman mode appears at ~281cm^{-1} for deposition potentials of -1.00V and -1.20V, which might be attributed to ZnS. As discussed in Chapter 4, reliable detection of ZnS by Raman spectroscopy typically requires the use of UV laser wavelengths to take advantage of resonance enhanced scattering; however, the Raman system used in this thesis employed a longer 488nm wavelength laser. In any case, no peak at 350cm^{-1} was identified, which would typically confirm ZnS phase. Further, no clear trends are observed in the Zn:S element ratios in the film that would suggest a stoichiometric relationship in the deposition, as might be expected with anomalous co-deposition.

At -1.20V, another significant shift in the morphology is observed. The deposit consists of a dense, small-grained film decorated with an abundance of micron-sized surface particulates, similar in appearance to those observed in Section 7.4.1. The relative Cu concentration decreases from -1.00V to -1.20V, evident as a decrease in Cu:Zn ratio and static Zn:Sn ratio. The absolute concentration of Cu monotonically decreases from -0.55V to -1.20V. Point-and-shoot EDS measurements (not shown) indicate that the surface overgrowths seen in the SEM image at -1.20V are composed of Cu, Zn and Sn. EDS cannot confirm the presence of S, due to peak overlap with Mo. No clear trends in the overgrowth composition are evident, however, as Cu:Sn and Cu:Zn peak ratios vary among different points measured on the overgrowth features.

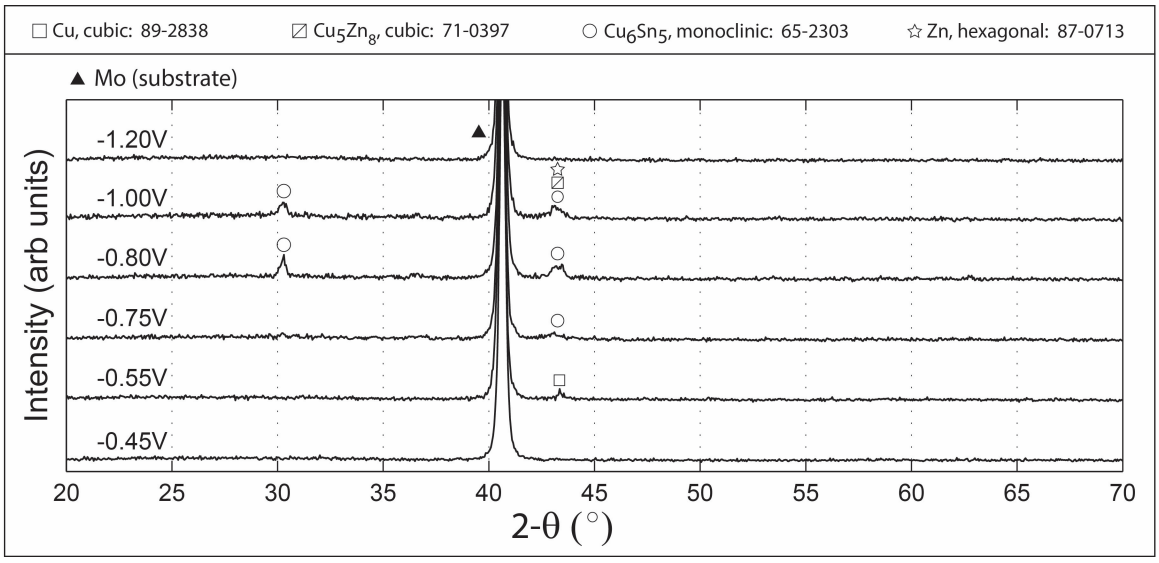

Fig. 7-28. X-ray diffractograms of co-electrodeposited CZTS precursors on (Guardian) Mo-substrates deposited at varying potentials (nominal bath composition)

Based on the onset of deposition for the different elements, the following assignments may be made for the cathodic peaks on the cyclic voltammagram:

- Weak cathodic peak at -0.055V (I): initial nucleation of elemental Cu
- Dominant cathodic peak at -0.55V (II): elemental Cu reduction
- Weak cathodic peak at -0.73V (III): Sn reduction process, possibly S reduction process
- Dominant cathodic peak at -0.77V (IV): Sn, S and Zn reduction processes, including potentially citrate deprotonation and hydrogen evolution processes (as detailed below)
- Dominant cathodic peak at -0.90V (V): Zn reduction process
- Weak cathodic peak at -1.14V (VI): possibly elemental Zn reduction

The peaks at -0.055V (I) and -0.55V (II) may clearly be assigned to elemental copper, supported by RBS, EDS and XRD identification of the deposited grains. The onset of Sn at -0.75 suggests that the peak at -0.73V (II) may be assigned to an elemental Sn reduction process. Notably, however, the presence of S in this film cannot be ruled out, and so other Sn reduction mechanisms, such as SnS_X, cannot be ruled out. Note that x-ray diffraction and Raman analysis found no evidence of SnS_X in the deposited films. The onset of significant S concentration at -0.80V suggests that the strong cathodic peak at -0.77V (III) is associated with S reduction process. Further reduction processes associated with Sn or Zn cannot be ruled out, however. The lack of large increases in the Sn and Zn concentrations at -0.80V suggests that the significant increase in current density evident at -0.77V (III) on the cyclic voltammagram likely is not associated with a sudden onset of other Sn

or Zn reduction processes. Consequently, a S reduction process represents the most likely source of cathodic peak at -0.77V (III), and as previously noted, deprotonation of sodium citrate may enhance S reduction process through increased H^+ concentrations at the electrode.

The significant rise in Zn concentration from at -1.00V suggests that the dominant cathodic peak at -0.90V (V) may be assigned to a Zn reduction process. As noted in the previous discussion, the deposition of Zn may proceed according to an underpotential or anomalous co-deposition mechanism, evidenced as a large negative shift in the onset of Zn deposition in similar baths without $Na_2S_2O_3$. Raman measurements suggest ZnS phases may be present in films deposited at -1.00V and -1.20V, although they cannot be definitively confirmed. The weak cathodic peak at -1.14V (VI) cannot be clearly assigned, although it may be associated with elemental Zn reduction processes. Cyclic voltammetry, performed on a similar bath without $Na_2S_2O_3$, shown in Fig. 8-2, indicates a well-defined cathodic peak at -1.14V assigned to elemental Zn reduction. The combination of Zn reduction processes, as well as cathodic S reduction process, may obscure trends in Zn:Sn ratios that may otherwise be evident with an anomalous co-deposition mechanism.

7.4.2.3 Time Evolution of Morphology

In order to investigate the nucleation behavior and morphology evolution with time, films were prepared with varying deposition times: 3sec, 30sec, 1min, 5min, and 15min. Using the nominal bath composition, depositions were performed on (Guardian) Mo-substrates at -1.00V. The morphologies of as-deposited films for increasing deposition time are shown in Fig. 7-29.

After 3sec, the deposit consists of individualized and small clusters of grains, each grain approximately 75nm in diameter. With increasing deposition time, the deposit completely covers the substrate. A 30sec deposition yields a densely packed film approximately 40nm thick, with grains ~150nm in diameter, as evident in Fig. 7-29. With increasing deposition time beyond 1min, the film roughness increases and the grains coarsen. After 5min, a significant roughening of the film is evident, with grains coarsening to ~300nm. By 15min, the deposit transitions to loosely-packed cauliflower and dendritic grains, consistent with diffusion-limited growth mechanisms. The film thickness increases approximately linearly with deposition time, up to 1.5μm at 15min.

The film nucleation appears qualitatively to proceed by progressive nucleation, evident as incomplete coverage of the substrate by the deposit after 3sec, seen in Fig. 7-29. In particular, a high magnification view film deposited for 3sec, shown below in Fig. 7-30, shows "availability" of nucleation sites, which are not populated by Cu grains. A linear increase in time of populated nucleation sites would confirm a progressive nucleation mechanism, but additional time steps are required to confirm [66]. More rigorous analyses of the nucleation behavior, by fitting of the current-time transients with instantaneous and progressive nucleation models, were inconclusive.

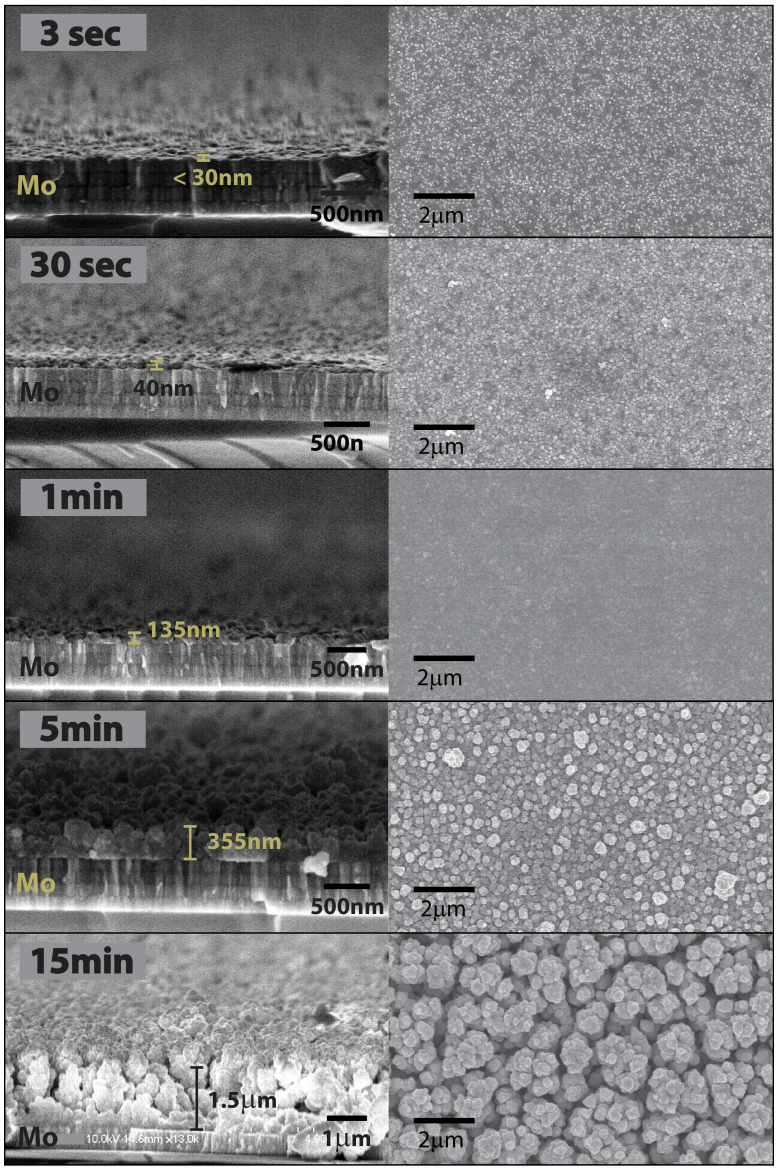

Fig. 7-29. Top-down and cross-sectional SEM images of co-electrodeposited CZTS precursors on (Guardian) Mo-substrates for deposition times of 3sec – 15min

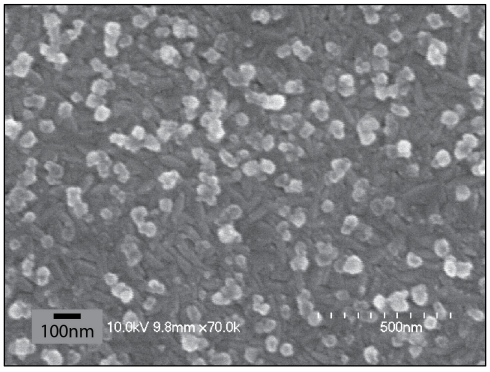

Fig. 7-30 High magnification SEM image of 3sec deposition

The transition from densely-packed, small-grained films to more loosely-packed, large-grained films that originates near 5min might be attributed to a shift in the transport properties of the electroactive species, resulting from exhaustion at the surface or in the bulk. As the chrono-amperogram in Fig. 7-31 shows, the onset of an additional reaction mechanism can be clearly seen at ~6min, evident as an increase in the current density. Hydrogen evolution at the electrode likely accounts for this time-delayed reaction, as a significant rate of bubble generation was visually evident after ~7.5min, confirming its onset.

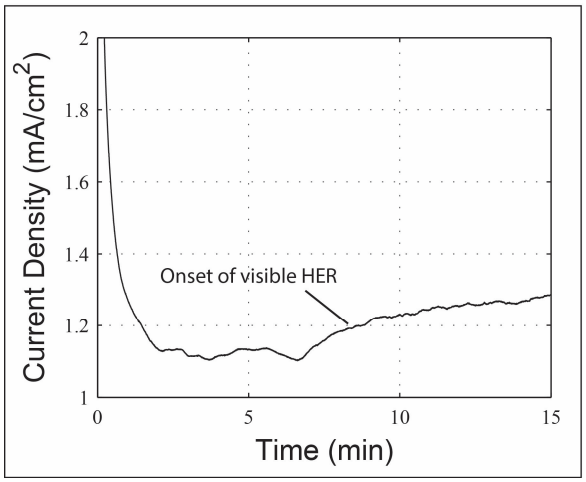

Fig. 7-31. Chrono-amperogram of co-electrodeposited CZTS precursor on (Guardian) Mo-substrate, 15min deposition

In the literature, the transition to dendritic growth modes has been shown to yield well-defined slope shifts in the chrono-amperograms, as described in Section 7.4.1.5. Comparison of the chrono-amperogram with Fig. 7-29 indicates good correlation between the transition time of the current density slope change and the transition to diffusion-limited growth features. However, later studies indicate that the shift in the chrono-amperogram results primarily from hydrogen evolution. Note: the source of the instabilities in current density at 1- 6min in Fig. 7-31 is unclear, and deposition currents associated with modified bath compositions in subsequent studies were significantly more stable in appearance.

7.4.2.4 Effects of Substrate

The section investigates the dependence of the as-deposited morphologies and compositions of CZTS precursors on the substrate type. Using the nominal bath composition, films were deposited at a constant potential of -1.00V for 25min onto an FTO-substrate, an (EMAT) Mo-substrate, and a (Guardian) Mo-substrate. The resulting film compositions are summarized in Table 7-18. Note the morphologies of the two Mo-substrates are nearly identical. The FTO-substrate demonstrates a similar morphology to the Mo-substrates, including dendritic features, except the film appears slightly more compact. For brevity, SEM images are omitted here.

The compositions of as-deposited films on the varying substrates were generally similar, although variations in the relative Sn and S concentrations were more pronounced between the two Mo-substrates and the FTO-substrate. The large film thicknesses and significant surface roughnesses prevent reliable determination of the compositions by RBS, but PIXE spectra support the reported trends in the element ratios in the films. Note also that the thickness of the film deposited on the (EMAT) Mo-substrate is significantly smaller than the thickness of the (Guardian) Mo- and FTO-substrates. The exact mechanism for this decrease in thickness is unknown, but chrono-amperograms confirm a significantly lower current density for the (EMAT) Mo-substrate compared to the (Guardian) Mo-substrate and the FTO-substrate.

Table 7-16. Composition of baseline co-electrodeposited CZTS precursors on varying substrates

Substrate	Atomic %					Cu:Zn	Zn:Sn	S:Metals	Thick (nm)
	Cu	Zn	Sn	S	O				
Guardian	35	9	18	21	17	3.8	0.52	0.33	1950
FTO	35	9	15	15	26	3.7	0.62	0.26	1940
EMAT Mo	32	8	17	20	23	3.9	0.47	0.35	1330

The cyclic voltammagrams (only forward sweep shown for clarity) for the FTO-, (EMAT) Mo-, and (Guardian) Mo-substrates with nominal bath conditions were measured from 0 to -1.50V at 10mV/s, as shown in Fig. 7-32. The voltammagram for each substrate indicates a series of cathodic peaks and HER onset at potentials more negative than -1.20V.

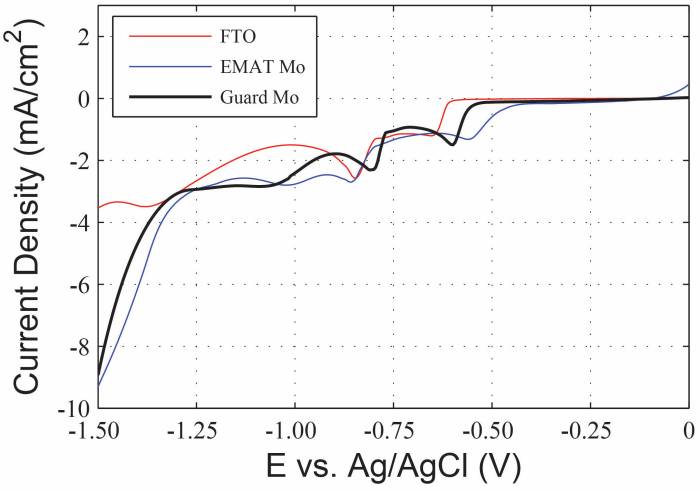

Fig. 7-32. Cyclic voltammagrams of nominal bath composition with FTO-, (EMAT) Mo-, and (Guardian) Mo-substrates

The cathodic peaks are summarized in Table 7-17, where the dominant, most-well defined reduction peaks are identified in bold. The voltammagram shapes are generally similar for the two Mo-substrates, although the dominant cathodic peaks and HER onset are slightly shifted. The

(EMAT) Mo-substrate has a significantly more-noble and weaker onset cathodic peak near -0.47V, previously associated with elemental Cu reduction. In [67], electrodeposition studies of $CuInSe_2$ showed that nuclei formed preferentially on the ridges of the Mo grains. The smaller grains in the (EMAT) Mo-substrates may therefore lower the activation overpotential associated with initial Cu nucleation by increasing the density of these ridges. The remaining cathodic peaks of the (EMAT) Mo-substrate do not exhibit any significant differences with the (Guardian) Mo-substrate, as they are spaced within 0.02V. HER onset, however, occurs at ~0.05V more-noble potentials.

Table 7-17. Cathodic peak locations of nominal bath composition for FTO-, (EMAT) Mo-, and (Guardian) Mo-substrates

Substrate	Cathodic Peak Locations (V)						HER Onset
FTO	-0.25	**-0.59**	-0.73	**-0.79**	**-1.02**	-1.20	-1.45
(EMAT) Mo	-0.18	**-0.47**	-0.73	**-0.80**	**-0.92**	**-1.13**	-1.24
(Guardian) Mo	-0.06	**-0.55**	-0.73	**-0.77**	**-0.90**	**-1.14**	-1.29

The cyclic voltammagram for the FTO-substrate exhibits notable differences from the Mo-substrates. First, the onset of the first dominant cathodic peak shifts more negative to -0.59V, which may also be related to increased grain size associated with FTO- compared to the Mo-substrates. More significantly, the depletion associated with the -0.79V cathodic peak is more exaggerated than the Mo-substrate. If a peak exists at -0.92V or at -1.13V, then it is masked by this large depletion curve. The overpotential for HER also shifts significantly to -1.45V for the FTO-substrate. From approximately 0V to -0.90V, the current densities of the FTO- and Mo-substrates are similar, while the current density for the FTO-substrate drops significantly beyond -0.9V. The mechanisms for the variations in cyclic voltammagram behavior for FTO- and Mo-substrates require additional study to identify them.

7.4.2.5 Effects of Bath Composition

The dependence of the as-deposited film morphologies and compositions of CZTS on the bath composition was investigated for (Guardian) Mo-substrates by varying each bath component while holding the others constant. Due to interactions of the electroactive species in solution, it is expected that the film composition will not change linearly with the bath component concentrations. In an effort to more quickly reach an optimum bath composition, the component concentrations were not varied relative to a single nominal bath. The baseline composition for each bath will be noted at the beginning of each section. The trends in film properties are expected to be general, however. **In order to improve Zn incorporation, all films are deposited at constant potential of -1.10V instead of -1.00V**.

$CuSO_4$ Concentration

The baseline composition for the investigation of $CuSO_4$ concentration was the following: 0.2M Citrate, 0.02M $ZnSO_4$, 0.014M $SnSO_4$, and 0.02M $Na_2S_2O_3$. The concentration of $CuSO_4$ was varied between 0.010M and 0.016M, and the resulting compositions and morphologies are summarized in Table 7-18 and Fig. 7-33, respectively.

Table 7-18. Compositions of co-electrodeposited CZTS precursors deposited with varying $CuSO_4$ concentrations

[$CuSO_4$]	Atomic %					Cu:Zn	Zn:Sn	S:Metals	Thick (nm)
	Cu	Zn	Sn	S	O				
0.010M	23	9	16	22	30	2.5	0.55	0.45	590
0.014M	28	11	13	17	30	2.5	0.88	0.33	760
0.016M	29	9	11	18	33	3.1	0.82	0.36	720

As expected, the relative Cu concentration in the film monotonically increased with increasing $CuSO_4$ concentration, evident as an increase in the Cu:[Zn+Sn] ratio. Conversely, the relative Sn concentration monotonically decreased with increasing $CuSO_4$ concentration. This inverse Cu and Sn relationship, associated with varying $CuSO_4$ concentration, was observed in all $Na_2S_2O_3$-containing baths with and without tartaric acid (see Section 7.4.1.4). Zn and S concentrations, however, did not show any clear trends with varying $CuSO_4$ concentration, except the absolute Zn concentration exhibits a maximum and S exhibits a minimum at 0.014M.

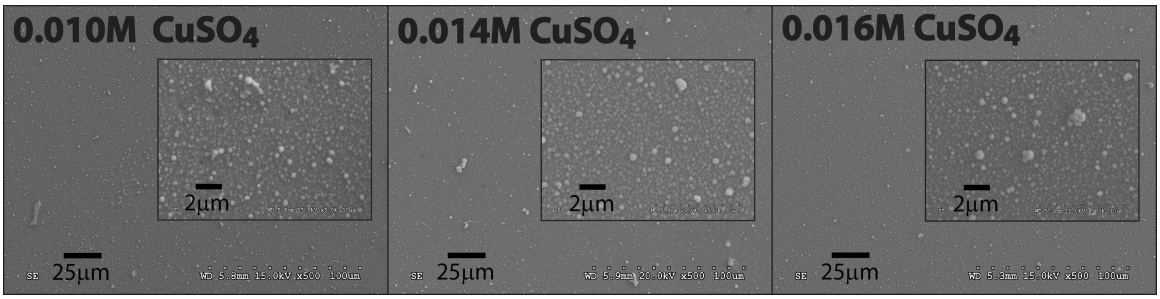

Fig. 7-33. SEM images of co-electrodeposited CZTS precursors on (Guardian) Mo-substrates deposited with varying $CuSO_4$ concentrations

The surface morphologies of as-deposited films do not vary strongly with increasing $CuSO_4$ concentration, as shown in Fig. 7-33 below. The films are significantly more compact, although thinner, than the longer deposition baseline films shown in Section 7.4.2.1. The reduction in dendritic features is attributed to the shorter deposition times and adjusted component concentrations. As Section 7.4.2.3 showed, films surfaces roughened significantly with increasing time; at 5min, the films deposited from Pawar's nominal bath (less tartaric acid), demonstrated significant roughness. The films deposited in this section show compact surfaces at 10min of deposition, demonstrating that the adjusted bath composition also contributed to improvement in the as-deposited morphologies. Note that the surfaces do not contain the large overgrowths

previously developed on all films deposited from baths containing tartaric acid. Small voids, attributed to hydrogen evolution reaction, are also evident in all the films.

$ZnSO_4$ Concentration

The baseline composition for the investigation of $ZnSO_4$ concentration was the following: 0.2M Citrate, 0.01M $CuSO_4$, 0.014M $SnSO_4$, and 0.02M $Na_2S_2O_3$. The concentration of $ZnSO_4$ was varied between 0.02M and 0.03M, and the resulting compositions and morphologies are summarized in Table 7-19 and Fig. 7-34, respectively.

Table 7-19. Compositions of co-electrodeposited CZTS precursors deposited with varying $ZnSO_4$ concentrations

[$ZnSO_4$]	Atomic %					Cu:Zn	Zn:Sn	S:Metals	Thick (nm)
	Cu	Zn	Sn	S	O				
0.020M	23	9	16	22	30	2.5	0.55	0.45	590
0.030M	22	10	15	20	33	2.2	0.66	0.41	660
0.040M	22	9	15	17	37	2.3	0.61	0.37	760

The relative Zn concentration increases slightly with increasing $ZnSO_4$, evident as a decrease in Cu:Zn and an increase in Zn:Sn ratios. The increase is not monotonic, however, with the relative Zn concentration dipping slightly again at 0.04M. This trend is contrary to the variation in Zn with $ZnSO_4$ concentration observed in Section 7.4.1.4 for baths containing tartaric acid. In that study, the relative Zn concentration in the film was shown to scale roughly with the $ZnSO_4$ concentration in the bath. Further, here the S concentration monotonically decreases with increasing $ZnSO_4$. Note the film thickness monotonically increases with increasing $ZnSO_4$ concentration.

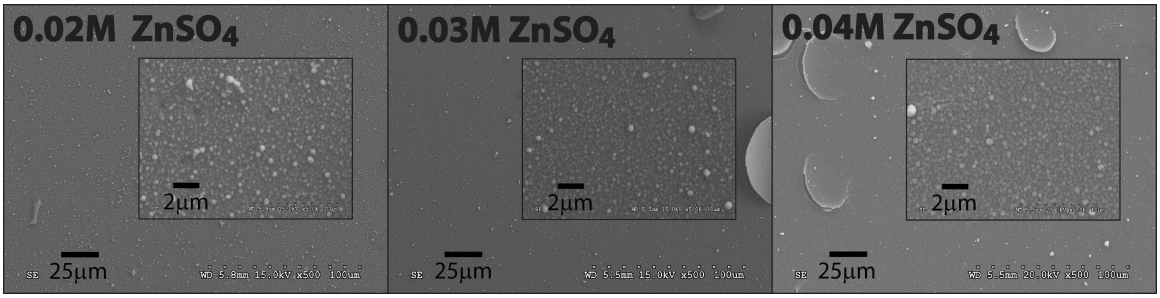

Fig. 7-34. SEM images of co-electrodeposited CZTS precursors on (Guardian) Mo-substrates deposited with varying $ZnSO_4$ concentrations

The surface morphologies of as-deposited films show evidence of film/substrate damage at $ZnSO_4$ concentrations of 0.03 and 0.04M, as shown in Fig. 7-34 below. All the films possess well-packed, small-grained structures but show evidence of small voids that are attributed to hydrogen evolution reaction. Films deposited at larger $ZnSO_4$ concentrations of 0.03 and 0.04M also contain large semicircular blisters.

As shown in Fig. 7-31, the deposition current demonstrates a relative period of stability, followed by delayed onset of an additional reaction that increases the current density. This reaction onset, and subsequent current density increase, was attributed to hydrogen evolution reaction and possibly transition to dendritic growth mode. Similar features are observed in the chrono-amperograms associated with the depositions performed here with varying $ZnSO_4$ concentrations (figure not shown for brevity). The onset of the current increase occurs at 7.8min, 7.4min, and 4.9min for 0.02M, 0.03M, and 0.04M $ZnSO_4$ concentrations, respectively. Note that bubbles generated at the surface were observed after the onset of the current increases. This association of earlier onset of hydrogen evolution reaction with damage to the film and substrate is regularly observed throughout the remaining studies, and the mechanisms of damage are discussed in more detail in Section 7.4.2.9. It will later be shown that stopping the deposition before the onset this transition mitigates damage to the film. The lack of diffusion-limited growth features suggests that the slope change in the chrono-amperogram more likely results from hydrogen evolution.

$SnSO_4$ Concentration

The baseline composition for the investigation of $SnSO_4$ concentration was the following: 0.2M Citrate, 0.01M $CuSO_4$, 0.02M $ZnSO_4$, and 0.02M $Na_2S_2O_3$. The concentration of $SnSO_4$ was varied between 0.010M and 0.016M, and the resulting compositions and morphologies are summarized in Table 7-20 and Fig. 7-35, respectively.

Table 7-20. Compositions of co-electrodeposited CZTS precursors deposited with varying $SnSO_4$ concentrations

[$SnSO_4$]	Atomic %					Cu:Zn	Zn:Sn	S:Metals	Thick (nm)
	Cu	Zn	Sn	S	O				
0.010M	25	11	11	22	31	2.2	1.1	0.46	500
0.014M	23	9	16	22	30	2.5	0.55	0.45	590
0.016M	18	9	18	20	35	2.0	0.53	0.44	800

As expected, the relative Sn concentration in the film monotonically increases with increasing $SnSO_4$ concentration, evident as an increase in the Sn:[Cu+Zn] ratio. Note this ratio changes approximately in proportion to the concentration changes in $SnSO_4$. Conversely, the relative Cu concentration monotonically decreases with increasing $SnSO_4$ concentration. This inverse Cu and Sn relationship has been noted several times before in this work. The Zn and S concentrations, however, do not show significant variations with changes in $SnSO_4$ concentration, although the absolute concentrations do show a maximum at the lowest $SnSO_4$ concentration. Note the film thickness monotonically increases with increasing $SnSO_4$ concentration.

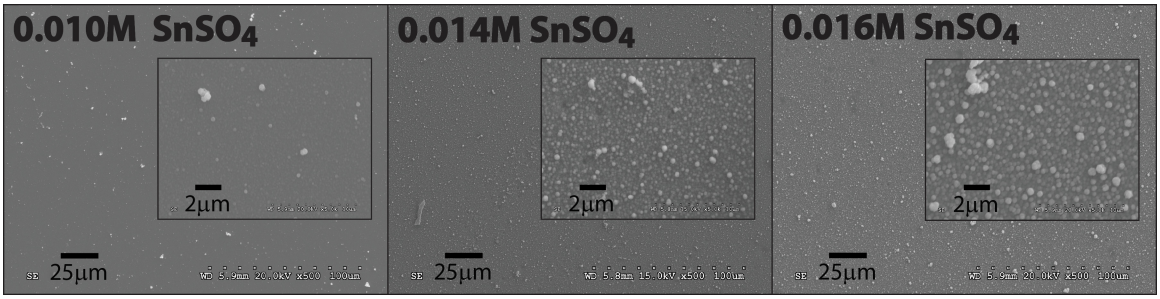

Fig. 7-35. SEM images of co-electrodeposited CZTS precursors on (Guardian) Mo-substrates deposited with varying $SnSO_4$ concentrations

The surface morphologies of as-deposited films exhibited well-packed, small-grained structure, with grain size increasing with increasing $SnSO_4$ concentration. Micron-sized features periodically decorate the film surfaces but show no strong trend with $SnSO_4$ concentration. Small voids, attributed to hydrogen evolution reaction, are also evident in all the films. Like the varying $ZnSO_4$ study in the previous section, increasing the $SnSO_4$ concentration causes a shift in the HER reaction to earlier times. However, the resulting film damage in this case was less severe, with the semicircular blisters generally absent.

$Na_2S_2O_3$ Concentration

The baseline composition for the investigation of $Na_2S_2O_3$ concentration was the following: 0.2M Citrate, 0.01M $CuSO_4$, 0.02M $ZnSO_4$, and 0.014M $SnSO_4$. The concentration of $Na_2S_2O_3$ was varied between 0.01M and 0.03M, and the resulting compositions and morphologies are summarized in Table 7-21 and Fig. 7-36, respectively.

Table 7-21. Compositions of co-electrodeposited CZTS precursors deposited with varying $Na_2S_2O_3$ concentrations, ◊ element present but cannot be reliably fitted

$[Na_2S_2O_3]$	Atomic %					Cu:Zn	Zn:Sn	S:Metals	Thick (nm)
	Cu	Zn	Sn	S	O				
0.010M	23	9	25	16	27	2.7	0.34	0.28	490
0.020M	23	9	16	22	31	2.5	0.55	0.45	590
0.030M	◊	◊	◊	◊	◊	1.8	0.71 (◊)	-	-

The severe roughness of the films deposited with 0.03M $Na_2S_2O_3$ prevents reliable fitting of the RBS spectrum. However, scaling of the PIXE peaks permits calculation of the Cu:Zn and Zn:Sn ratios. The relative Zn concentration increases with increasing $Na_2S_2O_3$ concentration, evident as decreasing Cu:Zn and increasing Zn:Sn ratios. Note the Cu:Zn ratios are calculated using the non-truncated composition values; therefore, the Cu:Zn ratios change for 0.01 and 0.02M $Na_2S_2O_3$, despite apparently constant Cu and Zn concentrations. The relative Sn concentration monotonically decreases with increasing $Na_2S_2O_3$, evident as a decreasing Sn:[Cu+Zn] ratio. Note

that in baths with tartaric acid (see Section 7.4.1.4), no clear trends in the cation ratios with varying $Na_2S_2O_3$ concentration were observed.

The S concentration increases slightly with an increase in $Na_2S_2O_3$ from 0.01 to 0.02M, evident as an increase in the absolute S concentration and in the S:metals ratio. At 0.03M $Na_2S_2O_3$, the calculated S concentrations cannot be reliably determined from RBS or PIXE due to S peak overlaps with Mo.

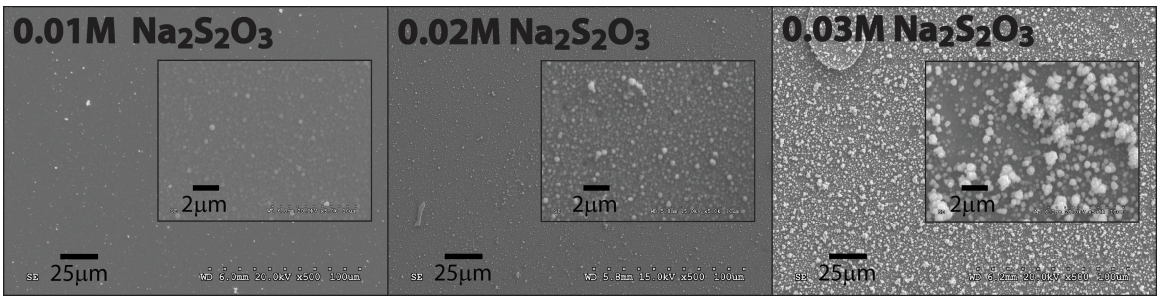

Fig. 7-36. SEM images of co-electrodeposited CZTS precursors on (Guardian) Mo-substrates deposited with varying $Na_2S_2O_3$ concentrations

The surface morphologies of as-deposited depend strongly on the concentration of $Na_2S_2O_3$, as shown in Fig. 7-36. The film deposited with the lowest concentration 0.01M of $Na_2S_2O_3$ exhibited the most compact, smallest-grained structure, with the least evidence of film damage. As the $Na_2S_2O_3$ concentration increased, the grains coarsened and voids developed in the film. At 0.03M, a significant morphology transition appears; films showed the large semicircular blisters also demonstrated at high $ZnSO_4$ concentrations, as well as the large overgrowths demonstrated in depositions from baths containing tartaric acid. Similar to previous $ZnSO_4$ and $SnSO_4$ studies, varying the $Na_2S_2O_3$ concentration modified the onset of HER and associated current rise. In this case, decreasing the $Na_2S_2O_3$ concentration delayed the onset. For 0.010M $Na_2S_2O_3$, no HER reaction was observed for the 10min duration of the deposition. For 0.03M, the HER reaction was observed near 5min.

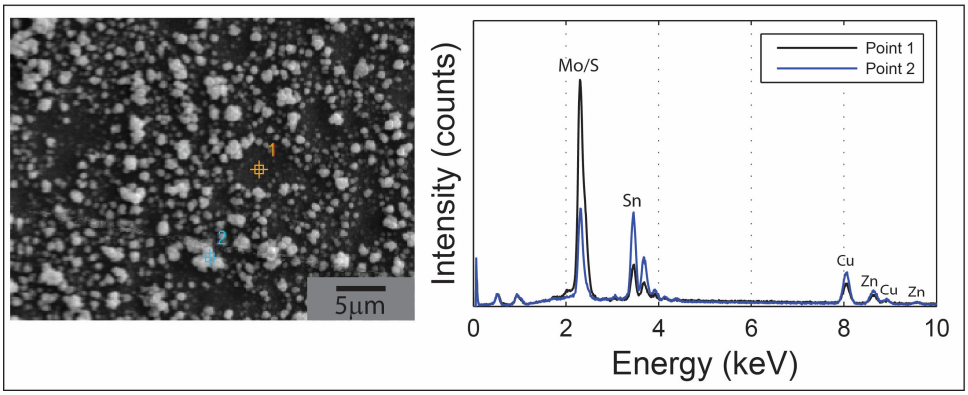

Fig. 7-37. Point-and-shoot EDS spectra for co-electrodeposited CZTS precursor (0.03M $Na_2S_2O_3$)

Point-and-shoot EDS measurements, shown in Fig. 7-37, indicated that the large surface particulates (Point 2) seen in the SEM image were Sn-rich. The EDS spectrum also indicated that Point 2 contains Cu, Zn and Mo/S. However, the relatively small particulate size may result in sampling of the surrounding film and substrate (e.g. the sample volume may be larger than the particulate).

Citrate Concentration

The baseline composition for the investigation of Citrate concentration was the following: 0.01M $CuSO_4$, 0.03M $ZnSO_4$, 0.01M $SnSO_4$, and 0.02M $Na_2S_2O_3$. The concentration of Citrate was varied between 0.1M and 0.3M, and the resulting compositions and morphologies are summarized in Table 7-22 and Fig. 7-38, respectively.

Table 7-22. Compositions of co-electrodeposited CZTS precursors deposited with varying Citrate concentrations

[Citrate]	Atomic %					Cu:Zn	Zn:Sn	S:Metals	Thick (nm)
	Cu	Zn	Sn	S	O				
0.10M	26	9	11	23	31	2.9	0.86	0.51	590
0.20M	24	12	10	18	36	2.0	1.2	0.39	510
0.30M	17	5	11	20	47	3.0	0.53	0.59	450

The cation ratios in the film, Cu:Zn and Zn:Sn, varied non-monotonically with increasing Citrate concentration, with the desired stoichiometries achieved at 0.20M Citrate. The relative Zn concentrations decreased significantly at 0.10M and 0.30M, evident as increased Cu:Zn and decreased Zn:Sn ratios. The absolute S concentration showed no significant variations with Citrate concentration, with values varying between 18–23at%. Note the film thickness decreases monotonically with increasing Citrate concentration.

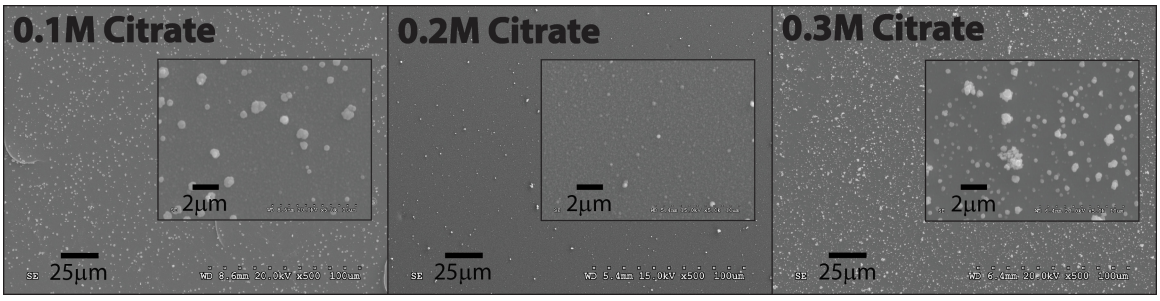

Fig. 7-38. SEM images of co-electrodeposited CZTS precursors on (Guardian) Mo-substrates deposited with varying Citrate concentrations

Like the compositions, the film morphologies are also optimum at 0.2M Citrate. At 0.1M and 0.3M Citrate, the surface morphologies exhibit semicircular blisters and overgrowth features. Similar to previous studies of varying component concentrations, varying the Citrate concentration modified the onset of HER and associated current rise. In this case, no HER reaction

was observed in the 0.2M Citrate sample for the 10min duration of the deposition. The 0.1M and 0.3M Citrate samples, however, showed onset of HER reaction near 5min.

Point-and-shoot EDS measurements, shown in Fig. 7-39, indicates that the large surface particulates (Point 2) seen in the SEM image were Cu-rich. The EDS spectrum also indicates that Point 2 contains Zn, Sn and Mo/S. However, the relatively small particulate size may result in sampling of the surrounding film and substrate (e.g. the sample volume may be larger than the particulate). Note that EDS point-and-shoot results for 0.1M Citrate (not shown) indicate the surface particulates were similarly Cu-rich.

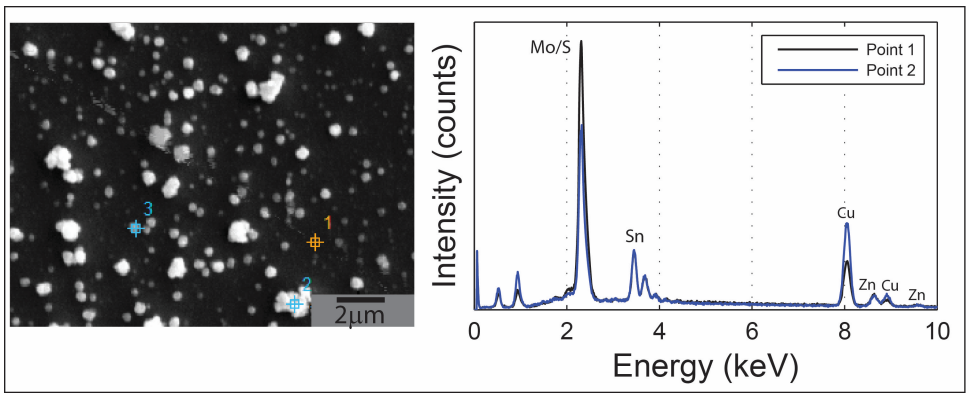

Fig. 7-39. Point-and-shoot EDS spectra for co-electrodeposited CZTS precursor (0.3M Citrate)

The effects of bath composition on the composition and morphology of as-deposited films may then be summarized as follows:

- Similar to baths with tartaric acid, the Cu and Sn concentrations in the films demonstrated an inverse relationship. For instance, increasing the $CuSO_4$ increased the Cu and decreased the Sn concentrations in the films. Conversely, increasing the $SnSO_4$ increased the Sn and decreased the Cu concentrations in the films. However, shifts in the Sn concentrations were significantly more pronounced than Cu in both cases.
- The relative Sn concentrations decreased significantly, the Zn concentrations increased significantly, and the S concentrations increased slightly with increasing $Na_2S_2O_3$ concentrations. At 0.03M $Na_2S_2O_3$, rough surface morphologies prevented reliable fitting of the RBS spectrum.
- The relative Zn concentrations increased slightly and the S concentrations monotonically decreased with increasing $ZnSO_4$ concentration. A contrary trend in Zn concentration was observed in baths with tartaric acid, which showed significant increases in relative Zn concentration with increasing $ZnSO_4$.

- The Cu:Sn ratio monotonically decreased with increasing Citrate concentration. However, the Cu:Zn ratio exhibited non-monotonic behavior with a minimum at 0.2M Citrate.
- The grain sizes of the deposited film generally increased with increasing concentrations of the metal sulfate precursors.
- Increasing $CuSO_4$ and $SnSO_4$ concentrations caused earlier onset of HER.
- Increasing $ZnSO_4$ concentration caused the formation of semicircular blisters and earlier onset of HER.
- Increasing $Na_2S_2O_3$ concentration increased the grain size, significantly increased the density of micron-sized Sn-rich particulates, caused the formation of semicircular blisters, and caused significantly earlier onset of HER.
- Increasing or decreasing Citrate concentration from nominal 0.02M increased the density of micron-sized, Cu-rich particulates and caused much earlier HER onset.

7.4.2.6 Effects of Bath Concentration

The properties of the as-deposited films depend not only on the ratios of the component concentrations, but the overall bath concentration. Under diffusional control, the partial current density of a depositing species depends on its bulk concentration, as given by the Cottrell equation (3-21); see Section 3.2.2.3 for further discussion. Consequently, increasing the overall bath concentration should result in higher deposition rates of the films. The previous sections have shown that longer deposition times can lead to rougher films with more damage, particularly after the onset of HER reactions that are identified by visible bubble generation on the film and an uptick in current density during deposition. Stopping the deposition before the onset of this detrimental reaction was shown to mitigate the damages to the film and substrate, but the film thicknesses were too thin to make useful photovoltaic absorber layers. Therefore, increasing the bath concentration was investigated as a possible way to increase the film thickness before the onset of the detrimental reactions.

Table 7-23. Compositions of co-electrodeposited CZTS precursors deposited with varying bath concentrations

Bath Concentration	Atomic %					Cu:Zn	Zn:Sn	S:Metals	Thick (nm)
	Cu	Zn	Sn	S	O				
1X	24	12	10	18	36	2.0	1.2	0.39	510
1.5X	26	12	10	20	32	2.2	1.1	0.41	830
2X	26	13	10	20	31	2.0	1.3	0.41	1140

The baseline composition for the investigation of bath concentration was the following: 0.2M Citrate, 0.01M $CuSO_4$, 0.03M $ZnSO_4$, 0.01M $SnSO_4$, and 0.02M $Na_2S_2O_3$. This bath composition was shown to yield film stoichiometries near the ideal Cu:Zn:Sn ratio of 1.8:1.2:1.0, as shown in Section 7.4.2.5. The bath concentration was increased up to 2X, such that the ratios of component concentrations remained constant (e.g. 2X bath: 0.4M Citrate, 0.02M $CuSO_4$, 0.06M $ZnSO_4$, 0.02M $SnSO_4$, 0.04M $Na_2S_2O_3$). The resulting compositions and morphologies are summarized in Table 7-23 and Fig. 7-40, respectively.

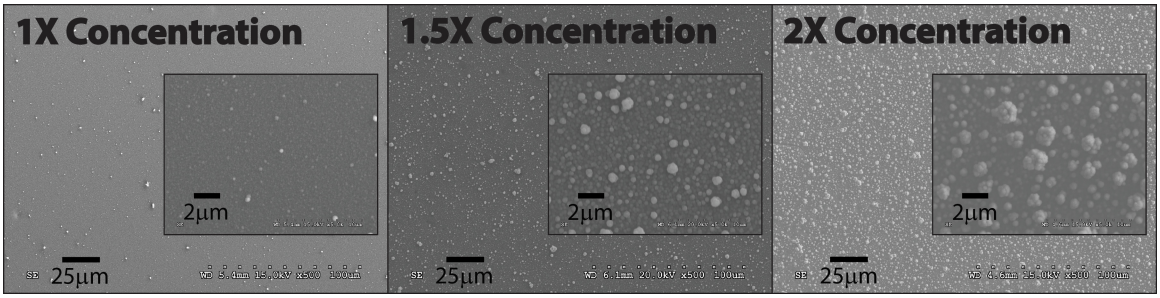

Fig. 7-40. SEM images of co-electrodeposited CZTS precursors on (Guardian) Mo-deposited with varying bath concentrations (component ratios were fixed)

The relative Sn concentration decreases slightly and the relative S concentration increases slightly with increasing bath concentration, evident as small increases in the Zn:Sn and S:metals ratios, respectively. However, the compositions of the as-deposited films do not depend strongly on the overall bath concentration. The film thickness scales approximately with the bath concentration, increasing by approximately a factor of two with 2X bath concentration, as expected.

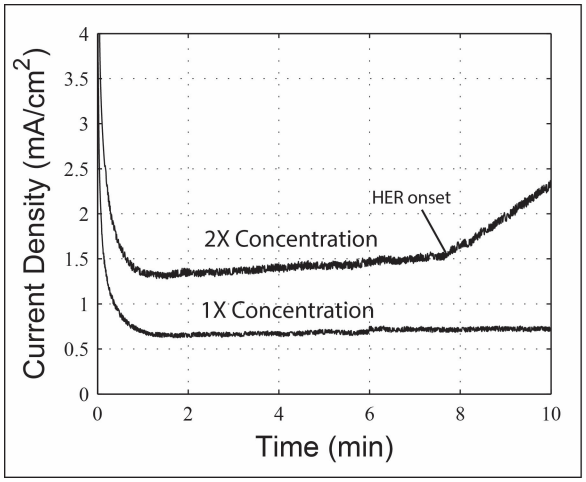

Fig. 7-41. Chrono-amperograms of co-electrodeposited CZTS precursors on (Guardian) Mo-substrates for 1X and 2X bath concentrations

The surface morphologies of as-deposited films exhibited well-packed, small-grained structure, with grain size increasing with increasing bath concentration. Small voids, attributed to hydrogen evolution reaction, were also evident in all the films. Further, at 2X bath concentration, cracks and semicircular blisters are also evident (more clear in other SEM images not shown here for brevity).

Increasing the bath concentration caused earlier onset of HER reaction and associated current rise, as shown in Fig. 7-41. This onset in HER and associated film damage is consistent with growth behavior observed in Section 7.4.2.5. Increasing the bath concentration did yield some gains in film thickness before the onset of detrimental HER reaction, however. For 2X bath concentration, if the deposition were to be stopped at 7min (prior to the onset of HER), then the film thickness would be 800nm (assuming linear growth), significantly larger than 510nm film associated with the 1X bath deposition.

7.4.2.7 Effects of Stirring

Like bath concentration, stirring was investigated as a means to increase the film thickness, while mitigating the film and substrate damage resulting from HER. Providing stirring during deposition, via magnetic stir bars, can modify the film growth behavior by altering the transport properties of the depositing species and possibly the H^+ and OH^- ions involved in hydrogen evolution reaction. Further, convective transport associated with stirring was expected to increase the deposition rate and therefore film thickness.

The baseline composition for the investigation of bath concentration was the following: 0.2M Citrate, 0.01M $CuSO_4$, 0.03M $ZnSO_4$, 0.01M $SnSO_4$, and 0.02M $Na_2S_2O_3$. This bath composition was shown to yield film stoichiometries near the ideal Cu:Zn:Sn ratio of 1.8:1.2:1.0, as shown in Section 7.4.2.5. Films were deposited from baths without stirring and from baths with stirring at 200rpm. The resulting compositions and morphologies are summarized in Table 7-24 and Fig. 7-42, respectively.

The relative Cu concentration increases significantly and the relative Zn concentration decreases significantly with stirring, while the absolute Sn and S concentrations do not vary. Stirring increases the film thickness by a factor of 5, yielding a film thickness near 2.5μm.

Table 7-24. Compositions of co-electrodeposited CZTS precursors deposited with varying stir rates

Stirring	Atomic %					Cu:Zn	Zn:Sn	S:Metals	Thick (nm)
	Cu	Zn	Sn	S	O				
None	24	12	10	18	36	2.0	1.2	0.39	510
200rpm	30	9	10	18	33	3.2	0.9	0.37	2500

The surface morphologies of quiescent and stirred films both exhibited compact structures. However, stirring significantly increased the grain size and roughness of the films. More voids, attributed to hydrogen evolution reaction, were also evident in all the films deposited with stirring. No cracks or semicircular blisters were observed, however. Further, the chrono-amperogram from deposition shows a steady rise in current but no time-delayed uptick in current density evident in other films with HER. No bubble generation was visible during deposition.

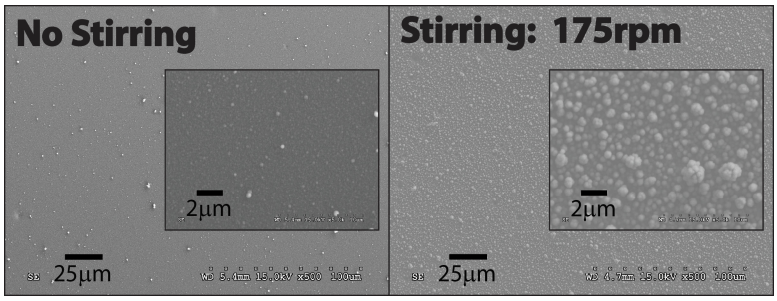

Fig. 7-42. SEM images of co-electrodeposited CZTS on (Guardian) Mo-substrates deposited from baths with and without stirring

After deposition, the films were visibly non-uniform, which is attributed to the electrode configuration in the bath. As shown in Chapter 3, the electrochemical cell did not employ a luggin capillary and the large reference electrode sat near the face of the working electrode (e.g. the substrate). When stirring, the bath rotated clockwise, stirring the bath towards the electrode. Subsequently, the flow was interrupted and slowed near the reference electrode tip. The velocity of the bath across the electrode face was therefore non-uniform, yielding non-uniform depositions. If the composition is properly adjusted to account for the relative increase in Cu and decrease in Zn in the film, then stirring represents a viable path to increase the film thickness, while mitigating the damaging effects associated with HER onset.

7.4.2.8 Effects of Galvanostatic Control

The properties of the as-deposited films depend not only on the bath composition but also on the deposition control method. The reduction mechanisms depend strongly on the overpotential applied, but the film morphology often depends strongly on the deposition current density, particularly its value relative to the limiting current density [68]. The effects of constant current (galvanostatic) control on the properties of as-deposited films are investigated here.

The baseline composition for the investigation of bath concentration was the following: 0.2M Citrate, 0.01M $CuSO_4$, 0.03M $ZnSO_4$, 0.01M $SnSO_4$, and 0.02M $Na_2S_2O_3$ This bath composition was shown to yield film stoichiometries near the ideal Cu:Zn:Sn ratio of 1.8:1.2:1.0, as shown in Section 7.4.2.5. Films were deposited with constant current densities varied between -0.34 and -1.59mA/cm^2, chosen based on the steady-state current densities observed with

potentiostatic control. The resulting compositions and morphologies are summarized in Table 7-25 and Fig. 7-43, respectively.

Table 7-25. Compositions of co-electrodeposited CZTS precursors deposited under galvanostatic control with varying current densities

Current Density	Atomic %					Cu:Zn	Zn:Sn	S:Metals	Thick (nm)
	Cu	Zn	Sn	S	O				
-0.34mA/cm^2	55	-	10	14	21	-	-	0.21	200
-0.68mA/cm^2	22	8	11	20	39	2.8	0.73	0.49	380
-1.59mA/cm^2	22	12	10	17	39	1.8	1.2	0.39	970

The film deposited at -1.59mA/cm^2 achieved exactly the desired stoichiometry, with slightly Cu-poor and slightly Zn-rich cation ratios. Further, the film was near the minimum required thickness of 1μm for use as a photovoltaic absorber layer.

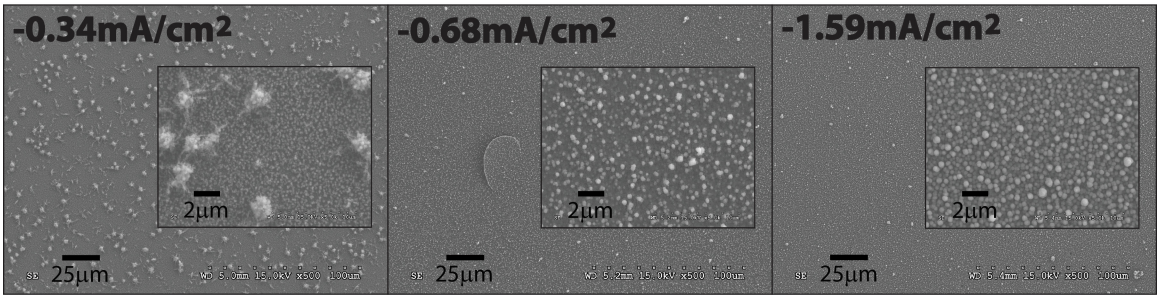

Fig. 7-43. SEM images of co-electrodeposited CZTS precursors on (Guardian) Mo-substrates deposited under galvanostatic control with varying current densities

The surface morphologies of the as-deposited films varied significantly with increasing current density. As the chrono-potentiogram in Fig. 7-44 shows, the constant current density deposition of -0.34mA/cm^2 settled into a nearly constant potential of -0.78V. The surface features seen in the SEM were similar in appearance to those observed in constant potential depositions at -0.75V and -0.80V, as shown in Fig. 7-25. At current densities of -0.68 and -1.59mA/cm^2, the films were compact with small grains and no evidence of large particulates on the surface. Further, few voids, typically attributed to hydrogen evolution, were evident on the film surfaces. However, large semicircular blisters appeared in both the higher current density samples. The film thickness roughly scaled with the current density, as expected.

No bubble generation was visibly evident for the lower current densities of -0.34 and -0.68mA/cm^2. However, vigorous bubble generation was evident for the current density of -1.59mA/cm^2. The time of visible onset of bubble generation was, unfortunately, not noted during the deposition. However, the clear transition of the potential near 3.5min from -1.23V to -1.06V indicates a sudden lowering of the overpotential for a new reaction, most likely hydrogen

evolution. This transition to lower potentials at constant current correlates with the transition to higher currents at constant potential observed in previous studies. Possible sources for the apparent lowering of the hydrogen overpotential are discussed in Section 7.4.2.9.

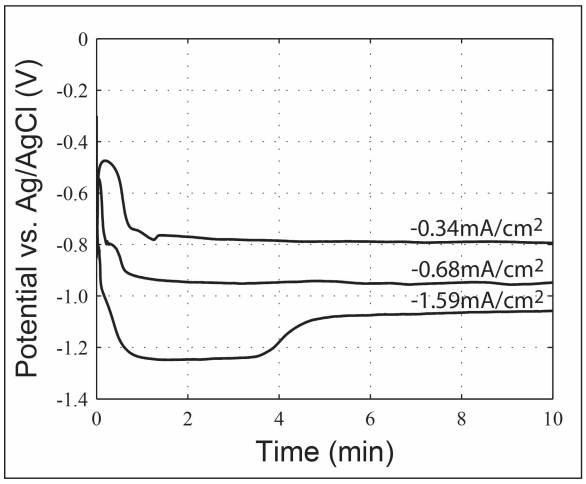

Fig. 7-44. Chrono-potentiograms of co-electrodeposited CZTS precursors on (Guardian) Mo-substrates deposited under galvanostatic control with varying current densities

7.4.2.9 Proposed Deposition Mechanisms

Substrate and Film Damage

Many types of damage to the deposited films and Mo-substrates are observed after electrodeposition, including substrate blistering, substrate pitting, film blistering, and film void formation. Fig. 7-45 shows examples of these damage modes, which are strongly linked to the onset of *visible hydrogen evolution reaction*, as described in the previous section (see Fig. 7-41).

Substrate blisters and pits are observed in samples that demonstrated visible onset of hydrogen evolution reaction during electrodeposition, although the onset of visible HER did not guarantee their formation. Substrate blisters are observed in the (Guardian) Mo-substrates but not the (EMAT) Mo-substrates, which is attributed to the high compressive-strain and multi-layer structure of the (Guardian) Mo films. A large rightward shift in the primary (110) x-ray diffraction peak (see Table 3-8) indicates high compressive-strain in the (Guardian) Mo films. Note that Guardian Industries provide the Mo-substrates as courtesy samples, and they were not optimized for this application. Further, the Mo film consists of four layers, as evident in the cross-sectional SEM image in Fig. 7-29. The substrate blistering may be attributed to the unique properties of this (Guardian) Mo film, such that damage to the Mo film results in buckling failures. H^+ ions associated with the HER reaction may diffuse in between the Mo layers, resulting in H_2 bubble generation and splitting/buckling of the upper layer(s). This failure mode is not seen in the single-layer, tensile-strained (EMAT) Mo films.

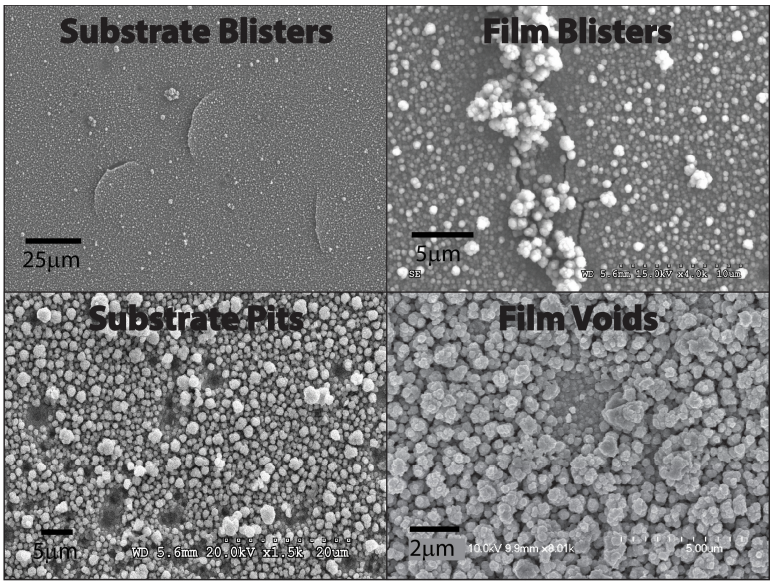

Fig. 7-45 SEM images of substrate and film damage modes in co-electrodeposited S-containing CZTS precursors on (Guardian) Mo-substrates

SEM images show the formation of pits in the sample, as shown in the bottom left of Fig. 7-45. However, it is unclear if these holes are simply voids in the deposited film or actual pits in the substrate. Point-and-shoot EDS measurements were inconclusive, as the detection of Mo in the pits may result from incomplete penetration of the pit through the Mo film. However, visible changes to the Mo film after deposition, as seen in Fig. 7-46, suggest the presence of pits. Similar changes to those shown are evident when visible onset of HER is active during electrodeposition, and they are present when blisters and pits are observed, when pits only are observed, and when minimal pits are observed. Since the molybdenum layer is optically thick, changes in the appearance of the back (glass-side) surface must indicate modifications to the Mo film itself.

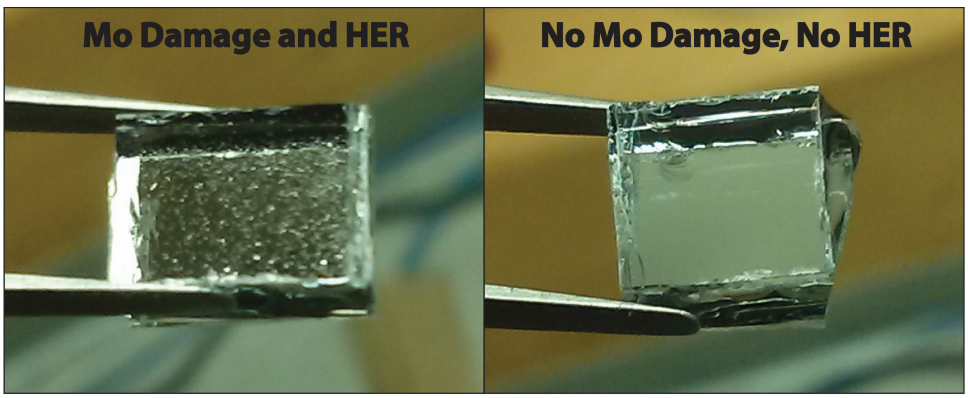

Fig. 7-46 Changes to the appearance of Mo film, associated with visible onset of HER during electrodeposition, observed through the back-side of the glass

Pitting corrosion could result from hydrogen evolution by raising the local pH or by creating local galvanic cells. Increasing the local pH can modify the thermodynamic stability of

the films, possibly inducing metal dissolution. Molybdenum, however, tends to form a passivation layer, which mitigates corrosion (e.g. dissolution of the metal) [69]. In fact, stainless steels frequently include molybdenum as an additive to improve corrosion resistance [70]. Soaking of the Mo sample in pH~14 NaOH solution confirmed no notable corrosion in the films. In corrosion studies of stainless steel, thiosulfate has been shown to accelerate pitting corrosion by blocking the adsorption of OH^- ions and preventing the formation of a passivation layer [70]. Molybdenum was shown, however, to decelerate this process [70]. Galvanic corrosion of the metal (e.g. dissolution) can result from coupling of the metal electrode reaction with the hydrogen evolution reaction [71] . Effectively, soluble metal ions form when electrons are scavenged by the hydrogen evolution reaction. That is, electrons are supplied to the hydrogen evolution reaction, Eqn. (3-33), via: $M(s) \rightarrow M^{2+} + 2e^-$ [71, 72].

These explanations are not particularly satisfying, however, given the prevalence of literature identifying molybdenum as a strong corrosion inhibitor [70] and stable catalyst in hydrogen production applications [73]. Note that no pits or blisters were observed in the co-electrodeposited metallic precursors, which were deposited from baths without $S_2O_3^{2-}$ and demonstrated no hydrogen evolution reaction. Additional investigations are required to more fully understand potential pitting mechanisms in the Mo films.

The film blisters and the film voids are simply attributed to hydrogen evolution. The film blisters are consistent with hydrogen bubble formation at the interface between the molybdenum and the depositing film, which eventually breaks through the depositing film surface. In studies of the electrodeposition of $CuInSe_2$, hydrogen evolution was shown to proceed preferentially at the Mo back contact [74]. The other voids result simply from local blocking of deposition or delamination of the film, consistent with the features identified in the leftmost image in Fig. 3-12.

Reduction Mechanisms

Examining the peak assignments for the (Guardian) Mo- substrate from Section 7.4.2.2, the onset of significant Cu deposition occurs at -0.55V, the onset of significant Sn deposition occurs at -0.75V, the onset of S deposition occurs at -0.80V, and the onset of significant Zn deposition occurs at -1.00V. The strong peak at -0.77V may be associated with a Sn reduction process, a S reduction process, citrate ion deprotonation and hydrogen evolution, or possibly a mix of all these mechanisms.

The deposition of Cu associated with the reduction peak at -0.55V in the voltammagram can be attributed to an elemental reduction process, as given by Eqn. (7-1). A small amount of nucleation proceeds at -0.45V. Well-defined grains, identified with x-ray diffraction and EDS, confirm the deposition of elemental Cu at these potentials. Contrary to depositions with tartaric acid, trace S concentrations are not found with the Cu deposition.

The deposition of Sn associated with the reduction peaks at -0.73V, and possibly -0.77V, in the voltammagram can be attributed most likely to elemental reduction process, as given by Eqn. (7-3). In baths without tartaric acid, the independence of Sn and S reduction processes is more well-defined, evident as the onset of significant Sn concentration at -0.75V with negligible S concentration. This independence might result from more widely separated reduction potentials for Sn and S or simply a fortuitously chosen deposition potential. The onset of S deposition at -0.80V suggests that the reduction peak at -0.77V may be assigned to $S_2O_3^{2-}$ reduction via Eqn. (7-5) or (7-6). Sn and Zn reduction may also contribute to the increase in deposition current near -0.77V. Similarly deep peaks attributed to Sn reduction were observed in electrodeposition of SnS films from $SnCl_2$ and $Na_2S_2O_3$ baths [37]. The small concentration of Zn at -0.80V makes primary attribution of the -0.77V reduction peak to Zn unlikely. Citrate ion deprotonation and hydrogen evolution may contribute to this peak, as well. However, since the metal-citrate species are expected to shift towards non-hydrogenated species with increasing pH, this reaction is considered less likely. Notably, the peaks at -0.73/-0.77V are shifted approximately 0.03 – 0.05V more negative than similar peaks in baths containing tartaric acid, but the peak shapes remain similar.

Similar to baths with tartaric acid, the Zn deposition mechanism remains generally unclear. Zn incorporation into the films first appears at -0.80V, although significant concentrations do not appear until -1.00V. It will be shown in Chapter 8 that in the absence of $Na_2S_2O_3$ (and tartaric acid), Zn deposition is delayed until < -1.14V. As noted in Section 7.4.1.5, this noble shift in deposition onset suggests that the thiosulfate may induce Zn deposition by underpotential or anomalous co-deposition mechanism. S-induced Zn deposition or co-reduction of Zn and S has been reported in the literature [30]. Note the weak cathodic peak at -1.14V corresponds well with the elemental Zn reduction peak observed in baths without $Na_2S_2O_3$.

Morphology Trends

As demonstrated in Section 7.4.2.1, the baseline **(Guardian) Mo film** was highly uniform, exhibiting diffusion-limited growth features consistent with cauliflower or dendrite growths. The improvement of the surface morphology with the removal of tartaric acid was discussed in Section 7.4.1.5. For deposition potentials up to -1.00V and deposition times of 10min, films are generally compact. At -0.75 and -0.80V, uniformly dispersed spherical particulates decorate the surface, which vary in size from 2 – 10μm and contain Cu, Sn, and possibly S. These particulates decrease in size, increase in population density, and decrease in Sn-richness with increasingly negative potential. The appearance of the particulates is similar to the **spongy deposit** type described by Popov [75] and briefly discussed in Section 7.4.1.5. These types of surface features are rare, but may form under low overpotentials and high exchange current densities [75]. Relative to the reduction peaks at -0.73V and -0.77V, the applied potentials at -0.75V and -0.80V represent relatively small overpotentials. These features disappear with increasing overpotential. At -1.00V,

the deposited film is compact with no large surface features evident. Alternatively, the large surface particulates may result from colloidal adsorption, as described in Section 7.4.1.5. At -1.20V, the film exhibits a powdery morphology, consistent in appearance with those deposited from baths with tartaric acid and similarly attributed to diffusion-limited growth mechanism and hydrogen co-deposition.

A study of the time evolution of the morphology on (Guardian) Mo-substrates, at -1.00V deposition potential, indicates the formation of compact films that coarsen and decrease in density with increasing deposition time. After 3sec, the deposit consists of individualized and small clusters of grains, each grain approximately 75nm in diameter. With increasing deposition time, the deposit completely covers the substrate. A 30sec deposition yields a densely packed film approximately 40nm thick, with grains ~150nm in diameter, as evident in Fig. 7-29. A clear morphology transition is evident after 5min, evident as a significant coarsening of the grains in the film. By 15min, the film morphology transitions to loosely-packed cauliflower and dendritic grains, consistent with diffusion-limited growth mechanisms. The transition from densely-packed, small-grained films to more loosely-packed, large-grained films that originates near 5min corresponds well with a shift in the transport properties of the electroactive species, resulting from exhaustion at the surface or in the bulk. Near this time of transition, the deposition current density experiences a well-defined uptick, consistent with the onset of hydrogen evolution reaction and possibly dendritic growth modes.

Modifying the concentrations of $CuSO_4$, $ZnSO_4$, and $SnSO_4$, and $Na_2S_2O_3$ in the bath significantly influenced the film morphologies, as well as the onset of HER and associated damage modes. Increasing the $CuSO_4$ and $SnSO_4$ concentrations increased the average grain sizes and decreased the transition times to HER onset. The grain size increases can be attributed to the higher deposition rates at higher metal sulfate concentrations, evident as larger film thicknesses for similar deposition times. Note the change in grain size was significantly more pronounced for increasing $SnSO_4$ than increasing $CuSO_4$ concentration. Increasing the $ZnSO_4$ concentration decreased the transition time to HER onset and caused the formation of semicircular blisters. Despite the increasing deposition rate, evident as increasing film thickness, the average grain size did not change significantly. Increasing the $Na_2S_2O_3$ concentration increased the grain size, significantly decreased the transition time to HER onset, caused the formation of semicircular blisters, and significantly increased the density of micron-sized Sn-rich particulates. Increasing or decreasing the Citrate concentration from nominal 0.02M significantly decreased the transition to HER onset and increased the density of micron-sized Cu-rich particulates.

The onset of the HER reaction during the deposition, identified by visible bubble generation on the film and an uptick in current density during deposition, introduces damage to

the substrate and to the films in the form of voids and blisters. Frequently, but not always, the formation of micron-sized particulates on the film surface accompanied this hydrogen evolution. The onset of HER may result from a lowering of the hydrogen overpotential and/or a depletion of one or more of the depositing species. Evidence exists to support both of these mechanisms, and one or both may be active. The noble shift in potential at HER onset during galvanostatic depositions and the decrease in transition time to HER onset for increasing component concentrations likely indicate a lowering of the hydrogen overpotential. The formation of micron-sized particulates, on the other hand, indicates a transition to diffusion-limited growth modes, consistent with a depletion of one more of the depositing species.

In the galvanostatic deposition at -1.59mA/cm^2, the deposition potential shifts more positive at the onset of HER, contrary to the shift in potential expected to result from depletion at the electrode. As discussed in [76], when the reacting species concentration at the electrode decreases to zero, the potential on the working electrode shifts *more negative* until the next electrode process satisfies the applied current. In this case, hydrogen evolution reaction represents the next electrode process. While the uncompensated resistance likely increases with a depletion of the depositing species at the electrode, possibly distorting the measured potential, the opposing trend observed in Fig. 7-44 cannot be practically accounted for by such deviations. In general, increasing the concentration of components in the bath decreased the transition time to HER onset, evident in Sections 7.4.2.5 and 7.4.2.6. The deposition rate increases with increasing component and bath concentrations, and similarities in the transition times to HER for similar thickness samples suggests a link between them. The apparent decrease in hydrogen overpotential observed during galvanostatic deposition and with increasing concentrations could result from evolving electrode properties with film growth. That is, at sufficient film thicknesses, it is possible that the effects of the substrate may be minimized such that the hydrogen overpotential shifts to values closer to those of the deposited film, which may be lower (see Table 3-5). However, thicker films did not always exhibit earlier HER onset; for instance, the 1.5X bath composition exhibited an earlier transition than the 2X bath composition, despite being significantly thinner. Other time-evolving factors, such as adsorption and species stabilities near the electrode surface, may also influence the hydrogen overpotential.

The formation of micron-sized particulates at high overpotentials (-1.20V in Fig. 7-25), high $Na_2S_2O_3$ concentrations (Fig. 7-36), and off-nominal Citrate concentrations (Fig. 7-38), indicates a transition to diffusion-limited growth modes, consistent with a depletion of one more of the depositing species. The growth features are consistent with the diffusion-limited growth features observed in Section 7.4.1. The Sn-rich surface particulates at high $Na_2S_2O_3$ concentrations and the Cu-rich surface particulates in high Citrate concentrations correspond to decreasing Sn concentrations and decreasing Cu concentrations, respectively, in the films. This correlation

suggests that Sn and Cu may experience depletion at the electrode or in the bulk, leading to the diffusion-limited growth behavior observed. The apparent rate-limiting behavior associated with Zn deposition, as described in the following section, also suggests that depletion triggers the onset of hydrogen evolution. As might be expected with rate-limited growth, diffusion-limited growth features are not evident despite the onset of HER.

The onset of HER represents the major obstacle to the fabrication of high quality S-containing precursors by co-electrodeposition method. The damage to the substrate and film can be avoided by stopping the deposition prior to the onset of HER; however, film thicknesses are limited to less than 400nm, too thin for viable use as photovoltaic absorber layers. Linearly sweeping the deposition potential to more-noble values during the deposition can delay the onset of HER. Further, stirring the solution cannot prevent hydrogen evolution, but it can effectively provide thicker films before its onset. These methods are used to fabricate optimized film compositions and morphologies, as discussed in Section 7.4.2.10. While viable deposition processes are demonstrated, further optimization may be achieved with a better understanding of the mechanisms by which the hydrogen evolution reaction activates. This remains for future work.

Composition Trends

As demonstrated in Section 7.4.2.5, the Cu and Sn concentrations in the film demonstrated an inverse relationship, such that increasing the $CuSO_4$ (and decreasing $SnSO_4$) concentration increased the Cu and decreased the Sn concentrations in the films. The changes in Cu:Sn ratios in the film were greater than the changes in the $CuSO_4$:$SnSO_4$, suggesting an interaction between the Cu and Sn deposition mechanism. A similar trend is observed in baths with and tartaric acid, which was attributed to possible interactions through thiosulfate complexation. See Section 7.4.1.5 for further discussion.

Unexpectedly, the relative Zn concentrations increased only slightly with increasing $ZnSO_4$ concentration. A contrary trend in Zn concentration was observed in baths with tartaric acid, which showed significant increases in relative Zn concentration with increasing $ZnSO_4$. The relatively static Zn concentration with significantly increasing $ZnSO_4$ suggests that the Zn reduction mechanism is rate-limited and not diffusion-limited. As discussed in the previous section, the more-noble onset of Zn reduction in the presence of $S_2O_3^{2-}$ suggests a S-induced underpotential deposition or anomalous co-deposition mechanism. In this case, the rate of Zn reduction would depend on the concentration of $S_2O_3^{2-}$ or S^{2-} ions and possibly H^+ ions available at the electrode. Increasing the Zn^{2+} ion concentration in the bath would have the effect of depleting these complementary ions faster. The earlier onset of hydrogen evolution reaction at 5.2min during the deposition, instead of 8.3min, is consistent with a faster rate of depletion. For baths with tartaric acid (Section 7.4.1.4) and baths without thiosulfate (Chapter 8), Zn

concentration in the film varies more predictably with $ZnSO_4$. In the metals-only baths without thiosulfate, Zn proceeds by elemental reduction mechanism and so the deposition rate increases proportionally with the concentration of $ZnSO_4$ (see Table 8-4 and 8-6). In baths with tartaric acid, the Zn concentration in the films also generally scales in proportion with the $ZnSO_4$ concentration (see Table 7-9). If the Zn reduction mechanism were mediated by H^+ ions, then the inconsistent behavior observed here may be attributed to a reduction in the H^+ concentration with increasing pH, compared to baths with tartaric acid. Note the relative S concentration monotonically decreased, and the Zn:S ratio monotonically increased, with increasing $ZnSO_4$ concentration. Since the exact Zn reduction mechanism remains unclear, it is not possible to assess the consistency of the trend in S concentration with the prior interpretation.

The $Na_2S_2O_3$ concentration in the bath demonstrated a significant effect on the composition and morphology of the films. With increasing $Na_2S_2O_3$, the relative Sn concentrations decreased significantly, and the relative Zn concentration increased significantly. However, the S concentrations increased only slightly with significantly increased $Na_2S_2O_3$ concentration. At the highest $Na_2S_2O_3$ concentrations of 0.03M, rough surface morphologies developed that prevented reliable fitting of the RBS spectra. Point-and-shoot EDS analysis identified the particulates on the surface as Sn-rich. Increasing $Na_2S_2O_3$ may reduce the activity of the Sn^{2+} ions by complexation with thiosulfate or formation of SnS_X colloids, as detailed in Section 7.4.1.5. Copper also complexes with thiosulfate, but the Cu concentration did not vary significantly with the $Na_2S_2O_3$ concentration. The increase in relative Zn concentration with increasing $Na_2S_2O_3$ fits generally with the interpretation of Zn reduction mechanism above. That is, Zn deposition is rate-limited by the availability of $Na_2S_2O_3$, so increasing $Na_2S_2O_3$ concentration increases the Zn deposition rate. However, the interpretation above also included H^+ mediation of the deposition, such that pH played an important role in the rate-limiting step of S available to react. Future work includes studies of the species stabilities with the varying bath conditions and the deposition kinetics, in order to assess this interpretation.

7.4.2.10 Optimization of Deposition Conditions

Numerous combinations of the deposition conditions examined in Sections 7.4.2.5 – 7.4.2.8 were investigated, in order to achieve films with the desired stoichiometry and thickness while minimizing damage to the films and substrate that results from detrimental side reactions, in particular HER. Four optimized deposition approaches are discussed here, denoted **Opt-1 to Opt-4**, consisting of three potential-controlled methods and one current-controlled method.

The potential-controlled deposition processes, labeled Opt-1 to Opt-3, demonstrated films with the desired compositions, smooth surface morphologies, and minimum voids or defects. The

bath composition used for these optimized depositions is summarized in Table 7-26, and the deposition processes are summarized in Table 7-27.

Table 7-26. Bath composition for optimized, potential-controlled co-electrodepositions of CZTS precursors on (Guardian) Mo-substrates: Opt-1 to Opt-3

Chemical Formula	Concentration [M]
$Na_3C_6H_5O_7$	0.20
$Cu(II)SO_4$	0.007
$Zn(II)SO_4$	0.030
$Sn(II)SO_4$	0.008
$Na_2S_2O_3$	0.017

Three approaches were taken in order to mitigate the damage caused by the time-delayed HER discussed in Section 7.4.2.9. In the first approach (Opt-1), the deposition was simply stopped before the onset of the reaction, limiting the total time deposition time to 4min. In the second approach (Opt-2), the voltage was linearly swept from the starting potential to more-noble potentials, in an effort to maintain the potential below the HER overpotential for the duration of the deposition. The idea was to balance the more negative potentials required to achieve necessary Zn incorporation, while taking advantage of the improved morphologies demonstrated at more-noble potentials. Note the Opt-2 process described in Table 7-27 includes an initial constant potential hold period of 60sec at -1.17V before the linear sweep starts. As shown in Table 7-28, Opt-1 and Opt-2 deposition processes yielded films too thin for use in absorber layers (< 400nm). In the third approach (Opt-3), stirring was used to improve the film thickness. Previous studies discussed in Section 7.4.2.7 indicated that continuous stirring resulted in Cu-rich, Zn-poor films with very large thickness. Consequently, a pulsed stirring approach was employed, in order to mitigate the stoichiometry deviations caused by stirring, while taking advantage of the film thickness improvements.

Table 7-27. Summary of optimized, potential-controlled co-electrodeposition processes for S-containing CZTS precursors

Deposition	Potential (V)	Control	Total Time (min)	Stirring
Opt-1	-1.16	Constant	4	None
Opt-2	-1.17 to -1.11	Linear Sweep (0.133mV/s)	~7.3	None
Opt-3	-1.17	Constant	8.7	200rpm (every 2min for 25sec)

In Opt-2 and Opt-3 depositions, the time of the HER onset was not known prior to deposition. For Opt-2, the deposition was stopped as soon as visible bubble generation was

observed. For Opt-3, visible bubbles were evident at 7.9min, but the deposition was allowed to continue for a brief period to investigate the effect of stirring on HER. Stirring had little effect on the bubble generation, and the deposition was stopped at 8.7min. The damage evident in the film may be reduced by using shorter deposition times. Assuming a constant deposition rate, stopping the deposition at 7.5min would yield a 750nm thick film. If the uniformity of the film can improved by optimizing the electrolyte flow behavior at the electrode, then pulsed stirring represents a promising method to achieve high-quality, S-containing CZTS precursors.

Table 7-28. Compositions of co-electrodeposited CZTS precursors fabricated using optimized deposition processes

Sample ID	Atomic %					Cu:Zn	Zn:Sn	S:Metals	Thick (nm)
	Cu	Zn	Sn	S	O				
Opt-1	20	14	10	13	43	1.4	1.4	0.30	320
Opt-2	20	14	11	15	40	1.4	1.3	0.33	400
Opt-3	23	15	13	19	30	1.6	1.2	0.38	875
Opt-4	22	12	10	17	39	1.8	1.2	0.39	970

The champion current-controlled process (Opt-4) was demonstrated in Section 7.4.2.8, using a constant current density of -1.59mA/cm^2. This galvanostatic deposition process used a similar but slightly modified bath composition compared to the potential-controlled processes (see Table 7-26): 0.2M $Na_3C_6H_5O_7$, 0.01M $CuSO_4$, 0.03M $ZnSO_4$, 0.01M $SnSO_4$, and 0.02M $Na_2S_2O_3$. As noted in Section 7.4.2.8, the onset of HER occurred approximately 3.5min into the 10min deposition.

The compositions and morphologies of the films deposited using the optimized processes are summarized in Table 7-28 and Fig. 7-47, respectively. Films deposited using the constant potential and linearly-swept potential, Opt-1 and Opt-2, demonstrated similar compositions with the desired element ratios of Cu:[Zn+Sn] near 0.8 and Zn:Sn near 1.3-1.4. The relative Zn concentrations were slightly higher than the desired 1.2–1.3 ratio, increasing the likelihood of ZnS formation during annealing. The relative Zn concentration can be easily reduced, however, by decreasing the deposition potential to slightly more-noble potentials. The films are too thin, however, to use as absorber layers in photovoltaic devices. Opt-3 and Opt-4 processes both yielded thicker films with higher S concentrations and metal element ratios close to the ideal Cu:Zn:Sn ratio of 1.8:1.2:1.0.

As Fig. 7-47 shows, the thinner Opt-1 and Opt-2 films have very fine grains with smooth surfaces, decorated with occasional particulates (~100nm). Macroscopically, the samples are highly specular with no evidence of damage to the films or substrates. The thicker Opt-3 film exhibits coarser grains (200 – 400nm), with micron-sized particulates periodically decorating the surface. Thickness and roughness varied across the film, with increasing grain size and increasing

number of voids in the thicker, rougher sections. Macroscopically, the samples were specular in the smoother, thinner sections and less reflective, in the rougher, thicker sections. Similar non-uniformities were found in stirring studies in Section 7.4.2.7, attributed primarily to the large reference electrode and generally poor electrode configuration. Voids similar to the one in Fig. 7-47 were uniformly distributed across the surface, although no semicircular blisters like those observed in Section 7.4.2.5 were present. The thickest, galvanostatically deposited film (Opt-4), exhibited the largest grains (500 – 700nm), with micron-sized particulates periodically decorating the surface. Note these particulates were evident in lower-magnification SEM images (not shown), and they were more dispersedly distributed than those on the Opt-3 film. Limited voids, typically associated with HER, were evident on the films. However, a relatively high density of semicircular blisters were present on the film (not shown). If these blisters could be eliminated, then the Opt-4 films would represent an ideal precursor layer.

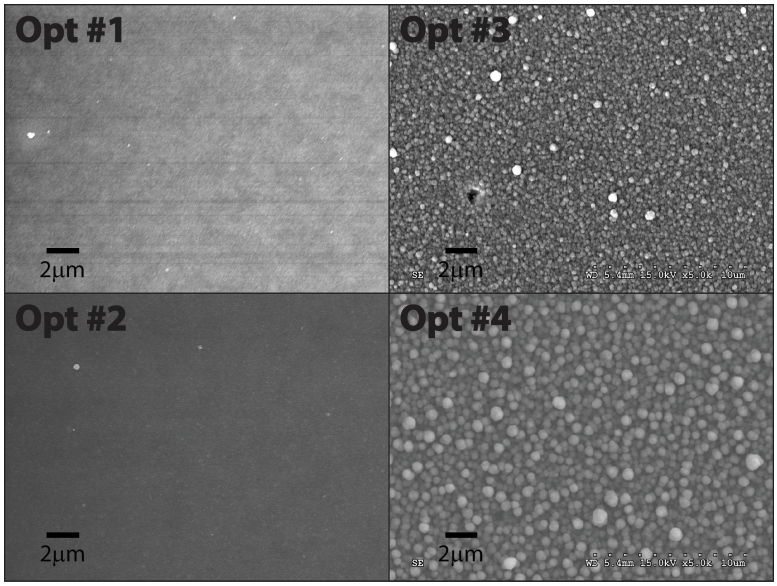

Fig. 7-47. SEM images of co-electrodeposited CZTS precursors fabricated using optimized deposition processes

Comparing the morphologies of the films deposited using the optimized deposition methods above (see Fig. 7-47) to the morphologies of the films deposited using the original Pawar's method (see Fig. 7-4 and Fig. 7-7), significant improvements in the deposition quality of the films are clearly evident. In particular, the optimized deposition processes reduced the density of large surface particulates, which dominated the surface morphologies of the films deposited using Pawar's method. Further, the optimized deposition processes significantly improved the compactness of the films, evident by comparing these films with the underlayers of the films deposited using Pawar's method (seen for instance, by examining sonicated films such as those in Section 7.4.1.6 or films presented in [6]).

7.4.2.11 Effects of Sulfur Annealing

In order to form the desired Cu_2ZnSnS_4 films, the S-containing CZTS precursors must be annealed in a reactive sulfur environment to fully sulfurize the films and prevent phase decomposition during crystal formation. Literature has shown that anneal temperatures over 500°C are required to achieve the desired kesterite crystal formation. For a detailed review of the crystal formation processes associated with CZTS, the reader is referred to Section 3.3.2.2.

Table 7-29. Summary of annealing temperature profiles

ID	Ramp (min)	Dwell (min)	Temp (°C)
TP1	40	10	585
TP2	5/ 5	30/ 10	200/ 560
TP3	30	60	560

Sulfur annealing was performed as described in Section 7.3.2, using 4.5– 26mg of elemental sulfur in the graphite annealing box with the samples. Three temperature profiles were investigated, as listed in Table 7-29. TP2 represents the optimum temperature profile determined in previous studies of S-containing CZTS precursors deposited by pulsed laser deposition (Chapter 6), which yielded films with the fewest voids and secondary phases. TP1 and TP3 were additional temperature profiles investigated in the sulfur annealing of pulsed laser deposited films (Chapter 6) and co-electrodeposited metallic CZTS precursors (Chapter 8), respectively, and they were studied here as a way to provide a basis of comparison.

Sulfur Annealing of Opt-1, using TP1: FTO-substrate

The film studied in this section was deposited using the optimized deposition process Opt-1 summarized in Table 7-26 and Table 7-27, and the film was sulfurized (25mg elemental sulfur) using temperature profile TP1 summarized in Table 7-29. Note this deposition was performed on an FTO-substrate, in order to investigate the role of the substrate in annealing and to provide a sample on a semi-transparent substrate that could be used for optical analysis. Preliminary work (not reported) demonstrated that slightly more negative potentials are required for FTO-substrates, in order to achieve similar stoichiometries to the (Guardian) Mo-substrates. Subsequently, this deposition was performed at a constant potential of -1.19V, instead of the -1.16V shown in Table 7-27. A longer deposition time of 8min was also employed, due to an improved tolerance to HER and to the desire to get thicker films. Finally, sulfur annealing with temperature profile TP1 was intended to be conducted at 560°C. However, a loose thermocouple resulted in higher actual temperatures during sulfur annealing, estimated as 585–595°C.

The compositions of the as-deposited and sulfur annealed films are summarized in Table 7-30. Note the as-deposited film was severely Cu-rich, likely resulting from a combination of two factors related to the change in deposition behavior associated with the FTO-substrate. First, the adjusted deposition potential of -1.19V overshot the required shift associated with the FTO-substrate, yielding highly Zn-rich films evident as a low Cu:Zn ratio of 1.3, compared to the desired 1.4 – 1.5 range. The Cu:Sn ratio of 1.55 was also too low, and should be in the range closer to 1.8. Given the inverse Cu:Sn ratio observed with varying $CuSO_4$ and $SnSO_4$ concentration, the as-deposited stoichiometry can be improved by slightly decreasing the deposition potential (more-noble) and slightly increasing the $CuSO_4$ concentration. This should simultaneously increase the Cu:Zn ratio, while maintaining the Zn:Sn ratio approximately constant.

Table 7-30. Compositions of Opt-1 CZTS films as-deposited and sulfur annealed using TP1 (on FTO-substrate)

Processing	Atomic %					Cu:Zn	Zn:Sn	S:Metals	Thick (nm)
	Cu	Zn	Sn	S	O				
As-Deposited	14	11	9	25	41	1.3	1.2	0.76	415
S Anneal	19	15	11	50	5	1.2	1.4	1.1	300

After sulfur annealing, the relative Zn concentration increases significantly and the relative Sn concentration decreases slightly, evident as a small decrease in Cu:Zn and large increase in Zn:Sn ratios. S:metals ratio of 1.1 indicates the complete sulfurization of the film. Typically, sulfurization expands the film thickness; for instance in [10], S-containing CZTS precursors with 14 – 18at% S concentration expanded by factors of 2 – 2.5X. However, all S-containing precursors fabricated in this thesis demonstrated a decrease in thickness with sulfur annealing, evident here as a decrease from 415 to 300nm. Composition changes after annealing, including the decrease in relative Sn concentration, are consistent with this decrease in thickness. As discussed in detail in Chapter 3, Sn often is preferentially lost during annealing as SnS. The sulfurized film composition is close to ideal, exhibiting Cu-poor, Zn-rich stoichiometry with a thickness: $Cu_{1.71}Zn_{1.38}Sn_{1.00}S_{4.55}$. The films, however, are slightly too Zn-rich, likely yielding excessive ZnS phases, which may detrimentally impact device performance. Note the film composition was nearly identical to the composition of the **Ar_2 + S Anneal** sample prepared in Section 8.4.7. The film thickness of 300nm was ideal for optical absorption studies performed in Section 7.4.2.12.

The surface morphologies of the as-deposited and sulfur annealed films are shown in Fig. 7-48. First, note the presence of a significant density of micron-sized particulates on the surface of the as-deposited films. It is unclear if the formation of these particulates resulted from the use of longer deposition times or the use of the FTO-substrate. Additional studies are required. Sulfurization did not appear to strongly modify the macroscopic surface morphology, with numerous surface particulates still decorating the surface. However, a higher magnification view

(not shown) indicates the presence of nano-sized grains defining all of the larger features shown. The surface morphology of the sulfurized film on FTO-substrate differed significantly from all other sulfurized films on Mo-substrates. Furthermore, films with generally similar composition (although Zn-deficient) and thickness (200nm) were deposited on (Guardian) Mo-substrates. Annealed under similar conditions, the film on Mo-substrate showed significant signs of decomposition, with only islands of CZTS film remaining after annealing. This suggests that, for very thin films in particular, the molybdenum layer may contribute to the destabilization of the film, consistent with the back contact decomposition mechanism discussed in Section 3.3.2.2.

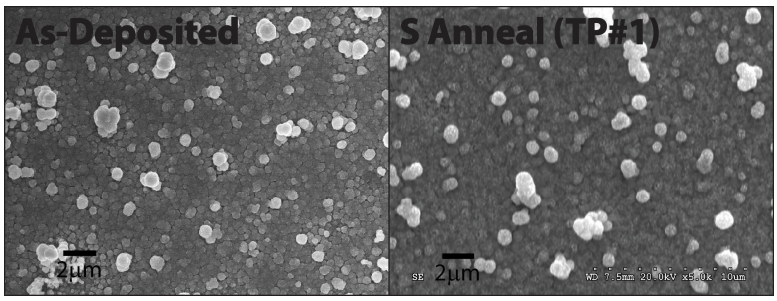

Fig. 7-48. SEM images of Opt-1 CZTS films as-deposited and sulfur annealed using TP1

Point-and-shoot EDS measurements of the surface of the sulfur annealed films, shown in Fig. 7-49, indicate that the large particulates are Sn-rich. Overlap in the Mo and S peaks in the EDS spectrum prevent definitive identification of S. The appearance and composition of the surface particulates are similar to those that appeared at high $Na_2S_2O_3$ concentrations in Section 7.4.2.5.

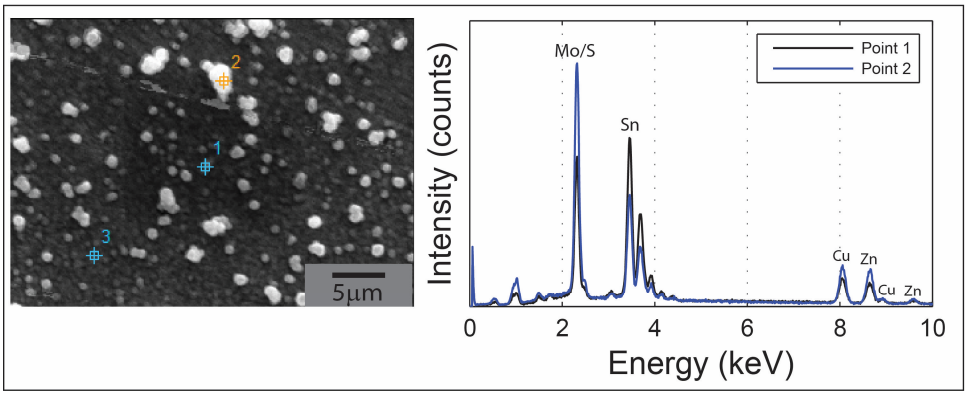

Fig. 7-49. Point-and-shoot EDS spectra of Opt-1 CZTS film after sulfuring annealing using TP1

The structural properties of the sulfurized film are presented in Fig. 7-50 and Fig. 7-51. The x-ray diffractrogram in Fig. 7-50 indicates the presence of a strong (112) peak at 28.56° (0.193° width) and three smaller (020)/(004), (220)/(024) and (132) peaks, which are attributed to kesterite CZTS. The sulfurized film exhibits significantly less preferred-orientation of the (112) peak than the pulsed laser deposited films presented in Section 6.4.6.2.

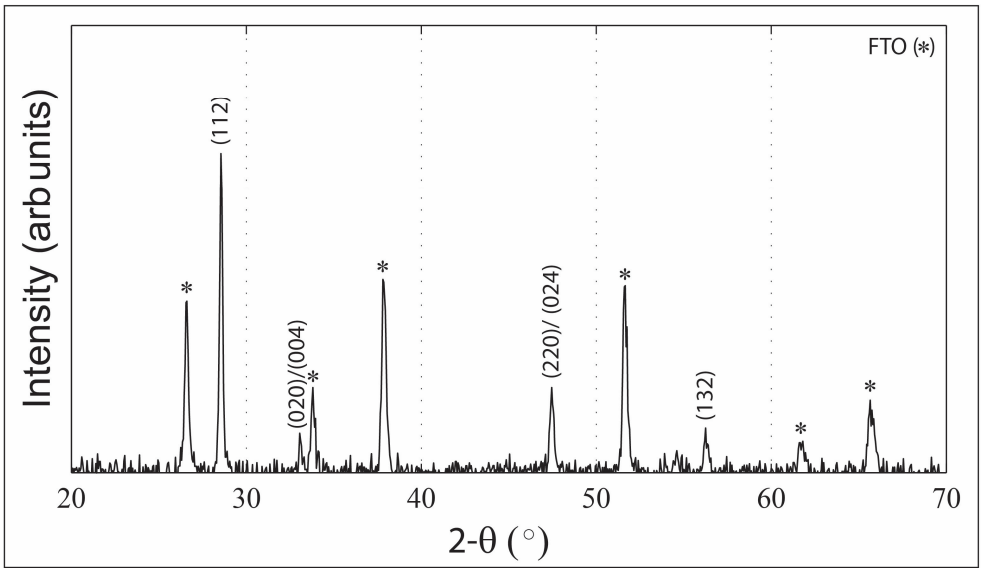

Fig. 7-50. X-ray diffractogram for Opt-1 CZTS film after sulfuring annealing using TP1

In the Raman spectrum in Fig. 7-51, characteristic CZTS Raman modes are evident at 254cm^{-1} (E-TO mode), 287cm^{-1} (A-mode), 336cm^{-1} (A-mode), 352cm^{-1} (E-TO mode) and 372cm^{-1} (B-LO mode). As determined in Section 6.4.6.2, the weak modes near 144, 163, and 276cm^{-1} are likely attributed to CZTS, as well. It was shown in Section 6.4.6.2 that properties of the dominant A-mode (near 338cm^{-1}) provide some indication of the phase-purity of the film, such that a broadening and blue shift in the peak can be attributed to increases in secondary phase Raman modes near 310 – 320cm^{-1}. Raman modes in this range have been attributed to SnS_2, $Cu_2Sn_3S_7$ and Cu_3SnS_4 [61-65]. Here, the films exhibit a subtle peak near 311cm^{-1} as well as moderate broadening in the dominant A-mode, possibly attributed to these phases.

Broad, low intensity peaks are evident at 405 and 478cm^{-1}, and similar peaks are observed in most other sulfurized CZTS thin films, including pulsed laser deposited and co-electrodeposited metallic precursor films. However, these peaks are not evident in concurrent measurements of other thin film samples (e.g. CIGSe), indicating that these peaks are not associated with a background signal. For the FTO-substrate, no common secondary phases exhibit modes near 405cm^{-1}, although $Cu_{2-X}S$ phases may contribute to modes near 475cm^{-1}. Since the secondary phase content likely depends strongly on the film composition and fabrication method, the presence of these low-intensity modes in all CZTS samples suggests that the modes are not associated with secondary phases. The peak at 405cm^{-1} may represent a higher-order mode of a peak located at 96cm^{-1} (not shown), and the peak at 478cm^{-1} may represent a higher-order mode of the located at 163cm^{-1}. Both the 96cm^{-1} and the 163cm^{-1} peaks have been associated with CZTS in the literature [77], and the 163cm^{-1} was previously identified as a CZTS mode in this work.

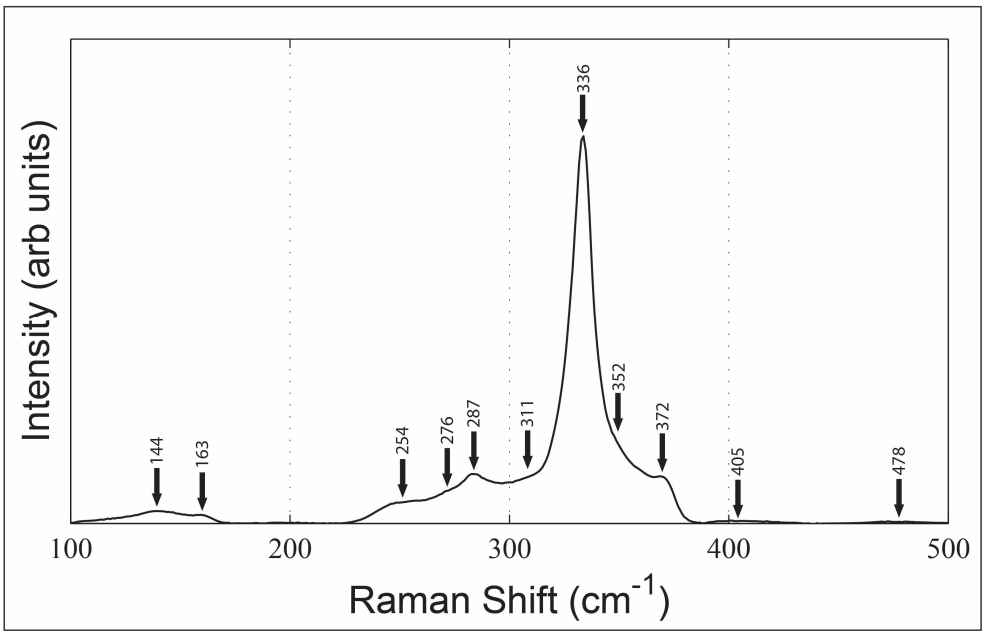

Fig. 7-51. Raman spectrum for Opt-1 CZTS film after sulfuring annealing using TP1

Sulfur Annealing of Opt-2, using TP2

The film studied in this section was deposited using the optimized deposition process Opt-2 summarized in Table 7-26 and Table 7-27, and the film was sulfurized (26mg elemental sulfur) using temperature profile TP2 summarized in Table 7-29.

The compositions of the as-deposited and sulfur annealed films are summarized in Table 7-31. The sulfurized film composition was close to ideal, exhibiting a Cu-poor, Zn-rich stoichiometry: $Cu_{1.79}Zn_{1.28}Sn_{1.00}S_{4.09}$. The S:metals ratio of 1 indicates the film was fully sulfurized. The film thickness of 395nm remains too thin for use as a photovoltaic absorber layer. Note the composition and the thickness do not change significantly with sulfurization, suggesting the least amount of film was lost for this sample compared to other S-containing samples.

Table 7-31. Compositions of Opt-2 CZTS films as-deposited and sulfur annealed using TP2

Processing	Atomic %					Cu:Zn	Zn:Sn	S:Metals	Thick (nm)
	Cu	Zn	Sn	S	O				
As-Deposited	20	14	11	15	40	1.4	1.3	0.33	400
S Anneal	20	14	11	45	10	1.4	1.3	1.0	395

The surface morphologies of the as-deposited and sulfur annealed films are shown in Fig. 7-52. The SEM image shows the as-deposited film was extremely smooth, with negligible particulates present on the surface. After annealing, the surface of the film was significantly more textured, with light-colored particulates up to several 100nm evident on the surface. Point-and-shoot EDS measurements on similar features in other films indicated that they were likely $Cu_{2-X}S$

phases. Note, however, that $Cu_{2-x}S$ nor other secondary phases can be discerned in the x-ray diffractogram or Raman spectrum of the film. The RBS spectrum exhibits a small decrease in Sn concentration near the surface of the film, likely indicating some decomposition of the film and evolution of Sn via SnS.

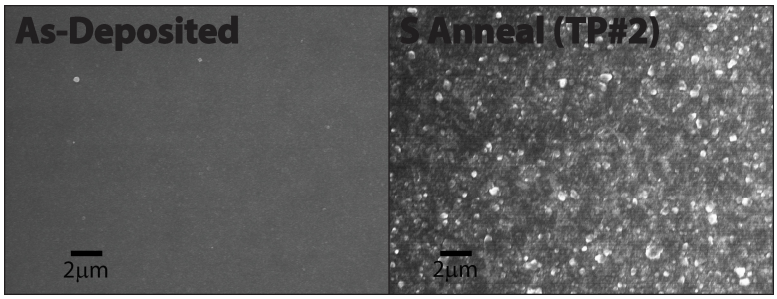

Fig. 7-52. SEM images of Opt-2 CZTS films as-deposited and sulfur annealed using TP2

The structural properties of the sulfurized film are presented in Fig. 7-53 and Fig. 7-54. The x-ray diffractrogram in Fig. 7-53 indicates the presence of strong (112) peak at 28.57° (0.207° width) and three smaller (020)/(004), (220)/(024) and (132) peaks, which are attributed to kesterite CZTS. Like other films fabricated by co-electrodeposition, the sulfurized film does not exhibit strong (112) texturing.

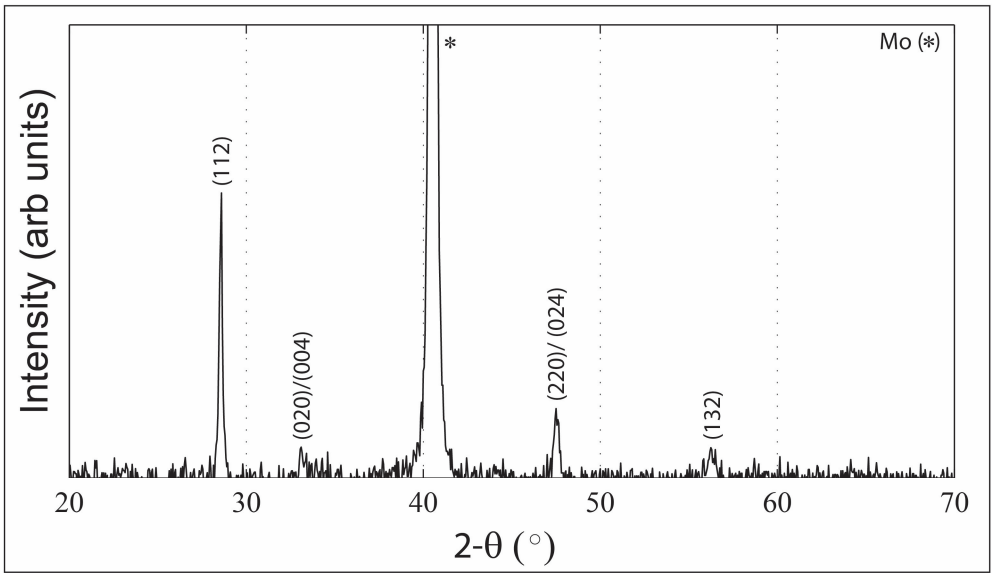

Fig. 7-53. X-ray diffractogram for Opt-2 CZTS films after sulfur annealing using TP2

In the Raman spectrum in Fig. 7-54, characteristic CZTS Raman modes are evident at 252cm^{-1} (E-TO mode), 287cm^{-1} (A-mode), 338cm^{-1} (A-mode), 352cm^{-1} (E-TO mode) and 374cm^{-1} (B-LO mode). The weak modes near 143, 163, and 273cm^{-1}, and the broad low-intensity modes near 408 and 483cm^{-1}, are also attributed to CZTS. As previously discussed, broadening and blue shift of the dominant A-mode likely indicate the presence of secondary phases. **The dominant A-**

mode exhibits a peak location closest to ideal (338cm^{-1}) and the smallest peak width for all films fabricated in this dissertation, suggesting that this film may be the most phase-pure. Prominent peaks at 287cm^{-1} and 365cm^{-1} complicate, but ultimately support, this interpretation. In particular, the three optimized S-containing CZTS precursors fabricated on Mo-substrates (Opt-2, Opt-3, and Opt-4) exhibit significantly larger peaks at 287cm^{-1} than all other CZTS films demonstrated in this dissertation, including pulsed laser deposited and co-electrodeposited metallic precursors. A new mode near 365cm^{-1} also emerges in the Raman spectra of these three optimized S-containing precursors.

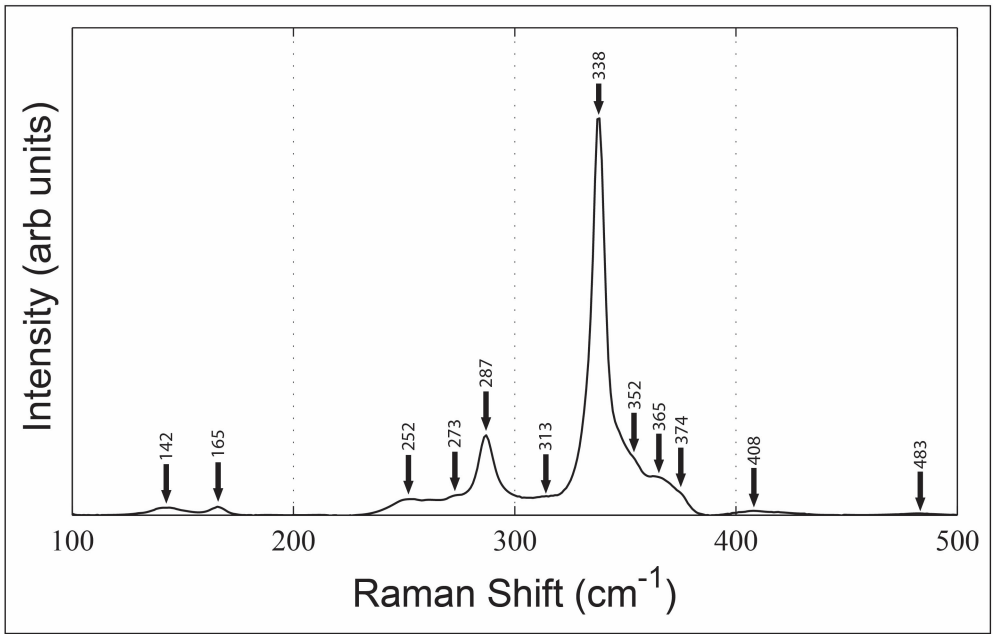

Fig. 7-54. Raman spectrum for Opt-2 CZTS films after sulfur annealing using TP2

The most common phases identified with the 287cm^{-1} mode include CZTS and ZnS, although MoS_2 also has a non-dominant peak at 286cm^{-1}. The absence of the more intense peaks near 383 and 406cm^{-1}, however, indicate that MoS_2 phases do not likely cause the observed increase in peak intensity at 287cm^{-1}. ZnS may contribute to the increase in peak intensity, although Raman measurements weakly detect ZnS when using 488nm excitation wavelength and weaker peaks are observed at 286cm^{-1} for more Zn-rich samples. More likely, the increase in peak intensity results from an increase in crystal quality of the sample (e.g. increase in effective correlation length). Similarly, the emergence of the peak at 365cm^{-1} may result from a sharpening of the characteristic modes at 352 and 374cm^{-1}, which masked the mode when the characteristic peaks were broader. Notably, a mode near 365cm^{-1} (E-LO) has been assigned to kesterite CZTS in literature [77, 78].

Sulfur Annealing of Opt-3, using TP2

The film studied in this section was deposited using the optimized deposition process Opt-3 summarized in Table 7-26 and Table 7-27, and the film was sulfurized (26mg elemental sulfur) using temperature profile TP2 summarized in Table 7-29.

Table 7-32. Compositions of Opt-3 CZTS films as-deposited and sulfur annealed using TP2

Processing	Atomic %					Cu:Zn	Zn:Sn	S:Metals	Thick (nm)
	Cu	Zn	Sn	S	O				
As-Deposited	23	15	13	19	30	1.6	1.2	0.38	875
S Anneal	20	16	9	50	5	1.3	1.7	1.1	620

Compositions of the as-deposited and sulfur annealed films are summarized in Table 7-32. The as-deposited film was close to the ideal composition and thickness, with Cu-poor and Zn-rich stoichiometry and thickness of 875nm. After sulfurization, however, the relative Zn concentration significantly increased and the Sn concentration significantly decreased, evident as a decrease in the Cu:Zn ratio and a substantial increase in the Zn:Sn ratio. The S:metals ratio of 1.1 indicates the film was fully-sulfurized. The significant shift in composition was accompanied by a significant reduction in film thickness from 875 to 620nm, consistent with decomposition of the film.

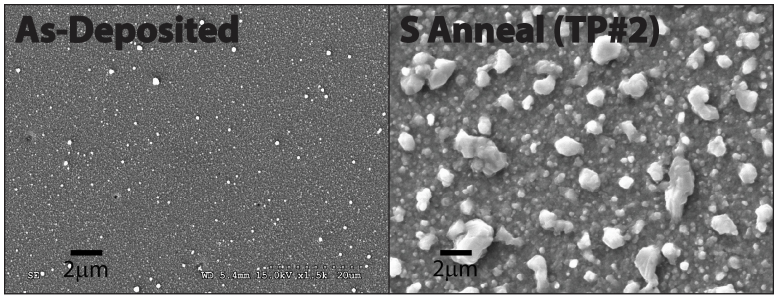

Fig. 7-55. SEM images of Opt-3 CZTS films as-deposited and sulfur annealed using TP2

The surface morphologies of the as-deposited and sulfur annealed films are shown in Fig. 7-55. The as-deposited film is smooth and small-grained, periodically decorated with voids and surface particulates (~100nm). After sulfurization, the film is dense with small grains (100-300nm) and no voids, but it is covered by a significant density of micron-sized particulates. Point-and-shoot EDS measurements of the sulfurized film (not shown) indicate that the composition of the surface particulates have similar compositions to the more compact film underneath. RBS measurements, however, indicate a severe through-thickness variation in the Sn concentration, with the film surface highly Sn-deficient. Considering the decrease in the film thickness and the severe Sn-gradient, these micron-sized particulates likely resulted from decomposition of the film around them rather than from phase precipitation associated with grain growth. Note that no secondary phases, such as $Cu_{2-X}S$, are evident in the Raman spectrum in Fig. 7-57.

The structural properties of the sulfurized film are presented in Fig. 7-56 and Fig. 7-57. The x-ray diffractrogram indicates the presence of strong (112) peak at 28.56° (0.211° width) and three smaller (020)/(004), (220)/(024) and (132) peaks, which are attributed to kesterite CZTS. Like other films fabricated by co-electrodeposition, the sulfurized film does not exhibit strong (112) texturing.

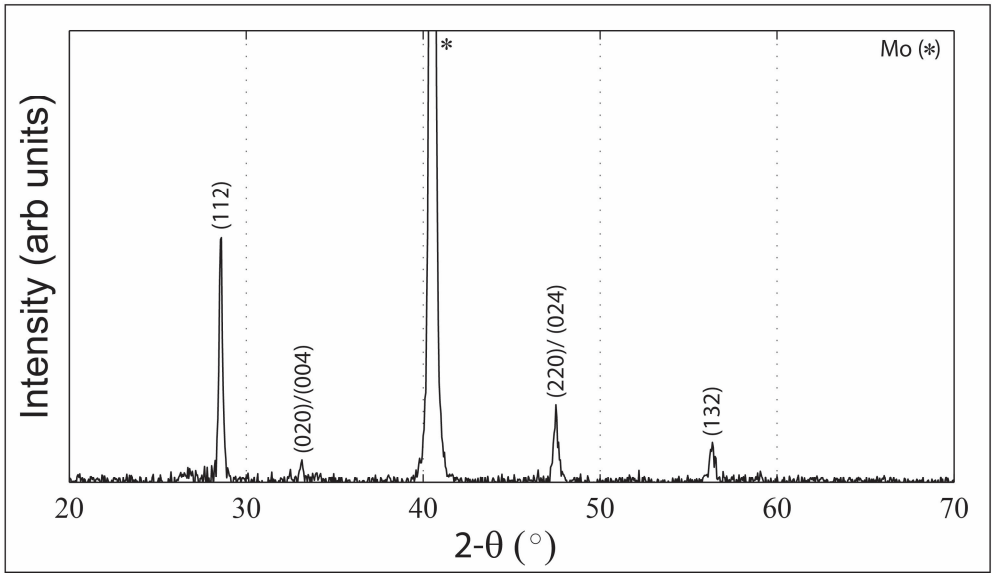

Fig. 7-56. X-ray diffractogram for Opt-3 CZTS after sulfur annealing using TP2

In the Raman spectrum in Fig. 7-57, characteristic CZTS Raman modes are evident at 253cm^{-1} (E-TO mode), 287cm^{-1} (A-mode), 337cm^{-1} (A-mode), 352cm^{-1} (E-TO mode) and 374cm^{-1} (B-LO mode). As determined in Section 6.4.6.2, the weak modes near 143, 163, and 272cm^{-1}, and the broad low-intensity modes near 412 and 481cm^{-1}, are likely attributed to CZTS, as well. Further, the emergent mode at 365cm^{-1} can also likely be attributed to E-LO CZTS mode, as discussed in the previous section. Compared to the Opt-2 film, the Opt-3 dominant A-mode slightly blue shifts to 337cm^{-1} and modestly broadens. However, the A-mode remains significantly sharper than all sulfurized pulsed laser deposited and co-electrodeposited metallic precursor films.

If the phase decomposition could be prevented, then this fabrication method would represent a viable pathway to high-quality films, with few voids, compositions of the desired stoichiometry (Cu:Zn:Sn = 1.8:1.2:1.0), and thicknesses on the order of 1μm suitable for use as photovoltaic absorber layers.

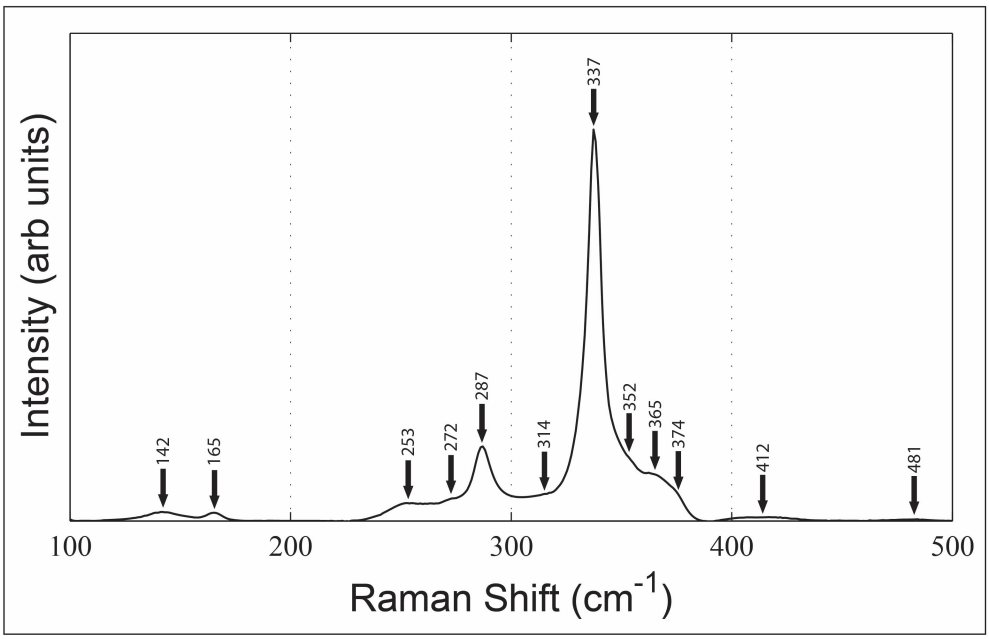

Fig. 7-57. Raman spectrum for Opt-3 CZTS after sulfur annealing using TP2

Sulfur Annealing of Opt-4, using TP2 and TP3

The films studied in this section were deposited using the optimized (galvanostatic) deposition process Opt-4 discussed in Section 7.4.2.10, and the films were sulfurized using the following two processes: S Anneal #1 (TP2, using 4.5mg elemental sulfur) and S Anneal #2 (TP3, using 26mg elemental sulfur).

Table 7-33. Compositions of Opt-4 CZTS films as-deposited and sulfur annealed using TP2 and TP3, * incomplete film coverage, ◊ element present but cannot be reliably fitted

Processing	Atomic %					Cu:Zn	Zn:Sn	S:Metals	Thick (nm)
	Cu	Zn	Sn	S	O				
As-Deposited	22	12	10	17	39	1.8	1.2	0.39	970
S Anneal #1*	22	12	11	55	-	1.9	1.1	1.2	720
S Anneal #2*	◊	◊	◊	◊	◊	0.79	-	-	-

The compositions of the as-deposited and sulfur annealed films are summarized in Table 7-33. The as-deposited film is close to the ideal composition and thickness, with Cu-poor and Zn-rich stoichiometry and thickness of 970nm. After sulfurization using TP2, metal element ratios in the **S Anneal #1** film remain approximately constant, indicating no element was preferentially lost by evaporation from the film. Further, the RBS spectrum (not shown) indicates no significant through-thickness variations in the composition, noting in particular that the Sn concentration remains approximately constant. The S:metals ratio of 1.2 indicates the film is fully-sulfurized, although the stoichiometric excess of S may indicate the presence of secondary phases. Despite no

significant shift in composition, the film thickness decreases significantly after sulfur annealing from 970 to 720nm.

After sulfurization using TP3, most of the **S Anneal #2** film was lost by decomposition, leaving loosely connected islands on the surface of the substrate as seen in Fig. 7-58. Incomplete film coverage prevents reliable composition analysis by RBS of **S Anneal #2**, although PIXE spectra can still be fitted to provide the Cu:Zn ratio shown in Table 7-33.

The surface morphologies of the as-deposited and sulfur annealed films are shown in Fig. 7-58. The as-deposited film is compact with moderately-sized grains (~500nm), negligible surface particulates, and periodic semi-circular blisters, as previously detailed. After sulfurization using TP2, the **S Anneal #1** film is porous with micron-sized grains. Significant patches of thinner, loosely populated sections of film (see top-right of TP2) are also evident in lower magnification SEM images (not shown). It is unclear if the morphology differences between Opt-3 and the Opt-4 (**S Anneal#1**) result from differences in the precursor structure or the amount of elemental sulfur used. In the as-deposited films, the Opt-4 grains are significantly larger (500 – 700nm) than the Opt-3 grains (200 – 400nm). Further, **S Anneal #1** was sulfurized using 4.5mg S instead of 25mg S, decreasing the sulfur overpressure and increasing the likelihood of elemental sulfur escape from the graphite box prior to achieving the final anneal temperature.

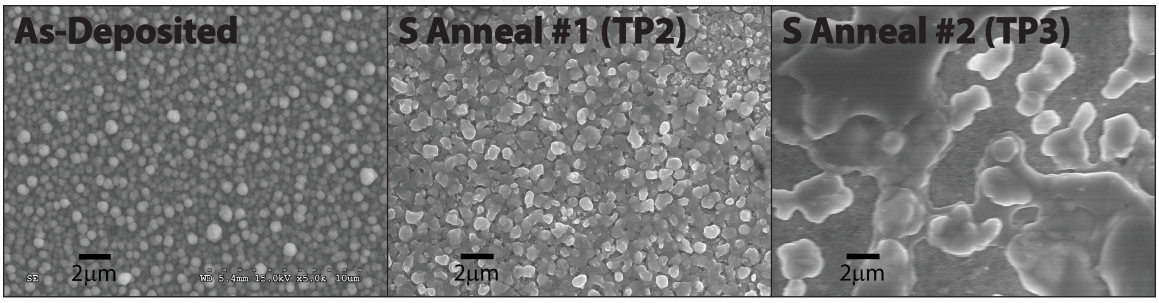

Fig. 7-58. SEM images of Opt-4 CZTS films as-deposited and sulfur annealed using TP2 and TP3

After sulfurization using TP3, the **S Anneal #2** film was almost completely decomposed, leaving only loosely connected islands of material, as described above. Such morphology changes are consistent with sulfurization of other S-containing CZTS precursors (on Mo-substrates) investigated using similar temperature profiles and masses of elemental sulfur. However, for co-electrodeposited metallic precursors, this temperature profile TP3 yields films with significantly different morphologies, which are defined by laterally-segregated regions of ZnS and large-grained CZTS phases (see Opt-2, **S Anneal** in Section 8.4.7).

The structural properties of the sulfurized film are presented in Fig. 7-59 and Fig. 7-60. The x-ray diffractrogram indicates the presence of strong (112) peak at 28.58° (0.200° width) and three smaller (020)/(004), (220)/(024) and (132) peaks, which are attributed to kesterite CZTS.

Like other films fabricated by co-electrodeposition, the sulfurized film does not exhibit strong (112) texturing.

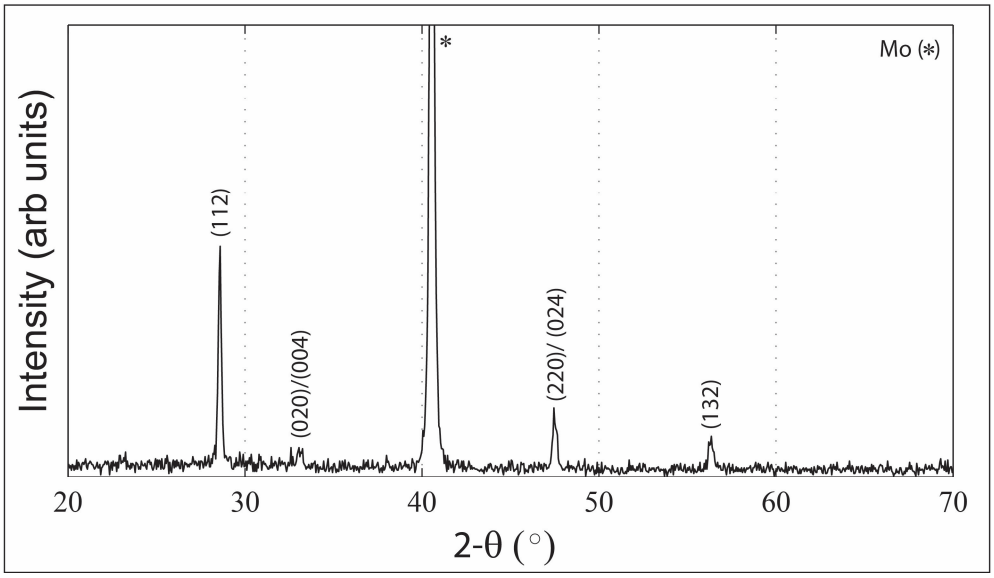

Fig. 7-59. X-ray diffractogram for Opt-4 CZTS film (S Anneal #1) after sulfur annealing using TP2

In the Raman spectrum in Fig. 7-60, characteristic CZTS Raman modes are evident at 252cm^{-1} (E-TO mode), 286cm^{-1} (A-mode), 337cm^{-1} (A-mode), 351cm^{-1} (E-TO mode) and 373cm^{-1} (B-LO mode). As determined in Section 6.4.6.2, the weak modes near 143, 163, 273, and 365cm^{-1}, and the broad low-intensity modes near 410 and 475cm^{-1}, are likely attributed to CZTS, as well. The dominant A-mode blue shift (337cm^{-1}) and broadening for the Opt-4 film are in between those observed in the Opt-2 and Opt-3 films. Again, the A-mode remains significantly sharper than all sulfurized pulsed laser deposited and co-electrodeposited metallic precursor films.

Note that the trend in diffraction peak width, representative of the crystallite size, does not follow the trend in Raman mode peak width, representative of the effective correlation length. The (112) peak width decreases from 0.211° to 0.200°, as follows: Opt-2 < Opt-4 < Opt-3. Differences in the diffraction and Raman peak trends can result from differences in the crystal scale probed by the two methods. For instance, defect-free crystal grains above ~100nm diameter demonstrate Raman scattering behavior close to that of a perfect crystal, as discussed in Section 4.2.2.1. Due to instrument broadening, however, x-ray diffraction typically cannot accurately estimate crystallite sizes less than about 100nm.

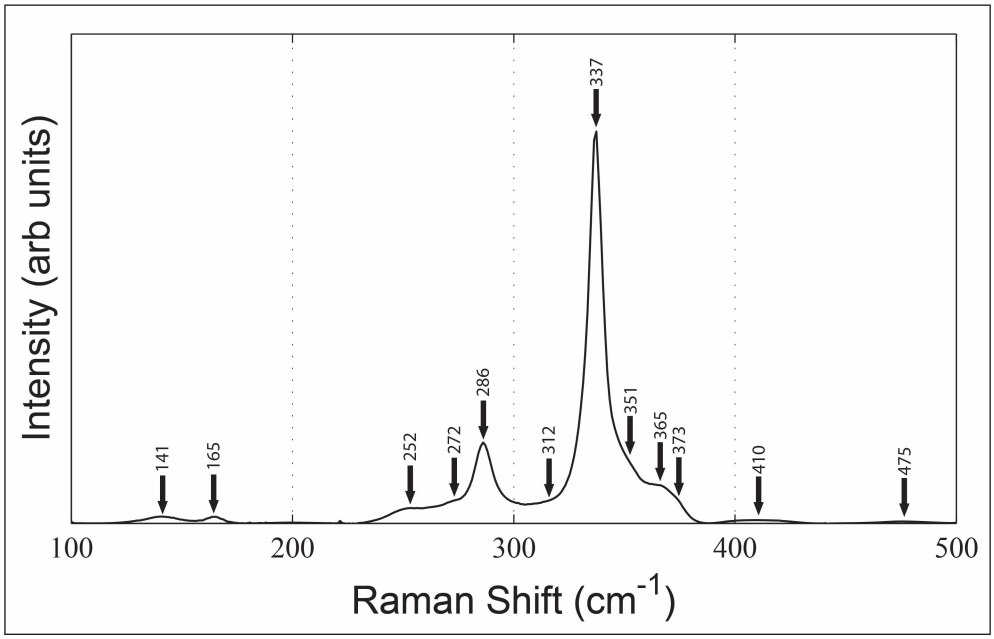

Fig. 7-60. Raman spectrum for Opt-4 CZTS film (S Anneal #1) after sulfur annealing using TP2

The effects of sulfur annealing on the formation of CZTS thin films from S-containing CZTS precursors may then be summarized as follows:

- Sulfurized S-containing precursors exhibit significantly smaller grains (< 1μm) than sulfurized metallic precursors
- Film thickness decreases after sulfurization for all S-containing precursors, contrary to literature that showed precursors with similar S-content increase film thickness by 2–2.5X after sulfurization [10]
- The film composition does not necessarily change with decreasing film thickness, indicating that in some cases the metal elements are lost to evaporation at similar rates
- Using an FTO back contact, instead of Mo back contact, improves the stability of thin precursor layers (<400nm) during sulfurization by preventing void and island formation. The increased film stability is attributed to the elimination of the back contact decomposition mechanism associated with Mo.
- Sulfurization with temperature profile TP2 yields the highest-quality films, evident as the least amount of film decomposition and the sharpest Raman spectra. Despite the short dwell time of 10min at the final anneal temperature, all films annealed using TP2 are fully-sulfurized, evident as S:metals ratios > 1.0.
- The sulfurization of co-electrodeposited S-containing CZTS precursors yielded the most phase-pure CZTS thin films produced in this dissertation. X-ray diffraction,

Raman spectra, film composition, and SEM/EDS are used to evaluate the phase-purity, such that the most phase-pure films exhibit the following:

- Diffraction peaks for CZTS are closest to the ideal positions and spectrum contains no additional peaks or shoulders from secondary phases
- Raman peaks (dominant A-mode) are closest to the ideal position of 338cm^{-1}, with least amount of blue shifting and broadening, and spectrum contains no additional peaks or shoulders from secondary phases
- Films are fully-sulfurized (S:metals = 1.0) with final metal element ratio Cu:Zn:Sn of 1.8:1.2:1.0.
- No surface segregated phases are evident on the SEM, confirmed by point-and-shoot EDS measurements of any significant surface particulates present

Note that ZnS cannot be reliably detected using the Raman system employed, due to 488nm excitation wavelength, and therefore the relative abundance of ZnS in the films cannot be compared. Further, the phase-purity of the film does not correlate with the grain size. Therefore, diffraction peaks for "less phase-pure" may exhibit sharper peaks, due to the scale of defects probed by x-ray diffraction and Raman spectroscopy.

7.4.2.12 Optical Properties

In order to study the optical properties of CZTS thin films fabricated by co-electrodeposition of S-containing precursors, films were electrodeposited on semi-transparent FTO substrates. The film used for this study was deposited using the Opt-1 co-electrodeposition process and sulfurized using temperature profile TP1, as described in the previous section. The composition, morphology, and structural properties of the film are summarized in Table 7-30, Fig. 7-48, and Fig. 7-50 and Fig. 7-51, respectively.

Fig. 7-61 shows the optical absorption and $(\alpha \cdot h\nu)^2$ vs. $h\nu$ plots for the sulfur annealed film. For comparison, the optical absorption plot also includes a representative absorption spectrum for a pulsed laser deposited sample (7min ramp / 10min dwell, see Table 6-9). The optical absorption coefficients were calculated, accounting for front surface reflections only, according to the relations in Table 4-13. The band gap was calculated using the fitting procedure for direct band gap materials, Eqn. (4-15) and (4-16), described in Section 4.3.1.2.

The optical absorption curve for the electrodeposited sample exhibits a nearly identical shape to the one shown for the pulsed laser deposited sample. However, the electrodeposited absorption curve shifts up ~ 4x10^{4}cm^{-1} compared to the pulsed laser deposited curve. This offset is attributed to effects from the FTO substrate not accounted for in the calculation of the

absorption coefficient for CZTS. In order to deduce the effects of the FTO substrate, transmission and reflection measurements were made on the FTO-substrate only. However, the absorption curve was unable to be shifted to the expected order of magnitude (e.g. matched to the pulsed laser deposited film), using the measured optical data from the FTO substrate. The inability to match the spectrum might result from modification of the FTO layer during sulfurization of the film; the optical properties for FTO were measured on an unannealed sample.

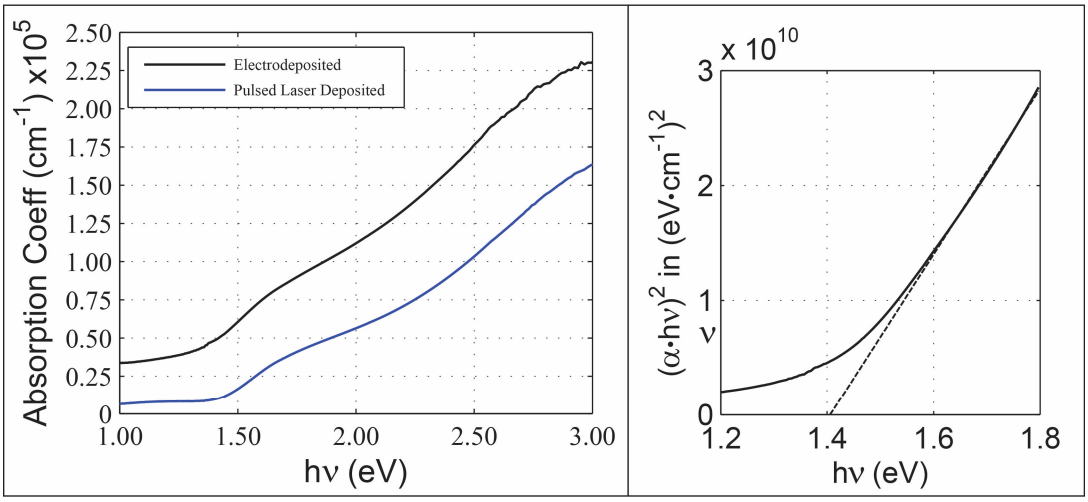

Fig. 7-61. Optical absorption coefficient curves for electrodeposited and pulsed laser deposited films; $(\alpha \cdot h\nu)^2$ vs. hν curve for electrodeposited film

The direct band gap was measured as 1.41eV by fitting the linear section of the $(\alpha \bullet h\nu)^2$ vs. hν curve near the band edge. However, the vertical offset in absorption coefficient directly modifies the vertical position of the $(\alpha \bullet h\nu)^2$, which subsequently modifies the abscissa crossing of the extrapolated line. That is, if the optical absorption coefficient is shifted down by a constant bias of $4x10^4 cm^{-1}$, the band gap shifts to 1.51eV, consistent with typical band gaps for CZTS and the band gaps for pulsed laser deposited films measured in Chapter 6. Future work includes investigating the effects of sulfur annealing on the optical properties of FTO and improving the calculation of absorption coefficient for CZTS on FTO-substrates.

7.4.2.13 Summary of Results

Films deposited on (Guardian) Mo-substrates, using Pawar's method and the original bath composition (less tartaric acid), exhibited uniform morphologies with cauliflower/dendrite growth features consistent with diffusion-limited growth modes. The as-deposited films were severely Zn-poor and S-poor. Cyclic voltammetry and deposition potential studies indicate similar reduction mechanisms for Cu, Zn, Sn, and S as those observed in baths containing tartaric acid. In baths with tartaric acid, increasing the $ZnSO_4$ concentration significantly increased the relative Zn concentration, but increasing the $Na_2S_2O_3$ did not significantly modify the relative Zn concentration. In baths without tartaric acid, however, increasing the $ZnSO_4$ did not significantly

modify the relative Zn concentration, but increasing the $Na_2S_2O_3$ significantly increased the relative Zn concentration. An S-induced underpotential or anomalous co-deposition was posited to cause rate-limiting deposition of Zn by S or $S_2O_3^{2-}$, such that increasing the $ZnSO_4$ did not modify its rate of deposition. The change in Zn dependence on $ZnSO_4$ concentration with the removal of tartaric acid was possibly attributed to changes in pH and associated concentration of H^+ ions, which mediate the thiosulfate reduction mechanism.

The onset of hydrogen evolution reaction, evident as bubble generation on the electrode and a well-defined uptick in cathodic current, was shown to cause damage to the substrate and to the films. Large semicircular blisters were attributed to buckling damage in the compressively-strained Mo film, resulting from hydrogen evolution on and within the multi-layer Mo film. Voids and blisters in the deposited film were also attributed to hydrogen evolution on the substrate and on the film. Hydrogen evolution also caused the formation of voids in the deposited films. Frequently, but not always, the formation of micron-sized particulates on the film surface accompanied this hydrogen evolution. Typically the hydrogen evolution started many minutes into the deposition, and this delayed onset may be attributed to a lowering of the hydrogen overpotential and/or a depletion of one or more of the depositing species. Evidence exists to support both of these mechanisms, and one or both may be active.

The onset of HER represents the major obstacle to the fabrication of high quality S-containing precursors by co-electrodeposition method. The damage to the substrate and film can be avoided by stopping the deposition prior to the onset of HER; however, film thicknesses are limited to less than 400nm, too thin for viable use as photovoltaic absorber layers. Linearly sweeping the deposition potential to more-noble values during the deposition can delay the onset of HER. Further, stirring the solution cannot prevent hydrogen evolution, but it can effectively provide thicker films before its onset. These methods are used to fabricate optimized film compositions and morphologies, as discussed in Section 7.4.2.10.

Sulfur annealing was performed on the S-containing CZTS precursors as described in Section 7.3.2, using 4.5– 26mg of elemental sulfur in the graphite annealing box with the samples. Three temperature profiles were investigated, as shown in Table 7-29. Similar to the pulsed laser deposited films, sulfurization with the two-step temperature profile TP2 (200°C / 560°C) yielded the highest-quality films. Despite the short dwell time of 10min at the final anneal temperature, all films annealed using the temperature profile TP2 are fully-sulfurized, evident as S:metals ratios > 1.0. The film with the most ideal stoichiometry and sharpest Raman spectrum was fabricated using the linear swept deposition potential (Opt-2 in Section 7.4.2.10). This film, however, is too thin (~400nm) for use in practical photovoltaic device. The film with the largest thickness and composition closest to the ideal stoichiometry was fabricated with the pulsed stirring method

(Opt-3 in Section 7.4.2.10). However, sulfurization yielded significant surface decomposition of the film, which is attributed to insufficient sulfur overpressure during annealing. Notably, the film thickness decreased after sulfurization, contrary to the literature which demonstrated thickness increases of 2 – 2.5X for similar composition precursors [10]. Sulfurized S-containing precursors exhibit significantly smaller grains (< 1μm) than sulfurized metallic precursors, consistent with the trends observed in literature [10]. In fact, the S-containing co-electrodeposited precursors yielded the highest-quality, most phase-pure films produced in this dissertation. X-ray diffraction, Raman spectra, film composition, and SEM/EDS are used to evaluate the quality and phase-purity as described in the summary section of Section 7.4.2.11.

Using an FTO back contact, instead of Mo back contact, improves the stability of thin precursor layers (< 400nm) during sulfurization by preventing void and island formation under similar annealing conditions. The increased film stability is attributed to the elimination of the back contact decomposition mechanism associated with molybdenum [79]. The fabrication of CZTS thin films on the semi-transparent FTO-substrate enabled the investigation of optical properties of the film. The optical absorption curve for the electrodeposited sample exhibits a nearly identical shape to the one shown for the pulsed laser deposited sample. However, the absorption curve for the co-electrodeposited film shifts up ~$4x10^4 cm^{-1}$ compared to the pulsed laser deposited curve. The measured direct band gap of 1.41eV is lower than the expected ~1.5eV reported in literature, which we attribute to the offset bias in the absorption coefficient. This offset bias in absorption coefficient is attributed to effects from the FTO-substrate not accounted for in the calculation of the absorption coefficient for CZTS. Future work includes investigating the effects of sulfur annealing on the optical properties of FTO and improving the calculation of absorption coefficient for CZTS on FTO-substrates.

Work remains to understand the deposition mechanisms active in the co-electrodeposition of S-containing precursors, including the delayed onset of HER. However, the work here demonstrates a pathway to high-quality CZTS precursors, with ideal Cu-poor, Zn-rich stoichiometries and compact surface morphologies. If the sulfurization process can provide better control and monitoring of the temperature and sulfur overpressure, then surface decomposition losses observed in the thicker precursors can likely be minimized. The generally similar quality of the optical absorption curve indicates that the co-electrodeposited precursors behave similarly to the pulsed laser deposited precursors. The high optical absorption coefficient and the band gap near 1.5eV indicate that the CZTS films have desirable characteristics for use as an absorber layer, consistent with the literature.

7.5 REFERENCES

[1] D. Mitzi, O. Gunawan, T. Todorov, K. Wang, S. Guha, The path towards a high-performance solution-processed kesterite solar cell, Solar Energy Materials & Solar Cells, 95 (2011) 1421 - 1436.

[2] W. Wang, M. Winkler, O. Gunawan, T. Gokmen, T. Todorov, Y. Zhu, D. Mitzi, Device Characteristics of CZTSSe Thin-Film Solar Cells with 12.6% Efficiency, Advanced Energy Materials, (2013).

[3] J.J. Scragg, Studies of Cu_2ZnSnS_4 films prepared by sulfurisation of electrodeposited precursors, in: Chemistry, University of Bath, 2010, pp. 244.

[4] F. Jiang, S. Ikeda, T. Harada, M. Matsumura, Pure Sulfide Cu2ZnSnS4 Thin Film Solar Cells Fabricated by Preheating an Electrodeposited Metallic Stack, Advanced Energy Materials, 4 (2013) 1 - 4.

[5] J. Lehner, M. Ganchev, M. Loorits, N. Revathi, T. Raadik, J. Raudoja, M. Grossberg, E. Mellikov, O. Volobujeva, Structural and compositional properties of CZTS thin films formed by rapid thermal annealing of electrodeposited layers, Journal of Crystal Growth, 380 (2013) 236 - 240.

[6] S.M. Pawar, B.S. Pawar, A.V. Moholkar, D.S. Choi, J.H. Yun, J.H. Moon, S.S. Kolekar, J.H. Kim, Single step electrosynthesis of Cu_2ZnSnS_4 (CZTS) thin films for solar cell application, Electrochimica Acta, 55 (2010) 4057-4061.

[7] H. Araki, Y. Kubo, K. Jimbo, W.S. Maw, H. Katagiri, M. Yamazaki, K. Oishi, A. Takeuchi, Preparation of Cu_2ZnSnS_4 thin films by sulfurization of co-electroplated Cu-Zn-Sn precursors, Phys. stat. sol. (c), 6 (2009) 1266-1268.

[8] J. Tao, J. liu, J. He, K. Zhang, J. Jiang, L. Sun, P. Yang, J. Chu, Synthesis and characterization of Cu_2ZnSnS_4 thin films by the sulfurization of co-electrodeposited Cu-Zn-Sn-S precursor layers for solar cell applications, The Royal Society of Chemistry Advances, 4 (2014) 23977 - 23984.

[9] C. Gougaud, D. Rai, S. Delbos, E. Chassaing, D. Lincot, Electrochemical Studies of One-Step Electrodeposition of Cu-Sn-Zn Layers from Aqueous Electrolytes for Photovoltaic Applications, Journal of the Electrochemical Society, 160 (2013) D485-D494.

[10] C. Platzer-Bjorkman, J. Scragg, H. Flammersberger, T. Kubart, M. Edoff, Influence of precursor sulfur content on film formation and compositional changes in Cu2ZnSnS4 films and solar cells, Solar Energy Materials & Solar Cells, 98 (2012) 110 - 117.

[11] B.S. Pawar, S.M. Pawar, K.V. Gurav, S.W. Shin, J.Y. Lee, S.S. Kolekar, J.H. Kim, Effect of Annealing Atmosphere on the Properties of Electrochemically Deposited Cu_2ZnSnS_4 (CZTS) Thin Films, ISRN Renewable Energy, 2011 (2011) 1-5.

[12] B. Ananthoju, F. Sonia, A. Kushwaha, D. Bahadur, N. Mehekar, M. Aslam, Improved structural and optical properties of Cu_2ZnSnS_4 thin films via optimized potential in single bath electrodeposition, Electrochimica Acta, 137 (2014) 154 - 163.

[13] Y. Cui, S. Zuo, J. Jiang, S. Yuan, J. Chu, Synthesis and characterization of co-electroplated Cu_2ZnSnS_4 thin films as potential photovoltaic material, Solar Energy Materials & Solar Cells, 95 (2011) 2136-2140.

[14] S. Delbos, Kesterite thin films for photovoltaics: a review, EPJ Photovoltaics, 3 (2012) 35004:p35001 - p35013.

[15] X. He, H. Shen, W. Wang, B. Zhang, Y. Dai, Y. Lu, Quaternary co-electrodeposition of the Cu_2ZnSnS_4 films as potential solar cell absorbers, J. Mater. Sci: Mater Electron, (2012).

[16] J. Iljina, R. Zhang, M. Ganchev, T. Raadik, O. Volobujeva, M. Altosaar, R. Traksmaa, E. Mellikov, Formation of Cu2ZnSnS4 absorber layers for solar cells by electrodeposition-annealing route, Thin Solid Films, 537 (2013) 85 - 89.

[17] M. Jeon, T. Shimizu, S. Shingubara, Cu_2ZnSnS_4 thin films and nanowires prepared by different single-step electrodeposition method in quaternary electrolyte, Materials Letters, 65 (2011) 2364-2367.

[18] M. Jeon, Y. Tanaka, T. Shimizu, S. Shingubara, Formation and characterization of single-step electrodeposited Cu_2ZnSnS_4 thin films: Effect of complexing agent volume, Energy Procedia, 10 (2011) 255-260.

[19] S. Lee, JongminKim, H.S. Woo, Y. Jo, A.I. Inamdar, S.M. Pawar, H. Kim, W. Jung, H. Im, Structural, morphological, compositional, and optical properties of single step electrodeposited Cu_2ZnSnS_4 (CZTS) thin films for solar cell application, Current Applied Physics, 14 (2014) 254 - 258.

[20] E.M. Mkawi, K. Ibrahim, M.K.M. Ali, M.A. Farrukh, A.S. Mohamed, Influence of triangle wave pulse on the properties of Cu_2ZnSnS_4 thin films prepared by single step electrodeposition, Solar Energy Materials & Solar Cells, 130 (2014) 91 - 98.

[21] B.S. Pawar, S.M. Pawar, S.W. Shin, D.S. Choi, C.J. Park, S.S. Kolekar, J.H. Kim, Effect of complexing agent on the properties of electrochemically deposited Cu_2ZnSnS_4 (CZTS) thin films, Applied Surface Science, 257 (2010) 1786-1791.

[22] S.M. Pawar, B.S. Pawar, K.V. Gurav, D.W. Bae, S.H. Kwon, S.S. Kolekar, J.H. Kim, Fabrication of Cu_2ZnSnS_4 Thin Film Solar Cell Using Single Step Electrodeposition Method, Japanese Journal of Applied Physics, 51 (2012) 10NC27:11 - 14.

[23] K. Ramasamy, M.A. Malik, P. O'Brien, Routes to Copper Zinc Tin Sulfide Cu_2ZnSnS_4 a Potential Material for Solar Cells, Chem. Commun., 48 (2012) 5703-5714.

[24] W. Septina, S. Ikeda, A. Kyoraiseki, T. Harada, M. Matsumura, $Cu_2ZnSn(S,Se)_4$ Thin Film Prepared from a Single-step Electrodeposited Cu-Zn-Sn-Se Precursor, in: Photovoltaic Specialists Conference (PVSC), 2012 38th IEEE, Austin, 2012, pp. 002702-002706.

[25] W. Septina, S. Ikeda, A. Kyoraiseki, T. Harada, M. Matsumura, Single-step electrodeposition of a microcrystalline $Cu_2ZnSnSe_4$ thin film with a kesterite structure, Electrochimica Acta, 88 (2013) 436-442.

[26] J. Tao, J. He, K. Zhang, J. Liu, Y. Dong, L. Sun, P. Yang, J. Chu, Effect of deposition potential on the properties of Cu2ZnSnS4 films for solar cell applications, Materials Letters, 135 (2014) 8 - 10.

[27] M. Valdes, M. Modibedi, M. Mathe, T. Hillie, M. Vazquez, Electrodeposited Cu_2ZnSnS_4 thin films, Electrochimica Acta, 128 (2014) 393.

[28] N.A. Shvab, V.D. Litovchenko, L.M. Rudkovskaya, Mechanism of Reduction of Thiosulfate Ions on the Cathode, Russian Journal of Applied Chemistry, 80 (2007) 1852 - 1855.

[29] M. Bouroushian, Electrochemistry of Metal Chalcogenides, Springer, Berlin, 2010.

[30] F.A. Kroger, Cathodic Deposition and Characterization of Metallic or Semiconducting Binary Alloys or Compounds, Journal of the Electrochemical Society: Solid-State Science and Tehcnology, 125 (1978) 2028 - 2034.

[31] R.S. Mane, C.D. Lokhande, Chemical deposition method for metal chalcogenide thin films, Materials Chemistry and Physics, 65 (2000) 1 - 31.

[32] C.D. Lokhande, A chemical method for tin disulphide thin film deposition, J. Phys. D: Appl. Phys., 23 (1990) 1703 - 1705.

[33] I. Grozdanov, C.K. Barlingay, S.K. Dey, M. Ristov, M. Najdoski, Experimental study of the copper thiosulfate system with respect to thin-fiml deposition, Thin Solid Films, 250 (1994) 67 - 71.

[34] P.P. Hankare, A.V. Jadhav, P.A. Chate, K.C. Rathod, P.A. Chavan, S.A. Ingole, Synthesis and characterization of tin sulphide thin films grown by chemical bath deposition technique, Journal of Alloys and Compounds, 463 (2008) 581 - 584.

[35] A. Tanusevski, Optical and photoelectric properties of SnS thin films prepared by chemical bath deposition, Semiconductor Science and Technology, 18 (2003) 501 - 505.

[36] F. Chen, W. Jie, X. Cai, Effects of supersaturation on CdS film growth from dilute solutions on glass substrate in chemical bath deposition process, Thin Solid Films, 516 (2008) 2823 - 2828.

[37] B. Subramanian, C. Sanjeeviraja, M. Jayachandran, Cathodic electrodeposition and analysis of SnS films for photoelectrochemical cells, Materials Chemistry and Physics, 71 (2001) 40 - 46.

[38] R.J. Tykodi, In Praise of Thiosulfate, Journal of Chemical Education, 67 (1990) 146 - 149.

[39] A.F. Clifford, The Prediction of Solubility Product Constants, J. Am. Chem. Soc., 79 (1957) 5404 - 5407.

[40] G.L. Miessler, D.A. Tarr, Inorganic Chemistry, Fourth ed., Pearson Prentice Hall, Boston, 2011.

[41] C.J. Huang, T.H. Meen, M.Y. Lai, W.R. Chen, Formation of $CuInSe_2$ thin films on flexible substrates by electrodeposition (ED) technique, Solar Energy Materials & Solar Cells, 82 (2004) 553 - 565.

[42] C. Guillen, E. Galiano, J. Herrero, Cathodic Electrodeposition of $CuInSe_2$ Thin Films, Thin Solid Films, 195 (1990) 137 - 146.

[43] K. Anuar, Z. Zainal, M.Z. Hussein, H. Ismail, Electrodeposition and characterization of Cu_2S thin films from aqueous solution, Journal of Materials Science: Materials in Electronics, 12 (2011) 147 - 152.

[44] B.W. Sanders, A.H. Kitai, The Electrodeposition of Thin Film Zinc Sulphide from Thiosulphate Solution, Journal of Crystal Growth, 100 (1990) 405 - 410.

[45] J.R.S. Brownson, C. Georges, G. Larramona, A. Jacob, B. Delatouche, C. Levy-Clement, Chemistry of Tin Monosulfide (δ-SnS) Electrodeposition: Effects of pH and Temperature with Tartaric Acid, Journal of the Electrochemical Society, 155 (2008) D40 - D46.

[46] S. Boonsalee, R.V. Gudavarthy, E.W. Bohannon, J.A. Switzer, Epitaxial Electrodeposition of Tin(II) Sulfide Nanodisks on Single-Crystal Au(100), Chem. Mater., 20 (2008) 5737.

[47] T. Yukawa, K. Kuwabara, K. Koumoto, Electrodeposition of CuInS2 from aqueous solution Part I. Electrodeposition of Cu-S film, Thin Solid Films, 280 (1996) 160 - 162.

[48] S.S. Dhasade, J.S. Patil, J.H. Kim, S.H. Han, M.C. Rath, V.J. Fulari, Synthesis of CuS nanorods grown at room temperature by electrodeposition method, Materials Chemistry and Physics, 137 (2012) 353 - 358.

[49] M. Ichimura, K. Takeuchi, Y. Ono, E. Arai, Electrochemical deposition of SnS thin films, Thin Solid Films, 361 - 362 (2000) 98 - 101.

[50] T. Mahalingam, C. Sanjeeviraja, Characterization of Electrodeposited Zinc Sulphide Thin Films, phys. stat. sol. (a), 129 (1992) K89 - K92.

[51] S. Cheng, G. Chen, Y. Chen, C. Huang, Effect of deposition potential and bath temperature on the electrodeposition of SnS film, Optical Materials, 29 (2006) 439 - 444.

[52] I. Volov, X. Sun, G. Gadikota, P. Shi, A.C. West, Electrodeposition of copper-tin film alloys for interconnect applications, Electrochimica Acta, 89 (2013) 792 - 797.

[53] A. Survila, Z. Mockus, S. Kanapeckaite, D. Brazinskiene, R. Juskenas, Surfactant Effects in Cu-Sn Alloy Deposition, Journal of the Electrochemical Society, 159 (2012) D296 - D302.

[54] N. Eliaz, E. Gileadi, Induced Codeposition of Alloys of Tungsten, Molybdenum, and Rhenium with Transition Metals, in: C. Vayenas (Ed.) Modern Aspects of Electrochemistry, Springer, New York, 2008.

[55] J. Torrent-Burgues, E. Guaus, Effect of tartaric acid in the electrodeposition of zinc, Journal of Applied Electrochemistry, 37 (2007) 643 - 651.

[56] N. Nikolic, K. Popov, Hydrogen Co-deposition Effects on the Structure of Electrodeposited Copper, in: S. Djokic (Ed.) Electrodeposition: Theory and Practice, Springer, New York, 2010.

[57] A. Taguchi, F. Bento, L. Mascaro, Nucleation and Growth of Tin-Zinc Electrodeposits on a Polycrystalline Platinum Electrode in Tartaric Acid, Journal of the Brazilian Chemical Society, 19 (2008) 727 - 733.

[58] O. Aaboubi, J. Douglade, X. Abenaqui, R. Boumedmed, J. VonHoff, Influence of tartaric acid on zinc electrodeposition from sulphate bath, Electrochimica Acta, 56 (2011) 7885 - 7889.

[59] M.M. Benjamin, J.O. Leckle, Effects of Complexation by Cl, SO_4, and S_2O_3 on Adsorption Behavior of Cd on Oxide Surfaces, Environmental Science and Technology, 16 (1982) 162 - 170.

[60] F.-x. Xiao, X.-n. Shen, F.-z. Ren, A. Volinsky, Additive effects on tin electrodepositing in acid sulfate electrolytes, International Journal of Minerals, Metallurgy and Materials, 20 (2013) 472 - 478.

[61] L.S. Price, I.P. Parkin, A. Hardy, R. Clark, Atmospheric Pressure Chemical Vapor Deposition of Tin Sulfides (SnS, Sn_2S_3, and SnS_2) on Glass, Chemistry of Materials, 11 (1999) 1792 - 1799.

[62] D. Berg, R. Djemour, L. Gutay, S. Siebentritt, P. Dale, X. Fontane, V. Izquiero-Roca, A. Perez-Rodriguez, Raman analysis of monoclinic Cu_2SnS_3 thin films, Applied Physics Letters, 100 (2012) 192103-192101 - 192103-192104.

[63] P.A. Fernandes, P.M.P. Salome, A.F.d. Cunha, A study of ternary Cu2SnS3 and Cu3SnS4 thin films prepared by sulfurizing stacked metal precursors, Journal of Physics D: Applied Physics, 43 (2010) 1-11.

[64] H. Guan, H. Shen, C. Gao, X. He, Structural and optical properties of Cu_2SnS_3 and Cu_3SnS_4 thin films by successive ionic layer adsorption and reaction, Journal of Materials Science: Materials in Electronics, 24 (2013) 1490 - 1494.

[65] A. Fairbrother, X. Fontane, V. Izquierdo-Roca, M. Espindola-Rodriguez, S. Lopez-Marino, M. Placidi, L. Calvo-Barrio, A. Perez-Rodriguez, E. Saucedo, On the formation mechanisms of Zn-rich Cu_2ZnSnS_4 films prepared by sulfurization of metallic stacks, Solar Energy Materials & Solar Cells, 112 (2013) 97 - 105.

[66] M. Paunovic, M. Schlesinger, Fundamentals of Electrochemical Deposition, John Wiley & Sons, Hoboken, 2006.

[67] O. Roussel, O. Ramdani, E. Chassaing, P.-P. Grand, M. Lamirand, A. Etcheberry, O. Kerrec, J.-F. Guillemoles, D. Lincot, First Stages of $CuInSe_2$ Electrodeposition from Cu(II)-In(III)-Se(IV) Acidic Solutions on Polycrystalline Mo Films, Journal of the Electrochemical Society, 155 (2008) D141 - D147.

[68] R. Winand, Electrodeposition of Metals and Alloys - New Results and Perspectives, Electrochimica Acta, 39 (1994) 1091 - 1105.

[69] W.A. Badawy, F.M. Al-Kharafi, Corrosion and passivation behaviors of molybdenum in aqueous solutions of different pH, Electrochimica Acta, 44 (1998) 693 - 702.

[70] T. Laitinen, Thiosulfate pitting corrosion of stainless steels in paper machine environment, in: Manufacturing Technology, VTT Technical Research Centre of Finland, Finland, 1999.

[71] Springer Handbook of Metrology and Testing, Springer-Verlag, New York, 2011.

[72] G.S. Frankel, Pitting Corrosion of Metals, Journal of the Electrochemical Society, 145 (1998) 2186 - 2198.

[73] W.A. Badawy, H.E. Feky, N.H. Helal, H.H. Mohammed, Cathodic hydrogen evolution on molybdenum in NaOH solutions, International Journal of Hydrogen Energy, 38 (2013) 9625 - 9632.

[74] H.-C. Huang, C.-S. Lin, W.-C. Chang, Electrodeposition of CIS films on the Mo back electrodes with different crystallites, Electrochimica Acta, 75 (2012) 20 - 27.

[75] K. Popov, S. Djokic, B. Grgur, Fundamental Aspects of Electrometallurgy, Kluwer Academic Publishers, New York, 2002.

[76] A.J. Bard, L.R. Faulkner, Electrochemical Methods: Fundamentals and Applications, Second ed., John Wiley & Sons, Hoboken, 2001.

[77] M. Dimietrievska, A. Fairbrother, X. Fontane, T. Jawhari, V. Izquierdo-Roca, E. Saucedo, A. Perez-Rodriguez, Multiwavelength excitation Raman scattering study of polycrystalline Cu_2ZnSnS_4 thin films, Applied Physics Letters, 104 (2014) 021901-021901 021901-021905.

[78] A. Khare, B. Himmetoglu, M. Johnson, D. Norris, M. Cococcioni, E. Aydil, Calculation of the lattice dynamics and Raman spectra of copper zinc tin chalcogenids and comparison to experiments, Journal of Applied Physics, 111 (2012) 083707-083701 - 083707-083709.

[79] J. Scragg, J. Watjen, M. Edoff, T. Ericson, T. Kubart, C. Platzer-Bjorkman, A Detrimental Reaction at the Molybdenum Back Contact in $Cu_2ZnSn(S,Se)_4$ Thin-Film Solar Cells, J. Am. Chem. Soc., 134 (2012) 19330 - 19333.

8 GROWTH BEHAVIOR OF CO-ELECTRODEPOSITED METALLIC CZT PRECURSORS

8.1 PURPOSE

The co-electrodeposition of S-containing CZTS precursors represents an attractive fabrication route because the presence of S in the precursor has been shown to improve the crystal growth properties of CZTS. In [1], S-content of 14-18at% in the precursor films significantly reduced Sn-loss and void formation, although also decreased the grain size, in the final films. The co-deposition of the S element, however, significantly complicates the growth behavior of the co-electrodeposited precursors, since the $S_2O_3^{2-}$ anion must be transported by diffusion (against the electric field in the cell) to the working electrode surface [2] and disproportionation of $S_2O_3^{2-}$ may cause precipitation of insoluble species [3, 4].

The elimination of $Na_2S_2O_3$ from the bath significantly simplifies the electrodeposition behavior, as will be shown in this chapter. In particular, co-electrodeposition of metallic CZT precursors allows easier deposition of compact films free of pits and particulates, simpler optimization of composition, greater bath stability, and potentially greater compatibility with existing plating technologies. As discussed above and in Section 7.1, however, films sulfurized from metallic precursors may exhibit greater Sn loss and increased void formation. To provide a basis for comparison with the S-containing CZTS precursors investigated in Chapter 7, metallic CZT precursors are investigated here.

Further, comprehensive studies on the effects of deposition parameters were not found in a review of the literature, and so the studies here were also meant to provide a foundation for future work on the subject. This chapter explores the co-electrodeposition of metallic CZT precursors, deposited and annealed under varying conditions, with the following objectives:

- Characterize the effects of the co-electrodeposition parameters on the as-deposited film compositions and morphologies.
- Determine deposition parameters that achieve the optimum as-deposited film composition and morphology. From Section 1.3 and 2.3.2, the desired film stoichiometry corresponds to a Cu:Zn:Sn metal ratio of approximately 1.8:1.2:1.0, and 1μm represents the minimum film thickness necessary for use in photovoltaic absorber layers.
- Investigate the role of the precursor composition and structure on crystal and secondary phase formation processes and determine their influence on film properties.
- Demonstrate the fabrication of high-quality films for use in fundamental material, interface studies, and device studies.

8.2 BACKGROUND

This section provides a brief review of the existing literature on co-electrodeposition of metallic CZT thin film precursors [4-14]. Most of the reported works performed the electrodepositions under constant potential using three-electrode cells, with varying reference electrodes, platinum or graphite counter electrodes, and Mo-coated or ITO/FTO-coated glass substrates [5, 7, 9-13]. Metal sulfates or metal chlorides typically provided the Cu, Zn, and Sn sources in the deposition bath [4, 5, 7, 9-13]. Other complexing agents (e.g. pyrophosphate [8]) have been investigated, but many works employed tri-sodium citrate or citric acid [4, 5, 7, 9, 10]. Table 8-1 shows typical deposition parameters demonstrated in the literature, and Table 8-2 shows reported effects of the deposition parameters on the properties of metallic CZT precursor films.

Table 8-1. Typical deposition parameters for metallic CZT precursors (literature results)

Deposition Parameter	Value	Reference
$[Cu^{2+}]$	0.003 – 0.02	[4-10, 12]
$[Zn^{2+}]$	0.005 – 0.20	
$[Sn^{2+}]$	0.003 – 0.01	
[Cit]	0.1 – 0.5	
pH	2.7 – 11	[4, 7-10, 12]
Deposition Potential (vs. Ag/AgCl)	-1.1 to -1.4V	[4, 7, 9, 10, 12]
Deposition Time	6 – 20min	[5, 8, 10]
Stirring	None	[5, 7, 12]

In literature, studies of co-electrodeposition of metallic CZT thin film precursors have focused on characterizing the precursor growth behavior, including the effects of bath composition and deposition potential on the as-deposited film properties, and characterizing the effects of sulfur or selenium annealing on the final film properties. A detailed investigation of the kinetics and mechanism of growth may be found in [4]. Device efficiencies of 1.7 – 5.8% have been reported for solar cells using CZTS absorber layers fabricated by two-step co-electrodeposition of metallic CZT precursors and sulfurization [4, 5, 9, 13].

Co-electrodeposition of metallic CZT precursors represents a greatly simplified process compared to S-containing precursors and potentially allows greater opportunities for optimization. Various approaches have been attempted, but the deposition method usually includes constant potential deposition from baths containing Cu-, Zn-, and Sn-metal salts, a complexing agent and sometimes a buffering agent. Typically, metal sulfates with M^{2+} metal ions have been employed, although Sn^{4+} ions have also been used [8]. The basic reduction processes associated with cathodic deposition of the metallic elements, similar to those in Section 7.2, have therefore been described as follows [4, 8, 9, 14]:

$$Cu^{2+} + 2e^- \rightarrow Cu(s) \quad (8\text{-}1)$$

$$Zn^{2+} + 2e^- \rightarrow Zn(s) \quad (8\text{-}2)$$

$$Sn^{2+} + 2e^- \rightarrow Sn(s) \quad (8\text{-}3)$$

$$Sn^{4+} + 2e^- \rightarrow Sn^{2+} \quad (8\text{-}4)$$

The investigation by Gougaud et. al. in [4] represents the most significant work to date on the kinetics and mechanism involved in the co-electrodeposition of metallic CZT precursors. The stabilities of metal-complex species and the reduction potentials of the electroactive species were investigated theoretically and experimentally, the diffusion constants for the electroactive species were measured, and the potential dependence of the film compositions were evaluated [4]. This work utilized a bath composition similar to Pawar's method but employed citric acid instead of tri-sodium citrate and eliminated sodium thiosulfate [4]. Given its relevance to the work performed in this dissertation, a brief review of the study by Gougaud is provided here [4]

As discussed in Section 3.2.3.3, citric acid was shown to complex primarily with Cu and Zn, while the tartaric acid was shown to complex primarily with Sn, when both complexing agents were present [4]. For pH values larger than 5, tin oxide may precipitate, and for pH values larger than 7, copper oxide and zinc oxide may precipitate [4]. For the nominal bath composition with citrate and tartrate, predicted values of the reduction potentials for Cu, Sn, and Zn, based on the complexing stabilities and resulting activities, were close to the values measured using cyclic voltammetry: -0.26V, -0.66V, and -1.21V (vs. Ag/AgCl), respectively [4]. The voltammagram also displayed a large peak at -1.01V not associated with metal reduction, which was attributed to hydrogen evolution. This HER was reported to proceed via citrate ion proton reduction [4]:

$$H_3AOH \leftrightarrow AOH^{3-} + 3H^+ \quad (8\text{-}5)$$

$$2H^+ + 2e^- \leftrightarrow H_2 \quad (8\text{-}6)$$

where H_3AOH represents the citric acid molecule $C_6H_8O_7$.

Due to its apparently negligible influence, tartaric acid was eventually eliminated from the deposition baths. Using partial electrolytes without tartaric acid, the diffusion constants of the electroactive species were determined via rotating disc electrode studies as follows: copper species = 4.4×10^{-6} cm^2/s and tin species = 1.9×10^{-6} cm^2/s. The zinc species diffusion could not be accurately determined due to parallel hydrogen evolution reaction [4]. At the final deposition potential (e.g. where Zn is depositing out in sufficient quantities), copper and tin are deposited under diffusion-limiting conditions, and the zinc co-deposits with hydrogen evolution reaction [4]. The as-deposited films were severely dendritic with features up to ~2μm length, although later selenization was shown to improve film compactness. In fact, the work reports the highest device efficiency (5.8%) demonstrated for solar cells fabricated with co-electrodeposited metallic precursors [4].

Other works have also reported rough, dendritic films [14], but features were less severe than those demonstrated in [4]. However, significantly more compact films have also been reported [5, 7].

Table 8-2. Process control variables and effects for metallic CZT precursors (literature results), * bath contains no complexing agent

Process Parameter	Variation	Film Effect	Rationale
Metal Cation Ratios	Increasing $[CuCl_2]$*	(1) Increased [Cu] in films (2) Did not modify [Zn], [Sn] in films (3) Increased large grains on surface of films and voids in film	Not discussed
	Increasing $[ZnCl_2]$:$[SnCl_2]$*	(1) Increased Zn:Sn in films (2) Negligibly modified [Cu] in films	Not discussed
Complexing Agent	Citric Acid	(1) Strongly complexes with Cu, Zn (2) Weakly complexes with Sn (3) Demonstrates reduction peak near -1.01V (vs. Ag/AgCl)	(1-2) Complexing species stabilities (3) Proton reduction of citrate ion facilities HER
	Tartaric Acid	In the presence of citric acid, does not dramatically alter deposition behavior	Not well understood
	Pyrophosphate	(1) Strongly complexes with Cu and weakly complexes with Zn (2) Does not complex with Sn (3) Shifts reduction potential between Cu-Zn-Sn closer than citrate	(1-3) Complexing species stabilities
Deposition Potential	Increasingly Negative	(1) Strongly increasing [Zn] in films (2) Moderately increasing Cu:Sn in films (3) Increasing dendrite formation	(1) Onset of Zn reduction (2) Not discussed (3) High overpotentials applied
Bath pH	Decreasing pH (more acidic)	(1) Strongly increasing [Zn] in films (2) Slightly decreasing Cu:Sn ratio	Not discussed
Substrate	FTO (compared to Mo)	More uniform, with smaller grains and smaller voids	Not discussed

Typically, co-electrodeposited metallic CZT precursor films possess combinations of Cu-Zn, Cu-Sn alloys, and elemental phases, depending on the film composition, as determined by

x-ray diffraction. Schurr reported that Cu-rich films were composed of Cu_3Sn and CuZn phases, while Cu-poor/near-stoichiometric films contained additional Cu_6Sn_5 and Sn phases [11]. Other works have reported similar phases, with some other Cu-Zn alloys, elemental Cu, and elemental Zn phases present as well [4, 5, 7, 10].

Many works have investigated the sulfur or selenium annealing of co-electrodeposited metallic CZT precursors [5, 7-11, 14]. "Soft," low-temperature alloy annealing in inert environment of the precursors prior to final crystal formation, has been shown to improve final films properties [10, 14]. However, soft annealing in reducing (H_2) environment did not improve the final film quality [7]. The most extensive work on the crystal formation processes associated with co-electrodeposited metallic CZT precursors was reported in [11]. For more information, the reader is referred back to Section 3.3.2.2, which extensively discuss the crystal formation processes associated with CZT and CZTS precursors.

The effects of varying $CuCl_2$, $ZnCl_2$ and $SnCl_2$ concentrations on the film properties were investigated in [12]. The deposition methodology presented is unclear, however, as the deposition bath included sodium thiosulfate as a buffering agent, but the study only refers to the deposition of metallic precursors. Neglecting this contradiction, the study showed that modifying the metal chloride concentration in the bath independently modified the depositing metal concentration, suggesting that the metals deposit independently without interaction in the bath or in the reduction process. SEM images show increasing grain size and decreasing grain density in films deposited with increasing $[CuCl_2]$:$[ZnCl_2+SnCl_2]$ [12]. No other works investigating the effects of component concentration were found.

A review of the literature found no works reporting the effects of complexing agent concentration or complexing agent type on the properties of as-deposited films. However, a detailed discussion of the effects of citric acid and tartaric acid on the stabilities of Cu-, Zn-, and Sn-complex species was provided in [4]. Besides tri-sodium citrate and citric acid, pyrophosphate has been used as a complexing agent and was noted to complex strongly with Cu as $[CuH_q(P_2O_7)_2]^{(6-q)-}$, while weakly complexing with Zn and not complexing with Sn [8]. Sn is expected to exist as free stannate ions, $Sn(OH)_6^{2-}$ [8]. In this work, pyrophosphate was reported to narrow the reduction potentials more efficiently than tri-sodium citrate [8]. Bath compositions and deposition conditions differed considerably from other reported methods, including the use of alkaline pH and galvanostatic control, preventing broader comparisons.

In [9] and [4], the effects of deposition potential on the properties of as-deposited films were reported. Using a bath containing metal sulfates, citric acid, and NaOH (to neutralize pH to 7), increasing the deposition potential from -1.16 to -1.21V (vs. Ag/AgCl) was shown to moderately increase the Cu:Sn ratio and substantially increase the Zn:Sn ratio in the deposited films [9]. The mechanism of these changes was not discussed, and the as-deposited morphologies were not reported [9]. In the work by Gougaud discussed previously, films were deposited from

baths containing metal sulfates, sodium citrate (citric acid), and supporting electrolyte potassium sulfate, using a rotating disk electrode (RDE) configuration [4]. The work reports the film composition versus the deposition potential, with stoichiometric films achieved at -1.46V (vs. Ag/AgCl) [4]. The poor quality of the as-deposited films, characterized by extreme dendrite morphologies, was attributed to the highly negative deposition potentials and subsequently large overpotentials required to achieve stoichiometric growth [4].

In the reviewed literature, co-electrodeposited metallic CZT precursors were deposited from baths with pH varying from 2.7 to 11 [4, 7-10, 12]. In [7], the effects of pH on the properties of as-deposited films were investigated, using baths composed of metal sulfates, sodium citrate, hydroquinone (antioxidant), and sulfuric acid buffering agent. With decreasing (more acidic) pH, the Cu:Sn ratio decreased slightly and the Zn:Sn ratio increased substantially. The mechanism of this increase, however, was not discussed [7]. As-deposited films were compact, with large spherical grains, with no noted dependence on the pH [7].

Co-electrodeposition of metallic CZT precursors has been performed using Mo-coated [4-6, 9-11, 13, 14], ITO-coated [7], and FTO-coated glass substrates [6, 12]. The effects of the substrate on the properties of deposited films was investigated in [6]. Films were grown on Mo- and FTO-coated glass substrates using a constant potential and the following bath components: copper sulfate, zinc chloride, tin stannate, and potassium sodium tartrate [6]. SEM images indicated that the as-deposited morphologies of films deposited on FTO-substrates were more uniform, with smaller voids and smaller grains than films deposited on Mo-substrates [6]. The reasons for these variations, however, were not discussed.

Finally, other deposition control methods have been investigated for co-electrodeposition of metallic CZT precursors, including galvanostatic control [8]. However, the investigation in [8] did not discuss the impact specifically of galvanostatic control on the deposition behavior. Given the unique bath composition used to deposit the films in [8], it is also difficult to compare the results of the work against other potentiostatic methods. The deposited films were able to achieve appropriate stoichiometries for CZTS materials, including Cu:[Zn+Sn] = 0.66 and Zn:Sn = 1.34 [8]. Morphologies of as-deposited films were noticeably rough with stripes and clusters of larger grains on the surface [8].

8.3 EXPERIMENTAL DETAILS

Single-layer films of Cu-Zn-Sn (CZT), up to 1.5μm thickness, were deposited on Mo-coated soda lime glass substrates using a modified version of **Pawar's method,** which eliminated tartaric acid and the sulfur-carrying $Na_2S_2O_3$ from the bath [15]. Using similar baths without $Na_2S_2O_3$, tartaric acid was shown to have negligible influence on the co-electrodeposition behavior [4]. The (Guardian) Mo-coated substrates used deposition areas of ~1.6 x 2cm. See Section 3.2.4 for more detailed descriptions of the electrodeposition system, deposition methodology, and substrate properties. Details specific to the individual studies are presented in following sections.

Metallic CZT precursor films were deposited from aqueous electrolyte baths with the nominal composition shown in Table 8-3, adapted from the bath composition in [15]. Constant potential depositions were performed at -1.00 to -1.25V vs. Ag/AgCl, using an AFCBP1 or WaveDriver 20 biopoteniostat. Sulfur annealing was performed using the Generation #2 annealing system design and methodology described in Section 3.3.3.3. Samples were nominally annealed at 560°C and passively cooled under flowing Argon to < 120°C. The masses of elemental sulfur and the temperature profiles used for annealing are noted in the discussion. Some precursor films were also soft annealed at low temperatures prior to sulfurization, as noted in the discussion.

Table 8-3. Nominal bath composition used for co-electrodeposition of metallic CZT precursors

Chemical Formula	Concentration [M]
$Na_3C_6H_5O_7$	0.20
$Cu(II)SO_4$	0.02
$Zn(II)SO_4$	0.01
$Sn(II)SO_4$	0.02

Film compositions and thicknesses were characterized using Rutherford back scattering (RBS) and particle-induced x-ray emission spectroscopy (PIXE) analyses, as detailed in Chapter 4. To help qualitatively identify compositions of large surface features, such as the likely ZnS phases seen in Fig. 8-12, point-and-shoot EDS spectra were measured, as detailed in Chapter 4. Crystal structures were analyzed by x-ray diffraction and Raman backscattering spectroscopy, and morphologies were assessed using scanning electron microscopy, as detailed in Chapter 4.

8.4 RESULTS AND DISCUSSION

Note that all deposition potentials referenced in Sections 8.4 and 0 refer to the Ag/AgCl reference electrode.

8.4.1 Baseline Film Properties

This section describes the baseline film properties and deposition characteristics associated with the original bath conditions shown in Table 8-3. Baseline films were deposited from the nominal bath composition above at -1.20V for 25 minutes. Preliminary work identified the Zn deposition onset at -1.14V, and so more negative (less noble) potentials are used for all depositions in this chapter.

The baseline films were well-adhering, such that rinsing and light nitrogen blow drying caused no visible loss of material from the films. The morphology of the as-deposited film was uniform, with a rough surface containing loosely-packed grains, as evident in Fig. 8-1. Voids in the films, attributed to hydrogen evolution, are also evident in the 500X image.

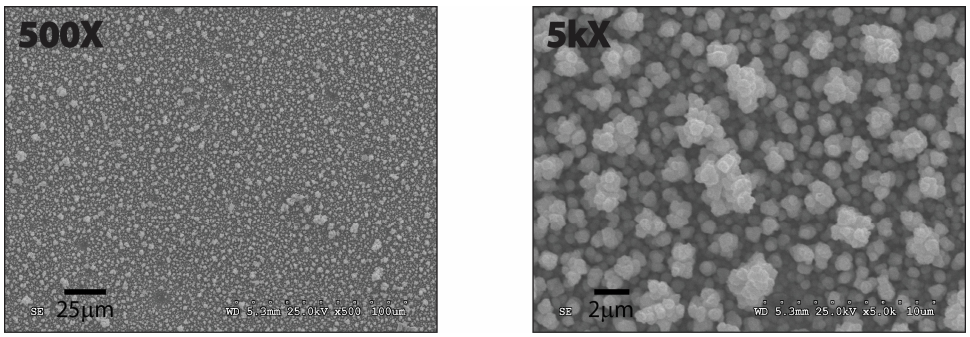

Fig. 8-1. SEM images of baseline co-electrodeposited metallic CZT precursor on Mo-substrate (Guardian)

The large film thickness, estimated as 1.5µm by RBS measurements, and the significant surface roughness prevent reliable determination of the composition by RBS. Table 8-4 shows the best estimate of the film composition and thickness. From Section 1.3 and 2.3.2, the desired film stoichiometry corresponds to a Cu:Zn:Sn metal ratio of approximately 1.8:1.2:1.0. The as-deposited film is severely Zn-deficient, evident as large Cu:Zn ratio and small Zn:Sn ratio. Note, however, the Cu:Sn ratio of 1.64 is near the desired value of 1.8.

Table 8-4. Composition and thickness of baseline co-electrodeposited metallic CZT precursor

Atomic %				Cu:Zn	Zn:Sn	Thick (nm)
Cu	Zn	Sn	O			
47	11	29	32	4.1	0.39	1500

The 25min deposition time yields extremely thick films (~1.5µm), and the poor roughness and loosely-packed grains are attributed to the long deposition time and associated diffusion-limited growth conditions. Note, the surface morphology is similar to films deposited from baths containing $Na_2S_2O_3$, which showed a transition to rougher, more dendritic surfaces with longer deposition times (see Section 7.4.2.3). In this case, shorter deposition times of 10min prevent this transition and yield significantly smoother films with few visible defects, as demonstrated in following sections. Note that after sulfurization the film thickness increases by a factor of 1.7 – 2.7X, as shown in Section 8.4.7, so a precursor film thickness of only ~350nm is required to achieve the desired final film thickness of ~ 1µm.

8.4.2 Cyclic Voltammetry

A cyclic voltammetry spectrum for the (Guardian) Mo-coated glass substrate with nominal bath conditions was measured from 0 to -1.50V at 10mV/s, as shown in Fig. 8-2. The voltammagram indicates a series of cathodic peaks labeled I – V. The onset of hydrogen evolution reaction (HER) occurs near -1.38V.

The dominant cathodic peaks at -0.32V (II), -0.65V (III), -0.95V (IV), and -1.14V (V) show sharp, well-defined drop-offs in cathodic current density consistent with mass-transfer limited conditions. Weaker peaks, evident as shifts in current density slope, are evident at -0.21V (I) and possibly -0.71V (unlabeled). A series of anodic oxidation peaks are also evident on the reverse

voltage sweep. While the Cu and Sn peaks were not explicitly verified here, the reduction peaks at -0.32V and -0.65V may tentatively be assigned to Cu and S, respectively. The peak at -1.14V can be assigned to Zn reduction, confirmed by as lack of Zn in films deposited at potentials more noble than -1.14V. These reduction potentials compare well with the peaks at -0.26V (Cu), -0.66V (Sn), and -1.21V (Zn) observed in the voltammagram in [4], which used a more acidic bath composition with different component concentrations.

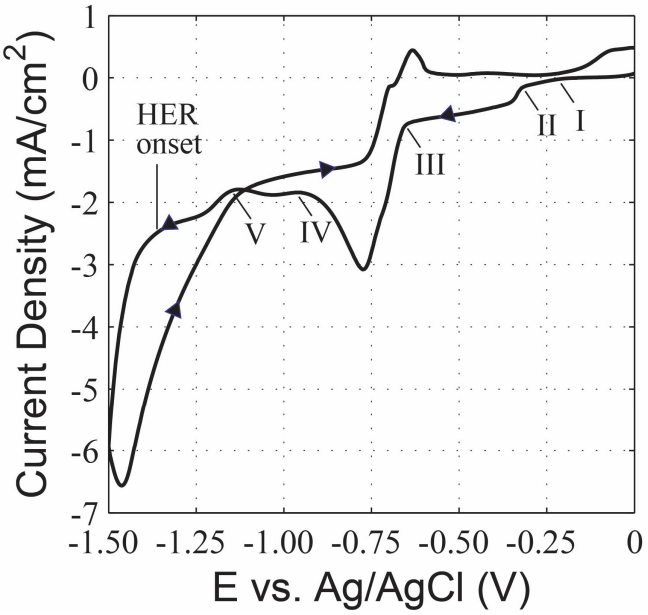

Fig. 8-2. Cyclic voltammagram of nominal bath composition with (Guardian) Mo-substrate

The removal of $Na_2S_2O_3$ significantly modifies the cyclic voltammagram for the nominal bath, as evident by comparing Fig. 8-2 with Fig. 7-24. The cathodic peaks are summarized in Table 8-5, where the dominant, most-well defined reduction peaks are identified in bold. In general, the reduction peaks shift to more noble values for the bath without $Na_2S_2O_3$. This may signify a reduction in the overpotentials associated with the reduction mechanisms or modifications to the reduction processes themselves. As Table 8-5 shows, the presence of $Na_2S_2O_3$ shifts the onset of HER to significantly more noble potentials.

Table 8-5. Cathodic peak locations for baths with and without $Na_2S_2O_3$ (no tartaric acid)

$Na_2S_2O_3$ Concentration	Cathodic Peak Locations (V)						HER Onset
0.02M	-0.06	**-0.55**	-0.73	**-0.77**	**-0.90**	**-1.14**	-1.29
None	-0.21	**-0.32**	**-0.65**	-0.71	**-0.95**	**-1.14**	-1.38

The as-deposited compositions and morphologies vary with the bath composition and deposition in a more predictable way for metallic CZT precursors than for S-containing CZTS precursors. For this reason, a systematic investigation of the cathodic peaks was not pursued here.

8.4.3 Effects of Bath Composition

The dependence of the as-deposited film morphologies and compositions of CZTS on the bath composition was investigated for (Guardian) Mo-substrates by varying a given bath component while holding the others constant. In an effort to more quickly reach an optimum bath composition, the component concentrations were not varied relative to a single nominal bath. The trends in film properties are expected to be general, however. The baseline composition for each bath will be noted at the beginning of each section. In order to improve Zn incorporation, higher $ZnSO_4$ concentrations of 0.02M are used hereafter. Further, the nominal deposition time was reduced to 10min to reduce film roughness and to achieve desired precursor film thickness.

8.4.3.1 $CuSO_4$ Concentration

The baseline composition for the investigation of $CuSO_4$ concentration was the following: 0.2M $Na_3C_6H_5O_7$, 0.02M $ZnSO_4$, and 0.02M $SnSO_4$. Films were grown at a constant potential of -1.19V for 10min, with the concentration of $CuSO_4$ varied between 0.016 and 0.02M. The resulting compositions and morphologies are summarized in Table 8-6 and Fig. 8-3, respectively.

Table 8-6. Compositions and thicknesses of co-electrodeposited metallic CZT precursors with varying $CuSO_4$ concentrations

[$CuSO_4$]	Atomic %				Cu:Zn	Zn:Sn	Thick (nm)
	Cu	Zn	Sn	O			
0.016M	31	21	35	13	1.5	0.59	500
0.020M	39	19	33	8.0	2.0	0.58	535

As expected, the relative Cu concentration in the film increases with increasing $CuSO_4$ concentration, evident as an increasing Cu:[Zn+Sn] ratio. However, the relative Zn and Sn concentrations do not vary significantly with increasing $CuSO_4$, evident as a static Zn:Sn ratio. This approximately independent rise in Cu concentration behaves contrary to $Na_2S_2O_3$-containing baths, which demonstrated inverse trends in the Cu:Sn ratios with varying $CuSO_4$ and $SnSO_4$ concentration. The independence of the Cu and Sn deposition rates in baths without $Na_2S_2O_3$ suggests that the presence of $Na_2S_2O_3$ causes an interaction between the Cu and Sn, either in the bulk species or through a modified or interactive reduction process. Similar independence of elemental deposition rates with $SnSO_4$ concentration and deposition potential is demonstrated in the following sections. Note the film thickness increases with increasing $CuSO_4$ concentration.

The surface morphologies of as-deposited films do not vary strongly with increasing $CuSO_4$ concentration, as shown in Fig. 8-3 above. The films both exhibit homogeneous surfaces with densely-packed grains (several hundred nm diameter), no large surface particulates, and negligible voids or substrate damage. The films are significantly more compact, although thinner, than the longer deposition baseline films shown in Section 8.4.1. The reduction in surface roughness is attributed primarily to the shorter deposition times. In general, the co-electrodeposited metallic CZT precursors exhibited significantly improved quality over the S-containing CZTS precursors,

with notable decreases in film and substrate damage. The samples were visually specular and highly uniform.

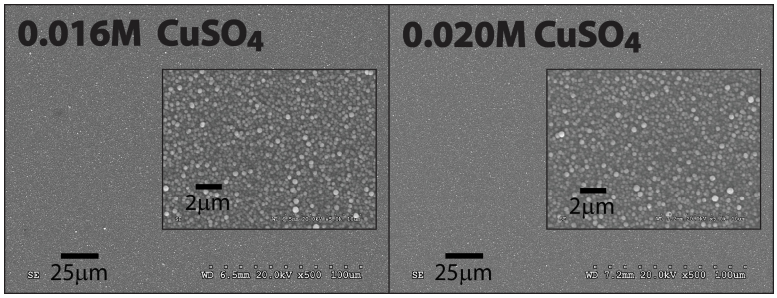

Fig. 8-3. SEM images of electrodeposited C-Z-T metal precursor films on Mo-coated glass substrates deposited from baths with varying [$CuSO_4$]

8.4.3.2 $SnSO_4$ Concentration

The baseline composition for the investigation of $SnSO_4$ concentration was the following: 0.2M $Na_3C_6H_5O_7$, 0.016M $CuSO_4$, and 0.02M $ZnSO_4$. Films were grown at a constant potential of -1.19V for 10min, with the concentration of $SnSO_4$ varied between 0.01 and 0.02M. The resulting compositions and morphologies are summarized in Table 8-7 and Fig. 8-5, respectively.

Table 8-7. Compositions and thicknesses of co-electrodeposited metallic CZT precursors with varying $SnSO_4$ concentrations

[$SnSO_4$]	Atomic %				Cu:Zn	Zn:Sn	Thick (nm)
	Cu	Zn	Sn	O			
0.0100M	41	30	22	7.0	1.4	1.4	365
0.0125M	40	29	26	6.0	1.4	1.1	360
0.0200M	31	21	35	13	1.5	0.59	500

The desired Cu-poor, Zn-rich stoichiometries, with element ratios near Cu:Zn:Sn of 1.8:1.2:1.0, are achieved at 0.01 – 0.0125M $SnSO_4$. As expected, the relative Sn concentration in the film increases with increasing $SnSO_4$ concentration, evident as an increasing Sn:[Cu+Zn] ratio. The relative Cu and Zn concentrations do not vary significantly with increasing $SnSO_4$, evident as a static Cu:Zn ratio. This approximately independent rise in Sn concentration with $SnSO_4$ behaves similarly to the rise in Cu concentration with $CuSO_4$ demonstrated in the previous section and contrary to previous studies with $Na_2S_2O_3$-containing baths. Note the film thickness generally increases with increasing $SnSO_4$ concentration.

The RBS spectra for the films deposited with varying $SnSO_4$ concentration indicate that all films exhibit significant composition grading, with higher Sn concentrations and lower Cu-Zn concentrations near the surface. Fig. 8-4 shows the RBS spectrum for 0.01M $SnSO_4$. It will be shown in Section 8.4.6 that sulfur annealing reduces these through-thickness composition gradients.

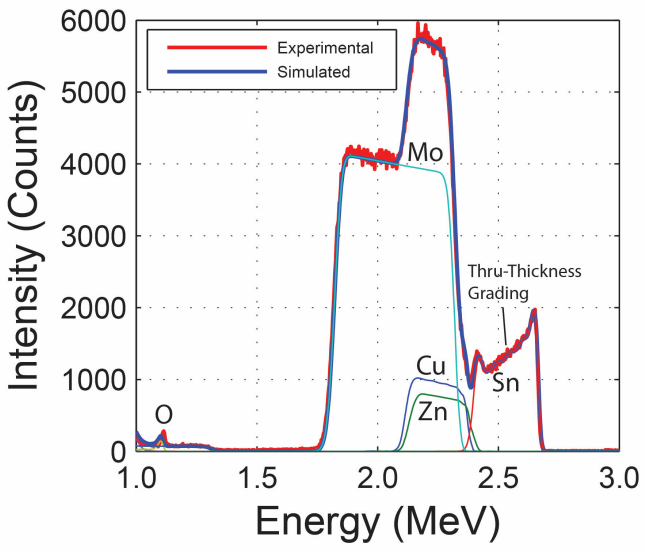

Fig. 8-4. Experimental and simulated RBS spectra of metallic CZT precursor electrodeposited (0.01M $SnSO_4$) on Mo-substrate

The surface morphologies of as-deposited films all exhibit homogeneous surfaces with densely packed grains, no large surface particulates, and negligible voids, as shown in Fig. 8-5. The films show a clear increase in the grain size, from approximately 130 to 300nm, with increasing $SnSO_4$ concentration. This increase in grain size may be attributed to the increased deposition rate associated with the increasing $SnSO_4$ concentration; as Table 8-7 shows, the film thickness increases from 365 to 500nm.

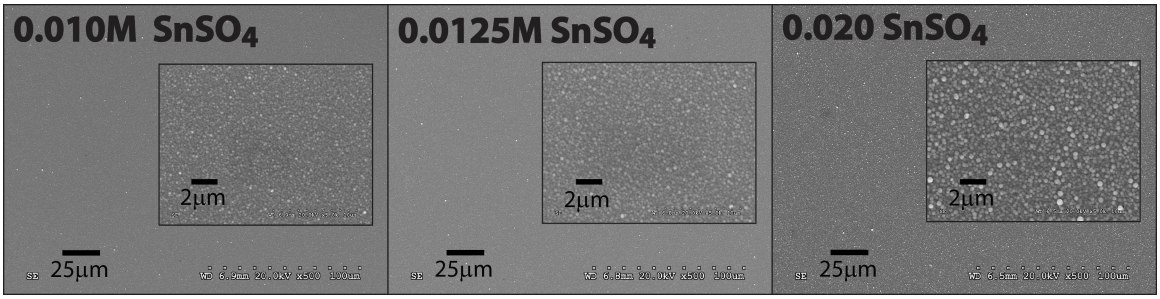

Fig. 8-5. SEM images of electrodeposited metallic CZT precursors on Mo-substrates deposited from baths with varying $SnSO_4$ concentration

8.4.4 Effects of Bath Concentration

As shown in Section 7.4.2.6, increasing the overall bath concentration can yield higher deposition rates of the films. Longer deposition times can yield rougher, less dense films, as shown in Section 8.4.1. Therefore, if films thicker than 1μm were desired, then increasing the bath concentration represents one possible path to increase film thickness while minimizing surface roughness.

The baseline composition for the investigation of bath concentration was the following: 0.2M $Na_3C_6H_5O_7$, 0.016M $CuSO_4$, 0.02M $ZnSO_4$ and 0.0125M $SnSO_4$. This bath composition was

shown to yield near ideal (although slightly too Zn-rich) Cu:Zn:Sn ratios in the films, as shown in Table 8-7. The bath concentration was varied between 1X and 2X, such that the ratios of component concentrations remained constant (e.g. 2X bath: 0.4M Citrate, 0.032M $CuSO_4$, 0.04M $ZnSO_4$, and 0.025M $SnSO_4$). Films were grown at a constant potential of -1.19V for 10min, and the resulting compositions and morphologies are summarized in Table 8-8 and Fig. 8-6, respectively.

Table 8-8. Compositions and thicknesses of co-electrodeposited metallic CZT precursors with varying overall bath concentrations

Bath Concentration	Atomic %				Cu:Zn	Zn:Sn	Thick (nm)
	Cu	Zn	Sn	O			
1X	40	29	26	6.0	1.4	1.1	360
2X	43 (◊)	25 (◊)	24 (◊)	◊	1.7	1.0	765

Due to peak overlap resulting from the much thicker films, the Cu-Zn and Sn concentrations in the 2X bath concentration film could not be reliably analyzed using RBS. PIXE spectra, however, indicated nearly identical Sn:[Cu+Zn] ratios for the baths deposited at 1X and 2X concentration. The Cu:Zn ratio, however, increased slightly from 1.4 to 1.7 with increasing bath concentration. Consequently, the film composition for the 2X bath concentration could be estimated, as shown in Table 8-9. Like the $Na_2S_2O_3$-containing baths, the compositions of the co-electrodeposited metallic precursors do not depend strongly on the overall bath concentration. The film thickness scales approximately with the bath concentration, increasing by approximately a factor of two with 2X bath concentration, as expected. For higher bath concentrations, the relative Zn concentration should be increased slightly, in order to achieve the desired Zn:Sn ratios of 1.1 – 1.2.

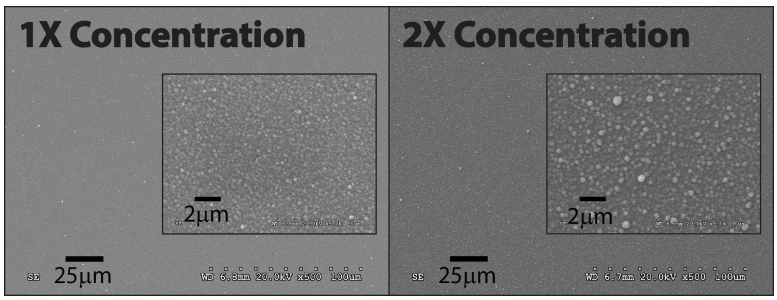

Fig. 8-6. SEM images of electrodeposited metallic CZT precursors on Mo-coated substrates deposited from baths with varying overall dilution

The surface morphologies of as-deposited films both exhibit homogeneous surfaces with densely packed grains, no large surface particulates, and negligible voids, as shown in Fig. 8-6. The films show a clear increase in the grain size, from approximately 250 to 450nm with increasing bath concentration. This increase in grain size may again be attributed to the increase in deposition rate associated with the increasing concentration; as Table 8-8 shows, the film thickness increases from 360 to 835nm.

8.4.5 Effects of Deposition Potential

Previous studies of the effects of deposition potential on compositions and morphologies of as-deposited films, discussed in Sections 7.4.1.2 and 7.4.2.2, indicated strong dependences of the relative Zn concentration on the deposition potential. This section investigates the composition dependence, particularly the Zn concentrations, of co-electrodeposited metallic precursors on the deposition potential.

The baseline composition for the investigation of bath concentration was the following: 0.2M $Na_3C_6H_5O_7$, 0.016M $CuSO_4$, 0.02M $ZnSO_4$ and 0.01M $SnSO_4$. Films were grown under constant potential for 10min, with the potential varied from -1.16 to -1.20V. The compositions of the as-deposited films are summarized in Table 8-9.

Table 8-9. Compositions and thicknesses of co-electrodeposited metallic CZT precursors with varying deposition potentials

Potential	Atomic %				Cu:Zn	Zn:Sn	Thick (nm)
	Cu	Zn	Sn	O			
-1.16V	46	18	24	12	2.6	0.74	325
-1.18V	43	28	23	6.0	1.5	1.2	330
-1.19V	41	30	22	7.0	1.4	1.4	365
-1.20V	38	30	21	11	1.3	1.4	435

Note the desired Cu-poor, Zn-rich stoichiometries are achieved in the potential range of -1.18V to -1.20V, with the most optimum stoichiometry achieved at -1.18V. As expected, the relative Zn concentration in the film increases with increasingly negative deposition potential, evident as a decreasing Cu:Zn and an increasing Zn:Sn ratio. The relative Cu and Sn concentrations do not vary significantly with increasingly negative potential, evident as a static Cu:Sn ratio between 1.8 and 1.9. This approximately independent rise in Zn concentration with increasingly negative potential behaves similarly to the independent rises in Cu and Sn with $CuSO_4$ and $SnSO_4$, respectively. Contrary to the $Na_2S_2O_3$-containing baths, the deposition rates of Cu, Zn, and Sn do not show any complicated interactions with varying bath composition or deposition potential. As literature has indicated, the deposition then likely proceeds by parallel, independent elemental reduction processes. Note the film thickness increases with increasingly negative deposition potential.

The surface morphologies of the as-deposited films all exhibit homogeneous surfaces with densely-packed grains, no large surface particulates, and negligible voids. SEM images are omitted here for brevity. The grains coarsen with increasingly negative deposition potential, which like previous samples, may be attributed to higher deposition rates.

8.4.6 Optimization of Deposition Conditions

Due to the general independence of Cu, Zn, and Sn deposition rates, optimization of the deposition process for metallic precursors was greatly simplified compared to S-containing

precursors. The ratios of the metals in the film can then be directly modified by adjusting ratios of the metal sulfates in the bath. As demonstrated in Table 8-11, the $[CuSO_4]$:$[SnSO_4]$ ratio in the bath approximately determines the Cu:Sn ratio in the deposited films. Further, the relative Zn concentration may be modulated by varying the deposition potential (at values more negative than the Zn reduction potential of -1.14V). In this work, the optimum deposition process for metallic CZT precursors used constant potentials of -1.18V to -1.19V for 10min with the bath composition shown in Table 8-10. Note that films with similar compositions and morphologies were achieved using similar, more acidic baths in [7].

Table 8-10. Optimized bath composition for co-electrodeposited metallic CZT precursors

Chemical Formula	Concentration [M]
$Na_3C_6H_5O_7$	0.20
$Cu(II)SO_4$	0.016
$Zn(II)SO_4$	0.02
$Sn(II)SO_4$	0.01 – 0.0125

The compositions of the films deposited using the optimized processes are summarized in Table 8-11. All films exhibited the desired Cu-poor, Zn-rich stoichiometries. However, Opt-2 demonstrates the stoichiometry most close to the ideal, with a Cu:[Zn+Sn] ratio of 0.8 and a Zn:Sn ratio of 1.2. While the precursor films are thin (~350nm), sulfurization yields final film thicknesses on the order of 1μm (as shown in Section 8.4.7), the minimum value required for use in photovoltaic absorber layers. Further, the precursor film thickness can be increased by increasing the bath concentration, as shown in Section 8.4.4.

Table 8-11. Compositions of optimized co-electrodeposited metallic CZT precursors

Sample ID	Potential	$[SnSO_4]$	Atomic %				Cu:Zn	Zn:Sn	Thick (nm)
			Cu	Zn	Sn	O			
Opt-1	-1.19V	0.0125M	40	29	26	6.0	1.4	1.1	360
Opt-2	-1.19V	0.010M	41	30	22	7.0	1.4	1.4	365
Opt-3	-1.18V	0.010M	43	28	23	6.0	1.5	1.2	330

The morphologies of the optimized precursor films, Opt-1 to Opt-3, are dense and small-grained, with negligible surface particulates. Macroscopically, the samples are highly specular (mirror-like) and uniform, with no evidence of damage to the film or substrate. Fig. 8-7 shows the surface morphology for Opt-1, generally representative of the optimized deposition process.

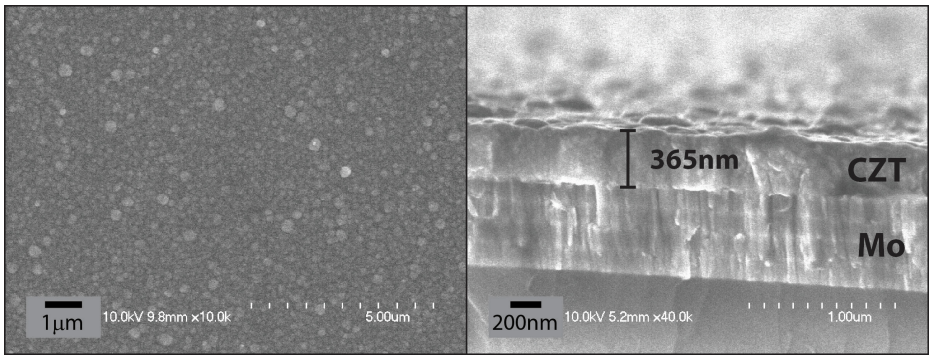

Fig. 8-7. Top-down and cross-sectional SEM images of film deposited using optimized deposition process, Opt-2

8.4.7 Effects of Sulfur Annealing

In order to form the desired Cu_2ZnSnS_4 films, the metallic CZT precursors must be annealed in a reactive sulfur environment. Literature has shown that anneal temperatures over 500°C are required to achieve the desired kesterite crystal formation. For a detailed review of the crystal formation processes associated with CZTS, the reader is referred to Section 3.3.2.2.

Table 8-12. Summary of annealing temperature profiles

ID	Ramp (min)	Dwell (min)	Temp (°C)
TP1	5/ 5	30/ 10	200/ 560
TP2	30	60	560

Sulfur annealing was performed as described in Section 8.3, using 24 – 27mg of elemental sulfur in the graphite annealing box with the samples. Two temperature profiles were investigated, as listed below in Table 8-12. TP1 represents the optimum temperature profile from previous studies of S-containing CZTS precursors deposited by pulsed laser deposition (Chapter 6) and co-electrodeposition (Chapter 7), which yielded films with the fewest voids and secondary phases. As will be shown in the follow section, this temperature profile yielded incomplete sulfurization of the metallic CZT precursors, and so the second temperature profile designated TP2 employed a longer dwell time. An additional low-temperature annealing operation of the metallic CZT precursors, performed in Argon background and prior to sulfurization, was also investigated in combination with TP2. This "soft" annealing step in inert environment has been shown in literature to improve the quality of sulfurized films.

Sulfur Annealing of Opt-1, using TP1

The film studied in this section was deposited using the optimized deposition process Opt-1 summarized in Table 8-10 and Table 8-11, and the film was sulfurized using temperature profile TP1 summarized in Table 8-12.

Table 8-13. Compositions of Opt-1 CZTS films as-deposited and sulfur annealed using TP1, * incomplete film coverage

Processing	Atomic %					Cu:Zn	Zn:Sn	S:Metals	Thick (nm)
	Cu	Zn	Sn	S	O				
As-Deposited	38	28	27	-	7.0	1.4	1.1	-	550
S Anneal*	23	17	14	44	2.0	1.4	1.2	0.83	960

The compositions of the as-deposited and sulfur annealed films are summarized in Table 8-13. After sulfur annealing, the film composition exhibited Cu:Zn and Zn:Sn ratios similar to those in the as-deposited film. The similarity of these ratios indicates that no metal elements (e.g. Sn) were preferentially lost by evaporation from the film with annealing. The S:metals ratio remains below 1, indicating incomplete sulfurization of the films. The film thickness increases from 550 to 960nm with sulfurization, exhibiting a thickness growth of 1.7X. For films annealed with TP2, the thickness grows by a factor of 2.7X (see Table 8-14). In this study, the deficiency in thickness growth can be attributed, at least part, to the incomplete sulfurization of the films. Apart from the S-deficiency, the sulfurized film composition and thickness are close to ideal, exhibiting Cu-poor, Zn-rich stoichiometry with a thickness near 1μm: $Cu_{1.67}Zn_{1.20}Sn_{1.00}S_{3.19}$.

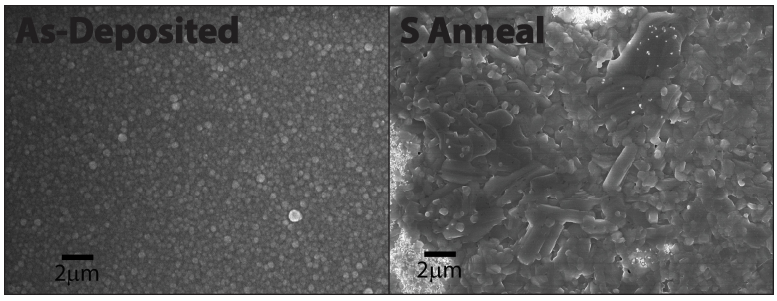

Fig. 8-8. SEM images of Opt-1 CZTS films as-deposited and sulfur annealed using TP1

The surface morphologies of the as-deposited and sulfur annealed films are shown in Fig. 8-8. Note the as-deposited film is uniform and compact, with negligible overgrowths present on the surface. The sulfurized film contains dense, large grains up to several μm with pinholes periodically decorating the grains. However, regions devoid of these large grains (bright spots), and which are composed of small pearl-like grains, are also evident in the SEM image. These bright regions can be seen in the lower left corner and upper middle edge of the S Anneal figure. Notably, lower magnification images (not shown for brevity) indicate these "voids" cover a significant portion of the film surface. Point-and-shoot EDS spectra of similar features in other films (see Fig. 8-12) demonstrate that these regions are Zn-rich, suggesting the small pearl-like grains occupying the voids are ZnS phase. Since the metal element ratios do not change significantly despite the presence of these large voids, then these voids must either result from evaporation of the metal elements in similar proportions or from phase segregation of CZTS and ZnS.

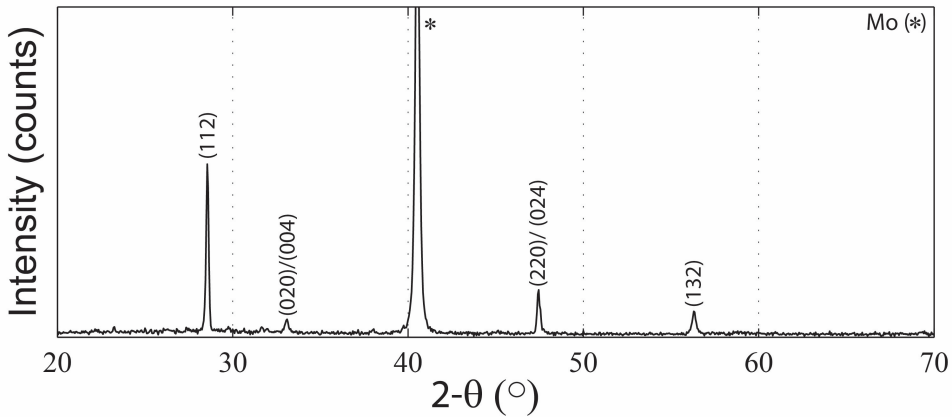

Fig. 8-9. X-ray diffractogram of Opt-1 CZTS films sulfur annealed using TP1

The structural properties of the sulfurized film are presented in Fig. 8-9 and Fig. 8-10. The x-ray diffractrogram indicates the presence of a strong (112) peak at 28.56° and three smaller (020)/(004), (220)/(024) and (132) peaks, which are attributed to kesterite CZTS. The film exhibits significantly less preferred-orientation of the (112) peak than the pulsed laser deposited films presented in Section 6.4.6.2. Similar to the pulsed laser deposited films from Chapter 6, the diffractogram indicates a shoulder in the (112) peak near 28.4°, evident under greater magnification, that suggests the presence of a secondary phase. Cubic-SnS (111), Hex(P-3m1)–SnS_2 (100), cubic(F-43m)–Cu_2SnS_3 (111) [16], orthorhombic(Pmn21)-Cu_3SnS_4 [16], $Cu_4Sn_7S_{16}$ (202/116), or various ZnS phases may contribute this shoulder to the diffraction peak.

Characteristic CZTS Raman modes are evident at 252cm^{-1} (E-TO mode), 287cm^{-1} (A-mode), 337cm^{-1} (A-mode), 350cm^{-1} (E-TO mode) and 372cm^{-1} (B-LO mode). As determined in Section 6.4.6.2, the weak modes near 143, 163, and 364cm^{-1} are likely attributed to CZTS, as well. Like x-ray diffraction, however, many of the common secondary phases share similar Raman mode locations, as noted in Section 4.2.3.

It was shown in Section 6.4.6.2 that properties of the dominant A-mode (near 338cm^{-1}) provide some indication of the phase-purity of the film, such that a widening and blue shift in the peak can be attributed to increases in secondary phase Raman modes near 310 – 320cm^{-1}. Raman modes in this range have been attributed to SnS_2, $Cu_2Sn_3S_7$ and Cu_3SnS_4 [16-20]. Here, a subtle peak near 314cm^{-1} may be attributed to these phases. Peaks at 157, 189, 218, and 264cm^{-1} clearly indicate the presence of SnS phases. Despite the clear presence of SnS phases, the dominant A-mode at 337cm^{-1} is sharp and close to the ideal location, suggesting that the film might contain a low concentration of secondary $Cu_XSn_YS_Z$ phases and crystallite defects. The sulfurized Opt-2 films presented in the next section possess A-modes that are wider but similarly positioned at 337cm^{-1} and possess no SnS phases.

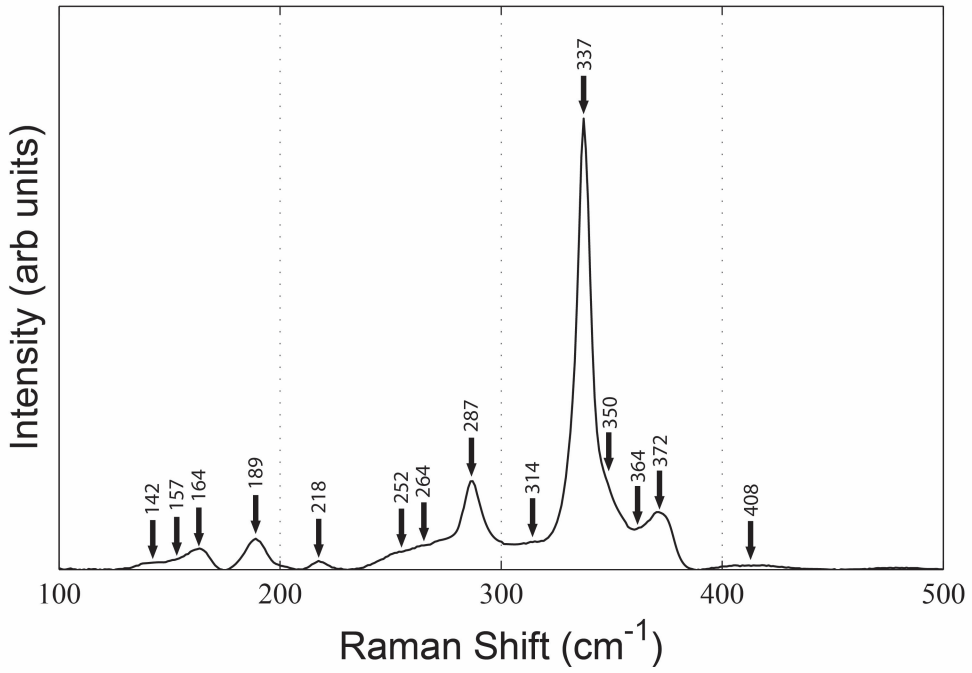

Fig. 8-10. Raman spectrum of Opt-1 CZTS films sulfur annealed using TP1

Sulfur Annealing of Opt-2, using TP2

The films studied in this section were deposited using the optimized deposition process Opt-2 summarized in Table 8-10 and Table 8-11, and the films were sulfurized using temperature profile TP2 summarized in Table 8-12. Additional pre- and post-processing of the films was performed, including annealing of the metallic CZT precursors in Ar_2 background and etching of the sulfurized films in hydrochloric acid. The film designated **Ar_2 + S Anneal** was annealed at 250°C for 4min, using a 3min ramp, in 600torr Ar_2 background prior to sulfurization. This annealing profile was chosen to promote metal alloying, while preventing Sn de-wetting and Zn evaporation, as detailed in the work in [21]. After this metal alloying step, films were sulfurized using temperature profile TP2. The film designated **S Anneal + HCl** was sulfurized using temperature profile TP2. After sulfurization, the film was etched in 1.5M HCl solution for 3min, then thoroughly rinsed with ultra-high purity water and blown dry with nitrogen.

The compositions of the as-deposited and sulfur annealed films are summarized in Table 8-14. Due to peak overlap resulting from incomplete film coverage, the Cu-Zn and S concentrations in the **S Anneal** and **S Anneal + HCl** films could not be reliably analyzed using RBS. The Sn edge, however, was well-defined allowing determination of the Sn concentration. By scaling the metal element peaks in the PIXE spectra of similar films that have well-defined RBS spectra, the remaining Cu and Zn concentrations in the **S Anneal** and **S Anneal + HCl** films could be estimated. Due to Mo-S peak overlap in both the RBS and PIXE spectra, however, the S concentration and S:metal ratios could not be estimated for these films.

Table 8-14. Compositions of Opt-2 CZTS films as-deposited and sulfur annealed using TP2, "Ar_2" indicates annealing of metallic CZT precursor prior to sulfurization, HCl indicates etching with HCl after sulfurization, * incomplete film coverage, ◊ element present but cannot be reliably fitted

Processing	Atomic %					Cu:Zn	Zn:Sn	S:Metals	Thick (nm)
	Cu	Zn	Sn	S	O				
As-Deposited	41	31	21	-	7.0	1.3	1.5	-	355
Ar_2 + S Anneal*	19	16	11	50	4.0	1.2	1.4	1.1	970
S Anneal*	19 (◊)	15 (◊)	11	◊	◊	1.2	1.4 (◊)	◊	◊
S Anneal + HCl*	19 (◊)	15 (◊)	11	◊	◊	1.3	1.4 (◊)	◊	◊

After sulfurization, the compositions of the three films exhibited Cu:Zn and Zn:Sn ratios similar to those in the as-deposited film. As before, the similarity of these ratios indicates that no metal elements (e.g. Sn) were preferentially lost by evaporation from the film with annealing. For the **Ar_2 + S Anneal** film, the S:metals ratio of 1.1 indicates the complete sulfurization of the film, an improvement from the sample annealed with temperature profile TP1. The film thickness increases from 355 to 970nm with sulfurization, exhibiting a thickness growth of 2.7X, similar to most fully-sulfurized metallic precursors investigated in this dissertation. The sulfurized film composition and thickness of **Ar_2 + S Anneal** are close to ideal, exhibiting Cu-poor, Zn-rich stoichiometry with a thickness near 1μm: $Cu_{1.70}Zn_{1.39}Sn_{1.00}S_{4.35}$. The film, however, is slightly too Zn-rich, likely yielding excessive ZnS phases, which may detrimentally impact device performance. Lowering the deposition potential to -1.18V, as shown for Opt-3 in Table 8-11, can reduce the relative Zn concentration and further improve the final film stoichiometry.

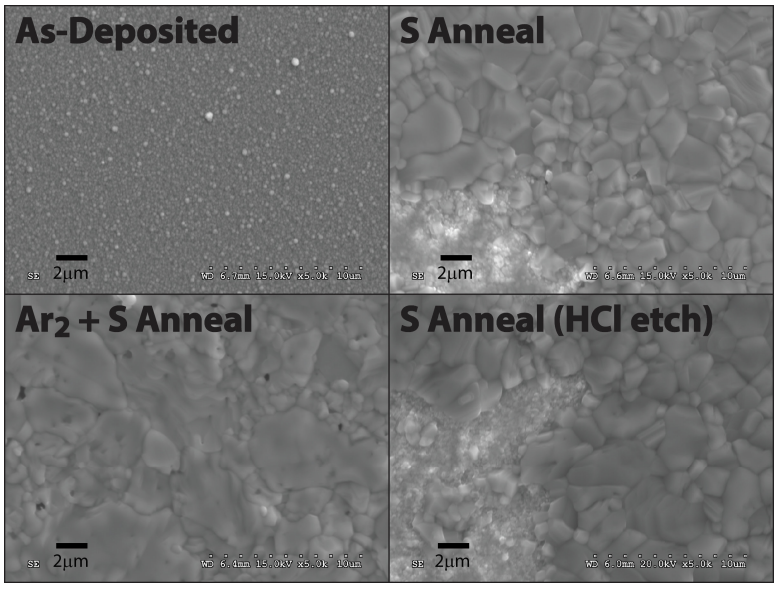

Fig. 8-11. SEM images of Opt-2 CZTS films as-deposited and sulfur annealed using TP2, Ar_2 indicates annealing of metallic CZT precursor prior to sulfurization, HCl indicates etching with HCl after sulfurization

The surface morphologies of the as-deposited and sulfur annealed films are shown in Fig. 8-11. Note the as-deposited film is uniform and compact, with negligible large overgrowths present on the surface. In the **Ar_2 + S Anneal** film, the grain size varies from approximately 1μm up to 10μm with clusters of smaller grains fitted between large grains. The film appears dense with pinholes up to ~1μm uniformly distributed on the surface. In the **S Anneal** film, the grain size varies from approximately 1μm up to 5μm with the grains more uniformly distributed and topographically rougher than those in the **Ar_2 + S Anneal** film. Fewer pinholes are present in the **S Anneal** film, but large portions of the film surface are composed of the bright, void regions also observed in the film annealed with temperature profile TP1 (see Fig. 8-1). Therefore, the inclusion of the soft Ar_2 anneal prior to sulfurization significantly improved the surface morphologies of the films by increasing grain size and dramatically reducing void formation.

Based on the SEM image of the **S Anneal** film, the nature of the bright void-regions was not immediately obvious. Note, however, that other works have demonstrated similar laterally-segregated regions of high Zn-concentration, with similar sizes and distributions [22, 23]. Because the films were highly Zn-rich and similar light-colored surface decorations have been attributed to ZnS in the literature [23, 24], ZnS was expected to compose these regions. It was not clear, however, if these features decorated the surface or displaced the film entirely. To investigate, the **S Anneal** film was diced in half and one piece was etched in HCl, in order to selectively etch away possible ZnS phases [22]. As Fig. 8-11 shows, however, HCl etching of the **S Anneal** film does not dramatically modify the structure or morphology of these voids, and no definitive conclusions can be drawn. Note the CZTS crystallites remain unaffected by etching.

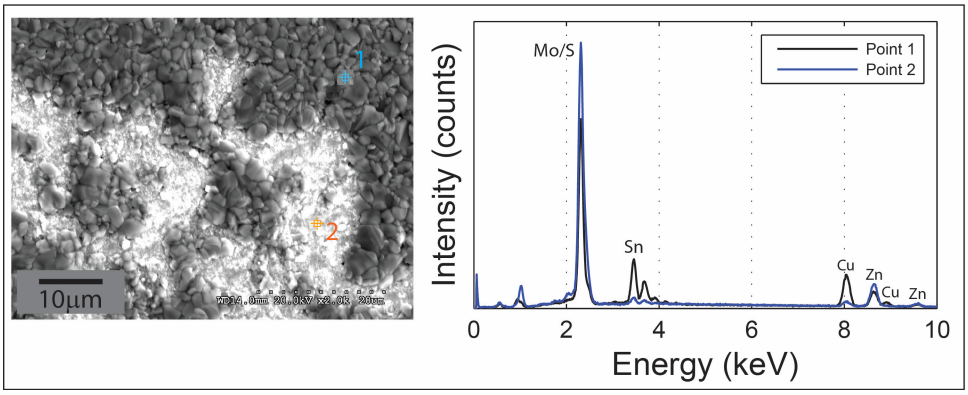

Fig. 8-12. EDS spectrum of Opt-2 CZTS film after sulfur annealing using TP2 and HCl etching

Point-and-shoot EDS measurements of the voids in the **S Anneal + HCl** film, shown in Fig. 8-12, indicate that the lighter colored regions are highly Zn-rich. Overlap of the Mo and S peaks in the EDS spectrum prevent definitive identification of sulfur in the features contained in the voids. However, given that the void features are highly Zn-rich, no elemental Zn peaks are present in x-ray diffraction, and the likely conversion of elemental Zn to ZnS with sulfur annealing, then these void features can be reasonably assigned to ZnS phases. HCl etching yielded a small increase in the Cu:Zn ratio, suggesting that a small amount of Zn may have been removed with etching.

Raman measurements, shown in Fig. 8-14, also indicate that HCl etching was effective in at least partially removing some of the Zn-structures present in these voids, evident as an increasing MoS_2 signal at 383 and 408cm^{-1}.

Since the metal element ratios in the **S Anneal** film do not change significantly from the as-deposited film, despite the presence of these large voids, then these voids must either result from evaporation of the metal elements in similar proportions or from phase segregation of CZTS and ZnS. Previous studies have shown that ZnS does not diffuse as efficiently as elemental Zn [25]. If not well-mixed prior to sulfurization, as in a stacked elemental layer configuration, the poor diffusion of ZnS can lead to its phase segregation. Hydrogen (H_2) environment was shown to enhance the diffusion of ZnS. Elemental Zn diffused more efficiently, but yielded lower relative Zn concentrations due to evaporative loss during annealing [25]. The improvement in morphology with the Ar_2 pre-anneal might be attributed to better mixing of the metal elements prior to sulfurization when the elements are more mobile. In studies in [21], pre-annealing demonstrated negligble effects on the final sulfurized film properties, although improvements in final film quality were demonstrated in [14].

To investigate the lateral uniformity of the as-deposited films, line scan EDS measurements (not shown) were taken over a similar scale as the morphology variations in the SEM image in Fig. 8-11. Measurements were spaced approximately 6 – 7μm apart over 100μm total length. Negligible variation in the Cu, Zn, and Sn peak intensities were observed. Consequently, the void formation, via lateral phase segregation or phase decomposition, was not likely caused by lateral variations in the as-deposited film composition. The as-deposited films do, however, exhibit severe through-thickness variations in the composition, as evident in Fig. 8-4. RBS measurements (not shown) indicate that the low-temperature Ar_2-annealing of the film improves but does not eliminate the composition gradient, with significant surface concentrations of Sn still evident. The impact of through-thickness mixing on grain and void formation, subsequently, remains unclear. If the relatively low mobility of ZnS in the films is responsible for the formation of the ZnS islands (e.g. the voids), then annealing in H_2 or H_2S environment may improve the film quality.

Note that while the short Ar_2-anneal prior to sulfurization significantly reduced the formation of voids in the **Ar_2 + S Anneal** films, temperature profile TP1 was not effective in reducing voids, despite containing a similar low-temperature step at 200°C in the profile. This discrepancy might be attributed to the longer dwell time at low temperature (30min vs. 4min), the lower temperature (200°C vs. 250°C), the significantly increased ramp rate to final anneal temperature (5min vs. 30min), or increased escape of elemental sulfur from the graphite box before final crystal formation. The incomplete sulfurization of the film annealed with temperature profile TP1 suggests that either the dwell time at the anneal temperature of 560°C was not long enough, or that insufficient sulfur overpressure remained in the graphite box, to complete the crystal formation. As discussed in Chapter 9, the sulfur annealing system requires greater control and

monitoring of the temperature at the film and the sulfur overpressure on the film surface, in order to more reliably evaluate the crystal formation processes. This evaluation remains for future work.

The structural properties of the sulfurized film are presented in Fig. 8-13 and Fig. 8-14. The x-ray diffractrograms indicate the presence of strong (112) peaks and three smaller (020)/(004), (220)/(024) and (132) peaks, which are attributed to kesterite CZTS. The (112) peak locations and FWHM widths for the **Ar_2 Anneal + Sanneal**, **S Anneal**, and **S Anneal + HCl** films are 28.54° (0.155°), 28.55° (0.158°), and 28.55° (0.159°), respectively. The slightly decreased peak width for the **Ar_2 + S Anneal** film is consistent with the slightly larger grain sizes evident in the SEM images in Fig. 8-11.

The films exhibit significantly less preferred-orientation of the (112) peak than the pulsed laser deposited films presented in Section 6.4.6.2. The shoulder in the (112) peak near 28.4°, evident in many other CZTS films, was not discernable in these diffractograms, suggesting possibly more phase-pure films. Further, no change in the (112) peak shape was evident after HCl etching.

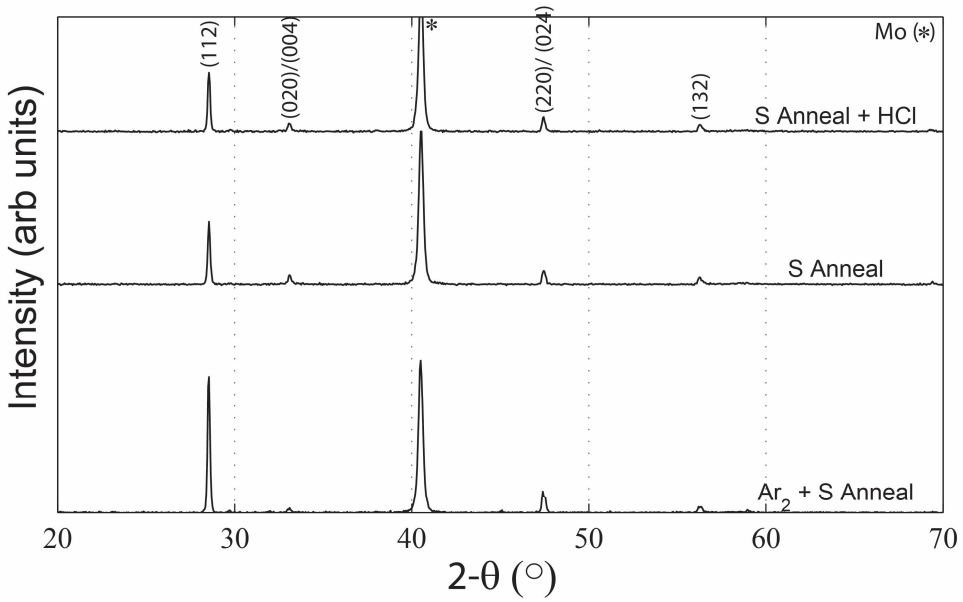

Fig. 8-13 X-ray diffractograms of Opt-2 CZTS films after sulfur annealing using TP2, Ar_2 indicates annealing of metallic CZT precursor prior to sulfurization, HCl indicates etching with HCl after sulfurization

For all sulfur annealed films in Fig. 8-14, characteristic CZTS Raman modes are evident at 254cm^{-1} (E-TO mode), 287cm^{-1} (A-mode), 337cm^{-1} (A-mode), 352cm^{-1} (E-TO mode) and 373cm^{-1} (B-LO mode). As determined in Section 6.4.6.2, the weak modes near 143, 163, 276, and 362cm^{-1} are likely attributed to CZTS, as well. Like x-ray diffraction, however, many of the common secondary phases share similar Raman mode locations, as noted in Section 4.2.3.

All films exhibit a subtle peak near 314cm^{-1} as indicated in the Raman spectrum, possibly attributed to SnS_2, $Cu_2Sn_3S_7$ or Cu_3SnS_4 phases [16-20]. The subtle peak near 276cm^{-1} has been identified in all CZTS films fabricated in this dissertation, and the peak may be associated with

Cu_2SnS_3 phases, although definitive identification is not possible without additional characteristic peaks [16]. No characteristic SnS or $Cu_{2-X}S$ Raman modes ($475cm^{-1}$) are present in the spectra. Note again the inability to reliably measure ZnS using our Raman system (non-UV wavelength). However, the dominant A-mode locations for all films of $337cm^{-1}$ are near the ideal position of $338cm^{-1}$ and consistent with the best co-electrodeposited S-containing films. However, the A-mode widths remain wider than those observed in films sulfurized using temperature profile TP1.

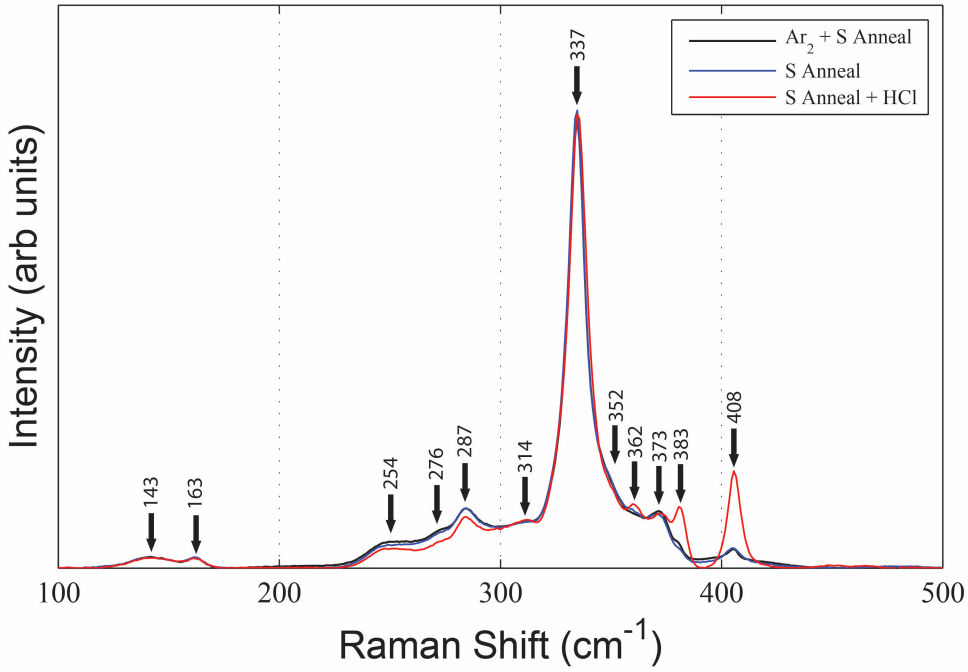

Fig. 8-14. Raman spectra of Opt-2 CZTS films after sulfur annealing using TP2, Ar_2 indicates annealing of metallic CZT precursor prior to sulfurization, HCl indicates etching with HCl after sulfurization

Remarkably, the Raman spectra for the **Ar_2 + S Anneal** and **S Anneal** samples are virtually identical with no notable deviations, despite dramatically different surface morphologies. HCl etching, on the other hand, causes notable shifts between the **S Anneal** and **S Anneal + HCl** films. In particular, the peak near $287cm^{-1}$ decreases, while well-defined peaks near 383 and $408cm^{-1}$ are significantly enhanced. Using a reference MoS_2 sample, in which a Mo-substrate was annealed in similar elemental sulfur environment, the Raman modes at 383 and $408cm^{-1}$ may be definitively attributed to MoS_2.

The decrease in intensity of the Raman mode at $287cm^{-1}$ and the increase in intensities of the modes at 383 and $408cm^{-1}$ may be explained by the preferential removal of ZnS phases by HCl etching. The removal of ZnS, in part or whole, from the bright void regions identified in Fig. 8-12, exposes the back contact surface composed of MoS_2, thereby enhancing the mode intensities at 383 and $408cm^{-1}$. Further, the weak decrease in the mode at $287cm^{-1}$ may indicate a decrease in ZnS concentration in the films. The exposure of the MoS_2 layer with HCl etching also confirms that bright void regions, attributed to ZnS, are not surface decorations and represent displaced films.

The effects of sulfur annealing on the formation of CZTS thin films from metallic CZT precursors may then be summarized as follows:

- Sulfurized metallic precursors exhibit significantly larger grains (up to 10μm) than sulfurized S-containing precursors (< 1μm)
- Sulfurized films tend to segregate into regions of CZTS and Zn-rich "voids", as confirmed by EDS and HCl etching. It is unclear if phase decomposition or phase segregation causes the formation of these distinct regions. The composition does not change significantly with annealing, suggesting that if phase decomposition was active, then the elements must be lost by evaporation in near-stoichiometric proportions. This type of phase segregation was not observed in sulfurized S-containing precursors.
- Low-temperature annealing in Ar_2 background prior to sulfurization significantly improves the uniformity of the films, generally eliminating the large phase-separated regions. However, the sulfurized film contains a significant density of pinholes that would detrimentally impact device performance. The improvement in film uniformity with the Ar_2 annealing step is not well-understood, but it may result from enhanced mixing of the elements prior to sulfurization.
- Temperature profile TP1 demonstrated large phase-separated regions, despite employing a low-temperature step similar to the one used with the successful **Ar_2 + S Anneal** sample. The comparative success of the Ar_2-annealed sample might be attributed to shorter dwell time at lower temperature, the slightly higher temperature of 250°C, the significantly decreased ramp rate to the final anneal temperature, or decreased escape of elemental sulfur from the graphite box before final crystal formation.
- Film thickness increased by factors of 1.7 to 2.7X with sulfurization
- Temperature profile TP1 yielded films with sharper Raman spectra than TP2, consistent with the pulsed laser deposited and co-electrodeposited S-containing precursors annealed with similar profiles, but the film was incompletely sulfurized and possessed SnS phases.
- Temperature profile TP2 yielded relatively phase-pure CZTS, confirmed by x-ray diffraction and Raman spectroscopy (noting that ZnS may not be reliably detected). The diffraction peak locations and Raman mode locations are close to ideal. The Raman A mode peaks at 337cm^{-1} were wider than those demonstrated in metallic and S-containing films that were sulfurized using temperature profile TP1.

8.5 SUMMARY OF RESULTS

CZTS thin films were fabricated by co-electrodeposition of metallic precursors and annealing in elemental sulfur, and they were characterized using Rutherford backscattering, particle-induced x-ray emission spectroscopy, SEM imaging, x-ray diffraction, and Raman spectroscopy.

The effects of bath composition, bath concentration and deposition potential on the deposited film properties were investigated. The metal deposition rates were determined to proceed independently, such that the ratios of the metals in the film can be directly modified by adjusting ratios of the metal sulfates in the bath. In particular, the $[CuSO_4]$:$[SnSO_4]$ ratio in the bath was shown to correlate approximately with the Cu:Sn ratio in the deposited films. For the same deposition time, increasing the bath concentration by a factor of 2X was shown to increase the film thickness by a factor of approximately 2X, as expected. The higher bath concentration yielded a slight reduction in the relative Zn concentration. The relative Zn concentration was shown to be independently adjustable by varying the deposition potential, at values more negative than the Zn reduction potential of -1.14V.

Annealing in elemental sulfur was investigated, in order to sulfurize the films and to form the desired kesterite CZTS phase. Sulfurized metallic precursors exhibit significantly larger grains (up to 10μm) than sulfurized S-containing precursors (< 1μm). However, the sulfurized films also tended to segregate into regions of CZTS and Zn-rich "voids." Low-temperature annealing in Ar_2 background prior to sulfurization significantly improved the uniformity of the films, generally eliminating these large phase-separated regions, although the final film contained a significant density of pinholes.

Note that annealing with temperature profile TP1 yielded incomplete sulfurization of the films, secondary SnS phases, and sharper Raman A-mode at $337cm^{-1}$. For the films sulfurized with temperature profile TP2, the diffraction peak locations and Raman mode locations are close to ideal, with no evidence of secondary $Cu_{2-x}S$ or SnS phases. Further, the Raman A-mode at $337cm^{-1}$ was moderately sharp but remained wider than the A-modes observed in metallic and S-containing precursors that were sulfurized using temperature profile TP1.

8.6 REFERENCES

[1] C. Platzer-Bjorkman, J. Scragg, H. Flammersberger, T. Kubart, M. Edoff, Influence of precursor sulfur content on film formation and compositional changes in Cu2ZnSnS4 films and solar cells, Solar Energy Materials & Solar Cells, 98 (2012) 110 - 117.

[2] M. Bouroushian, Electrochemistry of Metal Chalcogenides, Springer, Berlin, 2010.

[3] Y. Cui, S. Zuo, J. Jiang, S. Yuan, J. Chu, Synthesis and characterization of co-electroplated Cu_2ZnSnS_4 thin films as potential photovoltaic material, Solar Energy Materials & Solar Cells, 95 (2011) 2136-2140.

[4] C. Gougaud, D. Rai, S. Delbos, E. Chassaing, D. Lincot, Electrochemical Studies of One-Step Electrodeposition of Cu-Sn-Zn Layers from Aqueous Electrolytes for Photovoltaic Applications, Journal of the Electrochemical Society, 160 (2013) D485-D494.

[5] H. Araki, Y. Kubo, K. Jimbo, W.S. Maw, H. Katagiri, M. Yamazaki, K. Oishi, A. Takeuchi, Preparation of Cu_2ZnSnS_4 thin films by sulfurization of co-electroplated Cu-Zn-Sn precursors, Phys. stat. sol. (c), 6 (2009) 1266-1268.

[6] P. Sarswat, M. Free, A Comparative Study of Co-electrodeposited Cu_2ZnSnS_4 Absorber Material on Fluorinated Tin Oxide and Molybdenum Substrates, Journal of Electronic Materials, 41 (2012) 2210 - 2215.

[7] R. Juskenas, S. Kanapeckaite, V. Karpaviciene, Z. Mockus, V. Pakstas, A. Selskiene, R. Giraitis, G. Niaura, A two-step approach for electrochemical deposition of Cu-Zn-Sn and Se precursors for CZTSe solar cells, Solar Energy Materials & Solar Cells, 101 (2012) 277-282.

[8] M. Khalil, R. Bernasconi, L. Magagnin, CZTS layers for solar cells by an electrodeposition-annealing route, Electrochimica Acta, 145 (2014) 154 - 158.

[9] J. Li, Z.-w. Zhang, Y. Ou, W. Liu, G. Jiang, C.-f. Zhu, Preparation and characterization of $Cu_2ZnSnSe_4$ thin films by selenization of electrodeposited metal precursors, Materials Science Forum, 685 (2011) 105-109.

[10] J. Li, T. Ma, M. Wei, W. Liu, G. Jiang, C. Zhu, The $Cu_2ZnSnSe_4$ thin films solar cells synthesized by electrodeposition route, Applied Surface Science, 258 (2012) 6261-6265.

[11] R. Schurr, A. Holzing, S. Jost, R. Hock, T. Vob, J. Schulze, A. Kirbs, A. Ennaoui, M. Lux-Steiner, A. Weber, I. Kotschau, H.W. Schock, The crystallisation of Cu2ZnSnS4 thin film solar cell absorbers from co-electroplated Cu-Zn-Sn precursors, Thin Solid Films, 517 (2009) 2465 - 2468.

[12] Y. Wang, J. Ma, P. Liu, Y. Chen, R. Li, J. Gu, J. Lu, S.-e. Yang, X. Gao, Cu_2ZnSnS_4 films deposited by a co-electrodeposition-annealing route, Materials Letters, 77 (2012) 13-16.

[13] A. Ennaoui, M. Lux-Steiner, A. Weber, D. Abou-Ras, I. Kotschau, H.-W. Schock, R. Schurr, A. Holzing, S. Jost, R. Hock, T. Vob, J. Schulze, A. Kirbs, Cu2ZnSnS4 thin film solar cells from electroplated precursors: Novel low-cost perspective, Thin Solid Films, 517 (2009) 2511 - 2514.

[14] K.V. Gurav, S.M. Pawar, S.W. Shin, M.P. Suryawanshi, G.L. Agawane, P.S. Patil, J.H. Moon, J.H. Yun, J.H. Kim, Electrosynthesis of CZTS films by sulfurization of CZT precursor: Effect of soft annealing treatment, Applied Surface Science, 283 (2013) 74 - 80.

[15] S.M. Pawar, B.S. Pawar, A.V. Moholkar, D.S. Choi, J.H. Yun, J.H. Moon, S.S. Kolekar, J.H. Kim, Single step electrosynthesis of Cu_2ZnSnS_4 (CZTS) thin films for solar cell application, Electrochimica Acta, 55 (2010) 4057-4061.

[16] P.A. Fernandes, P.M.P. Salome, A.F.d. Cunha, A study of ternary Cu2SnS3 and Cu3SnS4 thin films prepared by sulfurizing stacked metal precursors, Journal of Physics D: Applied Physics, 43 (2010) 1-11.

[17] L.S. Price, I.P. Parkin, A. Hardy, R. Clark, Atmospheric Pressure Chemical Vapor Deposition of Tin Sulfides (SnS, Sn_2S_3, and SnS_2) on Glass, Chemistry of Materials, 11 (1999) 1792 - 1799.

[18] D. Berg, R. Djemour, L. Gutay, S. Siebentritt, P. Dale, X. Fontane, V. Izquiero-Roca, A. Perez-Rodriguez, Raman analysis of monoclinic Cu_2SnS_3 thin films, Applied Physics Letters, 100 (2012) 192103-192101 - 192103-192104.

[19] H. Guan, H. Shen, C. Gao, X. He, Structural and optical properties of Cu_2SnS_3 and Cu_3SnS_4 thin films by successive ionic layer adsorption and reaction, Journal of Materials Science: Materials in Electronics, 24 (2013) 1490 - 1494.

[20] A. Fairbrother, X. Fontane, V. Izquierdo-Roca, M. Espindola-Rodriguez, S. Lopez-Marino, M. Placidi, L. Calvo-Barrio, A. Perez-Rodriguez, E. Saucedo, On the formation mechanisms of Zn-rich Cu_2ZnSnS_4 films prepared by sulfurization of metallic stacks, Solar Energy Materials & Solar Cells, 112 (2013) 97 - 105.

[21] J.J. Scragg, Studies of Cu_2ZnSnS_4 films prepared by sulfurisation of electrodeposited precursors, in: Chemistry, University of Bath, 2010, pp. 244.

[22] A. Fairbrother, E. Garica-Hemme, V. Izquierdo-Roca, X. Fontane, F. Pulgarin-Agudelo, O. Vigil-Galan, A. Perez-Rodriguez, E. Saucedo, Development of a Selective Chemical Etch to Improve the Conversion Efficiency of Zn-Rich Cu_2ZnSnS_4 Solar Cellss, J. Am. Chem. Soc., 134 (2012) 8018 - 8021.

[23] J.J. Scragg, P.J. Dale, L.M. Peter, Synthesis and characterization of Cu_2ZnSnS_4 absorber layers by an electrodeposition-annealing route, Thin Solid Films, 517 (2009) 2481 - 2484.

[24] K. Zhang, Z. Su, L. Zhao, C. Yan, F. Liu, H. Cui, X. Hao, Y. Liu, Improving the conversion efficiency of Cu_2ZnSnS_4 solar cell by low pressure sulfurization, Applied Physics Letters, 104 (2014) 141101-141101 - 141101-141104.

[25] P.M.P. Salome, J. Malaquias, P.A. Fernandes, M.S. Ferreira, J.P. Leitao, A.F.d. Cunha, J.C. Gonzalez, F.N. Matinaga, G.M. Ribeiro, E.R. Viana, The influence of hydrogen in the incorporation of Zn during the growth of $Cu_2ZnSnSn_4$ thin films, Solar Energy Materials & Solar Cells, 95 (2011) 3482 - 3489.

9 CONCLUSIONS AND RECOMMENDATIONS

9.1 SUMMARY OF RESULTS

This dissertation investigated the growth behavior of $Cu(In,Ga)Se_2$ and Cu_2ZnSnS_4 thin films developed for use as photovoltaic absorber layers. The CIGSe thin films were fabricated by pulsed laser deposition, and the CZTS thin films were fabricated by pulsed laser deposition and co-electrodeposition methods. Pulsed laser deposition (PLD) represents a useful laboratory-scale fabrication tool that enables rapid fabrication of different material combinations and thin film deposition on insulating substrates, which facilitates the study of optical absorption and Hall Effect measurements. Electrodeposition (ED) represents a commercially viable synthesis tool that also enables rapid thin film deposition. Further, the scalability of electrodeposition has been demonstrated in large-scale industrial deployment of conventional metallic plating, and also in the semiconductor industry with copper damascene electroplating techniques [1].

CZTS thin films represent ideal absorber layers for single-junction photovoltaic devices, due to their direct band gaps of ~1.5eV and high optical absorption > $10^4 cm^{-1}$ above the band edge [1]. With more earth-abundant and less toxic component elements, the CZTS material system represents the next-generation version of the CIGSe system. Since they share similar crystal structure and electronic attributes, it is hoped that CZTS demonstrates a similar resilience in its opto-electronic properties to grain boundaries and to stoichiometric deviations that has afforded CIGSe devices much success [2]. Devices with moderately high efficiencies of 12.6% have been fabricated using Se-alloyed CZTSeS absorber layers [3].

In general, however, the fabrication of high-quality CZTSeS absorber layers has been extremely challenging, due to the narrow phase formation region for CZTSeS [1, 4], elemental and compound volatility [1, 5-7], and phase decomposition at the surface and back contacts [8, 9]. The difficulty in preventing Zn and SnS loss during film growth, associated with CZTS phase decomposition and the high vapor pressures of these components, has resulted in the comparative success of two-step (deposition reaction) fabrication processes over more conventional single-step processes [1, 8].

Despite the moderately high device efficiencies achieved, all aspects of CZTS device design merit continued investigation. Scalable and reliable fabrication methods that are capable of producing phase-pure, void-free CZTSeS absorber layers have yet to be demonstrated. Such advancements will require better understanding of the crystal formation processes and defect behavior of CZTSeS. Future improvements to the device performance will also likely require the optimization of the device architecture for CZTSeS, in order to enhance the stability and band alignments at the back contact and front contact interfaces. The work in this dissertation aims to improve understanding of the growth processes of CZTS thin films and to provide a pathway to

fabrication of high-quality absorber layers for use in photovoltaic devices. Reliable growth of high-quality CZTS thin films will enable investigation of the fundamental properties of CZTS, as well as device and interface behavior, necessary to improve device efficiency.

Early work exposed significant difficulties in controlling CZTS thin film growth, using both PLD and ED. Pulsed laser deposited CZTS films demonstrated significant deviations in stoichiometry relative to the sputtering target (Sn-rich) during deposition and void formation during subsequent sulfur annealing steps. Moreover, co-electrodeposited CZTS films exhibited rough, powdery morphologies, which deviated strongly from the reported behavior [10]. These fabrication challenges, and the gaps in relevant literature necessary to address them, prompted the systematic investigation of the growth behavior of CZTS by PLD and ED that forms the core of this work. CIGSe represents a mature material system with similar chemical and electronic properties to CZTS, and therefore it provided a valuable starting point and reference standard for investigation of CZTS. The major goals of this work included the following:

(1) Fabricate device-quality CIGSeS thin films for use as reference standards against which to evaluate the properties and behavior of CZTS thin films.

(2) Characterize the growth behavior of pulsed laser deposited and electrodeposited CZTS thin films by systematically investigating relevant deposition and annealing parameters.

(3) Identify the critical parameters in film growth, including the effects of deposition and annealing conditions and the precursor properties on the final CZTS film properties.

(4) Demonstrate high-quality CIGSeS and CZTS absorber layers fabricated by pulsed laser deposition and co-electrodeposition methods.

After many depositions and significant optimization effort, quality CZTS thin films were demonstrated using both pulsed laser deposition and co-electrodeposition. The work presented in this dissertation provides a greater understanding of the effects of deposition and annealing parameters on the growth behavior and proposes a possible pathway to reliable, scalable production of CZTS thin films.

9.1.1 Pulsed Laser Deposition of CIGSe

Thin film solar cells using CIGSe absorber layers have achieved high efficiencies, both in laboratory cells as well as commercial modules [2, 11]. Although the CIGSe material system has been studied for over two decades and commercial products are available on the market, understanding of the defect, grain and junction physics of CIGSe remains incomplete [12]. The CIGSe material system also serves as a relevant standard against which the next generation CZTS system can be evaluated.

Existing literature [13-15] showed that pulsed laser deposition of CISe and CIGSe thin films typically yielded materials with high carrier concentration ($>10^{18}$ cm^{-3}) and low hole mobilities (< 10 $cm^2/V{\cdot}s$) not adequate for use in photovoltaic device and interface studies. For

photovoltaic applications, optimum doping concentrations of 10^{15} – $10^{17}cm^{-3}$ and hole mobilities of 20 – $200cm^2/V{\cdot}s$ are needed [2, 11]. High hole concentrations have been correlated with large Cu:[In+Ga] ratios (>1) and attributed to acceptor-type Cu_{In} or V_{In} defects, as well as the formation of $Cu_{2-x}Se$ phases on the film surface [13-16].

Chapter 5 investigated the effects of substrate temperature, vacuum annealing and sulfur annealing on the composition, structure, morphology and opto-electronic properties of pulsed laser deposited CIGSe thin films. For all substrate temperatures, as-deposited films demonstrated Cu-rich, Se-deficient composition with high hole carrier concentrations and low Hall mobilities. Varying anneal temperatures from 300 to 500°C were investigated for vacuum and sulfur annealing, in order to improve the electronic quality of the films. Critical growth parameters and optimized fabrication parameters were identified, as summarized in Sections 9.1.1.1 and 9.1.1.2. Pulsed laser deposition with a substrate temperature of 450°C and annealing in sulfur environment yielded large-grained CIGSeS thin films with high electronic quality (e.g. hole concentrations near $10^{16}cm^{-3}$ and Hall mobilities up to $20cm^2/V{\cdot}s$). While the fabricated films are too thin for use in devices, they could be useful for interface studies. Thicker films can be readily fabricated by increasing the laser spot and/or increasing the deposition time.

9.1.1.1 Critical Growth Parameters

The most critical growth parameters identified in the pulsed laser deposition and annealing of CIGSe thin films include the following:

- Substrate temperature during deposition
- Sulfur environment during annealing

The substrate temperature significantly increased the grain size in the films. While the low mobilities in the as-deposited films was attributed to defect scattering and not grain boundary scattering, large grain sizes are still considered ideal for photovoltaic absorber layers. The incorporation of sulfur in even small amounts dramatically improves the electronic quality of the films, significantly decreasing the carrier concentration and increasing the Hall mobilities.

Increasing sulfur annealing temperature was shown to increase the incorporation of sulfur into the films and to decrease the presence of $Cu_{2-x}S$ phases formed during annealing. The sulfur overpressure, which depends on the annealing temperature and quantity of elemental sulfur included in the chamber, likely also plays an important role, as too high sulfur concentrations can lead to low carrier concentrations, particularly in Cu-poor films [11].

9.1.1.2 Optimized Fabrication Process

Based on the deposition studies in Chapter 5, the pulsed laser deposition parameters shown in Table 9-1 provided the highest quality CIGSe thin films. Using the Gen #1 annealing system with the parameters shown in Table 9-2, sulfur annealing dramatically improved the electronic quality of the films, decreasing the hole concentration several orders of magnitude and increasing the Hall hole mobility by an order of magnitude. As discussed in Section 3.3.3.3, the temperature

and sulfur overpressure were not well-controlled in the Gen #1 system. The sulfur overpressure, however, appears to be quite low based on the sulfur-gradient observed in the film and the generally-low quantities of sulfur incorporation.

Table 9-1. Optimized pulsed laser deposition parameters for CIGSe films

Deposition Condition	Value
Sputtering Target	$Cu_{1.00}In_{0.75}Ga_{0.25}Se_{2.00}$
Laser Energy	110mJ
Repetition Rate	7Hz
Target-Substrate Distance	4in
Background	Vacuum: $5x10^{-5}$ torr
Substrate Temperature	450°C
Deposition Time	2hr

Table 9-2. Optimized annealing parameters for pulsed laser deposited CIGSe films

Annealing Condition	Value
Temperature	400°C
Time	1hr
Background	Vacuum / Sulfur
Mass of Sulfur	13mg

Table 9-3. Properties of CIGSeS films fabricated using optimized deposition and annealing parameters

Film Properties	Value
Composition (Final)	$Cu_{1.05}In_{0.71}Ga_{0.29}Se_{1.71}S_{0.18}$
Thickness (Final)	110nm
(112) Peak Location	27.0°
(112) Peak Width	0.191°
Hole Concentration	$5x10^{16}cm^{-3}$
Hall Hole Mobility	19.3 $cm^2/V{\cdot}s$
Band Gap	1.17eV

Table 9-3 summarizes the properties of the highest performing films fabricated using the optimized deposition and annealing parameters. See Fig. 5-10 for representative film morphology. Note the film composition is slightly Cu-rich and slightly chalcogen-deficient, evident as Cu:[In+Ga] > 1 and [S+Se]:[Cu+In+Ga] < 1. The hole concentration and Hall mobility are consistent with device-quality absorber layers demonstrated in literature [2, 11], and the measured

band gap of 1.17eV is consistent with reported band gaps for CIGSe films with Ga-alloying ratios near Ga:[In+Ga] = 0.30 [2].

9.1.2 Pulsed Laser Deposition of CZTS

Pulsed laser deposition enabled rapid synthesis of the complex CZTS material, thin film deposition on insulating substrates, and evaluation of other critical growth parameters. Deposition on insulating substrates enabled the investigation of optical absorption and Hall measurements and also facilitated the investigation of CZTS crystal growth in the absence of destabilizing back contact materials. Electrodeposition, on the other hand, requires the use of conducting substrates, and films were deposited on either FTO-coated or Mo-coated glass substrates. Mo films, in particular, have demonstrated a strong destabilizing effect on the film during sulfur annealing [9]. Notably, pulsed laser deposition enabled larger sulfur-incorporation (up to 45at%) in the CZTS precursors than the electrodeposition method, thus providing a wide range of precursor compositions to be investigated. Sulfur concentrations were typically limited to less than 25at% in CZTS precursors deposited by co-electrodeposition. Finally, pulsed laser deposition with substrates above the crystal formation temperatures of CZTS enabled one-step fabrication of CZTS, thus providing comparison to the two-step deposition reaction method.

Chapter 6 investigated the effects of laser fluence, laser pulse repetition rate, target-substrate distance, substrate temperature, and sputtering target compositions on the composition, morphology and structure of the as-deposited films. Based on the results of these investigations, optimized pulsed laser deposition parameters were identified. Using optimized precursor films, the effects of varying sulfurization ramp times, dwell times, and temperature profiles on the final film compositions, structures, morphologies, resistivities, absorption coefficients and band gaps were investigated. Critical growth parameters and optimized fabrication parameters were identified, as summarized in Sections 9.1.2.1 and 9.1.2.2.

The two-step film growth process was shown to represent the most viable fabrication process, and proposed crystal growth mechanisms were discussed. Films with ideal compositions and structures were demonstrated. However, measured Hall mobilities in the film remained low, and the film surfaces possessed too many voids and splashed particles for use in devices. While the void formation appears connected to growth mechanisms specific to pulsed laser deposited CZTS thin films with high S-content, greater control of the sulfur overpressure may mitigate the observed film decomposition during annealing. Further, it is recommended that the S-content in the deposited precursor be reduced. This sulfur reduction should reduce the nuclei density in the deposited film and enhance the grain growth during annealing. Finally, reducing the laser fluence to the ablation threshold and re-conditioning the target prior to each deposition are expected to reduce the splashed particles.

9.1.2.1 Critical Growth Parameters

The most critical growth parameters identified in the pulsed laser deposition and annealing of CZTS thin films include the following:

- Laser fluence
- Sputtering target composition
- Substrate temperature during deposition
- Temperature profile during sulfurization

A laser ablation threshold fluence of ~2.5J/cm^2 was identified, above which the film composition no longer varied significantly with fluence. At laser fluences above the ablation threshold, as-deposited films were shown to be slightly Zn-poor, significantly Sn-rich, and S-poor compared to the sputtering target. The reason for the severe deviation in Sn concentration was not well-understood. However, the sputtering target compositions were shown to be reliably modified, in order to improve the cation ratios in the as-deposited films, achieving the desired Cu-poor, Zn-rich stoichiometries.

Increasing substrate temperature during deposition was shown to significantly impact the composition and quality of the deposited film. While smoother, larger-grained films were achieved at temperatures of 400 and 500°C, significant losses in Zn and Sn were demonstrated. These losses were attributed to losses of elemental Zn and SnS phases caused by their high vapor pressures at these elevated temperatures, and they indicate the need for a two-step fabrication approach as others have reported [1, 8], with the precursor films deposited at room temperature followed by a high temperature annealing step in sulfur background. Further, by employing a two-step fabrication approach, the back contact decomposition mechanism described in [9] can be mitigated by forming CZTS under S-rich environment.

Sulfur annealed films, in general, exhibited a decrease of Sn at the film surface and a decrease in overall film thickness, which stabilized at longer ramp times and longer dwell times. This time-dependent stabilization was explained in terms of kinetically-limited crystal growth, which we believe results from the large number of amorphous Cu-Sn-S and CZTS phase present in the as-deposited films, and the associated large number of nucleation sites therefore formed. These amorphous phases formed, despite room temperature deposition, via the high kinetic energies associated with pulsed laser deposition. While the slow crystal growth proceeds, volatile SnS phases are evolved from the films. The exact mechanism for this evolution remains unclear, however, as the sulfur overpressures employed in the annealing operation should prevent their evaporation.

The inclusion of a low-temperature (200°C) anneal step prior to crystal formation at 560°C was shown to significantly improve the phase purity and resistivity of the annealed film. The film sulfur annealed with this two-step temperature profile exhibited a (112) diffraction peak with the most negligible shoulder and a Raman A-mode with the smallest peak width. This film also demonstrated a decreased loss of Sn in the film, which was restricted to a smaller layer near the surface. We attribute this reduction in secondary phase formation, and the reduction of Sn loss,

to the healing of defects in the amorphous state, which reduces the number of nucleation sites and improves the kinetics associated with crystal formation. The improvement in phase purity and defect density likely yield the improved film resistivity.

9.1.2.2 Optimized Deposition Process

Based on the comprehensive deposition studies in Chapter 6, the pulsed laser deposition parameters shown in Table 9-4 provided precursor film stoichiometries with cation ratios closest to the ideal Cu:Zn:Sn ratio of 1.8:1.2:1.0.

Table 9-4. Optimized pulsed laser deposition parameters for CZTS precursors

Deposition Condition	Value
Sputtering Target	$Cu_{1.90}Zn_{1.25}Sn_{0.85}S_{4.25}$
Laser Fluence	> 2.6 J/cm^2
Repetition Rate	5Hz
Target-Substrate Distance	10cm
Background	Ar_2, 15mtorr, 2sccm
Substrate Temperature	Room Temperature
Deposition Time	45min

Table 9-5. Optimized annealing parameters for sulfurization of pulsed laser deposited CZTS precursors

Annealing Condition	Value
Temperature Profile	5min Ramp / 30min Dwell / 200°C 5min Ramp / 10min Dwell / 560°C
Background	600torr Ar_2 / Sulfur
Mass of Sulfur	> 4.5mg

Table 9-6. Properties of CZTS films fabricated using optimized deposition and annealing parameters

Film Properties	Value
Composition (Final)	$Cu_{1.89}Zn_{1.35}Sn_{1.00}S_{4.48}$
Thickness (Final)	300nm
(112) Peak Location	28.58°
(112) Peak Width	0.176°
A-Mode Location	336cm^{-1}
Resistivity	8.2x10^2 Ω·cm
Band Gap	1.55eV

The highest quality films were fabricated using the sulfur annealing parameters shown in Table 9-5. Film quality was evaluated by comparing diffraction and Raman peaks against their ideal locations, and by evaluating the diffraction and Raman peak widths. The Raman modes, more sensitive to the local defect environment, were the sharpest for these annealing parameters. This annealing temperature profile yielded the film with the least amount of surface decomposition, evident as a decrease in the Sn-gradient in the film and a decrease in the voids present in the film surface.

Table 9-6 summarizes the properties of the highest performing films fabricated using the optimized deposition (laser fluence of 3.5J/cm^2) and annealing parameters. See Fig. 6-17 for the associated film morphology. The film composition is slightly too Zn- and S-rich but close to the ideal composition. The Hall mobility remained too low to reliably determine the carrier concentrations and Hall mobility values from Hall effect measurements. Note, however, that a film resisitivity of 820Ω·cm would correspond to a hole concentration of 10^{16} – 10^{17}cm^{-3} for a Hall mobility in the range of 0.01 – 0.1cm^2/V·s. The measured band gap of 1.55eV is consistent with reported band gaps for CZTS films [17-20].

9.1.3 Co-Electrodeposition of S-containing CZTS Precursors

Significant efforts have been devoted to the investigation and optimization of CZTS thin films fabricated by the electrodeposition of metallic precursors in the stacked elemental layer (SEL) configuration; see for example [21-23]. As discussed in Section 3.2.1.2, however, single-step co-electrodeposition of the elements may improve the film homogeneity, while reducing the need for precise control of the film thickness. In the SEL configuration, the layer thicknesses directly correspond to the final film composition. Co-electrodeposition of metallic CZT and S-containing CZTS precursors have both been successfully demonstrated [10, 24-26]. As discussed in detail in Section 3.3.2.2, the S-content in the precursor films has been shown to significantly influence grain growth and void formation during annealing [6]. In particular in [6], S-content of 14-18at% in the precursor films significantly reduced Sn-loss and void formation, although also decreased the grain size, in the final films. Consequently, the co-electrodeposition of S-containing CZTS precursors may provide advantages over metal-only precursors.

To this author's knowledge, the first successful single-step co-electrodeposition of S-containing CZTS precursors with near-stoichiometric compositions was demonstrated by Pawar et. al [10]. As a first step for work in this dissertation, the co-electrodeposition process from [10] was reproduced. However, films fabricated using this method exhibited severely rough, powdery morphologies and highly Zn-poor, Sn-rich compositions, which deviated strongly from the reported film properties in the original work. In working to reconcile the deviations in deposition behavior, a gap in the literature was noted regarding the effects of the deposition parameters on the growth behavior of co-electrodeposited S-containing CZTS precursors. Consequently, in order to understand the growth behavior and to improve the quality of as-deposited films, the effects of deposition parameters on the film properties were systematically investigated.

Chapter 7 investigated the properties of "baseline" S-containing CZTS precursor films fabricated on FTO- and Mo-substrates using Pawar's method, which originally demonstrated the single-step deposition of near-stoichiometry CZTS thin films. As noted above, these baseline films exhibited severely rough, powdery morphologies and highly Zn-poor, Sn-rich compositions. Reduction mechanisms were proposed by comparing cyclic voltammagrams with films deposited at varying potentials. The effects of the bath composition on the composition and morphologies of as-deposited films were investigated by systematically varying the concentration of each component in the bath. The removal of tartaric acid was shown to dramatically improve the uniformity of the films and eliminate the powdery morphology.

The second half of Chapter 7 was devoted to the investigation of films deposited without tartaric acid. Baseline film properties and possible reduction mechanisms using the original bath composition less tartaric acid were similarly established. To improve film composition and morphology, bath component concentrations were then systematically modified to yield Cu-poor, Zn-rich films. Optimum bath compositions were successfully identified, although a delayed onset of damaging hydrogen evolution reaction was observed during growth. Stopping the deposition before its onset mitigated the damage caused by HER, but films were limited to small thicknesses. Stirring, increasing bath concentration, and galvanostatic control were investigated as possible methods to increase the film thickness before the onset of this reaction. Optimized co-electrodeposition processes were identified.

Finally, the effects of sulfur annealing on the properties of the films were investigated. Several temperature profiles were evaluated, but a two-step temperature profile yielded the highest quality films. Critical growth parameters and optimized fabrication parameters were identified, as summarized in Sections 9.1.3.1 and 9.1.3.2. As-deposited films were significantly S-deficient, although it is believed that this deficiency actually improves the quality of the films grown during sulfurization. After sulfur annealing, high-quality films with the desired stoichiometries and structures were demonstrated, but the film thicknesses were limited to ~400nm. Thicker precursor films were able to be fabricated, but these films experienced more significant surface decomposition during sulfurization. With additional optimization of the co-electrodeposition process and improved control of the sulfur overpressure, as discussed in Section 9.3, very high-quality films of the desired 1μm thickness appear readily achievable.

9.1.3.1 Critical Growth Parameters

The most critical growth parameters identified in the co-electrodeposition and sulfurization of S-containing CZTS precursors include the following:

- Presence of tartaric acid
- Bath component ratios
- Deposition potential
- Bath stirring

- Substrate properties
- Temperature profile during sulfurization

In general, the desired cation ratios in the film can be achieved through proper adjustment of the metal sulfate ratios in the bath and the deposition potential, for baths with and without tartaric acid. Sulfur concentrations greater than about 25at% are not able to be reliably incorporated during electrodeposition, with concentrations typically limited to 15 – 20at%. This work demonstrated that S concentrations in these ranges were adequate to improve film stability during sulfurization, consistent with [6]. By comparing cyclic voltammagrams with films deposited at varying potentials, reduction mechanisms for Cu, Sn, and S were primarily attributed to elemental reduction processes as given by Eqns. (7-1), (7-3), and (7-5), respectively. At potentials less than -1.14V, Zn deposition was attributed to a S-induced underpotential or anomalous co-deposition mechanism. The reduction of elemental Zn was believed to take place at potentials more negative than -1.14V, according to Eqn. (7-2).

The primary challenge in the co-electrodeposition of S-containing CZTS precursors involves minimizing diffusion-limited growth modes and hydrogen co-deposition, which yield powdery, poorly adhering films and cause damage to the substrate and the film. These two mechanisms were found to depend most strongly on the presence of tartaric acid, such that its removal significantly reduced hydrogen evolution and caused a transition to cauliflower morphology. This morphology transition is consistent with a growth mode transition from fully-diffusional to mixed activation-diffusion. These effects were attributed to an increase in pH from 4.5 to 6, with the removal of the tartaric acid, which is believed to yield shifts in the metal-complex species to non-hydrogenated species with higher charge states. However, additional species stability and kinetics studies are required to confirm this interpretation.

In the absence of tartaric acid, films are significantly more compact. However, at varying periods of time after the start of the electrodeposition, a hydrogen evolution reaction was frequently observed, evident as bubbles generated on the sample and a well-defined uptick in current. Substrate and film damage was strongly associated with the onset of this HER. Frequently, but not always, morphology transitions accompanied this transition, as well, with films becoming rougher or more powdery. In general, increasing the concentration of one or more components and increasing (more negative) the deposition potential decreased this transition time to HER onset. This delayed hydrogen evolution reaction was attributed to a lowering of the hydrogen overpotential and/or a depletion in one or more of the depositing species.

The type and quality of substrate was shown to modify the hydrogen overpotential and to influence the as-deposited film morphology. Cyclic voltammetry studies indicated that the FTO-substrates exhibited significantly higher hydrogen overpotential than the Mo-substrates. In baths containing tartaric acid, films deposited on FTO-substrates exhibited less powdery surface overgrowths than films deposited on (EMAT) Mo-substrates. Commercially fabricated Mo films,

provided by Guardian Industries, were more uniform with larger grains and less oxygen than in-house fabricated (EMAT) Mo films. Further, the (Guardian) Mo films possessed a quad-layer structure, evident from cross-sectional SEM, and significant built-in compressive strain, evident as a positive $\Delta\theta$ shift in the (110) diffraction peak. The (EMAT) Mo films, on the other hand, possessed a single layer structure and built-in tensile strain, evident as a negative $\Delta\theta$ shift in the (110) diffraction peak. In baths without tartaric acid, the hydrogen overpotential was approximately 0.05V more negative for the (Guardian) Mo-substrate than the (EMAT) Mo-substrate. However, hydrogen evolution caused more significant damage to the (Guardian) Mo-substrate than the (EMAT) Mo-substrate, which was attributed to the quad-layer structure and compressive-strain that enabled buckling at sites of hydrogen evolution on and within the Mo film. In baths without tartaric acid, the cyclic voltammagrams for the three substrates (see Fig 7-32) generally appeared similar but demonstrated some shifts in the reduction peak locations, which were most significant for the elemental Cu reduction peak near -0.55V and elemental Zn reduction peak near -1.14V.

Linearly sweeping the deposition potential to more noble values during deposition and providing pulsed stirring was shown to increase the deposited film thickness before the onset of HER. Linearly sweeping the voltage allowed the deposition of small-grained, extremely high-quality films with ideal compositions up to 400nm. With additional optimization of the voltage profile, thicker films might be possible. Providing pulsed stirring enabled the deposition of thick films (near 1μm) appropriate for use in photovoltaic devices. However, films were generally non-uniform due to the poorly controlled transport properties in the solution. Stirring was shown to increase the Cu:Zn ratio, and by pulsing the stirring, the film thickness was increased while maintaining the desired Cu:Zn ratio. Additional optimization may be possible by improving the transport uniformity, modifying the stirring rate, and adjusting the bath component concentrations to enable continuous stirring instead of pulsed stirring.

Similar to the pulsed laser deposited films, the inclusion of a low-temperature (200°C) anneal step prior to crystal formation at 560°C was shown to significantly improve the phase purity of the annealed film. This temperature profile yields films with sharper (112) diffraction peaks and Raman A-modes. The longer ramp and dwell temperature profile (30min / 60min / 560°C) resulted in significant decomposition of the films, leaving only islands of films after annealing.

9.1.3.2 Optimized Fabrication Process

Based on the comprehensive deposition studies in Chapter 7, the bath composition shown in Table 9-7 provided precursor film stoichiometries with cation ratios closest to the ideal Cu:Zn:Sn ratio of 1.8:1.2:1.0, when deposited at potentials close to -1.17V vs. Ag/AgCl. Note the deposition bath contains no tartaric acid, contrary to most reported methods.

Section 7.4.2.10 detailed a series of optimized deposition processes, and the two most promising methods (Opt-2 and Opt3) are shown in Table 9-8. Note both these methods involve

deposition under potential control. In the first approach listed, the potential was linearly swept from the starting potential to more noble potentials, in an effort to maintain the potential below the HER overpotential for the duration of the deposition. The goal was to balance the more negative potentials required to achieve necessary Zn incorporation, while taking advantage of the improved morphologies demonstrated at more noble potentials. Note this process includes an initial constant potential hold period of 60sec at -1.17V before the linear sweep starts.

Table 9-7. Optimized bath composition for co-electrodeposition of S-containing CZTS precursors

Chemical Formula	Concentration [M]
$Na_3C_6H_5O_7$	0.20
$Cu(II)SO_4$	0.007
$Zn(II)SO_4$	0.030
$Sn(II)SO_4$	0.008
$Na_2S_2O_3$	0.017

In the second approach listed, stirring was used to improve the film thickness. Previous studies discussed in Section 7.4.2.7 indicated that continuous stirring resulted in Cu-rich, Zn-poor films with very large thickness. Consequently, a pulsed stirring approach was employed, in order to mitigate the stoichiometry deviations caused by stirring, while taking advantage of the film thickness improvements.

The highest quality films were fabricated using the sulfur annealing parameters shown in Table 9-9. Film quality was evaluated by comparing diffraction and Raman peaks against their ideal locations, and by evaluating the diffraction and Raman peak widths. The Raman modes were the sharpest for these annealing parameters. This annealing temperature profile yielded films with the least amount of surface decomposition, evident as decrease loss of film thickness. Surface decomposition was more significant for thicker films, which was generally attributed to loss of sulfur overpressure during annealing.

Table 9-10 summarizes the properties of the highest performing film fabricated using the optimized deposition and annealing parameters. The film properties shown correspond to the sample deposited using a linearly swept potential, as described in Table 9-8. See Fig. 7-52 for the associated film morphology. Based on the film composition, the diffraction and Raman peak locations, and the sharpness of the dominant Raman A-mode, this film represents the highest quality film fabricated in this dissertation. However, the thickness remains too small for use in a photovoltaic device and further improvements to the deposition process are required to achieve thicker films.

Table 9-8. Optimized co-electrodeposition parameters for S-containing CZTS precursors

Potential (V)	Control	Total Time (min)	Stirring
-1.17 to -1.11	Linear Sweep (0.133mV/s)	~7.3	None
-1.17	Constant	8.7	200rpm (every 2min for 25sec)

Table 9-9. Optimized annealing parameters for sulfurization of co-electrodeposited S-containing CZTS precursors

Annealing Condition	Value
Temperature Profile	5min Ramp / 30min Dwell / 200°C 5min Ramp / 10min Dwell / 560°C
Background	600torr Ar_2 / Sulfur
Mass of Sulfur	25mg

Table 9-10. Properties of CZTS films fabricated using optimized deposition and annealing parameters

Film Properties	Value
Composition (Final)	$Cu_{1.79}Zn_{1.28}Sn_{1.00}S_{4.09}$
Thickness (Final)	395nm
(112) Peak Location	28.57°
(112) Peak Width	0.207°
A-Mode Location	338cm^{-1}

9.1.4 Co-Electrodeposition of Metallic CZT Precursors

The co-electrodeposition of S-containing CZTS precursors represents an attractive fabrication route because the presence of S in the precursor has been shown to improve the crystal growth properties of CZTS. In [6], S-content of 14-18at% in the precursor films significantly reduced Sn-loss and void formation, although also decreased the grain size, in the final films. The co-deposition of the S element, however, significantly complicates the growth behavior of the co-electrodeposited precursors, since the $S_2O_3^{2-}$ anion must be transported by diffusion (against the electric field in the cell) to the working electrode surface [27] and disproportionation of $S_2O_3^{2-}$ may cause precipitation of insoluble species [26, 28].

The elimination of $Na_2S_2O_3$ from the bath significantly simplifies the electrodeposition behavior, enabling easier deposition of compact films free of pits and particulates, simpler

optimization of composition, greater bath stability, and potentially greater compatibility with existing plating technologies. As discussed above and in Section 7.1, however, films sulfurized from metallic precursors may exhibit greater Sn loss and increased void formation. To provide a basis for comparison with the S-containing CZTS precursors investigated in Chapter 7, co-electrodeposition of metallic CZT precursors was investigated. Comprehensive studies on the effects of deposition parameters were not found in a review of the literature, and so the studies here were also meant to provide a foundation for future work on the subject.

Chapter 8 investigated the properties of "baseline" metallic CZT precursor films fabricated using a similar co-electrodeposition technique to the method in Chapter 7 (less tartaric acid and sodium thiosulfate). A cyclic voltammagram was presented and compared to the deposition bath with thiosulfate. Due to the simplified nature of the deposition, however, additional investigation of the reduction mechanisms was not pursued. The as-deposited films were highly compact, uniform and free of damage, and the metal ratios in the film could be directly controlled by modifying the metal sulfate concentration ratios in the bath. Varying bath concentrations were investigated, in order to determine the effect on film thickness and composition. Optimized co-electrodeposition processes were identified.

Finally, the effects of sulfur annealing on the properties of the films were investigated. Critical growth parameters and optimized fabrication parameters were identified, as summarized in Sections 9.1.4.1 and 9.1.4.2. After sulfurization, films demonstrated ideal compositions and structures but also significant phase segregation, with the film laterally divided into regions of large-grained CZTS and small-grained ZnS phases. Annealing in Argon at low temperature prior to sulfurization significantly improved the film homogeneity, although a significant density of pinholes remained. It is unclear if the lack of S-content in the precursors, the loss of sulfur overpressure, or both, contributed to the formation of voids and pinholes. Improved monitoring and control of the sulfur overpressure would enable distinguishing the two effects.

9.1.4.1 Critical Growth Parameters

The most critical growth parameters identified in the co-electrodeposition and sulfurization of CZT metallic precursors include the following:

- Bath component ratios
- Deposition potential
- Soft anneal in Argon prior to sulfurization

The metal deposition rates were determined to proceed independently, such that the ratios of the metals in the film can be directly modified by adjusting ratios of the metal sulfates in the bath. In particular, the $[CuSO_4]$:$[SnSO_4]$ ratio in the bath was shown to correlate approximately with the Cu:Sn ratio in the deposited films. The relative Zn concentration was shown to be independently adjustable by varying the deposition potential, at values more negative than the Zn reduction potential of -1.14V.

The two-step annealing temperature profile, shown in Table 9-5 and Table 9-9, yielded incomplete sulfurization (S:metals < 1), large voids, and SnS phases in the film. However, the Raman spectrum for this film possessed sharpest peaks for any of the sulfurized metallic precursors. Sulfur annealing with the longer ramp and dwell time temperature profile, shown in Table 9-13, yielded films with segregated regions of CZTS and Zn-rich "voids." Low-temperature annealing in Argon background prior to sulfurization significantly improved the uniformity of the films, generally eliminating these large phase-separated regions, although the final film contained a significant density of pinholes. The improvement in morphology was possibly attributed to enhanced mixing of the elements prior to sulfurization.

9.1.4.2 Optimized Fabrication Process

Based on the deposition studies in Chapter 8, the bath composition shown in Table 9-11 provided precursor film stoichiometries with cation ratios closest to the ideal Cu:Zn:Sn ratio of 1.8:1.2:1.0, when deposited at potentials near -1.18 to -1.19V. The relative Zn concentration can be directly adjusted by varying the $ZnSO_4$ concentration or by varying the deposition potential at values more negative than the Zn reduction onset at -1.14V.

Table 9-11. Optimized bath composition for co-electrodeposition of metallic CZT precursors

Chemical Formula	Concentration [M]
$Na_3C_6H_5O_7$	0.20
$Cu(II)SO_4$	0.016
$Zn(II)SO_4$	0.020
$Sn(II)SO_4$	0.010 – 0.0125

Section 8.4.6 detailed a series of optimized deposition processes, which are effectively summarized in Table 9-12. Within the window of varying $SnSO_4$ concentrations (0.010 – 0.0125M) and varying deposition potentials (-1.18 to -1.19V), the desired Cu-poor, Zn-rich films are demonstrated. Note however, the most ideal precursor composition was demonstrated at 0.01M $SnSO_4$ and -1.19V. While the precursor films are thin (~350nm), sulfurization yields final film thicknesses on the order of 1μm (as shown in Section 8.4.7), the minimum value required for use in photovoltaic absorber layers. Further, the precursor film thickness can be increased by increasing the bath concentration, as shown in Section 8.4.4. The co-electrodeposition of metallic CZT was significantly easier to control than S-containing CZTS precursors, in order to give the desired stoichiometries, thickness, and film morphologies. However, sulfurization generally yielded films with more voids.

The highest quality films, with the least amount of voids and CZTS-ZnS phase segregation, were fabricated using the sulfur annealing parameters shown in Table 9-13. Prior to sulfurization, the metallic precursors were annealed in inert Argon environment at low temperatures for short

duration, denoted as a **soft anneal**. This was believed to promote mixing of the precursors. The film was subsequently sulfurized according to the parameters shown in Table 9-13.

Table 9-14 summarizes the properties of the highest performing films fabricated using the optimized deposition and annealing parameters. The film properties shown are for the sample co-deposited using 0.01M SnSO4 and a constant potential of -1.19V. The films are Zn- and S-rich, but generally close to the ideal composition. The thickness is close to the minimum necessary for use in photovoltaic devices.

Table 9-12. Optimized co-electrodeposition parameters for metallic CZT precursors

Deposition Condition	Value
Potential	-1.18 to -1.19V
Stirring	None
Deposition Time	10min

Table 9-13. Optimized annealing parameters for sulfurization of co-electrodeposited metallic CZT precursors

Annealing Step	Annealing Condition	Value
Soft Anneal	Temperature Profile	3min Ramp / 4min Dwell / 250°C
	Background	600torr Ar_2
Sulfurization	Temperature Profile	30min Ramp / 60min Dwell / 560°C
	Background	600torr Ar_2 / Sulfur
	Mass of Sulfur	25mg

Table 9-14. Properties of CZTS films fabricated using optimized deposition and annealing parameters

Film Properties	Value
Composition (Final)	$Cu_{1.70}Zn_{1.39}Sn_{1.00}S_{4.39}$
Thickness (Final)	970nm
(112) Peak Location	28.54°
(112) Peak Width	0.155°
A-Mode Location	337cm^{-1}

9.2 MAJOR CONCLUSIONS

9.2.1 The Suitability of Pulsed Laser Deposition and Co-Electrodeposition Methods

CIGSe thin films with device-quality carrier concentrations and Hall mobilities have been demonstrated using pulsed laser deposition. The stability of the CIGSe system under vacuum allows the single step fabrication of large-grained films by pulsed laser deposition. However, films required additional annealing in sulfur environment, in order to achieve the desired electronic quality. The demonstrated carrier concentrations and Hall mobilities represent significant improvement compared to the properties of pulsed laser deposited CIGSe thin films reported in the reviewed literature. To validate the feasibility of this fabrication method for devices studies, thicker films on Mo-coated glass substrates must be demonstrated. While conventional co-evaporation clearly remains a higher quality fabrication approach, the successful growth by pulsed laser deposition demonstrated in this dissertation provides an alternative, practical pathway to laboratory-scale synthesis of CIGSe thin films.

Fabrication of CZTS thin films with the desired film compositions and crystal structures were demonstrated using a two-step pulsed laser deposition and sulfurization method. However, splashed particles and voids in the film indicate the need for additional optimization of the fabrication approach. In order to fully-sulfurize the film and to prevent phase decomposition at the back contact (if Mo substrate used) and the film surface, a sulfur overpressure must be maintained throughout the crystal growth. The current inability to provide this background during pulsed laser deposition requires a two-step deposition approach, in which precursor films are pulsed laser deposited at low temperatures and then sulfurized.

To improve the morphology and structure quality of the final films, the density of splashed particles must be significantly reduced and the S-content in the precursor films should be reduced. The splashed particles locally destabilize the film, accelerating phase decomposition around the particles, and will cause shunts at the heterojunctions of photovoltaic devices. Limiting the laser fluence near the ablation threshold, re-conditioning the target between depositions, and increasing the target-substrate distance should mitigate the formation and deposition of splashed particles. The high S-content in the precursor films appears detrimental to crystal growth, as discussed in more detail in Section 9.2.2. The work in this dissertation, consistent with literature [6, 29], indicates that lower S-content in the precursor films enhances grain growth. Increasing the S-concentration in the precursors increases the number of potential nucleation sites, thereby limiting grain growth and also possibly defect healing [6].

The high kinetic energy associated with pulsed laser deposition may increase the density of nucleation centers. In fact, the Raman spectrum in Fig. 6-5 suggests the presence of amorphous CZTS phases in films pulsed laser deposited at room temperature. Decreasing the S-content in the pulsed laser deposited CZTS precursors should decrease the density of nucleation centers. The decrease in nucleation centers should enhance grain growth, possibly also mitigating void formation that was attributed to kinetically-limited growth mechanisms. See Section 6.4.6.3 for a

discussion of this void formation mechanism. Further, the enhanced grain formation and possible defect healing may also help improve the low Hall mobilities demonstrated in these films. With these modifications, the pulsed laser deposition growth of high-quality CZTS thin films adequate for use in photovoltaic device studies might be possible.

Fabrication of CZTS thin films with the desired film compositions and crystal structures were demonstrated with co-electrodeposited S-containing and metallic precursors. In general, the co-electrodeposition of high-quality metallic precursors was easier than S-containing precursors, using common, low-toxicity plating components such as metal sulfates and tri-sodium citrate. Co-electrodeposited metallic precursors were dense, smooth, and free of damage. Film compositions were easily adjusted by modifying the ratio of metal sulfate concentrations in the bath, with the metal deposition rates scaling nearly linearly with the metal sulfate concentrations. Deposition times of only 10min yielded precursor films with appropriate thicknesses to form ~1μm thick films after sulfurization.

For co-electrodeposition of S-containing precursors, the introduction of the sulfur source ($Na_2S_2O_3$) significantly complicates the deposition behavior of the films. Disproportionation reactions of $S_2O_3^{2-}$ can induce the formation of sulfur and metal-sulfide colloids. While the deposition of these insoluble species was avoided in the optimized baths, the thiosulfate generally introduces instability into the deposition bath. Further, the presence of $S_2O_3^{2-}$ in the bath caused non-linear interactions in the Cu and Sn, evident as larger changes in the Cu:Sn ratio in the film than associated changes in the $[CuSO_4]$:$[SnSO_4]$ ratio in the bath. Most importantly, hydrogen evolution and diffusion-limited growth modes were significantly more active in depositions from baths containing $Na_2S_2O_3$. These reactions caused damage to the Mo substrate and the film, yielding blisters and possibly pitting, although these damage modes are partially attributed to the properties of the Mo film as discussed in Section 9.2.3. In general, deposition times, and subsequently the film thicknesses, were limited by the transition time for the onset of HER. The highest quality film fabricated was limited to 400nm, relying on a potential sweep technique to help delay the onset of the hydrogen evolution reaction. However, other methods to increase the film thickness, including pulsed stirring, have demonstrated promise.

While the co-electrodeposition of metallic precursors was easier than S-containing precursors, the final film formation of S-containing precursors was more successful than metallic precursors. As will be discussed in the following section, the inclusion of S on the order of 15 – 25at% significantly improved film stability during sulfur annealing. Sulfurization of the metallic precursors yielded films with large grains but also significant phase segregation, with laterally segregated regions of CZTS and ZnS. Soft annealing in Argon background prior to sulfurization improved the film uniformity, but a non-negligible density of pinholes remained. Sulfurization of S-containing precursors yielded films with smaller grains without phase segregation, although surface decomposition of the films was evident. CZTS thin film fabrication by co-electrodeposition of S-containing precursors currently represents a more viable approach than co-

electrodeposition of metallic precursors. However, improved control of the sulfur overpressure may improve the film quality of sulfurized metallic precursors. With further optimization as discussed in Section 9.3, it is believed that co-electrodeposition and sulfurization of S-containing and metallic precursors will provide a fast, scalable, reliable technique to produce high-quality CZTS thin films.

9.2.2 S-containing Precursors vs. Metallic Precursors

In order to study the effect of S-content in the precursors on the crystal growth processes, sulfurization was performed on a wide range of precursor compositions: 1) metallic precursors with no sulfur were deposited by co-electrodeposition on Mo-substrates, 2) partially-sulfurized precursors with 15-25at% of sulfur were deposited co-electrodeposition on Mo-substrates, and 3) highly-sulfurized precursors with 35-45at% of sulfur were deposited by pulsed laser deposition on soda lime glass substrates.

Metallic precursors yielded films with the largest grains (up to 10μm) but also the largest voids after sulfurization. SEM images reveal large regions of laterally phase-segregated fields, consisting of small-grained ZnS and large-grained CZTS. The regions of large-grained CZTS are well-packed, however, with few voids. Low-temperature soft annealing of the precursors in inert Argon background prior to sulfurization significantly improved the film uniformity, although micron-sized voids periodically decorated the surface and a higher density of pinholes developed in between the large CZTS grains. Further, grains were similarly sized but much flatter than those observed in films sulfurized without the soft anneal. Sulfurized metallic precursors with and without the soft anneal demonstrated similar Raman spectra with similar peak locations and similar peak widths of dominant A-mode, indicating similar crystal quality.

Partially-sulfurized precursors yielded films with small grains (< 1μm) and few voids after sulfurization, depending on the film thickness and annealing parameters. Larger grains with more voids were demonstrated in films sulfurized with lower amounts of elemental sulfur in the graphite box (e.g. lower sulfur overpressure), consistent with the trends observed in [21]. In general, the S-containing precursors were more stable during sulfurization than the metallic precursors. Whereas metallic precursors primarily exhibited lateral phase-segregation with "voids" consisting of small-grained ZnS phases, the S-containing precursors primarily exhibited through-thickness film loss resulting from the surface decomposition mechanism. In particular, thick S-containing precursors demonstrated Sn loss at their surfaces, consistent with SnS evolution. As discussed in Section 9.2.4, the sulfur annealing system requires better control of the sulfur overpressure, in order to more reliably assess the relative effects of the precursor composition. However, the relative trends in crystal growth behavior are considered self-consistent and based on the work in this dissertation, S-containing precursors are expected to yield more homogeneous, smaller-grained films than metallic precursors. Note that CZTS films fabricated by sulfurization of co-electrodeposited S-containing precursors demonstrated the sharpest, most well-defined Raman spectra for any films in this dissertation, with the least evidence of secondary phases.

Highly-sulfurized precursors yielded films with small grains (< 1μm) and varying densities of voids after sulfurization. These films were generally stable during sulfur annealing, but demonstrated some void formation that was dependent on the temperature profile and the presence of splashed particles. Two factors make direct comparison of these pulsed laser deposited films with the co-electrodeposited films: 1) the pulsed laser deposited on inert soda lime glass rather than on reactive Mo film and 2) the high kinetic energy associated with pulsed laser deposition likely increases the density of nucleation centers in the precursors compared to co-electrodeposition. As discussed above, better control of the sulfur overpressure is required to reliably assess the effects of precursor composition, but the relative trends in crystal growth behavior are considered self-consistent. The sulfur annealing of highly-sulfurized precursors indicates increased film stability compared to metallic precursors. However, less S-content may improve the overall film quality, as the highest quality pulsed laser deposited film exhibited a less sharp Raman peak than those observed in metallic and S-containing precursors.

In general, including sulfur in the precursors increased the stability of the films during sulfur annealing. A two-step sulfur annealing profile (5min/30min/200°C + 5min/10min/560°C) yielded the sharpest, most-well defined Raman peaks in the metallic, partially-sulfurized, highly-sulfurized precursors. In the metallic precursors, however, this temperature profile yielded incomplete sulfurization and the Raman spectrum indicated the presence of secondary SnS phases. Extending the dwell time at 560°C may improve the properties of the deposited films, if the sulfur overpressure can be properly maintained to prevent phase decomposition and void formation. The results of this dissertation suggest that, while high-quality metallic precursors can more easily be fabricated by co-electrodeposition, higher quality films can ultimately be produced using S-containing precursors. With further optimization, as discussed in Section 9.3, it is believed that a co-electrodeposition of S-containing CZTS precursors represents a viable pathway to commercially scalable fabrication of high-quality films for photovoltaic devices.

9.2.3 The Role of the Substrate

The substrate was shown to play strong roles in the growth behavior during electrodeposition and during sulfurization. The type and quality of the substrate influenced the hydrogen overpotential, as well as the morphology of films deposited by electrodeposition. For baths with tartaric acid, the hydrogen overpotential for FTO-substrate was significantly larger than the (EMAT) Mo-substrates, and the morphology of films deposited on (EMAT) Mo-substrates were significantly more powdery and poorly adhering. For baths without tartaric acid, the FTO-substrate exhibited the highest hydrogen overpotential, although the (Guardian) and (EMAT) Mo-substrates demonstrated sufficiently large overpotentials to prevent hydrogen evolution and to enable high-quality depositions. Notably, the delayed onset HER, a detrimental side reaction observed during co-electrodeposition of S-containing precursors, does not appear strongly related to the hydrogen overpotentials of the substrate. The reaction was attributed to a lowering of the hydrogen overpotential by the *depositing film* or the depletion of one or more species in the bath. The onset of HER at similar times for films deposited on FTO- and (Guardian) Mo-substrate using

similar parameters supports this interpretation. The quad-layer structure and built-in compressive strain of the (Guardian) Mo films were believed to contribute to the severe damage modes (e.g. semicircular blisters) caused by the hydrogen evolution.

With respect to sulfurization, FTO-substrates and Mo-substrates suffer from degraded conductivity and film decomposition issues, respectively. It has been shown that sulfurization at the required crystal growth temperatures (> 500°C) can significantly decrease the conductivity of FTO films [30], which would significantly increase the series resistance and decrease the efficiency in photovoltaic devices. In this work, films deposited on FTO-substrates demonstrated improve stability during sulfurization, which can be attributed to elimination of the detrimental back contact reaction of Mo with CZTS. For Mo-substrates, high sulfur overpressures must be maintained in order to mitigate this destabilizing reaction. However, this sulfur overpressure increases the growth rate of MoS_2 at the back contact via direct reaction with diffusing sulfur, and high series resistances have been attributed to thick interfacial MoS_2 layers. Scragg notes the tradeoff between thinner MoS_2 layers and more CZTS phase decomposition and thicker MoS_2 layers with less CZTS phase decomposition, suggesting that the former represents the better approach [9].

9.2.4 The Role of the Sulfur Annealing System

Some degree of film decomposition was observed for all CZTS precursor types. In general, including sulfur in the precursors (15-20at%) and decreasing dwell time at the crystal formation temperature (560°C) decreased void formation in the sulfurized films. Sufficiently large sulfur overpressures should mitigate both surface and back contact decomposition, although small partial pressures of SnS are required to complete halt the surface decomposition process [8]. The observed film decomposition therefore suggests that the amount of elemental sulfur included in the graphite box, and the seal between the base and the lid of the graphite box, are not sufficient to prevent escape of the sulfur gas and subsequent loss of overpressure. However, the extent of this overpressure loss remains unclear.

Note the observed trends with varying sulfur annealing parameters are considered self-consistent, since the same annealing system was used for all samples. That is, the general conclusions remain valid: the two-step temperature profile is optimum for S-containing precursors, the soft anneal of metallic precursors prior to sulfurization is optimum for metallic precursors, and the S-containing precursors are generally more stable than the metallic precursors during sulfurization. It is likely, however, that maintaining a constant sulfur overpressure during annealing will modify the film growth and longer dwell times may prove beneficial. In fact, the sulfur overpressure may represent an important control variable to be optimized. That is, the sulfur overpressure may demonstrate an optimum profile similar to the temperature profile. For instance, low sulfur overpressure at low temperatures and early periods in the annealing process might promote grain growth, while higher overpressures may be necessary at higher temperatures and later periods in the annealing process to prevent film decomposition.

The film temperature represents an important parameter in crystal formation processes. However, the Gen #2 annealing system, described in Section 3.3.3.3, did not allow highly accurate monitoring of the temperature at the film surface. The annealing temperature was modulated using a temperature controller and a thermocouple embedded in the heater block. Another thermocouple embedded in the graphite box base provided additional monitoring. Temperature gradients exist across the bolted interface between the heater block and the graphite box, between the graphite box and the sample, and between the back of the glass and the film. While the temperature drops within the graphite and the sample were not generally considered severe, better in situ monitoring at the film surface would improve process reliability.

9.3 FUTURE WORK

The work in this dissertation demonstrated a viable pathway to the fabrication of CZTS films from co-electrodeposition of S-containing and metallic precursors. However, work remains to fully characterize the kinetics and mechanism of deposition, in particular the Zn reduction mechanism and the source of the delayed onset HER. With additional optimization, the linearly swept potential and pulsed stirring methods should yield thick, high-quality precursor films. Alternative back contacts may help mitigate the damage caused by hydrogen evolution during electrodeposition, and more generally a sulfur-stable back contact would significantly simplify fabrication and improve device performance. Finally, the development of a sulfur annealing system with accurate monitoring and tunable sulfur overpressure would enable significantly enhanced optimization of the crystal growth parameters. Such a system would enable more reliable comparison of crystal growth behavior of S-containing and metallic precursors during annealing.

The comprehensive studies in Chapter 7 of co-electrodeposition of S-containing CZTS precursors suggested that Cu, Sn and S are reduced according to elemental reduction processes via Eqns. (7-1), (7-3), and (7-5), respectively. For potentials more noble than -1.14V, Zn appears to deposit by an S-induced underpotential deposition or anomalous co-deposition mechanism. Several other important deposition mechanisms were also identified, including the following:

- Reduction in powdery, diffusion-limited growth features with removal of tartaric acid
- Non-linear dependence of Cu and Sn on the $CuSO_4$:$SnSO_4$ ratio, such that changes in Cu:Sn in the film are larger than the changes in $CuSO_4$:$SnSO_4$
- Delayed onset of HER during deposition from baths without tartaric acid
- Rate-limited deposition of Zn with apparent dependence on S^{2-} or $S_2O_3^{2-}$

Possible mechanisms were identified for each of these reactions, including shifts in the metal-complex species, interactions of the elements via metal-thiosulfate complexes, evolving hydrogen overpotential, depletion in the baths, and S-induced underpotential or anomalous co-deposition. In order to confirm the proposed mechanisms, more comprehensive kinetics and

species stabilities studies are required. For instance, electrochemical impedance spectroscopy, rotating disk electrode diffusions studies, and pH dependent speciation analyses could help clarify these mechanisms. While the effects of tartaric acid and sodium thiosulfate on the metal-complex speciation in the bath are of particular interest, the most important next steps are to determine the mechanism of delayed HER onset and to mitigate it. High-quality CZTS precursors were demonstrated, but thicker films were difficult to achieve due to this HER reaction.

Significant opportunities for optimization remain with regards to the stirring and bath concentration parameters. The use of a luggin capillary reference electrode set-up will decrease the uncompensated resistance and improve the measurement accuracy of the potential, as well as limit the mass transport disturbance and improve deposition uniformity. Alternative electrode configurations and agitation methods may also enhance the deposition uniformity. Finally, a combination of increased bath concentration and low RPM stirring may facilitate the growth of thicker films while minimizing HER onset.

In addition to mitigating the hydrogen evolution reaction, the substrate should be made more resilient to damage from the reaction. For instance, a high-quality Mo film with a bilayer structure and less compressive-strain could reduce the formation of semicircular blisters caused by hydrogen evolution. However, future studies should also include alternative back contacts that are more stable during sulfurization. These back contacts should also have a large hydrogen overpotential with resilience to damage from hydrogen evolution.

In order to reliably optimize the sulfurization parameters and improve the crystal formation behavior, the sulfur annealing system must improve monitoring and control of the sulfur overpressure. This will help better distinguish the effects of precursor properties on the crystal formation processes and will enable more sophisticated optimization techniques, such as varying sulfur overpressure during annealing.

9.4 OUTLOOK

CZTS represents a challenging material system, defined by a narrow phase window for single-phase kesterite structure, which results from the quaternary nature of CZTS. Consequently, a large number of native defects and secondary phases are possible, which can significantly influence on the electronic behavior of the films. For instance, high carrier concentrations and deep level defects have been attributed to Cu_{Zn} defects, which have low formation energies [31, 32]. The highest performing devices have been fabricated using Cu-poor, Zn-rich absorber layers [1], which has been attributed to the promotion of well-behaving V_{Cu} defects and inhibition of detrimental Cu_{Zn} defects [33, 34]. However, Zn-rich films also tend to form ZnS phases [21, 35, 36], which may increase film resistivities [37].

Further, Mo back contact and surface decomposition mechanisms have been identified, which make final crystal formation difficult. These mechanisms impose requirements on the

sulfur and SnS overpressures necessary to prevent phase decomposition and SnS evolution at the top surface and phase decomposition of CZTS into its binary metal-sulfide components at the Mo back contact interface [8, 9]. The structure and composition of the precursors have been shown to strongly influence the grain growth [6, 21], secondary phase formation [6, 21], and decomposition mechanisms [6, 8, 9]. While work continues to optimize the precursor film properties and crystal growth conditions, the identification of alternative back contacts, which remain stable during sulfurization and satisfy conventional back contact requirements, represents an urgent need in the field [1, 9].

Despite all of the fabrication challenges, high efficiency devices have been demonstrated, which indicate the promise for the CZTS material system. Wet solution techniques, such as nano-ink spin coating and stacked elemental layer electrodeposition, have so far yielded the highest performing devices. Recently, moderate device efficiencies of 3.6% were achieved using co-electrodeposited S-containing CZTS precursors [38]. In this device, the CZTS layer was electrodeposited using a two-step deposition potential method similar to the linearly swept potential method used to deposit optimized films in this thesis.

The work in this dissertation provides a comprehensive foundation on which to further improve the deposition of co-electrodeposited S-containing and metallic precursors. The growth of high-quality CZTS precursors was demonstrated and a pathway to additional optimization recommended. With minor adjustments in the electrodeposition process, and improved monitoring and control of the sulfur overpressure, it is believed that very high-quality CZTS films can be reliably fabricated using a two-step co-electrodeposition and sulfurization process. Notably, the co-electrodeposition method represents a simple fabrication method that utilizes low-toxicity components, complies with existing plating technologies, and provides high throughput. The demonstration of such a process would represent a significant step forward in the development of the earth-abundant, low-toxicity CZTS material system.

9.5 REFERENCES

[1] D. Mitzi, O. Gunawan, T. Todorov, K. Wang, S. Guha, The path towards a high-performance solution-processed kesterite solar cell, Solar Energy Materials & Solar Cells, 95 (2011) 1421 - 1436.

[2] W. Shafarman, S. Siebentritt, L. Stolt, Cu(InGa)Se_2 Solar Cells, in: A. Luque, S. Hegedus (Eds.) Handbook of Photovoltaics Science and Engineering, John Wiley & Sons, West Sussex, 2011.

[3] W. Wang, M. Winkler, O. Gunawan, T. Gokmen, T. Todorov, Y. Zhu, D. Mitzi, Device Characteristics of CZTSSe Thin-Film Solar Cells with 12.6% Efficiency, Advanced Energy Materials, (2013).

[4] I.D. Olekseyuk, I.V. Dudchak, L.V. Piskach, Phase equilibria in the Cu_2S-ZnS-SnS_2 system, Journal of Alloys and Compounds, 368 (2004) 135 - 143.

[5] P.M.P. Salome, J. Malaquias, P.A. Fernandes, M.S. Ferreira, J.P. Leitao, A.F.d. Cunha, J.C. Gonzalez, F.N. Matinaga, G.M. Ribeiro, E.R. Viana, The influence of hydrogen in the incorporation of Zn during the growth of $Cu_2ZnSnSn_4$ thin films, Solar Energy Materials & Solar Cells, 95 (2011) 3482 - 3489.

[6] C. Platzer-Bjorkman, J. Scragg, H. Flammersberger, T. Kubart, M. Edoff, Influence of precursor sulfur content on film formation and compositional changes in Cu2ZnSnS4 films and solar cells, Solar Energy Materials & Solar Cells, 98 (2012) 110 - 117.

[7] A. Weber, R. Mainz, H.W. Schock, On the Sn loss from thin films of the material system Cu-Zn-Sn-S in high vacuum, Journal of Applied Physics, 107 (2010) 013516-013511 - 013516-013516.

[8] J. Scragg, T. Ericson, T. Kubart, M. Edoff, C. Platzer-Bjorkmann, Chemical Insights into the Instability of Cu_2ZnSnS_4 Films during Annealing, Chemistry of Materials, 23 (2011) 4625–4633.

[9] J. Scragg, J. Watjen, M. Edoff, T. Ericson, T. Kubart, C. Platzer-Bjorkman, A Detrimental Reaction at the Molybdenum Back Contact in $Cu_2ZnSn(S,Se)_4$ Thin-Film Solar Cells, J. Am. Chem. Soc., 134 (2012) 19330 - 19333.

[10] S.M. Pawar, B.S. Pawar, A.V. Moholkar, D.S. Choi, J.H. Yun, J.H. Moon, S.S. Kolekar, J.H. Kim, Single step electrosynthesis of Cu_2ZnSnS_4 (CZTS) thin films for solar cell application, Electrochimica Acta, 55 (2010) 4057-4061.

[11] R. Scheer, H.-W. Schock, Chalcogenide Photovoltaics: Physics, Technology, and Thin Film Devices, Wiley-VCH, Weinheim, 2011.

[12] P. Jackson, D. Hariskos, E. Lotter, S. Paetel, R. Wuerz, R. Menner, W. Wischmann, M. Powalla, New world record efficiency for $Cu(In,Ga)Se_2$ thin-film solar cells beyond 20%, Progress in Photovoltaics: Research & Applications, 19 (2011) 894 - 897.

[13] Y.H. Jo, B.C. Mohanty, Y.S. Cho, Crystallization and surface segregation in $CuIn_{0.7}Ga_{0.3}Se_2$ thin films on Cu foils grown by pulsed laser deposition, Applied Surface Science, 256 (2010) 6819-6823.

[14] Y.H. Jo, B.C. Mohanty, Y.S. Cho, Enhanced electrical properties of pulsed laser-deposited $CuIn_{0.7}Ga_{0.3}Se_2$ thin films via processing control, Solar Energy, 84 (2010) 2213-2218.

[15] D.H. Yeon, B.C. Mohanty, Y.H. Jo, Y.S. Cho, Preparation and electrical properties of $CuInSe_2$ thin films by pulsed laser deposition using excess Se targets, J. Mater. Res., 25 (2010) 1936-1942.

[16] S.M.F. Hasan, M.A.S.K.M. Mannan, The optical and electrical properties of copper indium di-selenide thin, Optical Materials, 14 (2000) 329-336.

[17] S. Chen, A. Walsh, J.-H. Yang, X.G. Gong, L. Sun, P.-X. Yang, J.-H. Chu, S.-H. Wei, Compositional dependence of structural and electronic properties of $Cu_2ZnSn(S,Se)_4$ alloys for thin film solar cells, Physical Review B, 83 (2011) 125201-125201 - 125201-125205.

[18] J. He, L. Sun, S. Chen, Y. Chen, P. Yang, J. Chu, Composition dependence of structure and optical properites of $Cu_2ZnSn(S,Se)_4$ solid solutions: An experimental study, Journal of Alloys and Compounds, 511 (2012) 129-132.

[19] S. Ji, T. Shi, X. Qiu, J. Zhang, G. Xu, C. Chen, Z. Jiang, C. Ye, A Route to Phase Controllable $Cu_2ZnSn(S_{1-x}Se_x)_4$ Nanocrystals with Tunable Enregy Bands, Scientific Reports, 3 (2013) 1 - 7.

[20] C. Persson, Electronic and optical properties of Cu_2ZnSnS_4 and $Cu_2ZnSnSe_4$, Journal of Applied Physics, 107 (2010) 053710-053711 - 053710-053718.

[21] J.J. Scragg, Studies of Cu_2ZnSnS_4 films prepared by sulfurisation of electrodeposited precursors, in: Chemistry, University of Bath, 2010, pp. 244.

[22] F. Jiang, S. Ikeda, T. Harada, M. Matsumura, Pure Sulfide Cu2ZnSnS4 Thin Film Solar Cells Fabricated by Preheating an Electrodeposited Metallic Stack, Advanced Energy Materials, 4 (2013) 1 - 4.

[23] J. Lehner, M. Ganchev, M. Loorits, N. Revathi, T. Raadik, J. Raudoja, M. Grossberg, E. Mellikov, O. Volobujeva, Structural and compositional properties of CZTS thin films formed by rapid thermal annealing of electrodeposited layers, Journal of Crystal Growth, 380 (2013) 236 - 240.

[24] H. Araki, Y. Kubo, K. Jimbo, W.S. Maw, H. Katagiri, M. Yamazaki, K. Oishi, A. Takeuchi, Preparation of Cu_2ZnSnS_4 thin films by sulfurization of co-electroplated Cu-Zn-Sn precursors, Phys. stat. sol. (c), 6 (2009) 1266-1268.

[25] J. Tao, J. liu, J. He, K. Zhang, J. Jiang, L. Sun, P. Yang, J. Chu, Synthesis and characterization of Cu_2ZnSnS_4 thin films by the sulfurization of co-electrodeposited Cu-Zn-Sn-S precursor layers for solar cell applications, The Royal Society of Chemistry Advances, 4 (2014) 23977 - 23984.

[26] C. Gougaud, D. Rai, S. Delbos, E. Chassaing, D. Lincot, Electrochemical Studies of One-Step Electrodeposition of Cu-Sn-Zn Layers from Aqueous Electrolytes for Photovoltaic Applications, Journal of the Electrochemical Society, 160 (2013) D485-D494.

[27] M. Bouroushian, Electrochemistry of Metal Chalcogenides, Springer, Berlin, 2010.

[28] Y. Cui, S. Zuo, J. Jiang, S. Yuan, J. Chu, Synthesis and characterization of co-electroplated Cu_2ZnSnS_4 thin films as potential photovoltaic material, Solar Energy Materials & Solar Cells, 95 (2011) 2136-2140.

[29] J.J. Scragg, P.J. Dale, L.M. Peter, Synthesis and characterization of Cu_2ZnSnS_4 absorber layers by an electrodeposition-annealing route, Thin Solid Films, 517 (2009) 2481 - 2484.

[30] P. Sarswat, M. Free, A Comparative Study of Co-electrodeposited Cu_2ZnSnS_4 Absorber Material on Fluorinated Tin Oxide and Molybdenum Substrates, Journal of Electronic Materials, 41 (2012) 2210 - 2215.

[31] S. Chen, J.-H. Yang, X.G. Gong, A. Walsh, S.-H. Wei, Intrinsic point defects and complexes in the quaternary kesterite semiconductor Cu_2ZnSnS_4, Physical Review B, 245204 (2010) 245204-245201 245204-245210.

[32] A. Nagoya, R. Asahi, Defect formation and phase stability of Cu_2ZnSnS_4 photovoltaic materials, Physical Review B, 81 (2010) 113202-113201 - 113202 - 113204.

[33] A. Walsh, S. Chen, S.-H. Wei, X.-G. Gong, Kesterite Thin-Film Solar Cells: Advances in Materials Modelling of Cu_2ZnSnS_4, Advanced Energy Materials, 2 (2012) 400 - 409.

[34] S. Chen, X.G. Gong, A. Wlash, S. Wei, Defect physics of hte kesterite thin-film solar cell absorber Cu_2ZnSnS_4, Applied Physics Letters, 96 (2010) 021902-021901 - 021902-021903.

[35] A. Fairbrother, X. Fontane, V. Izquierdo-Roca, M. Espindola-Rodriguez, S. Lopez-Marino, M. Placidi, L. Calvo-Barrio, A. Perez-Rodriguez, E. Saucedo, On the formation mechanisms of Zn-rich Cu_2ZnSnS_4 films prepared by sulfurization of metallic stacks, Solar Energy Materials & Solar Cells, 112 (2013) 97 - 105.

[36] F. Hergert, R. Hock, Predicted formation reactions for the solid-state syntheses of the semiconductor materials Cu_2SnX_3 and Cu_2ZnSnX_4 (X=S,Se) starting from binary chalcogenides, Thin Solid Films, 515 (2007) 5953 - 5956.

[37] B. Mendis, M. Goodman, J. Major, A. Taylor, K. Durose, D. Halliday, The role of secondary phase precipication on grain boundary electrical activity in Cu_2ZnSnS_4 (CZTS) photovoltaic absorber layer material, Journal of Applied Physics, 112 (2012) 124508-124501 - 124508-124510.

[38] J. Tao, J. He, K. Zhang, J. Liu, Y. Dong, L. Sun, P. Yang, J. Chu, Effect of deposition potential on the properties of Cu2ZnSnS4 films for solar cell applications, Materials Letters, 135 (2014) 8 - 10.